THÈSE DE DOCTORAT

Soutenue à Aix-Marseille Université
Prévu le 21 février 2022 par

Enrico Soldati

Improved in Vivo Diagnosis of Bone Quality in the Context of Osteoporosis

Discipline
Sciences pour l'ingénieur

Spécialité
Mécanique et Physique des fluides

École doctorale
ED 353 Sciences pour l'ingénieur : mécanique, physique, micro et nanoélectronique

Laboratoire/Partenaires de recherche
Laboratoire IUSTI UMR CNRS 7343
Laboratoire ISM UMR CNRS 7287
Laboratoire CRMBM UMR CNRS 7339
Assistance Publique Hôpital de Marseille (APHM)

Composition du jury

Martine COHEN-SOLAL AP-HP - Hôpital Lariboisière	Rapporteuse
Quentin GRIMAL Sorbonne Université	Rapporteur
Françoise PEYRIN Université de Lyon	Examinatrice
Jerome VICENTE Aix Marseille Université	Directeur de thèse
Martine PITHIOUX Aix Marseille Université	Co-directrice de thèse
David BENDAHAN Aix Marseille Université	Co-directeur de thèse
Sandrine GUIS Aix Marseille Université	Invitée
Mossadek TALBY Aix Marseille Université	Invité
Emil Malucelli Bologna University	Invité

Affidavit

I, undersigned, Enrico Soldati, hereby declare that the work presented in this manuscript is my own work, carried out under the scientific direction of Jerome Vicente, Martine Pithioux and David Bendahan, in accordance with the principles of honesty, integrity and responsibility inherent to the research mission. The research work and the writing of this manuscript have been carried out in compliance with both the French national charter for Research Integrity and the Aix-Marseille University charter on the fight against plagiarism.

This work has not been submitted previously either in this country or in another country in the same or in a similar version to any other examination body.

Place Marseille, date 22 novembre 2021

Liste de publications et participation aux conférences

1) Liste des publications[1] réalisées dans le cadre du projet de thèse :

1. Soldati E, Rossi F, Vicente J, Guenoun D, Pithioux M, Iotti S, Malucelli E, Bendahan D. Survey of MRI Usefulness for the Clinical Assessment of Bone Microstructure. Int J Mol Sci. 2021 Mar 2;22(5):2509. doi: 10.3390/ijms22052509. PMID: 33801539; PMCID: PMC7958958.
2. Soldati E, Escoffier L, Gabriel S, Ogier AC, Chagnaud C, Mattei JP, Cammilleri S, Bendahan D, Guis S. Assessment of in vivo bone microarchitecture changes in an anti-TNFα treated psoriatic arthritic patient. PLoS One. 2021 May 19;16(5):e0251788. doi: 10.1371/journal.pone.0251788. PMID: 34010320; PMCID: PMC8133422.
3. Soldati E, Vicente J, Guenoun D, Bendahan D, Pithioux M. Validation and Optimization of Proximal Femurs Microstructure Analysis Using High Field and Ultra-High Field MRI. Diagnostics (Basel). 2021 Sep 2;11(9):1603. doi: 10.3390/diagnostics11091603. PMID: 34573945; PMCID: PMC8466948.
4. Soldati E, Guenoun D, Pithioux M, Bendahan D and Vicente J. Assessment of Bone Microarchitecture in Fresh Cadaveric Human Femurs : What could be the Clinical Relevance of Ultra-High Field MRI ? (**submitted in Diagnostics**)
5. Soldati E, Roseren F, Avellan S, Guenoun D, Catelli E, Sciutto G, Iotti S, Malucelli E, Mancini L, Vicente J, Bendahan D, Pithioux M. Multiscale femoral neck imaging and multimodal trabeculae quality characterization of one osteoporotic and aged-matched healthy subject (**draft article**)
6. Soldati E, Vicente J, Macías-Pérez LA, Guenoun D, Catelli E, Sciutto G, Iotti S, Malucelli E, Gorni G, Marini C, Pithioux M, Bendahan D. Fracture risk assessment in the proximal femur based on bone microarchitecture and hydroxyapatite crystallinity investigation: a multimodal and multiscale approach (**draft article**)

[1] Cette liste comprend les articles publiés, les articles soumis à publication et les articles en préparation ainsi que les livres, chapitres de livre et/ou toutes formes de valorisation des résultats des travaux propres à la discipline du projet de thèse. La référence aux publications doit suivre les règles standards de bibliographie et doit être conforme à la charte des publications d'AMU.

2) Participation aux conférences2 et écoles d'été au cours de la période de thèse :

1. Journée de l'école doctoral (11/07/2019), oral presentation.
2. interdisciplinary DOC2AMU meeting (06/11/2019), oral presentation.
3. annual ISMRM meeting going virtual (08-14/08/2020), 2 poster presentation.
4. Seminar at APHM, (17/09/2020), oral presentation.
5. ECTS congress digital (22-24/10/2020), poster presentation
6. Séminaire CRMBM (16/09/2021), oral presentation.

[2] Le terme « conférence » est générique. Il désigne à la fois « conférence », « congrès », « workshop », « colloques », « rencontres nationales et/ou internationales » … etc.
Indiquer si vous avez fait une présentation orale ou sous forme de poster.

Abstract

This study aimed to improve the *in vivo* diagnosis of osteoporosis using MRI. Despite the largely recognized burden of osteoporosis, an accurate diagnostic tool is still lacking and bone microarchitecture features are not taking into consideration although playing an important role in bone structural resistance.

In this study, it has been first evaluated the MRI ability to assess bone morphology and follow up the therapy delivery on in vivo patients. Then comparing MRI and μCT on cadaveric proximal femurs it has been evaluated the minimum pixel size to assess the bone trabeculae. Moreover, by comparing the bone morphological parameters obtained from MRI with different field strengths (3T vs. 7T) and pulse sequences (GRE vs. TSE) an optimized approach has been presented and validated. The macroscale investigation based on clinical BMD and bone morphology using fracture test as reference have showed that bone morphology provided additional information to the bone health state and fracture risk assessment showing that osteoporosis deteriorates the trabecular architecture.

The changes due to osteoporosis and lower investigative scales (micro-, nano- and molecular) have been questioned using a multimodal approach. The results showed that the femoral neck resulted the proximal femur subregion more affected by osteoporosis and hence at in general higher risk fragility fracture compared to both femoral head and great trochanter. Moreover, while no stoichiometric changes in the hydroxyapatite (HA) chemical composition can be associated to mineral maturation, anatomical site or osteoporosis, differences in the HA crystal could be associated to the local order and microarchitecture.

Keywords : MRI, μCT, bone morphology, bone microarchitecture, osteoporosis, Hydroxyapatite, fragility fracture risk

Résumé

Cette étude visait à améliorer le diagnostic in vivo de l'ostéoporose par IRM. Malgré le fardeau largement reconnu de l'ostéoporose, un outil de diagnostic précis fait toujours défaut et les caractéristiques de la microarchitecture osseuse ne sont pas prises en compte bien qu'elles jouent un rôle important dans la résistance structurelle des os.

Dans cette étude, d'abord a été évalué la capacité de l'IRM à estimer la morphologie osseuse et à suivre l'administration de la thérapie sur des patients in vivo. Ensuite, en comparant l'IRM et le µCT sur des fémurs proximaux cadavériques, il a été évalué la taille de pixel minimale pour évaluer les travées osseuses. En comparant les paramètres morphologiques des os obtenus par IRM avec différentes intensités de champ (3T vs 7T) et séquences d'impulsions (GRE vs TSE), une approche optimisée a été présentée et validée. L'enquête à grande échelle basée sur la DMO clinique et la morphologie osseuse utilisant le test de fracture comme référence a montré que la morphologie osseuse fournissait des informations supplémentaires sur l'état de santé des os et l'évaluation du risque de fracture montrant que l'ostéoporose détériore l'architecture trabéculaire.

Les changements dus à l'ostéoporose et aux échelles d'investigation inférieures (micro-, nano- et moléculaire) ont été interrogés en utilisant une approche multimodale. Les résultats ont montré que le col fémoral entraînait la sous-région proximale du fémur plus touchée par l'ostéoporose et donc, en général, à risque plus élevé de fracture de fragilité par rapport à la tête fémorale et au grand trochanter. Toutefois, aucun changement stoechiométrique dans la composition chimique de l'hydroxyapatite (HA) ne puisse être associé à la maturation minérale, au site anatomique ou à l'ostéoporose, des différences dans le cristal de HA pourraient être associées à l'ordre local et à la microarchitecture.

Mots clés : IRM, µCT, morphologie osseuse, microarchitecture osseuse, ostéoporose, Hydroxyapatite, risque de fracture de fragilité

Acknowledgement

Firstly, I would like to thanks my Chefs, Martine, Jerome et David. From the very beginning you have believed in me and have given me the possibility to prove my worth to others and most importantly to myself. I would like you to know that these past years working together, shoulder to shoulder, have made me grow both as a researcher and as a person. I am really glad with the relationship we have established from the very beginning and which, over time, has only improved and strengthened. Every meeting, exchange of opinion and chat, scientific or not, was extremely precious to me and I hope I was able to absorb as much as possible because, to me, you all represent inspiring models.

A special thanks goes to my non-Academic partner AP-HM and particularly to Sandrine for the support and the kindness, hopefully it is the beginning of a strong relationship. Moreover, I would thank the European Union's Horizon 2020 research and innovation programme, the Regional Council of Provence- Alpes-Côte d'Azur, A*MIDEX, and all the people involved in project organization and funding administration that have made this experience possible.

Then, I would like to thank all the colleagues met during these years that, even though I wasn't always there, they always made me feel part of a group, and most importantly, a friend. Coming to work, knowing that you were there, has been beautiful and has never been that easy. I will remember you all with great affection.

I would also like to thank my lifetime friends, you know who you are with no need of citation. You always have been there and made me feel as I never left home. Every time I was back, you did not lose any occasion to organize a dinner, an apero, to stop by the house just for a quick greeting, to send a message for knowing how I was doing or to have come to visit me in Marseille. You were, and always will be, very precious, and I hope we will have more time to be together in the next years.

A special thanks goes to my special, extremely international, group of "Marseilleise" friends, and in particular to Annalisa, Luis, Emily, Farah and Natalie, that have made these "French" years we had together an unique experience! Our soirées RACLETTE-VIN were unforgivable and without you they will never be the same in the future. I would like you to know that even though we won't be able to see each other as frequently as it has been (not that it was that frequently, but this was my bad) during these years, you will always have an Italian fiend to get in contact with at any occasion. It will be a great

pleasure to remember all the old good times and to create new memories, which for sure will be memorable and will remain unforgettable.

I would also like to thank my grandparents and my aunt for all the Sundays lunch we had together and for all those where you have videocalled me to made me feel at home with you. Thank you also to remember me who I am, where I came from and why I was doing what I was doing. A special thought goes to my grandfather Walther, for sure you would have climbed mountains, got across after storm rivers and even closed the "Fil-Mec" to come and share with me this happy and festive day, but that unfortunately you have to enjoy it, let's say, online on the network. Be sure that if I made it to this new beginning point it is also thank to both you and Donatella.

I would like to thank also my Ville di Montecoronaro enlarged, basically in-law, family for all the time spent together these years, which was not much but invaluable. I hope we will share more of it in the next future.

It is not easy to thank my own Family mostly because there are too many things to be grateful for. You have always been there to support any decision I made, first listening, then advising, sometimes shouting (as we like to discuss family business) but always pushing me to do my best and to improve myself. If I made it until here, I do what I do and I am who I am, it's thank to you. Grazie.

Last but not least, Elisa. You endured these years where we have been further apart while we would have wanted the exact contrary. You supported my decision to go to Marseille and experience, as you would playfully call it, a sort of ERASMUS+++ (where last two pluses are due to the fact that it has been way too long). You planned all the holidays we had (that a travel planning scansate proprio), even making the almost only destination I chose (Romania) an unforgettable experience. You even acknowledged yourself and made me acknowledge you to have made me fashionable (as much as you could and with the raw material you got at least, which has not been easy according to you). However, what I really want to acknowledge you about is that you made Home the place where You are. Ti Amo.

Index

Affidavit **2**
Liste de publications et participation aux conférences **3**
Abstract **5**
Résumé **6**
Acknowledgement **7**
IndexIntroduction **9**
Introduction **13**
Aim of the Thesis 14
Manuscript Structure 17
Chapter 1: State of the Art **19**
Part I : Bone Function and Multiscale Structure **21**
Part II : Survey of MRI Usefulness for the Clinical Assessment of Bone Microstructure (published article) **31**
1. Introduction **33**
1.1. Bone Disorders and Investigative Tools 33
1.2. Bone Microstructure 34
2. Bone Pathologies and Clinical Approach **35**
2.1. Principal Bone Pathologies 35
2.2. Clinical Approach 38
3. MRI Based Approach **39**
3.1. Technical Considerations for Clinical Usefulness 40
3.2. Microstructure Investigation 42
3.3. Microstructure vs. DXA 44
3.4. Voxel Size and Microstructure 44
3.5. Main Magnetic Field Strength Effect 46
3.6. Comparison with CT Measurements 47
3.7. Reported Limitations 50
4. Prospectives **52**
4.1. Magnetic Resonance Spectroscopy vs. Chemical Shift Encoding-MRI 52
4.2. MR Susceptibility 54
4.3. Solid State MRI 56
5. Conclusion **59**

Conclusion of the Chapter **61**
Chapter 2: Assessment of In Vivo Bone Microarchitecture Changes in an anti-TNFα Treated Psoriatic Arthritic Patient (published article) **65**
1. Introduction **67**
2. Materials and Methods **68**
2.1. Subject Recruitment 68
2.2. Imaging Techniques 69
2.3. PET-MRI fusion and Analysis 69
3. Results **73**
3.1. PET-FNa 73
3.2. MRI Microarchitecture 74
4. Discussion **77**
5. Conclusion **79**
Conclusion of the Chapter **81**
Chapter 3: Materials and Methods **83**
1. Sample Collection and Preparation **85**
2. Multiscale and Multimodal Bone Characterization Experimental Techniques **89**
2.1. Macroscale 90
2.1.1. High Resolution Magnetic Resonance Imaging 90
2.1.2. X-ray micro Computed Tomography 92
2.1.3. Biomechanical Tests 93
2.2. Microscale 95
2.2.1. Synchrotron Radiation X-ray micro Computed Tomography 95
2.2.2. Microindentation 97
2.3. Nano- and Molecular Scale 99
2.3.1. X-ray Absorption Spectroscopy 99
2.3.2. Infrared Spectroscopy 107
3. Image Processing and Analysis **109**
Conclusion of the Chapter **119**
Chapter 4: Assessment of Bone Microarchitecture in Fresh Cadaveric Human Femurs : What could be the Clinical Relevance of Ultra-High Field MRI ? (submitted article) **121**
1. Introduction **123**
2. Sample Preparation **125**
2.1. Materials and Methods 125
2.2. Results and Discussion 127
3. MRI Microstructure Quantification **129**
3.1. Materials and Methods 129

3.2. Results and Discussion 132
4. Reproducibility Analysis 136
4.1. Materials and Methods 136
4.2. Results and Discussion 136
4.2.1. Sample preparation 136
4.2.2. Bone Morphology Quantification 136
4.2.3. Resolution Effect 138
5. Correlation between DXA-BMD and MRI Morphology 139
6. Conclusion 141
Conclusion of the Chapter 143
Chapter 5: Validation and Optimization of Proximal Femurs Microstructure Analysis Using High Field and Ultra-High Field MRI (published article) 147
1. Introduction 149
2. Materials and Methods 151
2.1. Sample Preparation 151
2.2. Imaging 152
2.3. Image Analysis 153
2.4. Mechanical Testing 158
3. Results 159
3.1. Registration Quality 159
3.2. Selection of the Optimal MRI Sequence 160
3.3. Correlation between DXA-BMD and Microarchitecture 163
3.4. Correlation between DXA-BMD and both µCT- and MR- Derived BMD 165
3.5. Correlation between Failure Load and Bone Morphology 167
4. Discussion 168
5. Conclusion 172
Conclusion of the Chapter 173
Chapter 6: Multiscale Femoral Neck Imaging and Multimodal Trabeculae Quality Characterization of one Osteoporotic and Aged-Matched Healthy Subject (draft article) 175
1. Introduction 177
2. Materials and Methods 180
2.1. Sample Collection and Preparation 180
2.2. X-ray Microtomography 181
2.3. Microindentation 185
2.4. Infra-Red Fourier Transform 186
2.5. Statistical Analysis 187
3. Results 188

3.1. Multiscale Bone Morphology ... 188
3.2. Trabeculae Mechanical Properties ... 194
3.3. ATR-FTIR Results ... 196
4. Discussion ... 198
5. Conclusion ... 204
Conclusion of the Chapter ... 205
Chapter 7 : Fracture Risk Assessment in the Proximal Femur Based on Bone Microarchitecture and Hydroxyapatite Crystallinity Investigation: a Multimodal and Multiscale Approach (draft article) ... 209
1. Introduction ... 211
2. Materials and Methods ... 213
2.1. Sample Collection ... 213
2.2. Biomechanical Fracture Tests ... 215
2.3. μCT Imaging and Analysis ... 215
2.4. X-ray Absorption Spectroscopy ... 216
2.5. Statistical Analysis ... 218
3. Results ... 218
3.1. Biomechanical Fracture Tests ... 218
3.2. Bone Morphology ... 219
3.3. Calcium K-edge Spectroscopy ... 222
3.4. Bone Fracture Predictivity Risk Assessment ... 226
4. Discussion ... 235
5. Conclusion ... 238
General Conclusion ... 239
Long Résumé de Thèse ... 243
List of Figures ... 261
List of Tables ... 271
Bibliography ... 273

Introduction

Bones have multiple fundamental functions in humans, it is possible to separate between 3 types of functions: (i) mechanical, bones provide protection to inner organs, locomotive allowing the movement but also sensorial transmitting the sound and supportive of all soft tissues; (ii) hemopoietic, synthesizing the white blood cells; and (iii) metabolic, they consists in a stock of minerals, lipids and growth factors, they are able to detoxify the body from many heavy metals and their endocrine secretion, among others, is responsible to regulate the phosphorous secretion and through osteocalcin, to lower blood sugar. Bone is a tissue that continuously absorb and replace itself maintaining the homeostasis, which allow the tissue to resist also to all the external forces to which it is subjected in daily life of all humans. Changes in the bone resistance may lead to an increased susceptibility to fractures mainly accounted by a reduced bone strength and quality. While both determinants are tightly linked to several parameters related to bone geometry, macroarchitecture, microarchitecture, microlesions, bone mineralization and bone remodeling, many bone diseases, i.e. osteoporosis, are currently diagnosed on the basis of the single measurement of bone mineral density (BMD). BMD is considered as an index of bone mass loss and on that basis as a predictor of osteoporotic fracture. However, the limitations of BMD measurements have been clearly acknowledged given that a significant percentage of osteoporotic fractures are occurring in patients with normal BMD. Bone is in fact a porous material and it has been largely acknowledged that BMD cannot take into account other morphometric parameters which are critical for the bone mechanical behavior. BMD neither takes into account bone porosity nor distribution, shape and organization of bone pores. Accordingly, the scientific community is still lacking a reliable and sensitive diagnostic method of bone quality which should be ideally based on bone resistance measurements in vivo.

Magnetic Resonance Imaging (MRI) has been used over the last decades as a non-invasive tool of choice for the diagnosis of a large number of disorders and it is able to provide highly contrasted and highly resolved images which offer qualitative and functional information. Recent technological developments have made possible a further improvement of image resolution with the use of ultra-high magnetic field (7T). Images with a resolution of 150 µm are now obtainable within a reasonable time (10 minutes). Such a resolution has opened up new opportunities to investigate bone microarchitecture and to assess in vivo the trabecular bone density. Although of interest, this index (BMD)

and the corresponding indices related to trabecular thickness and trabecular density have never been submitted to a robust comparative analysis with in vivo measurements of bone resistance. Such a comparative analysis should provide an unquestionable basis supporting the potential of ultra-high field MRI in the field of bone quality. If these microarchitecture indices assessed using a non-invasive technique are proved to be related to bone resistance, they could be used in addition to BMD, as sensitive diagnostic indices and to assay the efficiency of therapeutic strategies.

Moreover, bone quality not only depends on the density and the morphology of its solid phase but also from other factors as the bone mineralization. Therefore, a multiscale and multimodal investigation of the osteoporosis effect on bones is of great interest knowing that a deeper understanding of the mechanism of this disease, that causes fragility fractures in 1 of 3 women and 1 of 5 men aged 50 years or older and is highly debilitating, could open the possibility to perform early diagnosis and to begin new therapeutic trials.

Overall, there is a need to design new imaging approaches of bone resistance which could be complementary to BMD. These approaches should provide key information regarding the mechanical behavior and remodeling of bones thereby improving the reliability and sensitivity of diagnostic procedures, the risk stratification and follow-up of therapeutic strategy.

Aim of the Thesis

The general aim of our study was to improve the *in vivo* diagnosis of osteoporosis using MRI. Osteoporosis is a systemic bone disease characterized by reduced bone resistance and increased occurrence of fragility fractures. Osteoporosis is currently diagnosed using dual X-energy absorptiometry which provide information of the bone density while to increase the diagnostic tool accuracy the bone microarchitecture could be added since the bone inner structure plays an important role in the structural resistance. Bone microarchitecture could be assessed in vivo using both X-ray computed tomography and MRI which is recognized as totally non-invasive. In this study, A multimodal and multiscale analysis have been performed focused only in the bone quality of the proximal femur, which represent an important osteoporotic site, one of the most invalidating, and a deep anatomical site not easily assessable using neither CT nor MRI due to its position, far from the skin surface. However, the UHF MRI could provide image resolution in the same range of bone trabeculae also in these deep anatomical site, which instead remain not assessable using high resolution CT techniques, i.e. high resolution peripheral quantitative computed tomography (HRpQCT).

This multimodal and multiscale approach included i) μCT scanning of cadaveric proximal femurs which intends to provide the ground truth inner trabecular architecture, ii) MRI scanning of the same specimens at 3T and 7T for comparative purposes and iii) biomechanical destructive tests. Additional scanning methods such as synchrotron X-ray tomography, X-ray absorptiometry spectroscopy, Fourier transform infrared and microindentation were used in smaller specimens and so in order to assess the mechanical properties of trabeculae, osteocyte's lacunae network and the hydroxyapatite crystal composition and structure. In Figure I.1 it is presented the overview and the timeline of this thesis project. In particular, it is reported the sample collection, the timeline of submission and acceptance/rejection of synchrotron proposals to perform further examination at bone micro and molecular scale. Finally, Fig I.1 reports all the experimentation techniques, their investigation scale and the Chapter of the thesis where their corresponding results will be presented and discussed.

The first aim of the thesis was to investigate the possibility to assess proximal femur microarchitecture using MR technology and to increase the osteoporosis diagnostic accuracy using information derived from the bone inner morphology.

The second aim was to investigate differences in the bone quality at the nano and molecular scale to evaluate at which level osteoporosis starts its deterioration activity, therefore providing direct implications in pre-clinical research, therapeutic strategy, and eventually clinical practice.

In order to study the bone at different scales, several investigative techniques have been applied. The macroscale have been investigated applying imaging modalities and biomechanical techniques using instruments at disposal in our laboratories. The smaller scales have been investigated using both in-house instruments or devices from other laboratories after the establishment of a collaborative regime based on mutual interests, and techniques at disposal in synchrotron facilities (X-ray absorption spectroscopy and synchrotron micro computed tomography). However, if the collaboration with different laboratories has been created based on mutual interests and hence immediate, to access synchrotron facilities it is necessary that the submitted proposal is accepted and a beamtime allocated. Therefore, from proposal submission to acceptance are usually required between 3 to 4 months and between 5 to 7 months before beamtime. These delays require a meticulous planning of the experiments and the timeline in Figure I.1 is necessary to understand the motif applied to perform the essays.

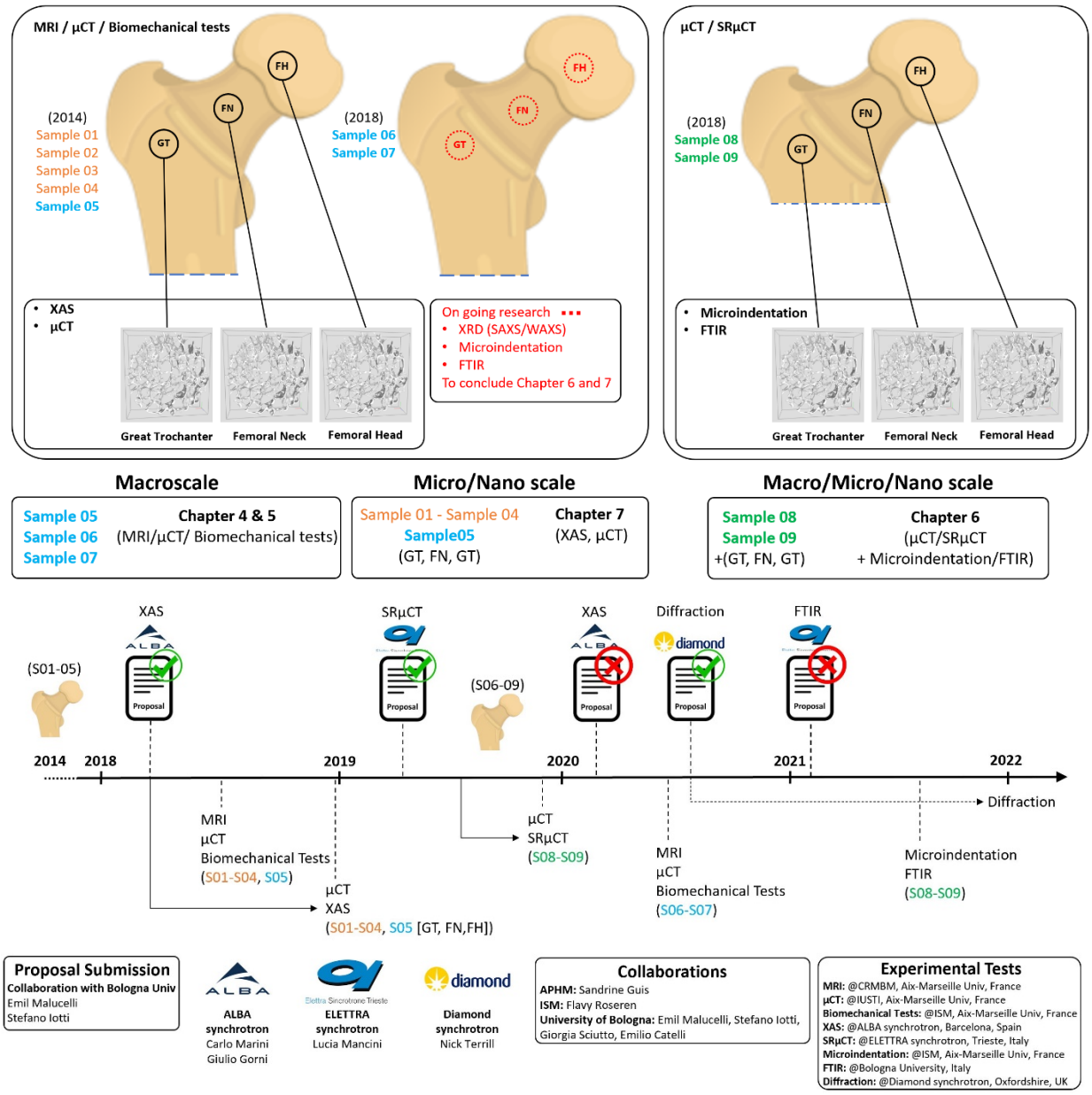

Figure I. 1: overview and timeline of the sample collection and acquisition performed. "MRI" refers to magnetic resonance imaging, "µCT" refers to industrial X-ray computed tomography, "SRµCT" refers to synchrotron radiation X-ray computed tomography, "XAS" refers to X-ray absorption spectroscopy, "FTIR" refers to Fourier transform infrared, "GT" refers to great trochanter, "FN" refers to femoral neck and "FH" refers to femoral head.

Manuscript Structure

This thesis manuscript aim to characterize the bone quality using a multiscale and multimodal approach, moreover showing differences both in vivo, between patients affected by bone disorders and controls, and ex vivo using healthy and osteoporotic cadaveric samples. However, the collection of cadaveric samples is extremely complicated due to both ethical regulation and effective lack of human bodies donated to research, therefore during this thesis project it has been tried to optimize the samples in our possession by a multimodal and multiscale systematic characterization.

The manuscript is organized as follows:

Chapter 1 presents a survey of the literature, showing the most important bone disorders and investigative tools. Moreover, it depicts the conventional clinical approach and the applicability of an approach based on MRI. Finally, it describes the upcoming MRI applications, which could provide additional biomarkers for the bone quality assessment.

Chapter 2 presents an in vivo study of knee microarchitecture assessment of a patient affected by psoriatic arthritis. This study shows a direct application of Ultra-High Field MRI to quantify bone microarchitecture anomalies in patient compared to controls, moreover presenting a reliable assessment of the bone quality, illness risk stratification and for the follow-up of therapeutic strategies.

Chapter 3, dedicated to the materials and methods, presents the sample database collected during the thesis and the their preparation protocol depending on the experimental characterization techniques used. In addition, all the multiscale and multimodal bone characterization experimental techniques have been presented.

Chapter 4 presents an ex vivo study on the clinical relevance of UHF MRI by assessing the bone microarchitecture in cadaveric proximal femurs. First, it depicts the sample preparation protocol for large cadaveric femurs to reduce artefacts due to magnetic susceptibility effects, then it shows the bone morphology quantification techniques and the effect of the resolution on the morphological analysis. Finally, correlations between clinical standard bone mineral density measurements and bone morphology are presented.

Chapter 5 presents an ex vivo study aim to optimize the proximal femurs microarchitecture analysis from MRI acquisitions. The microarchitecture parameters of the same proximal femurs acquired using different imaging techniques μCT and MRI 3T and 7T have and sequences gradient re-called echo and turbo spin echo have been compared. Moreover, it presents the correlation between clinical standard BMD to bone

morphology and to BMD derived from image analysis and the correlation between bone morphology and bone failure load derived from biomechanical fracture test.

Chapter 6 presents a multiscale and multimodal analysis of two femurs neck, one osteoporotic and one control. It depicts the bone quality from the macroscale (μCT at 51 μm^3 and 5 μm^3) to the microscale (X-ray synchrotron μCT at 0.9 μm^3 and microindentation) and to the molecular scale (Fourier Transform Infra-Red). Morphology at macroscale, changes in the osteocytes lacunae morphology and distribution have been investigated and variations in the trabecular mechanical properties and in the hydroxyapatite types, collagen fibrils and proteins have been assessed.

Chapter 7 presents the investigation of the hydroxyapatite molecular changes due to osteoporosis. Using X-ray absorption spectroscopy the Calcium K-edge has been investigated in 15 samples from 5 different patients (3 osteoporotic women and 2 controls, 1 female and 1 male). Differences in both Calcium and Phosphorous ratio and hydroxyapatite crystallinity order have been assessed as for their relevance in the osteoporotic/control classification.

Finally, a general conclusion is presented as for an opening to new perspectives. In addition, an overall conclusion chapter by chapter is also presented in French at the end of the manuscript.

Chapter 1: State of the Art

Part I: Bone Function and Multiscale Structure

Part II: Survey of MRI Usefulness for the Clinical Assessment of Bone Microstructure (published article)

Cite:

Soldati E, Rossi F, Vicente J, Guenoun D, Pithioux M, Iotti S, Malucelli E, Bendahan D. Survey of MRI Usefulness for the Clinical Assessment of Bone Microstructure. Int J Mol Sci. 2021 Mar 2;22(5):2509. doi: 10.3390/ijms22052509. PMID: 33801539; PMCID: PMC7958958.

Authors

Enrico Soldati, Francesca Rossi, Jerome Vicente, Daphne Guenoun, Martine Pithioux, Stefano Iotti, Emil Malucelli and David Bendahan

Part I : Bone Function and Multiscale Structure

Bone is a mineralized tissue that solves multiple functions including mechanical, metabolic, and hematopoietic. Bone mechanical properties involve resist to mechanical load, provide support to soft tissues, protect the vital internal organs, permit the movement providing insertional points for the skeletal muscles and store the bone marrow. Among the multiple metabolic functions, the most important are the ability of storing minerals, in particular calcium with the aim to control the metabolic balance (homeostasis). Calcium is fundamental for the regulation of the muscular and nerve activity and for the blood coagulation maintaining the calcium concentration constant. Moreover, it provides detoxification from heavy metals and other extraneous elements removing them from the bloodstream (S. C. Cowin 1999).

During life, the bone is in constant mutation, called bone remodeling. The bone remodeling is the result of an antagonistic process of formation and resorption of the mineral tissue aiming to maintain the integrity of the skeleton. The integrity of a healthy skeleton depends on the interactive process of three cells: osteoblast (bone forming cells), osteoclast (bone absorptive cells) and osteocytes (able to measure the bone solicitation state, inhibiting or encouraging the bone formation or absorption).

Bone is a multiphase material composed of a solid phase and a viscoelastic component (Fig. 1.1). The solid phase is considered as hierarchical, anisotropic, and heterogeneous and is composed of 65% of inorganic matrix (mostly calcium hydroxyapatite crystals) and 35% of organic matrix (type I collagen, proteoglycans, and bound water) (X. Wang et al. 2010). While the inorganic matrix is characterized by a high rigidity, a high resistivity, and an elastic behavior, the organic matrix is deformable thereby providing the tissue with tensile strength. Due to the combination of these two materials, bone tissue is simultaneously deformable and rigid (Fratzl and Gupta 2007). The solid phase creates a shell for the bone marrow, which is the viscoelastic component. The bone marrow on the other hand has a double function. It provides nutriments to the solid phase allowing higher regenerative rate and is able, due to its viscoelastic properties, to spread the dynamics of an impulsive action, reducing the risk of fractures due to impacts (Nyman et al. 2006a). Bone tissue is composed of both trabecular and cortical bone phases. Cortical

bone covers the whole surface of the bone. It is compact, dense, and characterized by overlapped and parallel lamellae, which provide a large resistivity (X. Wang et al. 2010). Trabecular bone is the inner compartment of bone tissue. It is composed of 25% of bone and 75% of marrow (S. C. Cowin 1999). At the microstructural level, trabecular bone appears as a complex 3D network of interconnected trabeculae rods and plates responsible for tissue resistance to loading forces. The bone inner architecture is an important contributor to bone strength independent of bone mass (X. Wang et al. 2010). It is characterized by a high porosity so that trabecular bone is lighter and less dense than cortical bone. In fact, cortical bone mainly works in compression while trabecular bone principally works in flexion and torsion reaching a higher area under the stress–strain curve (S. C. Cowin 1999).

Bone is actually a dynamic porous structure and its porosity can change as a result of pathological processes but also as an adaptive response to mechanical or physiological stimuli. This change in both cortical and trabecular bone porosity can strongly affect the corresponding mechanical properties (S. C. Cowin 1999).

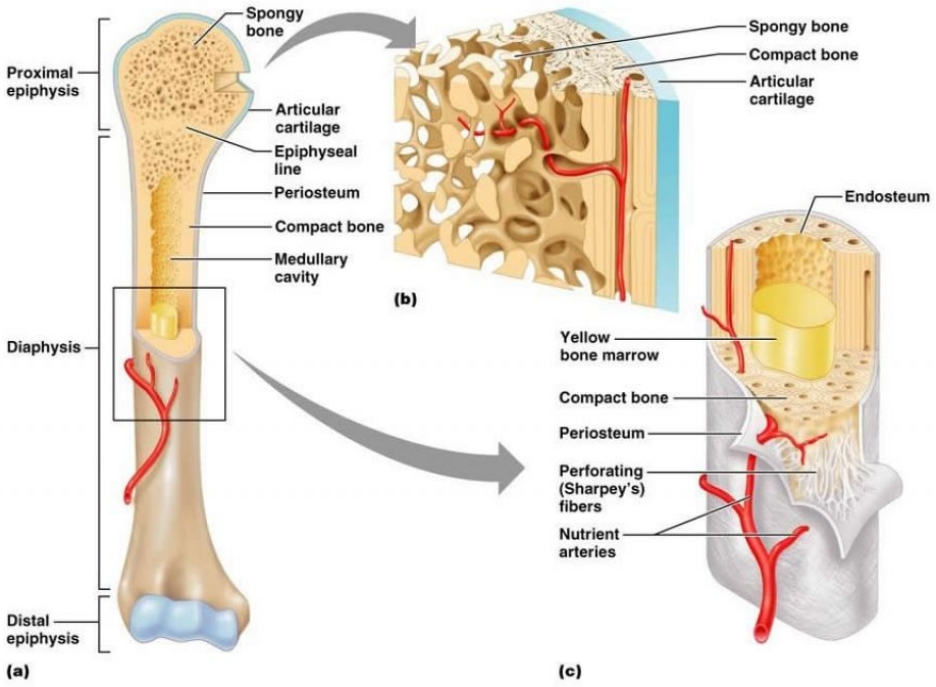

Figure 1. 1: Bone Structure.

The complexity of bone properties finds its origin from its structure (Fig. 1.2). The hierarchical structure of the bone requires an interpretation of the structural behavior at different levels. Therefore, to fully understand bone mechanical properties it is important to understand the properties of its different component phases and their structural

relationship at multiscale levels. The bone hierarchical structure can be classified and investigated as:

- **Macrostructure** (from 100 µm to 1 mm): cortical and trabecular bone.
- **Microstructure** (from 1 µm to 100 µm): Haversian systems, osteons, single trabeculae, osteocytes lacunae.
- **Nanostructure** (< 1 µm): collagen fibrils and embedded minerals.

The resulting structure, however being anisotropic, is highly oriented and (Rho, Kuhn-Spearing, and Zioupos 1998).

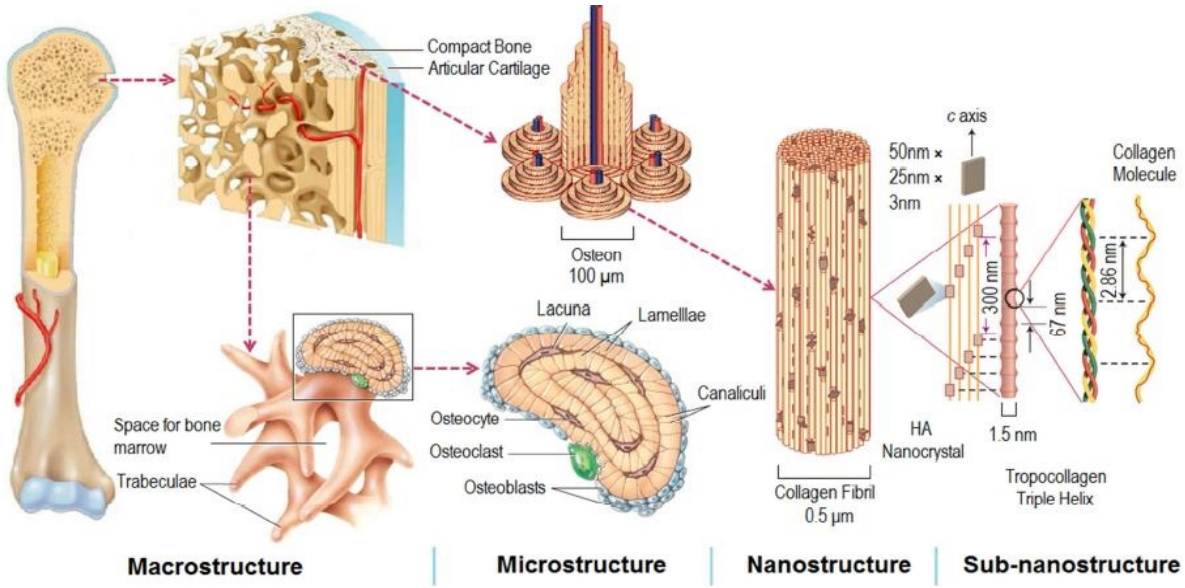

Figure 1. 2: Bone hierarchical structure.

Macrostructure

Macroscopically, it is possible to remark that bones have different shape and sizes depending by the anatomical position and the function they have to attend. However, at the macroscale all bones are characterized by two architectural structures, called cortical and cancellous/trabecular bone. It is important to notice that both cortical and trabecular bone are mainly composed by HA crystals and collagen while their arrangement differs accordingly to their maturity (S. Cowin 2001; Khurama 2009).

Long bones, as for femurs, are generally composed by diaphysis, metaphysis, and epiphysis. The diaphysis is the central tubular part, it is characterized by a thick external cortical bone and inner trabecular bone surrounding a medullary cavity which contains yellow bone marrow, high in fat. Moving towards the extremities of the bone there are two extended edges, metaphysis, disks of cartilage growing during childhood which is how the bones get longer as child gets taller. Bones are ending in epiphysis mainly

composed by trabecular bone within a thin cortical bone and filled with red marrow, responsible for producing blood cells.

Cortical bone covers the whole surface of the bone, is principally found in the diaphysis as a thick cylinder and as an outer shell of trabecular bone at both the proximal and distal ends of bones. The trabecular bone is instead located within the cortical shell, in medullary cavities at the end of long bones and in between the opposite faces of the cortical bone in the diaphysis (Fig. 1.3) (X. Wang et al. 2010).

Trabecular bone represents the 20% of the total skeleton mass with a porosity in the range 45-95%, whereas the cortical bone accounts for the 80% of skeleton mass with a porosity in range 5-10%. It is necessary to underline that bone are a dynamics porous structures and therefore their porosity depends not only because of pathological conditions but also by the position, the function as an adaptive response to mechanical or physiological stimulus. Changes in the porosity, that may occur in both cortical and trabecular bone, strongly affect bone's mechanical properties. However, since the cortical bone is as dense as possible and with lamellae organized to optimize the structure, properties does not vary greatly between different cortical tissues (S. Cowin 2001).

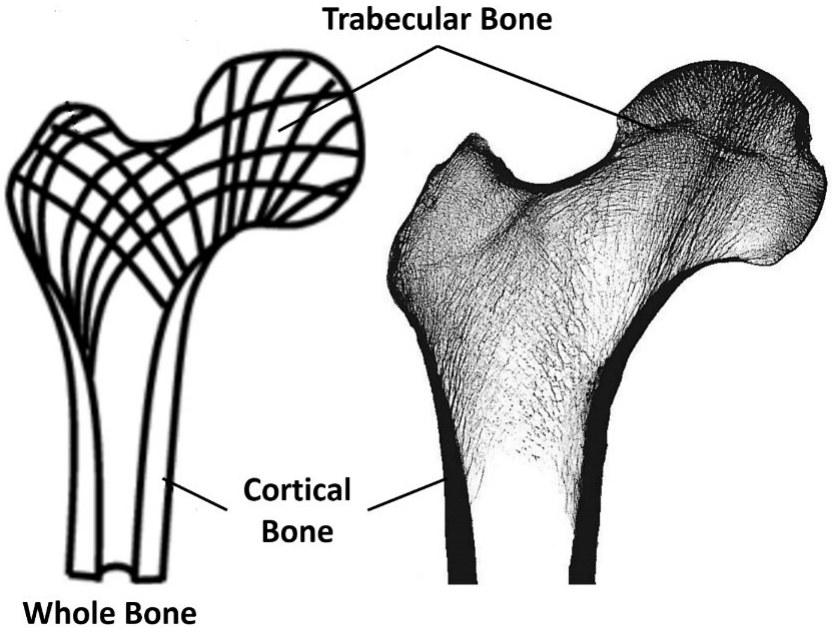

Figure 1. 3: Trabecular and cortical bone.

The cortical bone is compact and characterized by overlapped and parallel lamellae to provide maximal resistivity, it is very dense and therefore very resistant it is possible to individuate three different dispositions of the lamellae. The principal component is the osteon (or Haversian systems), cylindrical and concentric structure of 200-250 μm of diameter composed by several concentric lamellae. Osteon may reach some cm of length

and in the center, they present the capillary space where the blood flows. Osteons born around the capillary because the bone needs collagen and nutrients to grow. Between lamellae there are the osteocyte lacunae where there are the osteocytes, important for the bone mechanic-regulation, and these lacunae are interconnected between them forming a complex network able to exchange signals about the mechanic load. Given that osteons are cylindrical structure, the space between them is filled by interstitial lamellae which are the remnant of previous osteons, hence forming the older part of the bone. The third family of lamellae are the circumferential or peripherical lamellae which bandage the osteons, they can reach a dimension of some cm^2 and cover whole portions of the bone. Their role is to pack the osteons providing a smooth surface able to resister to higher strain than rough surfaces (S. C. Cowin 1999; S. C. Cowin and Doty 2007; S. Cowin 2001; Martin et al. 2015).

The trabecular or spongy bone is a network of short and interconnected struts or trabeculae, which are characterized by different shapes and sizes, but arranged along a preferential directionality. It is characterized by high porosity, which makes trabecular bone lighter and less dense than cortical bone. It also has a large surface area and the interstitial space is filled with marrow, both red and yellow, which has not only the function of providing nutrients but also concur to bone rigidity. As a matter of fact, marrow is a viscous fluid, incompressible and bounded by the cortical shell, which reacts according to the strain velocity. The minimum trabecular size is in order of 100 μm of diameter but it can also reach several hundred of μm as for the pores, or the space between trabeculae, which may vary from few micrometers to millimeters. Trabecular bone is much more metabolically active than cortical bone thanks to higher surface to volume ratio directly connected to bone marrow. It is much more deformable than cortical bone even though it is composed by the same material. Trabecular composition and structure generate a more compliant and deformable material. Moreover, the preferential directionality, along the principal stress lines, of trabeculae provides maximum strength and the regenerative power permits realignment in case of changes of stress directions (X. Wang et al. 2010; Wolff 1986; Murugan and Ramakrishna 2005; Rho, Kuhn-Spearing, and Zioupos 1998).

The trabecular properties of the proximal femur head have been investigated in this thesis using both μCT and MRI and the mechanical behavior of the whole proximal femurs have been assessed using biomechanical fracture tests with a specific assay which simulates sideways fall on the great trochanter. The results corresponding to the macroscale investigation of the trabecular phase are presented in Chapter 2, 4 and 5. The cortical macroscale properties have been assessed in the femoral neck using μCT and the corresponding results are shown in Chapter 6.

Microstructure

Microscopically, lamellae are composed by parallel collagen fibrils, reinforced by crystals, forming an average structure thickness between 3 and 7 μm (Rho, Kuhn-Spearing, and Zioupos 1998). Collagen fibrils are principally oriented in the same direction, permitting an high collagen density per unit volume, and they are organized in bundles of 1-2 μm of diameter (Ascenzi et al. 1979).

Each lamella contains an ellipsoidal cavity, named lacunae, usually aligned with their long axis parallel to the long axis of the lamella. Inside the cavities made by the lacunae there are located the osteocytes (bone cells buried in the matrix) (Fig. 1.4). The osteocytes functions as mechano-sensory cells, and they are responsible for the coordination of relate cells activities. Each osteocyte has several cytoplasmatic processes forming a 3D network that permits the connection with similar processes of neighbouring cells (up to 12).

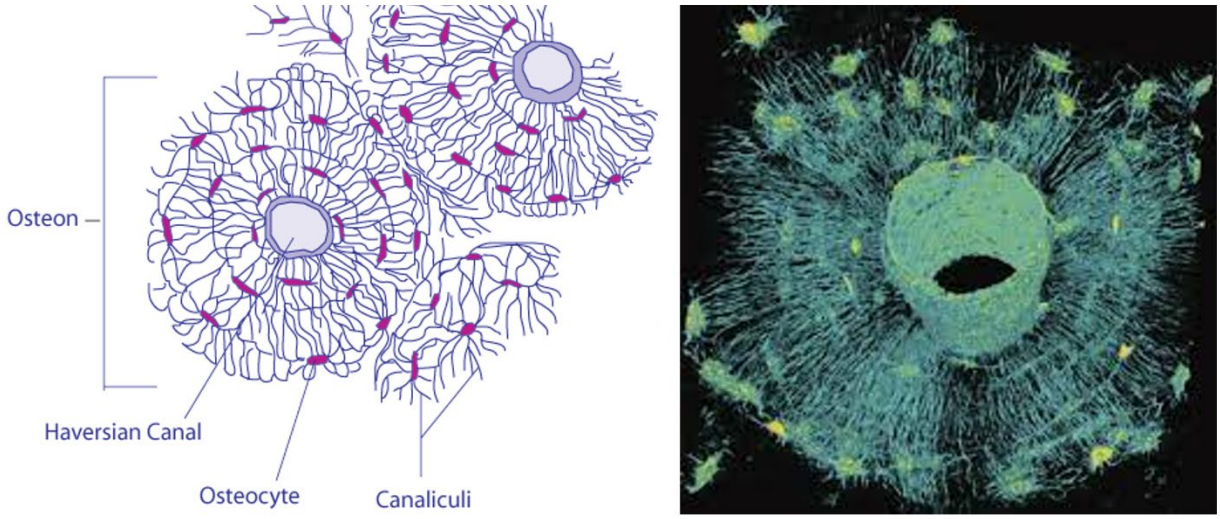

Figure 1. 4: (left) Osteocytes network and canaliculi scheme, (right) 3D rendering of the osteocyte network organized around a Haversian canal **(reproduced from Med. Phys. 39 (4), April 2012).**

These processes lie inside small channels (range 0.1 μm of radius), known as canaliculi and that provides connections between lacunae and the Haversian canal (Pacureanu et al. 2012). This network is commonly referred as lacunae-canaliculi network (LCN) and provides to the bone the ability to respond to changes in the mechanical loading. It is well accepted that osteocytes receive mechanical signals directly through deformation of the solid bone matrix, and/or indirectly through fluid motion in the LCN. The potential direct mechanisms include sensing of the strain magnitude, gradients, rates, energy density and loading frequency as well as cycle number. On the contrary, the potential of the indirect mechanisms includes sensing the fluid pressure, shear stresses and streaming potentials (S. C. Cowin and Doty 2007; Scheiner et al. 2010). The total volume of lacunae and canaliculi is contributing to 10% of the total porosity (X. Wang et al. 2010).

In this thesis study the osteocytes lacunae morphology and distribution have been assessed using synchrotron radiation micro-computed tomography and the trabeculae tissue properties have been investigated using microindentation of multiple samples extracted from three different regions of the proximal femur (great trochanter, femoral neck and femoral head). The corresponding results have been presented in Chapter 6.

Nanostructure

The nanostructure of both cortical and trabecular bone is formed by a composite of mineral crystals and collagen fibrils. Bone mineral is stiff and fragile while the collagen fibrils are much softer and resistant. The individual characteristics of both mineral crystals and collagen along with their interaction are crucial for the bone mechanical performance (Fratzl 2005). At nanoscale, groups of collagen molecules aggregate forming the mineralized collagen fibrils, of about 100 nm of diameter (Landis et al., n.d.), which themselves group together to form mineralized collagen fibers (Rho, Kuhn-Spearing, and Zioupos 1998) (Fig. 1.5).

Collagen fibrils are composed by collagen molecules also named tropocollagen. Tropocollagen is a highly reactive molecule, that spontaneous perform fibrillogenesis creating a supramolecular structure, which formation is intrinsically linked with the collagen cross-linking (Rho, Kuhn-Spearing, and Zioupos 1998; Ottani et al. 2002). In fact, the longitudinal distribution of polar and hydrophobic residues along the length of the tropocollagen helix results in staggered, lateral intermolecular interaction through the process of cross-linking during fibrillogenesis (Ottani et al. 2002). This method of self-assembling results in observed molecular axial stagger within collagen fibrils and this axis stagger results in a gap region between the tropocollagen ends, vitals for the healthy mineralization process. The gap regions became centers of ossification which is believed to encourage the spontaneous precipitation of mineral from the extracellular matrix to the existing mineral nucleus (Landis et al., n.d.). The mineralization process is predominantly intrafibrillar and the mineral crystals platelets grow to form the observed mineral plates and extend along the fibril surface forming a reinforcing apatite ring around the fibrils (Ottani et al. 2002). The mineral crystals (2 to 7 nm thick, 15 to 200 nm length and 10 to 80 nm width) tend to grow exhibiting a specifically oriented crystalline, with the c-axis of the mineral crystal being approximately aligned with the long axis of the associated fibrils (Fratzl 2005; Rho, Kuhn-Spearing, and Zioupos 1998).

Mineralization enhances the fibril stiffness firstly because the intrafibrillar mineral platelets strengthen the collage fibrils in tension and compression along the fibril axis and in shear in the platelets plane, while preserving the fibrils flexibility not pronouncing the

bending rigidity. Secondly, the extracellular mineralization further strengthens the fibrils in all remaining deformation modes (Nikolov and Raabe 2008).

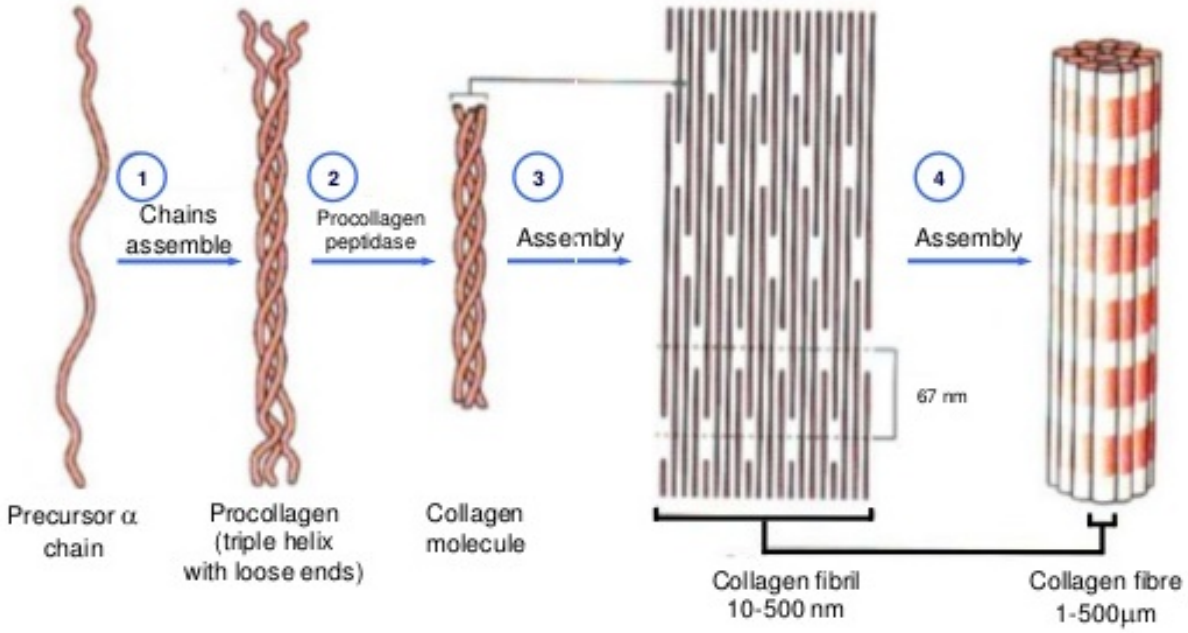

Figure 1. 5: Collagen fiber structure.

The bone mineral component is mostly composed of Hydroxyapatite (HA) (Fig. 1.6) and other elements like sodium, magnesium, zinc, etc. in trace quantity. The HA accounts for 60% of bone and it is the primary component of the entire bone (Mow and Huiskes 2004).

The bone mineral is analogous to the naturally available ceramic hydroxyapatite. The chemical formula for the HA is $Ca_{10}(PO_4)_6(OH)_2$, and the actual bone mineral has some impurities added to the structure of this ceramic compound. The global crystallographic structure mostly depends on the characteristic of the anion PO_4^{3-} and mostly on his tetraedric geometry. The bidimensional structure monolayer coming from the association of these anions have a hexagonal symmetry. The three dimensional multilayer structure resulting from the overlap of multiple monolayers it will tend to the minimum bulk (Landi et al. 2003a).

Often the OH^- and PO_4^{3-} are replaced by other compounds like carbonate (Fig. 1.6). This results in formation of carbonate hydroxyapatite (Rey et al. 2011; Rey 1991). The calcium can also be replaced by element like strontium or magnesium. These replacements increase the imperfection in the apatite, and it makes the mineral to be more soluble. These substitutions result in reduction of size of the crystal. The fluoride ion occupying the OH^- site is an exception to the above statement. In this case, the mineral is less soluble, and their crystal size is comparatively larger. The presence of carbonate and the different type of carbonate that substitute the bone mineral are well studied. The

carbonate ions replacing the OH^- sites in HA are called type A carbonate apatite ($Ca_{10-x/2}(PO_4)_{6-x}(CO_3)_x(OH)_2$) while if the carbonate ion replaces the phosphate sites, they are called type B carbonate apatite ($Ca_{10-x/2}(PO_4)_{6-x}(CO_3)_x$) (Madupalli, Pavan, and Tecklenburg 2017a). The carbonate ion can replace both monovalent and trivalent anionic sites and they are called type AB carbonate apatite.

The carbonate content in the bone is about 4-8 wt.% and it depends on the age of the individual. The B-type carbonation is the preferential carbonate substitution found in the bone with a A/B ratio in the range 0.7-0.9, and a higher value of the A/B ratio was observed in old tissue, compared to young tissue. The presence of B-carbonate in the apatite was shown to cause a decrease in crystallinity and an increase in solubility in both in vitro and *in vivo* tests. Moreover, the A-carbonate surface showed a lower affinity for the human trabecular osteoblastic cell, compared to HA, this is demonstrated by the lower cell attachment and collagen production which was attributed to a decrease of the polar component of the surface of the A-carbonated biomaterial (Landi et al. 2003a).

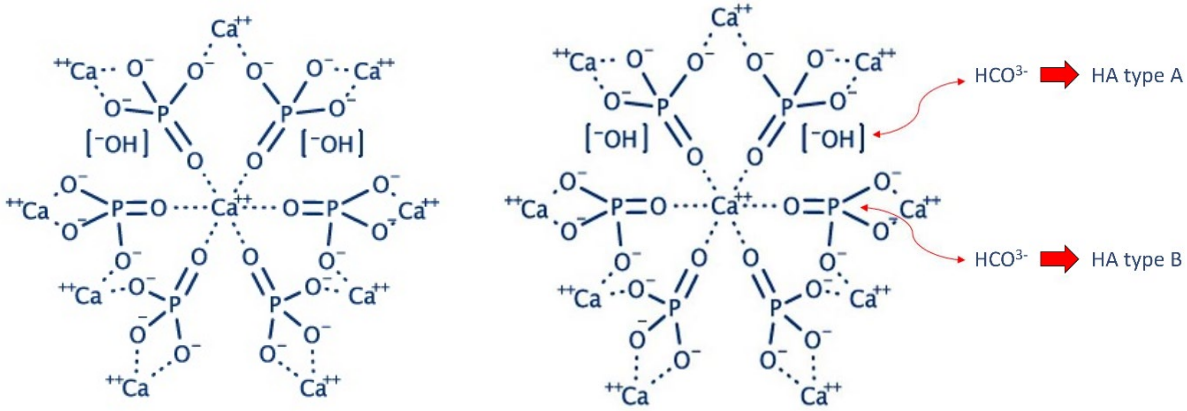

Figure 1. 6: (left) Hydroxyapatite (HA) molecular structure, (right) HA type A and B substitutes.

It is pointed out that a gross sample of bone tissue contains crystals of bone mineral of very widely different age. This is because bone tissue is being continuously formed and resorbed. The new bone tissue contains the very youngest bone crystals, and in most instances the tissue being resorbed is among the oldest and therefore the crystals removed or dissolved are also among the oldest. Therefore, the age distribution of crystals in any gross sample of bone will contain a certain proportion of the very youngest crystals and a certain proportion of the very oldest crystals, as well as a distribution of crystals of all other ages, depending on the age of the patient or animal, the rates of bone formation, and the rates and location of bone resorption. It is generally true that this distribution will be skewed toward the youngest crystals in very young animals in which bone turnover is very rapid, and toward older crystals in the older, more mature animals, in which new bone formation (and therefore new, young crystal formation) and bone

turnover are relatively low (A.L. Boskey and Coleman 2010). The specific distribution of the bone crystals as a function of the age of the animal can therefore vary widely, depending on the rate of turnover, bone formation, resorption, and other biological factors. The most obvious change that occurs in the crystals of bone with aging is an increase in their crystallinity, despite the tendency of carbonate ions to stabilize amorphous states, the ordered structure of the ion constituents in the vicinity of the carbonate ions nonetheless appears to occur rapidly during the growth and aging of the bone crystals, even as the content of carbonate ion increases. This progressive increase in the crystallinity of the crystals, despite an increase in the carbonate ion concentration, is analogous to what occurs in synthetic samples. This indicates that carbonate ions are not a predominant factor in the biological regulation or control of the crystallinity of apatite crystals. In the crystals of young, whole bone, the increase of the CO_3 is indicative of a more organized structure of the atomic lattice of the regions in the vicinity of carbonate ions in both the A and B positions. This can probably be related in part to the progressive but moderate increase in the size of the crystals during maturation and aging (Wopenka and Pasteris 2005).

In this PhD project the nano and molecular scale have been investigated using two spectroscopic techniques, i.e. the X-ray absorption spectroscopy and the Fourier transform infrared, and the differences between osteoporotic and controls have been presented. The while FTIR spectroscopy was used to assess the HA carbonation and the collagen cross-links and the results have been presented in Chapter 6 while the XAS of the Calcium K-edge has been used to assess the HA crystallinity order and the changes in the Calcium neighbor and the corresponding results have been presented in Chapter 7.

Part II : Survey of MRI Usefulness for the Clinical Assessment of Bone Microstructure (published article)

Cite:

Soldati E, Rossi F, Vicente J, Guenoun D, Pithioux M, Iotti S, Malucelli E, Bendahan D. Survey of MRI Usefulness for the Clinical Assessment of Bone Microstructure. Int J Mol Sci. 2021 Mar 2;22(5):2509. doi: 10.3390/ijms22052509. PMID: 33801539; PMCID: PMC7958958.

Authors

Enrico Soldati [1,2,3,*], Francesca Rossi [4], Jerome Vicente [2], Daphne Guenoun [3,5], Martine Pithioux [3,6], Stefano Iotti [4,7], Emil Malucelli [4] and David Bendahan [1]

Abstract

Bone microarchitecture has been shown to provide useful information regarding the evaluation of skeleton quality with an added value to areal bone mineral density, which can be used for the diagnosis of several bone diseases. Bone mineral density estimated from dual-energy x-ray absorptiometry (DXA) has shown to be a limited tool to identify patients' risk stratification and therapy delivery. Magnetic resonance imaging (MRI) has been proposed as another technique to assess bone quality and fracture risk by evaluating the bone structure and microarchitecture. To date, MRI is the only completely non-invasive and non-ionizing imaging modality that can assess both cortical and trabecular bone in vivo. In this review article, we reported a survey regarding the clinically relevant

Affiliation

[1] Aix Marseille University, CNRS, CRMBM, Marseille, France
[2] Aix Marseille University, CNRS, IUSTI, Marseille, France
[3] Aix Marseille University, CNRS, ISM, Marseille, France
[4] University of Bologna, Department of Pharmacy and Biotechnology, Bologna, Italy
[5] Institute for Locomotion, Department of Radiology, Sainte-Marguerite Hospital, Aix Marseille University, APHM, CNRS, ISM, Marseille, France;
[6] Institute for Locomotion, Department of Orthopaedics and Traumatology, Sainte-Marguerite Hospital, Aix Marseille University, APHM, CNRS, ISM, Marseille, France;
[7] National Institute of Biostructures and Biosystems, Rome, Italy
* Correspondence: enrico.soldati@univ-amu.fr

information MRI could provide for the assessment of the inner trabecular morphology of different bone segments. The last section will be devoted to the upcoming MRI applications (MR spectroscopy and chemical shift encoding MRI, solid state MRI and quantitative susceptibility mapping), which could provide additional biomarkers for the assessment of bone microarchitecture.

Keywords: MRI; bone microarchitecture; bone morphology; bone quality.

1. Introduction

1.1. Bone Disorders and Investigative Tools

A large number of studies have demonstrated the substantial burden of bone disorders worldwide (Vos et al. 2012; Lim et al. 2012; Murray 2012). Considered as the second greatest cause of disability (Vos et al. 2012), musculoskeletal pathologies account for 6.8% of total disability worldwide (Lim et al. 2012). Bone pathologies are usually affecting the bones solid phase, which is composed of both cortical and cancellous/trabecular types of bone. Bone alterations commonly include cortical shell thinning, increased porosity of both cortical and trabecular bone phases (Woolf 2015; Johnell and Kanis 2006), and reduced density, volume, and regenerative power. These bone modifications generally account for a reduced resistivity and flexibility eventually leading to an increased risk of fragility fractures accompanied by long-term disabilities. Recent studies have shown that people over the age of 50 with a high risk of osteoporotic fractures represented more than 150 million people worldwide with 137 million women (Odén et al. 2015). This number is expected to exceed 300 million by 2040 (Odén et al. 2015). Fragility fractures lead to more than half a million hospitalizations each year in North America alone, with an annual direct cost, which has been estimated to be $17 billion dollars in 2005. This cost is expected to rise by almost 50% by 2025 (Burge et al. 2007). Overall, the early identification of bone fragility risk is a major health issue (van Oostwaard 2018). In the clinical context, bone disorders are usually assessed using dual-energy X-ray absorptiometry (DXA), which is able to assess the bone mineral density (BMD). The BMD score is then compared to a reference range of values calculated in healthy (25–35 years old) volunteers taking into account sex and ethnicity. Accordingly, a score (T-score) is generated indicating how far, in terms of SD (standard deviation), the measured BMD is from the reference values. A T-score between −1 and −2.5 indicates a low bone mass or osteopenia while a value lower than −2.5 is indicative of osteoporosis. The corresponding method has good sensitivity (around 88% for both men and post-menopausal women), but the specificity is poor (around 41% for post-menopausal women and 55% for men) (Nayak et al. 2015a) resulting in a low clinical diagnostic accuracy (70%) (Humadi, Alhadithi, and Alkudiari 2010a). In addition, DXA measurements do not take into consideration microarchitectural alterations, which have also been recognized as part of the structural picture in osteoporosis. Of interest, bone microarchitecture can be assessed using quantitative

computed tomography (qCT) (Sharma, Toussaint, Elder, Masterson, et al. 2018; Boutroy et al. 2005a). Given that both DXA and qCT are both radiative imaging techniques, non-radiative alternatives would be of great interest. Over the last decades, magnetic resonance imaging (MRI) (Majumdar et al. 1996a; Seifert et al. 2014a; Karamat, Darvish-Molla, and Santos-Diaz 2016a) has been indicated as a non-ionizing and non-invasive technique.

Using MRI, a large number of studies have attempted to assess bone microarchitecture in bone disorders and more particularly in osteoporosis (Majumdar et al. 1999a; Roland Krug et al. 2008a; G. Chang, Honig, et al. 2015a; Chamith S. Rajapakse et al. 2018a). The corresponding studies have been conducted at different magnetic field strengths, using different Radio Frequency coils and pulse sequences. Although, the results were compelling, the sensitivity of the corresponding microarchitecture metrics for diagnostic purposes and the assessment of the disease severity is still a matter of debate.

On the basis of a comparative survey of MRI, computed tomography, and DXA-based metrics, we intended to address the issues related to the diagnostic potential of the corresponding metrics and their capacity to predict disease severity. The final section will be devoted to potential perspectives offered by magnetic resonance spectroscopy (MRS) and chemical shift encoding (CSE-MRI), solid-state MRI, and quantitative susceptibility mapping (QSM).

1.2. Bone Microstructure

Bone is a multiphase material composed of a solid phase and a viscoelastic component. The solid phase is considered as hierarchical, anisotropic, and heterogeneous and is composed of 65% of inorganic matrix (mostly calcium hydroxyapatite crystals) and 35% of organic matrix (type I collagen, proteoglycans, and bound water) (X. Wang et al. 2010). While the inorganic matrix is characterized by a high rigidity, a high resistivity, and an elastic behavior, the organic matrix is deformable thereby providing the tissue with tensile strength. Due to the combination of these two materials, bone tissue is simultaneously deformable and rigid (Fratzl and Gupta 2007). The solid phase creates a shell for the bone marrow, which is the viscoelastic component. The bone marrow on the other hand has a double function. It provides nutriments to the solid phase allowing higher regenerative rate and is able, due to its viscoelastic properties, to spread the dynamics of an impulsive action, reducing the risk of fractures due to impacts (Nyman et al. 2006a). Bone tissue is composed of both trabecular and cortical bone phases. Cortical bone covers the whole surface of the bone. It is compact, dense, and characterized by overlapped and parallel lamellae, which provide a large resistivity (X. Wang et al. 2010).

Trabecular bone is the inner compartment of bone tissue. It is composed of 25% of bone and 75% of marrow (S. C. Cowin 1999). At the microstructural level, trabecular bone appears as a complex 3D network of interconnected trabeculae rods and plates responsible for tissue resistance to loading forces. The bone inner architecture is an important contributor to bone strength independent of bone mass (X. Wang et al. 2010). It is characterized by a high porosity so that trabecular bone is lighter and less dense than cortical bone. In fact, cortical bone mainly works in compression while trabecular bone principally works in flexion and torsion reaching a higher area under the stress–strain curve (S. C. Cowin 1999).

Bone is actually a dynamic porous structure and this porosity can change as a result of pathological processes but also as an adaptive response to mechanical or physiological stimuli. This change in both cortical and trabecular bone porosity can strongly affect the corresponding mechanical properties (S. C. Cowin 1999).

2. Bone Pathologies and Clinical Approach

2.1. Principal Bone Pathologies

Pathologies of the bone microstructure are quite common and may derive from multiple factors. Musculoskeletal (MSK) complaints are the second most common reason for consulting a medical doctor and account for 10%–20% of primary care visits (Woolf 2015). They are also among the leading causes of long-term disability and the leading cause for long-term absence from work in numerous countries (Woolf 2015; Brage, Nygard, and Tellnes 1998). Worldwide, the total number of MSK disability adjusted life years (DALYs) significantly increased from 80.2 million in 2000 to 107.9 million in 2015 ($p < 0.001$) with the total number of MSK years lived with disability (YLDs) increasing from 77.4 million to 103.8 million. Overall, MSK diseases represent the second cause of YLDs worldwide (Sebbag et al. 2019).

The most common pathology related to bone microstructure alterations is osteoporosis in which bone density and volume of bone segments or specific bone regions can be progressively reduced. Patients with osteoporosis are at high risk of having one or more fragility fractures, which eventually lead to a physical debilitation and potentially to a downward spiral in physical and mental health. Johnell et al. reported that 9 million osteoporotic fractures occurred in 2000, 1.6 million in the hip, 1.7 million in the wrist, and

1.4 million in the vertebrae (Johnell and Kanis 2006). Only in the five largest countries in Europe plus Sweden (EU6), the number of fragility fractures were estimated at 2.7 million in 2017 with an associated annual cost of €37.5 billion and both fragility fractures and associated annual cost are expected to increase by 23% in 2030 (for the International Osteoporosis Foundation et al. 2020). A large Chinese epidemiological survey using DXA among people aged fifty years or older demonstrated the prevalence of osteoporosis in males (6.46%) than females (29.13%) meaning that there are 10 million men and 40 million women with osteoporosis only in China (Cheng et al. 2020). The current DALYs per 100 individuals age 50 years or more were estimated at 21 years, which is higher than the estimates for stroke or chronic obstructive pulmonary disease (for the International Osteoporosis Foundation et al. 2020). Moreover, it has been reported that if all patients who fracture in the EU6 were enrolled into fracture liaison services, at least 19,000 fractures every year might be avoided (for the International Osteoporosis Foundation et al. 2020). Finally, Kemmak et al. reported that the direct annual cost of treating osteoporotic fractures of people on average is between 5000 and 6500 billion USD in Canada, Europe, and USA alone, not taking into account indirect costs, i.e., disability and loss of productivity (kemmak et al. 2020).

Osteoporosis may be linked to ageing, particularly in postmenopausal women, or can occur as a result of specific conditions, i.e., diabetes, anorexia nervosa, and obesity or treatments, i.e., corticosteroid. Indeed, corticosteroid-induced osteoporosis is the most common form of secondary osteoporosis and the first cause in young people. Bone loss occurs early after the initiation of corticosteroid therapy and is correlated to dose and treatment duration (Bartl and Bartl 2017). Fragility fractures have been associated with early mortality and increased morbidity having a significant effect on the quality of life of both patients affected by diabetes (Keenan and Maddaloni 2016; S. C. Chen et al. 2019; Abdalrahaman et al. 2017), anorexia nervosa (Singhal et al. 2018; Fazeli and Klibanski 2019), and obesity (Fintini et al. 2020; Cordes et al. 2016; 2015).

Additionally, a number of childhood diseases cause rickets, a physical condition resulting from a delayed calcium phosphate mineral deposition in growing bones, which may lead to skeletal deformities (Ganie et al. 2016). In adults, the equivalent disease is called osteomalacia and may have devastating consequences if not diagnosed and treated (Minisola et al. 2017; Florenzano et al. 2021). Patients with chronic renal disease are at risk of developing a complex bone disease known as renal osteodystrophy, which is responsible for an increasing bone resorption due to an increased osteoclast activity (Sharma, Toussaint, Elder, Masterson, et al. 2018; Ruderman et al. 2020).

Paget's disease is a chronic progressive bone disorder occurring in middle-aged or older adults and which commonly affect spine, pelvis, legs, or skull (Winn, Lalam, and

Cassar-Pullicino 2017; Gennari et al. 2019). The most likely etiology is a slow paramyxoviral viral infection in generally susceptible individuals, however the exact cause is unknown (Kravets 2018). It appears to arise more or less simultaneously in one or more skeletal sites, remaining restricted there. In long bones the disease first appears in the region of the proximal epiphysis and advances along the shaft at a rate of 8 mm/yr (Cundy 2018). Paget's disease is initially characterized by bone resorption, disorganized bone deposition, resulting in pathological bone remodeling where the osteoclastic activity is predominant, is then followed by a mixed phase of osteoclast and osteoblast with osteoblasts prevailing, and end with an inactive phase where the osteoblastic activity declines (Winn, Lalam, and Cassar-Pullicino 2017). The leading edge of this advance is often visible as a V-shaped "lytic wedge" reflecting osteoclastic resorption (Cundy 2018). Moreover, it has been noticed that an elevated serum alkaline phosphatase level correlated with the disease activity (Kravets 2018). Diagnosis and follow-up are usually based on imaging modalities in order to assess disease status, bone microarchitecture and metabolic activity. MRI is invaluable for the assessment of complications, i.e., spinal stenosis and sarcomatous degeneration (Winn, Lalam, and Cassar-Pullicino 2017). An early diagnosis of this disease can minimize the impact on the patient quality of life (Appelman-Dijkstra and Papapoulos 2018).

Many genetic and developmental disorders can affect the skeleton. Among them, the most common is the osteogenesis imperfecta (Palomo, Vilaça, and Lazaretti-Castro 2017). Osteogenesis Imperfecta (OI) is a systemic connective tissue disorder characterized by low bone mass and bone fragility causing significant morbidity due to pain, immobility, skeletal deformities, and growth deficiency. Moreover, it is the most prevalent heritable bone fragility disorder in children (Palomo, Vilaça, and Lazaretti-Castro 2017; Rossi, Lee, and Marom 2019; Trejo and Rauch 2016; Marini et al. 2017; Hoyer-Kuhn, Netzer, and Semler 2015). OI is a skeletal dysplasia characterized by bone fragility and high incidence of fractures that may occur with minimal or no trauma (Rossi, Lee, and Marom 2019; Marini et al. 2017). Fractures may involve atypical locations. Vertebral fractures occur in about 70% of OI patients. Joint hypermobility is also common and gray or blue scleral hue is a predominant OI feature (Rossi, Lee, and Marom 2019; Marini et al. 2017). Moreover, severe OI may present prenatally by detection of in utero fractures and shortening of long bones on prenatal ultrasound (Palomo, Vilaça, and Lazaretti-Castro 2017; Rossi, Lee, and Marom 2019; Marini et al. 2017). OI is currently diagnosed using patient history, clinical examination, lumbar spine BMD, bone biochemistry, and image analysis (CT and/or MRI scans) (Palomo, Vilaça, and Lazaretti-Castro 2017; Marini et al. 2017; Hermie, Horvath, and Van Cauter 2017). Interestingly, Ashinsky et al. have shown that multiparametric classification using quantitative MRI could detect at the skin level

differences between OI patients and unaffected individuals, suggesting the potential of MRI for the clinical OI diagnosis (Ashinsky et al. 2016). However, the molecular diagnosis using DNA sequence analysis can pinpoint the exact OI cause and provide information about the recurrence risk to affected individuals and their families (Palomo, Vilaça, and Lazaretti-Castro 2017; Trejo and Rauch 2016). There is no cure for OI and among the clinical and chirurgical therapies (largely supportive at present), the bisphosphonate therapy has shown remarkable effect where treatment efficacy and follow ups are usually assessed though image analysis (Palomo, Vilaça, and Lazaretti-Castro 2017; Hermie, Horvath, and Van Cauter 2017; Dwan et al. 2016).

Lastly, some skeletal disorders can result from primary or secondary tumors. Primary bone tumors are rare, accounting for < 0.2% of malignant neoplasms registered in the EUROCARE (European Cancer Registry based study on survival and care of cancer patients) database (Casali et al. 2018), and in particular osteosarcoma (OS) represents < 1% of all cancers diagnosed in the United States (Harrison et al. 2018). OS is classically described as a high grade spindle shaped neoplasm with malignant cells that produce osteoid (Harrison et al. 2018). However, OS is the first primary cancer of bone (incidence: 0.3 per 100,000 per year) with a relatively high incidence in the second decade of life (incidence: 0.8–1.1 per 100,000 per year at age 15–19 years) (Casali et al. 2018). Most of the OSs of younger patients arise in the metaphysis of long bones with the most common sites being the extremities (distal femur, proximal tibia, and proximal humerus) (Harrison et al. 2018), while the axial tumor sites increases with age. Conventional radiography is the first radiological investigation. However, MRI investigation of the whole compartment with adjacent joints is regarded today as the best modality for local staging of extremities and pelvic tumors (Casali et al. 2018; Hao et al. 2020). The final diagnosis as for the disease grading is based on biopsy, histology, and molecular assessment. Curative treatment consists of chemotherapy and surgery (Casali et al. 2018; Hao et al. 2020). In the case of chemotherapy treatment, dynamic MRI is reliable for the evaluation of changes in tumor vascularity (Hao et al. 2020; Saleh et al. 2020).

2.2. Clinical Approach

The clinical evaluation of bone status is mainly based on the dual-energy X-ray absorptiometry (DXA), which gives information about the bone mineral density (BMD). The whole body or a bone segment is scanned using X-rays and a 2D projection of bone density is evaluated using a standard reference. Although this technique has been classified as being minimally invasive, the radiation deposition dose for a whole body DXA examination is 0.0042 mSv, and can reach up to 0.009 mSv and 0.013 mSv

respectively for the hip and the spine examination (Damilakis et al. 2010a). DXA is the most common screening evaluation test for osteoporosis and body composition (whole body percent fat). Since the proportion of cortical bone is often larger, DXA is more sensitive to the presence and quality of the cortical bone. DXA can then be considered as poorly sensitive to trabecular bone alterations. Accordingly, recent studies have shown that DXA is not well suited to discriminate between patients with and without fragility fractures while this would be possible with quantitative microarchitecture analysis (G. Chang, Honig, et al. 2015a; G. Chang, Deniz, et al. 2014a; Agten et al. 2018; D. Guenoun et al. 2020a).

For clinical applications, bone inner morphology can be assessed using quantitative computed tomography (qCT), an X-ray based technique, which could be used to assess central and peripheral skeletal sites. The acquired volumes of interests are reconstructed from a stack of images, which can reach n = 900 images for a 45-cm abdominal-thorax scan, with a radiation deposition dose of 0.06–0.3 mSv/image. On that basis, this technique is considered as highly radiative (Damilakis et al. 2010a; Rad et al. 2011). On the contrary to DXA, the tomographic reconstruction and the resolution power of qCT can provide information related to the inner bone morphology. For deep bone segments, the corresponding image resolution ranges between 0.160 and 0.300 mm due to radiations issues (Adams 2009). For bone extremities, i.e., radii and tibiae, qCT can be replaced by high-resolution peripheral computed tomography (HR-pQCT), which provides a higher resolution, i.e., between 0.040 and 0.150 mm (Boutroy et al. 2005a; Adams 2009). Due to a low benefit–risk ratio, qCT and HR-pQCT are not currently used for the diagnosis of bone diseases in clinical practice.

3. MRI Based Approach

A non-invasive alternative to DXA and qCT could be MRI. Over the last two decades, a large number of studies have intended to assess bone microstructure using MRI. The initial investigations have been performed using T1-weighted spin echo sequences characterized by short TR (<1200 ms) and short TE (<25 ms) in distal radius and calcaneus (Majumdar et al. 1999a; 1997a; Ladinsky et al. 2007; Thomas M. Link et al. 1998). Due to technical advances, tibiae (Roland Krug et al. 2008a; X. H. Zhang et al. 2008; N. Zhang et al. 2013), spine (Majumdar et al. 1997a; Chamith S. Rajapakse et al. 2012a), and proximal

femur (G. Chang, Honig, et al. 2015a; G. Chang, Deniz, et al. 2014a; Roland Krug et al. 2005a; G. Chang, Rajapakse, et al. 2015a) have been investigated. MRI of trabecular microstructure can be obtained by imaging the marrow phase inside the bone segment, which appears as a hyperintense signal in conventional MR images. Using higher field MRI, i.e., 3T one can expect an increased signal to noise ratio (SNR), which can be translated either in a reduced acquisition time or an increased image resolution. Over the last decades, due to the higher availability of high-field (HF) MRI scanners, a large number of studies have been dedicated to the MRI assessment of osteoporosis (Roland Krug et al. 2008a; G. Chang, Honig, et al. 2015a; G. Chang, Deniz, et al. 2014a; D. Guenoun et al. 2020a; N. Zhang et al. 2013; Roland Krug et al. 2005a; G. Chang, Rajapakse, et al. 2015a). Very recently, clinical FDA and CE-approved ultra-high field (i.e., 7T UHF) MRI scanners with announced MSK applications have become available. Their clinical availability is still poor and the coming results will be of utmost importance to decide about the future of UHF MRI for clinical purposes.

Using MRI, the most common extrapolated features are the bone volume fraction (BVF), the trabecular thickness (Tb.Th), spacing (Tb.Sp), and number (Tb.N) (G. Chang, Honig, et al. 2015a; D. Guenoun et al. 2020a).

3.1. Technical Considerations for Clinical Usefulness

A signal to noise ratio (SNR) of 10 has been reported as the minimum value for the investigation of bone microarchitecture (Wehrli 2007). The scan time considered acceptable for clinical examination has to range between 10 and 15 min. As a result, the minimum voxel size, which has been obtained at 1.5T was between 0.135 and 0.250 mm while the slice thickness was between 0.3 and 1.5 mm. One has to keep in mind that SNR would be higher for superficial anatomical sites (radius or calcaneus compared to deeper anatomical sites, e.g., proximal femur) leading to higher resolution or shorter acquisition time. Moreover, SNR can be increased at higher field strengths and/or using multichannel coils (Wehrli 2007; Brown et al. 2014; Techawiboonwong et al. 2005a; G. Chang et al. 2017b).

MRI pulse sequences such as gradient recalled echo (GRE) and spin echo (SE) have also been tested at different field strengths (Roland Krug et al. 2008a; 2005a; R. Krug et al. 2008a). It has been shown that SE sequences were less susceptible to partial volume effects as compared to GRE sequences and that GRE were more sensitive to trabecular broadening than SE. These results indicate that SE sequences would provide more accurate results regarding trabecular characteristics (R. Krug et al. 2008a; Roland Krug et

al. 2008a). However, the use of these pulse sequences might be problematic using ultra-high field (UHF) MRI considering power-deposition issues.

A list of the main literature references, scanned regions, sequences, and principal MRI setup parameters is reported in Table 1.1.

Table 1. 1 : List of the main magnetic resonance imaging (MRI) parameters and sequences.

Anatomical Site	Clinical History	Specimen /Patient	Acq. Time	Slice Thickness [mm]	Pix. Size [mm]	FOV [mm]	MRI Seq.	Main Field	N°	Reference
distal radii	type 2 diabetes	patient	12 min 9 s	1	0.195 × 0.195	100 × 100	FSE	1T	[78]	Pritchard et al.
calcaneus	osteoporotic hip fractures	patient	15 min 15 s	0.5	0.195 × 0.195	100 × 100	GE	1.5T	[67]	Link et al.
distal radii	healthy	patient	16 min 25 s	0.5	0.156 × 0.156	80 × 45	3D FLASE	1.5T	[75]	Techawiboonwong et al.
distal radii	healthy	patient	3 min 15 s	0.5	0.156 × 0.156	80 × 45	3D SSFP	1.5T	[75]	Techawiboonwong et al.
distal radii	NA	specimen	15 min	0.3	0.156 × 0.156	80	GE	1.5T	[13]	Majumdar et al.
lumbar spine	osteoporotic	patient	16 min	0.7	0.156 × 0.156	80 × 80	GE	1.5T	[65]	Majumdar et al.
distal radii	hip fractures	patient	NA	0.5	0.156 × 0.156	80 × 80	GE	1.5T	[16]	Majumdar et al.
distal radii	NA	specimen	58 min (1) 16 min (2)	0.3 (1) 0.9 (2)	0.153 × 0.153	49×78	SE	1.5T	[79]	Link et al.
prox. femur	NA	specimen	74 min (1) 27 min (2)	0.3 (1) 0.9 (2)	0.195 × 0.195	75 × 100	SE	1.5T	[80]	Link et al.
prox. femur	healthy	patient	6 min 12 s	1.5	0.234 × 0.234	NA	3D FIESTA	1.5T	[71]	Krug et al.
distal tibiae	NA	specimen	40 min	0.16	0.160 × 0.160	70 × 63	3D FLASE	1.5T	[81]	Rajapakse et al.
lumbar spine	NA	specimen	15 min 23 s	0.41	0.137 × 0.137	70 × 64 × 13	3D FLASE	1.5T	[70]	Rajapakse et al.
distal radii(1) distal tibiae(2)	osteopenic and osteoporotic	patient	12 min (1) 16 min (2)	0.4	0.137 × 0.137	70 × 40(1) 70 × 50(2)	3D FLASE	1.5T	[66]	Ladinsky et al.
distal femur	cerebral palsy (children)	patient	9 min 52 s	0.7	0.175 × 0.175	90	3D fast GE	1.5T	[82]	Modlesky et al.
distal radii(1) distal tibi.ae(2)	osteoporotic	patient	12 min (1) 16 min (2)	0.41	0.137 × 0.137	70 × 40 × 13 (1) 70 × 50 × 13 (2)	3D FLASE	1.5T	[83]	Rajapakse et al.
prox. femur	NA	specimen	16 min 55 s	1.1	0.21 × 0.21	120	TSE	3T	[84]	Soldati et al.
prox. femur	healthy	patient	12 min 43 s	1.5	0.234 × 0.235	NA	3D FIESTA	3T	[71]	Krug et al.
distal radii, distal tibiae	NA	specimen	< 10 min	0.5	0.156 × 0.156	NA	GE	3T	[77]	Krug et al.
distal radii, distal tibiae	NA	specimen	< 10 min	0.5	0.156 × 0.156	NA	GRE	3T	[77]	Krug et al.
distal radii, distal tibiae	NA	specimen	< 10 min	0.5	0.156 × 0.156	NA	SE	3T	[77]	Krug et al.
distal tibiae	osteoporotic	patient	15 min	0.41	0.137 × 0.137	70 × 64 × 13	3D FLASE	3T	[69]	Zhang et al.
prox. femur	fragility fractured	patient	25 min 30 s	1.5	0.234 × 0.234	120	FLASH	3T	[60]	Chang et al.

prox. femur	long-term glucocorticoid	patient	15 min 18 s	1.5	0.234 × 0.234	100	FLASH	3T	[72]	Chang et al.
distal radii	HR+ breast cancer	patient	7 min	0.34	0.170 × 0.170	65	GE	3T	[85]	Baum et al.
distal femur	osteoarthritis	patient	9 min 18 s	1	0.180 × 0.180	100	3D B-FFE	3T	[86]	Liu et al.
prox. tibia	osteoarthritis	patient	3 min	2.8	0.230 × 0.240	120 × 123	SE	3T	[87]	MacKey et al.
prox. tibia, distal femur	osteoarthritis	patient	NA	1	0.195 × 0.195	100	FIESTA-c	3T	[88]	Chiba et al.
prox. tibia, distal femur	osteoarthritis	patient	NA	1	0.195 × 0.195	160	SPGR	3T	[88]	Chiba et al.
distal tibiae	NA	specimen	7 min	0.41	0.137 × 0.137	70 × 53 × 13	3D FLASE	3T	[19]	Rajapakse et al.
prox. femur	NA	specimen	16 min 45 s	1.5	0.13 × 0.13	130	TSE	7T	[89]	Soldati et al.
prox. femur	NA	specimen	37 min 36 s	0.5	0.170 × 0.170	140 × 140	GRE	7T	[62]	Guenoun et al.
distal tibiae	healthy	patient	19 min 10 s	0.5	0.156 × 0.156	NA	SE	7T	[17]	Krug et al.
distal tibiae	healthy	patient	18 min 25 s	0.5	0.156 × 0.157	NA	FP	7T	[17]	Krug et al.
vertebrae (1 axial, 2 sagittal)	NA	specimen	34 min (1) 51 min (2)	0.4 (1) 0.5 (2)	0.170 × 0.170	140 × 140	GRE	7T	[90]	Guenoun et al.
distal femur	fragility fractured	patient	7 min 9 s	1	0.234 × 0.234	120	FLASH	7T	[18]	Chang et al.
femurs, tibiae, vertebrae	NA	specimen	120 min	0.05	0.05 × 0.05	6.4 × 6.4 × 25.6	SE	9.4T	[91]	Rajapakse et al.

3.2. Microstructure Investigation

In the majority of MRI literature, the morphological parameters that are reported are BVF, Tb.Th, Tb.Sp, and Tb.N (Roland Krug et al. 2005a; R. Krug et al. 2008a; Hipp et al. 2009). In addition, some groups have proposed some other features such as an erosion index, trabecular rod- and plate-like structures, trabecular plate-to-rod ratio, trabecular isolation, and fractal lacunarity (G. Chang, Honig, et al. 2015a; Zaia et al. 2021).

These microarchitectural parameters have been generated from the post processing of both 2D and 3D images. The corresponding analyses were performed in binarized images or in original grey level intensities. All these approaches have tried to take into account partial volume effects occurring given the poor resolution of MRI as compared to the trabeculae dimension (D. Guenoun et al. 2020a; Chamith S. Rajapakse et al. 2010a; Soldati, Bendahan, et al. 2020). So far, no standard reference has been suggested.

Studies performed at different MRI field strength in postmenopausal woman with fragility fractures have illustrated microstructural alterations (reduced BVF and increased Tb.Sp) whereas DXA T-scores were unchanged. In a study conducted in distal radii at 1.5T, Kijowsky et al. showed that post-menopausal woman had a slightly lower (−9%) bone volume fraction and a higher erosion index (+17%) compared to controls (Kijowski et al. 2012). Krug et al. in a study conducted on the proximal femurs of six

healthy males and females using both 1.5T and 3T MRI showed good correlation (r up to 0.86) between structural parameters obtained from the two different field strengths. However, they reported that bone structure of the proximal femur was substantially better depicted at 3T than 1.5T (Roland Krug et al. 2005a). Microstructure alterations have been reported in a large variety of cases including chronic kidney disease (CKD) (Sharma, Toussaint, Elder, Masterson, et al. 2018; Ruderman et al. 2020), HIV-infection (Kazakia et al. 2018) glucocorticoid-induced osteoporosis (G. Chang, Rajapakse, et al. 2015a), or disuse osteoporosis (Modlesky, Subramanian, and Miller 2008).

In a 3T MRI study conducted in distal tibiae of 20 patients with CKD, Ruderman et al. reported trabecular deterioration together with reduced cortical thickness (Ruderman et al. 2020). Moreover, a study conducted on 30 patients affected by end stage renal disease (ESRD) it has been shown that Tb.N, Tb.Th, and whole bone stiffness were significantly lower ($p < 0.01$) is ESRD compared to controls (Leonard et al. 2019). A similar study conducted on distal tibiae of 11 kidney transplant recipient patients have high-lightened post-transplant deterioration in trabecular bone quality (Sharma, Toussaint, Elder, Rajapakse, et al. 2018). In a study conducted in proximal femurs at 3T, glucocorticoid treated patients had a largely reduced (−50.3%) Tb.N, trabecular plate-to-rod ratio (−20.1%), and a largely increased (+191%) Tb.Sp (G. Chang, Rajapakse, et al. 2015a). Patients with a disuse osteoporosis displayed similar anomalies for BVF (−30%), Tb.N (−21%), Tb.Th (−12%), and Tb.Sp (+48%) (Modlesky, Subramanian, and Miller 2008). Chang et al. (G. Chang, Honig, et al. 2015a) further supported and extended these results in a study conducted in distal femur at 7T. In 31 subjects with fragility fractures, they reported a lower BVF (–3%), Tb.N (–6%), and erosion index (–6%). Moreover, in a 7T MRI study conducted in the distal radius of 24 women, Griffin et al. reported a trabecular bone microarchitecture gradient with an overall higher quality (+123% BVF, +16% Tb.N) distally (epiphysis) than proximally (diaphysis) (Griffin et al. 2017).

Ultra-high field MRI can provide images with a smaller pixel size (0.156×0.156 mm) as compared to the resolution achieved at lower field strength (0.234×0.234 mm for example at 3T (Roland Krug et al. 2005a)(Roland Krug et al. 2008a)). In a dual 3T-7T study conducted in distal tibiae of 10 healthy volunteers, Krug et al. reported that metrics computed at higher field strength were different than those quantified from 3T MR images. More specifically, UHF measurements illustrated increased BVF (+22%) and Tb.Th (+25%) whereas Tb.Sp (−21%) and Tb.N (−4%) were both decreased (Roland Krug et al. 2008b). These results suggest a higher discriminative power of UHF MRI for trabecular features.

3.3. Microstructure vs. DXA

In a study conducted in 32 postmenopausal women, Kang et al. showed a good correlation between DXA-based BMD and MRI T2 and T2 * in calcaneus ($r = -0.8$, $p < 0.001$) and spine ($r = -0.53$, $p = 0.002$) (Kang et al. 1999). Similar results have been reported for the femoral neck (Majumdar et al. 1997a; Guglielmi et al. 1996) with a good correlation ($r = 0.74$, $p < 0.001$) between DXA-based BMD and T2 * values (Arokoski et al. 2002a). T2 * relaxation time illustrates the susceptibility differences between trabecular and bone marrow leading to signal loss due to magnetic field inhomogeneities. MRI-derived T2 * has been shown to correlate with DXA results in several anatomical areas such as calcaneus, distal radius, and Ward's area in the femoral neck (Brismar 2000; Stephan Grampp et al. 1996). Based on T2 * measurements, Schmeel et al. reported a significant difference between benign and malignant neoplastic vertebral compression fractures (VCFs). A 72% diagnostic accuracy was computed (Schmeel, Luetkens, Feißt, et al. 2018). Furthermore, a strong negative correlation was found between the pelvic bone marrow adipose tissue (BMAT) calculated in 56 healthy women using MRI and the corresponding DXA-based BMD ($r = -0.646$, $p < 0.001$) (Shen et al. 2007). The negative correlation indicates that patients with decreased bone mineral density are characterized by an increased fat content in bone marrow (Shen et al. 2007; Griffith et al. 2005; Woods et al. 2020).

Based on highly resolved MR images (0.150–0.300 mm in-plane pixel size), Chang et al. showed a lack of significant correlation between DXA-computed BMD T-scores and MRI computed microarchitectural parameters in the femoral neck in both controls and glucocorticoid-treated patients (G. Chang, Rajapakse, et al. 2015a; G. Chang et al. 2018a). Similar results were also reported more recently in subchondral tibiae (Agten et al. 2018), proximal femurs (D. Guenoun et al. 2020a; Soldati, Bendahan, et al. 2020), vertebrae (Daphne Guenoun et al. 2017a), and on patients affected by diabetes (S. C. Chen et al. 2019; Abdalrahaman et al. 2017). Guenoun et al. reported that the combination of BVF and BMD was able to improve the prediction of the failure stress (from $r2 = 0.384$ for BMD alone to $r2 = 0.414$). All the presented results suggest that although density and structure metrics illustrate bone quality, microarchitectural parameters provide additional information regarding skeletal fragility.

3.4. Voxel Size and Microstructure

Results from the literature showed that image resolution is a key parameter for the assessment of bone microarchitecture. Importantly, a distinction must be made between in-plane and through-planes resolution. For specific oriented plane (mostly

perpendicular to the trabecular), an in-plane MRI pixel size in the same order of magnitude than Tb.Th dimension is enough to measure morphological parameters similar to those extrapolated using gold standard method and so both ex vivo (μCT) (Soldati, Bendahan, et al. 2020; Soldati, Pithioux, et al. 2020) and in vivo (HR-pQCT) (R. Krug et al. 2008a). If one intends to assess bone microstructure using small isovolumetric voxels (0.15 mm), close to the actual thickness of the trabeculae, with an acceptable SNR, acquisition times would exceed the in vivo acceptable duration. One can increase the SNR and reduce the acquisition time with an increased slice thickness while keeping the plane pixel size constant. Accordingly, the radius morphological parameters computed from similar in-plane pixel sizes and different slice thicknesses (0.156×0.156×0.3 mm (Majumdar et al. 1996a), 0.156×0.156×0.5 mm (Majumdar et al. 1999a; Kindler et al. 2017), 0.156×0.156×0.7 mm (Majumdar et al. 1997a), and 0.153×0.153×0.9 mm (Thomas M. Link et al. 2003a)) were comparable. In fact, the bone inner microarchitecture appeared to be a mixture of oriented plates- and rod-like structures. The parallel trabecular plates structures are separated by bone marrow and are perpendicular to the coronal plane (Koshi 2017). On that basis, increasing the in-plane pixel size should provide more accurate results independently of the slice thickness. As reported by Mulder et al., the calculated volume of ellipsoid at high resolution (0.1×0.1 mm) is independent from the anisotropy factor but related to the orientation (Mulder et al. 2019a).

Different studies performed in distal radii at 1.5T, using similar in-plane pixel size and using different slice thicknesses above 0.3 mm, reported comparable morphological results (Majumdar et al. 1996a; 1999a; Kijowski et al. 2012). However, in a study conducted by Majumdar et al. in 39 distal radii specimens acquired using 1.5T MRI and contact radiograph, 0.9-mm thick MR images performed better than those obtained from 0.3-mm images. This was explained with the significantly higher SNR (18.2 in 0.9-mm thick images and 9.3 in 0.3-mm sections) (Thomas M. Link et al. 2003a). Similar results were obtained in vivo in distal radii scanned at 1.5T (0.156×0.156×0.5 mm) with an acceptable SNR around 10 (Techawiboonwong et al. 2005a). Moreover, wrists and distal tibiae scanned in patients using 1.5T with pixel sizes in the same range of trabecular thickness (0.156×0.156×0.410 mm (Ladinsky et al. 2007) and 0.137×0.137×0.410 mm (C. S. Rajapakse et al. 2014)) reporting lower acquisition time for wrist (12 min) than for tibiae (16 min) and good image quality in both anatomical regions. In a second study conducted by Majumdar et al., 31 cadaveric proximal femurs were scanned at 1.5T with an in-plane pixel size of 0.195×0.195 and comparing two different slice thicknesses (0.9 and 0.3 mm). The SNR achieved was 25.2 and 13.8 for the larger and smaller slice thickness respectively. The corresponding acquisition times were very long (27:19 and 73:14 min), i.e., much longer than what could be accepted in clinics (T.M. Link et al. 2003).

The knee articulation has also been assessed in the study of Rajapakse et al., 17 distal tibiae specimens were scanned at 3T (0.137×0.137×0.410 mm) in 7 min (Chamith S. Rajapakse et al. 2018a). These results where extended in vivo by Zhang et al., in the distal tibiae of 20 postmenopausal women with osteoporosis. The scanning time using 3T MRI (0.137×0.137×0.410 mm) was less than 15 min (N. Zhang et al. 2013). Krug et al. further confirmed these results in a study comparing 3T MRI (0.156×0.156×0.5 mm) and X-ray based techniques both ex vivo (5 tibiae and 3 radii) and in vivo (5 radii and 6 tibiae). While the scanning time was less than 10 min, correlations were reported between both methods and so for the whole set of parameters, i.e., BVF ($r = 0.83$) and Tb.Sp ($r = 0.7$) (R. Krug et al. 2008b). Liu et al. also reported 3T MR images (pixel size 0.180×0.180 mm, acq. time 9:18 min) of 92 distal femurs divided in three groups (without osteoarthritis, mild osteoarthritis, and severe osteoarthritis) reporting progressively lower BVF and higher erosion index from healthy patients to those affected by severe osteoarthritis (C. Liu et al. 2018), extending previous results (C. Liu et al. 2017; MacKay et al. 2017; Bolbos et al. 2008).

3.5. Main Magnetic Field Strength Effect

The technical advantages of moving from 1.5T to 3T or 7T MR scanners were clearly visible in the acquisition of deeper anatomical sites keeping the spatial pixel size in the same order of the trabecular thickness, the acquisition time (acq. Time), and the SNR (>10) being clinically compatible. On that basis, 7T MR scanners have been tested mostly for the acquisition of distal and proximal femur, which represent a clinical important fracture site and one of the most invalidating (van Oostwaard 2018).

In a comparative study conducted in vivo in proximal femur at 1.5 and 3T, Krug et al., reported as expected a 1.6 time-SNR increase together with a corresponding contrast-to-noise ratio (CNR) increase at higher magnetic field. While the 3T images clearly showed the trabecular bone structure, the image resolution did not allow a proper trabecular morphological analysis (Roland Krug et al. 2005a). In a more recent study in the knee joint of 16 healthy volunteers scanned at 1.5T (0.6×0.6×0.6 mm, acq. time 7:15 min) and 3T (0.5×0.5×0.5 mm, acq. time 6:51 min), Abdulaal et al. reported significantly higher SNR ($p < 0.05$) allowing a better trabecular characterization at 3T than 1.5T (Abdulaal, n.d.). Moreover, 3T MRI could be used to successfully scan radii with an in-plane pixel size comparable to the trabecular thickness and an acquisition time (10 min) lower than what commonly needed at 1.5T (Kindler et al. 2017; Folkesson et al. 2011). Jarraya et al., on a study conducted in 50 distal radii scanned at both 3T (0.2×0.2×2.0 mm, acq. time 4:29 min) and 7T MR (0.125×0.125×2.0 mm, acq. time 3:16 min), reported a statistical significant difference of horizontal and fractal dimensions between patients with chronic wrist

disease and controls (Jarraya et al. 2021). A similar comparative analysis has been performed between 3T and 7T MRI (0.156×0.156×0.5 mm, acq. time lower than 10 min) and HR-pQCT. Krug et al. showed that tibial trabecular structures were over-represented at higher field strength. Due to susceptibility-induced broadening smaller trabeculae normally not visible due to partial volume effects may be emphasized at 7T (Roland Krug et al. 2008b). Moreover, using UHF MRI (0.234×0.234×1.0 mm, acq. time 7 min), Chang et al. reported that microarchitectural parameters could discriminate between patients and controls and could detect bone deterioration in women with fragility fractures for whom BMD was normal (G. Chang, Honig, et al. 2015a). In addition to the effects of magnetic field strength, Krug et al. also assessed the potential differences between GRE and TSE sequences at 7T. SNR was slightly higher for GRE sequences (13.2 vs. 11.9) while the bone marrow signal was more homogeneous using TSE sequences. This large homogeneity is related to a reduced susceptibility-induced broadening of the trabeculae so that the morphological analysis showed decreased BVF (−13%) and Tb.Th (−23%). These values were closer to those reported using the HR-pQCT reference method (Roland Krug et al. 2008b). Furthermore, in a study conducted in three cadaveric proximal femurs scanned at 7T (0.130×0.130×1.5 mm, acq. time 16 min) and using μCT, Soldati et al. reported no statistical difference between the methods and so for the whole set of morphological parameters (Soldati, Bendahan, et al. 2020). These preliminary results strongly suggest that UHF MRI could be of interest for the in vivo assessment of bone microarchitecture particularly for the deep anatomical regions.

3.6. Comparison with CT Measurements

Validation of the bone morphological parameters derived from the high-resolution MR images has usually been performed through the comparison with X-ray based techniques (qCT, HRpQCT, and μCT).

Ex-vivo

Ex vivo studies have been performed in different body parts. However, due to the samples size (<5 cm3) and the commonly used preparation protocols (replacement of marrow), they remain poorly representative of the in vivo conditions (Hipp et al. 2009; Majumdar et al. 1996a; Thomas M. Link et al. 2003a; Soldati, Bendahan, et al. 2020; Weiger, Stampanoni, and Pruessmann 2013). One of the first studies validating MR bone structure measurements was performed by Hipp et al. in cubic bovine trabecular bone from several anatomical sites using optical and micro-MRI methods. BVF and Tb.N were linearly related (r2 = 0.81 and r2 = 0.53 respectively) and did not differ statistically (p =

0.96 and p = 0.17) (Hipp et al. 2009; Weiger, Stampanoni, and Pruessmann 2013). These results were confirmed and extended in human specimens by Majumdar et al., in a study conducted in 7 cubic specimens of trabecular bone extracted from cadaveric radii scanned at 1.5T (0.156×0.156×0.3 mm) and using μCT (0.018 mm isovolumetric). The results showed a good correlation for the whole set of metrics with BVF and Tb.Th performing the best (r = 0.77 and 0.87 respectively) and Tb.Sp and Tb.N the worst (r = 0.53 and 0.6 respectively). However a significative statistical difference (p > 0.01) was reported for all the calculated features (Majumdar et al. 1996a). MRI images with an in plane pixel-size lower than the smallest trabecular thickness order (0.1 mm) are not easily reachable. On that basis, one cannot expect to fully characterize it.

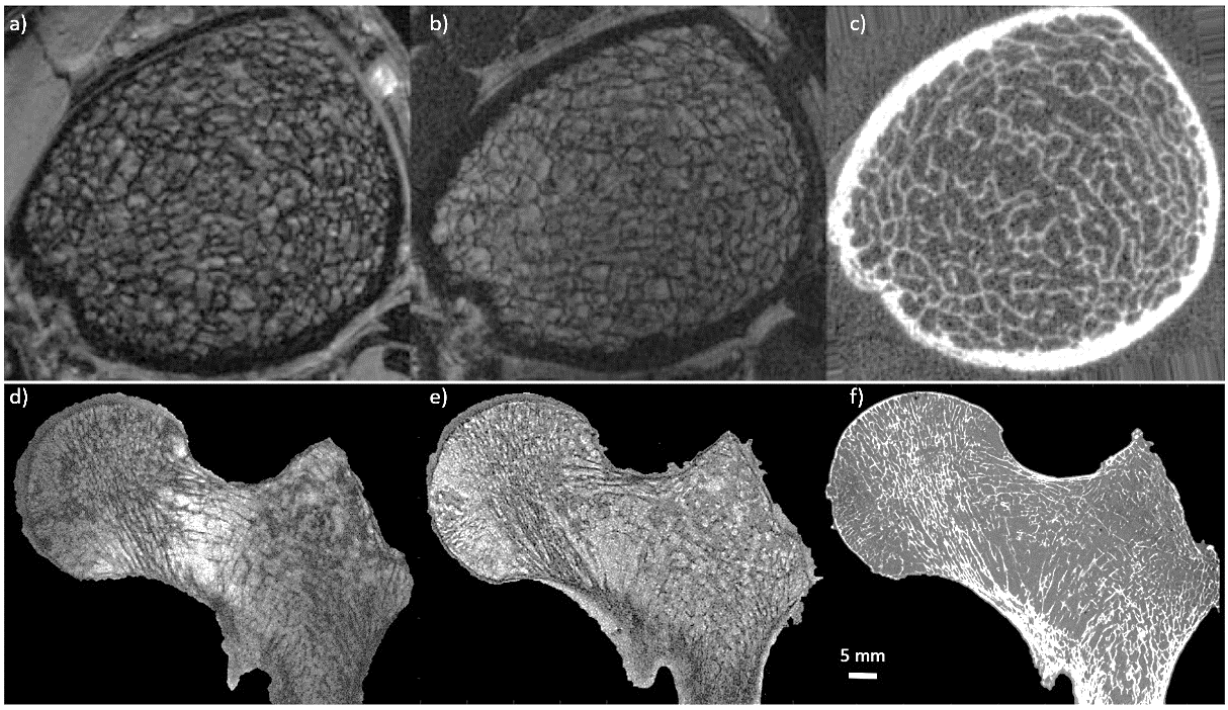

Figure 1. 7: Comparison between MRI and CT. (first row) MR images of in vivo distal tibia acquired using gradient echo sequence at 7T MRI (a) (0.156×0.156×0.5 mm) and 3T MRI (b) (0.156×0.156×0.5 mm), and compared with high-resolution peripheral computed tomography (HR-pQCT) (c) (0.082 mm^3) (**reproduced from J. of Mag. Res. Im. 27:854–859 (2008)**). (second row) MR images of cadaveric proximal femur acquired using turbo spin echo sequence at 7T MRI (d) (0.13×0.13×1.5 mm) and 3T MRI (e) (0.21×0.21×1.1 mm), and compared with μCT (f) (0.051 mm^3). Note that using MRI, the trabecular bone appears black and bone marrow delivers the bright signal whereas for HR-pQCT and μCT the trabecular bone is shown bright. Additionally, note that the trabecular network is clearly more enhanced at 7T compared to 3T.

Moreover, these findings were further extended in a larger study conducted in 39 distal radius specimens scanned at 1.5T MRI (0.152×0.152×0.9 mm) and using contact radiography (0.05 mm isovolumetric). The results showed a significant correlation (r > 0.61) between bone microstructure parameters derived from both methods with Tb.Sp

and BVF providing the highest correlations (r = 0.69 and p = 0.75 respectively) (Thomas M. Link et al. 2003a). More recently, Rajakapse et al. conducted a study in 13 cylindrical specimens (7 proximal femurs, 3 proximal tibiae, and 3 third lumbar vertebrae) extracted from 7 human donors and computed microarchitectural parameters using 9.4T micro-MRI (0.050 mm isovolumetric) and μCT (0.021 mm isovolumetric). Architectural parameters were found to highly correlate between these two modalities with a slope close to unity (r2 ranging from 0.78 to 0.97) (Chamith S. Rajapakse et al. 2009a). In a more recent study conducted in three cadaveric entire proximal femurs evaluating the trabecular morphology using 7T MRI (0.13×0.13×1.5 mm) and comparing the results with those acquired using μCT (0.051 mm isovolumetric) (Fig. 1.7), Soldati et al. showed a good intraclass correlation coefficient for all the parameters (ICC > 0.54) between 7T and μCT (Soldati, Bendahan, et al. 2020) illustrating that bone morphological metrics of human specimens can be properly assessed using MRI. Moreover, due to the comparison between MR images and gold standard high-resolution CT images, it has been shown that trabecular features derived from images with a similar pixel size provide statistically comparable results. However, when assessing bone trabeculae using MRI, partial volume effects will occur and will affect image segmentation and trabeculae quantification.

In-Vivo

The MRI potential for the bone microstructure has also been assessed in vivo in anatomical regions more affected by osteoporosis, i.e., tibiae and radii, vertebrae (Majumdar et al. 1997a; H.-Z. Wu et al. 2020; Bandirali et al., n.d.), distal (G. Chang, Honig, et al. 2015a; C. Liu et al. 2017; 2018; Chiba et al. 2012; Bolbos et al. 2008), and proximal femurs (G. Chang, Deniz, et al. 2014a; Roland Krug et al. 2005a; G. Chang, Rajapakse, et al. 2015a). Microarchitectural parameters extrapolated from 3T MRI (0.156×0.156×0.5 mm) and compared to HR-pQCT of tibiae and radii of 11 healthy volunteers showed good correlation for BVF (r = 0.83) and Tb.Sp (r = 0.7) in tibiae and good correlation for all the microarchitecture parameters investigated in radii (r = 0.65, 0.95, 0.83, and 0.63 for BVF, Tb.N, Tb.Sp, and Tb.Th respectively) (R. Krug et al. 2008a). Kazakia et al. extended these results in a study conducted in tibiae and radii of 52 postmenopausal scanned at 3T MRI (0.156×0.156×0.5 mm) and using HR-pQCT. A significant correlation between MRI and HR-pQCT has been reported for Tb.N (r2 = 0.52) and Tb.Sp (r2 = 0.54–0.60) with no statistical difference for these two parameters. Poor correlations were reported for BVF and Tb.Th (r2 = 0.18–0.34) (Kazakia et al. 2007). Similar results were also reported by Folkesson et al., in a study conducted in 52 postmenopausal women scanned at 3T (0.156×0.156×0.5 mm) and using HR-pQCT in both tibiae and radii. All the structural parameters derived from MRI were highly

correlated to those obtained from HR-pQCT (Tb.N was equal to 0.68 and 0.73 and Tb.Sp was equal to 0.77 and 0.67 for tibiae and radii respectively) with the exception of BVF and Tb.Th for which correlations were less significant (BVF was equal to 0.61 and 0.39 and Tb.Th was equal to 0.43 and 0.32 for tibiae and radii respectively) (Folkesson et al. 2011). Furthermore, Krug et al. confirmed and extended these results in a study conducted in distal tibiae of 10 healthy volunteers scanned at 3T and 7T (0.156×0.156×0.5 mm for both techniques). The results showed that microarchitectural parameters extracted from HR-pQCT images had higher correlation with those extracted from 7T MR images (r equal to 0.73 for BVF, 0.69 for Tb.N, 0.89 for Tb.Sp, and 0.13 for Tb.Th) as compared to 3T MR images (r = 0.83, 0.49, 0.67, and 0.15 for BVF, Tb.N, Tb.Sp, and Tb.N respectively) (Fig. 1.7). Interestingly, the corresponding absolute values did only differ by 0.6% for 7T and 3% for 3T (Roland Krug et al. 2008b). All the findings reported above indicate good correlations for Tb.Sp and Tb.N between MRI and HR-pQCT. In contrast, this was not the case for BVF and Tb.Th. The limited resolution in MRI leads to partial volume effects responsible for the exclusion of the smallest trabeculae, while susceptibility artifacts enhance the remaining trabeculae leading to an overestimation of Tb.Th. This double effect seems limited when using UHF MRI. Indeed, good correlations were found between MRI and HR-pQCT metrics although a poor correlation was still existing for Tb.Th.

3.7. Reported Limitations

The main limitation reported regarding the bone morphology evaluation using MRI is related to partial volume effects resulting from the ratio between the resolution offered by the MR machines and the trabecular dimension. The minimum trabecular size is in the order of 0.1 mm. If the pixel size is larger than this limit, trabecular broadening would occur. In the worst possible scenario, trabecular broadening would cause the disappearance or the aggregation of the finest trabeculae leading to over- or underestimation of the main morphological characteristics (Majumdar et al. 1996a; D. Guenoun et al. 2020a; Roland Krug et al. 2008b; Chamith S. Rajapakse et al. 2009a; Soldati, Bendahan, et al. 2020). Majumdar et al. reported an overestimation of the BVF (3 times) and the Tb.Th (3 times) and an underestimation of the Tb.Sp (1.6 times) in the MR images (0.156×0.156×0.3 mm) compared to the 18-µm µCT images (Majumdar et al. 1996a). Many studies conducted in different anatomical sites both in vivo and in vitro have shown that increasing the main magnetic field strength may emphasize small trabecular structures, normally not visible due to partial volume effects and susceptibility-induced broadening (Roland Krug et al. 2008b; Soldati, Bendahan, et al. 2020). Moreover, several studies have

shown that spin echo sequence are less prone to partial volume effects than gradient echo ones (R. Krug et al. 2008a; Roland Krug et al. 2008b; Soldati, Pithioux, et al. 2020). In particular, Krug et al. compared gradient echo and spin echo sequences at 7T and the results showed that SE sequence provided decreased BVF (−13%) and Tb.Th (−23%) and an increase in Tb.N (13%) and Tb.Sp (1%) as compared to gradient echo (Roland Krug et al. 2008b). SE sequences have shown their higher discriminative power to resolve the bone microstructure due to a more homogeneous bone marrow signal. However, at UHF spin-echo sequences should be used carefully due to a specific absorption rate (SAR) that limits the number of acquirable images. Soldati et al. reported a maximum number of 10 acquired images using a turbo spin echo sequence at 7T in approximately 16 min.

MR imaging conducted in cadaveric specimens may suffer from an additional limitation related to air bubbles trapped in the trabecular network and leading to magnetic susceptibility effects (Chamith S. Rajapakse et al. 2009a; Soldati, Bendahan, et al. 2020). Air bubbles provide grey level intensities similar to the bone signal so that pixel misclassification could be expected. In order to properly perform MRI acquisition of cadaveric specimens air bubbles have to be removed using different strategies that have been reported and validated through images analysis (Chamith S. Rajapakse et al. 2009a; Soldati, Bendahan, et al. 2020; R. Krug et al. 2008b). The common strategy used mainly for small specimens (<5 cm3) is related to the bone marrow removal through a gentle water jet, the immersion in 1 mM Gd-DTPA saline solution to simulate the bone marrow magnetic response and the removal of air bubbles using centrifugation (approximately between 5× to 6× g, for 5 min) (Majumdar et al. 1996a; R. Krug et al. 2008b; Chamith S. Rajapakse et al. 2009a). Hipp et al. reported an alternative solution consisting in filling marrow spaces with confectioners' sugar to provide contrast between bone and marrow (Hipp et al. 2009). More recently, Soldati et al. reported no trabecular misclassification due to air bubbles by combining vacuum application and vibrational forces to large cadaveric specimens (entire proximal femurs) immersed in 1 mM Gd-DTPA saline solution (Soldati, Bendahan, et al. 2020).

4. Prospectives

In this chapter we provide an overview of the most recent results reported in the literature, which are related to the assessment of bone marrow using magnetic resonance spectroscopy and chemical shift encoding MRI, bone phosphorus content, and bone mineral density using solid-state MRI and quantitative susceptibility measurements. These techniques are considered promising to further investigate bone quality.

4.1. Magnetic Resonance Spectroscopy vs. Chemical Shift Encoding-MRI

Several MRI studies have shown that bone marrow, which is mainly composed by adipocytes (yellow marrow regions) and hematopoietic red blood cells (red marrow regions), may play a key role in the bone health and metabolism. Moreover, it has been reported that distinct alterations become increasingly evident when comparing osteoporotic subjects to controls (Fazeli et al. 2013; Sollmann et al. 2020). The bone marrow fat content can be assessed from bone marrow fat fraction (BMFF) and proton density fat fraction (PDFF) measurements (Sollmann et al. 2020; Reeder, Hu, and Sirlin 2012). Bone marrow has been actually investigated using magnetic resonance spectroscopy (MRS) and chemical shift encoding based water fat MRI (CSE-MRI).

Up to now, the most frequently used technique for bone marrow quantification has been the single-voxel proton MRS, which is also considered the gold-standard. Based on a localized scheme, water and fat components can be quantified on the basis of their respective resonance frequencies. Point-resolved spectroscopy (PRESS) and stimulated echo acquisition mode (STEAM) have been mainly used. Given that the STEAM sequence allows shorter TEs as compared to PRESS, a higher signal can be expected for the short-T2 water component of the BM spectrum (Sollmann et al. 2020).

MRS has been used to assess BMFF at the spine level (S. C. Chen et al. 2019; Singhal et al. 2018; Cordes et al. 2015; R. Chang et al. 2020; He, Fang, and Li 2019; Karampinos et al., n.d.; Sheu et al. 2018) and fewer studies have been devoted to the proximal femur (Manenti et al. 2013; Pietro 2015; Ismail et al. 2021). Correlations between BMFF and BMD or T-scores have been repeatedly reported. BMFF is elevated in osteoporotic patients and negative correlations have been reported between BMFF and BMD. He et al., in a study conducted in L2–L4 vertebrae of 123 subjects (49 with normal bone density, 38 with osteopenia and 36 with osteoporosis) scanned using PRESS at 3T (voxel size 15×15×15 mm^3) showed that BMFF was increased in patients with reduced BMD values while the

metrics were negatively correlated ($r = -0.82$, $p < 0.001$) (He, Fang, and Li 2019), further confirming previous results on the lumbar spine (L1-L2) and proximal femurs (E. W. Yu et al. 2017). In a study conducted in femoral neck of 33 postmenopausal woman using 3T MRS (PRESS sequence, single voxel 15×15×15 mm^3), Di Pietro et al. reported larger content of methylene (L13), glycerol (L41,L43), and total lipid in osteoporotic subjects (Pietro 2015). There changes suggest that MRS of bone marrow lipid profiles from peripheral skeletal sites might be a promising screening tool to identify individuals with or at risk of developing osteoporosis (Pietro 2015; Singhal and Bredella 2019).

CSE-MRI can be used to obtain a spatially resolved quantification of BMFF. Multi-echo GRE sequences are commonly used with an appropriate selection of experimental parameters (i.e., small flip angle to reduce T1 bias, and distinct correction of T2* decay effects during the postprocessing stage) (Sollmann et al. 2020; Karampinos et al., n.d.; 2018; Ruschke, n.d.). T2* decay effects have to be particularly considered when measuring the PDFF. In fact, T2* of trabecular bone is reduced due to microscopic magnetic field inhomogeneity effects (Sollmann et al. 2020).

A good agreement has been reported between BMFF measured using MRS and CSE-MRI for both spine and proximal femur (G. Li et al. 2017; Ruschke et al. 2017; Martel, Leporq, Saxena, et al. 2018). At the spine level, BMFF has been reported as increased in osteoporotic patients and inversely correlated with BMD and T-scores (Sollmann et al. 2020; G. Li et al. 2017; Y. Zhao et al. 2019). At the proximal femur level, Martel et al., reported a higher saturation (+14.7% to +43.3%), and a lower mono- (−11.4% to −33%) and polyunsaturation (−52% to −83%) in postmenopausal women. More specifically, red marrow of postmenopausal women showed a lower fat content (−16% to −24%) and a decreased polyunsaturation (−80% to −120%) in the femoral neck, greater trochanter, and Ward's triangle (Martel, Leporq, Bruno, et al. 2018). In another study, it has been reported that PDFF derived from CSE-MRI would discriminate benign osteoporotic and malignant vertebral fractures. Accordingly, Schmeel et al. reported that both PDFF and PDFFratio (fracture PDFF/normal vertebrae PDFF) of malignant VCFs were significantly lower as compared to acute benign (PDFF, 3.48±3.30% vs. 23.99±11.86% ($p < 0.001$) and PDFFratio, 0.09±0.09 vs. 0.49±0.24 ($p < 0.001$)). The corresponding areas under the curve were 0.98 and 0.97 for PDFF and PDFFratio respectively providing a 96% and 95% accuracy for the discrimination between acute benign and malignant VCFs (Schmeel, Luetkens, Enkirch, et al. 2018). CSE-MRI conducted in 156 subjects at 3T (8 echoes 3D spoiled gradient echo sequence, voxel size 0.98×0.98×4.00 mm, acq. time 1:17 min), showed that vertebral bone marrow heterogeneity is primarily dependent on sex and age but not on anatomical location suggesting that future studies should investigate the bone marrow heterogeneity with regards to aging and disease (Dieckmeyer et al. 2020). Baum et al. in a study

conducted on the whole spine of 28 young and healthy patients using CSE-MRI at 3T (8 echoes, acq. time 3:15 min), extend these results reporting that the repeatability of PDFF measurements expressed an averaged absolute precision error of 1.7% over C3-L5 (Baum et al. 2015).

MRS and CSE-MRI have enabled the evaluation of the nonmineralized bone compartment and the extraction of the PDFF. The marrow adipose tissue has shown to have a role in bone health, through its paracrine and endocrine interaction with the other bone components. However, the implication of marrow adipose tissue in physiological and pathological conditions remains unclear (Gómez et al. 2020).

4.2. MR Susceptibility

Magnetic susceptibility is the macroscopic physical quantity that describes the tissue's induced magnetization in the presence of an external magnetic field. Since the early days of MRI, susceptibility quantification has been considered as of paramount interest given that it is related to the tissue's chemical composition. Even a small susceptibility change can lead to field distortions that could be quantified. This has been achieved through SWI (susceptibility weighted imaging) (Haacke, Xu, and Cheng, n.d.; Rauscher et al. 2006) and quantitative aspects could be computed from MRI phase and magnitude signals by means of QSM (quantitative susceptibility mapping) (Schweser 2015; Deistung, Schweser, and Reichenbach 2017).

Dense calcified tissues, such as bone, show a strong diamagnetic behavior. On that basis, QSM (Dimov et al. 2018) could be used to assess bone mineral changes (W. Chen et al. 2014). Although QSM has been largely developed for brain imaging (Haacke et al. 2015; W. Li, Wu, and Liu 2011), the corresponding applications for bone are still considered very challenging. Cortical bone has a very low signal using conventional echo times GRE imaging and water connected to the crystalline mineral structures or to the collagen matrix has an ultrashort transverse relaxation time ($T2^* = 300$ μs (Jiang Du et al., n.d.)) thereby showing a non-meaningful signal for QSM. In order to overcome this issue, ultrashort echo-time (UTE) GRE imaging (Dimov et al. 2018) has been developed to obtain phase information for reliable QSM, which may be used in the evaluation of BMD (Y. Chen et al. 2018).

For example, correlations between QSM and BMD have been studied through clinical MRI sequences in spine and ankle trabecular bones (Y. Chen et al. 2018; Diefenbach et al. 2019). In Chen et al. (Y. Chen et al. 2018), the efficacy of QSM in the assessment of osteoporosis for post-menopausal women was investigated. The L3 vertebrae body of 70 post-menopausal women was studied through a multi-GRE UTE sequence on a 3T MR

system (TR = 20 ms, TE = 0.142, 2.4, 4.6, and 6.8 ms, voxel size = 1.0×1.0×2.0 mm, and acq. time = 10 min) and a qCT examination. Based on qCT values, individuals were divided into normal and affected by osteopenia or osteoporosis. The QSM values were higher for the osteoporosis group than in either the normal or the osteopenia group ($p < 0.001$) and showed an highly negative correlation with qCT values ($r = -0.72$, $p < 0.001$) (Y. Chen et al. 2018).

Non-UTE multi-GRE sequences can be applied to QSM: ankle in vivo imaging was performed by Diefenbach et al. using a time-interleaved gradient-echo sequence (TIM-GRE) at 3T (9 echoes, TEmin = 1.25 ms with $\Delta TE = 0.7$ ms, voxel size = 1.5×1.5×1.5 mm, and acq. time = 7 min) in order to evaluate the feasibility of QSM for trabecular bone imaging and investigate its sensitivity for measuring trabecular bone density (Diefenbach et al. 2019). Mean susceptibility values in calcaneus regions with different trabecular bone density were compared to CT attenuation values. In highly trabecularized regions, qCT values showed significant correlation with lower susceptibility values ($r = -0.8$, $p = 0.001$) (Diefenbach et al. 2019). In addition, differences in calcaneus trabecularization were outlined in QSM maps in good agreement with qCT and high resolution MR images.

Furthermore, cones 3D UTE-MRI techniques have recently been developed showing similar susceptibility values but faster scanning process if compared with other different sampling strategies (Lu et al. 2019). In Jerban et al. (Jerban, Lu, et al. 2019), cones 3D UTE-MRI was implemented for ex vivo QSM in order to investigate correlations of susceptibility with volumetric intracortical BMD in human tibial cortical bone. Nine tibial midshaft cortical bones specimens were scanned in a 3T clinical scanner with a cones 3D UTE-MRI sequence for QSM (TE = 0.032, 0.2, 0.4, 1.2, 1.8, and 2.4 ms, voxel size = 0.5×0.5×2.0 mm, and acq. time = 20 min) and with high-resolution μCT for BMD estimation (Fig. 1.8). Average QSM values were calculated in one slice (2 mm thickness) at the middle of the specimen and showed a strong correlation with volumetric BMD ($r = -0.82$, $p = 0.01$) and bone porosity ($r = 0.72$, $p = 0.01$). Results in this study highlight the potential of 3D cones UTE-MRI QSM as a possible future tool in the in vivo diagnosis of bone diseases that can be detected through mineral level variations in cortical bone.

Despite its potential in providing an x-ray radiation free approach to quantify susceptibility in bone tissue, QSM suffers from some limitations. Data processing is relatively complex and still under study while data acquisition times are too long if compared to clinical MRI sequences. Furthermore, bone susceptibility variations due to soft surrounding tissues should be taken into account in future in vivo clinical studies and applications.

4.3. Solid State MRI

Solid state MRI has been recently described in a review by Seifert and Wehrli (Seifert and Wehrli 2016). One of the main issued faced by MRI of the solid part of bones is the extremely weak MR signal. In order to acquire the fast decaying (i.e., short T2*) ^{1}H and ^{31}P MRI signals in bone, the time between signal excitation, encoding, and acquisition must be shorter than the one used in conventional MRI sequences (Seifert and Wehrli 2016; Gervais, Bonhomme, and Laurencin 2020). Hence, to image short-T2* tissues three solid state radial pulse sequences have emerged: ultrashort echo time (UTE) (Glover, Pauly, and Bradshaw 1992), zero echo time (ZTE) (Weiger, Pruessmann, and Hennel 2011; Jerban et al. 2020), and sweep imaging with Fourier transformation (SWIFT) (Idiyatullin et al. 2006; 2012; Mastrogiacomo et al. 2019). The main strategy to image short-T2* tissue is to reduce the time delay between the end of the signal excitation and the beginning of encoding and acquisition. In UTE, the time delay is reduced by beginning the signal encoding and acquisition simultaneously and immediately after the MRI system's transmit/receive switching dead time has elapsed (Glover, Pauly, and Bradshaw 1992; Takizawa et al. 2013). In ZTE, signal encoding is begun simultaneously with the excitation, but the time delay to signal acquisition is still dictated by the transmit/receive dead time resulting in the loss of the first data points in the acquisition (Kuethe et al. 1999; Y. Wu et al. 2003; Grodzki, Jakob, and Heismann 2012). In SWIFT, the three steps (excitation, encoding, and acquisition) are performed in a finely interleaved (gapped) (Idiyatullin et al. 2006) of fully simultaneous (continuous) (Idiyatullin et al. 2012) manner, allowing the in vivo imaging of teeth, where the T2* is even shorter than that of bone (Idiyatullin et al. 2014). All these sequences have been used ex vivo and in vivo applying whole-body MRI scanners at different field strengths. However, in the case of in vivo solid-state NMR of tibial shafts, a minimum voxel size of 0.98 mm^3 for ^{1}H and 2.5 mm^3 for ^{31}P is required to have enough SNR at an acceptable acquisition time (<10 min for ^{1}H and <25 min for ^{31}P) and to avoid SAR limitation (Seifert and Wehrli 2016; X. Zhao et al. 2017).

Solid-state MRI could be used to compute total bone water (TW), water bound to the collagen matrix (BW), and pore water (PW). Several consistent studies from different groups have been reported for bone extremities (Rad et al. 2011; X. Zhao et al. 2017; Techawiboonwong et al. 2008; Manhard et al. 2015; J. Chen et al. 2016) showing also the ability to differentiate between pre- and post-menopausal women. Techawiboonwong et al., in a study conducted in distal tibiae of pre-menopausal and post-menopausal women (n = 5 for each group) scanned using an UTE sequence at 3T MRI (pixel size 0.3×0.3×8.0 mm and acq. time = 9 min) reported a difference in the TW concentration of 17.4% and 28.7% respectively for the pre- and post-menopausal groups (Techawiboonwong et al.

2008). Moreover, BW and PW were acquired in vivo tibiae and wrist of 5 volunteers using 3T MR scanner (isotropic pixel size of 1.5 mm in the leg and 1.2 in the wrist and acq. time = 8–14 min per acquisition) reporting a mean BW of 34.86±2.59 M and a mean PW 6.14±1.97 M, similar to previously ex vivo observations (Manhard et al. 2015; J. Chen et al. 2016; Jerban, Ma, et al. 2019).

Using ^{31}P NMR, solid-state MRI could also be used to quantitatively assess the mass of bone mineral in bone tissue (Kaflak, Chmielewski, and Kolodziejski 2016). An ex vivo study conducted in 16 tibiae specimens acquired using ZTE ^{31}P at 7T (pixel size = 3.84 mm isovolumetric and acq. time = 3 h and 3 min) and ^{1}H at 3T (pixel size = 1.17 mm isovolumetric and acq. time = 26 min and 45 sec) by Seifert et al. (Fig. 1.8), reported a mean bone mineral ^{31}P density of 6.74±1.22 M and mean BW ^{1}H density of 31.3±4.2 M (Seifert et al. 2014a). In addition, ^{31}P and BW densities correlated positively with pQCT density (^{31}P: r2 = 0.46, $p < 0.05$; BW: $r^2 = 0.50$, and $p < 0.005$), showing that MRI-based measurements are able to detect inter-subject variations in apparent mineral and osteoid density in human cortical bone using clinical hardware (Seifert et al. 2014a; Chamith S. Rajapakse et al. 2015). However, Tamimi et al. in a study conducted on trabecular femur head samples collected from patients who had hip fractures and individuals with osteoarthritis reported no differences in neither ^{1}H nor ^{31}P between the two groups (Tamimi et al. 2020).

In a more recent study performed on in vivo tibiae of 10 healthy subjects, Zhao et al. acquired at 3T ^{1}H UTE (pixel size = 0.98 mm^3 and acq. time = 8:20 min) and ^{31}P ZTE (pixel size = 2.5 mm^3 and acq. time = 22:30 min). They showed no differences in the ^{31}P concentration in healthy adults across 50-years of age (X. Zhao, Song, and Wehrli 2018) and a strong positive correlation ($r = 0.98$, $p < 0.0001$) between bone mineral content (BMC) measured using ^{31}P MRI and HR-pQCT (X. Zhao et al. 2017), further extending previous in vivo studies (C. Li et al. 2014).

Therefore, solid-state MRI has shown its potential as translational techniques into clinical research and practice providing information related to the mineral composition of bone tissue, bound, and pore water. However spatial resolution, SNR, and scan time remain key challenges for the solid state MRI (Seifert and Wehrli 2016; X. Zhao et al. 2017; Yon et al. 2017). These three characteristics are dependent on each other and a trade-off has to be established to retrieve useful information in a clinically acceptable acquisition time. Usually, a SNR higher or equal to 10 is recommended and, to maintain the acquisition time in an acceptable range, the voxel size is enlarged along the bone axis where features are considered to be constant.

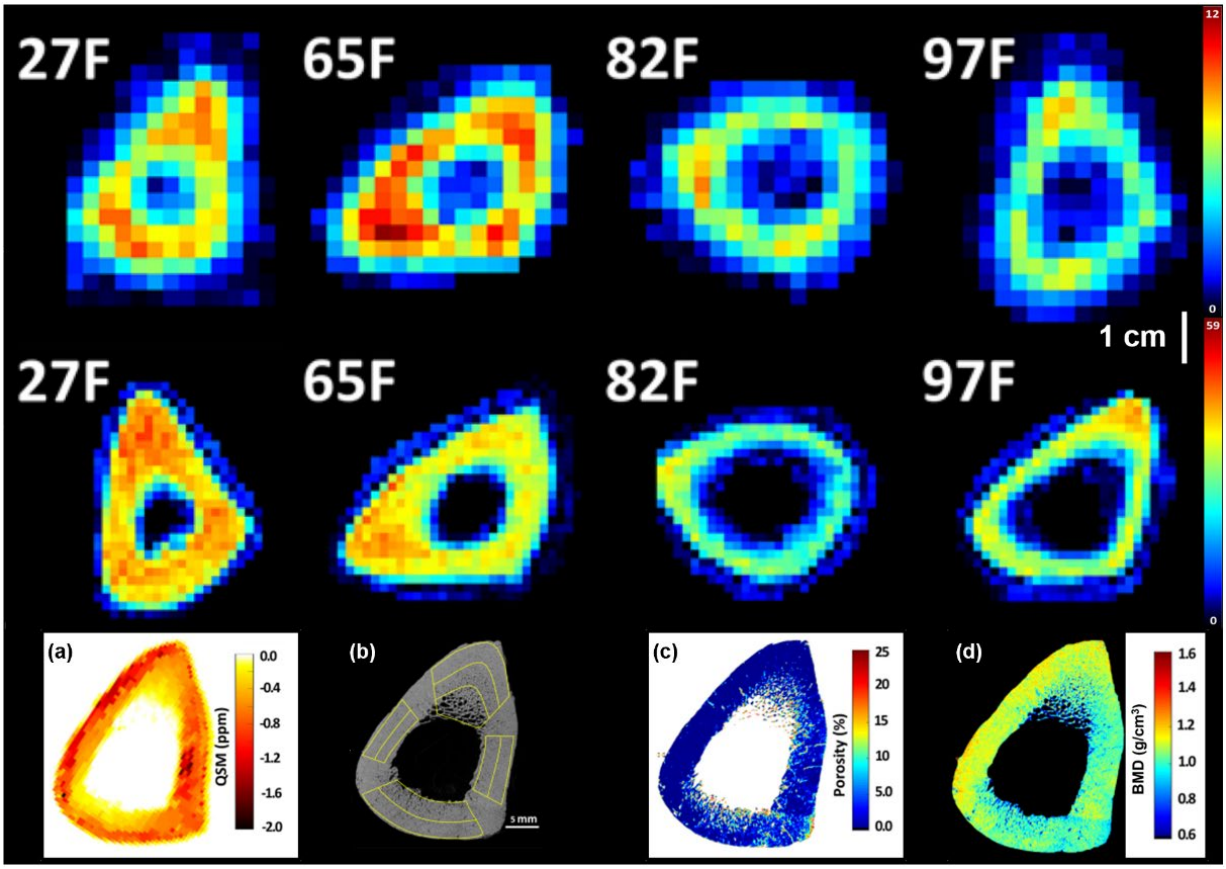

Figure 1. 8: Solid state MRI and quantitative susceptibility mapping. (first row) Maps of bone mineral ^{31}P density, and bound water density (second row) in central slices of 4 human tibial cortical bone specimens. Age and gender of bone specimen donors are indicated. Bone mineral ^{31}P and bound water ^{1}H densities are markedly lower in bones from elderly female donors than from younger females or males. ^{31}P maps also suffer from increased point spread function blurring because of the lower gyromagnetic ratio and shorter $T2^*$ of ^{31}P. (**reproduced from NMR Biomed. 27: 739–748 (2014)**) (third row) (a) QSM map obtained through Cones 3D UTE-MRI scans (0.5×0.5×2 mm voxel size) of a tibial midshaft cortical bone (45-year-old female), (b) one μCT slice at 9 μm isotropic voxel size, (c) μCT-based porosity, and (d) BMD map of the same specimen. Local maxima in the QSM map correspond to high BMD regions and low porosity values in μCT-based maps (**reproduced from Magn. Res. Im. 62: 104–110 (2019)**).

5. Conclusion

Over the last decades, the multiple technical improvements that have been made in MRI have opened new MRI applications such as a bone microarchitecture assessment. Up to now, most of the MRI studies conducted in bones have been performed using 1.5T and 3T scanners. However, results obtained at UHF showed the technical advantages and the higher discriminative power of 7T MRI for the assessment of the bone microstructure of the most proximal anatomic locations, including those more affected by osteoporotic fractures. The advantages provided by UHF MRI have shown great potential on the bone microstructure assessment and made this technique almost ready for a daily clinical application.

Moreover, bone morphological parameters derived from both specimens and patients acquired using MRI were shown to provide features in the same range of those derived with the gold-standard X-rays techniques, with the great advantage of being completely non-invasive for the patients. In addition, MRI was also shown to be able to provide supplementary information about the mineral content, i.e., phosphorous density, not accessible using X-rays techniques. Furthermore, MRI microarchitecture analysis was able to evaluate changes related to age and/or pathology suggesting the great clinical potential for MRI in evaluating different bone pathologies, assessing the risk stratification, and following the therapy delivery.

Up to now, BMD derived from DXA measurements was the only parameter used to identify bone related pathologies. Several studies have demonstrated that microarchitectural parameters provide additional information regarding the skeletal fragility and should be integrated with BMD to provide a more comprehensive view of the bone quality. MRI is completely radiation free, and the application of UHF MRI made accessible the anatomical regions further away from the skin surface, with a resolution in the same range of trabecular thickness, and in an acquisition time compatible for in vivo clinical use. Moreover, MRI, and in particular UHF MRI, showed to provide bone morphological parameters in the same range of gold standard analysis both in specimens and patients.

Finally, MSC and CSE-MRI, solid state MRI, and QSM have shown to be useable in in vivo acquisitions providing bone marrow fat quantification, mineral composition of bone tissue, bound, and pore water, and magnetic susceptibility quantification. However, for the clinical application of solid state MRI and QSM acquisition times would have to be reduced. MRI could certainly be added to BMD measurements for a complete analysis of bone quality, health, and metabolism.

Conclusion of the Chapter

In this first chapter, it has been presented the bone function and structure focusing on it multiscale hierarchy. The principal bone pathologies and the most common clinical approaches to evaluate the bone quality and healthy state have been discussed, confirming the doubts of using the DXA derived BMD as a only investigative tools and supporting the need to provide additional information regarding the bone microarchitecture. Then, it has been presented the available imaging techniques to assess the bone inner morphology presenting the advantages and disadvantages of each technique and suggesting that UHF MRI could provide a non-invasive approach to solve this problem, although reporting the necessity of a resolution in the same order of the trabeculae dimension (100-150 μm). Finally, new investigative MRI techniques could allow to assess both the patient bone microarchitecture and BMD in a completely non-invasive and radiation-free approach.

As reported, the most common pathology related to bone microstructure alterations is osteoporosis and therefore it is the bone pathology it has been decided to investigate during this thesis. In osteoporosis, bone density and volume of segments or specific bone regions can be progressively reduced. Patients with osteoporosis are at high risk of having one or more fragility fractures, which eventually lead to a physical debilitation and potentially to a downward spiral in physical and mental health. The hidden mechanism of osteoporosis is an imbalance between bone production and resorption leading to a decreased bone mass. Usually, bone is in constant remodelling and up to 10% of the entire bone mass at a time may undergo bone remodeling. An interplay of different mechanisms underlies the development of fragile bone tissues, among them insufficient mass and strength during growth, excessive bone resorption and inadequate formation of new bone during remodeling are the most important (Paccou et al., n.d.). Hormonal factors play an important role in the in the bone resorption rate as for the menopause that because of a lack of estrogen increases the bone resorption and inhibits new bone formation. Other factors as the Calcium metabolism have been significant for the bone turnover (Bendtzen 2015). Osteoporotic trabecular bone not only loses density, but the microarchitecture is also disrupted, the smallest trabeculae breaks creating microcracks that are replaced by weaker bones (Osterhoff et al. 2017). Cortical bone when affected by osteoporosis decreased its density losing part of its strength and rigidity. The site more often affected by osteoporotic fractures are wrist, spine and hip and are characterized by a relatively high trabecular to cortical bone ratio. The sites of fracture rely on trabecular bone for strength and absorption of load since are in correspondence of joints (Oftadeh

et al. 2015). The intense remodeling of these bone regions causes these areas to progressively degenerate when the remodeling in imbalanced. Bone degradation is supposed to begin between 30 and 35 years old and women may lose up to 50% while men about 30% (Koda-Kimble et al. 2008). Osteoporosis may be linked to ageing, particularly in postmenopausal women, or can occur as a result of specific conditions, i.e., diabetes, anorexia nervosa, and obesity or treatments, i.e., corticosteroid (Fig. 1.9). Indeed, corticosteroid-induced osteoporosis is the most common form of secondary osteoporosis and the first cause in young people. Bone loss occurs early after the initiation of corticosteroid therapy and is correlated to dose and treatment duration (Bartl and Bartl 2017). Fragility fractures have been associated with early mortality and increased morbidity having a significant effect on the quality of life of both patients affected by diabetes (Keenan and Maddaloni 2016; S. C. Chen et al. 2019; Abdalrahaman et al. 2017), anorexia nervosa (Singhal et al. 2018; Fazeli and Klibanski 2019), and obesity (Fintini et al. 2020; Cordes et al. 2016; 2015).

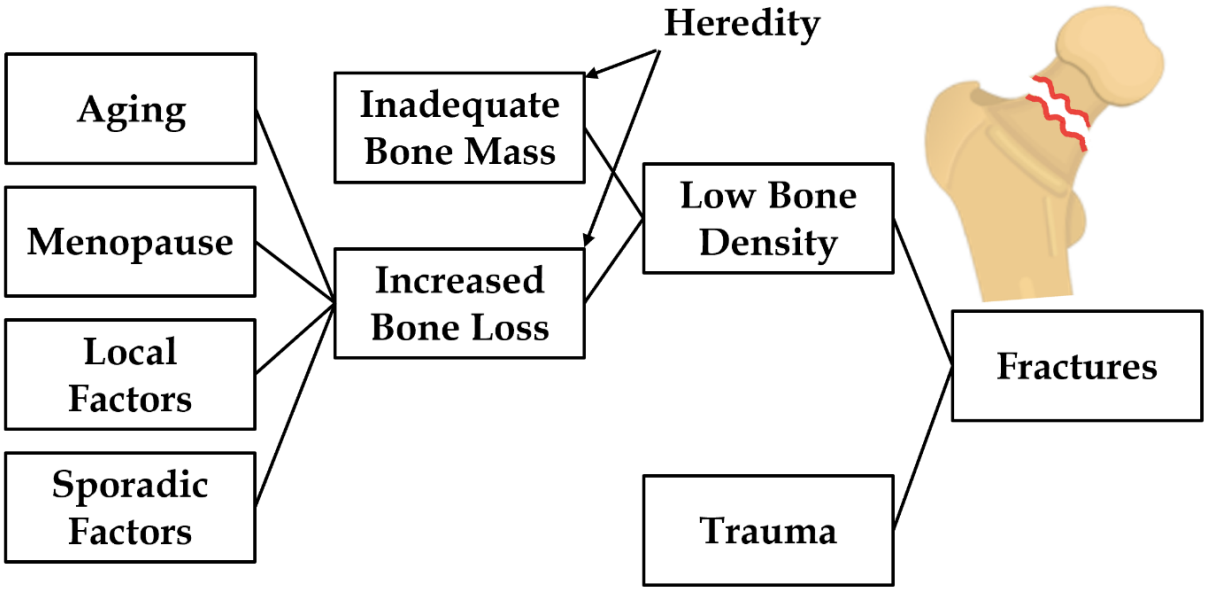

Figure 1. 9: Factors leading to bone fractures.

Similarly to osteoporosis, which is the main objective of this thesis and is further analyzed in the following chapters, the psoriatic arthritis is a bone disease responsible do degrade bone trabeculae. The psoriatic arthritis is here introduced because before the beginning of this thesis, one patient affected by psoriatic arthritis and eight gender- and aged-matched controls have been acquired using UHF MRI in the knee. This study was completed at the beginning of this PhD, when the patient has been assessed using UHF MRI a second time after one year of treatment. The MR images from this clinical study have been used to investigate the knee microarchitecture and the retrieved parameters

have been compared between the patient and the controls to evaluate the MRI applicability to both in vivo bone microarchitectural assessment and to follow-up of therapeutic strategies. This study showed both the limitation and the potentialities of the in vivo bone microarchitecture assessment using MR imaging technology at the beginning of this thesis.

Chapter 2: Assessment of In Vivo Bone Microarchitecture Changes in an anti-TNFα Treated Psoriatic Arthritic Patient (published article)

Cite

Soldati E, Escoffier L, Gabriel S, Ogier AC, Chagnaud C, Mattei JP, Cammilleri S, Bendahan D, Guis S. Assessment of in vivo bone microarchitecture changes in an anti-TNFα treated psoriatic arthritic patient. PLoS One. 2021 May 19;16(5):e0251788. doi: 10.1371/journal.pone.0251788. PMID: 34010320; PMCID: PMC8133422.

Authors

Enrico Soldati [1,2,3,*], Lucas Escoffier [4], Sophie Gabriel [5], Augustin C. Ogier [1,6], Christophe Chagnaud [4], Jean P. Mattei [1,4], Serge Cammilleri [5], David Bendahan [1] and Sandrine Guis [1,4]

Abstract

Psoriatic arthritis (PsA) is an inflammatory rheumatic disease, mediated in part by TNFα and associated with bone loss. Anti-TNFα treatment should inhibit this phenomenon and reduce the systemic bone loss. Ultra-high field MRI (UHF MRI) may be used to quantify bone microarchitecture (BM) *in-vivo*. In this study, we quantified BM using UHF MRI in a PsA patient and followed up the changes related to anti-TNFα treatment.

Affiliations

[1] Aix-Marseille University, CNRS, CRMBM-CEMEREM, Marseille, France,
[2] Aix-Marseille University, CNRS, IUSTI, Marseille, France,
[3] Aix-Marseille University, CNRS, ISM, Marseille, France,
[4] Aix-Marseille University, Service de Rhumatologie, AP-HM, Marseille, France,
[5] Aix-Marseille University, Service de Médecine Nucléaire, AP-HM, Institut Fresnel, Marseille, France,
[6] Aix-Marseille University, Université de Toulon, CNRS, LIS, Marseille, France
* Correspondence: enrico.soldati@univ-amu.fr

A non-treated PsA patient with knee arthritis and 7 gender-matched controls were scanned using a gradient re-echo sequence at UHF MRI. After a year of Adalimumab treatment, the patient underwent a second UHF MRI. A PET-FNa imaging was performed before and after treatment to identify and localize the abnormal metabolic areas. BM was characterized using typical morphological parameters quantified in 32 regions of interest (ROIs) located in the patella, proximal tibia, and distal femur.

Before treatment, the BM parameters were statistically different from controls in 24/32 ROIs with differences reaching up to 38%. After treatment, BM parameters were normalized for 15 out of 24 ROIs. The hypermetabolic areas disclosed by PET-FNa before the treatment partly resumed after the treatment.

Thanks to UHF MRI, we quantified *in vivo* BM anomalies in a PsA patient, and we illustrated a major reversion after one year of treatment. Moreover, BM results highlighted that the abnormalities were not only localized in hypermetabolic regions identified by PET-FNa, suggesting that the bone loss was global and not related to inflammation.

1. Introduction

Psoriatic arthritis (PsA) is an inflammatory rheumatic joint disease associated with psoriasis in which axial and peripheral joints can display an elevated inflammatory status (Griffiths and Barker 2007). PsA has been initially described by Moll and Wright as a seronegative inflammatory arthritis that occurs most of the time in the presence of psoriasis (Moll and Wright 1973). It was initially thought to be rare but recent studies indicated that it might occur in up to 30% of patients with psoriasis (Ogdie and Weiss 2015; Villani et al. 2015). The most commonly involved sites include Achilles tendon, quadriceps tendon, knee, wrist and ankle (Tang et al. 2020). These sites are usually assessed using ultrasound imaging which could detect both clinically active and non-active sites. Most of the times sites are clinically active. The main clinical presentations are swollen, tender joints, stiffness and pain, scaly skin patches, nail pitting, eye redness (Coates and Helliwell 2017) but also asymmetric oligo-arthritis, polyarthritis, dactylitis and enthesis (Griffiths and Barker 2007; Ritchlin, Colbert, and Gladman 2017). The PsA clinical presentation is frequently associated with structural changes such as bone erosion and formation i.e. ankylosis or periostitis (Tang et al. 2020; Perez-Chada and Merola 2020). Bone erosion could lead to fragility fractures which is a relevant clinical event and one of the major complication of many bone disorders such as osteoporosis. While the prevalence of osteoporosis in PsA is still a matter of debate (Attia et al. 2011; Del Puente et al. 2015), previous studies have shown that fragility fractures should be considered when evaluating the global picture of PsA patients (Del Puente et al. 2015). Psoriasis and psoriatic arthritis are characterized by tissue infiltration by activated T cells thereby resulting in an increased TNFa, IL 17 and IL 23 production (Ritchlin, Colbert, and Gladman 2017; Leijten et al. 2015; Kocijan et al. 2015). Synovial tissue and entheses are more particularly affected (Menon et al. 2014). This pro inflammatory status can be an effective trigger of osteoclasts differentiation and activation through the expression of the receptor activator of nuclear factor kappa B ligand (RANKL)(Ritchlin et al. 2003).

The increased cell activity and the corresponding elevated inflammatory status due to PsA could be assessed using positron emission tomography (PET), which is able to assess the abnormal accumulation of radiotracer in specific areas (Rosen et al. 2011; Chaudhari et al. 2016). The systemic bone loss resulting in a reduced bone mineral density (BMD) and the role of TNFa antibodies in this process are a matter of debate in psoriatic arthritis

(Perez-Chada and Merola 2020; Ogdie et al. 2017a; Chandran et al. 2016a)(Di Munno and Ferro 2019; Hoff, Kavanaugh, and Haugeberg 2013; Maruotti, Corrado, and Cantatore 2014). Using dual energy X-ray absorptiometry (DXA) (Briot et al. 2018), reduced BMD (g/cm^2) values have been reported in PsA patients as compared to controls and so regardless of sex, menopausal status, or age (lumbar spine 1.112 *vs.*. 1.326; femoral neck 0.870 *vs.*. 1.006; total body 1.125 *vs.*. 1.203) (Frediani et al., n.d.). However, bone micro architecture has never been documented as part of this bone alteration process. Interestingly, magnetic resonance imaging (MRI) and more particularly ultra-high field MRI (UHF MRI) has been reported as a promising tool for the assessment of bone microarchitecture given the high resolution of the corresponding images (G. Chang et al. 2017a). Over the last few years, this non-radiating imaging technique has shown promising results regarding spine, knee, and femur trabeculation in osteoporosis (G. Chang, Honig, et al. 2015b; Daphne Guenoun et al. 2017b; D. Guenoun et al. 2020b). So far, the corresponding changes in psoriatic arthritis have never been assessed.

The purpose of the present study was to investigate bone trabeculation in a patient with psoriatic arthritis using UHF MRI and to assess changes related to a TNFa antibodies therapeutic strategy.

2. Materials and Methods

2.1. Subject Recruitment

This study received institutional review board approval by the "Comité de protection des personnes sud Méditerranée I" (approval number 2016-A000427-44). Written informed consent was obtained from all the recruited subjects. One PsA patient (male, 18 years old, body mass index (BMI) = 14.53 kg/m^2) affected by axial and peripheral psoriatic arthritis, was assessed before and after a one-year Adalimumab treatment. The patient experienced knee arthritis six months before the first appointment and had cutaneous *vulgaris psoriasis* in elbow and knee only (Psoriasis Area Severity Index (PASI) = 1.8). The whole set of other pathologies leading to comorbidities and reduced BMI values were excluded. The patient was naïve of any conventional synthetic Disease Modifying Anti-Rheumatic Drug (CsDMARD), biological Disease Modifying Anti-Rheumatic Drug (bDMARD) or targeted synthetic Disease Modifying Anti-Rheumatic Drug (tsDMARD). Seven healthy volunteers with no sign of trabecular bone diseases or

osteopenia (all males, mean age = 21.6 years [interquartile range (IQR) = 1 year], mean BMI = 21.32 kg/m^2 [IQR = 1.29 kg/m^2]) were included in the control group.

2.2. Imaging Techniques

MRI scanning

The patient and the volunteers underwent 7T MRI (MAGNETOM, Siemens Healthineers, Germany) of the knee joint (distal femur, proximal tibia and patella). All subjects were scanned using a 28-channel knee coil and a 3D gradient recalled echo sequence (3D GRE, TR/TE = 15/4.36 ms, flip angle = 12°, bandwidth = 326 Hz/pixel, field of view = 180*180 mm, matrix = 768 x 768, in-plane voxel dimension 0.234 x 0.234 mm, slice thickness = 1.5 mm, 64 sagittal planes, acquisition time = 5 minutes 56 seconds). This protocol is similar to what has been previously used for knee scanning at 3T (Chiba et al. 2012; Bolbos et al. 2008). The PsA patient was scanned once before treatment and once after one year of treatment. During MRI scanning, the patients' knee was immobilized by sandbags and secured by Velcro straps to avoid involuntary movements.

PET scanning

As part of the usual follow-up procedure, the PsA patient underwent two CT/PET FNa scanning, once before treatment and once after one year of treatment. The sodium fluoride radiotracer (Cisnaf©) was administrated intravenously (3MBq/kg) and images were acquired 60 min after the injection on a Biograph 16 tomograph (Siemens, Healthineers, Germany), coupled to a low dose CT scanner with standard parameters (CT: 80 mA, 120 kV without contrast; 2 min per bed-PET- step of 15 cm) (de Arcocha et al. 2012; Albano, Giubbini, and Bertagna 2018). CT/PET FNa images were iteratively reconstructed in a 128x128 matrix and 60 cm field of view, with and without attenuation correction in the transaxial, coronal and sagittal planes. The patient did not require special preparation. He was asked to be hydrated in order to activate the rapid washout of the radiotracer, to reduce the radiation dose and to improve the images quality.

2.3. PET-MRI fusion and Analysis

PET-MRI fusion

MR and CT/PET FNa images (de Arcocha et al. 2012) were acquired using two different scanners. Given that bones were clearly visible in both CT and MR images, the

four bones (femur, tibia, fibula, and patella) were used as landmarks for the registration of both images. More specifically, bones were delineated semi-automatically in each stack of images and linear affine registrations were computed independently between each bone using FSL-FLIRT (Jenkinson et al. 2002). Each local affine transformation was then merged into a global 3D deformation field through the implementation (described in (Makki et al. 2019)) of the log-euclidean poly-affine framework proposed by Arsigny *et al.* (Arsigny et al. 2009). The resulting deformation field was used to overlay the PET maps on the highly resolved and contrasted 7T MR anatomical images as previously reported (Cammilleri et al. 2019) (Fig. 2.1).

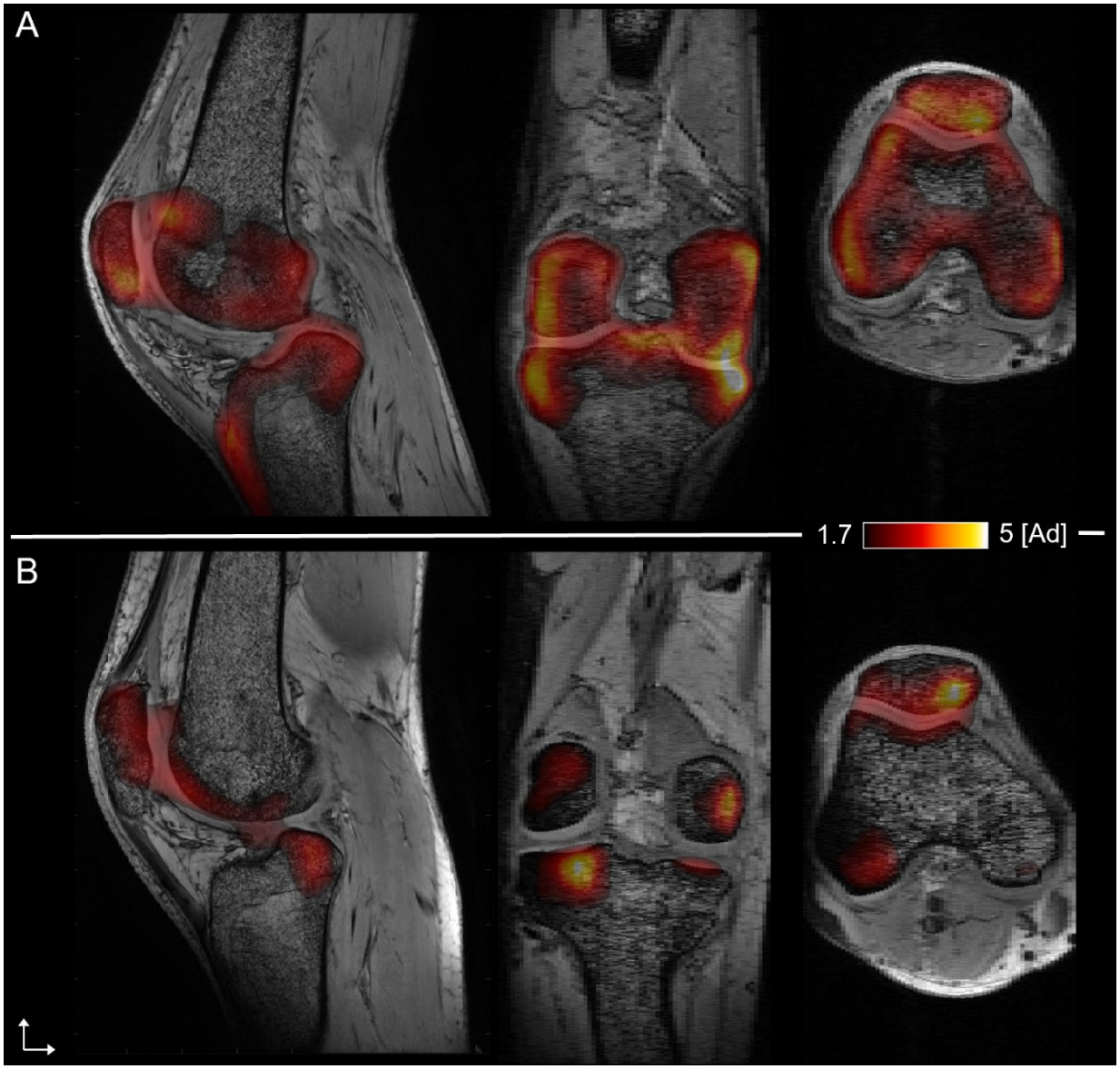

Figure 2. 1: merged PET-UHF MRI. Sagittal, coronal, and axial plane of merged PET-UHF MRI of the knee articulation of the patient before (A) and after (B) treatment by TNF-antibodies. "[Ad]" refers to a dimensional. Values higher or equal to 2.5 are considered indicative of "hypermetabolic" activity.

PET-MR Analysis

Fused PET-MR images were visually evaluated by an expert (SG) with the aim of identifying and localizing the hypermetabolic regions before and after the treatment. The visual inspection of fused images was crucial in order to identify the regions with hyperintense signals.

Bone volume fraction maps representing the relative volume of bone within each voxel were generated from the GRE images. The initial images were linearly scaled in order to cover the range from 0 (pure bone) to 255 (pure marrow) (G. Chang, Rajapakse, et al. 2015b; Chamith S. Rajapakse et al. 2012b). In each image, distal femur, proximal tibia and patella were delineated using the Chan-Vese algorithm, which showed to be robust for the separation between bone, tendons and cartilage in the knee (Jiang et al. 2008; Aprovitola and Gallo 2016). The corresponding filled contours were used as masks on which a 10-pixels closing process was applied (2.34 mm) in all directions in order to eliminate all the cortical bone (Fig. 2.2). Several region of interests (ROI) where identified in different locations of the trabecular bone in order to fully investigate the trabecular network.

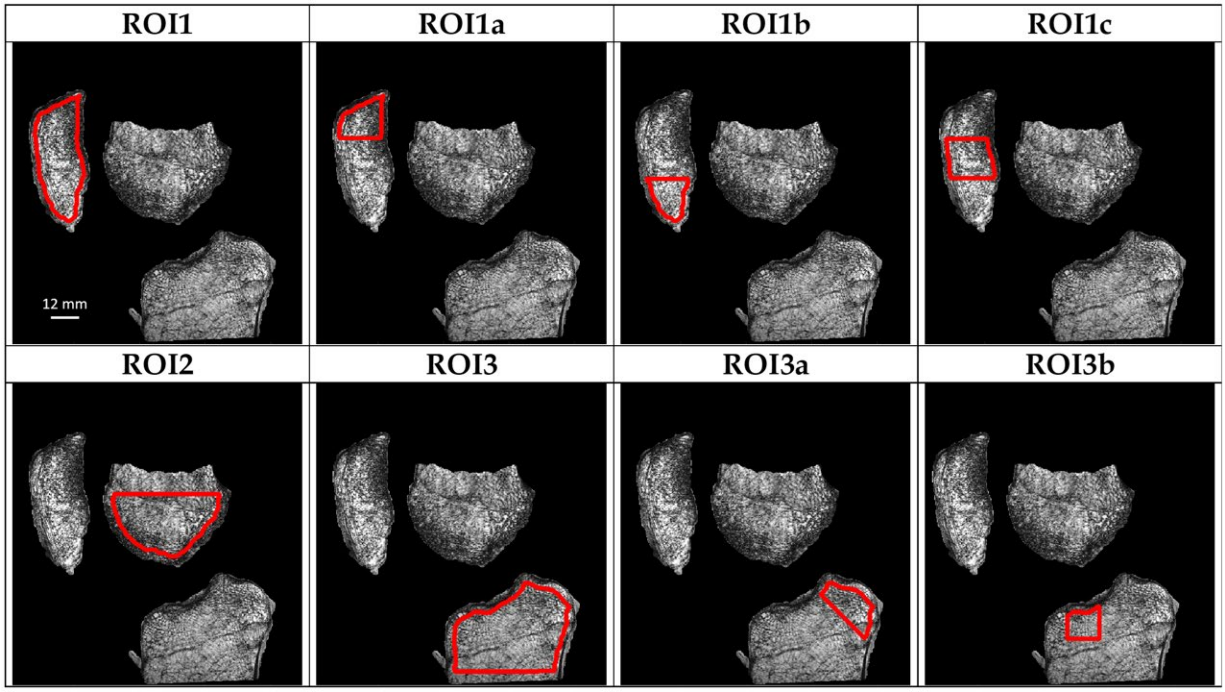

Figure 2. 2: ROIs identification. PsA patient after treatment BVF maps showing the multiple ROIs identified in red.

ROIs selection

The ROIs selection was based on the PET-FNa results. Accordingly they were selected in regions with hyper-intense signals before the Adalimumab treatment and were selected in the same regions after the treatment regardless of the signal intensity.

Patella : The first set of ROIs (ROI1, ROI1a, ROI1b and ROI1c) were located in the patella region and referred respectively to the trabecular space of the whole patella, the upper and lower third of the trabecular region where the quadriceps and patellar tendons are respectively attached and the central third of the patella (Fig. 2.2).

Distal Femur : ROI2 was located in the distal femur epiphysis as illustrated in Fig. 2.2.

Proximal Tibia : The final set of ROIs (ROI3, ROI3a and ROI3b) were positioned in the proximal tibia. ROI3 refers to the trabecular space of the proximal tibia epiphysis. ROI3a represents the trabecular part of the tibia where the medial collateral ligand is attached and ROI3b represents the trabecular part of the tibia where there was no hypermetabolic activity on the basis of the PET FNa signal. (Fig. 2.2).

Bone Microstructure Evaluation

To reduce the computational costs from the 3D ROIs, three 2D centrally located MRI planes were selected for each subject i.e. the image with the highest ROI surface together with the N_{+1} and N_{-1} images.

ROIs were then binarized using an automatic local thresholding as previously described (Dougherty and Kunzelmann 2007a) and three independent metrics were computed. The bone volume fraction (BVF) which refers to the ratio between bone and the total volume, the trabecular thickness (Tb.Th) and spacing (Tb.Sp). Tb.Th and Tb.Sp were extrapolated using iMorph (E. Brun, Ferrero, and Vicente 2017a) which can generate an aperture map (AM) derived from a distance transformation map. The AM was retrieved from the maximal balls diameter enclosed in the bone (Tb.Th) and in the marrow (Tb.Sp) phases (Fig 2.2). Finally the trabecular number (Tb.N) was computed as the ratio between the BVF and the Tb.Th.

Student's T-tests were used in order to assess the morphological parameters differences between the control group and the PsA patient before and after the TNF treatment. For each subject, three measurements were obtained for each metric and each ROI. A p-value lower than 0.01 was considered as significant.

Standardized Uptake Values

A semi-quantitative analysis of PET images was performed as previously described in order to generate the Standardized Uptake Values (SUV) (de Arcocha et al. 2012; Rosen et al. 2011). SUV were computed as the ratio between the signal intensity within each pixel of the image scaled to the concentration of the total injected radioactivity (3 MBq/Kg). The corresponding results refer the pixel-based metabolic. A SUV of 2.5 or higher is generally considered to be indicative of an "hypermetabolic" region. Finally, mean and maximal values were computed within each ROI.

3. Results

3.1. PET-FNa

Hypermetabolism evolution

The visual inspection of the initial set of PET images showed intense polyarticular hyperintense signals preferentially involving the knees, the left hip, the right ankle, the elbows, and more moderately the spine, the feet and the hands. As illustrated in Fig 2.1, large hyperintensities were observed in the knee. The second set of PET image recorded after one year of treatment, showed an unequivocal reduction in most of the hypermetabolic regions affecting the joints of the axial and appendicular skeleton and more particularly the knee. The whole set of ROIs showed reduced hyperintensities whereas no more hyperintense signal was visible for ROI2 and ROI3b.

SUV results

SUV were quantified in all the knees ROIs before and after one year of treatment and the corresponding values are indicated in Table 2.1. Before the treatment, SUVmean was abnormal in 5 over 8 ROIs. The abnormal values were concentrated in all the patellar ROIs (2.7±0.1) and ROI3a (2.8). SUVmax averaged over the whole set of ROIs was 3.67±0.41. After the treatment, SUV were no longer larger than 2.5 in almost all the ROIs while the averaged SUVmax was also significantly reduced i.e. 2.86±0.86. Large SUV values (i.e. between 1.7 and 2.5) were still visible in all the patella ROIs and ROI3a (Table 2.1).

Table 2. 1: SUV results before and after treatment for all identified ROIs.

	Before Treatment		After Treatment	
	SUVmean	**SUVmax**	**SUVmean**	**SUVmax**
ROI1	2.7±0.5	3.79	2.1±0.6	3.77
ROI1a	2.6±0.4	3.72	2.4±0.4	3.18
ROI1b	2.9±0.5	3.77	1.6±0.5	3.02
ROI1c	2.7±0.4	3.79	2.3±0.6	3.69
ROI2	1.9±0.5	3.34	1.2±0.6	3.32
ROI3	1.9±0.5	4.06	1.0±0.3	2.41
ROI3a	2.8±0.4	4.06	1.3±0.4	2.41
ROI3b	2.0±0.2	2.82	0.7±0.1	1.12

SUV mean (SUVmean) values are presented as mean ± SD and SUV maximum (SUVmax) values of the investigated ROIs before and after one year of treatment.

3.2. MRI Microarchitecture

Regarding the MRI-based micro-architecture measurements performed before the treatment, the patient was outside the control range for multiple metrics and multiple localizations (24 out of 32 measurements were statistically different from the controls). However, after one year of treatment the microarchitectural parameters differences between the PsA patient and the healthy references were reduced and the parameters were approaching or within the control range (only 9 out of 32 measurements were still statistically different than controls) (Table 2.2).

Table 2. 2: Microarchitecture characteristics per ROI.

			Controls	P. before treatment	P. after Treatment
Patella	ROI1	BVF	0.375±0.015	0.297±0.011 *	0.373±0.016
		Tb.Th	0.258±0.005	0.257±0.004	0.276±0.003 *
		Tb.Sp	0.429±0.065	0.643±0.036 *	0.470±0.013
		Tb.N	1.455±0.076	1.132±0.068 *	1.347±0.008
	ROI1a	BVF	0.393±0.008	0.339±0.018 *	0.401±0.010
		Tb.Th	0.255±0.013	0.254±0.022	0.266±0.014
		Tb.Sp	0.364±0.032	0.477±0.058	0.365±0.008
		Tb.N	1.550±0.074	1.301±0.136	1.493±0.073
	ROI1b	BVF	0.355±0.035	0.222±0.064 *	0.328±0.027
		Tb.Th	0.261±0.010	0.250±0.015	0.285±0.004 *
		Tb.Sp	0.469±0.117	0.651±0.057 *	0.532±0.064
		Tb.N	1.366±0.114	0.994±0.090 *	1.116±0.083
	ROI1c	BVF	0.377±0.015	0.295±0.026 *	0.375±0.016
		Tb.Th	0.207±0.008	0.213±0.005	0.225±0.003 *
		Tb.Sp	0.366±0.042	0.632±0.096 *	0.424±0.005
		Tb.N	1.746±0.250	1.409±0.119 *	1.661±0.024
Distal Femur	ROI2	BVF	0.354±0.048	0.257±0.015 *	0.312±0.007
		Tb.Th	0.261±0.005	0.260±0.006	0.269±0.006
		Tb.Sp	0.516±0.140	0.769±0.025 *	0.656±0.009
		Tb.N	1.342±0.187	1.016±0.020 *	1.173±0.054
Proximal Tibia	ROI3	BVF	0.337±0.019	0.219±0.015 *	0.256±0.012 *
		Tb.Th	0.266±0.011	0.245±0.004 *	0.257±0.008
		Tb.Sp	0.562±0.087	0.924±0.029 *	0.866±0.053 *
		Tb.N	1.261±0.109	0.879±0.051 *	0.985±0.043 *
	ROI3a	BVF	0.381±0.009	0.307±0.016 *	0.335±0.018
		Tb.Th	0.258±0.008	0.260±0.009	0.267±0.012
		Tb.Sp	0.426±0.060	0.594±0.012 *	0.570±0.016 *

		Tb.N	1.468±0.073	1.185±0.047 *	1.241±0.029 *
	ROI3b	**BVF**	0.376±0.018	0.242±0.024 *	0.285±0.013 *
		Tb.Th	0.220±0.015	0.192±0.005 *	0.202±0.011
		Tb.Sp	0.418±0.061	0.636±0.054 *	0.539±0.033
		Tb.N	1.689±0.148	1.255±0.183 *	1.432±0.094

Data are presented as mean ± SD. "P." refers as patient. BVF: Bone volume fraction, Tb.Th: Trabecular Thickness, Tb.Sp: Trabecular Space, Tb.N: Trabecular number. * indicates a statistically significant difference ($p < 0.01$) with the Healthy reference values.

Patella

Before the treatment and considering the four ROIs delineated in the patellar region, BVF of the patient was always significantly lower as compared to controls with a mean difference of -23±10%. The Tb.Th difference was always below 5% ($p>0.01$ for all the four ROIs), with a general mean of 0.25±0.03 mm for the controls and 0.24±0.02 mm for the patient. The Tb.Sp difference was statistically significant for ROI1, ROI1b and ROI1c but not for ROI1a with the patient having larger trabecular spaces as compared to controls and therefore a positive difference mean of 48±18%. Similar results were found for Tb.N and a significant difference was found for ROI1, ROI1b and ROI1c but not for ROI1a with a general mean difference of -21±5%.

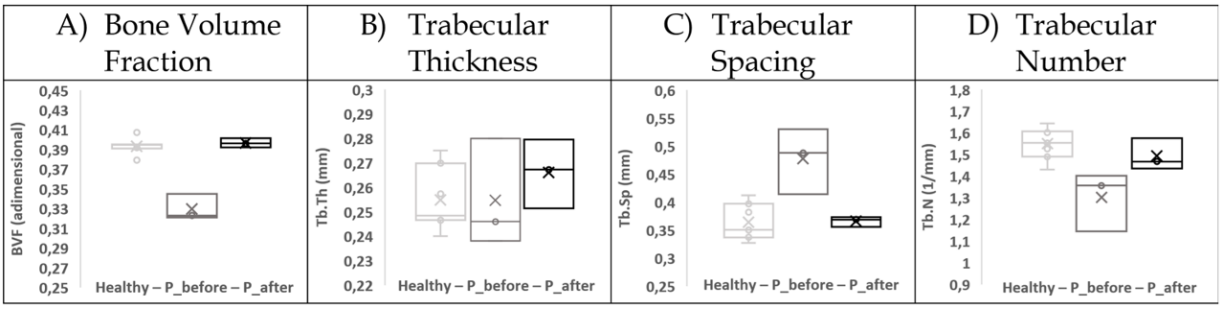

Figure 2. 3: ROI1a extrapolated features box plot. Box plot for each extrapolated feature for the control reference (Healthy), patient before (P_before) and after (P_after) one year of anti-TNFα treatment in the trabecular region where the quadricep tendon attaches the patella (ROI1a).

Following the 12-month TNF treatment, most of the micro-architecture metrics but Tb.Th reversed to normal values. BVF increased in the four patella's ROIs thereby reducing the differences with controls to a non-significant mean value of -2±4%. Similar results were quantified for Tb.Sp and Tb.N with a non-significant difference with controls for any of the patella's ROIs and a new overall patient mean difference of 10±7% for Tb.Sp and -9±7% for Tb.N. On the contrary, after the treatment, Tb.Th became significantly larger with a significant difference (up to 9%) with controls and so for ROI1, ROI1b and ROI1c (Fig. 2.3 and Table 2.2).

Distal Femur

In the distal femur (ROI2) the difference between the healthy reference and the patient before the treatment was more than 20% for all the parameters (-27% for BVF, 49% for Tb.Sp and -24% for Tb.N) except for Tb.Th for which the difference was less than 1%.

The image analysis after the treatment still showed increased BVF and Tb.N values while Tb.Sp values were reduced. The corresponding differences between the patient and the control values were -12%, -13% and +27% respectively. Similar to the results found in the patella, the Tb.Th increased becoming 3% thicker than controls. The difference between the control and the patient values after the treatment was statistically significant ($p>0.01$) for none of the micro-architectural parameters evaluated (Table 2.2).

Proximal Tibia

The three ROIs (ROI3, ROI3a and ROI3b) located in the proximal tibia region also showed statistically differences between patient and control values for the whole set of MRI metrics. The only normal value was found for Tb.Th in ROI3a. More particularly, the differences between the patient and the controls were -30±9% for BVF, 52±12% for Tb.Sp, -25±6% for Tb.N and -7±7% for Tb.Th.

After the 12 month-TNF treatment, the bone microstructure differences were reduced, although remaining statistically significant in most of the cases. For the BVF, the difference was reduced to -20±7% and remained statistically significant for ROI3 and ROI3b. The Tb.Th difference was also reduced to -3±6% thereby becoming not statistically significant for any of the three tibial ROIs. The Tb.Sp difference slightly decreased to 39±13% but remained statistically significant ($p<0.01$) for ROI3 and ROI3a but not for ROI3b. The Tb.N difference also decreased to -18±4% but remained statistically significant for ROI3 and ROI3a but not for ROI3b (Table 2.2).

4. Discussion

In the present study, we assessed bone microarchitecture in a PsA patient in order to document the potential bone quality changes associated with his inflammatory status. We also assessed the microarchitecture modification resulting from a one-year anti-TNF treatment. We mainly found that PET-FNa/MRI showed a largely inflamed knee articulation with some specific hypermetabolic regions in the vicinity of ligament and tendons in the patella, the distal femur, and the proximal tibia. Microarchitectural changes quantified using UHF MRI were affecting the whole bone segments and were not localized within the hypermetabolic regions only. After a year of TNF treatment, the combined PET-UHF MRI approach showed highly reduced hypermetabolic regions and an improvement for most of the microarchitectural parameters and the BMI increased from 14.5 to 18.9 kg/m^2 reaching the normal range (18.5-24.9 kg/m^2) (Weir and Jan 2020).

Before the treatment, all the microarchitecture metrics were significantly different with respect to the control values and so in at least one ROI. Using HR-pQCT on the distal radius of a group of 50 PsA patients and comparing the bone microarchitecture results to those from controls, Kocijan *et al.* reported significantly reduced BVF and Tb.N, increased Tb.Sp and almost constant Tb.Th (Kocijan et al. 2015). Compared to our study, Kocijan *et al.* reported lower bone microstructure parameters differences between PsA patients and controls (-11.9%, -7.1%, +9.1%,-1.5% respectively for BVF, Tb.N, Tb.Sp and Tb.Th *vs.*. an overall difference mean for all the ROIs analyzed of -26% for BVF, -23% for Tb.N, +50% for Tb.Sp and -3% for Tb.Th). However, these discrepancies could be explained by the different anatomical investigated sites (distal radii *vs.*. knee articulation) and by the age and body mass index of the PsA patients (51±13y, 27.9±5.1 kg/m^2 *vs.*. 18y, 14.5 kg/m^2). Although previous DXA measurements have been controversial regarding BMD changes in PsA patients (Perez-Chada and Merola 2020; Ogdie et al. 2017a; Chandran et al. 2016a), our results further support those obtained using a radiating imaging technique and confirm abnormalities of trabecular bone in PsA patients so that osteoporotic changes might be expected in PsA.

In the field of rheumatologic inflammatory disorders, our study is the first to address the bone microarchitecture issue using UHF MRI, although previous studies involving the use of UHF MRI have reported promising results in osteoporosis (G. Chang, Honig, et al. 2015b; Daphne Guenoun et al. 2017b; D. Guenoun et al. 2020b; Soldati, Rossi, et al. 2021). As an example, Chang *et al.* (G. Chang, Honig, et al. 2015b) found abnormal trabecular characteristics including BVF in the distal femur of subjects with fragility fractures whereas the DXA T-score was normal. Of interest, BVF, Tb.Sp and Tb.N were

abnormal in the majority (7/8) of ROIs in the present study whereas Tb.Th was abnormal in a limited number (2/8) of ROIs. These results further support those previously reported by Kocijan *et al* (Kocijan et al. 2015) and Chang *et al.* (G. Chang, Honig, et al. 2015b) regarding the larger sensitivity of BVF, Tb.Sp and Tb.N to bone micro-architecture alterations as compared to Tb.Th. In fact, Kocijan *et al.* (Kocijan et al. 2015) reported no difference in Tb.Th between PA patients and healthy controls in distal radii while Chang *et al.* (G. Chang, Honig, et al. 2015b) found normal distal femur Tb.Th in patients with fragility fractures.

Trabecular abnormalities detected using UHF MRI were found in all the hypermetabolic regions detected using PET-FNa, showing that microarchitecture deterioration was affecting the whole bone segments. The PET analysis has been shown to reflect bone remodeling and has been used in several studies on osteoporosis (Blake, Park-Holohan, and Fogelman 2002; Frost et al. 2003; Raynor et al. 2017; Uchida et al. 2009). In our case, PET-FNa allowed to localize specific ROIs characterized by elevated hypermetabolic activity before treatment and ROIs presenting partial or full remission after treatment.

After a year of anti-TNF treatment, the trabecular parameters clearly illustrated that the knee of the patient was in clinical remission from his PsA status. The trabecular parameters reversal might result from the decreased inflammatory status leading to a reduced osteoclastic bone resorption activity. In PsA, Hoff *et al.* (Hoff, Kavanaugh, and Haugeberg 2013) have showed that 24 weeks of Infliximab treatment can stop the bone loss. In multiple studies conducted in rheumatoid arthritis (RA) patients, the TNF blocking strategy has been associated with an increase of biological markers indicating bone formation and a decrease of those illustrating bone resorption (Vis et al. 2003; 2006; Lange et al. 2005). In both RA and Ankylosing spondylitis (AS), the efficiency of anti-TNF agents on bone loss has also been confirmed through BMD measurements using DXA (Vis et al. 2006; Lange et al. 2005; Marotte et al. 2007; Wijbrandts et al. 2009; Güler-Yüksel et al. 2008). Our PET-FNa/MRI measurements also supported the efficiency of the anti-TNF strategy. In fact, UHF MRI allowed us to assess and quantify the microarchitectural parameters in the hypermetabolic ROIs assessed through the PET-FNa. In our study, UHF MRI showed an almost homogeneous microarchitecture deterioration before treatment and a partial or a complete remission after one year of treatment. These results are also in agreement with those previously reported as a result of bisphosphonates treatment in osteoporotic patients (Frost et al. 2003; Uchida et al. 2009).

A few limitations have to be acknowledged in the present study. Although, this preliminary study was conducted in a PsA patient, we have quantified morphological parameters in several UHF MR images from 3 different bone segments (patella, distal

femur, and proximal tibia) and using 8 different ROIs. Moreover, the results of the PsA patient were compared both temporally, i.e. before and after the treatment, and against the control group. One might wonder whether the reported changes are gender specific given that we assessed male subjects only and the inclusion of female subjects would be of interest. Additionally, it could be of interest to assess other bones regions with an elevated bone turnover such as the sacroiliac joint, spine and other peripheral joints. However, one has to keep in mind that the availability of dedicated coils for UHF MRI is rather reduced. One could also argue that partial volume effects might have biased the results. Such an effect can occur when pixels size in a given MR image is larger than the trabecular thickness (100 μm). Our protocol was similar to previously reported knee MRI acquisitions (Chiba et al. 2012; Bolbos et al. 2008). The partial volume error if any was expected to be the same for all the MR images so that the comparison was still valid.

5. Conclusion

The investigation of bone microarchitecture in patients affected by PsA is of interest for a reliable assessment of bone quality, illness risk stratification and for the follow-up of therapeutic strategy. Up to now, PsA patients have been mainly treated using CsDMARD, bDMARD and tsDMARD (Gossec et al. 2020) and the effects on bone microarchitecture have never been documented. However, the administration of anti-TNF may inhibit the osteoclastic action of bone resorption triggered by the inflammatory response. Moreover, the application of UHF MRI might be of high interest to investigate bone microarchitecture in the future for specific clinical situations, such as osteoporosis.

Conclusion of the Chapter

In this chapter, it has been shown the limitations and the potentialities of the in vivo applicability of MR imaging for the assessment of bone microarchitecture. Firstly, it has been exploited the MR technical limitations, GRE sequences have been used in order to assess all the knee volume in a single scan, however the image resolution was not sufficient to resolve the bone inner morphology. Although, this article showed that the UHF MRI was able to assess the bone most common characteristics, and from their analysis, to discriminate the PsA patient from the controls. Moreover, it has been shown the improvement of the bone quality after one year of treatment therefore showing the potential use of MRI for illness risk stratification and for the follow-up of therapeutic strategy (Fig. 2.4).

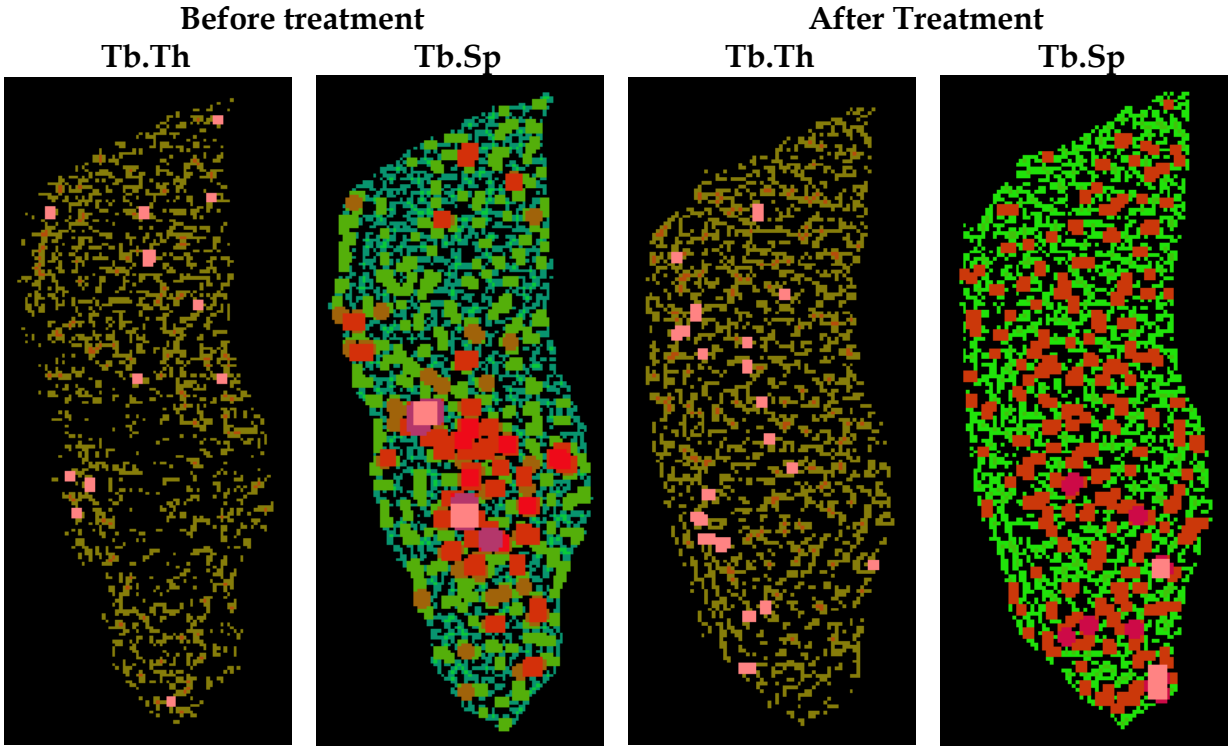

Figure 2. 4: Bone Morphology characterization. Trabecular thickness and spacing of the PsA patient's patella before and after one year of anti-TNF treatment.

This chapter have shown the additional value that UHF MR imaging of the bone microarchitecture could provide to the clinical practice in the bone quality assessment, however reporting the need of technical improvement and optimization in both the acquisition sequence and setups, but also in the image analysis. The investigation of different MRI sequences, but also the optimization between image resolution, acquisition

time, specific absorption rate, SNR, … is of great interest to increase the in vivo applicability of the bone microarchitecture assessment in the clinical practice.

In the next chapter, it has been presented all the experimental techniques and setups that have been applied in this thesis project. The first aim was to assess the bone quality and provide an optimized approach for the use of UHF MRI for bone microarchitecture assessment of proximal femurs in the clinical practice. Moreover, the second aim was to investigate the effect that osteoporosis have in the multiscale hierarchical bone structure, therefore the bone trabecular phase has been analyzed using a multiscale and multimodal approach able to investigate both the micro-, nano- and molecular scale.

Chapter 3: Materials and Methods

In this section we will present the all the cadaveric samples that have been provided by the pathological department of LaTimone medical school, AixMarseille University, Marseille, France, and the techniques used for retrieving and preparing the different sized of bone samples. Moreover, we will introduce all the experimental acquisition techniques, sequence and procedure, and the biomechanical testing setup.

1. Sample Collection and Preparation

Cadaveric human femurs have been collected thanks to the collaboration with the pathological department of LaTimone medical school, AixMarseille University. All procedures followed were in accordance with the ethical standards of the responsible committee on human experimentation of the thanatopraxy laboratory, University School of Medicine, Hôpital de la Timone, Marseille, France that provided the bodies coming from body donation and with the Helsinki Declaration of 1975, as revised in 2000. The whole set of collected samples are shown in Table 3.1, after bone collection, gender, age and height have been listed, in addition standard dual-energy X-ray absorptiometry (DXA) analysis was performed to classify them as healthy or osteoporotic. A schematic representation of the different femurs used for the analysis at different levels are shown in Figure 3.1.

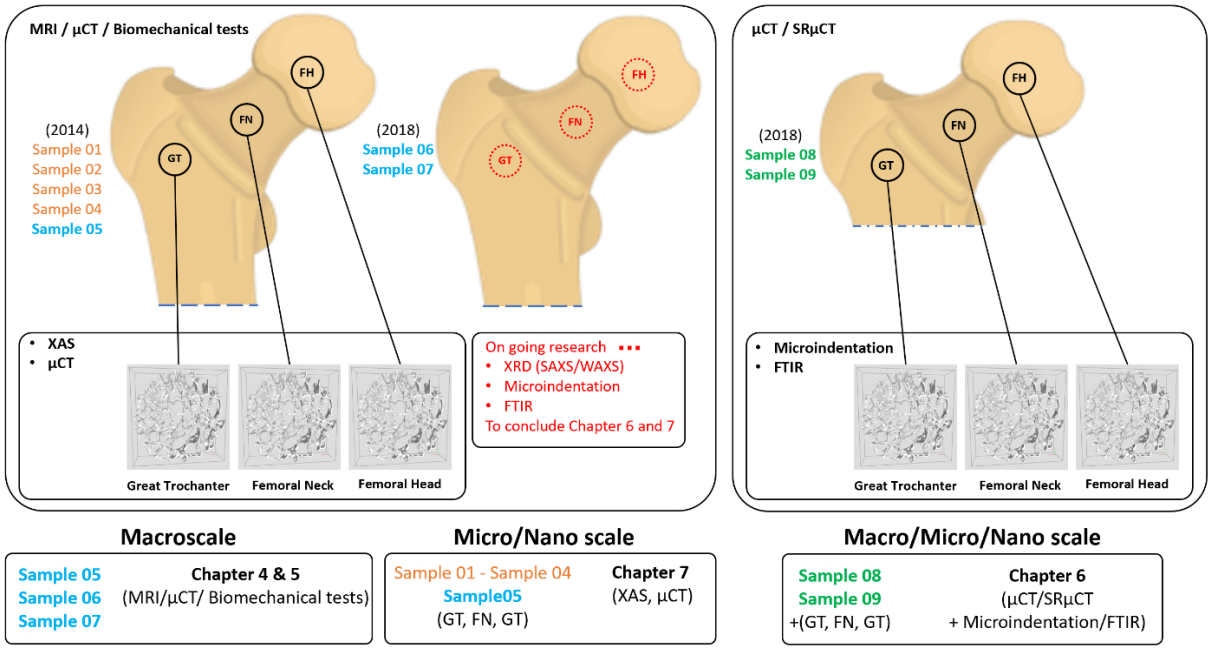

Figure 3. 1: Schematic representation of the different femurs and sample used in all the experimental setups and examination performed.

The macroscale study have been conducted on whole proximal femurs. The micro and nanoscale study was instead focused on small subregions of the proximal femur chosen to provide an overall characterization of the whole femur epiphysis. First, all epiphysis

were scanned intact to assess the bone inner morphology. Then, based on the preliminary μCT investigative scan providing information of the sites more affected by osteoporosis and characterized by higher bone mineral density or bone volume fraction, three small specimens (10 mm of diameter and 2 mm of thickness) were extracted from each proximal femur respectively in the great trochanter, femoral neck and femoral head region.

Table 3. 1: Description of the collected samples.

	ID	Gender	Leg Pos	Age (y)	DXA (g/cm²)	
					FN	WPF
Sample01	3414	Male	Right	80	0.796	0.884
Sample02	7414	Female	Right	89	0.416	0.508
Sample03	5114	Female	Left	83	0.608	0.651
Sample04	9214	Female	Right	83	0.562	0.701
Sample05	4514	Female	Left	82	0.784	0.831
Sample06	147_18	Female	Left	95	0.963	1.309
Sample07	56_18	Female	Left	96	0.543	0.503
Sample08	147_18	Female	Right	95	0.932	0.939
Sample09	56_18	Female	Right	96	0.552	0.480

Leg pos: leg position; DXA: dual-energy x-ray absorptiometry; FN: femoral neck, WPF: whole proximal femur.

Bone Sample Preparation Gold Standard

Analysis on bone samples is usually made on small specimens (<5 cm^3). Such specimens, which origin from different bones and regions, may present different shapes and sizes according to the manner of their retrieval. They may present cylindrical shape if retrieved by drilling (usually used for vertebrae) or may present cubical shape (usually used for femurs, tibiae and radii), in both cases flat and parallel faces, suited for mechanical testing, were obtained using a bandsaw. The samples are usually kept frozen (<-25°C) until use to avoid bone decomposition processes. Before undertake image acquisitions, specimens are thawed and the marrow is removed by immersing the bone in hypochlorite for 1 day and rinsed repeatedly with hot water (H. Chung et al. 1993) or using a gentle water jet (Chamith S. Rajapakse et al. 2009a). the rationale for marrow removal is dual, firstly, once removing the cortex and cutting the bone, contact with oxygen leads to a transformation of haemoglobin in hematopoietic marrow from the diamagnetic oxy to the paramagnetic deoxy state. The cellular confinement of paramagnetic deoxyhemoglobin leads to intrinsic gradients, which cause considerable further shortening of the effective transverse relaxation time during MRI acquisition.

Secondly, cutting the intact bone causes fluid leaking resulting in air cavities which are deleterious to both NMR microscopy and T_2^* measurements leading to local field distortions caused by different susceptibility between air and marrow tissue. However, bone marrow has to be replaced in order to obtain enough signal to acquire MR images, therefore specimens are usually suspended in distilled water (H. Chung et al. 1993) or in other aqueous solutions as 1 mM Gd-DTPA seen to shorten the longitudinal relaxation time to about 300 ms, consistent with fatty marrow (Chamith S. Rajapakse et al. 2009a; H.-W. Chung et al. 2009). The suspension in aqueous solution do not prevent by itself the presence of air bubbles trapped in the trabecular network neither lead to their substitution, hence air bubbles removal methods have been investigated. The most common technique to remove remaining air inclusions is through centrifugation, applying between 1500 and 2000 rpm (approximately 6×g) for 5 minutes (Chamith S. Rajapakse et al. 2009a; X. S. Liu, Cohen, et al. 2010).

Large Femur Preparation Protocol

According to the size of human femurs, the centrifugation technique previously used for small bone specimens is not suitable. On that basis, we designed and tested an in-house sample preparation protocol on one cadaveric femur.

The femurs were cut using a bandsaw along the axial direction (22 cm section proximal to the femur head) and immobilized into a resin support with an inclination of 15 degrees (Fig. 3.2a) that corresponds to the *in vivo* maximum stress of the hip articulation (Koshi 2017). The specimens were then ultimately frozen at –25°C.

Before the MRI and µCT acquisitions, the sample was thawed overnight, placed in a 2500 ml cylindrical plastic jar filled with a 1 mM Gd-DTPA saline solution (Fig. 3.2b). The MRI and µCT acquisition were performed sequentially in order to avoid repetitive frozen/unfrozen cycles. To mimic *in vivo* conditions, the diameter of the container reproduced the distance between the femur head and the skin surface (approximately between 5-7 cm). The container was then placed on a vibrating surface while successive low-pressure cycles were applied for 30 minutes using the vacuum pump (Fig. 3.2d, 3.2e). Each cycle was composed by 5 minutes of active pumping below 50 mbar and 5 minutes of relaxing time at 150 mbar hence avoiding the water saturation pressure. The preparation setup is shown in Fig. 3.2.

Different vibrating amplitude (0.1 to 1.5 mm) were used during the pumping cycles in order to generate different mechanical energies adapted to different bubbles sizes (from 20 µm to 2.5 mm of diameters) and allowing their displacement inside the bone.

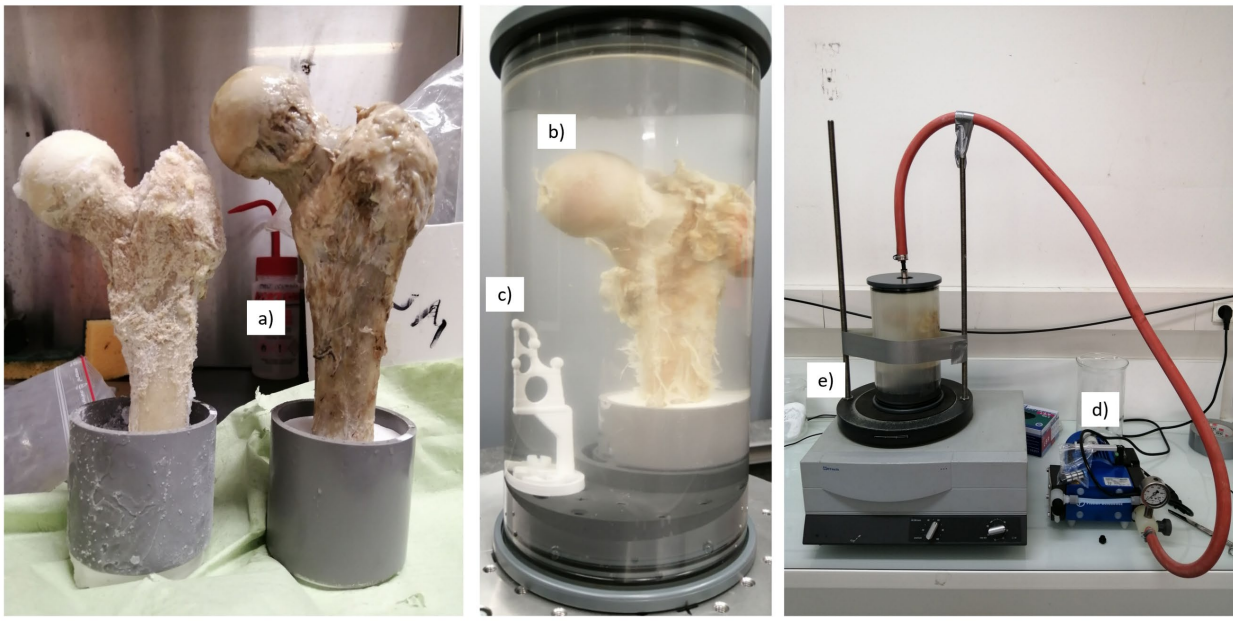

Figure 3. 2: Sample preparation. a) unfrozen femur head. b) cylindric plastic jar filled by 1mM Gd-DTPA saline solution. c) 3D-printed tool used for 3D volumes registration. d) vacuum pump. e) vibrating surfaces.

Small Specimen Extraction and Conservation

The small specimen (10 mm of diameter and 2 mm of thickness) used in this translational study were individuated and extracted using the following procedure.

Whole proximal femurs were scanned using X-ray microtomography at resolution between 51 and 62 μm^3, depending on the femur anatomical dimensions, in order to assess the complete trabecular network. The µCT images allowed to individuate the bone sections more affected by osteoporosis or more significative at microstructural level (higher bone mineral density/bone volume fraction) in three different regions of the proximal femur, the great trochanter (GT), the femoral neck (FN) and the femoral head (FH). Based on the 3D image analysis, specimens were first cored using drill press equipped with a hollow tip with an internal diameter of 10 mm and under constant water irrigation and then small disks of 2 mm width were selected and extracted cutting the trabecular core using a saw equipped with a diamond disk (Fig. 3.3).

The samples were conserved at low temperature (<-25°C) until use. Since different experimental techniques required different preparation protocols, a sample preparation paragraph is presented in each applied experimental technique.

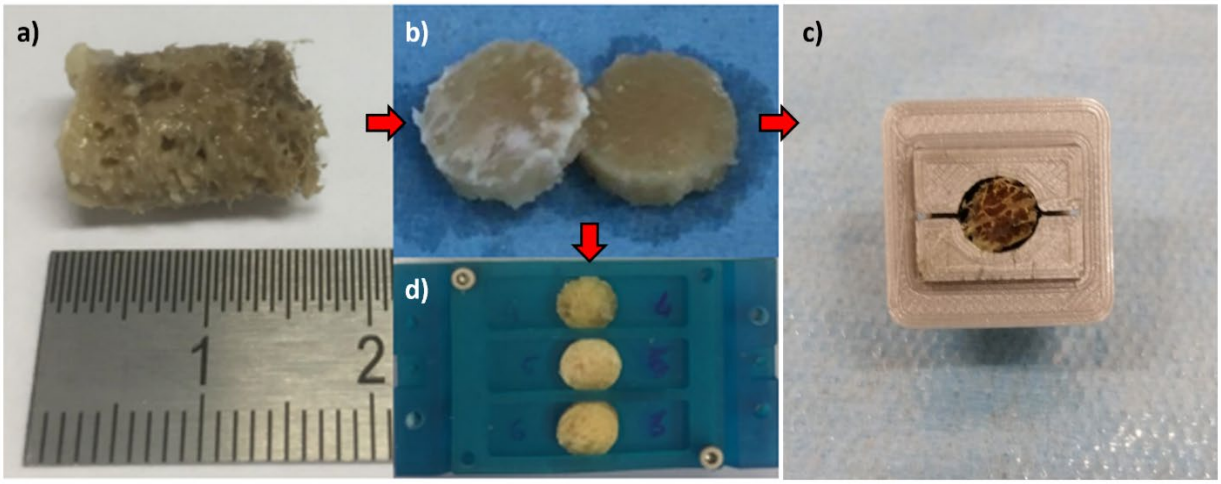

Figure 3. 3: Small sample extraction and conservation. a) core drilled from the proximal femur, b) extracted trabecular disks, c) and d) trabecular disks stored in sample holder for further experiments.

2. Multiscale and Multimodal Bone Characterization Experimental Techniques

In this section we will present all the experimental techniques used in this thesis work. The experimental techniques have been divided accordingly to the scale they have been used to investigate to. Therefore, the macroscale have been investigated using MRI, μCT and biomechanical tests applied to the whole bone; the microscale have been inspected using the synchrotron radiation μCT and the microindentation applied to three small sub-regions of each analyzed proximal femur; the nano and molecular scale have been investigated using X-ray absorption spectroscopy and Fourier transform infrared applied on the three different regions (great trochanter, femoral neck and head) of the examined proximal femurs.

2.1. Macroscale

2.1.1. High Resolution Magnetic Resonance Imaging

The most common MRI acquisition is done on the hydrogen proton ^1H and the reason is that since human body is composed approximately by 60-65% of water it represents the molecule present in higher quantity and concentration.

As previously explained all the spins of the protons are aligned along the main direction of the static magnetic field (B_0) and an application of a second RF pulse can tip the net polarization vector sideways (with a so called 90° pulse), or even reverse it (with the 180° pulse). The protons will come into phase with the RF pulse and therefore each other. The recovery of longitudinal magnetization is called longitudinal or T_1 relaxation and occurs exponentially with the time constant T_1. The loss of phase coherence in the transverse plane is called transverse or T_2 relaxation. T_1 is associated with the enthalpy of the spin system, or the number of nuclei with parallel versus anti-parallel spin, while T_2 is associated with the entropy of the system, or the number of nuclei in phase. When the radio frequency pulse is turned off, the transverse vector component produces an oscillating magnetic field which induces a small current. This small current is recorded by the receiver coil creating a signal called free induction decay (FID) and reconstructed into an image.

Table 3. 2: List of main parameters used for MRI acquisitions.

Seq.	TR/TE (ms)	Flip Angle (°)	FoV (mm)	Bandwidth (Hz/Px)	NeX	Voxel size (mm)	Slice Thickness (mm)	Slices	Acq.Time (min:sec)
7T TSE*	642 / 18	180	93*130	160	2	0.13x0.13	1.5	20	11:49
7T GRE*	12 / 4.85	12	120*175	325	3	0.18x0.18	0.5	64	13:30
7T TSE	1040 / 14	150	97*130	244	2	0.13x0.13	1.5	10	17:45
7T GRE	11 / 5.60	12	120*175	330	3	0.18x0.18	1	48	9:27
3T TSE	1170 / 12	140	119*119	255	2	0.21x0.21	1.1	36	16:45
3T GRE	16.5 / 7.78	10	120*120	130	2	0.23x0.23	1.1	40	11:17

TSE: turbo spin echo, GRE: gradient re-called echo, TR: repetition time, TE: echo time, FoV: field of view and NeX: number of excitations. The "*" refers to the pulse sequences performed using the new 7T MAGNETOM TERRA scanner recently approved for clinical applications.

In MRI the static magnetic field is augmented by a field gradient coil to vary across the scanned region to associate different spatial location with different precession frequencies, so that only those spatial regions where precession frequencies and RF frequency matches will experience an excitation. Usually, these field gradients are modulated to sweep across the region to be scanned, and the variety of both RF and

gradient pulse sequences gives MRI its versatility. Change of the field gradient spreads the corresponding FID signal in the frequency domain, and this signal can be recovered and measured by a refocusing gradient (to create a so called "gradient echo"), or by a radio frequency pulse (to create a "spin echo"). The whole process can be repeated when some T_1-relaxation has occurred, and the thermal equilibrium of the spins has been restored and the time between two successive excitations of the same slice is called repetition time (TR). Usually, in soft tissues T_1 is around one second and T_2 is a few tens of milliseconds, however these values may vary between different tissues as well as different external magnetic fields being responsible of excellent contrast between soft tissues. In addition, MRI contrast agents, i.e. Gadolinium, can be applied in order to shorten the relaxation parameters, especially T_1.

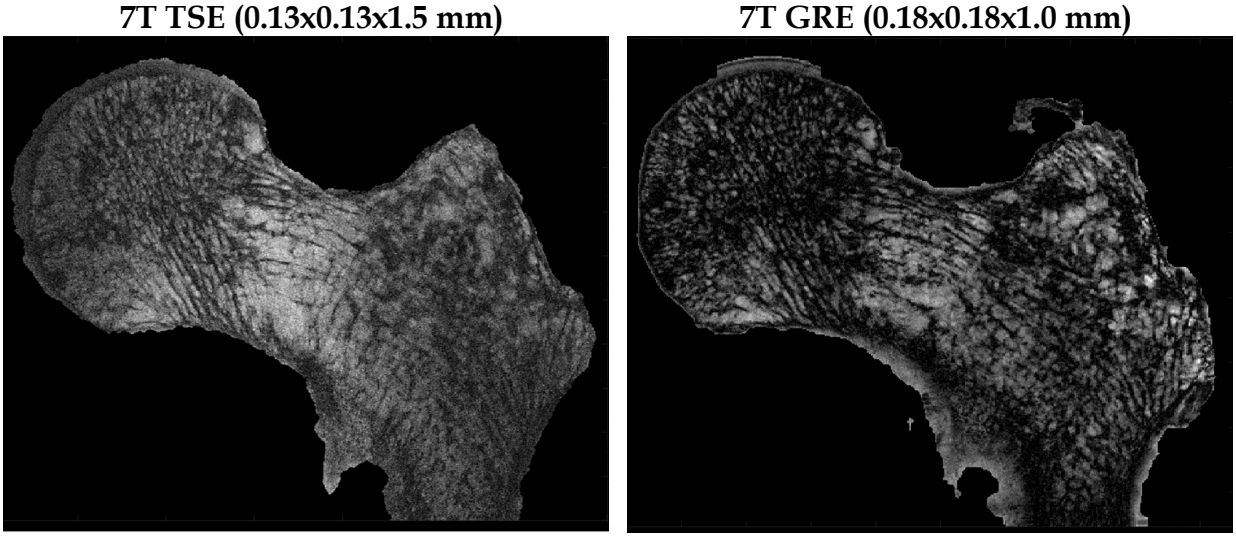

Figure 3. 4: Proximal femur coronal plane acquired using (a) 7T turbo spin echo (TSE) MRI, and (b) 7T gradient re-called echo (GRE) MRI.

In the present study four different MRI acquisitions were performed i.e. two pulse sequences (turbo spin echo (TSE) and gradient echo (GRE)) using two different scanners (3T Verio and 7T MAGNETOM, Siemens Healthineers, Germany). 3T MRI acquisitions were performed using a flexible 16Ch Heart coil, while 7T MRI was performed using a 28Ch Knee coil. The corresponding sequence parameters were similar to those used in the literature (G. Chang, Honig, et al. 2014a; Techawiboonwong et al. 2005a; Roland Krug et al. 2008a) and adapted to our sample size (Table 3.2). For the whole set of acquisitions, Coronal slices were acquired to cover the entire femoral head with the highest resolution using an acceptable acquisition time for clinical applications (14±4 minutes) (Fig. 3.4). Finally, TSE and GRE were also performed using the new 7T MRI (MAGNETOM TERRA,

Siemens Healthineers, Germany) using the same 28Ch Knee coil as the previously reported, however this 7T MRI differs from the previous 7T scanner since it has recently received the certification for being applied in clinics. All the applied parameters are reported in Table 3.2 with the name of the sequence followed by an asterisk (*).

2.1.2. X-ray micro Computed Tomography

X-ray microtomography (μCT) is a non-destructive technique that uses X-rays to create a cross-section of a physical object that can be used to create a virtual 3D model from the computer analysis of the object X-ray absorption (Fig. 3.5). the prefix micro- indicates that the smallest pixel size achievable is in the micrometer range. μCT has application in several fields, medical imaging and industrial computed tomography for the material analysis but also archaeology for the analysis of the sarcophagi contents. In clinical CT scanners usually the specimen or patient is stationary, and the X-ray tube and detector are rotating around while in industrial setup the X-ray tube and detector are stationary, and the specimen rotates.

The law of the X-ray absorption explains how, given an X-ray beam of initial intensity I_0, it is attenuated of a characteristic intensity $I(t)$ which is exponentially decreasing according to the mass attenuation coefficient (μ) and the travelled path in the object t. the mass attenuation coefficient depends by the density (ρ) of the crossed material and from the energy (E) of the X-ray beam.

$$I(t) = I_0 e^{-\mu t}$$

Hence, the X-ray beam when crossing a material is attenuated the more it crosses materials with high-atomic numbers, the lower is the energy and the greater is the thickness of the material. On the contrary, if the X-ray beam crosses a low-density material, travels a small thickness and the energy is high, the attenuation is lower. This explains why radiographies of higher-density material are brighter (maximal attenuation) and objects with lower-density appear darker (minimal attenuation). The principle of the tomographic reconstruction is that acquiring many radiographic projections on the same object from many angles it is possible to reconstruct the object in two dimensions. The third dimension is given by the application of complex algorithms able to elaborate pixels of successive scans. Each scan is represented by a 2D matrix where the smallest element, named pixel, has a gray-scale value corresponding to the measure of the beam attenuation in that specific point of the object. After the application of these reconstructive algorithms the obtained output is a digital image in which are represented

the density distribution for each slice of an object where the smallest element is the voxel. The smallest is the volume represented by the voxel the highest is the spatial resolution.

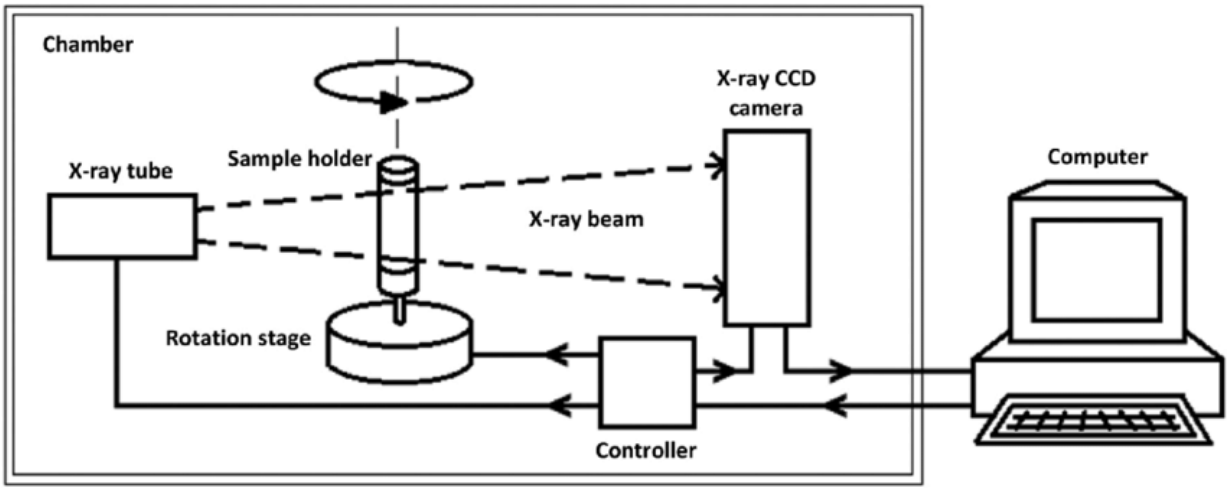

Figure 3. 5: X-ray microtomography setup.

In the present study, μCT images were acquired using Rx-Solution EasyTom XL ULTRA microtomograph ('RX Solutions SAS, 3D X-Ray Tomography Systems.', n.d.), with a 150 kV X-Ray Hamamatsu Tube allowing a focus spot size of 5 μm. In order to acquire the complete femur head volume, an isovolumetric voxel size between 51 and 62 μm^3 were chosen accordingly to the anatomical dimensions of the proximal femurs using an X-ray source voltage of 150 kV, a current of 343 mA, a frame rate of 8 images/s, and 1440 projections. Each projection was calculated on the average of 10 images to enhance the signal to noise ratio. The acquisition time was 40 minutes. Additional scans of the extracted small specimens have been acquired using an isovolumetric voxel size of 25 μm^3 (X-ray source voltage of 129 kV, a current of 219 mA, a frame rate of 6 images/s, and 1440 projections, each projection was calculated on the average of 10 images to enhance the SNR and the acquisition time was 30 minutes).

2.1.3. Biomechanical Tests

The mechanical behavior of entire bone organs is not trivial to be predicted since bone is a composite hierarchical material and therefore its mechanical response depends from both the properties of the material of which it is composed, and from the geometric spatial architecture in which the bone is arranged. A complete understanding of the relationship of these two bone characteristics is of great importance to both researchers and clinicians, as it would provide information about the normal behavior of whole bones during physiological activities, would identify areas of peak stresses which are more likely to

fracture during intense activity, and would allow the prediction of the effects caused by various pathological processes and drug treatments (Sharir, Barak, and Shahar 2008).

The samples (from Sample 01 to Sample 07) were loaded to failure in an universal testing machine (Instron 5566, Instron, Canton, MA, USA). The femurs were placed within the loading apparatus so as to simulate a sideways fall on the greater trochanter (Manske et al. 2009; Eckstein et al. 2003). Specimens were first fixed in resin (Epoxy Axon F23) at 15° internal rotation and then the femoral heads were oriented at 10° adduction within the testing machine. The load was applied to the greater trochanter (displacement rate 10 mm/min) through a pad, which simulated a soft tissue cover, and the femoral head was covered with resin to ensure force distribution over a greater surface area. Large femur biomechanical fracture test setup is shown in Fig. 3.6. Failure load (in MPa) was defined as the first local maximum after which the load declined by more than 10% divided by the bone surface at the fracture site (Le Corroller et al. 2012). Fractures were visually classified according to clinical criteria (femoral neck, intertrochanteric, subtrochanteric, or isolated greater trochanteric fractures) (D. Guenoun et al. 2020a). Finally, to assess the correlation between mechanical tests and bone morphology the linear regression between fracture load and both BMD (DXA-derived and derived from µCT and MR images) and microarchitectural parameters has been computed.

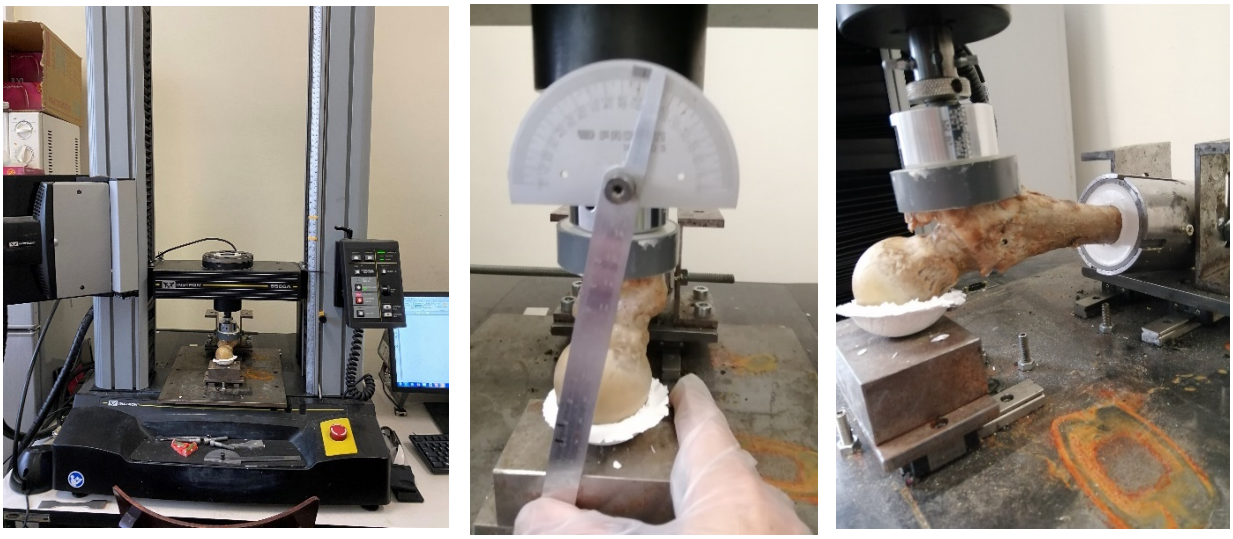

Figure 3. 6: Large femur biomechanical fracture test setup.

2.2. Microscale

2.2.1. Synchrotron Radiation X-ray micro Computed Tomography

The SYRMEP (SYnchrotron Radiation for MEdical Physics) beamline of the Elettra synchrotron laboratory (Basovizza [Trieste], Italy), beamline has been designed for research in medical diagnostic radiology, material science and life science application. The use of monochromatic and laminar shaped beams allows, in principles, an improvement of the clinical image quality and an absorbed dose reduction. Moreover, the spatial coherence of the SYRMEP source, provided by the phase-contrast techniques, is used to overcome the poor absorption contrast of biological samples.

The SYRMEP light source is a bending magnet and the horizontal acceptance covered by the front-end light-port is 7 mrad. The beamline setup showed in Fig. 3.7, provides a monochromatic and laminar-section X-ray beam with a maximum area of 160x5 mm^2 at a distance of 23 meters from the source. The monochromator is based on a double Si (111) crystals working in Bragg configuration and covers the whole angular acceptance of the beamline. The crystals assembly is equipped with high precision motion stages to set the Bragg angle and to perform the fine angular alignments between the two crystals and translating the second crystal along a linear guide of an angle of approximately 3° with respect to the beam direction makes the fixed exit of the beam. The resulting configuration of the exit beam is a beam parallel to the incident one with vertical displacement of 20 mm. the useful energy range is 8.3–35 KeV with the intrinsic energy resolution of the monochromator of 10^{-4} is reduced to about $4x10^{-3}$ due to the natural divergence of the beam.

Among the different captor configuration, the use of 16-bit air cooled CCD camera allows large field of view and small pixel size. In particular the camera quantum efficiency of 45% at 550nm at the scintillator emission wavelength, interline transfer air cooled CCD sensor with typical ΔT of > 55 OC allowing shutter less simultaneous exposure and read out cycles, a large field of view, continuously adjustable from 13.294x13.294 mm, down to 2.105x2.105 mm, variable data transfer rate 1 and 12MHz, on-chip up to 8x8 pixel binning, sub-area readout and up to 2048x2048 pixel resolution. Frame rate at 16-bit digitization: 2 fps unbinned.

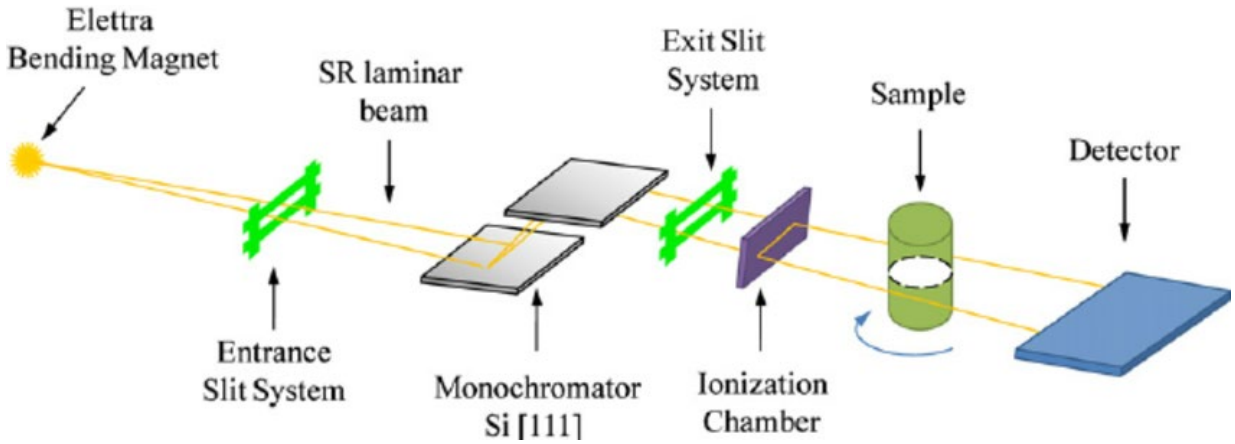

Figure 3. 7: X-ray synchrotron microtomography setup at the SYRMEP (SYnchrotron Radiation for MEdical Physics) beamline (Basovizza [Trieste], Italy).

In the current study, two proximal femurs (Sample 08 and Sample 09) have been cut using a bandsaw along the axial direction (7 cm section proximal to the femur head) to completely remove the femoral diaphysis whose encumbrance would not have allowed the sample accommodation in the acquisition setup. The samples were kept at -25° before and after performing the image acquisition while they were acquired at room temperature (15°C). Synchrotron radiation propagation-based phase-contrast SR-μCT was used to obtain the 3D virtual reconstruction of the microstructure of examined bone volumes. The center core across the whole length of femoral neck was imaged at the SYRMEP beamline, employing a filtered (1.5 mm Si +1 mm Al) polychromatic X-ray beam delivered by a bending magnet source in transmission geometry and using a mean energy of 27 KeV. The detector used was a water-cooled, 16-bit, scientific Complementary metal–oxide–semiconductor (sCMOS) macroscope camera (Hamamatsu C11440–22C) with a 2048 ×2048 pixels chip with two GGG:Eu scintillator screen (respectively 45 and 17 μm thick) through a high numerical aperture optics. The effective pixel size of the detector were set at 5.0×5.0 μm² and 0.9×0.9 μm² (obtained respectively using the scintillator of 45 and 17 μm of thickness), yielding a maximum field of view of about 10.2×10.2 mm² and 1.8×1.8 mm² respectively. The sample- to-detector (propagation) distance was set at 150 mm. A set of 1200 projections were recorded, with continuous sample rotation over a 180-degree scan angle and an exposure time per projection of 2.5 s.

Each set of acquired raw images was processed using the SYRMEP Tomo Project (STP) software suite, developed in-house at Elettra (F. Brun et al. 2015) based on the ASTRA Toolbox (van Aarle et al. 2015), to perform the CT reconstruction employing the Filtered Back-Propagation algorithm using a filter (Baker et al. 2012) to reduce the so-called ring artefacts in the reconstructed slices. A single-distance phase retrieval algorithm was

applied to projection images before CT reconstruction (Paganin et al. 2002), setting a γ parameter (ratio between the real and imaginary parts of the complex refraction index of the material under investigation) of 50 and 20 for SRμCT images with a voxel size of 5 and 0.9 μm^3 respectively.

2.2.2. Microindentation

The small trabecular specimens extracted from the great trochanter, femoral neck and femoral head of the Sample 08 and Sample 09 were mounted in ABS custom cuboid sample holders (Fig. 3.8). The sample holder have been strategically designed to immobilize the trabecular specimens therefore simplifying their manipulation during the grinding and the microindentation procedures which were performed following the protocol previously validated by Renault *et al.* (Renault et al. 2020) which will be only briefly summarized below.

The marrow trapped in the trabecular phase has been completely removed using a gentle water jet followed by an ultrasonic bath of 5 minutes (Philippe K Zysset et al. 1999). The distal surface of each specimen was polished with a polishing machine ESC-200-GTL (ESCIL®, Chassieu, France) with carbide papers (P600, P1200, P2500) under constant water irrigation. Subsequently, finer polishing was performed using a diamond solution using four different particle sizes (6, 3, 1 and 0.25 μm), which were applied in succession. The sample was cleaned with a gentle waterjet and via a 2-minute ultrasonic bath between each polishing step. Prior to mechanical testing, the sample preparation was controlled and validated under the optical microscope. Finally, the specimens were stored in their tubes with a solution containing calcium (50 mg/L) and sodium azide (0.01%) to prevent bone mineral matrix dissolving and avoid collagen degradation respectively (Gustafson et al. 1996). The tubes were then kept refrigerated at 4°C before indentation phase began.

The trabecular bone of the whole set of specimens has been characterized using a microindentation apparatus (Tester NHT², Anton Paar ®, Switzerland and Austria) equipped with a sharp Berkovich diamond indenter (tip diameter: 120 nm, elastic modulus: 1141 GPa and Poisson's ratio: 0.07) in a thermally controlled room at 23 °C and on a pneumatic antivibration table. For the indentation tests, the sample was set in a watertight support filled with calcium buffered saline up to the level of the polished surface. A total of 40 points were selected using a x20 microscopic objective on five different trabeculae located on the polished surface of the sample. A special attention was made on the placement of the points to avoid any border effect and therefore, indentation points were situated along the trabecular centerline. In addition, each indentation point

has been verified at magnitude x100 to avoid any surface irregularities (i.e. porosity). Before each set of indentation, a calibration session test was made on a fused silica reference sample, the mean values obtained were 71.3±1.6 GPa, knowing that the reference data was 72 GPa.

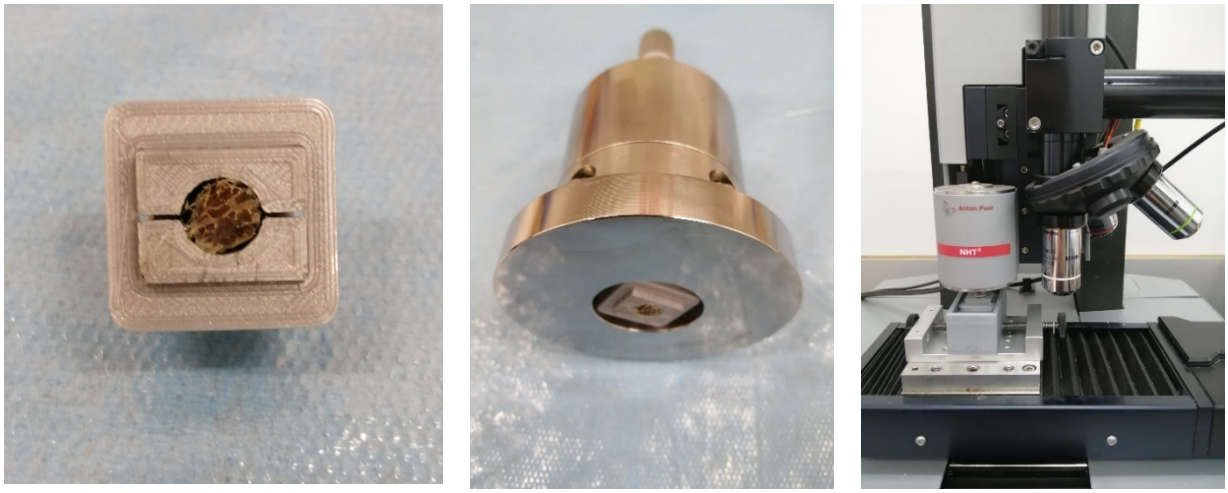

Figure 3. 8: Microindentation test setup.

The bone trabeculae were then indented using a trapezoidal loading profile (30 s: 60 s: 30 s, max load 40 mN) in the distal (polished) surface of each sample. The 60 s plateau time, higher than that found in the literature, was chosen from initial tests because wet tissue displays more viscous mechanical behavior. The sample hardness (H) and elastic modulus (E_s) were calculated using the Oliver and Pharr method (Oliver and Pharr 1992). The hardness corresponded to the mean pression under the tip at maximal depth, H = Pmax/Ac, where Pmax is the maximum load and Ac the contact area, while the elastic modulus was calculated using the unloading tangent from the indent load-displacement curve (Oliver and Pharr 1992) derived from the equation:

$$\frac{1}{Er} = \frac{(1-\nu_s^2)}{E_s} + \frac{(1-\nu_i^2)}{E_{it}}$$

where E_{it} and ν_i are the known elastic modulus and Poisson's ratio of the indenter and E_r the reduced modulus. In this study, the Poisson's ratio was assumed to be 0.3, since the relative error, by varying the Poisson's ratio from 0.2 to 0.4, was found to be less than 8% in elastic modulus (P. K. Zysset 2009; D. Wu et al. 2018).

The mean and standard deviation for elastic moduli and the hardness, both expressed in GPa, were obtained for all the different tested specimens.

2.3. Nano- and Molecular Scale

2.3.1. X-ray Absorption Spectroscopy

The X-Ray Absorptiometry Spectroscopy (XAS) study the absorbing coefficient of a substance in function of the incident radiation energy of the X-Ray (D. C. Koningsberger and R. Prins 1988; de Groot and Kotani 2008; Yano and Yachandra 2009; Henderson, de Groot, and Moulton 2014).

The interaction between radiation-subjects at the energy considered is represented by the photoelectron absorption, where a photon ejects an electron from an inner state (core electron) of an atom at the right energy. A photon is absorbed, and an electron is excited from a core state to an empty state (Yano and Yachandra 2009; Penner-Hahn, n.d.; Gherase and Fleming 2019). To excite an electron in a given core-level, the photon energy has to be equal or higher than the binding energy of this core-level. This give rise to the opening of a new absorption channel when the photon energy is scanned. The energy of an absorption edge therefore corresponds to the core-level energy, which is characteristic for each element, making XAS an element-selective technique (de Groot and Kotani 2008; Yano and Yachandra 2009; Henderson, de Groot, and Moulton 2014). With XAS It is possible to measure anything and with most elements of the periodic table without the need of any assumption of symmetry or periodicity (Yano and Yachandra 2009; Bazin et al. 2014). It is possible to measure crystals or liquids or mixed phases, thin films, engineered materials and so on… however it is important to individuate the beamline that covers the absorber edge energy. During the acquisition an incident X-ray of energy E is absorbed, destroying a core electron of binding energy E0 and emitting a photoelectron with kinetic energy (E-E0) (Henderson, de Groot, and Moulton 2014; Penner-Hahn, n.d.). The core state is eventually filled ejecting a fluorescence X-ray. In XAS it is measured the dipole mediated transition of the electron in a deep core state into an unoccupied state ruled by the Fermi Golden Rule (Henderson, de Groot, and Moulton 2014; de Groot 2001).

The X-ray absorption spectroscopy setup at CLÆSS (Core Level Absorption & Emission Spectroscopies) beamline of the ALBA Synchrotron (Barcelona, Spain) is represented in Fig. 3.9.

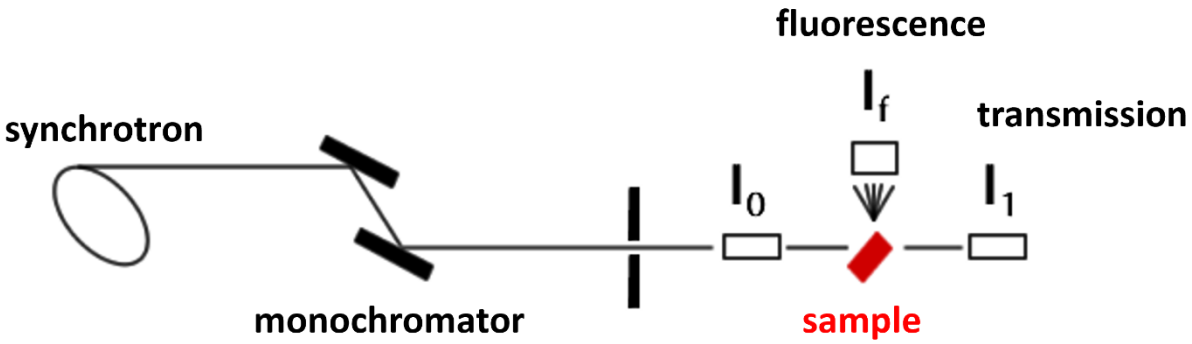

Figure 3. 9: X-ray absorption spectroscopy setup at CLÆSS (Core Level Absorption & Emission Spectroscopies) beamline of the ALBA Synchrotron (Barcelona, Spain).

The measurement's goal of XAS are about the atomic and electronic structure of the material measured, both qualitative and quantitative about the local structure of the excited absorbing element and it is possible to investigate (de Groot and Kotani 2008; Yano and Yachandra 2009; Henderson, de Groot, and Moulton 2014; Penner-Hahn, n.d.; Eisenberger and Kincaid 1978):

- Valence: the charge state of the absorber
- Species: what kind of atoms surround the absorber
- Number: how many of those surrounding atoms there are
- Distance: how far away surrounding atoms are
- Disorder: how atoms are distributed due to thermal motion on structural disorder

The X-ray absorption spectrum is usually divided into two regimes: the X-ray absorption near-edge spectroscopy (XANES), the region from before the threshold to 60-100 eV after the threshold and the extended X-ray absorption fine-structure spectroscopy (EXAFS) region which goes until the end of the spectrum (Fig. 3.10) (Yano and Yachandra 2009; Henderson, de Groot, and Moulton 2014; Penner-Hahn, n.d.; Gherase and Fleming 2019; de Groot 2001; Bazin et al. 2014). Although the two have the same physical origin, this distinction is convenient for the interpretation. XANES is strongly sensitive to formal oxidation state and coordination chemistry (octahedral, tetrahedral coordination) of the absorbing atom, while EXAFS is used to determine the distances, coordination number, and species of the neighbors of the absorbing atom (de Groot and Kotani 2008; Yano and Yachandra 2009; Carpentier et al. 2010; Sepulcre et al. 2004).

XAS methodology is an element specific methodology, so that it is possible to focus only on one element without interference from other elements present in the sample, and it is also possible to study the structural environment of each atom selectively (de Groot and Kotani 2008; Bazin et al. 2014; Gherase and Fleming 2019; Sepulcre et al. 2004; Sindhupakorn and Kidkhunthod 2021). Moreover, the atom of interest is never silent with

respect to XAS spectra while this is not always the case with respect to optical or other spectroscopic methodologies. XAS is not limited by the sample state as it is sensitive only to the local site structure (Corbett et al. 2007). Finally, damages to biological samples could be caused by X-rays however the diffusion of free radicals and hydrated electrons (both produced in biological samples by X-rays) can be minimized by the use of low temperatures (Yano and Yachandra 2009; Corbett et al. 2007).

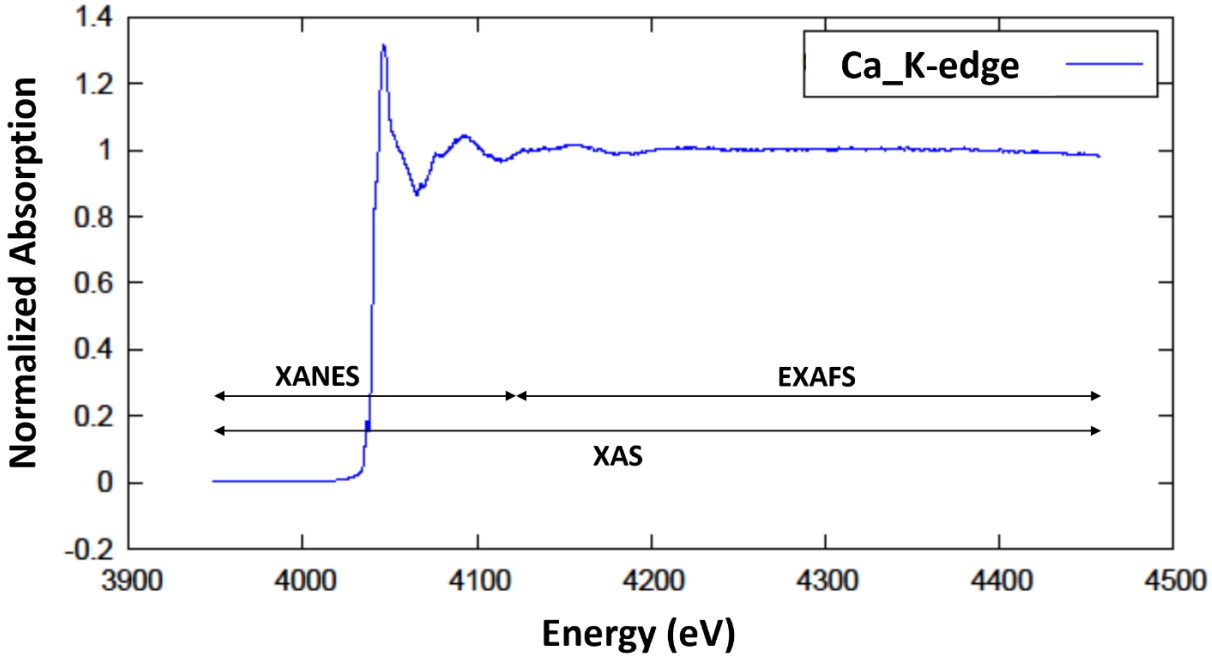

Figure 3. 10: X-ray absorption spectroscopy of Calcium K-edge showing both the X-ray absorption near-edge spectroscopy (XANES) and extended X-ray absorption fine-structure spectroscopy (EXAFS) regions.

XANES

The interpretation of XANES is complicated by the fact that there is not a simple analytic (or even physical) description of XANES (Penner-Hahn, n.d.; Sepulcre et al. 2004). It is clear, that the edge position and shape is sensitive to formal valence state, ligand type, and coordination environment (Rehr and Ankudinov 2001). If nothing else, XANES can be used as a fingerprint to identify phases (Penner-Hahn, n.d.; Sepulcre et al. 2004). Although the lack of a simple analytic expression complicates XANES interpretation, it can be described qualitatively (and nearly quantitatively) in terms of coordination chemistry, molecular orbitals, band-structure and multiple-scattering (Penner-Hahn, n.d.; Gherase and Fleming 2019; Rehr and Ankudinov 2001). These chemical and physical interpretations are all related, it all boils down to determining which electronic states the photoelectron can fill. In particular, for K shell absorption, where the core-level is a 1*s* state, the photo-electron has to end up in a *p* state (in general,

the photo-electric effect changes the orbital quantum number l to $l \pm 1$) (Yano and Yachandra 2009; Henderson, de Groot, and Moulton 2014). Thus, even if there are available states with the right energy, there might be no 1s absorption if there are no available p states. For EXAFS, where the energies are well-above the threshold energy, this is rarely an important concern. For XANES, on the other hand, this can play a very important role and the spectra are especially sensitive to such hybridization (Henderson, de Groot, and Moulton 2014). Moreover, an important and common application for XANES is to use the shift of the edge position to determine the valence state (de Groot and Kotani 2008). It is possible to show the valence dependence of ions and oxides ions. With good model spectra, the ratio between oxides can be determined with very good precision and reliability. The heights and positions of pre-edge peaks can also be reliably used to empirically determine oxidation states and coordination chemistry (Henderson, de Groot, and Moulton 2014; Penner-Hahn, n.d.; Nguyen et al. 2011). These approaches of assigning formal valence state based on edge features and as a fingerprinting technique makes XANES somewhat easier to crudely interpret than EXAFS, even if a complete physical understanding of all spectral features is not available. For many systems, XANES analysis based on linear combinations of known spectra from "model compounds" is sufficient to tell rations of valence states and/or phases (de Groot and Kotani 2008; Yano and Yachandra 2009; Henderson, de Groot, and Moulton 2014; Penner-Hahn, n.d.). More sophisticated linear algebra techniques such as Principle Components Analysis and Factor Analysis can and are also be applied to XANES spectra.

EXAFS

EXAFS refers to the details of how X-rays are absorbed by an atom at energies near and above the core-level binding energies of that atom. Specifically, EXAFS is the oscillatory behavior of an atom's X-ray absorption coefficient above an absorption edge due to the chemical and physical state of the atom (de Groot and Kotani 2008; Eisenberger and Kincaid 1978). The origin of these oscillations is of quantum mechanical nature. In fact, the photo electron has to be considered as a spherical wave which propagates away from the absorbing atom (Rehr and Albers 2000; Sayers, Stern, and Lytle 1971; Sepulcre et al. 2004). This propagating wave eventually interacts with the electronic potentials of the neighbor atoms and part of this wave is back scattered towards the origin, therefore generating an interference phenomena between the outgoing wave and the back scattered wavelets (Yano and Yachandra 2009; Rehr and Albers 2000). This interference gives rise to a modulation of the absorption probability. The EXAFS signal, which contains the information on the local structure, can be isolated and the frequencies in the signal are directly proportional to the bond distances between the absorber atom and its

neighbors (Henderson, de Groot, and Moulton 2014; Penner-Hahn, n.d.; Rehr and Albers 2000). EXAFS spectra are especially sensitive to the formal oxidation state, coordination chemistry, and the distances, coordination number and species of the atoms immediately surrounding the selected element (Yano and Yachandra 2009; Gherase and Fleming 2019; Sepulcre et al. 2004). Because of this dependence, EXAFS provides a practical way to determine the chemical state and local atomic structure for a selected atomic species (Henderson, de Groot, and Moulton 2014; Penner-Hahn, n.d.; Gherase and Fleming 2019; Rehr and Albers 2000). EXAFS spectra can be measured for essentially every element on the periodic table (Eisenberger and Kincaid 1978). Importantly, crystallinity is not required for EXAFS measurements, making it one of the few structural probes available for non-crystalline and highly disordered materials, including solutions (Eisenberger and Kincaid 1978).

XAS acquisition

In the current study, the small samples extracted in the three regions of the proximal femur (great trochanter, femoral neck and femoral head) from Sample01 to Sample05 were simply kept stored at -25°C before and after acquisition. The acquisition has been performed keeping the samples in an under vacuum (10^{-2} bar) liquid nitrogen cryostat (LN_2-cryo) environment at -80°C, which allows fully automatized X-ray absorption measurements in both transmission and fluorescence modes. The K-edge spectroscopy is a spectroscopic technique used to study the electronic structures of transition metal atoms and complexes. This method measures X-ray absorption caused by the excitation of a 1*s* electron to valence bound states localized on the metal, which creates a characteristic absorption peak called the K-edge. Calcium K-edge XAS measurements were collected in the fluorescence mode at the CLÆSS (Core Level Absorption & Emission Spectroscopies) beamline of the ALBA Synchrotron (Barcelona, Spain) using a single channel silicon drift detector. The synchrotron radiation of a wiggler source was monochromatized by means of a Si(111) double crystal monochromator. The focus at the sample position was 200x200 µm. The calibration of the monochromator was performed by measuring the spectrum of the Calcium Phosphate $Ca_3(PO_4)_2$ pellet measured in transmission mode. The absolute energy reproducibility of the measured spectra was ±0.1 eV. The incoming energy resolution around the Calcium K-edge can be estimated below 0.4 eV. The incoming and outcoming flux have been measured by two customized ionization chambers to have respectively the ~10 and 75% of absorbance.

The spectra, between 45 to 55 per sample depending on the sample size, have been selected and acquired following a grid with a step size of 1.25mm, were measured in fluorescence using a 6-channel silicon drift detector (SDD) (Xspress'3 from Quantum

Detectors). Energy scans were made from 3950 to 4460 eV using an integration time of 0.5 s per point.

CLÆSS Spectra Analysis

Synchrotron raw data were analyzed with the collaboration of CLAESS beamline team. Firstly, the raw spectra were imported in an opensource software, Demeter (v0.9.26)(Ravel and Newville 2005), which is a comprehensive opensource system for processing and analyzing X-ray Absorption Spectroscopy data. Demeter includes three sub-softwares Artemis, Athena and Hephaestus. In our study Athena is the only software used, whose main function is to import and process XAS data which can be summed in three main steps: (i) import raw data and convert it to μ(E), (ii) normalize the data to make the measurements independent from sample details and detector setup, (iii) determine the background function and subtract it from the data in order to generate EXAFS fine-structure function X(k).

The normalization process aims to regularize the data with respect to variations in the sample preparation sample thickness, absorber concentration, detector and amplifier settings and any other measurements aspects and this step is crucial for the comparison with the theory. The normalization of a spectrum is controlled by the pre-edge and post-edge range, which defines two regions of the data, respectively before and after the edge (E0). A line is regressed to the data in the pre-edge range and a quadratic polynomial is regressed to the data in the post-edge range. Athena also uses all the data in the ranges in the regressions, hence providing the regressions relatively insensitive to exact value of boundaries. The criteria for a good pre- and post-edge lines are subjective but as a main principle they must be chosen in order to pass through the middle of the data of their respective ranges. The position of the pre- and post-edge line (Fig. 3.11a) are shown be the little orange markers. The pre-edge line is extrapolated to all energies in the measurement range data and subtracted to μ(E) with the consequent effect to put the pre-edge portion of the data to the y=0 axis. The normalization constant, μ0(E0), is evaluated by extrapolating the pre- and post-edge lines to E0 and subtracting the E0-crossing of the pre-edge line from the E0-crossing of the post-edge line, the outcome difference is the edge step parameter. A flattened spectrum is then retrieved by subtracting the difference in slope and the quadrature between the pre- and the post-edge lines from the data, after E0. This step has the effect to push the oscillatory part to the y=1 line and is used because the features extrapolation and further computations usually benefit from using flattened data rather than simply normalized data. Once normalized, in the spectra might still be present some spurious points which might be removed performing the so-called

deglitching. An example of a spectrum before and after normalization is presented in Figure 3.11.

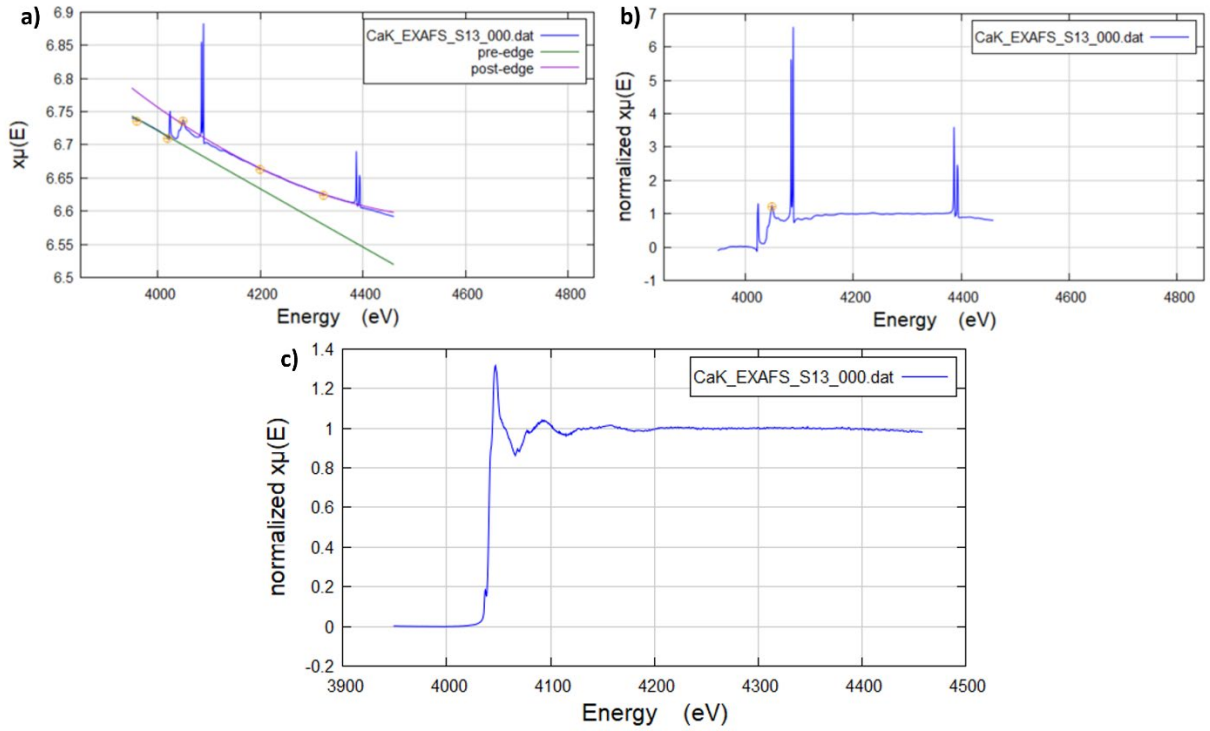

Figure 3. 11: X-ray absorption spectroscopy spectrum. a) Spectrum after positioning of the pre- and post-edge lines, b) spectrum after normalization and before deglitching, c) final XAS normalized spectrum, ready to be analyzed.

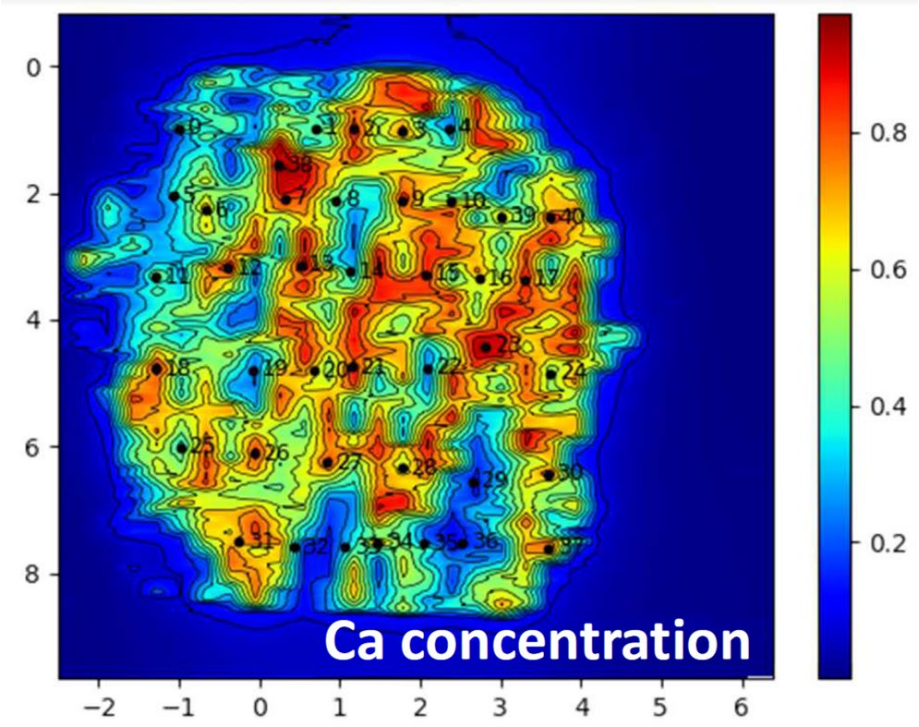

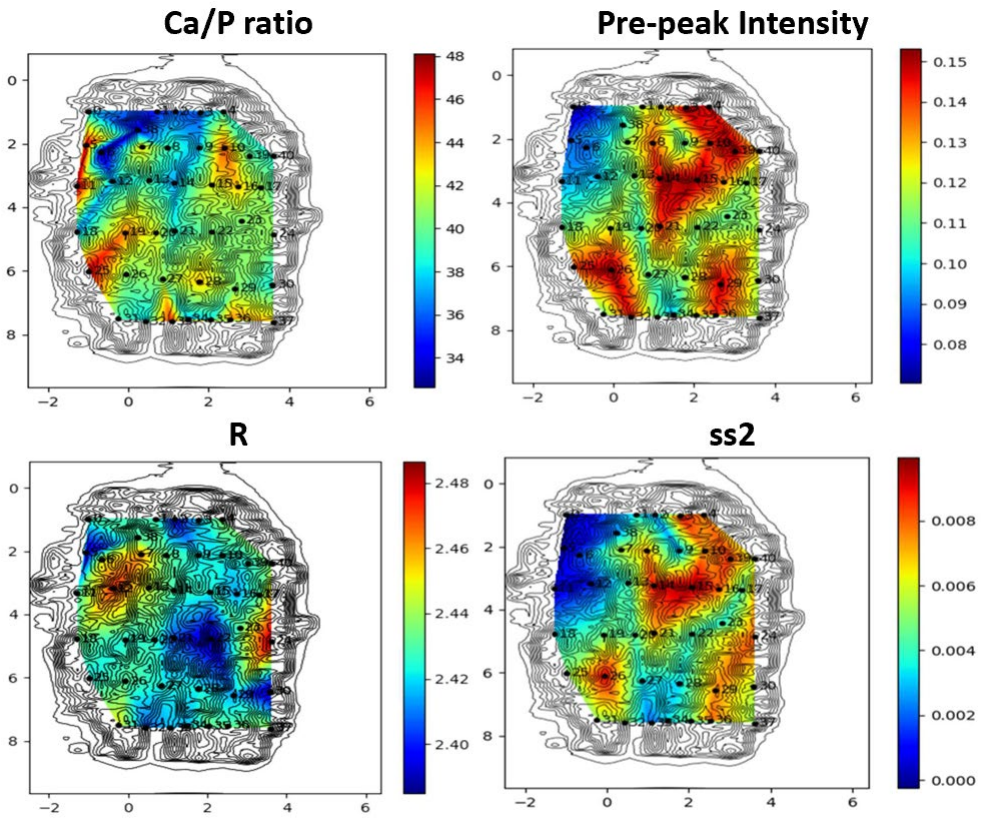

Figure 3. 12: Kernel density estimation of the derived features at CLÆSS beamline of the ALBA Synchrotron.

From each spectrum it has been possible to extrapolate four features: (i) the pre-peak area (I_G) providing a direct information on what is next to the Calcium element, (ii) the R distance representing the mean distance between the calcium and its closest atom, the oxygen, (iii) the ss2 which is the order degree of the Calcium structure providing information on the hydroxyapatite crystallinity, and (iv) the Ca/P ratio (MapRatio) which is the ratio between the calcium and the phosphorous. The features have been calculated on the basis of kernel density estimation (KDE), which in statics is non-parametric way to estimate the probability density function of a variable and it is a fundamental data smoothing problem where interferences about the population are made, based on a finite data sample. Therefore, we were able to provide a map for each of the described feature as shown in Figure 3.12.

2.3.2. Infrared Spectroscopy

Infrared (IR) spectroscopy is an absorbing spectroscopy technique normally used in the field of analytical chemistry and material characterization, as well as in physical chemistry for the study of the chemical bonds (Peter R. Griffiths and James De Haseth 2007; Taylor and Donnelly 2020). When an infrared photon is absorbed by a molecule, this molecule shifts from a fundamental vibrational state to an excited vibrational state (Peter R. Griffiths and James De Haseth 2007; A. Boskey and Pleshkocamacho 2007). These shifts are responsible for an IR spectrum where typically in the x-axis there are the frequencies expressed in wavenumber (v expressed in cm^{-1}), and in the y-axis there is the percentage of transmitted radiation, transmittance. Therefore, there will be transitions between vibrational energetic levels and the spectrum will be characterized by a peak (with variable heights) for each transition. In particular, the Fourier-Transform IR spectroscopy (FTIR) uses an interferometer which allows the scan of all the frequencies in the infrared radiation generated by the source (Peter Larkin 2011). An example of both infrared spectroscopy setup and IR spectra are shown in Figure 3.13. Among the several advantages with respect to conventional IR, it provides higher performances increasing the SNR, reducing the acquisition time and the resolution power which is maintained constant along all the IR spectrum (Taylor and Donnelly 2020). Through a detailed analysis of the absorption spectra, it is possible to derive information of subtle interactions with the surrounding groups of a molecule, and in case of FTIR analysis of bone, the spectra provide information on all bone tissue components (Peter Larkin 2011; Brian C. Smith 2011). In fact, the protein and mineral constituents produce an intense and structure-sensitive infrared modes, providing information for both the mineral (carbonate substituting in the apatite lattice and phosphate from the apatite itself) and collagen (Amide I, II and III) (Brian C. Smith 2011).

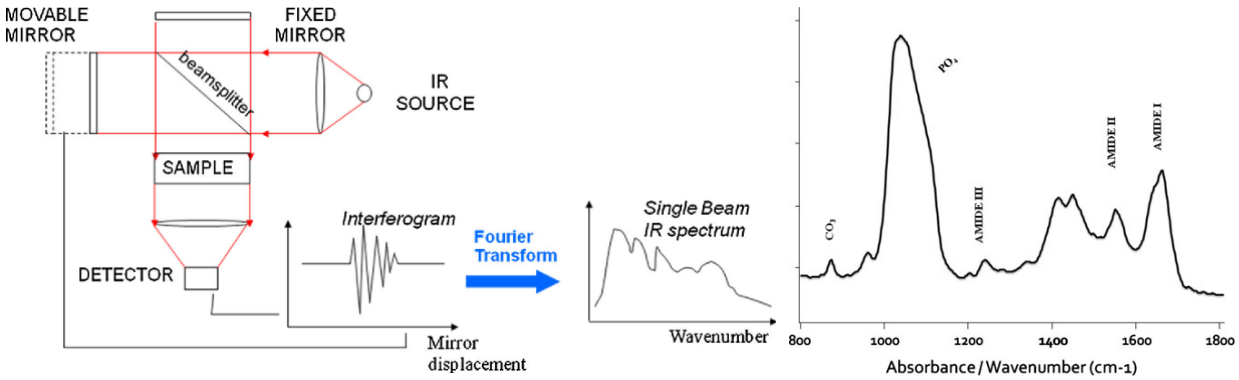

Figure 3. 13: Infrared Spectroscopy. a) Fourier Transform Infra-Red (FTIR) spectroscopy setup and b) FTIR spectra of bone sample showing principal tissue components and corresponding wavelength positions.

The most frequently reported parameters of FTIR spectroscopy regarding bone mineral properties are the mineral to matrix ratio, the mineral maturity/crystallinity, and the collagen maturity usually expressed as the ratio of the major Type I bone collagen crosslinks (Paschalis 2019a; Stockhausen et al. 2021; F. Z. Ren and Leng 2011; Landi et al. 2003b). The integrated area under an infrared band is directly proportional to the amount of species that generates the band. Therefore, the ratio between the integrated phosphate and any of the amide bands (usually Amide I) represent the amount of mineral normalized to the amount of collagen present, providing a measure of BMD that is seen to correlate with ash weight measurements (Faibish, Ott, and Boskey 2006). However, this BMD measurement provide information on the amount of mineral per volume analyzed per amount of collagen present whereas conventional BMD parameters express the amount of mineral per volume. On the other hand, it may provide a description about the mineralization differentiating between hypo- or hyper-mineralized because it encompasses the major constituent of the bone. Through spectroscopic and mathematic analysis of the phosphate band, spectral regions have been identified and correlated with the various chemical environments present in biological apatites, allowing the monitoring of the calcium phosphate crystal maturity (Chappard et al. 2016). Mineral characteristic varies with tissue age as a result of the dynamic physical chemistry status of the crystals bathing in biological fluids. Hence, in the same specimen it is possible to find variable mineral maturity. As a function of age not only the carbonate content but also the type of substitution may vary influencing the solubility and the crystallinity (size and shape) of the apatite crystals (Faibish, Ott, and Boskey 2006). Among the type of substitutes the most studied are the Type A, where a carbonate is in the hydroxyl position of the apatite, and Type B where a carbonate is in the phosphate, and labile which represents loosely adsorbed carbonate on the crystal surfaces (Landi et al. 2003b). The contribution of the mineral maturity/crystallinity in determining bone strength may be represented in an increased bone fragility due to and increased maturity/crystallinity of the apatites (Paschalis 2019a; F. Z. Ren and Leng 2011). Analysis of the two major mineralizing Type I collagen crosslinks (pyr and dehydrodihydroxynorleucine) in this, histologically stained bone sections allowed the establishment of their spatial distribution variation as a function of anatomic location, cellular activity and tissue age (Schmidt et al. 2017a). As a result, it is feasible to describe differences between healthy and diseased bone independently by the status of bone turnover.

IR analysis of bone tissue has proven to be a valuable tool in the field of osteoporosis and other conditions affecting bone quality (Faibish, Ott, and Boskey 2006; Zhai et al. 2019a; Huang et al. 2003). The fact that it allows the analysis of anatomic section at microscopic level, makes IR feasible for the detection of differences between normal and

osteoporotic human bone both at mineral maturity/crystallinity and collagen crosslink ratio both invariably higher in osteoporotic bone.

In the current study, in order to assess the mineral maturity/crystallinity the attenuated total reflection Fourier transform infra-red (ATR-FTIR) measurements were obtained using a Thermo Nicolet iS50 FTIR spectrometer (Thermo Fisher Scientific Co., Waltham, MA, USA) equipped with a deuterated triglycine sulphate (DTGS) detector. The ATR spectra were recorded using a diamond ATR Smart Orbit™ accessory (from Thermo Optec) in the Mid-IR spectral range 4000-527 cm^{-1}, averaging 64 scans for each measure and 64 scans for the background. The spectral resolution is 4 cm^{-1}. For each bone sample, a small fragment was collected and analyzed. The fragments were first grinded in an agate mortar and the powder obtained was successively placed on the ATR diamond crystal. Pressure was applied to the powder to optimize the contact with the diamond crystal. Several replicate spectra were acquired for each fragment. The spectra selected for interpretation are those which presented the highest signal-to-noise ratio.

3. Image Processing and Analysis

Image Registration

Image registration was necessary to perform morphological analysis in the same bone region. Due to the difference in the slice thickness between MR and μCT images, the image alignment according to the same coronal plane is of utmost importance to obtain the same region of interest for the morphological analysis. Therefore, MRI and μCT images were co-registered in the coronal plane using a 3D-printed plastic registration tool positioned inside the plastic jar as shown in Figure 3.2c. In particular, the MRI alignment was performed during the acquisition by positioning the scan regions accordingly to the 3D-printed registration tool, while the μCT alignment along the same coronal plane was performed during the post-processing volume reconstruction step.

After the manual 3D alignment, an automatic 2D registration was used between one MR slice and a stack of 60 consecutive μCT slices (N_{reg}) centered in the MRI absolute location to find the μCT image that better corresponded to the MRI one. The registration efficiency was assessed on the basis of the normalized cross-correlation (NCC), which measures the similarity between template and image by searching the location of the maximum value in the image matrices, as previously reported (Hisham et al. 2015a).

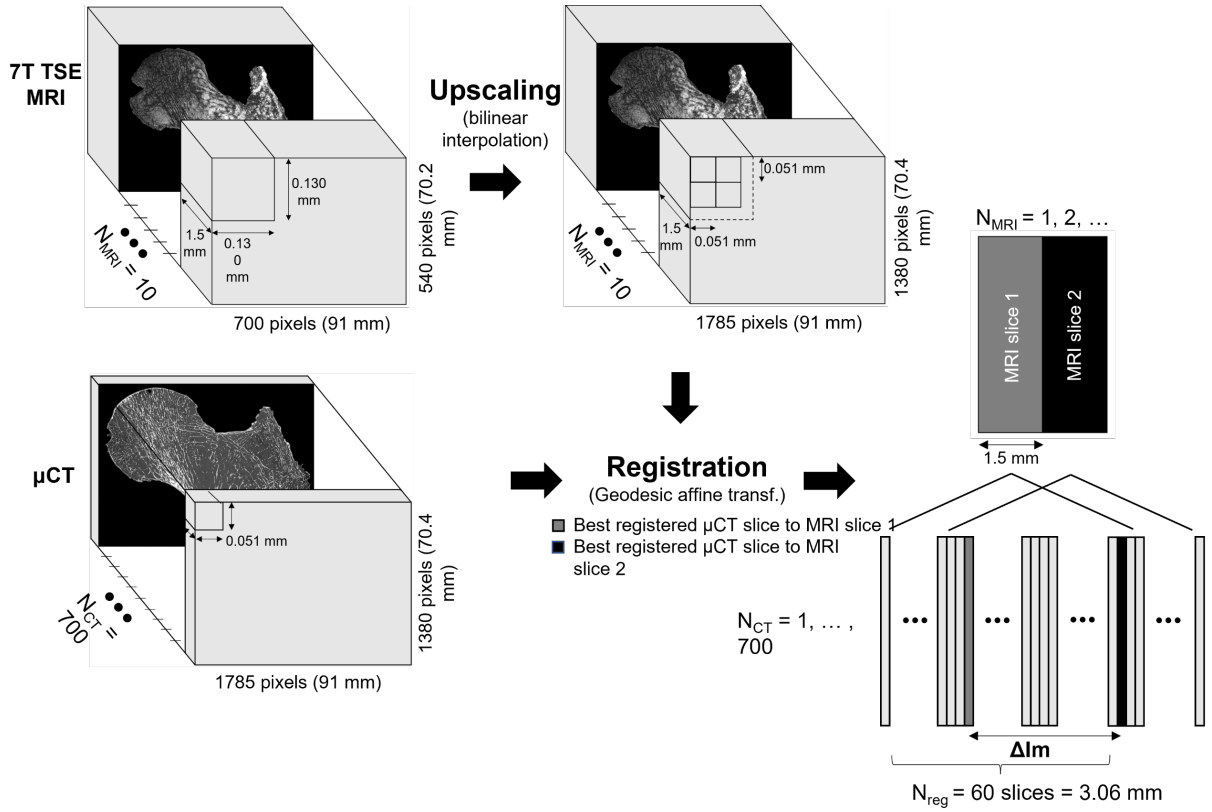

Figure 3. 14: Registration workflow.

For each stack of 60 µCT images, we selected the µCT slice with the highest NCC score as the slice that better registered with the corresponding MRI one. The MRI images were first upscaled to the µCT matrix size (1785×1380 pixels) using the bilinear interpolation in order to work in a unique reference frame (Dachena et al. 2019). The registration was then performed using a MATLAB (MathWorks, R2020b) built-in function, imregister, with a multimodal approach and a geometric affine transformation (Figure 3.14). Moreover, we defined the number of µCT images between two consecutive best-registered µCT slices as ΔIm. Considering that MR images were recorded with a space between slices equal to the slice thickness and in order to reduce the cross-talk effects, we also defined the distance between consecutive MRI slices as the expected ΔIm (expΔIm) (expressed in the number of µCT images). The expΔIm, which is unique for each MRI sequence, was calculated from the ratio between the sum of slice thickness and space between slices, and the µCT slice thickness. It is now possible to evaluate the registration quality by comparing the ΔIm mean values found between two consecutive best-registered µCT slices and the expΔIm. Moreover, to maximize the region of interest (ROI), the registration process was performed on the 3 central MRI slices characterized by the higher femur head surface. The morphological parameter analysis was performed on 2D slices.

Bone Morphological Quantification

Conventional histomorphometric parameters were quantified and compared in registered µCT/MR images using their original resolutions. Since the binarization of the solid part of MR images was not trivial, the Sauvola filter, an automatic local thresholding technique particularly useful when the background is not uniform with a window size of 10×10 pixels, was applied (Dougherty and Kunzelmann 2007b) to eliminate possible biases due to manual thresholding and to take into account important contrast variations observed in images. The segmentation of the µCT images was straightforward, since the contrast was high and the voxel size was smaller than the trabecular thickness.

Three independent parameters were extrapolated from all the binarized ROIs for the multimodal and multiscale comparative analysis (Lam et al. 2011a; Pierre-Marie Robitaille and Lawrence Berliner 2006). The bone volume fraction (BVF) was calculated as the ratio between bone volume and total volume. The trabecular thickness (Tb.Th) and the trabecular spacing (Tb.Sp) were extrapolated using the distance transformation map, from which the aperture map was derived using the software iMorph (iMorph_v2.0.0, AixMarseille University, Marseille, France) (E. Brun, Ferrero, and Vicente 2017b; E. Brun et al., n.d.). The aperture map previously used for the 2D and 3D morphology evaluation of porous matters in several fields (E. Brun, Ferrero, and Vicente 2017b) gives the diameter of the maximal disk totally enclosed and containing this voxel for every pixel. Tb.Th and Tb.Sp were then deduced from the mean values of the aperture map distribution, respectively, in the solid and the marrow phase. The trabecular number (Tb.N) was derived from the ratio between BVF and Tb.Th. The aperture map has been previously used for the 3D morphological evaluation of porous materials in different fields (E. Brun, Ferrero, and Vicente 2017b; Burghardt, Link, and Majumdar 2011a). The aperture map approach, compared to the commonly used mean intercept length technique, provides local information with a sub-voxel precision (E. Brun, Ferrero, and Vicente 2017b; Johansson et al. 2019).

Three additional morphological parameters were also assessed, i.e., the principal and secondary trabecular orientation (Tb.OrP and Tb.OrS, respectively) and the trabecular interconnectivity (Tb.Int). The local orientation of each pixel was computed using multiple 2D local Hessian matrices, each one resulting from the second-order derivatives of the gray level image convolved with a Gaussian matrix of fixed standard deviations (σ from 1 to 5). The eigenvalues and eigenvectors of the five 2D Hessian matrices were calculated and the eigenvectors corresponding to the largest eigenvalues were kept. The orientation was then calculated from the four-quadrant inverse tangent ($\tan^{-1}$) from the eigenvectors translating the main orientation (Ian Goodfellow, Yoshua Bengio, and

Aaron Courville 2016). The orientation distribution was computed considering the local orientation of binarized solid voxels only. In order to identify the first and second main directions of the trabeculae, the 2 Gaussian curves fitting method was applied using an in-house MATLAB code based on built-in function *fitnlm*, which was adapted to resolve the following model:

$$Y = a + m * x + \frac{1}{\sigma_1\sqrt{2\pi}} * e^{-\frac{1}{2}\left(\frac{x-\mu_1}{\sigma_1}\right)^2} + \frac{1}{\sigma_2\sqrt{2\pi}} * e^{-\frac{1}{2}\left(\frac{x-\mu_2}{\sigma_2}\right)^2}$$

where a is the y-intercept, m is the slope, and μ_1, σ_1 and μ_2, σ_2 are, respectively, the mean and SD of the first and second Gaussian curves.

Tb.OrP was expressed as the mean±SD of the principal fitted Gaussian curve; Tb.OrS is presented as the difference between absolute mean secondary orientation and the main principal orientation. Trabecular interconnectivity was computed as the standard deviation of the whole trabecular orientation distribution from the main principal trabecular orientation. Tb.Int represents the trabecular orientation variability and could provide information about the bone adaptability to stresses coming from different directions (Figure 3.15).

A one-way analysis of variance (factor = imaging modality) was carried out to assess the statistical effect of the imaging modality on the different morphological parameters. A p-value lower than 0.01 was considered as statistically significant. Linear regression was performed to address the functional relationship between the different imaging modalities. In addition, a Bland–Altman (BA) analysis was used to assess the agreement between the imaging modalities. The BA analysis allows the identification of any systematic difference between the measurements or possible outliers, and it is usually used to investigate any possible relationship of discrepancies between the measurements and the true value. Intraclass correlation coefficients (ICCs) were also calculated as previously reported (Koo and Li 2016a) and the agreement was considered as low (ICC<0.5), good (0.5<ICC<0.75) or excellent (ICC>0.75). Moreover, the clinical relevance of bone microarchitecture was assessed by calculating the linear regression between BMD, determined from the DXA scan, and the morphological parameters computed from the image analysis of the different imaging techniques and sequences.

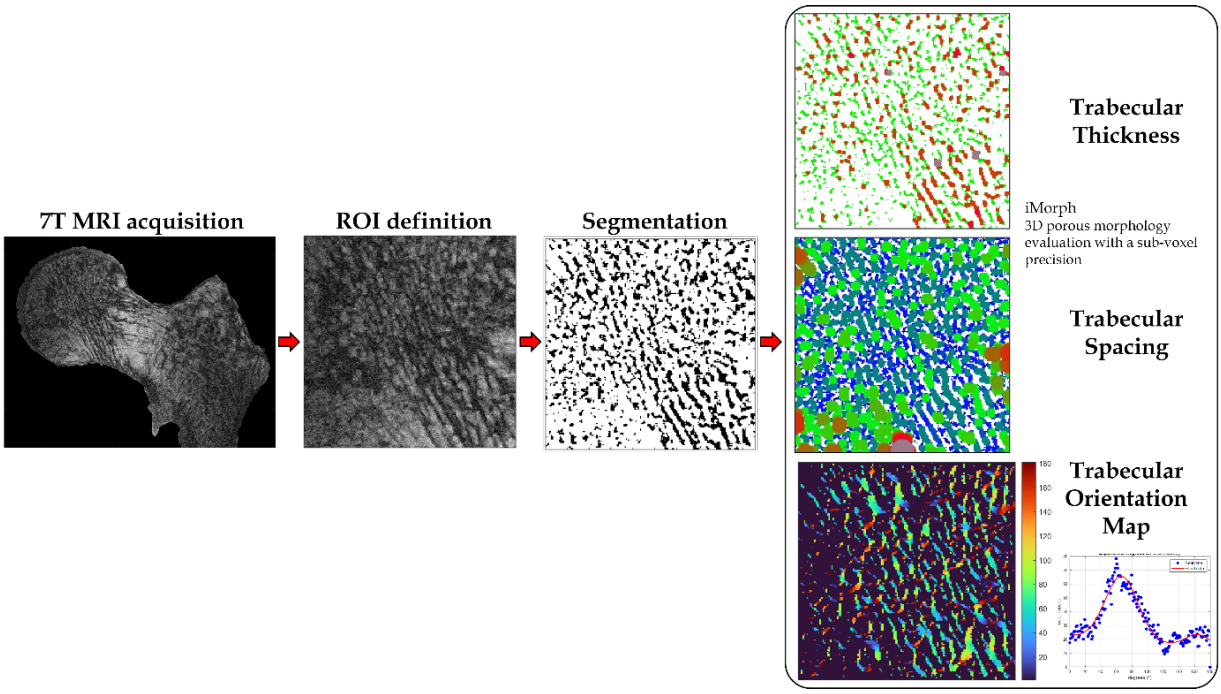

Figure 3. 15: Preprocessing and elaboration steps for the microarchitecture characteristics assessment.

Bone Mineral Density Assessment

BMD was also assessed using μCT and 7T MR images for comparison purposes. Two approaches were proposed and applied: one volumetric method, using all μCT images which provided a complete 3D bone reconstruction (Arokoski et al. 2002a), and one areal method, using the μCT and MR images with higher 2D bone surface, hence corresponding to the central coronal plane.

The BMD-DXA from the specific region of the femur neck were retrieved and the ROI used to calculate it, was individuated. Femur neck ROI was chosen as it represents one of the regions more affected by fragility fractures due to osteoporosis and one of the most commonly occurring due to sideways fall. The angle between the long bone axis and the femur head was individuated and the stack of images were oriented to obtain the ROI of the femur neck perpendicular to the y-axis (see Figure 3.16).

Firstly, using all the μCT images, a volumetric region of interest (VOI) in correspondence of the ROI used to evaluate the femur neck BMD-DXA was individuated manually. The number of bone voxels was assessed by applying the same threshold as described in the previous section. Bone mineral content ($BMC_{(1)}$) was calculated as the product of bone voxels for the bone density adjusted for porosity (ρ = 1.2 g Ca/cm^3) (Laval-Jeantet et al. 1983a). To provide the BMD comparable to conventional BMD-DXA

(expressed in g/cm²), in case of 3D µCT, the $BMC_{(1)}$ was divided by the bone surface of the central coronal plane of the VOI analyzed.

The same concept was applied to calculate BMD from a 2D image for both µCT and 7T MRIs. After the positioning of the ROI in accordance with the ROI used for the DXA analysis in the femur neck, the central coronal image in the ROI was selected and binarized. The vector crossing the bone surface in the middle was individuated and used as the rotation axis.

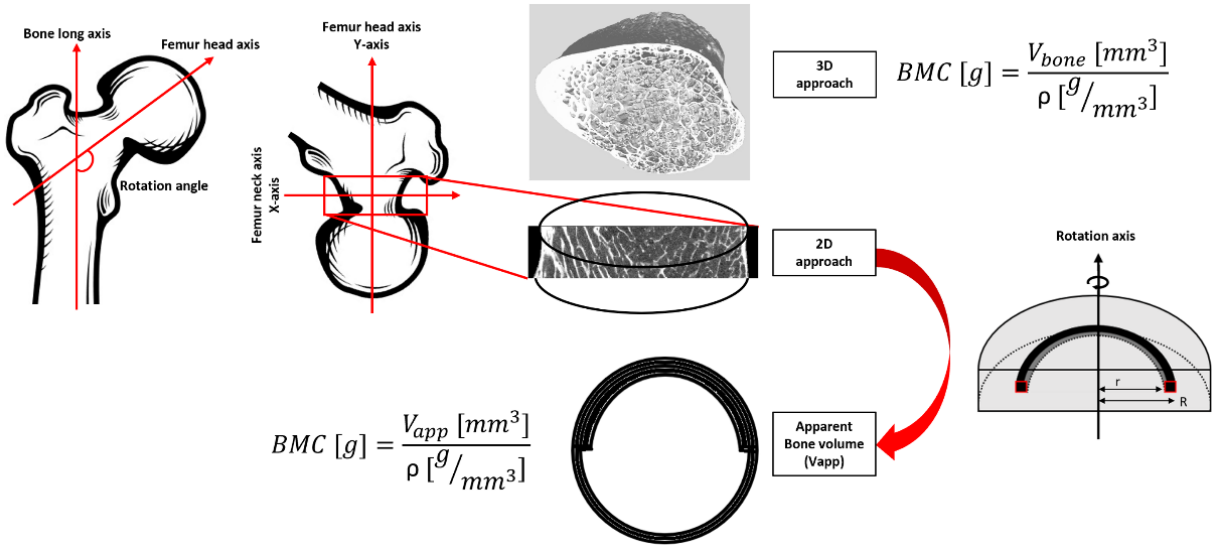

Figure 3. 16: Workflow for numerical bone mineral density estimation.

The volume that each bone pixel depicts over a rotation of 180° around the rotation axis was calculated using the volume ring formula, hence integrating the 2D surface to obtain an apparent bone volume (V_{app}) of the femur neck. The calculation was performed assuming unit height, and major (R) and minor (r) radii were assessed with respect to the rotation axis (Figure 3.16). The rotation of the 2D surface around the central coronal plane of the femur neck was made on the basis of the femur neck anatomy. In fact, the cortical thickness, which represents the most representative bone region for the BMD, is not homogeneous. The bottom cortical layer of the femur's neck is thicker than the upper layer. On that basis, a rotation over 2π of a surface expressing both the superior and inferior cortical layers, would provide a more reliable approximation of the total femur neck volume. Once obtained, the apparent bone volume, $BMC_{(2)}$ and BMD were derived as previously described. Finally, to assess the correlation between techniques, the linear regression was computed between BMD derived from DXA scans and those calculated from µCT and 7T MRIs in the same femoral neck ROI.

Sub-voxel processing

The sub-voxel processing (SubVoxel), first reported by Huang et al. (Hwang and Wehrli 2002), is an empirical algorithm (rather than one derived from mathematical theory), and it is based on the assumption that smaller voxels are more likely to have high bone volume fraction (BVF) and that bone is generally in close proximity to more bone. The main principle of the algorithm is the partitioning of each voxel into eight sub-voxels by strictly enforcing bone mass conservation. The total BVF in the original voxel is divided among the sub-voxels. The precise amount allocated to each sub-voxel is determined by the amount ad location of bone outside the voxel but adjacent to the sub-voxel. Thus, bone tends to be concentrated in the area of the voxel that closest to other bone. The images are assumed to be BVF maps where the value of each voxel is equal to the volume fraction occupied by bone.

In sub-voxel processing the voxel is first partitioned and each sub-voxel is assigned with a weight ($w_{subvoxels}$) computed as the sum of the BVFs from all the voxel adjacent to it, where the number of adjacent voxels is 2N-1, with N being the dimensionality of the image array. The bone is then partitioned among the sub-voxels according to their fractional weights. The absolute volume of bone in the voxel (BV_{voxel}) is then equal to the product of BVF of the voxel (BVF_{voxel}), the bone volume fraction of the voxel, and the volume of the voxel (V_{voxel}). To enforce conservation of bone mass, the volume of bone allocated to a sub-voxel ($BV_{subvoxel}$) may be assumed to be weight of the sub-voxel divided by the sum of the sub-voxels weights multiplied by the original bone volume of the voxel. Subsequentially, the BVF assigned to each sub-voxel ($BVF_{subvoxel}$) is then the calculated bone volume of the sub-voxel divided by the volume of the sub-voxel

$$BVF_{subvoxel} = \frac{BV_{subvoxel}}{V_{subvoxel}} = \frac{w_{subvoxel}}{w_{total}} \times BVF_{voxel} \times \frac{V_{voxel}}{V_{subvoxel}} = \frac{w_{subvoxel}}{w_{total}} \times BVF_{voxel} \times 2^N$$

It is important to note that the product $BVF_{voxel} \times 2^N$ is equal to the sum of BVF from all the sub-voxels in the voxel.

If the BVF in the voxel is particularly high, a sub-voxel may be assigned an unrealistic BVF > 1 because the sub-voxels are smaller than the original voxel. In that case, the sub-voxel is assigned a BVF of 1 and the residual bone is partitioned among the other sub-voxels according to the remaining weights.

Zero filled interpolation

The ZFI or Sinc Interpolation (extensively reported in previous publications (Yaroslavsky 2002; Sato et al. 2000; Khaire and Shelkikar 2013)) is a function that up samples a given input y[n,m] by an integer factor using the Fourier Domain. The principle is that the up-sampling is carried out by zero-padding in the input domain between the samples, then at the Fourier domain, the single spectrum (out of the repetition of spectrums) is taken while zeroing the rest of the spectrum, i.e. by doing a low pass filtering with

$$F_{cutoff} = {}^{PI}/_{upSample\_factor}$$

and finally performing the inverse fast Fourier transform (IFFT) to the distribution. Since it has been computed a zero-padding operation in time, it is necessary to multiply by the Fourier gain. The final workflow is shown in Figure 3.17.

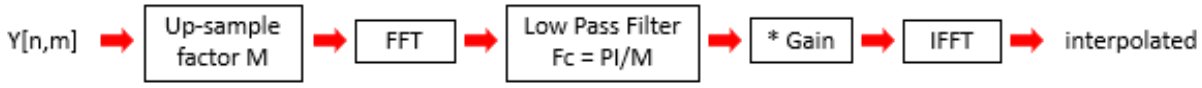

Figure 3. 17: Sinc Interpolation workflow.

It is important to note that the zero-padding must be such that the D.C. frequency remains the D.C. frequency and that the zero-padding is applied to both positive and negative frequencies. The zero-padding condenses the frequency therefore yielding to a longer series in the image domain, but without any additional information, thus the operation must be an interpolation. Finally, since there is an interpolation between the samples of a given distribution, the output array will have the size of the input array minus one, multiplied by the up-sample factor plus one.

Osteocytes Lacunae Characterization

Thanks to the extremely high resolution provided by SRμCT images at 0.9 μm^3, the image field of view was focused on a single trabecula (Fig. 3.18) and the osteocytes lacunae (OL) became assessable. To do so, focusing on the solid phase of the volume of interest, the threshold that better differentiated the bone from the OL was selected manually. The thresholding effect has been evaluated by comparing the retrieved morphological characteristics using two other thresholds (respectively +5% and -5% of the best individuated threshold). A second volumetric threshold of 100 voxels (73 μm^3) was selected to identify possible small pores derived from in-homogeneities in the image illumination, and these misclassified regions were re-added to the solid phase. Once the bone volumes were correctly segmented, the bone porosity was measured from the bone

volume and the osteocytes lacunae, vascular and canal network. Second, the osteocytes lacunae were individuated as those regions composed by a volume in range 73 to 1000 μm^3 chosen in accordance to the mean and standard deviation of OL previously find in the literature (van Oers, Wang, and Bacabac 2015; Dong et al. 2014). This approach allowed us to separate the OL from the vascular and the canal network characterized by higher volumes (in range of thousands voxels) (Fig. 3.18) (Dong et al. 2014; Carter et al. 2013). Finally, each OL was characterized individually extrapolating its volume, surface, size, shape, sphericity, and fractal anisotropy) and as an interconnected network by evaluating their region of action. In particular, in each OL the principal axes (a, b and c) of the maximum inscribed ellipsoid have been calculated, and from them it has been characterized the OL shape by deriving the aspect ratios ($\frac{a}{b}, \frac{b}{c}, \frac{a}{c} and\ \frac{a}{(b+c)}$). Then the surface (S) and the sphericity index (Fsph) (Benouali et al. 2005) have been derived respectively by the formula:

$$S_{OL} = 4 * \pi * (a^p b^p + a^p c^p + b^p c^p)^{1/p} \quad , with\ p = ln(3)/ln(2)$$

$$Fsph = 6 * V_{OL} * \left(\pi / {S_{OL}}^3\right)^{0.5}$$

Where V_{OL} and S_{OL} are respectively the volume and the outer surface of the OL. Moreover, the fractal anisotropy (Özarslan, Vemuri, and Mareci 2005) which reflects the axonal diameter and is an extension of the concept of eccentricity of conic sections in 3 dimensions, normalized to the unit range, has been calculated using the formula:

$$\sqrt{\frac{3}{2}} * \frac{\sqrt{(a-\lambda)^2+(b-\lambda)^2+(c-\lambda)^2}}{\sqrt{a^2+b^2+c^2}} \quad , where\ \lambda = (a+b+c)/3$$

Finally, the region of action could be considered as a 3D bone neighboring around the OL in which the osteocytes sense and transmit information. It is derived by applying the Voronoi map which calculates the minimum path between the closest OL and differs from the OL density because it is calculated for each OL singularly.

SRμCT at 0.9 μm³	**Osteocytes Lacunae Distribution**	**Osteocytes Lacunae Network**

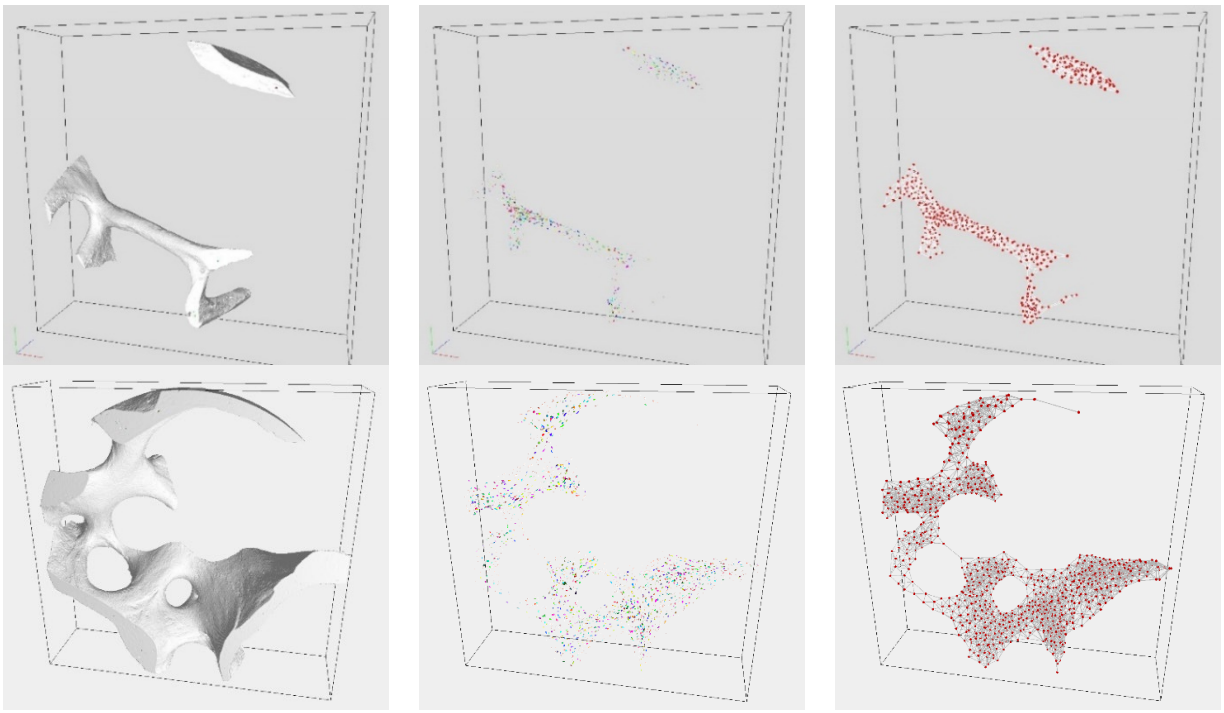

Figure 3. 18: Synchrotron radiation X-ray micro computed tomography at 0.9 μm^3. (first column) Bone solid phase in the field of view, (second column) osteocytes lacunae distribution embedded in the bone solid phase and (third column) osteocytes lacunae network, where the red dots are the barycenter of the ellipsoid inscribed in the osteocytes lacunae and the white lines shows their connectivity (Delaunay graph that is the Voronoi graph dual) between osteocytes lacunae.

Conclusion of the Chapter

In the present chapter have been reported all the collected samples, experimental techniques used for their investigations, and the preparation protocols specific for each technique. The reported experimental techniques have been divided into three main groups, i.e. macroscale, microscale and nano/molecular scale, depending on the investigative interest. In the macroscale have been proposed two different imaging techniques (magnetic resonance imaging and computed tomography) and one biomechanical tests for the whole proximal femur which simulates the sideways fall on the greater trochanter. The proximal femur microscale investigation has been performed on multiple sub-samples extracted from three different regions of the proximal femur (great trochanter, femoral neck and femoral head) based on synchrotron radiation micro computed tomography and microindentation tests on trabeculae. The SRμCT is able to reduce the image pixel size in order to completely resolve the bone microarchitecture and characterize the bone osteocytes lacunae while microindentation is able to characterize the material properties of trabeculae. The nano and molecular scale has been investigated based on two spectroscopic techniques which were also applied to small specimens of the three different proximal femur regions previously described. The X-ray absorption spectroscopy has been performed to investigate changes in the Calcium neighbors of the bone hydroxyapatite crystal due to osteoporosis while the infrared Fourier transform aimed to assess differences in the bone mineral properties usually reported as mineral to matrix ratio, the mineral maturity/crystallinity, and the collagen maturity. Finally, the last paragraph reported the image analysis performed to characterize the bone microarchitecture from MR and μCT images, and the osteocytes lacunae assessed using SRμCT. In particular it has been reported the registration process to individuate the same MR and μCT image so that the microarchitecture analysis were performed in the same proximal femur regions. Moreover, it has been reported the microarchitectural parameters usually retrieved in the literature, which were here derived using an optimized approach using the iMorph aperture map which provide sub-voxel precision and the proposed new parameter trabecular interconnectivity able to provide information about the bone adaptability to stresses coming from different directions. Finally, it has been presented two techniques reported in the literature able to reduce the image resolution in the post-processing by dividing each original pixel in four new subpixels while strictly enforcing bone mass conservation.

In Figure 3.1 it has been presented an overview of this PhD thesis study, showing how the collected samples have been repartitioned between the different studies and

examinations to optimized the results assembled during this research project. In the next chapter, it is presented a study on the optimized preparation protocol for the MRI acquisition of large cadaveric samples and in particular proximal femurs. Moreover, it is evaluated the effect that image resolution has on the assessment of the microarchitectural parameters. The research study presented in Chapter 4 aimed to validate the sample preparation protocol developed for large cadaveric bone samples, and to individuate the image resolution limit necessary to characterize the bone inner microarchitecture.

Chapter 4: Assessment of Bone Microarchitecture in Fresh Cadaveric Human Femurs : What could be the Clinical Relevance of Ultra-High Field MRI ? (submitted article)

Authors

Enrico Soldati [1,2,3,*], Daphne Guenoun [3,4], Martine Pithioux [3,5], David Bendahan [2] and Jerome Vicente [1]

Abstract

MRI could be the tool of choice for bone microarchitecture assessment, but the technique is still suffering from a low resolution as compared to the trabecular dimension. A clear comparative analysis between MRI and high-resolution X-Ray micro-tomography (µCT) regarding the microarchitecture metrics is still lacking.

In the present study, we performed a comparative analysis between µCT and 7T MRI with the aim of assessing the effects of image resolution on the microarchitecture metrics accuracy. We also addressed the issue of air bubbles artefacts in cadaveric bones.

Three fresh cadaveric femur heads have been scanned using turbo spin echo sequence at 7T MRI and µCT at high resolution (0.051 mm). The samples were submitted to a vacuum procedure combined with vibration to reduce the air bubbles volume.

Affiliations

[1] Aix Marseille University, CNRS, IUSTI, Marseille, France
[2] Aix Marseille University, CNRS, CRMBM, Marseille, France
[3] Aix Marseille University, CNRS, ISM, Marseille, France
[4] Institute for Locomotion, Department of Orthopaedics and Traumatology, Sainte-Marguerite Hospital, Aix Marseille University, APHM, CNRS, ISM, Marseille, France;
[5] Institute for Locomotion, Department of Radiology, Sainte-Marguerite Hospital, Aix Marseille University, APHM, CNRS, ISM, Marseille, France;
* correspondence : enrico.soldati@univ-amu.fr

Trabecular interconnectivity, a new metric, and conventional histomorphometric parameters, were quantified using MR images and compared to those derived from µCT at full resolution and at downsized resolutions (0.102 and 0.153 mm). One-way ANOVA, linear regression, Bland-Altman analysis and interclass correlation coefficients were performed for comparative analysis purposes. The correlations between these morphological parameters and bone mineral density (BMD) has been evaluated.

The amount of air bubbles was reduced by 99.8% in less than 30 minutes leaving partial volume effects as the only source of bias. The morphological parameters quantified with 7T MRI were similar and not statistically different ($p>0.01$) to those computed from µCT images with error up to 8% for both bone volume fraction and trabecular spacing. No linear correlation was found between BMD and all morphological parameters, but trabecular interconnectivity ($R^2 = 0.69$ for 7T MRI-BMD).

These results strongly suggest that 7T MRI could be of interest for the in-vivo assessment of bone microarchitecture providing additional information about bone health status and quality.

Keywords: Osteoporosis, MRI, Cadaveric Human Femur, Bone Morphology, Resolution Effect, Air Bubbles Artefacts.

1. Introduction

In the context of osteoporosis, bone fragility is commonly assessed using dual energy X-ray absorptiometry (DXA), which can measure the areal (two-dimensional) apparent bone mineral density (BMD in g/cm^2). The term 'apparent' refers to the fact that this density represents the mineral mass within the bone volume illuminated by the X-ray beam, including the bone matrix and the pore spaces. Quantitative computed tomography (qCT) and magnetic resonance imaging (MRI) could add a third dimension, yielding volumetric apparent BMD (in g/cm^3) (Seifert et al. 2014b).

On the contrary to qCT, MRI is a non-radiative technique, but the image resolution obtained with conventional clinical MRI is not sufficient to depict the trabecular dimension, i.e. 100 µm. On that basis, partial volume effects can occur and are expected to bias the quantification. So far, micro-architecture analyses using MRI have mainly been conducted in extremities such as wrist (R. Krug et al. 2008a) and knee (proximal tibiae (R. Krug et al. 2008a; Roland Krug et al. 2008a; Chamith S. Rajapakse et al. 2018a), distal femurs (G. Chang, Honig, et al. 2015a; C. Liu et al. 2018)) but not extensively in the proximal femur which is a clinical important fracture site and one of the most invalidating (van Oostwaard 2018). Proximal femur has been assessed previously using 1.5T (T.M. Link et al. 2003), 3T (G. Chang et al. 2018b) and 7T MRI (D. Guenoun et al. 2020a). However, few studies have reported a comparative analysis between ultra-high field (UHF) MRI and high resolution X-ray tomography so that the issue of image resolution for the assessment of proximal femur trabecular microarchitecture has been scarcely addressed. According to femur dimension, conventional micro tomography (µCT) can provide image resolution twice the minimum size of trabeculae and is able to distinguish bone and bone marrow thanks to their different X-Ray absorption rates. However, µCT cannot be used in humans because of the high radiation exposure. On the contrary, MRI is commonly used in humans, but the corresponding resolution is not high enough to properly investigate bone microarchitecture. More recently, it has been shown that UHF MRI can provide image resolution in the order of magnitude of the trabecular dimension, suggesting interesting perspectives for the investigation of bone microarchitecture in vivo (Karamat, Darvish-Molla, and Santos-Diaz 2016b; Roland Krug et al. 2008a; Soldati, Rossi, et al. 2021).

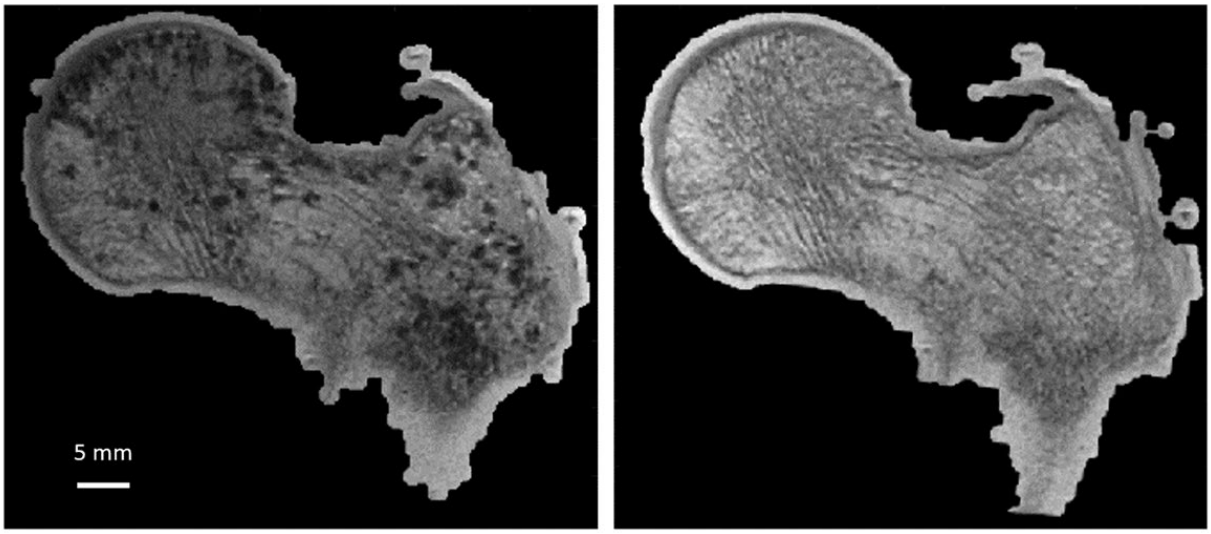

Figure 4. 1: Sample one same coronal plane before and after bubble removing. Sample05 (S05) same coronal plane for 3T MRI images (0.21x0.21x1.1 mm) before (left) and after (right) the application of air bubble reduction protocol.

The first aim of the present study was to assess proximal femur head morphological parameters from ultra-high field MR images acquired using an in-plane resolution (0.130 mm) close to trabecular dimension and to compare the results with the metrics quantified from full resolution μCT images. As these measurements were planned to be performed in cadaveric samples, we expected, as previously reported, the occurrence of image artefacts due to the presence of air bubbles (Chamith S. Rajapakse et al. 2018b; X. S. Liu, Zhang, et al. 2010). Air that leaks into the marrow space during sample preparation or during the decomposition process creates signal voids that could be misclassified as "bone" signal. In addition, air inclusions cause magnetic susceptibility artefacts leading to artificial broadening of trabecular bone thickness during MRI acquisitions (Fig. 4.1). Very few methods have been developed so far to handle this issue. Bone marrow removal using a gentle water jet has been reported and combined to centrifugation in order to remove the air bubbles trapped in the marrow spaces (Seifert et al. 2014b; X. S. Liu, Zhang, et al. 2010; Chamith S. Rajapakse et al. 2009b; 2010b). However, this method is poorly suited for whole bones segments and has been usually applied on small trabecular samples. Moreover, with this kind of pre-processing mechanical properties of the femur structure are modified given that dry and hydrated bones are known to have different biomechanical properties (Nyman et al. 2006b; Bembey et al. 2006). In that context, biomechanical tests would be biased. Samples freezing may limit tissue decomposition, which is a source of air bubbles generation. However, it has been reported that MR images of unfrozen samples are characterized by a substantially lower SNR (Chamith S.

Rajapakse et al. 2018b) and a poor contrast between bone and background so that image segmentation can also be compromised (Chamith S. Rajapakse et al. 2018b).

The second aim of the study was to develop a new sample preparation protocol considering that removing air bubbles is essential to provide meaningful MR images in large cadaveric human samples. For obvious ethical reasons, measurements could not be performed in a large number of human samples.

Overall, the present comparative analysis conducted in intact human proximal femurs was expected to provide valuable insights for the potential use of Ultra-High Field MRI as a non-invasive alternative assessment method of bone microarchitecture.

2. Sample Preparation

2.1. Materials and Methods

All procedures followed were in accordance with the ethical standards of the responsible committee on human experimentation of the thanatopraxy laboratory, University School of Medicine, Hôpital de la Timone, Marseille, France that provided the bodies coming from body donation and with the Helsinki Declaration of 1975, as revised in 2000.

A first femur (Sample05) from a female donor (89 years old) was initially scanned using conventional DXA (give BMD = 0.83 g/cm^2). It was then cut using a bandsaw along the axial direction (22 cm section proximal to the femur head) and immobilized into a resin support with an inclination of 15 degrees (Fig. 4.2) that corresponds to the in vivo maximum stress position of the hip articulation (Koshi, n.d.). The specimen was then frozen at – 25°C.

Before the MRI and µCT acquisitions, the sample was thawed overnight, placed in a 2500 ml cylindrical plastic jar filled with a 1 mM Gd-DTPA saline solution (Fig. 4.2). The MRI and µCT acquisitions were performed sequentially to avoid repetitive frozen/unfrozen cycles. To mimic in vivo conditions, the diameter of the container reproduced the distance between the femur head and the skin surface (approximately 5 to 7 cm). The container was then placed on a vibrating surface while successive low-pressure cycles were applied for 30 minutes using the vacuum pump (Fig. 4.2). Each cycle was composed by 5 minutes of active pumping below 50 mbar and 5 minutes of relaxing

time at 150 mbar hence avoiding the water saturation pressure. The preparation setup is shown in Fig. 4.2. Different vibrating amplitudes (0.1 to 1.5 mm) were used during the pumping cycles to generate different mechanical energies adapted to different bubbles sizes (from 20 µm to 2.5 mm of diameters (Fig. 4.3) and allowing their displacement inside the bone.

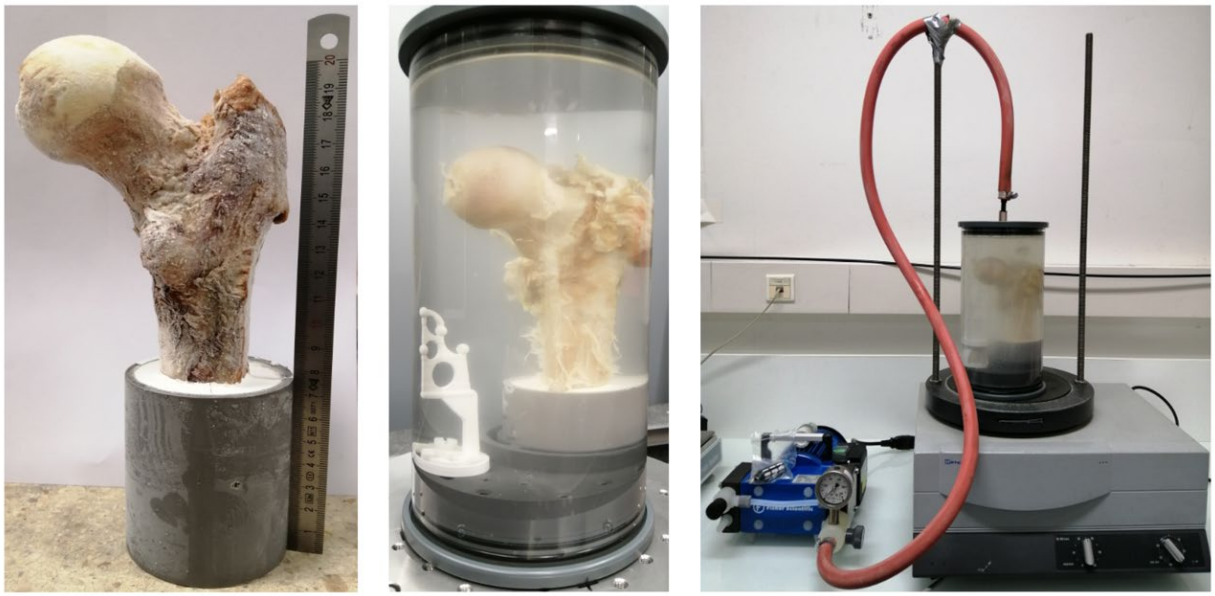

Figure 4. 2: Sample preparation setup. First Fresh sample (S05) preparation. a.(left) unfrozen femur head. b.(middle) cylindric plastic jar filled by 1mM Gd-DTPA saline solution with 3D-printed tool (bottom left) used for 3D volumes registration. c. (Right) vacuum pump and vibrating surfaces.

To quantify the effect of the successive pumping cycles, a 3D µCT acquisition have been performed before and after each cycle reporting the total volume of bubbles still present inside the bone microarchitecture. The segmentation of air bubbles was straightforward because bone, bone marrow and air have very different X-ray absorption values as shown in Fig. 4.2. Air bubbles volume (Ab.V in μm^3 and in %) was computed within the complete 3D bone volume.

2.2. Results and Discussion

As illustrated in Fig. 4.3, air bubbles were clearly visible as darker pixels in µCT images. The corresponding air volumes present inside S05 was 12.4 cm^3 (Table 4.1). During the vacuum procedure, the air bubbles movement from the bottom cross section was clearly visible. Three vacuum cycles were applied and the total amount of air bubbles still present in the bone microstructure was very largely reduced (Ab.V < 0.5%) (Table 4.1). Moreover, the residual amount of air bubbles after each vacuum cycle has been evaluated in the case of S05. The results showed that the first vacuum cycle led to a significantly large reduction (98.7%) of the air volume while the remaining air volume was completely removed after two additional cycles (Fig. 4.3 and Table 4.1).

So far, cadaveric bone imaging using 7T MRI has mainly been performed in small specimens (<5 cm^3) (Seifert et al. 2014b; Chamith S. Rajapakse et al. 2018b) with the expected limitations due to a poor representative picture of the entire bone. Investigations of large samples would be of interest but are not trivial given that they can be biased by the presence of air bubbles. Other kinds of sample preparation aiming at eliminating the bubble artefacts have been previously reported (Seifert et al. 2014b; X. S. Liu, Zhang, et al. 2010; Chamith S. Rajapakse et al. 2009b).

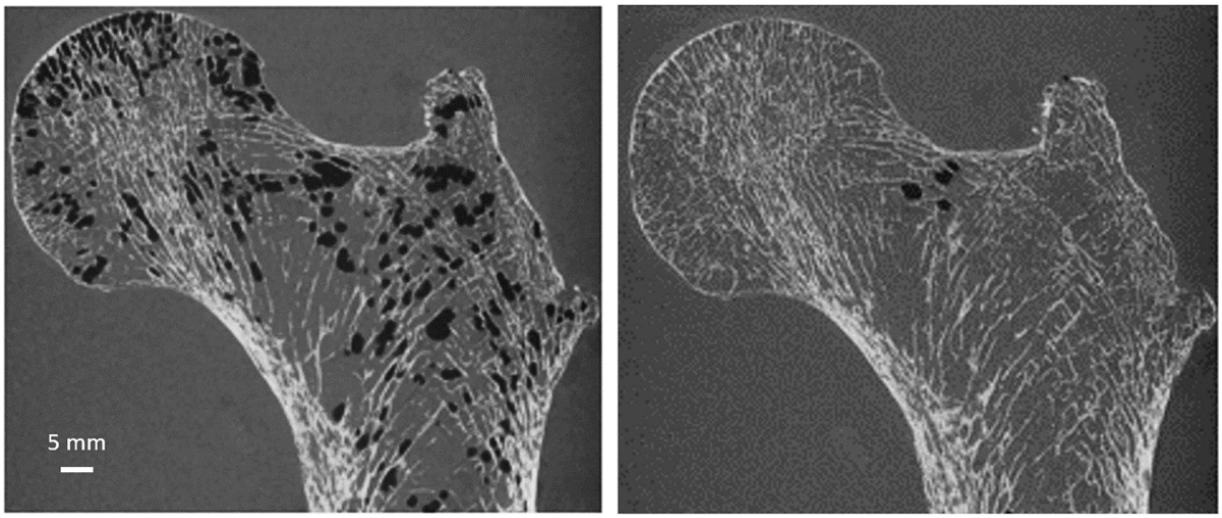

Figure 4. 3: Same coronal µCT plane before and after sample preparation. Same S05 µCT coronal plane before (left) and after (right) the application of our sample preparation technique and acquired at 0.051 mm isovolumetric resolution.

Considering that bubbles are trapped in the bone marrow, a gentle water jet has been used as a removal process. A 1 mM Gd-DTPA saline solution was then added to mimic the bone marrow magnetic response while the additional air bubbles trapped in the trabecular network were removed using centrifugation (1500 to 2000 rpm, approximately

6× g, for 5 minutes) (Seifert et al. 2014b; Chamith S. Rajapakse et al. 2009b; Majumdar et al. 1996a). Magnetic susceptibility artefacts were successfully removed using this process (Chamith S. Rajapakse et al. 2009b; Majumdar et al. 1996a). However, such a centrifugation process is not feasible for entire bone segments given the sample dimensions. In addition, one has to keep in mind that bone marrow removal would lead to changes in bone biomechanical properties given that dry and hydrated bone behave differently.

Table 4. 1: Air bubbles reduction.

	Ab.V (mm^3)				**Ab.V (%)**
	No Vacuum	**Cycle 1**	**Cycle 2**	**Cycle 3**	
Sample05	12427	154	103	27	0.22

Absolute and relative air bubble volumes for the first sample (S05) and pumping cycles.

In a work conducted on mid-diaphysis of human cadaveric bones dried at different temperatures, Neyman et al., showed that stiffness linearly increased with an increased water loss. In addition, they showed that this water loss was associated with a decrease of both bone strength and toughness (Nyman et al. 2006b). Moreover, Bembey et al. showed that an increased hydration was associated with a 43% decrease in stiffness while a decrease resulted in a 20% increase in bone stiffness (Bembey et al. 2006). In our study, the vacuum procedure, combined with vibrational shear, uniformly pushed the physiological solution inside the bone without modifying the inner microarchitecture while replacing the air bubbles and keeping the bone marrow. The bone marrow viscoelastic biomechanical response was thus preserved so that potential biomechanical tests could provide representative results.

3. MRI Microstructure Quantification

3.1. Materials and Methods

MRI Imaging

The specimen was scanned at 7T (MAGNETOM, Siemens Healthineers, Germany) using a turbo spin echo (TSE) sequence and a 28Ch Knee coil (TR/TE = 1040ms/14ms, bandwidth = 244 Hz/Px, FOV = 130°, resolution = 0.130x0.130x1.5 mm, space between slices = 1.95 mm, NeX = 2, number of images = 10, scan time = 17:45 min). The sequence parameters were similar to those reported in the literature (G. Chang, Honig, et al. 2014b; Techawiboonwong et al. 2005b; Roland Krug et al. 2008a) and adapted to our samples size. In the present study, we used a turbo spin echo sequence which is designed as pairs of radio frequency pulses, one excitation pulse and a 180° refocusing pulse. This sequence is considered as less sensitive to susceptibility arfefacts (Chamith S. Rajapakse et al. 2009b; Roland Krug et al. 2008a; Thomas M. Link et al. 2003b; R. Krug et al. 2008a). Coronal slices were acquired to cover the entire femoral head with the highest resolution.

µCT Imaging

µCT images were acquired using Rx-Solution EasyTom XL ULTRA microtomograph ('RX Solutions SAS, 3D X-Ray Tomography Systems.', n.d.), with a 150 kV X-Ray Hamamatsu Tube allowing a focus spot size of 5 µm. To cover the whole femoral head, an isovolumetric voxel size of 0.051 mm has been chosen. The other parameters were, 343 mA current, 150 V voltage, 8 images/s and 1440 projections over 360 degrees of rotation. Each projection was obtained from the average of 10 images to increase the signal to noise ratio. The acquisition lasted approximatively 40 minutes.

Image Registration

MRI and µCT images were co-registered in the coronal plane using a 3D registration tool (Fig. 4.2). For the µCT acquisition, the alignment along the coronal plane was made during the post processing volume reconstruction step. For the MRI acquisition, the alignment was performed before the acquisition.

After a 3D alignment of all the different stacks of images along the same coronal plane, an automatic 2D registration between each 7T MR slice with an appropriate stack of 60 consecutives µCT slices covering two times the 7T MR slice volume was performed (Fig. 4.4). The efficiency of the registration process was quantified using a correlation score

(Fig. 4.4). Both the 2D registration process and the correlation score were performed using an in-house build code based on MATLAB build-in functions: *imregister* with a multimodal approach and a geometric affine transformation, and corr2, returning the 2D correlation coefficient between pictures with similar sizes. Before registration, the image with the lowest resolution was upscaled and resized. Moreover, to maximize the region of interest (ROI), the registration process has been performed on the 3 central MRI slices which were characterized by the higher femur head surface. The morphological parameter analysis was then performed on these 2D MRI slices and their respective registered µCT slices.

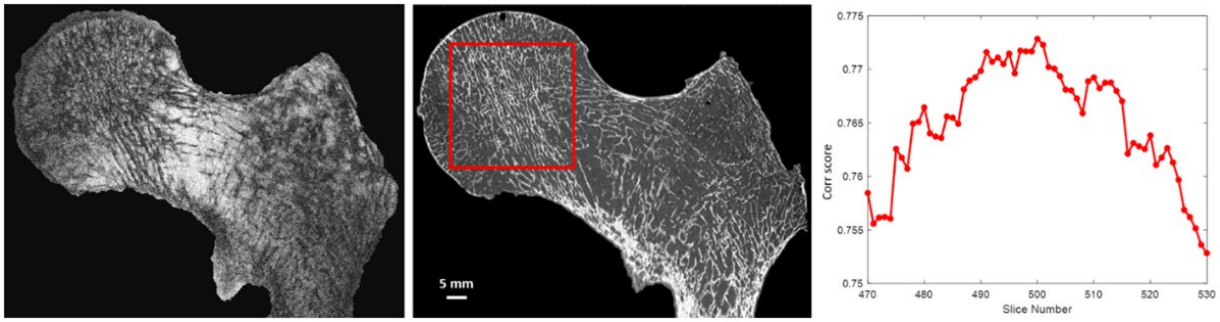

Figure 4. 4: 7TMRI - µCT image registration. (left) 7T MR image, (center) µCT - 7T MRI best registration with highlighted ROI, (right) correlation score of one 7T MR image with a stack of 60 consecutive µCT images of the first analyzed sample (S05).

Microstructure Quantification

Conventional histomorphometric parameters were quantified and compared between 3 registered MR/µCT images using their original resolutions. As the binarization of the solid part was not trivial in MR images, an automatic local threshold has been applied as previously described (Dougherty and Kunzelmann 2007a) to eliminate possible biases due to manual thresholding and to take into account important contrast variations observed in images. The µCT binarization was straightforward as the contrast was high and the voxel size was smaller than the trabecular thickness.

Based on the binarized ROIs, three independent parameters have been calculated. Bone volume fraction (BVF) refers to the ratio between the bone volume and the total volume. Trabecular thickness (Tb.Th) and spacing (Tb.Sp) were extrapolated using the distance transformation map from which it has been derived the aperture map (AM) using the software iMorph (E. Brun, Ferrero, and Vicente 2017a). The AM gives for every pixel of the bone the diameter of the maximal disk totally enclosed in the bone and containing this voxel. Tb.Th was then deduced from the mean value of the AM distribution. Tb.Sp was quantified from similar computations in the marrow phase. The trabecular number (Tb.N) was then calculated as the ratio between BVF and Tb.Th. The aperture map has been previously used for the 3D morphological evaluation of porous

materials in different fields (E. Brun, Ferrero, and Vicente 2017a; Burghardt, Link, and Majumdar 2011b; Soldati, Escoffier, et al. 2020) and has been applied here for 2D images. The AM approach, compared to the commonly used mean intercept length (MIL) technique, provides local information with a sub-voxel precision (E. Brun, Ferrero, and Vicente 2017a; Johansson et al. 2019).

Trabeculae Orientation Quantification

The principal and secondary trabecular orientation (Tb.OrP and Tb.OrS) have been deduced from the computation of the local orientation distribution of bone pixels. Based on the local orientation distribution, an original morphological parameter related to the trabecular interconnectivity (Tb.Int) has been computed. It actually represents the trabeculae orientation variability around the deduced principal trabecular orientation (Fig. 4.5).

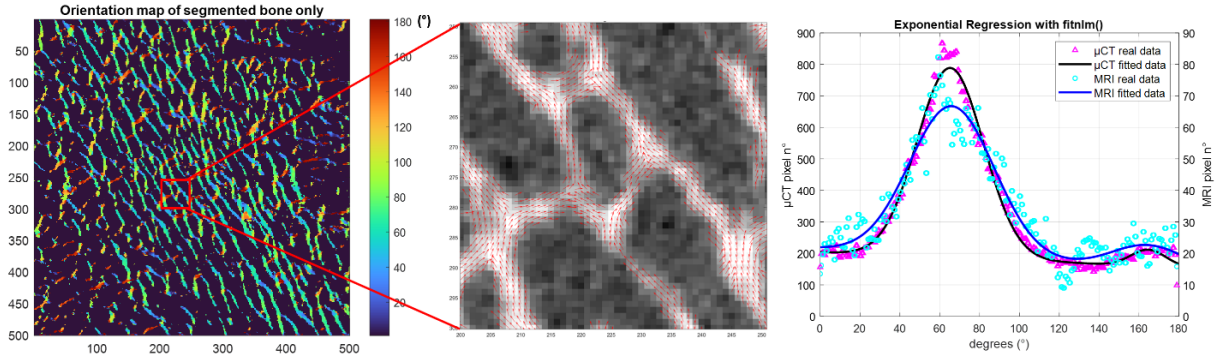

Figure 4. 5: Trabecular orientation quantification. (left) S05 µCT orientation map of the segmented bone phase. (center) µCT local orientation at pixel level. (right) Trabeculae orientation distribution expressed between 0 and 180 degrees obtained from all bone pixels - purple (µCT) - light blue (7T MRI), and gaussian curve fitting - black (µCT) - blue line (7T MRI).

Local orientation of each pixel has been computed using 2D local Hessian matrix obtained directly from grey levels. For every pixel, 5 different 2D Hessian matrixes have been generated, each one resulting from the second order derivatives of the gray level image convolved with a gaussian matrix of fixed standard deviations (σ from 1 to 5). The eigenvalues and eigenvectors of the five 2D Hessian matrices have been calculated and the eigenvectors corresponding to the largest eigenvalues have been kept. The orientation has then been calculated from the four-quadrant inverse tangent (tan-1) from the eigenvectors translating the main orientation (Ian Goodfellow, Yoshua Bengio, and Aaron Courville 2016). In order to keep the only direction of the solid bone phase, the orientation distribution was computed considering the local orientation of binarized solid voxels only. Moreover, in order to identify the first and second main directions of the trabeculae, a 2 gaussian curves fitting has been applied using an in-house MATLAB code

based on build-in functions *fitnlm*. Tb.OrP was expressed as the mean ± SD of the principal fitted gaussian curve. As the secondary orientation was supposed to be perpendicular to the main trabeculae orientation, Tb.OrS has been presented as the difference between absolute mean secondary orientation and the main principal orientation. In order to assess the angular variability around the principal direction Tb.OrP, Tb.Int has been computed as the standard deviation of the whole trabecular orientation distribution from the main principal trabecular orientation.

One could hypothesize that for high trabecular interconnectivity values, trabecular bone would display a wide range of multiple directions which could illustrate an important bone adaptability to stresses coming from different directions.

Effect of Image Resolution on the Morphological Quantification

To quantify the effect of the resolution on morphological parameters, the original high resolution µCT images were downsized by a factor 2 (degµCT2) and 3 (degµCT3). Pixels were merged by blocks of 8 and 27 leading to a voxel size of 0.102 mm and 0.153 mm respectively. The degraded µCT images together with full scale µCT and 7T MRI provided the appropriate datasets for a multimodal and complete multiscale comparative analysis.

3.2. Results and Discussion

Bone Morphology Quantification

As illustrated in Table 4.2 the microarchitecture parameters computed from the 7T MR images were comparable to those derived from µCT images. The S05 corresponding errors calculated for each images were higher for Tb.Th (10% and 11% for the first and third analyzed images respectively) while no difference was identified for the principal trabecular orientation (absolute error lower than 5% in all cases). Overall, the morphological parameters showed mean errors always lower than 9% with absolute errors ranging from 0 to 8% for BVF, 3 to 11% for Tb.Th, 1 to 8% for Tb.Sp, 0 to 8% for Tb.N, 1 to 3% for Tb.OrP, 4 to 5% for Tb.OrS and 0 to 9% for Tb.Int.

The computed µCT and MRI parameters reported in the present study are similar to those previously reported in femurs and radius (Majumdar et al. 1996a; Burghardt, Link, and Majumdar 2011b; Soldati, Escoffier, et al. 2020; Tjong et al. 2012a; Roland Krug et al. 2005b; Majumdar et al. 1999b), and extend previous results by adding new parameters (Tb.OrP, Tb.OrS and Tb.Int) for the quantification of trabecular health quality. Using µCT imaging of radii recorded with a 0.041 mm isovolumetric resolution, Tjong et al. (Tjong

et al. 2012a) reported BVF, Tb.Th and Tb.Sp values of 0.21, 0.21 and 0.72. The BVF (0.28) and Tb.Sp (0.87) values reported by Majumdar et al. using 1.5T MRI (0.156x0.156 in plane resolution) were similar (Majumdar et al. 1996a; 1999b). On the contrary, the Tb.Th (0.53) values they reported were larger (Majumdar et al. 1996a; 1999b) compared to our study, and the discrepancies could result from partial volume effects. The histomorphometric values reported by Krug et al. (Roland Krug et al. 2005b) from 3T MR images with a 0.23*0.23 mm in plane resolution were similar i.e. 0.32 (BVF), 0.27 (Tb.Th) and 0.56 (Tb.Sp).

Table 4. 2: Morphological characteristics between registered µCT – 7T MR images.

			BVF	Tb.Th	Tb.Sp	Tb.N	Tb.OrP	Tb.OrS	Tb.Int
S05 (DXA-BMD = 0.83 g/cm²)	im1	µCT	0.25±0.01	0.26±0.01	0.86±0.04	0.96±0.02	67±12	95±6	23.22
		7T MRI	0.25±0.01	0.28±0.01	0.92±0.08	0.89±0.04	65±14	90±6	21.96
	im2	µCT	0.26±0.02	0.26±0.01	0.82±0.05	0.99±0.03	68±12	ND	22.34
		7T MRI	0.24±0.01	0.27±0.02	0.82±0.08	0.93±0.04	69±14	ND	20.29
	im3	µCT	0.23±0.01	0.24±0.01	0.90±0.05	0.96±0.03	68±12	87±7	24.03
		7T MRI	0.25±0.01	0.26±0.02	0.97±0.06	0.95±0.03	70±13	77±14	23.96
S06 (DXA-BMD = 1.31 g/cm²)	im1	µCT	0.24±0.01	0.26±0.01	0.92±0.03	0.93±0.04	67±13	ND	24.66
		7T MRI	0.26±0.02	0.26±0.01	0.98±0.05	0.90±0.04	68±13	83±4	25.06
	im2	µCT	0.23±0.01	0.26±0.01	0.96±0.04	0.87±0.05	65±12	2±7	26.03
		7T MRI	0.24±0.03	0.27±0.01	0.99±0.06	0.91±0.04	64±15	ND	23.96
	im3	µCT	0.21±0.02	0.24±0.01	0.98±0.05	0.88±0.03	70±12	ND	25.3
		7T MRI	0.22±0.02	0.26±0.01	1.02±0.06	0.83±0.05	69±13	ND	28.04
S07 (DXA-BMD = 0.50 g/cm²)	im1	µCT	0.21±0.01	0.24±0.02	0.88±0.02	0.84±0.03	66±10	97±5	20.61
		7T MRI	0.22±0.01	0.24±0.02	0.92±0.03	0.83±0.02	65±13	100±4	18.87
	im2	µCT	0.20±0.01	0.23±0.01	0.87±0.04	0.88±0.03	68±10	93±8	21.98
		7T MRI	0.22±0.01	0.22±0.02	0.90±0.05	0.83±0.02	66±10	97±8	20.29
	im3	µCT	0.22±0.01	0.25±0.01	0.90±0.03	0.89±0.04	69±11	95±8	21.68
		7T MRI	0.24±0.01	0.26±0.02	0.96±0.04	0.85±0.03	68±12	112±15	21.46
S05 max diff %			8%	11%	8%	8%	3%	5%	9%
S06 max diff %			8%	8%	7%	5%	2%	ND	8%
S07 max diff %			6%	5%	6%	6%	3%	4%	8%

Morphological characteristics expressed as mean±SD for the three registered µCT-7T MRI images (im) for all the three different samples (S) with the corresponding maximum percentage difference (max diff%). BVF: Bone volume fraction, Tb.Th: Trabecular Thickness, Tb.Sp: Trabecular Space, Tb.N: Trabecular number, Tb.OrP: Principal trabecular orientation, Tb.OrS: Secondary trabecular orientation, Tb.Int: Trabecular Interconnectivity. ND indicates not detected data.

In agreement with the present results, literature results supported that, considering µCT measurements as the ground-truth, MRI measurements may under or overestimate bone morphological parameters given the partial volume effects (Majumdar et al. 1996a; Gonzalezballester 2002). Accordingly, MR image resolution would be the main limitation for the assessment of the inner trabeculae network which was found to be in the range of 0.100 to 0.150 mm in-plane regardless the pixel thickness. On that basis, more accurate results might be obtained for a higher MRI in-plane resolution.

Resolution Effect

As shown in Fig. 4.6, the progressive degradation of the image resolution was tightly linked to a bias regarding the whole set of microarchitecture metrics with Tb.Th being the most sensitive parameter and BVF the less. More specifically, BVF did not change significantly when the image resolution was downsized by a factor of 2 and 3. The corresponding errors were 4% and 1% respectively. On the contrary, the trabecular characteristics i.e., thickness, space, and number were more sensitive to the image resolution. The error regarding the trabecular thickness progressively increased from a mean error of 6±3% for degµCT2 to 44% for degµCT3 (for the second analyzed image of S05). Similar results were obtained for Tb.Sp and Tb.N with errors progressively increasing from ≤10% (degµCT2) to >15% (degµCT3). Trabecular interconnectivity showed similar results with absolute errors up to 8% for images degraded by a factor of 2 and up to 14% for images degraded by a factor of 3. The principal and secondary trabecular orientations showed comparable results with absolute errors always lower than 10% through the different degradations.

Our comparative analysis between µCT images obtained at different resolutions clearly supports the hypothesis that more accurate results might be obtained for a higher MRI in-plane resolution since it illustrated a progressive bias for the whole set of histomorphometric variables but BVF, Tb.OrP and Tb.OrS which remained in the same range through the different degradations. The progressive resolution degradation led to the almost complete replacement of the thinnest trabeculae by the bone-marrow signal. On that basis both the Tb.Th and Tb.Sp values were increased. These results suggest that the resolution threshold providing a proper basis for the assessment of bone trabecular structure should be between 0.100 and 0.150 mm thereby confirming and extending previous comparative analyses between industrial µCT and high-resolution quantitative CT (HR-pQCT) conducted in human vertebra (Roland Krug et al. 2005b), wrist (Tjong et al. 2012a), and tibia (Boutroy et al. 2005b; Tjong et al. 2012a; Burghardt, Link, and Majumdar 2011b; Ian Goodfellow, Yoshua Bengio, and Aaron Courville 2016). Tjong et al. (Tjong et al. 2012a) compared µCT (voxel size=0.018 mm^3) of cadaveric radii with HR-

pQCT images (0.041 mm^3, 0.082 mm^3 and 0.123 mm^3 voxel sizes) and reported that the strongest correlations and the smallest errors were obtained for HR-pQCT at 0.041 mm.

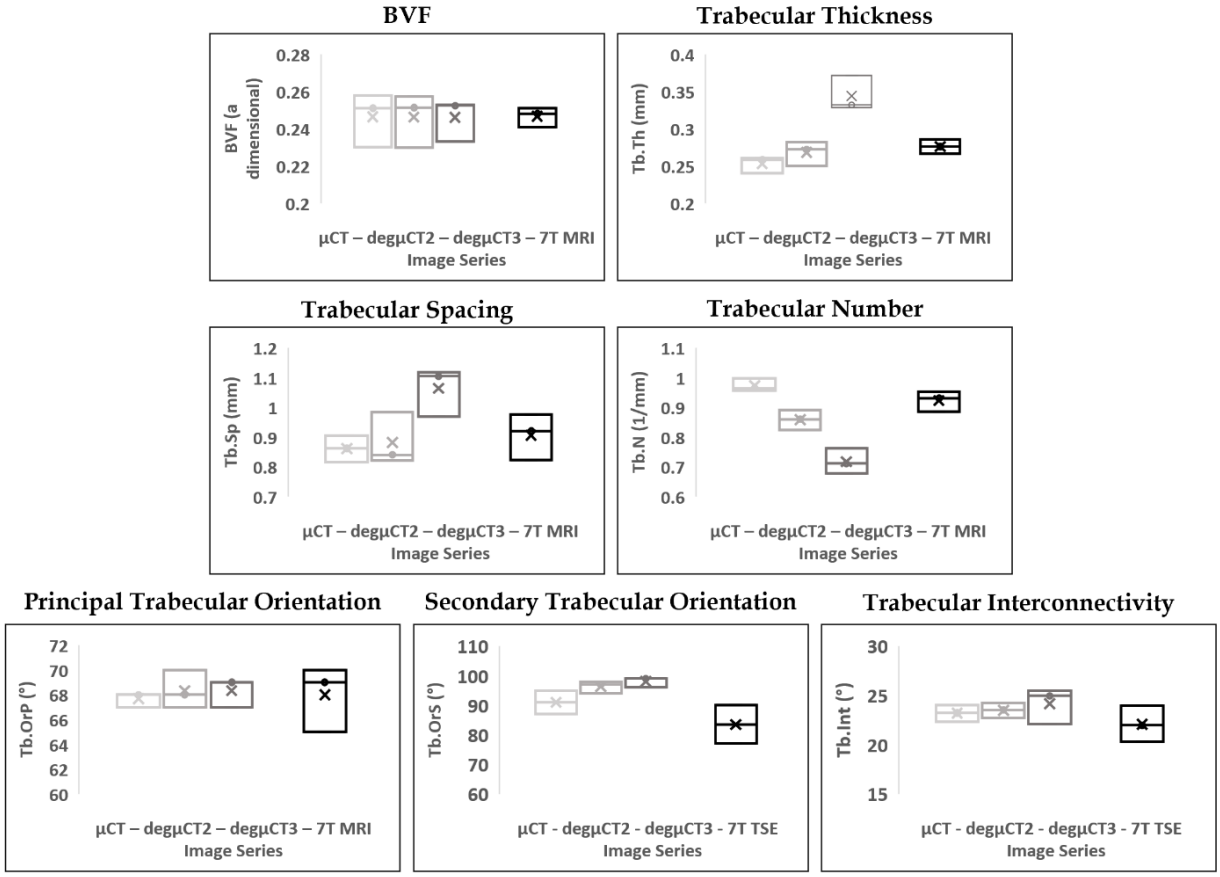

Figure 4. 6: Resolution effect on the Sample05 morphology quantification. Box plot for S05 bone volume fraction, trabecular thickness, spacing, number, principal and secondary orientation, and trabecular interconnectivity for the reference value of the µCT, the degraded µCT at 2 (degµCT2) and 3 (degµCT3) times the original µCT spatial resolution, and the 7T turbo spin echo (TSE) MRI.

On the contrary, the microstructural measurements computed from the HR-pQCT acquisition at 0.123 mm did show moderate or non-significant correlations with µCT data acquired at 0.018 mm (Tjong et al. 2012a). The comparative analysis previously performed between 3T and 7T MRI comes as an additional support (Roland Krug et al. 2008a). The MRI in plane voxel sizes reported in previous studies (0.156x0.156x0.3 mm (Majumdar et al. 1996a), 0.156x0.156x0.5 mm (Majumdar et al. 1999b), 0.156x0.156x0.7 mm (Majumdar et al. 1997b) and 0.153x0.153x0.9 mm (Thomas M. Link et al. 2003b)) for radius images were close to our in-plane voxel size at 7T (0.130 mm). Although, the slice thickness (1.5mm) used in the present study was larger than those previously reported, we obtained comparable morphological results. Using MR images with a non-isovolumetric voxel size, one can expect the mixing of bone-marrow and bone structures.

However, the parallel trabecular plates structures separated by bone marrow appeared to be orthogonal to central coronal planes (Koshi, n.d.). On that basis, increasing the in-plane resolution should enhance the signal to noise ratio. As reported by Mulder et al., the calculated volume of an ellipsoid object with the main axis oriented orthogonally to the slice thickness at high resolution (0.1x0.1 mm) was independent from the anisotropy factor (Mulder et al. 2019b). In the present study, the quantification of the trabecular orientation has shown to be independent from resolution and acquisition modality.

4. Reproducibility Analysis

4.1. Materials and Methods

Two additional complete fresh femur heads (an amount which was limited for obvious ethical reasons) from female donor with conventional DXA BMD of 1.31 and 0.50 g/cm^2 respectively for Sample06 (93 years old) and Sample07 (96 years old) has been acquired using both µCT and 7T MRI to demonstrate the reproducibility of the analysis and the robustness of the study design.

4.2. Results and Discussion

4.2.1. Sample preparation

Our in-house sample preparation protocol has been tested on the two additional cadaveric femurs. The results were comparable to those obtained for S05. The total air bubbles amount was reduced by more than 99.5% after the third vacuum pumping cycle (from 9438 mm^3 to 38 mm^3 and from 10335 mm^3 to 12 mm^3 for Sample06 and Sample07 respectively) so that the only expected bias on the morphological analysis may be related to partial volume effect due to the reduced image resolution.

4.2.2. Bone Morphology Quantification

The classical histomorphometric parameters computed from the 7T MR images were comparable to those derived from µCT images. The overall corresponding absolute errors were 8% for BVF, Tb.Th and Tb.N and 7% for Tb.Sp (see Table 4.2). The new evaluated

parameters showed similar results, the principal and secondary trabecular orientations appeared to be consistent for all the samples and they showed an absolute error lower than 5% in all cases. The trabecular interconnectivity maximum error were never exceeding 9%.

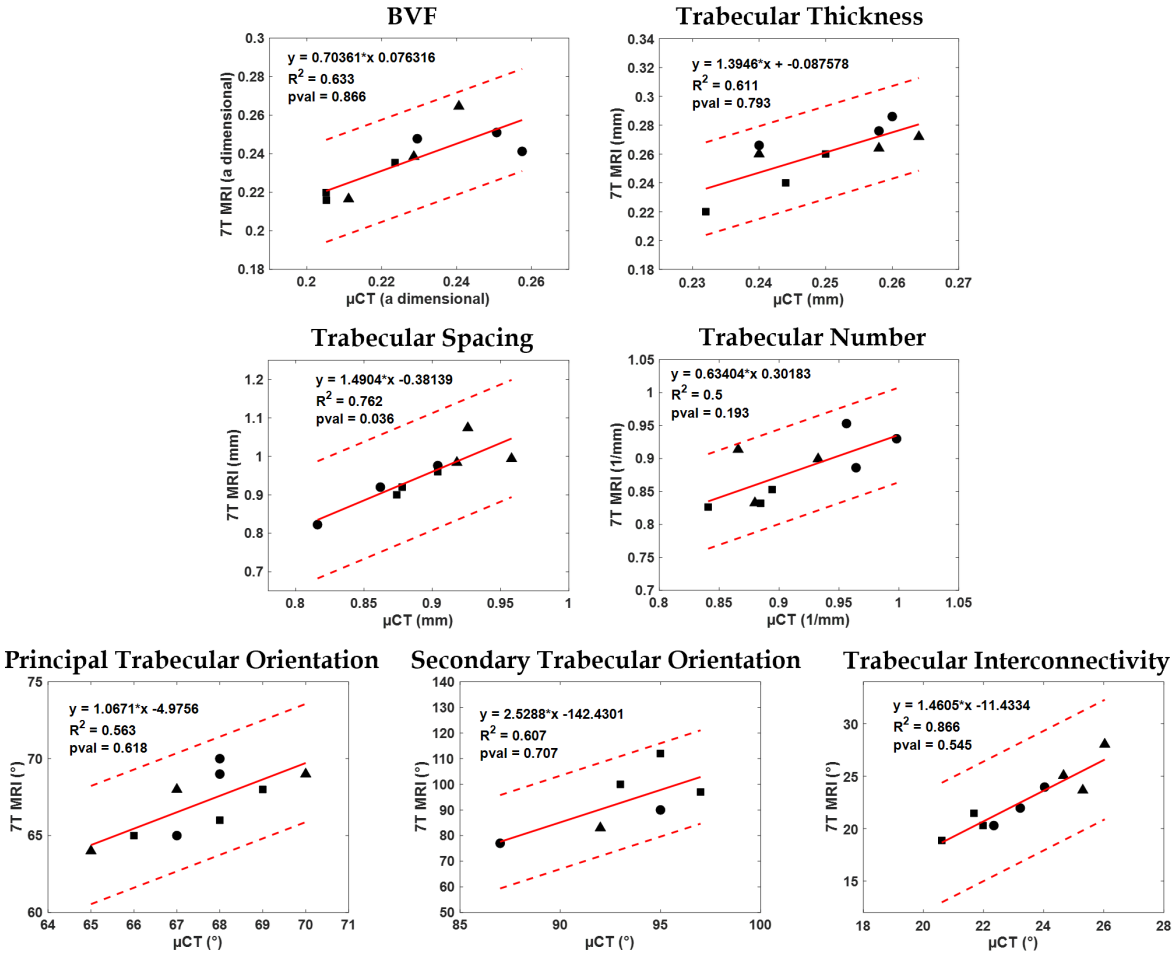

Figure 4. 7: Reproducibility analysis: µCT – 7T MRI linear regression. Linear regression between 7T MRI and reference µCT for bone volume fraction, trabecular thickness, spacing, number principal and secondary orientation, and trabecular interconnectivity for each of the 3 images of S05 '●', S06 '▲' and S07 '■'. – Each graph shows the slope, the coefficient of determination (R^2), the p-values (p-value<0.01 stands for representative feature and the degree of confidence (±2SD).

A one-way analysis of variance (one-way ANOVA) was performed to assess the difference between morphological parameters computed in 7T MR and µCT images using all the 9 µCT-7T MRI available images (3 registered images for each of the 3 analyzed samples). A p-value lower than 0.01 was considered as significant. The linear regression between given morphological parameters computed from different images was calculated to address their functional relationship. The results showed no significant

statistical difference between 7T MRI and full resolution µCT for the whole set of morphological features.

The Bland-Altman (BA) analysis was conducted to assess the agreement between the imaging techniques. The intraclass correlation coefficients (ICC) were also calculated as previously described (Koo and Li 2016b) and the agreement was considered as low (ICC<0.5), good (0.5<ICC<0.75) or excellent (ICC>0.75). The coefficients of determination (R^2), which are reported in Fig. 4.7, were computed when considering the reference µCT ranged between 0.50 and 0.87 for the whole set of evaluated parameters. The corresponding bias were calculated thanks to the Bland-Altman analysis. A mean bias of 5.3% was quantified between 7T MRI and the reference µCT for the four classical morphological parameters. The corresponding bias for Tb.OrP, Tb.OrS and Tb.Int were 2.3%, 4.7% and 5.4% respectively. ICC values came as an additional support and all parameters were classified as good, BVF (0.72), Tb.Th (0.61), Tb.Sp (0.65), Tb.N (0.62) and Tb.OrS (0.53) or excellent, Tb.OrP (0.81) and Tb.Int (0.84).

4.2.3. Resolution Effect

The morphological analyses performed on S06 and S07 showed effects similar to those initially observed for S05 due to image degradation. More specifically, BVF did not change significantly when the image resolution was downsized by a factor of 2 and 3. The corresponding errors were 4% and 10% respectively. On the contrary, the trabecular characteristics i.e. thickness, space, and number were more sensitive. The error regarding the trabecular thickness progressively increased from 4% for degµCT2 to 44% for degµCT3. Similar results were obtained for Tb.Sp, and Tb.N with errors always lower than 9% for degµCT2 but always greater than 15% for degµCT3. Principal and secondary trabecular orientations showed similar results with absolute errors always lower than 5% and so regardless of the image resolution. Errors related to trabecular interconnectivity ranged from 6% for degCT2 to 12% and 14% for degCT3 respectively.

These results were further confirmed by the ICC values which ranged between 0.62 (good) and 0.98 (excellent) for degµCT2. For degµCT3, ICC values were excellent for BVF (0.94), Tb.OrP (0.90), good for Tb.Int (0.62) and low for the other parameters (between 0.27 to 0.42). Coefficient of determinations (R^2) were computed for both µCT degraded by a factor of 2 and 3 with respect to full resolution µCT reference. The results showed decreased R^2 values through degradations with R^2 values ranging from 0.52 to 0.76 for µCT degraded by a factor of 2 to values ranging from 0.08 to 0.66 for µCT degraded by a factor of 3. The corresponding bias were calculated thanks to the Bland-Altman analysis. A mean bias of 5.8% for the BVF, Tb.Th, Tb.Sp and Tb.N was found between the full

resolution µCT and degraded µCT by a factor of 2 while slightly lower biases were found for Tb.OrP (1.8%), Tb.OrS (3%) and Tb.Int (4%). In general, degCT3 showed higher biases than degCT2 for all the evaluated parameters with Tb.OrP and Tb.OrS performing the best (3% and 4.5% respectively) and Tb.Th (24%) the worst.

5. Correlation between DXA-BMD and MRI Morphology

The linear regression between the whole set of derived microarchitectural parameters and BMD derived from standard DXA analysis, for the three analyzed samples, have also been assessed to determine their correlation. Parameters computed from both µCT and 7T MR images poorly agreed with DXA-BMD values. Those computed from full resolution µCT showed no linear correlation (0.23 for BVF, 0.21 for Tb.Th, 0.26 for Tb.Sp, 0.49 for Tb.N, 0.02 for Tb.OrP and 0.01 for Tb.OrS) with BMD, while good correlations was found for Tb.Int (0.87). Similar results were found between BMD and morphological parameters computed from 7T MRI. Poor linear correlations were found for the whole set of parameters (0.2 for BVF, 0.22 for Tb.Th, 0.33 for Tb.Sp, 0.29 for Tb.N, 0.11 for Tb.OrP and 0.20 for Tb.OrS) but Tb.Int for which a moderate correlation (0.69) was identified (Fig. 4.8).

The correlation between the derived morphological parameters and the clinical standard BMD showed a poor agreement for all the morphological parameters extrapolated from µCT and 7T MR images and BMD. As expected, higher correlations were found for Tb.Sp, Tb.N and Tb.Int since osteoporosis is expected to reduce the amount of bone, fragilizing the microarchitecture. No correlation was found for principal and secondary trabecular orientation, suggesting that trabeculae are oriented according to the main stress direction which does not vary due to osteoporosis. A poor correlation was found for Tb.Th which was almost similar in the different samples. Similar results were reported by Majumdar et al. (Majumdar et al. 1997b) on in vivo distal radii. Moderate correlations between morphological parameters and BMD were observed with higher correlations for Tb.N and Tb.Sp (0.51 and 0.41 respectively).

The progressive increasing of trabecular interconnectivity with higher BMD, may suggest that trabeculae oriented along the main stress direction provided a more varied orientation profile (wider range of trabeculae oriented surrounding the individuated

Tb.OrP). On that basis, one may suggest that femurs with higher trabecular interconnectivity are able to promote the dynamics spread of an impulsive action coming from a greater range of the usual bone working point. Moreover, in case of osteoporosis the first resorbing trabeculae are the less mechanically solicited structures with orientations between the main principal and secondary orientations, leading to reduced Tb.Int values. The standard deviation depicted by the gaussian curve fitting of the main trabecular orientation clearly support this hypothesis showing a reduction of 15% from both S05 and S06 to S07 (Table 4.2). Therefore, in case of femurs with lower BMD, Tb.Int seemed to suggest an increased bone fragility and a consequent increased risk of fracture.

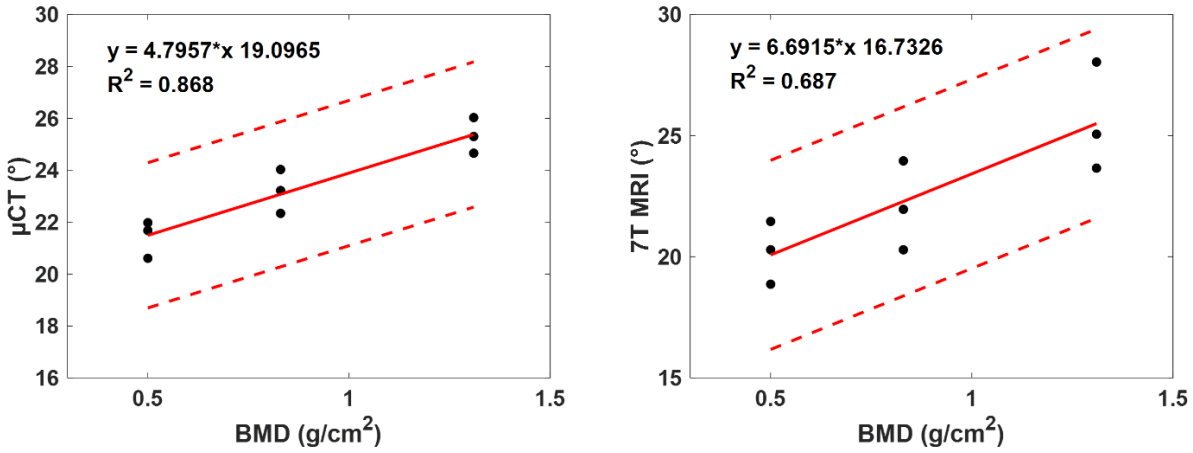

Figure 4. 8: Linear regression between DXA derived BMD and trabecular interconnectivity. Linear regression between DXA derived bone mineral density (BMD) and trabecular interconnectivity for µCT (left) and 7T MRI (right). – Each graph shows the slope, the coefficient of determination (R^2) and the degree of confidence (±2SD).

The structural organization of bone microarchitecture appeared to be a promising parameter for the evaluation of the quality and the dynamics of bone remodeling. Although, conventional histomorphometric parameters reflects the local dimensions of bone structures, yet they do not appear to be representative of the topological and structural characteristics. Due to osteoporosis, despite expected variations in the local bone dimensions, an even stronger impact could be expected on the structure's topology. This explains the moderate and poor correlations between the evaluated microarchitectural parameters and the BMD and further supports the clinical relevance of the microarchitecture analysis. Nevertheless, diagnostic clinical power might be improved if the microarchitecture analysis takes also into account the structural topological aspects. In fact, previous studies have shown that bone density and structure have to be considered as separate characteristics that could be integrated to provide a complete overview of the bone quality and health (Majumdar et al. 1997b; G. Chang et al.

2018b; D. Guenoun et al. 2020a). In the present study Tb.Int showed to correlate with BMD and suggested to be able to discriminate between healthy and pathological bones.

6. Conclusion

The investigation of large cadaveric fresh human bones is of utmost importance if one intends to reliably assess bone quality in both healthy and pathological situations. In the present study, we intended to address the issue related to air bubbles and image resolution for the histomorphometric assessment of bone using MRI.

The vacuum procedure we designed allowed an efficient removal of artefacts related to air bubbles so that the results obtained with ultra-high field MRI were comparable to those obtained using µCT and not affected by previously reported air magnetic susceptibility effects, therefore leaving partial volume effects as the only source of bias.

The comparative analysis between 7T MR images and full resolution µCT references showed that morphological characteristics computed from the 7T MR images were consistent and not statistically different with those obtained using µCT at a comparable resolution. The largest correlation was observed between 7T MRI and µCT both at 0.051 mm and 0.102 mm isovolumetric resolution. Accordingly, MR image resolution would be the main limitation for the assessment of the inner trabeculae network which was found to be in the range of 0.100 to 0.150 mm in-plane regardless the pixel thickness. Ultra-high field MRI offers such a resolution and, on that basis, more accurate results might be obtained for a higher MRI in-plane resolution.

The results related to full resolution, and progressive degraded µCT images, and MRI comes to an additional support showing that MRI can be appropriately used for a reliable assessment of bone quality as long as the in-plane resolution is in the same range of the trabecular thickness dimension (0.100 mm).

Finally, the results showed that bone microarchitecture analysis could provide additional tool for the assessment of bone fragility and fracture risk. Hence, the combination of bone structure organization, morphological parameters and BMD could provide a more comprehensive view of the bone health status and quality.

Conclusion of the Chapter

In this chapter, we have reported the necessity to perform large cadaveric image acquisition to investigate the difficulties and potentialities of applying MR technology on in vivo bones. However, acquiring large cadaveric bones present several issues, the most important is the decomposition process responsible to generate air bubbles between trabeculae. The air bubbles trapped between trabeculae when scanned using MRI creates artefacts due to air susceptibility effect, therefore the need to develop a sample preparation protocol to reduce artefacts due to air bubbles is of utmost importance. In the present chapter it has been presented a possible preparation protocol designed for large cadaveric anatomical samples and the protocol has been validated using μCT image analysis.

The second aim of this chapter was to investigate the effect of the resolution in the image analysis of trabeculae. To do so, the μCT images have been degraded by two and three times and the derived morphological parameters have been compared between different resolution images and among techniques (μCT vs. MRI). This investigation had a double purpose, the first was to individuate the resolution limit necessary to characterize the bone microarchitecture and the second aim was to assess if the μCT and MRI were providing the same bone morphological information. The designed approach revealed that both MRI and μCT could be used to assess the bone microarchitecture, however it is important to designed both the image acquisition techniques to have an in plane pixel size between 100 and 150 μm independently from the pixel thickness.

Finally, this chapter presented a new trabecular parameter, i.e. trabecular interconnectivity, which describe the angular variability around the principal trabecular direction. The Tb.Int has been shown to moderately correlate with the clinical standard DXA derived BMD while all the other investigated morphological parameters showed poor correlation. therefore, our hypothesis that bone microarchitecture could provide additional information to BMD in the clinical practice has been further supported.

MRI is a powerful tool for the quantification of tissue morphology non-invasively. However, when the voxel size is larger than the analyzed structure partial volume blurring occurs complicating the accuracy of the measurements. Acquisitions at higher resolution are possible but at the expenses of SNR and thus not presenting a valuable alternative. The resolution constraints are still the major obstacle for the development of MRI as a tool for quantifying trabecular bone microarchitecture in-vivo, with the final purpose of increasing the fracture risk prediction. As trabecular thickness (80 - 150 μm)

is typically less than the voxel size achievable in-vivo (around 150 μm), accurate structural information are difficult to obtain.

In the present work, among the image resolution enhancement technique appliable in the post-processing present in the literature, we identified and tested the sub-voxel processing (SubVoxel) and the zero filled interpolation (ZFI) or Sinc interpolation. The two resolution enhancement techniques have been applied on both μCT and MR images of three different proximal femurs. The images have been analyzed using iMorph retrieving BVF and trabecular thickness and spacing and the characteristics have been compared to those derived from the original images of both μCT and MRI.

The μCT resolution enhanced images showed morphological parameters in the same range with those derived using the original. In particular, the committed errors on the morphological parameters were always lower than 8%, the images enhanced using Sinc interpolation showed reduced BVF and Tb.Th (-4% than the μCT reference) and increased Tb.Sp (+7%). The μCT images enhanced using SubVoxel resolution showed increased BVF (+2%) and reduced Tb.Th and Tb.Sp (-7% and -6% respectively) when compared to the μCT reference. Similar results were assessed comparing the MR images enhanced to the MRI reference. The committed errors were always lower than 8%. In particular, the MR images enhanced using Sinc interpolation showed reduced BVF (-1%) and Tb.Sp (-3%) and increased Tb.Th (+5%), while the images enhanced using the SubVoxel technique showed increased BVF and Tb.Th (+6% and +4% respectively) and reduced Tb.Sp (-8%). The statistical analysis conducted using the Student T-test showed no significant difference between original and enhanced images using both Sinc interpolation and SubVoxel techniques for all the morphological characteristics analysed.

The image analysis showed that both Sinc interpolation and SubVoxel resolution provided images twice the dimension of the original, therefore providing images with half pixel dimension. Moreover, the results showed errors on the BVF lower than 4% and never statistically different from the original images meaning that the bone mass was conserved using both resolution enhanced techniques. Slightly higher differences were reported for the morphological characteristics as Tb.Th and Tb.Sp. In particular, the absolute committed errors using μCT images were up to 7% for the Tb.Sp retrieved using Sinc interpolated μCT images, while using MR images the absolute committed errors were up to 8% for the Tb.Sp retrieved using SubVoxel enhanced MR images. Both the techniques resulted suitable for reducing the pixel dimension while keeping the bone mass, however enhanced images did not provide additional information nor more trustful information of the bone morphology while the time needed to obtain the morphological outputs were quadrupled. Previous articles have shown the possibility to enhance the image resolution using both the Sinc interpolation (Yaroslavsky 2002; Khaire

and Shelkikar 2013) and the SubVoxel resolution (Hwang and Wehrli 2002) techniques reporting better defined contours. Hwang et al. on a study conducted using MR images (137x137x350 μm) of two radii reported that the application of SubVoxel resolution successfully alleviate partial volume blurring in tomographic images of binary systems (Hwang and Wehrli 2002), however the morphological parameters were obtained using images that have been binarized using a manually selected threshold while in our case an adapted local threshold have been used for the binarization of MR images. Moreover, the application of the aperture map using iMorph is able to provide a morphological analysis using a subvoxel precision that could also explain why in our case the morphological parameters assessed using both μCT and MRI did not change after the application of image enhanced techniques. Sinc interpolation have shown to provide the same deblurring effect reported using SubVoxel resolution on the characterization of the structure contours using both MRI (Puri, n.d.) and CT (Zoroofi et al. 2003) however it has been mostly applied to increase the voxel size in the z-axes rather than in-plane. In our case, increasing the in-plane pixel size using Sinc interpolation and analyzing the images using the SubVoxel precision provided by the aperture map did not show improvement in the morphological analysis of bone structures.

UHF MRI have proven to provide resolution images able to acquire bone trabeculae, however an optimized approach for the bone microarchitecture assessment is of great interest. Therefore, the next chapter focuses on the bone morphological analysis of three cadaveric proximal femur acquired using MR different main magnetic fields (3T vs. 7T) and pulse sequences (TSE vs. GRE). The comparison between the different MR main field strengths and sequence to the reference μCT would provide the optimal MRI setup that could also be applied in the clinical practice.

Chapter 5: Validation and Optimization of Proximal Femurs Microstructure Analysis Using High Field and Ultra-High Field MRI (published article)

Cite

Soldati E, Vicente J, Guenoun D, Bendahan D, Pithioux M. Validation and Optimization of Proximal Femurs Microstructure Analysis Using High Field and Ultra-High Field MRI. Diagnostics (Basel). 2021 Sep 2;11(9):1603. doi: 10.3390/diagnostics11091603. PMID: 34573945; PMCID: PMC8466948.

Authors

Enrico Soldati [1,2,3,*] , Jerome Vicente [1] , Daphne Guenoun [3,4] , David Bendahan [2] and Martine Pithioux [3,5]

Abstract

Trabecular bone could be assessed non-invasively using MRI. However, MRI does not yet provide resolutions lower than trabecular thickness and a comparative analysis between different MRI sequences at different field strengths and X-ray microtomography (µCT) is still missing. In this study, we compared bone microstructure parameters and bone mineral density (BMD) computed using various MRI approaches, i.e., turbo spin echo (TSE) and gradient recalled echo (GRE) images used at different magnetic fields, i.e., 7T and 3T. The corresponding parameters computed from µCT images and BMD derived from dual-energy X-ray absorptiometry (DXA) were used as the ground truth. The correlation between morphological parameters, BMD and fracture load assessed by

Affiliation

[1] Aix Marseille Univ, CNRS, IUSTI, Marseille, France;
[2] Aix Marseille Univ, CNRS, CRMBM, Marseille, France;
[3] Aix Marseille Univ, CNRS, ISM, Marseille, France;
[4] Institute for Locomotion, Department of Radiology, Sainte-Marguerite Hospital, Aix Marseille University, APHM, CNRS, ISM, Marseille, France;
[5] Institute for Locomotion, Department of Orthopaedics and Traumatology, Sainte-Marguerite Hospital, Aix Marseille University, APHM, CNRS, ISM, Marseille, France;
* Correspondence: enrico.soldati@univ-amu.fr

mechanical compression tests was evaluated. Histomorphometric parameters showed a good agreement between 7T TSE and µCT, with 8% error for trabecular thickness with no significative statistical difference and a good intraclass correlation coefficient (ICC > 0.5) for all the extrapolated parameters. No correlation was found between DXA-BMD and all morphological parameters, except for trabecular interconnectivity ($R^2 > 0.69$). Good correlation (p-value < 0.05) was found between failure load and trabecular interconnectivity ($R^2 > 0.79$). These results suggest that MRI could be of interest for bone microstructure assessment. Moreover, the combination of morphological parameters and BMD could provide a more comprehensive view of bone quality.

Keywords: osteoporosis; ultra-high field MRI; µCT; turbo spin echo; cadaveric human femur; bone morphology; air bubbles artefacts; gradient echo; bone microarchitecture; biomechanical fracture test.

1. Introduction

Low bone mineral density (BMD) and microarchitectural alterations are both responsible for osteoporosis, a bone disorder that leads to an increased sensitivity to fractures (G. Chang et al. 2018b). The economic burden of osteoporosis in Europe has been estimated to 37 billion euros (28 million patients) in 2010 and is expected to increase by 25% in 2025 (Hernlund et al. 2013). To alleviate this economic pressure and increase the quality of life of patients, the early diagnosis of osteoporosis is a critical issue. Osteoporosis is currently diagnosed on the basis of bone mineral density (BMD) measurements using dual energy X-ray absorptiometry (DXA). Previous studies have shown that DXA has a poor sensitivity. Schuil et al. reported that only 44% of all non-vertebral fractures occurred in women with a T-score lower than -2.5 SD and in men this percentage is even lower (21%) (Schuit et al. 2004). Although the DXA sensitivity increases to 88% for both men and post-menopausal women when considering DXA-determined osteoporosis and low bone density (T-score below -2.0 SD), the ability to discriminate the healthy patients, i.e. specificity, is poor (around 41% for post-menopausal woman and 55% for men) (Nayak et al. 2015b), resulting in a low clinical discriminative accuracy (70%) (Humadi, Alhadithi, and Alkudiari 2010b; Soldati, Rossi, et al. 2021). In addition, DXA measurements do not take into consideration microarchitectural alterations which are also part of the structural picture of osteoporosis. Considering the whole set of aspects, the diagnostic accuracy of osteoporosis might be expected to increase. Magnetic Resonance Imaging (MRI), quantitative computed tomography (qCT), and high-resolution peripheral computed tomography (HRpQCT) can be used to assess bone microarchitecture. Whereas qCT and HRpQCT are highly radiative techniques (>100 times larger than DXA) (Lam et al. 2011b; Damilakis et al. 2010b), MRI is recognized as totally non-invasive (Fig. 5.1).

So far, most of the MRI studies on bone microstructure have been carried out at conventional (1.5T) and high (3T) magnetic fields. Ultra-high magnetic field (7T) MRI is offering a higher resolution and has been used more recently (D. Guenoun et al. 2020c; G. Chang et al. 2017b; Roland Krug et al. 2008a). Most of the time, superficial bones such as distal radii and tibiae have been assessed (Majumdar et al. 1997b; R. Krug et al. 2008a; Magland, Wald, and Wehrli 2009; Chamith S. Rajapakse et al. 2018a) while deeper bones such as the proximal femur microarchitecture have been more scarcely analyzed (G. Chang et al. 2018b; G. Chang, Deniz, et al. 2014b). From a technical point of view, different

MRI pulse sequences such as gradient recalled echo (GRE) and spin echo (SE) have been used. Gradient-echo type of sequences have shown to provide the highest possible signal-to-noise (SNR) efficiency, while spin-echo sequences are less prone to off-resonance intravoxel signal cancellation due to susceptibility differences between bone and bone marrow (Roland Krug et al. 2008a). The corresponding results regarding bone volume fraction (BVF), trabecular thickness (Tb.Th), spacing (Tb.Sp), and number (Tb.N) have been compared to DXA (G. Chang et al. 2018b; D. Guenoun et al. 2020c), qCT (Majumdar et al. 1997b; R. Krug et al. 2008a; Roland Krug et al. 2008a) and X-ray microtomography (µCT) (Majumdar et al. 1996b; Tjong et al. 2012a; Burghardt, Link, and Majumdar 2011b). Using linear regression good correlations (r) have been reported between 3T and 7T MRI and qCT on in vivo and ex vivo radii and tibiae ($r > 0.69$) (Roland Krug et al. 2008a; R. Krug et al. 2008a), between qCT and µCT on cadaveric radii ($r > 0.89$) (Tjong et al. 2012a), and moderate to good correlation ($0.53 < r < 0.87$) was found between 1.5T MRI and µCT on cadaveric specimens of distal radii (Majumdar et al. 1996b). MRI can suffer from partial volume effects that could be responsible for the discrepancies between MRI and X-rays techniques. Previous studies have shown that Spin echo (SE) sequences would provide more accurate results regarding trabecular characteristics due the less proneness to susceptibility-induced broadening of the trabeculae (R. Krug et al. 2008a; Roland Krug et al. 2008a). The use of these pulse sequences might be problematic using Ultra-High field (UHF) MRI considering power-deposition issues, that will reduce the number of acquirable images in a single scan (Pierre-Marie Robitaille and Lawrence Berliner 2006). However, the full 3D acquisition of the thickest bones could be assessed using multiple scans per a single MRI session. On that basis, the higher resolution provided by UHF MRI might be compromised if one intends to use SE sequences.

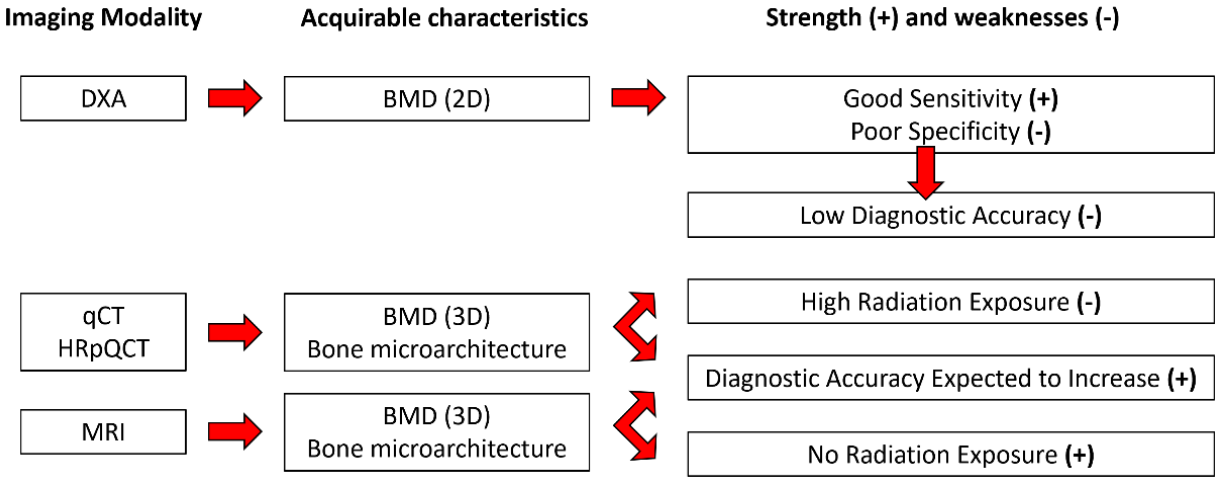

Figure 5. 1: Available characteristics from each imaging modality with their corresponding strength (+) and weaknesses (-).

In that context, a comparative analysis between high and ultra-high field MRI of intact proximal femurs taking into consideration the issue of pulse sequences (SE vs. GRE) would be of great interest. Such a comparative analysis could address the issues of image resolution needed for trabecular microarchitecture assessment, partial volume effects and specific power deposition of each imaging modality. For ex vivo measurements, susceptibility effects related to air bubbled trapped in the trabecular network should also be considered. Considering that these details are missing in the literature, we intended to compare, in the present study, the trabecular characteristics of three intact femur heads using µCT and 7T MRI using both SE and GRE pulse sequences. We aimed at identifying the effects of different techniques (µCT vs. high-field MRI vs. UHF MRI) and pulse sequences (SE vs. GRE) on the trabecular network characteristics and to compare the corresponding metrics using those from µCT as the gold standard. Moreover, microarchitecture characteristics from all the different imaging modalities were also compared with failure load assessed during biomechanical compression tests. The corresponding results should assess the link between trabecular characteristics and proximal femur risk of fracture and offer an assessment frame of the potential use of MRI as a non-invasive tool of bone microarchitecture in vivo.

2. Materials and Methods

2.1. Sample Preparation

All procedures were done in accordance with the ethical standards of the responsible committee on human experimentation of the thanatopraxy laboratory, University School of Medicine, Hôpital de la Timone, Marseille, France that provided the bodies coming from donation and in accordance with the Helsinki Declaration of 1975, as revised in 2000.

Three cadaveric femurs (S05, S06, S07), were initially scanned using conventional DXA (total femur BMD equal to 0.83 g/cm², 1.31 g/cm² and 0.50 g/cm² respectively for S05, S06 and S07) and then prepared according to an original vacuum procedure as previously reported (E Soldati et al. 2020) in order to remove air bubbles trapped in the trabecular network. After an overnight defreezing process, the femur was placed inside a plastic jar filled with a physiological solution doped with 1 mM Gd-DTPA (E Soldati et al. 2020). The container was then placed on a vibrating surface while low pressure cycles where applied. Each cycle had 5 minutes of active pumping (pressure lower than 50 mbar) and 5 minutes of resting time (150 mbar). Different vibrating amplitudes (0.1 to 1.5 mm) were

used to cope with different bubbles size displacement (from 20 µm to 2.5 mm diameter). The application of three cycles ensured the removal of more than 99% of air bubbles (E Soldati et al. 2020).

2.2. Imaging

µCT Imaging

µCT images of the three samples were acquired using Rx-Solution EasyTom XL ULTRA microtomograph ('RX Solutions SAS, 3D X-Ray Tomography Systems.', n.d.), with a 150 kV X-Ray Hamamatsu Tube allowing a focus spot size of 5 µm. In order to acquire the complete femur head volume, an isovolumetric voxel size of 0.05 mm was chosen using an X-ray source voltage of 150 kV, a current of 343 mA, a frame rate of 8 images/s, and 1440 projections over 360 degrees of rotation. Each projection resulted from the average of 10 images in order to enhance the signal to noise ratio. The acquisition time was approximately 40 minutes.

MRI Imaging

All the three femurs were scanned using two pulse sequences (turbo spin echo (TSE) and gradient recalled-echo (GRE)) using UHF MRI (7T MAGNETOM, Siemens Healthineers, Germany). For comparative purpose one femur head (S05) was also scanned at 3T (Verio Siemens Healthineers, Germany) with both TSE and GRE sequences. 7T MRI were performed using a 28Ch Knee coil, while 3T MRI acquisitions were performed using a flexible 16Ch Heart coil. The corresponding sequence parameters were similar to those used in the literature (Roland Krug et al. 2008a; G. Chang, Honig, et al. 2014b; Techawiboonwong et al. 2005b) and adapted to our sample size (Table 5.1). The acquisition time was set to be acceptable for clinical applications (14±4 minutes) while the voxel size was pushed to the machine limit.

Table 5. 1: List of main parameters used for MRI acquisitions.

Seq.	TR/TE (ms)	Flip Angle (°)	FoV (mm)	Bandwidth (Hz/Px)	NeX	Voxel Size (mm)	Slice Thickness (mm)	Slices	Acq.Time (min:sec)
7T TSE	1040/14	150	97 × 130	244	2	0.13 × 0.13	1.5	10	17:45
7T GRE	11/5.60	12	120 × 175	330	3	0.18 × 0.18	1	48	9:27
3T TSE	1170/12	140	119 × 119	255	2	0.21 × 0.21	1.1	36	16:45
3T GRE	16.5/7.78	10	120 × 120	130	2	0.23 × 0.23	1.1	40	11:17

TR: repetition time, TE: echo time, FoV: field of view and NeX: number of excitations.

2.3. Image Analysis

Image Registration

For each of the three scanned femurs, MRI and µCT images were co-registered in the coronal plane thanks to a 3D printed plastic registration tool positioned inside the plastic jar. The µCT alignment along the coronal plane was performed during the post-processing volume reconstruction step. For the MRI acquisitions, this alignment was performed before the acquisition. After the manual 3D alignment, an automatic 2D registration was used between one MR slice and a stack of 60 consecutive µCT slices (N_{reg}) centered in the MRI absolute location to find the µCT image that better correspond to the MRI one. The registration efficiency was assessed on the basis of the normalized cross-correlation (NCC), which measures the similarity between template and image by searching the location of the maximum value in the image matrices, as previously reported (Hisham et al. 2015b). For each stack of 60 µCT images we selected the µCT slice with the highest NCC score as the slice that better registered with the corresponding MRI one. The MRI images were first upscaled to the µCT matrix size (1785x1380 pixels) using the bilinear interpolation and so in order to work in a unique reference frame (Dachena et al. 2019). The registration was then performed using a MATLAB (MathWorks, R2020b) built-in function, *imregister*, with a multimodal approach and a geometric affine transformation (Fig. 5.2). Moreover, considering that MR images were recorded with a space between slices equal to the slice thickness and so in order to reduce the cross-talk effects, we also defined as ΔIm the number of µCT images between two consecutive best registered µCT slices. The mean values of ΔIm were also reported to evaluate the registration quality by comparing the distances between two consecutive, best registered, µCT slices with consecutives MRI slice distance which represents the expected ΔIm and are computed dividing the slice thickness and the space between slices of each MRI sequence by the µCT slice thickness. Moreover, to maximize the region of interest (ROI), the registration process has been performed on the 3 central MRI slices characterized by the higher femur head surface. Furthermore, since 3T and 7T MR images were targeting the same central bone region, we obtained very close registered µCT presenting similar morphological parameters values. Thus, we decided to report here only the series of µCT data corresponding to the 7T TSE registration. The morphological parameter analysis was performed on 2D slices.

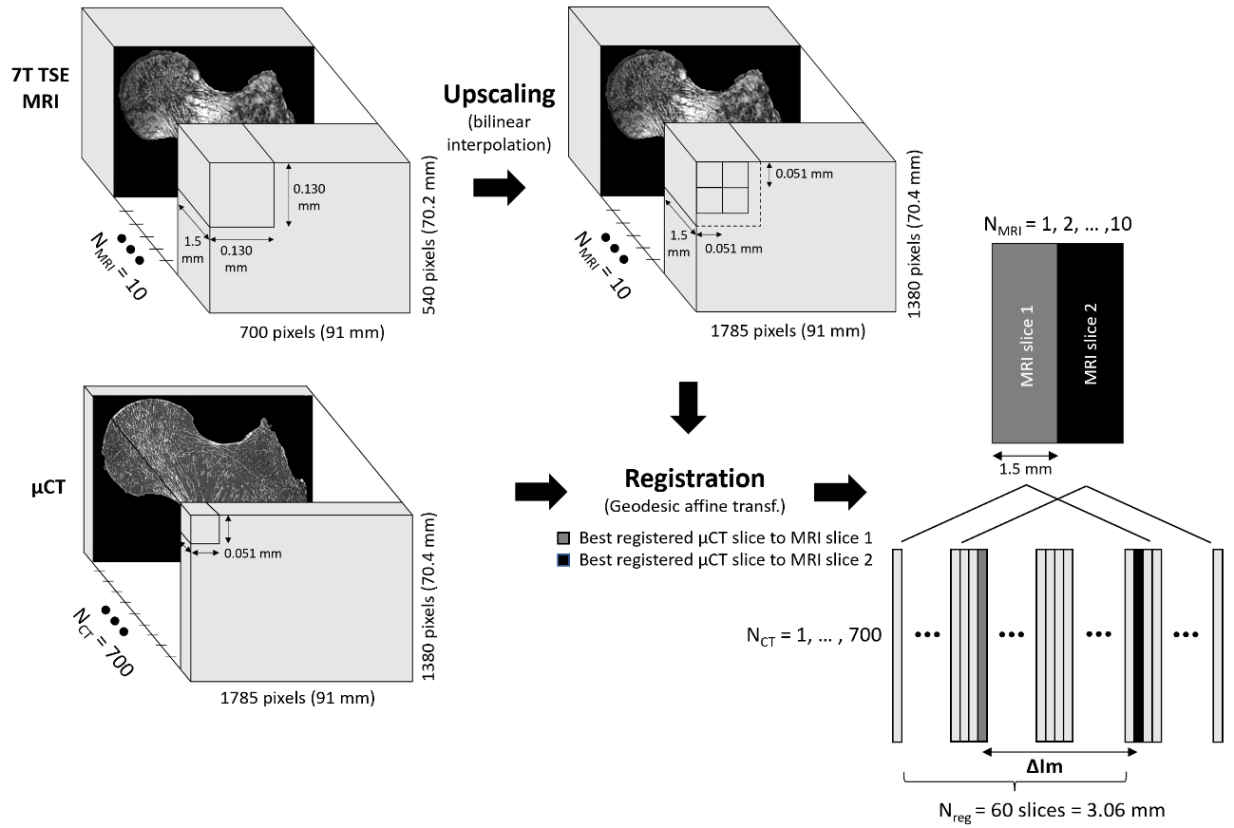

Figure 5. 2: Registration workflow.

Bone Morphological Quantification

Conventional histomorphometric parameters were quantified and compared in registered µCT/MR images using their original resolutions. Since the binarization of the solid part of MR images was not trivial, the Sauvola filter, an automatic local thresholding technique particularly useful when the background is not uniform with a window size of 10x10 pixels, has been applied (Dougherty and Kunzelmann 2007a) to eliminate possible biases due to manual thresholding and to take into account important contrast variations observed in images. The segmentation of the µCT images was straightforward since the contrast was high and the voxel size was smaller than the trabecular thickness.

Three independent parameters were extrapolated from all the binarized ROIs for the multimodal and multiscale comparative analysis (Majumdar et al. 1997b; G. Chang, Honig, et al. 2014b). The bone volume fraction (BVF) was calculated as the ratio between bone volume and total volume. The trabecular thickness (Tb.Th) and the trabecular spacing (Tb.Sp) were extrapolated using the distance transformation map from which it has been derived the aperture map using the software iMorph (version 2.0.0) (E. Brun, Ferrero, and Vicente 2017a). The aperture map previously used for the 2D and 3D

morphology evaluation of porous matters in several fields (E. Brun, Ferrero, and Vicente 2017a) gives for every pixel the diameter of the maximal disk totally enclosed and containing this voxel. Tb.Th and Tb.Sp were then deduced from the mean values of the aperture map distribution respectively in the solid and the marrow phase. The trabecular number (Tb.N) was derived from the ratio between BVF and Tb.Th. The aperture map has been previously used for the 3D morphological evaluation of porous materials in different fields (E. Brun, Ferrero, and Vicente 2017a; Burghardt, Link, and Majumdar 2011b). The aperture map approach, compared to the commonly used mean intercept length technique, provides local information with a sub-voxel precision (E. Brun, Ferrero, and Vicente 2017a; Johansson et al. 2019).

Three additional morphological parameters have also been assessed, i.e., the principal and secondary trabecular orientation (Tb.OrP and Tb.OrS respectively) and the trabecular interconnectivity (Tb.Int). The local orientation of each pixel has been computed using multiple 2D local Hessian matrix, each one resulting from the second order derivatives of the gray level image convolved with a gaussian matrix of fixed standard deviations (σ from 1 to 5). The eigenvalues and eigenvectors of the five 2D Hessian matrices have been calculated and the eigenvectors corresponding to the largest eigenvalues have been kept. The orientation has then been calculated from the four-quadrant inverse tangent ($\tan^{-1}$) from the eigenvectors translating the main orientation (Ian Goodfellow, Yoshua Bengio, and Aaron Courville 2016). The orientation distribution was computed considering the local orientation of binarized solid voxels only. In order to identify the first and second main directions of the trabeculae, a 2 gaussian curves fitting has been applied using an in-house MATLAB code based on built-in function *fitnlm* which was adapted to resolve the following model:

$$Y = a + m * x + \frac{1}{\sigma_1\sqrt{2\pi}} * e^{-\frac{1}{2}\left(\frac{x-\mu_1}{\sigma_1}\right)^2} + \frac{1}{\sigma_2\sqrt{2\pi}} * e^{-\frac{1}{2}\left(\frac{x-\mu_2}{\sigma_2}\right)^2}$$

Where a is the y-intercept, m is the slope, and μ_1, σ_1 and μ_2, σ_2 are respectively the mean and SD of the first and second gaussian curves.

Tb.OrP was expressed as the mean ± SD of the principal fitted gaussian curve, Tb.OrS is presented as the difference between absolute mean secondary orientation and the main principal orientation. Trabecular interconnectivity has been computed as the standard deviation of the whole trabecular orientation distribution from the main principal trabecular orientation. Tb.Int represents the trabecular orientation variability and could provide information about the bone adaptability to stresses coming from different directions (Fig. 5.3).

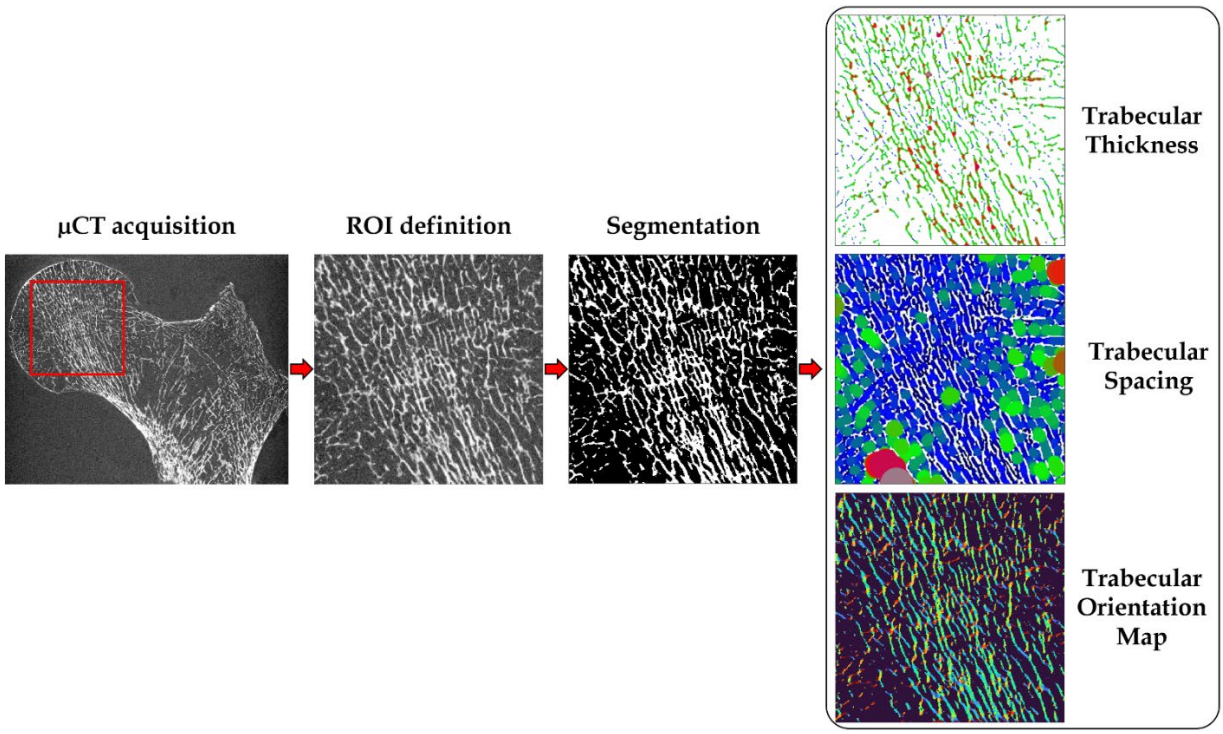

Figure 5. 3: Preprocessing and elaboration steps for the microarchitecture characteristics assessment.

A one-way analysis of variance (factor = imaging modality) was carried out to assess the statistical effect of the imaging modality on the different morphological parameters. A p-value lower than 0.01 was considered as statistically significant. Linear regression was performed to address the functional relationship between the different imaging modalities. In addition, a Bland-Altman (BA) analysis was used to assess the agreement between the imaging modalities. The BA analysis allows the identification of any systematic difference between the measurements or possible outliers and it is usually used to investigate any possible relationship of discrepancies between the measurements and the true value. Intraclass correlation coefficients (ICC) were also calculated as previously reported (Koo and Li 2016b) and the agreement was considered as low (ICC<0.5), good (0.5<ICC<0.75) or excellent (ICC>0.75). Moreover, the clinical relevance of bone microarchitecture was assessed by calculating the linear regression between BMD, determined from DXA scan, and the morphological parameters computed from the image analysis of the different imaging techniques and sequences.

Bone Mineral Density Assessment

BMD was also assessed using µCT and 7T MR images for comparison purposes. Two approaches have been proposed and applied. One volumetric using all µCT images which provided a complete 3D bone reconstruction (Arokoski et al. 2002a; Kröger et al.

1995), and one areal using the μCT and MR image with higher 2D bone surface, hence corresponding to the central coronal plane.

The BMD-DXA from the specific region of the femur neck (BMD = 0.78, 0.96 and 0.54 g/cm² for S05, S06 and S07 respectively) were retrieved and the ROI used to calculate it has been individuated. Femur neck ROI was chosen as it represents one of the regions more affected by fragility fractures due to osteoporosis (Ramponi, Kaufmann, and Drahnak 2018) and one of the most occurring due to sideways fall. The angle between the long bone axis and the femur head was individuated and the stack of images were oriented to obtain the ROI of the femur neck perpendicular to the y-axis (see Fig. 5.4).

Firstly, using all the μCT images a volumetric region of interest (VOI) in correspondence of the ROI used to evaluate the femur neck BMD-DXA was individuated manually. The number of bone voxels was assessed by applying the same threshold as described in the previous section. Bone mineral content ($BMC_{(1)}$) was calculated as the product of bone voxels for the bone density adjusted for porosity (ρ = 1.2 g Ca/cm^3) (Laval-Jeantet et al. 1983b). To provide the BMD comparable to conventional BMD-DXA (expressed in g/cm²), in case of 3D μCT, the $BMC_{(1)}$ was divided by the bone surface of the central coronal plane of the VOI analyzed.

The same concept was applied to calculate BMD from a 2D image for both μCT and 7T MRIs. After the positioning of the ROI in accordance with the ROI used for the DXA analysis in the femur neck, the central coronal image in the ROI was selected and binarized. The vector crossing the bone surface in the middle was individuated and used as rotation axis. The volume that each bone pixel depicts over a rotation of 180° around the rotation axis was calculated using the volume ring formula, hence integrating the 2D surface to obtain an apparent bone volume (V_{app}) of the femur neck. The calculation was performed assuming unit height, and major (R) and minor (r) radius assessed with respect to the rotation axis (Fig. 5.4). The rotation of the 2D surface around the central coronal plane of the femur neck was made on the basis of the femur neck anatomy. In fact, the cortical thickness, which represents the most representative bone region for the BMD, is not homogeneous. The bottom cortical layer of the femur's neck is thicker than the upper layer. On that basis, a surface rotation, expressing both the superior and inferior cortical layers, over 2π would provide a more reliable approximation of the total femur neck volume. Once obtained the apparent bone volume, $BMC_{(2)}$ and BMD were derived as previously described. Finally, to assess the correlation between techniques, the linear regression was computed between BMD derived from DXA scans and those calculated from μCT and 7T MRIs in the same femoral neck ROI.

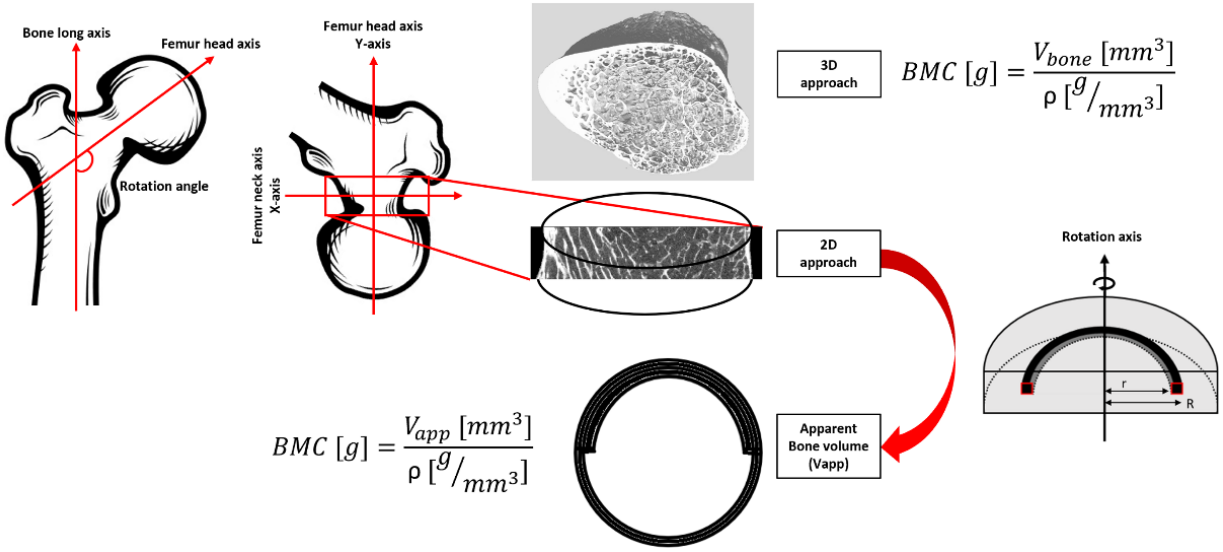

Figure 5. 4: Workflow for bone mineral density estimation.

2.4. Mechanical Testing

Each specimen was loaded to failure in an universal testing machine (Instron 5566, Instron, Canton, MA, USA). Each femur was placed within the loading apparatus so as to simulate a sideways fall on the greater trochanter (Manske et al. 2009; Eckstein et al. 2003). Each specimens was first fixed in resin (Epoxy Axon F23) at 15° internal rotation and then the femoral head were oriented at 10° adduction within the testing machine. The load was applied to the greater trochanter (displacement rate 10 mm/min) through a pad, which simulated a soft tissue cover, and the femoral head was covered with resin to ensure force distribution over a larger surface area. Failure load (in MPa) was defined as the first local maximum after which the load declined by more than 10% divided by the bone surface at the fracture site (Le Corroller et al. 2012). Fractures were visually classified according to clinical criteria (femoral neck, intertrochanteric, subtrochanteric, or isolated greater trochanteric fractures) (D. Guenoun et al. 2020a). Finally, to assess the correlation between mechanical tests and bone morphology the linear regression between fracture load and both BMD (DXA-derived and derived from µCT and MR images) and microarchitectural parameters has been computed and the coefficient of determination (R^2) have been reported.

3. Results

3.1. Registration Quality

The optimal registration between MRIs and μCT slices are illustrated in Fig. 5.5. In Table 5.2 are presented the mean and standard deviation of the NCC scores for the femur (S05) scanned both at 3T and 7T. Similar results were obtained between 7T MR and μCT images for the other two samples. As indicated, the results showed that the registration was more efficient using the TSE sequence as compared to the GRE. The corresponding increase was 20% at 3T and 7% at 7T. Considering the GRE images, an improved registration (13%) was quantified at 7T as compared to 3T.

Table 5. 2: S05 normalized cross-correlation (NCC) scores and ΔIm, the number between two consecutive best registered μCT images used to evaluate the registration efficiency for the four stacks of MRI images.

S05	7T TSE−μCT	7T GRE−μCT	3T TSE−μCT	3T GRE−μCT
NCC score	0.93 ± 0.01	0.86 ± 0.01	0.94 ± 0.01	0.75 ± 0.01
ΔIm	67 ± 7 (59)	36 ± 13 (39)	42 ± 16 (43)	50 ± 18 (43)

ΔIm are presented as mean ± SD. expΔIm values are presented in brackets.

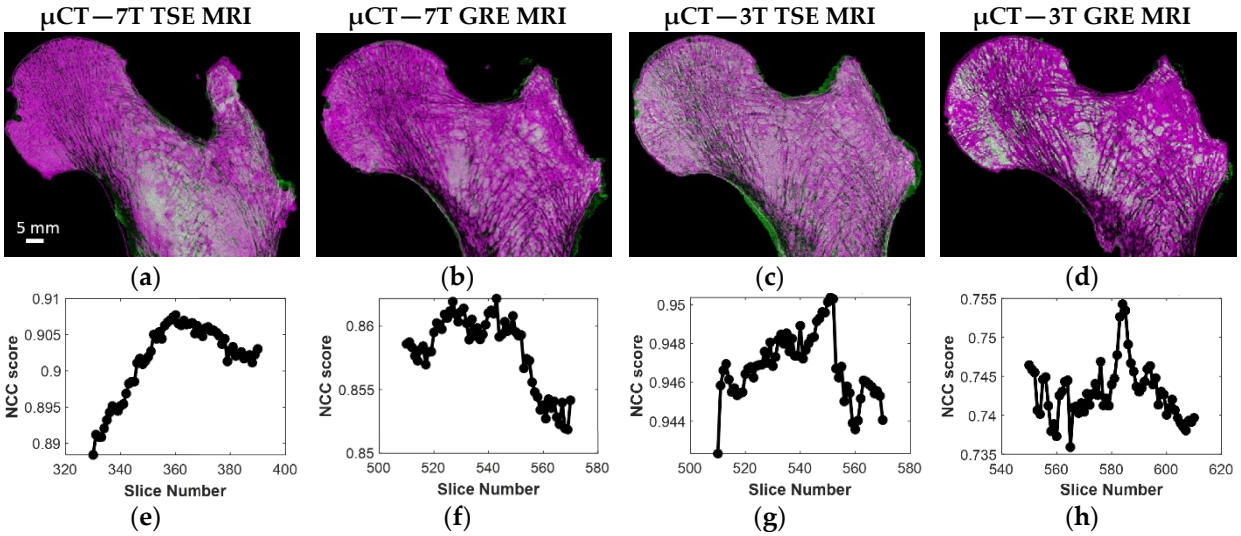

Figure 5. 5: (a–d) S05 best registration for the four different MRI acquisitions with μCT; (e–h) corresponding NCC efficiency profile.

The registration efficiency scores were similar at 3T (0.94) and 7T (0.93) regarding TSE images. Moreover, the ΔIm mean values were found to be in the same range of the expected ΔIm values (presented in brackets) which are the number of μCT slices between two consecutive MR images. More particularly the 7T TSE showed the lowest standard

deviation. In addition, considering all the three samples scanned at 7T, TSE images showed generally higher efficiency than GRE images (0.91±0.03 vs. 0.87±0.02). Moreover, ΔIm mean values were found in the same range to the expected results for both techniques (TSE and GRE) but TSE showed lower standard deviation (66±9 (59) vs. 38±14 (39) respectively for TSE and GRE at 7T). Overall, the registration results showed that we were able to register multimodal and multiscale images with different voxel dimensions.

3.2. Selection of the Optimal MRI Sequence

The same registered coronal plane for the four different MRI acquisitions and µCT with the corresponding ROIs are shown in the first row of Fig. 5.6. The binarized voxels of the respective ROIs are shown in the second row of Fig. 5.6. In Table 5.3 are reported the morphological parameters derived as "mean ± SD" for each sample and imaging modality with the absolute errors calculated on each feature for both TSE and GRE sequence performed with respect to the µCT reference. Clearly, TSE sequences provided a better contrast, so the inner trabecular network was more easily identifiable (Fig. 5.6) and this for all the scanned samples acquired using both 3T and 7T MRI.

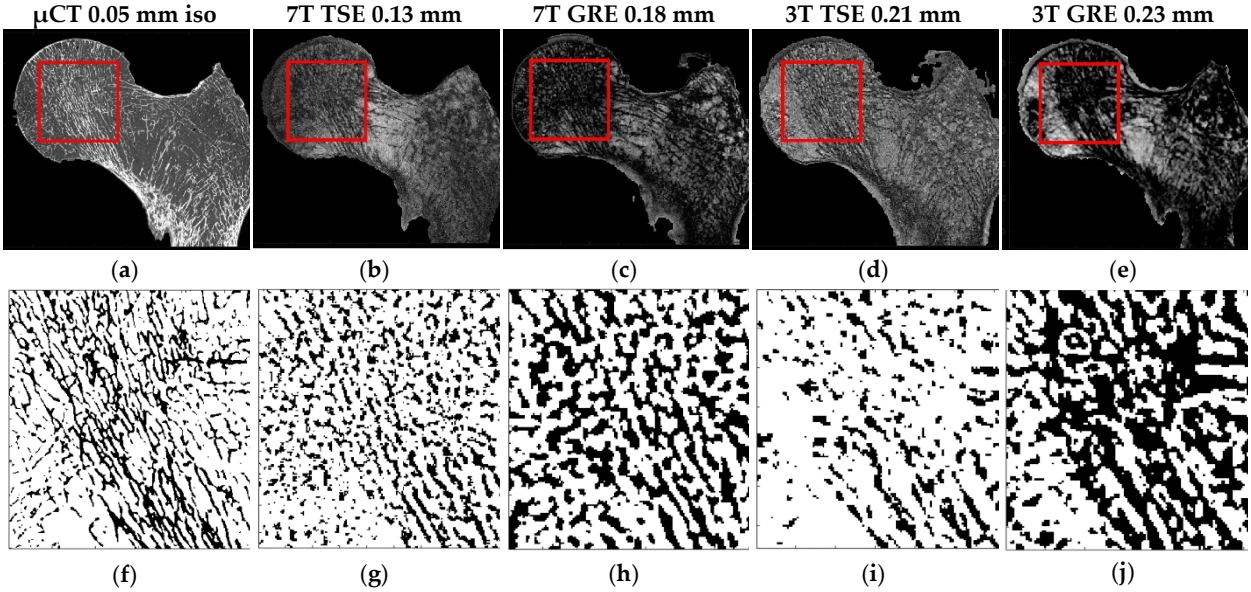

Figure 5. 6: (a–e) S05 same coronal planes of the (a) µCT and four different MRI acquisitions ((b) 7T TSE, (c) 7T GRE, (d) 3T TSE and (e) 3T GRE). The red square identify the ROI extrapolated from all the registered images. (f–j) Corresponding ROI binarized (automatic local thresholding with a window size of 10×10 pixels).

Moreover, considering the morphological features quantified on UHF images conducted on the three samples, the corresponding errors, taking µCT as a reference, were lower for TSE sequence (maximum errors always lower than 12% for all the

characteristics) than GRE (maximum errors up to 63% for BVF, 107% for Tb.Th and 35% for Tb.Sp) (Table 5.3 and Fig. 5.7).

Table 5. 3: Morphological characteristics between registered µCT—7T MR images.

		BVF	Tb.Th	Tb.Sp	Tb.N	Tb.OrP	Tb.OrS	Tb.Int
S05 (BMD-DXA = 0.83	µCT	0.23 ± 0.01	0.25 ± 0.01	0.86 ± 0.04	0.97 ± 0.03	67 ± 11	165 ± 6	23.84 ± 0.66
	7T TSE	0.24 ± 0.01	0.26 ± 0.02	0.92 ± 0.04	0.92 ± 0.03	67 ± 13	161 ± 10	22.41 ± 1.50
	Max diff%	8%	6%	8%	8%	1%	3%	9%
	7T GRE	0.36 ± 0.01	0.50 ± 0.03	1.02 ± 0.03	0.71 ± 0.03	62 ± 12	167 ± 10	21.44 ± 1.20
	Max diff%	63%	107%	27%	32%	10%	5%	13%
S06 (BMD-DXA = 1.31	µCT	0.24 ± 0.01	0.25 ± 0.01	0.93 ± 0.02	0.89 ± 0.04	69 ± 12	165 ± 7	24.83 ± 1.18
	7T TSE	0.24 ± 0.02	0.26 ± 0.01	0.96 ± 0.05	0.89 ± 0.05	67 ± 14	160 ± 9	25.08 ± 1.31
	Max diff%	10%	7%	5%	7%	7%	4%	5%
	7T GRE	0.34 ± 0.01	0.40 ± 0.02	0.89 ± 0.08	0.85 ± 0.03	68 ± 14	162 ± 10	23.21 ± 1.29
	Max diff%	57%	64%	13%	9%	4%	3%	8%
S07 (BMD-DXA = 0.50	µCT	0.21 ± 0.01	0.24 ± 0.01	0.88 ± 0.03	0.87 ± 0.03	68 ± 10	163 ± 7	21.33 ± 0.46
	7T TSE	0.22 ± 0.01	0.24 ± 0.02	0.89 ± 0.06	0.84 ± 0.02	68 ± 12	164 ± 11	20.56 ± 0.77
	Max diff%	11%	12%	5%	6%	3%	2%	6%
	7T GRE	0.32 ± 0.01	0.37 ± 0.04	1.08 ± 0.09	0.88 ± 0.11	61 ± 12	159 ± 9	19.60 ± 1.27
	Max diff%	55%	70%	35%	12%	17%	9%	12%

Morphological characteristics are expressed as mean ± SD for the three registered µCT-7T MRI images for all the three different samples (S) for both turbo spin echo (TSE) and gradient recalled echo (GRE) with the corresponding maximum percentage difference (max diff%). BVF: bone volume fraction, Tb.Th: trabecular thickness, Tb.Sp: trabecular spacing, Tb.N: trabecular number, Tb.OrP: principal trabecular orientation, Tb.OrS: secondary trabecular orientation, Tb.Int: trabecular interconnectivity.

The statistical analysis, conducted on three 2D images per bone sample using the one-way ANOVA showed no significant statistical difference ($p > 0.01$) between 7T TSE and the µCT reference for the whole set of parameters. The coefficient of determination (R2), calculated to address their functional relationship, ranged from 0.52 for Tb.N to 0.81 for Tb.Int. The corresponding bias (considering µCT as a reference) was determined thanks to the Bland-Altman analysis and resulted in a mean bias of 4.8% for the whole set of morphological parameters. The interclass correlation coefficient came as an additional support and all parameters were classified as good (ICC ranging from 0.53 for Tb.Th to 0.73 for Tb.OrP) or excellent (ICC = 0.80 for Tb.Int). Different results were obtained using the 7T GRE images. The one-way ANOVA showed a significant statistical difference for three out of seven morphological parameters analyzed (BVF, Tb.Th and Tb.Int). The coefficient of determination (R^2) ranged from 0.11 for Tb.Th to 0.63 for Tb.OrP and the Bland-Altman analysis showed higher biases for all the parameters (ranging from 2.0% for Tb.OrS to 51.1% for Tb.Th) with a mean bias of 20.6%. The ICC values were generally lower than those derived using 7T TSE and were classified as poor (BVF, Tb.Th and

TbOrS) or good (Tb.Sp, Tb.N, Tb.OrP and Tb.Int) with Tb.Th performing the worst (ICC = 0.11) and Tb.Int the best (ICC = 0.73).

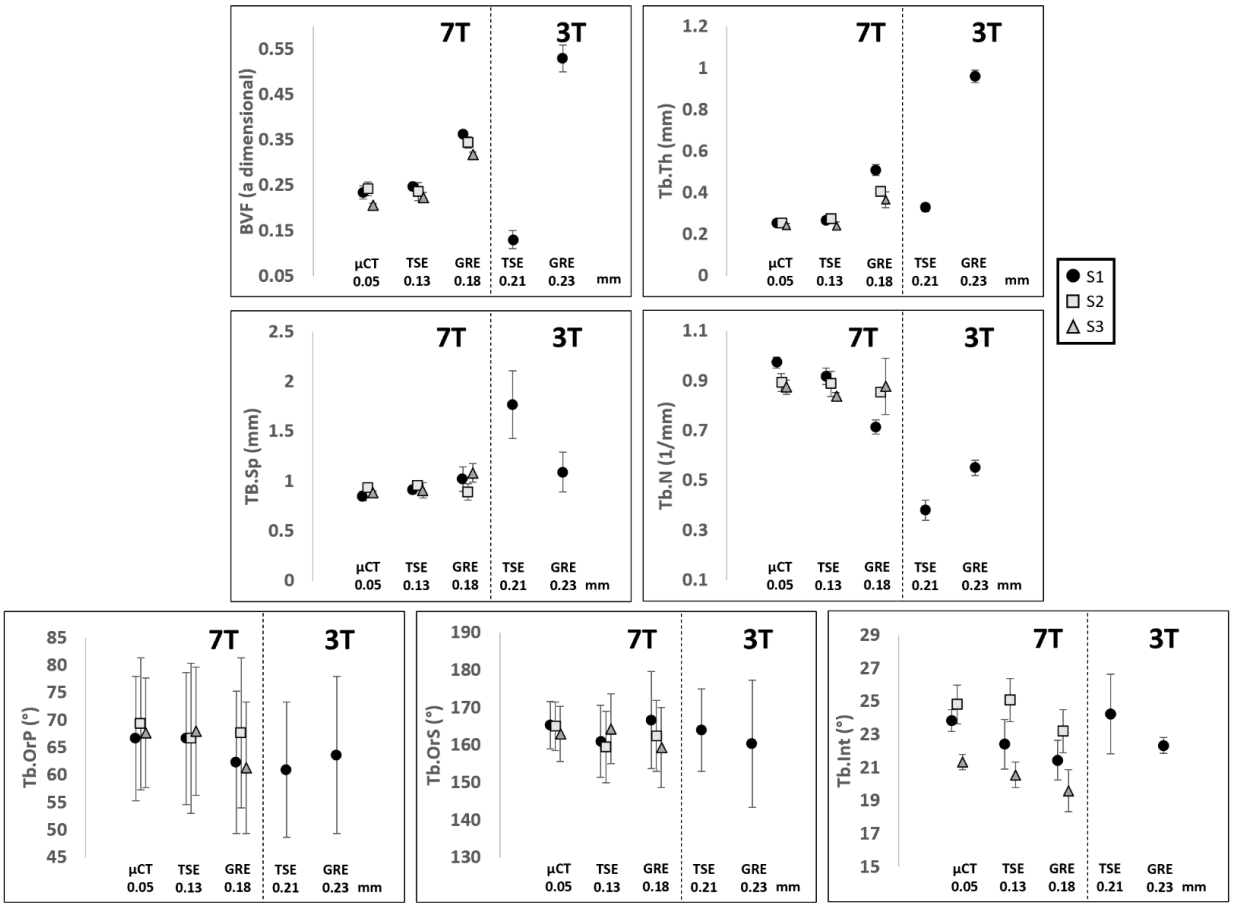

Figure 5. 7: Data shows mean and SD of, respectively, BVF: bone volume fraction, Tb.Th: trabecular thickness, Tb.Sp: trabecular spacing, Tb.N: trabecular number, Tb.OrP: principal trabecular orientation, Tb.OrS: secondary trabecular orientation and Tb.Int: trabecular interconnectivity of the three analyzed samples S05 '●', S06 '■' and S07 '▲' scanned with different scanners (µCT and MRI), field strengths (3T and 7T), sequences (TSE and GRE) and resolution.

Interestingly, the analysis conducted on a single femur (S05) using both 3T and 7T MRI showed that the corresponding error committed on morphological features quantified on UHF images, taking µCT as a reference, was the lowest and so regardless of the magnetic field strength (Fig. 5.7). As a matter of example, BVF error was reduced by 50% and 71% from 3T to 7T for TSE and GRE respectively. Similar results were obtained for all the conventional morphological parameters with a mean reduction of the committed error of 58% from 3T to 7T TSE and of 69% from 3T to 7T GRE. The largest reduction was 100% for the Tb.Sp from 3T to 7T TSE and 178% for the Tb.Th from 3T to 7T GRE. The morphological characteristics derived from gray level intensities showed very similar results between 3T and 7T with errors compared to µCT reference always lower than 11%

for both TSE and GRE. Considering the MRI pulse sequences at 3T, TSE did not systematically perform better than GRE. In fact, errors were reduced for BVF (81%) and Tb.Th (249%) and were increased for Tb.Sp (80%) and Tb.N (17%). Moreover, the results also showed that images acquired at 7T did not always provide better results as compared to 3T. In fact, when comparing 3T TSE with 7T GRE, the committed errors were lower for BVF (mean error equal to 48% for 3T TSE and 63% for 7T GRE) and for Tb.Th (mean error equal to 33% for 3T TSE and to 107% for 7T GRE).

3.3. Correlation between DXA-BMD and Microarchitecture

The linear regression between the morphological parameters and BMD derived from clinical DXA, for the three analyzed samples, has also been assessed to determine whether these two analyses were providing the similar information and, if appliable, the relation with a specific MR sequence (Fig. 5.8).

No linear correlation was assessed between µCT morphological parameters and BMD for the majority of the morphological parameters analyzed (R^2 equal to 0.20 for Tb.Th, 0.42 for Tb.Sp, 0.01 for Tb.N, 0.16 for Tb.OrP, 0.15 for Tb.OrS). However, BVF and Tb.Int showed respectively modest (R^2 = 0.50) and good (R^2 = 0.73) correlations. 7T MR images showed similar results i.e. no linear correlation was found for all morphological characteristics using TSE sequence (R^2 equal to 0.40 for BVF, 0.23 for Tb.Th, 0.31 for Tb.Sp, 0.16 for Tb.N, 0.01 for Tb.OrP and 0.30 for Tb.OrS) or GRE (R^2 equal to 0.22 for BVF, 0.02 for Tb.Th, 0.47 for Tb.Sp, 0.01 for Tb.N, 0.38 for Tb.OrP and 0.04 for Tb.OrS) but trabecular interconnectivity which presented the highest correlation (R^2 equal to 0.77 for 7T TSE and 0.66 for 7T GRE).

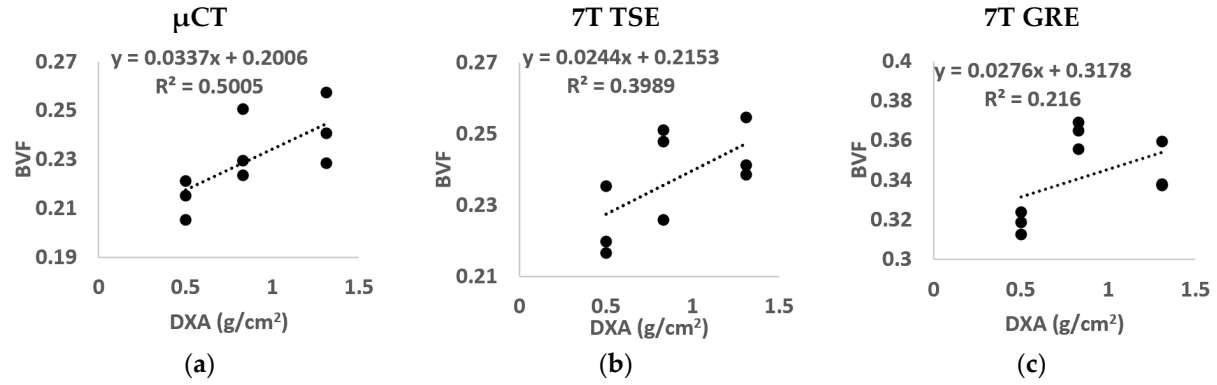

(**a**) (**b**) (**c**)

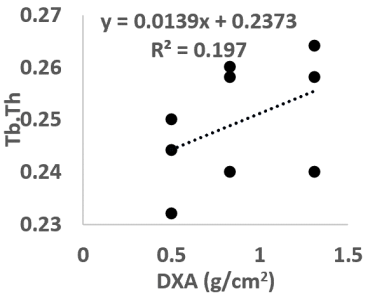

(d)

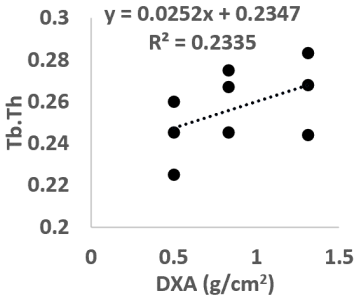

(e)

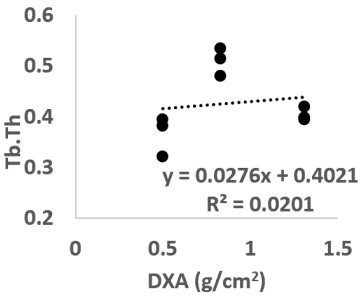

(f)

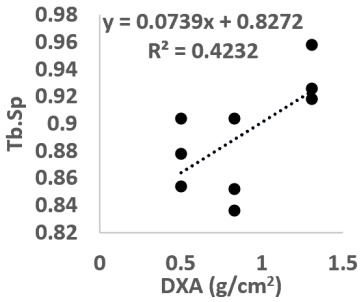

(g)

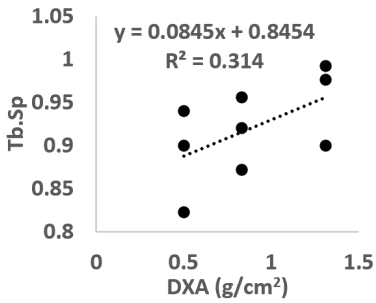

(h)

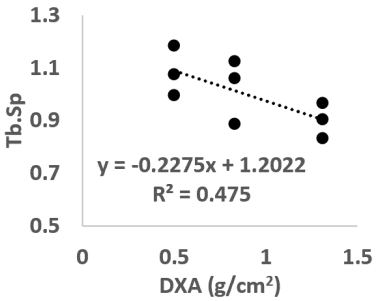

(i)

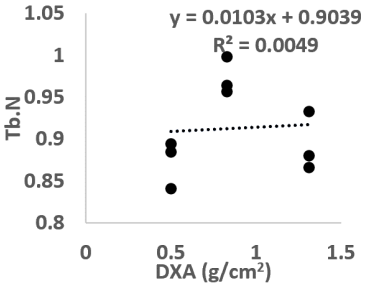

(j)

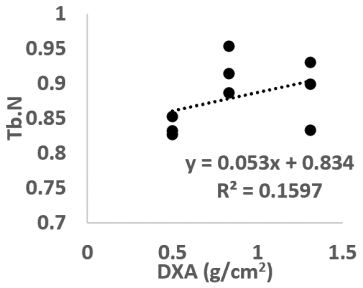

(k)

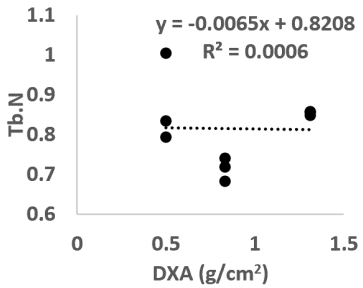

(l)

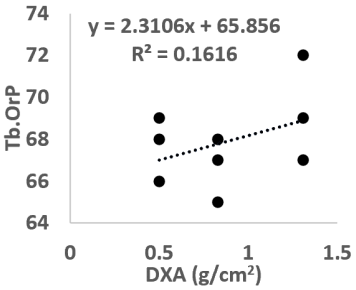

(m)

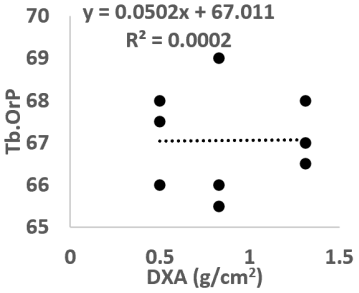

(n)

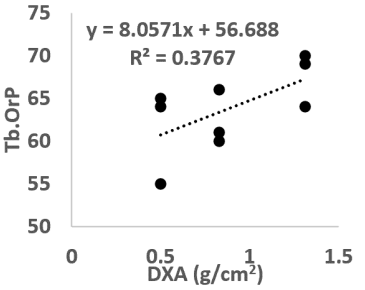

(o)

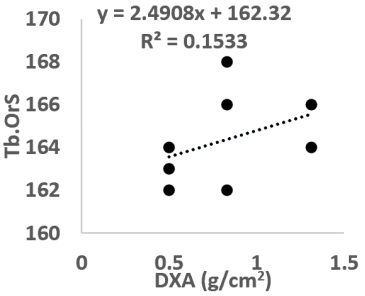

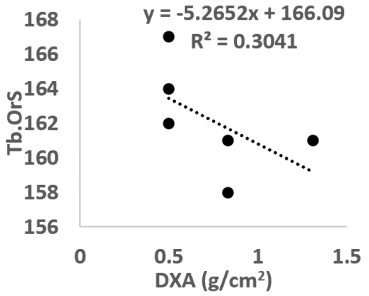

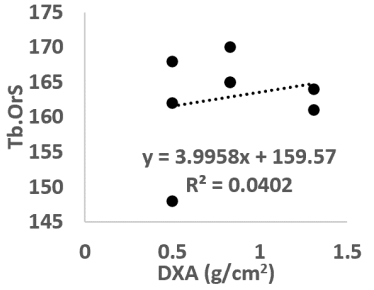

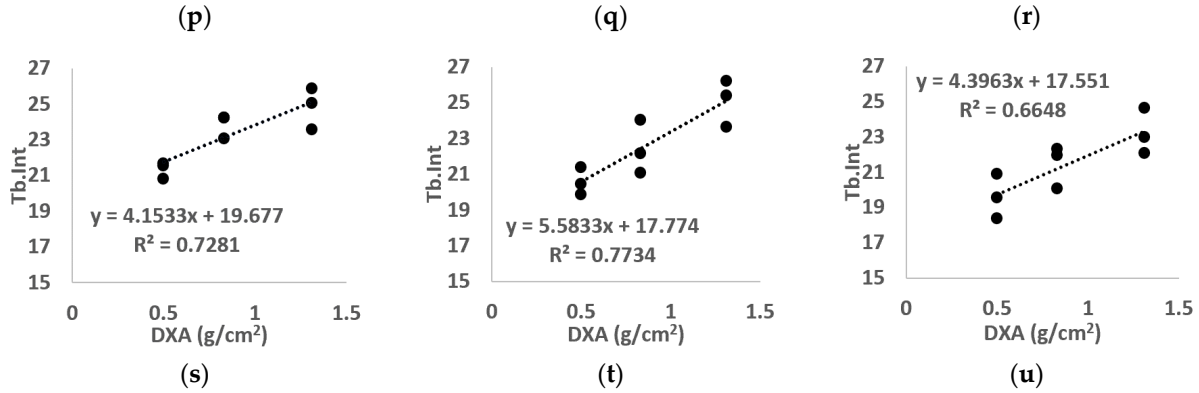

Figure 5. 8: Linear regression between BMD calculated using standard DXA and all morphological parameters ((a-c) BVF, (d-f) Tb.Th, (g-i) Tb.Sp, (j-l) Tb.N, (m-o) Tb.OrP, (p-r) Tb.OrP, (s-u) Tb.Int) derived from µCT (left), 7T TSE MR (middle) and 7T GRE MR (right) images. "BVF" refers to bone volume fraction, "Tb.Th" refers to trabecular thickness, "Tb.Sp" refers to trabecular spacing, "Tb.N" refers to trabecular number, "Tb.OrP" refers to principal trabecula orientation, "Tb.OrS" refers to secondary trabecular orientation, "Tb.Int" refers to trabecular interconnectivity.

3.4. Correlation between DXA-BMD and both µCT- and MR- Derived BMD

The BMD derived from µCT images (using both 3D and 2D approach) and 7T MR images (2D approach only) are presented in Fig. 5.9. The results showed values in the same range of the BMD determined using DXA scans for all the imaging techniques with mean errors equal to 6% for µCT 3D, 15% for µCT 2D, 12% for TSE 2D and 49% for GRE 2D. Moreover, the linear regression between BMD calculated using DXA and the BMD derived from µCT images, using both the 3D and the 2D approach, showed good correlation ($R^2 = 0.94$ for 3D µCT and $R^2 = 0.85$ for 2D µCT). Similar results were obtained using the 2D approach on 7T TSE images ($R^2 = 0.77$) while the BMD derived using 7T GRE showed poor correlation ($R^2 = 0.24$).

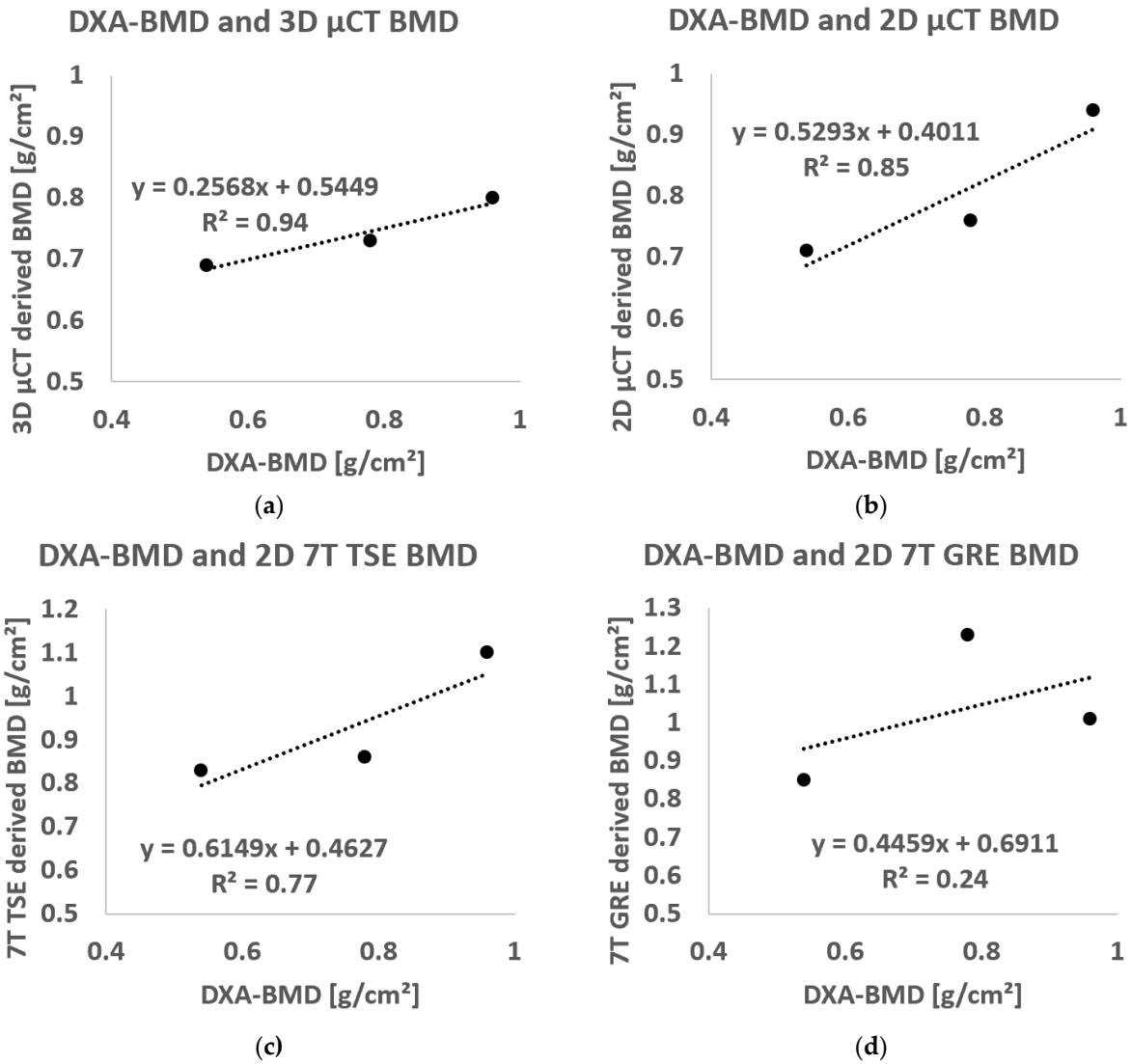

Figure 5. 9: Linear regression between BMD calculated using standard DXA analysis and BMD derived using (a) µCT 3D approach, (b) µCT 2D approach, (c) TSE 2D approach and (d) GRE 2D approach.

3.5. Correlation between Failure Load and Bone Morphology

We observed one femoral neck and two intertrochanteric fractures with a mean failure load equal to 1733.6 N (SD, 524.6 N) over a mean femoral neck surface of 800.9 mm² (SD, 195.8 mm²) derived from high-resolution µCT images in correspondence of the bone fracture site. The resulting mean fracture strain was 2.15 MPa (SD, 0.22 MPa) with a mean work equal to 0.067 J (SD, 0.04 J).

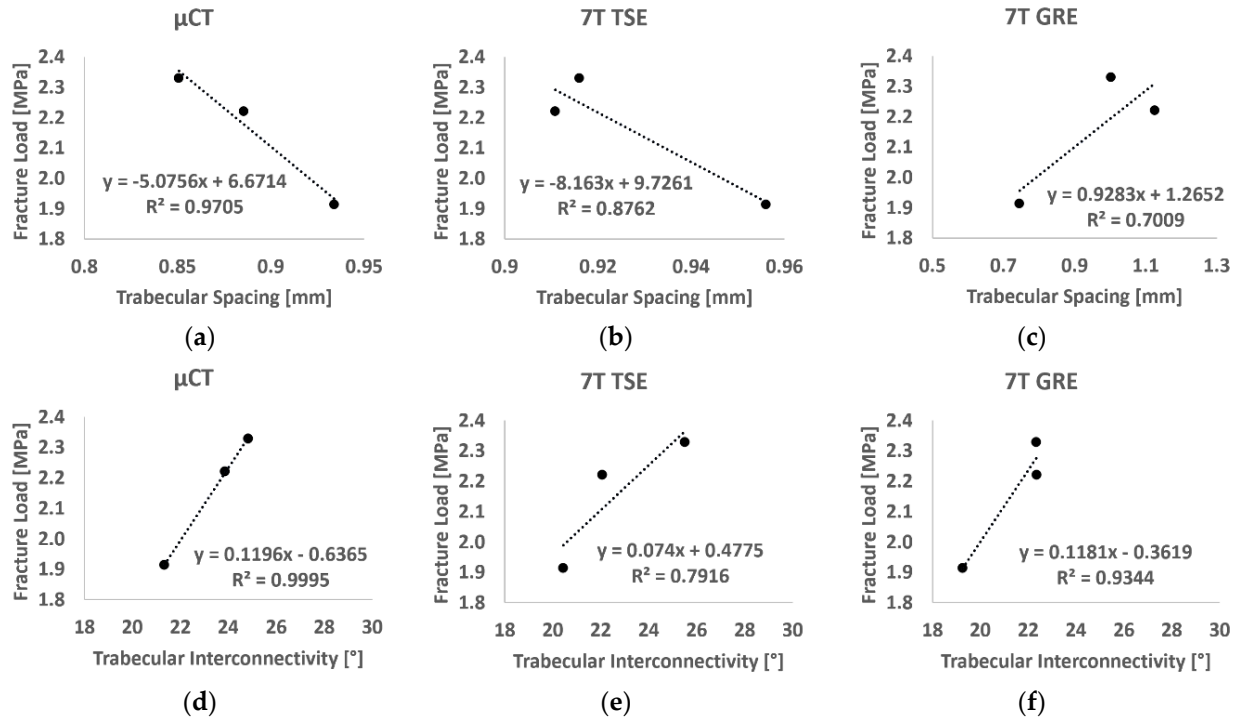

Figure 5. 10: Linear regression between fracture load and trabecular spacing (a-c) and trabecular interconnectivity (d-f) derived from µCT images (left), 7T TSE (middle) and 7T GRE (right).

The linear regression between DXA derived-BMD at the femoral neck region and fracture strain showed a poor correlation (R^2 = 0.43). Higher correlations were found using µCT derived-BMD (R^2 = 0.66 for the 3D µCT and R^2 = 0.88 for 2D µCT). Similar result was obtained using the BMD derived from the 2D approach on TSE images (R^2 = 0.87) while poor correlation (R^2 = 0.11) was found using GRE images. Moreover, the linear regression between failure strain and microarchitecture parameters derived in the femur head showed excellent to good correlations for both Tb.Sp (R^2 = 0.97, 0.88 and 0.70 respectively derived from µCT, 7T TSE and 7T GRE) and Tb.Int (R^2 = 0.999, 0.792 and 0.934 respectively for µCT, 7T TSE and 7T GRE) (Fig. 5.10). However, poor correlations were found for BVF (R^2 < 0.22), Tb.Th (R^2 < 0.25) and Tb.N (R^2 <0.36) among all the used imaging modalities in this study.

4. Discussion

The investigation of complete cadaveric bone segments is of interest for a reliable assessment of bone quality and bone disorders. Up to now, cadaveric bone imaging using MRI has been mainly performed in small specimens (<5 cm3) (Chamith S. Rajapakse et al. 2018a; Seifert et al. 2014b) with the consequence of a poor representative characterization of the entire bone. Large bone specimens' investigations could provide a more complete picture as long as magnetic susceptibility artefacts issues due to bubbles trapped inside the trabecular network are removed as previously described (E Soldati et al. 2020). High and ultra-high field MRI is of interest given the high images resolution that can be achieved using a reasonable acquisition time, but power deposition can be an issue for a certain type of MRI sequences. A comparative analysis between different MRI sequences (performed at different main field strengths) and µCT of proximal femurs trabecular network could be of interest for the clinical application of in vivo non-invasive microarchitecture analysis of one of the most invalidating osteoporotic site and more in general of deep bone segments.

In the present study we addressed the issue related to MRI sequence selection, at high and ultra-high field for the histomorphometric assessment of large bone segments in vivo.

Considering that previous studies have indicated that TSE sequences were less susceptible to partial volume effects as compared to GRE sequences (R. Krug et al. 2008a), one might expect different effects for the bone micro-architecture quantification. Our results regarding bone micro-architecture further confirm and extend those from previous studies conducted at 1.5T (Majumdar et al. 1999b), 3T (R. Krug et al. 2008a; Roland Krug et al. 2005b) and 7T (Roland Krug et al. 2008a). The TSE sequence was indeed less prone to partial volume effects errors as compared to GRE and so regardless the magnetic field strength and the investigated bone segment. These stronger partial volume effects on GRE sequences created opposite effects on Tb.Th and Tb.Sp. In fact, Tb.Th computed from GRE images was largely overestimated (249% at 3T and 107% at 7T) with respect to µCT reference values, likely as a result of bigger trabeculae thickening and aggregation of the thinnest. The same phenomenon, i.e. trabecular thickening and aggregation, led to a space reduction between the biggest trabeculae and also between the thinnest so that the computed Tb.Sp values were similar to those computed from µCT images. Previous measurements performed at 3T on tibiae and radii indicated that trabeculae are more accurately depicted using spin-echo type sequence, whereas gradient-echo sequences would lead to trabecular broadening (R. Krug et al. 2008a). Krug

et al. also suggested that trabecular structure can be enhanced using gradient-echo sequences so that smaller trabeculae would disappear due to partial volume effects (R. Krug et al. 2008a). In agreement with the present results, Majumdar et al. (Roland Krug et al. 2008a) also indicated that structural parameters computed from distal tibia images recorded at 7T were closer to reference µCT values as compared to those acquired at 3T. They also reported that spin-echo sequences revealed a more homogeneous bone marrow signal than gradient-echo ones, hence reducing the susceptibility-induced broadening effects of the trabeculae (Roland Krug et al. 2008a). Furthermore, they showed that since trabecular structure is overemphasized at higher field strength due to susceptibility-induced broadening, smaller trabeculae, usually not visible due to partial volume effects, may be emphasized at 7T (Roland Krug et al. 2008a). Therefore, the application of a higher main magnetic field strength may provide a more accurate trabecular network identification.

Of interest, the morphological parameters computed from TSE images recorded at 7T were in agreement with the µCT reference values for all the three acquired femur specimens and with those from previous works (Roland Krug et al. 2008a; Majumdar et al. 1997b; 1996b; Tjong et al. 2012a; Burghardt, Link, and Majumdar 2011b; Majumdar et al. 1999b; Soldati, Escoffier, et al. 2021). For the whole set of microarchitecture features, the committed errors were always lower than 12% and the corresponding mean bias was low (<5%). In young healthy subjects, Majumdar et al. (Roland Krug et al. 2008a), showed similar tibiae morphological parameters for both gradient- and spin-echo sequences recorded at ultra-high field (0.45 for BVF, 0.26 mm for Tb.Th and 0.33 mm for Tb.Sp with spin-echo, and 0.50 for BVF, 0.33 for Tb.Th and 0.33 for Tb.Sp with gradient-echo). Similarly to our results, they showed an overestimation of BVF and Tb.Th for gradient-echo as compared to spin-echo, while the identification of the Tb.Sp was consistent between the two sequences. Moreover, the values differences (higher BVF and lower Tb.Sp) might be due to the different conditions and anatomical site (healthy, young, and in vivo tibiae vs. old and cadaveric proximal femurs in our case). Our results are in agreement with those from Tjong et al. (Tjong et al. 2012a), in a study conducted using µCT (voxel size 18 µm isovolumetric) and HRpQCT (voxel sizes 41 µm isovolumetric) on cadaveric radii. The corresponding morphological parameters (0.21±0.06 for BVF, 0.75±0.15 mm for Tb.Sp and 0.21±0.01 mm for Tb.Th) were in the same range than those we computed in a different anatomical site.

The linear regression between morphological parameters and BMD assessed for all the different imaging techniques (µCT, 7T TSE and 7T GRE) showed a poor correlation (R^2<0.47 for all the parameters but Tb.Int (R^2 between 0.66 and 0.77 for the three different imaging modalities). Among the conventional morphological parameters higher

correlations were found for Tb.Sp, in particular for 7T GRE images (R^2 equal to 0.47), while Tb.Th usually showed the lowest. Similar effect has been assessed previously. Majumdar et al. (Majumdar et al. 1997b) showed moderate correlations for Tb.Sp (0.41 respectively) on in vivo distal radii acquired using a modified gradient echo imaging sequence at 1.5T. Moreover, Chang et al. showed no linear regression between microarchitectural parameters and BMD on a study conducted on the hip of 60 postmenopausal woman scanned using 3T MRI (G. Chang et al. 2018b). The poor correlation assessed between the morphological parameters and the BMD extended previous results showing that bone density and structure are two distinct characteristics. However both are essential for defining the clinical state of bone (G. Chang et al. 2018b; D. Guenoun et al. 2020c; Majumdar et al. 1997b). The highest correlations were found for trabecular interconnectivity, which provided good correlation for all the three different imaging modalities. The progressive decreasing of trabecular interconnectivity with lower BMD may suggest a reduced trabecular orientation profile and a reduced dynamic spread of impulsive actions. On that basis, Tb.Int seemed to suggest an increased bone fragility and a consequent increased risk of fracture.

The 2D approach for deriving the BMD has been proposed due to the fact that MR images are usually acquired using a slice thickness at least 3 times bigger than the pixel size, a distance factor/slice gap equal to the slice thickness to reduce the cross-talk effects, and a single acquisition using 7T TSE is not able to depict the whole femur head segment. Therefore, the potential to derive a BMD approximation using the central coronal plane only of the proximal femur is of great interest. The correlation between BMD derived from DXA scans and computed using the BMC from 2D and 3D μCT, and 2D 7T MR images, in approximately the same femoral neck ROI, showed good to moderate correlation for all the techniques but 7T GRE. In particular, the BMDs computed from 2D TSE images showed values in the same range of conventional DXA with a comparable standard deviation. Similar results have been assessed previously by Kroger et al., in a study conducted in 32 volunteers comparing BMD derived from DXA and 1.5T MR images in the lumbar vertebra L3 assessing a good correlation ($r = 0.665$) (Kröger et al. 1995). The results were further confirmed and extended by Arokoski et al. in a study conducted in the femoral neck of 28 people using DXA and a spin echo sequence (TR/TE = 730/11 ms) at 1.5T MRI where BMD derived from these two techniques provided a good correlation ($r = 0.74$) (Arokoski et al. 2002b). The results seemed to suggest that MR images can be used to assess both bone microstructure and mineral density in multiple bone regions with good accuracy compared to gold standard X-ray techniques.

The mechanical tests provided failure load values in the same range with those from previous studies (Le Corroller et al. 2012; D. Guenoun et al. 2020a; Manske et al. 2009).

Moreover, the linear regression between failure load and BMD derived using DXA was similar to a previous study conducted by Guenoun et al. on 10 samples ($R^2 = 0.415$) (D. Guenoun et al. 2020a). Interestingly, the linear regression between the fracture strain and both trabecular spacing and trabecular interconnectivity showed good correlation regardless the imaging modality ($R^2 > 0.79$). This result clearly supports the hypothesis that microarchitectural parameters could provide additional information to BMD on the bone health and fracture risk assessment.

Our results showed that the registration between MRI and µCT images converged for both GRE and TSE images recorded at both high and ultra-high fields. Previous studies related to multimodal registration have been conducted for images with similar voxels dimensions and used approaches based on entropy, correlation, and pixels intensities differences (Studholme, Hill, and Hawkes 1997; Penney et al. 1998). More recently, Wafi et al. reported that NCC was a robust registration approach based on illumination changes. However, the corresponding computational cost was high, and the technique was sensitive to thin line structures as reported by Penney et al. (Hisham et al. 2015b; Penney et al. 1998; Andronache, Cattin, and Székely 2006). Our results related to the registration process showed that TSE images always provided a better result, for both NCC and ΔIm, as compared to GRE images and so regardless of the magnetic field strength. This better performance might also be related to voxel resolution for both TSE vs. GRE and 3T vs. 7T. In fact, for a given field strength, a reduced in-plane resolution (0.13 vs. 0.18 mm at 7T and 0.21 vs. 0.23 mm respectively for TSE and GRE at 7T and 3T) is converted in greater NCC scores and lower ΔIm standard deviations. However, while an increased NCC score and ΔIm closest to the reference were obtained for GRE images from 3T to 7T, an opposite effect was computed for TSE images i.e. a slightly decreased NCC and a more different mean ΔIm value as compared to the expected values, while the standard deviation decreased from 16 to 7, corresponding to a decreased µCT range of 0.46 mm. This effect might be explained by the slice thickness (from 1.1 mm at 3T to 1.5 mm at 7T), which is due to the smaller number of acquirable images. Zhao et al. supported this hypothesis, showing that images with the same resolution (both in-plane and through-planes) can be registered accurately with more confidence (C. Zhao et al. 2016). Therefore, the NCC method can be considered as an optimized approach for images i.e. µCT and MRI with a 20 to 30-fold difference in slice thickness.

Some limitations must be acknowledged in the present study. Due to specific absorption rate (SAR), the number of images acquirable using TSE at 7T was strictly limited. In order to acquire the whole bone segment, multiple acquisitions could be performed as long as pauses are allowed between acquisitions. Moreover, although tissue alterations due to sample freezing-defreezing process could have been expected, our

morphological evaluation provided results similar to those in previous studies conducted in vivo and ex vivo (Majumdar et al. 1999b; Roland Krug et al. 2005b) suggesting a limited effect of this process. Finally, the study has been conducted in a limited number of cadaveric femurs. The number was limited for obvious ethical reasons.

5. Conclusion

Overall, in agreement with previous studies, the present results obtained from three cadaveric proximal femur heads, showed that TSE images were less prone to partial volume effects and trabecular broadening than GRE images and so regardless the magnetic field strength. Our results extended previous results and showed that the higher field strength, the smaller the committed errors and the larger the agreement with µCT reference values. Furthermore, the morphological and statistical analyses showed that TSE sequence at 7T could be used in vivo for evaluating bone microstructure of deep bone segments with a very good approximation as compared to µCT gold standard. Moreover, our results showed that the BMD derived from both µCT and 7T TSE images positively correlated with the clinical standard BMD derived using DXA and that trabecular interconnectivity presented higher correlation to fracture load than those derived using BMD.

Therefore, our results clearly suggest that UHF MRI could be of interest as an in vivo and non-invasive imaging modality for the assessment of both bone microarchitecture and mineral density, and could provide a more comprehensive view of bone quality and fracture risk than DXA alone.

Conclusion of the Chapter

In this chapter, it has been presented an optimized approach for the bone microarchitectural assessment of the proximal femurs. It has been shown that using UHF MRI the obtained morphological parameters were comparable to those derived from μCT reference, however this was not the case for MRI at 3T. The sequence effect has also been exploited, showing that TSE sequence are less prone to partial volume effects and have to be preferred to GRE ones. The different MRI acquisitions have been performed reducing the pixel size to the machine and sequence limit in an in vivo appliable acquisition time. The obtained results further support the hypothesis that to assess the bone trabeculae the image resolution has to be in the same order of the trabecular thickness.

MR technology is a developing field with the main aim to provide better diagnostic tools while increasing the patient comfort. In the last decades, the technical advantages has been focused on increasing the MR main field strength up to the new 7T which has also been released for clinical use. Increasing the main field strength provide higher SNR while keeping the acquisition time almost constant and therefore not affecting the patient comfort.

The images previously reported in this manuscript were acquired using the 7T MAGNETOM (Siemens Healthineers, Germany) which was a UHF MR machine for research use only. As previously reported, the 7T MAGNETOM was able to assess proximal femur microarchitecture, however presenting some limitations, i.e. the number of acquirable images per scan session was limited by the SAR deposition and the acquisition time was at the extreme limit of the in vivo applicability. Although, only recently a new UHF MR scanner, the 7T MAGNETOM Terra (Siemens Healthineers, Germany) has been release for clinical use. The application of the previously presented scanning protocol showed great advantages as compared to the previously described scanner. The SAR deposition on patients has been drastically reduced, allowing the acquisition of an increased number of images per a single scan (from 10 to 20) while reducing the acquisition time to 11:59 min leading to a more acceptable acquisition time for patients applicability. However, the image quality remained unchanged.

The technical advantages just described provided MR images with comparable quality than before, however they allowed the acquisition of the whole proximal femur in a single scan and using a more acceptable acquisition time for patients. Therefore, both the patient comfort and the protocol applicability in clinical practice resulted increased.

In the next chapter, it is presented a multiscale and multimodal analysis of two proximal femur neck (one osteoporotic and one healthy). The femoral neck has been chosen since it represents one of anatomical regions most affected by osteoporosis and one with high mortality risk. The multiscale analysis depicts the bone morphology from the macroscale to the microscale with the assessment of the osteocytes lacunae morphology and distribution. In addition, the bone quality has also been assessed using a multimodal approach and the trabecular mechanical properties have been assessed using microindentation while the mineralization and the carbonate accumulation have been exploited using FTIR.

Chapter 6: Multiscale Femoral Neck Imaging and Multimodal Trabeculae Quality Characterization of one Osteoporotic and Aged-Matched Healthy Subject (draft article)

Authors

Enrico Soldati [1,2,3], Flavy Roseren [2], Sebastien Avellan [2], Daphne Guenoun [2,4], Emilio Catelli [5], Giorgia Sciutto [5], Stefano Iotti [6], Emil Malucelli [6], Lucia Mancini [7], Jerome Vicente[1], David Bendahan [3] and Martine Pithioux [2,8].

Affiliation

[1] Aix Marseille University, CNRS, IUSTI, Marseille, France;
[2] Aix Marseille University, CNRS, ISM, Marseille, France;
[3] Aix Marseille University, CNRS, CRMBM, Marseille, France;
[4] Institute for Locomotion, Department of Radiology, Sainte-Marguerite Hospital, Aix Marseille University, APHM, CNRS, ISM, Marseille, France;
[5] University of Bologna, Department of Chemistry "G. Ciamician", Ravenna, Italy;
[6] University of Bologna, Department of Pharmacy and Biotechnology, Bologna, Italy;
[7] Elettra-Sincrotrone Trieste S.C.p.A., Basovizza, Trieste, Italy;
[8] Institute for Locomotion, Department of Orthopaedics and Traumatology, Sainte-Marguerite Hospital, Aix Marseille University, APHM, CNRS, ISM, Marseille, France;

1. Introduction

Bone is a dynamic tissue in which old bone is continuously resorbed and replaced by new bone maintaining the mineral homeostasis and the integrity of bone structure throughout a process called bone remodeling (Tresguerres et al. 2020). Bone remodeling is a multiscale process and recent works have highlighted the major role of osteocytes in maintaining the bone mass and volume. Osteocytes, the most abundant bone cells, are stocked in lacunar voids distributed throughout the entire bone and interconnected by canaliculi and play a role in the anabolic response to mechanical stimuli (Tresguerres et al. 2020; Hinton, Rackard, and Kennedy 2018). This osteocytes mechanism, called mechanotransduction, has been shown to be responsible for the release of soluble factors that induce either bone resorption or bone formation, acting on the cells on the bone surface (Yavropoulou and Yovos, n.d.; van Oers, Wang, and Bacabac 2015). Since the osteocytes system is believed to act as a key regulator of skeletal homeostasis, many bone diseases were suggested to be associated with changes or general disorganization in the osteocytes morphology and network (Knothe Tate et al. 2004). Conventional microscopic 2D imaging techniques have been previously applied (Qiu et al. 2006; Sasaki et al. 2015; Katsamenis et al. 2013; Ashique et al. 2017), however presenting some uncertainty because the slicing direction may bias the results due to missing information about the third dimension. To overcome this issue, many 3D imaging modalities have been investigated (Hasegawa et al. 2018; Genthial et al. 2017; Kamel-ElSayed et al. 2015), among those synchrotron radiation CT (SR CT), which is able to provide an isotropic spatial resolution and relatively large field of view (7.73 to 42.8 mm^3 for SR microCT, 0.26 to 1.03 mm^3 for SR nanoCT, which is also able to acquire the canalicular system compared to the SR microCT) (B. Yu et al. 2020; Dong et al. 2014; Carter et al. 2013). Despite the increasing interest in the osteocytes, data on human bone remains scarce and they are generally limited to a very small field of views. In addition, the available data come from a large variety of different imaging techniques at different spatial resolutions. Therefore, a complete morphological analysis of osteocytes lacunae (OL) from healthy and pathological bones is of great interest, since changes could be related to decreased activity in the bone remodeling process. Changes of lacunar shapes were observed in osteopenia, osteopetrosis and osteoarthritis based on imaging of one sample in human knees (van Hove et al. 2009). However, few studies assessed the osteocytes morphology changes related to osteoporosis, which represent one of the most common bone diseases (for the International Osteoporosis Foundation et al. 2020).

Osteoporosis is a systemic bone disease characterized by a reduced bone mineral density and thinning of both cortical and trabecular phase due to the bone resorption. Bone degradation due to osteoporosis usually lead to fragility fractures and the most affected bones are the upper limb (30.7%), the distal lower limb (15.1%) and the femoral neck (14.0%) (Bouyer et al. 2020). The increased susceptibility to fragility fractures usually accounts by reduced bone strength and quality. While both determinants are tightly linked to several parameters related to bone geometry, macro- and micro-architecture, bone mineralization, and bone remodeling, osteoporosis is currently diagnosed on the basis of the single measurement of bone mineral density (BMD) assessed by performing a dual-energy X-ray absorptiometry (DXA) acquisition (Soldati, Rossi, et al. 2021). BMD is considered as an index of bone mass loss and on that basis as a predictor of osteoporotic fracture. However, it has been acknowledged that bone strength depends not only on bone quantity but also on the shape and hierarchical structure and thus, the diagnostic value of BMD has been largely questioned (Soldati, Rossi, et al. 2021; G. Chang et al. 2017b). In fact, the extracellular matrix (ECM) of the bone is highly related to the mechanical properties of the bone tissue. The organic phase represents 35% of the ECM and is mainly comprised of type I collagen at 82% and the rest represent the non-collagenous protein (10%), lipides (3%), proteoglycan and the fundamental substance (5%). Each of those component plays an important role in the mechanical properties of the bone tissue (D. Wu et al. 2018). It has also been shown at the macroscale that the post-yield behavior of the bone, which characterizes the capacity of absorbing the energy before failure, is linked to the organic phase and its alteration has been associated with changes in the mechanical behavior, making bones more ductile or brittle (Alford, Kozloff, and Hankenson 2015). Concerning the mineral phase, it represents 65% of the ECM and plays an important role in the tissue rigidity. Gupta et al. showed that the bone elastic modulus is highly influenced by the amount of local mineral present at the microscale, therefore highlighting the link between the mineral content and the bone tissue mechanical properties (Gupta et al. 2005). Moreover, it is important to note that the mechanical behavior of bone at a macroscale is directly conditioned by the smaller scales (Rodriguez-Florez, Oyen, and Shefelbine 2013; Fantner et al. 2007; Poundarik et al. 2012). In altered ECM, the mineral part of the bone will be also affected leading to modulations in the mechanical behavior (Alford, Kozloff, and Hankenson 2015). Recent studies have shown that the ECM is responsible of the mineralization process and influences the density of the crystal composition (Adele L. Boskey 1996). Hence, the multimodal analysis is of great interest since it would allow the characterization of the bone mechanical properties, level of mineralization, carbonate accumulation and collagen cross-links, providing reliable indicators of the bone material properties.

In clinical practice, bone geometry, and bone macro- and microarchitecture has been successively assessed by using MRI and X-ray techniques, i.e. qCT and HRpQCT, which are able to acquire bones with a pixel size of 0.18×0.18×0.6 mm^3 and isotropic pixel sizes between 61 to 82 μm^3 respectively (Ohs, Collins, and Atkins 2020). However, using HRpQCT the proximal femur is not acquirable due to its anatomical position, so that its complete microarchitecture characterization is trivial. The bone quality and mineralization has been also assessed using reference point indentation (RPI) (Gong et al. 2014). RPI is a microindentation technique which directly measures mechanical properties in patients in a fast, safe, feasible and minimally invasive way (Pérez-Sáez et al. 2017; Soldado-Folgado et al. 2020; Ovejero Crespo 2020; Diez-Perez et al. 2010). However, further validation of this technique is required as only few trials has been done clinically and more understanding of the relation of RPI and material properties of the bone is needed. Moreover, the in vivo microindentation measures the resistance of the cortical bone, neglecting the characterization of the mechanical and tissue properties at the trabecular level, which could provide additional information on the bone resistance and quality. While the characterization of neither the osteocytes network nor the trabecular composition and mechanical properties could not be added in the clinics due to its inaccessibility using clinical diagnostic tools, the corresponding results could provide a better understanding of the bone quality, therefore providing direct implications in pre-clinical research, therapeutic strategy, and eventually clinical practice.

The aim of the article is to characterized the bone quality in the femoral neck, which represents the bone region where 14% of all the fragility fractures occurs in the elderly, one of the most invalidating, and with high mortality risk (4.3% in-hospital death in patients with mean age of 79.5 years) (Bouyer et al. 2020). In this paper, we present a femoral neck comparison between one osteoporotic patient diagnosed using BMD analysis and one aged- and gender-matched control using a multiscale and multimodal approach. The femoral neck morphology has been assessed using industrial microtomography (μCT) at 51 μm^3 and comparing the results with those derived using SRμCT at 5 μm^3 voxel size. Moreover, we explore the possibility offered by SR microCT (SRμCT) at 0.9 μm^3 for the 3D quantification of osteocytes lacunae. Finally, bone trabecular quality has been assessed by performing mechanical and a spectroscopic characterization assays. To do so, the microindentation and the Fourier transform infrared spectroscopy have been carried out to assess the differences in the trabeculae mechanical properties, the mineralization as well as carbonate accumulation among several anatomical regions of the same proximal femur and between subjects (osteoporotic vs. control).

2. Materials and Methods

All procedures followed were in accordance with the ethical standards of the responsible committee on human experimentation of the thanatopraxy laboratory, University School of Medicine, Hôpital de la Timone, Marseille, France that provided the bodies coming from body donation and with the Helsinki Declaration of 1975, as revised in 2000.

2.1. Sample Collection and Preparation

Two femurs from female donors were initially scanned using conventional DXA (Table 6.1). They were then cut using a bandsaw along the axial direction right below the lesser trochanter (approximately 10 to 12 cm section proximal to the femur head) and then the specimen were stored at -25°C. The whole proximal femurs were kept at -25°C before and after performing the image acquisition while they were acquired at room temperature (15°C).

Table 6. 1: Sample description.

	Gender	Age (y)	Leg Pos	Height (m)	DXA (g/cm²)		
					Total	Neck	Troch.
Control (S8)	Female	95	Right	1.63	0.939	0.932	0.883
OsteopS (S9)	Female	96	Right	1.65	0.480	0.552	0.419

OsteopS stands for Osteoporotic sample, Neck refers to proximal femur neck and Troch. stands for Great Trochanter.

Sample Extraction and Preparation for Microindentation Test

Three small samples for each condition were extracted from the proximal femurs to characterize the mechanical properties of lamellar bone. Three regions of interest were cored in the great trochanter (GT), the femoral neck (FN) and in the femoral head (FH) using a drill press equipped with a hollow tip with an internal diameter of 10 mm and under constant water irrigation. The samples were harvested perpendicular to the coronal plane and kept frozen at -25°C until microindentation assays. Leading a total of 3 samples per condition (osteoporotic and control), one for each proximal femur region of interest. As the assays begun, the specimen had their marrow completely removed using a soft water jet followed by an ultrasonic bath of 5 minutes (Philippe K Zysset et al. 1999). The trabecular specimen was then mounted in ABS custom cuboid sample holders (Fig. 6.1). This sample holder allowed the grinding and the application of the microindentation protocol without moving the trabecular specimen. The

protocol used for microindentation was validated by Renault et al. (Renault et al. 2020) and will be briefly summarized below. The surface of each specimen was polished with a polishing machine ESC-200-GTL (ESCIL®, Chassieu, France) with carbide papers (P600, P1200, P2500) under constant water irrigation. Subsequently, finer polishing was performed using a diamond slurry using four different particle sizes (6, 3, 1 and 0.25 µm), which were applied in succession. The sample was cleaned with a gentle waterjet and via a 2-minute ultrasonic bath between each polishing step. Prior to mechanical testing, the sample preparation was controlled and validated under the optical microscope where the bone microstructure had to appear as clear as in Fig. 6.1. Finally, the specimens were stored in their tubes with a solution containing calcium (50 mg/L) and sodium azide (0.01%) to prevent bone mineral matrix dissolving and avoid collagen degradation respectively (Gustafson et al. 1996). The tubes were then kept refrigerated at 4°C before indentation phase began.

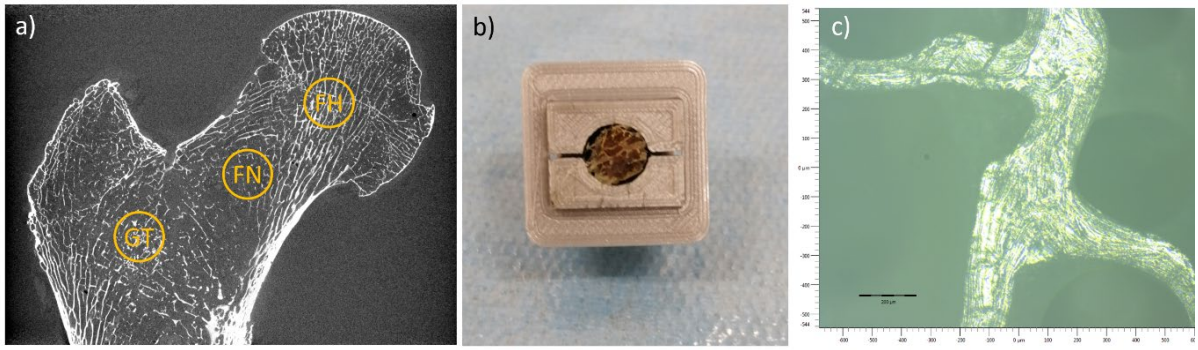

Figure 6. 1: Sample extraction and preparation. a) localization of the three different bone regions extracted from each proximal femur, "GT" refers to great trochanter, "FN" refers to femoral neck and "FH" refers to femoral head; b) trabecular sample stored in the designed sample holder after sample preparation protocol; c) microscopic investigation of the preparation protocol efficacy before microindentation essays.

2.2. X-ray Microtomography

µCT images of both the proximal femurs were acquired using Rx-Solution EasyTom XL ULTRA microtomograph ('RX Solutions SAS, 3D X-Ray Tomography Systems.', n.d.), with a 150 kV X-Ray Hamamatsu Tube allowing a focus spot size of 5 µm. To cover the whole femoral head, an isovolumetric voxel size of 0.051 mm has been chosen. The other parameters were, 343 mA current, 150 V voltage, 8 images/s and 1440 projections over 360 degrees of rotation. Each projection was obtained from the average of 10 images to increase the signal to noise ratio. The acquisition lasted approximatively 40 minutes.

Synchrotron radiation propagation-based phase-contrast (SRµCT) was used to obtain the 3D virtual reconstruction of the microstructure of examined bone volumes.

The center core across the whole length of femoral neck was imaged at the SYRMEP (SYnchrotron Radiation for MEdical Physics) beamline of the Elettra synchrotron laboratory (Basovizza [Trieste], Italy), employing a filtered (1.5 mm Si +1 mm Al) polychromatic X-ray beam delivered by a bending magnet source in transmission geometry and using a mean energy of 27 KeV. The detector used was a water-cooled, 16-bit, scientific Complementary metal–oxide–semiconductor (sCMOS) macroscope camera (Hamamatsu C11440–22C) with a 2048×2048 pixels chip coupled with two GGG:Eu scintillator screen (respectively 45 and 17 μm thick) through a high numerical aperture optics. The effective pixel size of the detector was set at 5.0×5.0 μm^2 and 0.9×0.9 μm^2 (obtained respectively using the scintillator of 45 and 17 μm of thickness), yielding a maximum field of view of about 10.2×10.2 mm^2 and 1.8×1.8 mm^2 respectively. The sample-to-detector (propagation) distance was set at 150 mm. A set of 1200 projections were recorded, with continuous sample rotation over a 180-degree scan angle and an exposure time per projection of 2.5 s.

Each set of acquired raw images was processed using the SYRMEP Tomo Project (STP) software suite, developed in-house at Elettra (F. Brun et al. 2015) based on the ASTRA Toolbox (van Aarle et al. 2015), to perform the CT reconstruction employing the Filtered Back-Propagation algorithm using a filter (Baker et al. 2012) to reduce the so-called ring artefacts in the reconstructed slices. A single-distance phase retrieval algorithm was applied to projection images before CT reconstruction (Paganin et al. 2002), setting a γ parameter (ratio between the real and imaginary parts of the complex refraction index of the material under investigation) of 50 and 20 for SRμCT images with a voxel size of 5 and 0.9 μm^3 respectively.

Image Post-Processing and Analysis

μCT (51 μm^3) and SRμCT (5 μm^3)

The total femoral neck volume acquired at 51 μm^3 (Fig. 6.2b) has been first manually divided in two different regions of interests (ROIs), one keeping the cortical phase and one the trabecular phase. The binarization of both ROIs were straightforward as the contrast was high and the voxel size was smaller than the trabecular thickness. Based on binarized ROIs it has been calculated the bone mineral content (BMC), derived from the total bone volume present in both the cortical and the trabecular ROI and multiplied by the bone tissue mineral density (ρ = 1.2 g/cm^3) (Laval-Jeantet et al. 1983a; Tassani et al. 2011). Moreover, in the trabecular phase it has been calculated the bone volume fraction (BVF), which refers to the ratio between the bone volume and the total volume, the trabecular thickness (Tb.Th) and spacing (Tb.Sp), which provide information about the trabecular diameters and distance between two trabeculae respectively. In the cortical phase, it has been calculated the cortical thickness (Ct.Th) which refers to the thickness of the outer femoral neck shell. Tb.Th, Tb.Sp and Ct.Th

have been extrapolated using the distance transformation map from which it has been derived the aperture map using the software iMorph (iMorph_v2.0.0, AixMarseille University, Marseille, France) (E. Brun, Ferrero, and Vicente 2017a; E. Brun et al., n.d.). The aperture map provides for every pixel of the bone the diameter of the maximal disk totally enclosed in the bone and containing this voxel. Tb.Th and Ct.Th were then deduced from the mean values of the aperture map distribution. Tb.Sp was quantified from similar computations in the marrow phase of the trabecular ROI. The aperture map has been previously used for the 3D morphological evaluation of porous materials in different fields (E. Brun, Ferrero, and Vicente 2017a; Burghardt, Link, and Majumdar 2011b; Soldati, Escoffier, et al. 2020) and provides local information with a sub-voxel precision (E. Brun, Ferrero, and Vicente 2017a; Johansson et al. 2019). The central femoral neck core acquired using the SRμCT at 5 μm^3 (Fig. 6.2c), in which was present the trabecular phase only, followed the same image analysis and using iMorph the same bone characteristics were retrieved.

The bone cortical characteristics have been compared between the osteoporotic subject and the control using μCT images. The trabecular characteristics have been compared using μCT and SRμCT singularly and between acquisition techniques evaluating the informative contribution by reducing the voxel size by an order of magnitude.

SRμCT (0.9 μm^3)

The stack of synchrotron images at 0.9 μm^3 followed a different path. Thanks to the extremely high resolution the image field of view was focused on a single trabecula (Fig. 6.2d) and the osteocytes lacunae (OL) became assessable. To do so, the images were normalized to obtain the same gray level dynamics, and the same optimum binarization threshold, that better differentiated the bone from the OL, was selected manually. The thresholding effect has been evaluated by comparing the retrieved morphological characteristics using two other thresholds (respectively +5% and -5% of the best individuated threshold). A second volumetric threshold of 100 voxels (73 μm^3) was selected to identify possible small pores derived from in-homogeneities in the image illumination, and these misclassified regions were re-added to the solid phase. Once the bone volumes were correctly segmented, the bone porosity was measured from the bone volume and the osteocytes lacunae, vascular and canal network. Second, the osteocytes lacunae were individuated as those regions composed by a volume in range 73 to 1000 μm^3 chosen in accordance to the mean and standard deviation of OL previously find in the literature (van Oers, Wang, and Bacabac 2015; Dong et al. 2014). This approach allowed us to separate the OL from the vascular and the canal network characterized by higher volumes (in range of thousands voxels) (Fig. 6.2e and 6.2f) (Dong et al. 2014; Carter et al. 2013).

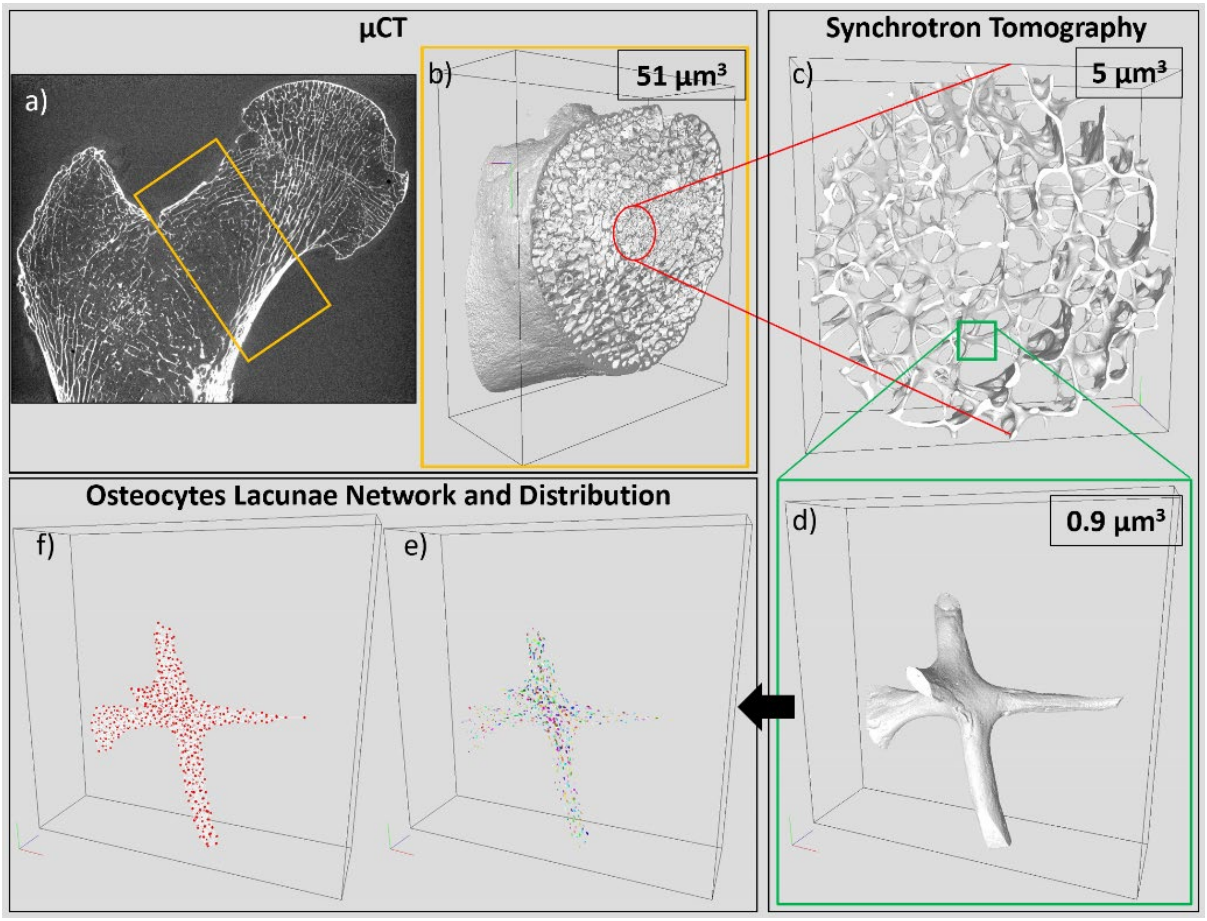

Figure 6. 2: multiscale characterization of femoral neck morphology acquired using μCT (51 μm³) and SRμCT (5 and 0.9 μm³). a) Proximal femur coronal plane acquired using μCT at 51 μm³ showing the femoral neck ROI (orange rectangle) used to assess clinical standard bone mineral density using dual-energy X-ray absorptiometry; b) whole femoral neck acquired using μCT at 51 μm³; c) central core of the femoral neck trabecular phase scanned using SRμCT at 5 μm³; d) single trabecula acquired using SRμCT at 0.9 μm³; e) osteocytes lacunae distribution and f) osteocytes lacune network.

Finally, each OL was characterized individually extrapolating its volume, surface, size, shape, sphericity, and fractal anisotropy) and as an interconnected network by evaluating their region of action. In particular, in each OL the principal axes (a, b and c) of the maximum inscribed ellipsoid have been calculated, and from them it has been characterized the OL shape by deriving the aspect ratios ($\frac{a}{b}, \frac{b}{c}, \frac{a}{c} and \frac{a}{(b+c)}$). Then the surface (S) and the sphericity index (Fsph) (Benouali et al. 2005) have been derived respectively by the formula:

$$S_{OL} = 4 * \pi * (a^p b^p + a^p c^p + b^p c^p)^{1/p} \quad , with\ p = ln(3)/ln(2)$$

$$Fsph = 6 * V_{OL} * \left(\pi / {S_{OL}}^3\right)^{0.5}$$

Where V_{OL} and S_{OL} are respectively the volume and the outer surface of the OL. Moreover, the fractal anisotropy (Özarslan, Vemuri, and Mareci 2005) which reflects

the axonal diameter and is an extension of the concept of eccentricity of conic sections in 3 dimensions, normalized to the unit range, has been calculated using the formula:

$$\sqrt{\frac{3}{2}} * \frac{\sqrt{(a-\lambda)^2+(b-\lambda)^2+(c-\lambda)^2}}{\sqrt{a^2+b^2+c^2}} \quad , where\ \lambda = {}^{(a+b+c)}/_{3}$$

Finally, the region of action could be considered as a 3D bone neighboring around the OL in which the osteocytes sense and transmit information. It is derived by applying the Voronoi map which calculates the minimum path between the closest OL and differs from the OL density because it is calculated for each OL singularly.

2.3. Microindentation

The trabecular bone of the whole set of specimens has been characterized using a microindentation apparatus (Tester NHT², Anton Paar ®, Switzerland and Austria) equipped with a sharp Berkovich diamond indenter (tip diameter: 120 nm, elastic modulus: 1141 GPa and Poisson's ratio: 0.07) in a thermally controlled room at 23 °C and on a pneumatic antivibration table. For the indentation tests, the sample was set in a watertight support filled with calcium buffered saline up to the level of the polished surface. A total of 40 points were selected using a x20 microscopic objective on five different trabeculae located on the polished surface of the sample. A special attention was made on the placement of the points to avoid any border effect and therefore, indentation points were situated along the trabecular centerline. In addition, each indentation point has been verified at magnitude x100 to avoid any surface irregularities (i.e. porosity). Before each set of indentation, a calibration session test was made on a fused silica reference sample, the mean values obtained were 71.3±1.6 GPa, knowing that the reference data was 72 GPa.

The bone trabeculae were then indented using a trapezoidal loading profile (30 s: 60 s: 30 s, max load 40 mN) as shown in Fig. 6.3 in the distal (polished) surface of each sample. The 60 s plateau time, higher than that found in the literature, was chosen from initial tests because wet tissue displays more viscous mechanical behavior. The sample hardness (H) and elastic modulus (E_s) were calculated using the Oliver and Pharr method (Oliver and Pharr 1992). The hardness corresponded to the mean pression under the tip at maximal depth, H=Pmax/Ac, where Pmax is the maximum load and Ac the contact area, while the elastic modulus was calculated using the unloading tangent from the indent load-displacement curve (Oliver and Pharr 1992) derived from the equation:

$$\frac{1}{Er} = \frac{(1-\nu_s^2)}{E_s} + \frac{(1-\nu_i^2)}{E_{it}}$$

where E_{it} and ν_i are the known elastic modulus and Poisson's ratio of the indenter and E_r the reduced modulus. In this study, the Poisson's ratio was assumed to be 0.3,

since the relative error, by varying the Poisson's ratio from 0.2 to 0.4, was found to be less than 8% in elastic modulus (D. Wu et al. 2018; P. K. Zysset 2009).

The mean and standard deviation for elastic moduli and the hardness, both expressed in GPa, were obtained for the osteoporotic subject and the control.

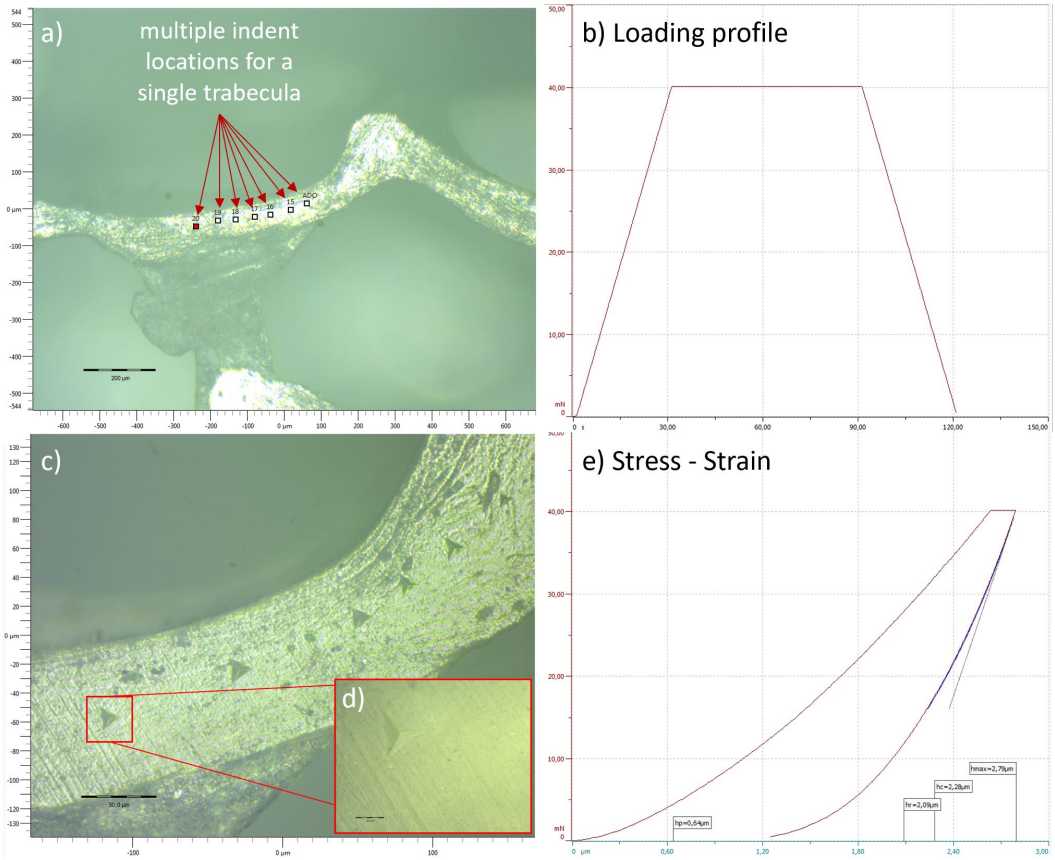

Figure 6. 3: Trabeculae micro indentation. a) manually placed indents locations for each selected trabecula, b) indentation trapezoidal loading profile, c) stress-strain plot showing a single load–unload cycle, d) indented area and e) view of a single indent at original magnification x100.

2.4. Infra-Red Fourier Transform

The attenuated total reflection Fourier transform infra-red (ATR-FTIR) measurements were obtained using a Thermo Nicolet iS50 FTIR spectrometer (Thermo Fisher Scientific Co., Waltham, MA, USA) equipped with a deuterated triglycine sulphate (DTGS) detector. The ATR spectra were recorded using a diamond ATR Smart Orbit™ accessory (from Thermo Optec) in the Mid-IR spectral range 4000-527 cm^{-1}, averaging 64 scans for each measure and 64 scans for the background. The spectral resolution is 4 cm^{-1}. For each bone sample, a small fragment was collected and analyzed. The fragments were first grinded in an agate mortar and the powder obtained was successively placed on the ATR diamond crystal. Pressure was applied to the powder to optimize the contact with the diamond crystal. Several replicate

spectra were acquired for each fragment. The spectra selected for interpretation are those which presented the highest signal-to-noise ratio.

A qualitative analysis of the spectra have been conducted considering the range 527-1800 and 2550-4000 cm^{-1}, where the most important features connected to bones component are visible. In all the spectra, the phosphate features of hydroxyapatite ($Ca_{10}(PO_4)_6(OH)_2$) could be found at 962 cm^{-1} (symmetric stretching, ν_s), 1090 and 1010 cm^{-1} (antisymmetric stretching ν_a), 555 and 559 cm^{-1} (bending mode, δ) (F. Ren, Ding, and Leng 2014). The carbonate group (CO_3^{2-}), a common substituent in the hydroxyapatite molecule, lead to the bands at 870, 879 (bending mode, δ), 1409, 1444 and 1468 cm^{-1} (antisymmetric stretching, ν_3). An additional band of the carbonate group could be present at 1540 cm^{-1}, but not diagnostic as often covered from contributions from other compounds (F. Z. Ren and Leng 2011). The presence of the organic matrix is visible from the CH and NH bands respectively at around 3000 cm^{-1} and 3300 cm^{-1} (antisymmetric stretching, ν_a). Additional bands connected to the organic matrix respectively at 1637 (Amide I), 1550 (Amide II), and 1239 cm^{-1} (Amide III) allows identifying a proteinaceous-based compound (Paschalis 2019b; Schmidt et al. 2017b; Zhai et al. 2019b). Moreover, the carbonate group can replace either PO_4^{3-} or OH^- groups in hydroxyapatite. When the substitutions happen at PO_4^{3-} sites, the compound is defined as B-type carbonated apatite (B-CAp); if the substitution is at OH^- sites, is the A-type carbonated apatite (A-CAp) (F. Z. Ren and Leng 2011; Madupalli, Pavan, and Tecklenburg 2017b). A-CAp and B-CAp can be distinguished by FTIR spectroscopy respectively using the bands at 1546 cm^{-1} and 1465 cm^{-1}.

2.5. Statistical Analysis

For the morphological parameters obtained using image processing, the Student T-test has been calculated for each of the OL characteristics to assess whether the average value of the osteoporotic distribution differs significantly from the control reference value. Moreover, the linear regression and the coefficient of correlation (R^2) has been calculated to evaluate the dependency of the OL characteristics and the volume of bone for each volume of interest (VOI) analyzed.

Regarding the trabeculae mechanical parameters, first a normality test (Shapiro-Wilk test) has been applied to assess if the normal distribution was respected using a p-value with a significance level alpha of 0.05 as a threshold. Since the Shapiro-Wilk test showed that the normal distribution was not respected, Kruskal-Wallis test and a multiple pairwise comparisons were performed using Dunn's test with a Bonferroni correction in order to assess differences between ROIs (femoral head vs. femoral neck vs. great trochanter) while the Mann-Whitney U test has applied to assess differences among groups (osteoporotic vs. control).

3. Results

3.1. Multiscale Bone Morphology

Macro- and microscale

The osteoporotic and the control femoral neck region of interest is shown in Fig. 6.4. The image analysis conducted using μCT images at 51 μm^3 in the cortical ROI showed a similar average cortical thickness of the cortical shell with the osteoporotic bone being 2% thinner than the control (0.72±0.48 mm and 0.74±0.52 mm respectively for the osteoporotic and the control). Moreover, the morphological analysis performed on the ROI which include the whole trabecular phase of the femoral neck showed higher differences between the two subjects with the osteoporotic subject presenting lower BVF (-13%) and Tb.Th (-12%) and higher Tb.Sp (+8%) compared to the control (Table 6.2 and Fig. 6.5). The analysis on the BMC of both the cortical and the trabecular ROI showed similar results comparing the osteoporotic to the control for the cortical ROI (3% higher BMC for the osteoporotic compared to the control, respectively 1.72 vs. 1.67 g/mm^3). However, this was not the case in the trabecular ROI, where the results showed that the BMC was +21% higher for the control than the osteoporotic (1.41 vs. 1.11 g/mm^3).

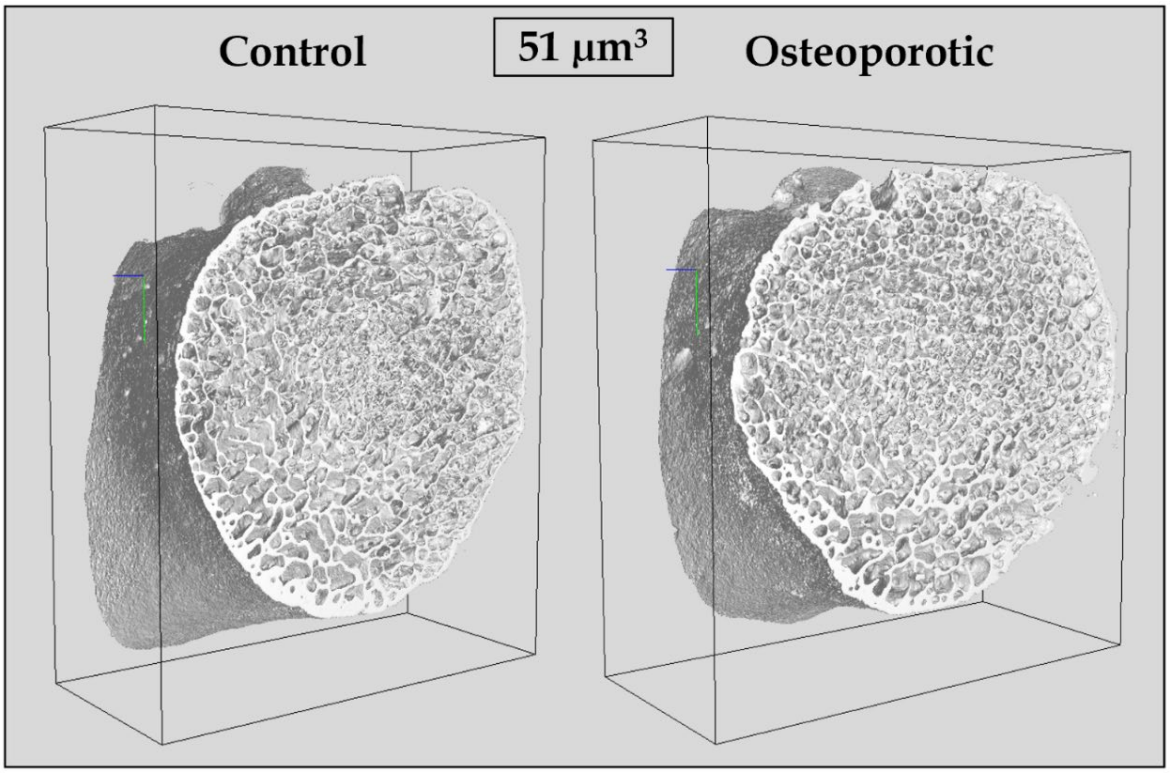

Figure 6. 4: 3D morphology of the whole femoral neck acquired using μCT at 51 μm^3.

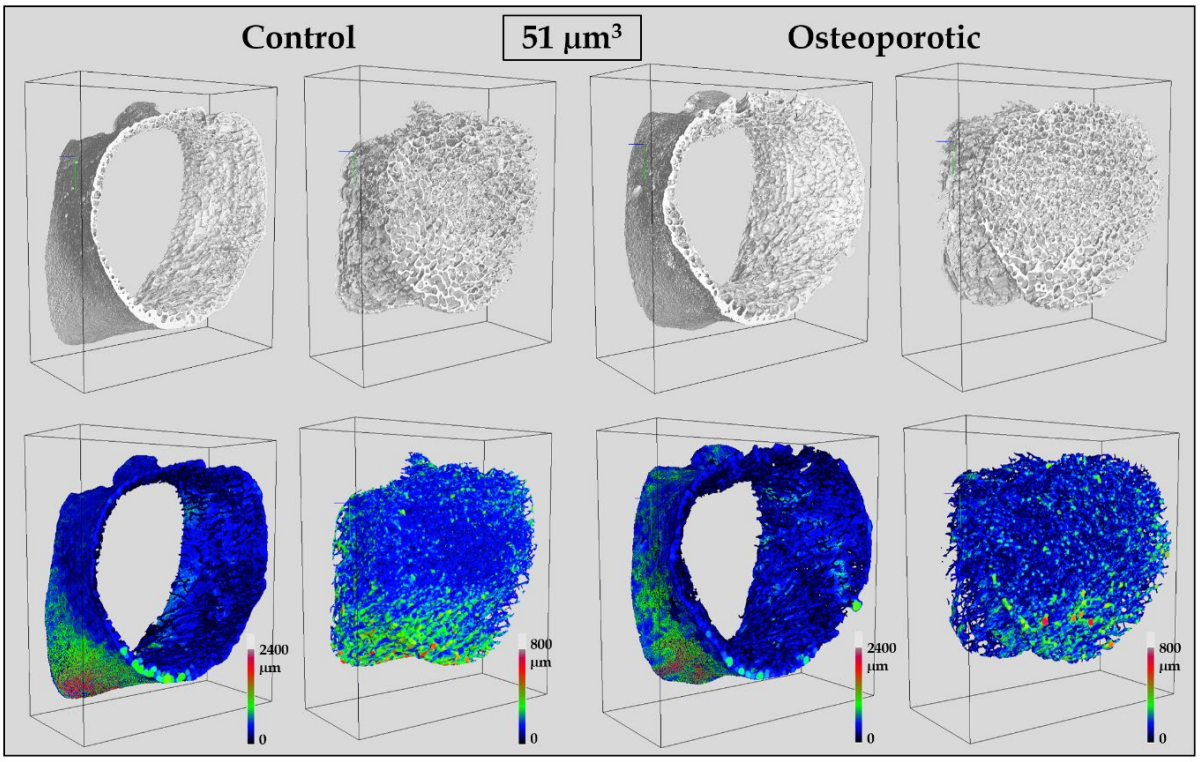

Figure 6. 5: 3D morphology of the osteoporotic and control femoral necks acquired using µCT at 51 µm³ showing the cortical and trabecular phase alone (first row) and bone thickness (second row).

The morphology analysis performed in the central core of the femoral neck acquired using SEµCT at 5 µm showed similar results (Table 6.2 and Fig. 6.6). Although, the SRµCT showed mean values different than those derived from µCT images, the Tb.Th and the BVF acquired using SRµCT were respectively -35% and -56% lower and the Tb.Sp wad +17% higher than those derived from µCT, the trend between osteoporotic and control was comparable. In particular, the osteoporotic subject presented reduced Tb.Th (-5%) and BVF (-33%) and increased Tb.Sp (+28%) compared to the control.

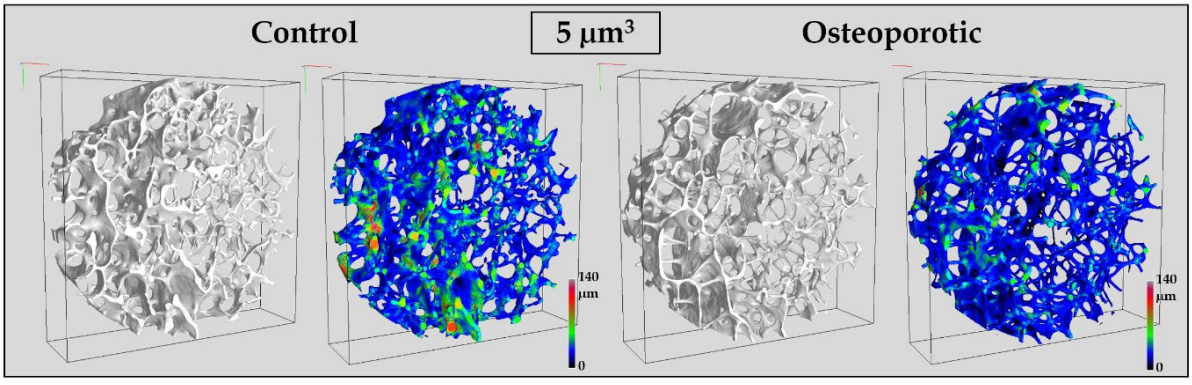

Figure 6. 6 : 3D morphology and trabecular thickness of the femoral neck central core acquired using SRµCT at 5 µm³ of both the control and the osteoporotic subject.

Lastly, using the SRμCT acquisition at 5 μm it was possible to assess the smallest trabeculae in the analyzed ROI. Specifically, evaluating the aperture map distribution profile of the solid phase and considering 1×10^6 occurrence as a threshold to assess the minimum trabeculae expression, the osteoporotic subject presented a minimum trabecular thickness 9% smaller than the minimum Tb.Th depicted by the control (0.052±0.005 mm vs. 0.057±0.003 mm respectively for the osteoporotic and the control).

Table 6. 2: Femoral neck morphological characteristics.

	Whole Femoral Neck (51 μm³)				**Femoral Neck Core (5 μm³)**			
	Ct.Th (mm)	**Tb.Th (mm)**	**Tb.Sp (mm)**	**BVF**	**Tb.Th (mm)**	**Tb.Sp (mm)**	**BVF**	**min Tb.Th (mm)**
Control (S8)	0.74±0.52	0.21±0.10	1.03±0.51	0.158	0.13±0.06	1.10±0.29	0.079	0.057±0.003
OsteopS (S9)	0.73±0.48	0.18±0.11	1.11±0.59	0.137	0.12±0.06	1.41±0.47	0.053	0.052±0.005
Diff	-2%	-12%	8%	-13%	-5%	28%	-33%	-8%

Data are presented as mean±SD. Ct.Th: cortical thickness; Tb.Th: trabecular thickness; Tb.Sp: trabecular spacing; BVF: bone volume fraction; min Tb.Th: minimum values of trabecular thickness.

Osteocytes Lacunae Characteristics

The image analysis conducted using SRμCT images at 0.9 μm³ allowed the individualization of the osteocytes embedded in the solid bone phase and in Table 6.3 and Fig. 6.7 are reported the osteocytes lacunae morphological parameters. Firstly the total number of OL per bone volume has been analyzed and the results showed a slightly lower density (-3%) in the osteoporotic subject as compared to the control. However, the mean OL density showed the opposite effect with the osteoporotic subject presenting higher density (+3%) as compared to the control. The results of the Voronoi map showed that the osteoporotic subject had in general 5% lower region of action than the control (5.67×10^4 μm^{-3} vs. 5.96×10^4 μm^{-3}). Moreover, the mean OL volume of the osteoporotic subject resulted 25% greater than those from the healthy (358.1 μm³ vs. 287.1 μm³ respectively for the osteoporotic and the control). The osteoporotic higher OL volume is also reflected in the principal axes (a, b and c) of the inscribed ellipsoid inside the OL which were 8% greater in the osteoporotic OL compared to the control and with 16% higher surface (225.5±13.7 μm² vs. 195.0±10.1 μm²). However, no difference was assessed in the axes of the inscribed ellipsoid in the osteocytes, nor in the osteocytes shape, (the aspect ratios where the osteoporotic OL showed 1% greater a/b, a/c and a/(b+c) and no difference was assessed for b/c). Moreover, although the sphericity index and the fractal anisotropy showed no difference in the mean values between the osteoporotic and the control subject (0% and 1% respectively), the control showed much higher intervariability (0.798±0.009 vs.

0.795±0.024 for the sphericity index respectively of the osteoporotic subject and the control and 0.467±0.015 vs. 0.462±0.023 for the fractal anisotropy).

Table 6. 3: morphometric parameters of osteocytes lacunae (OL).

Total Values		**OsteopS (S9)**	**Control (S8)**	**Diff**
Nb of Analyzed Regions		5	5	-
Bone Volume (mm^3)		0.28	0.45	-
OL Number		4030	6649	-
OL Volume (mm^3)		0.0016	0.0023	-
OL Density (10^4 mm^{-3})		1.44	1.49	-3%
Lacunar Porosity (%)		0.59%	0.52%	+13%
Mean values		**OsteopS (S9) (mean±SD)**	**Control (S8) (mean±SD)**	**Diff**
OL Volume (μm^3)		358.08±165.00	287.10±160.00	25%*
OL Surface (μm^2)		225.53±13.75	195.00±10.11	16%*
Lacunar Density (10^4 mm^{-3})		1.60±0.33	1.56±0.16	3%
OL Region of Action (10^4 μm^{-3})		5.7±2.7	6.0±4.0	-5%
OL Principal Axes (μm)	**a (length)**	12.13±0.46	11.18±0.57	8%
	b (width)	6.68±0.32	6.19±0.13	8%*
	c (depth)	4.40±0.13	4.09±0.12	8%*
OL Shape (Ad)	**a/b**	1.90±0.11	1.89±0.09	1%
	b/c	1.54±0.06	1.53±0.06	1%
	a/c	2.85±0.07	2.82±0.17	1%
	a/(b+c)	1.13±0.05	1.12±0.05	1%
OL Sphericity (Ad)		0.80±0.01	0.79±0.02	0%
OL Fractal Anisotropy (Ad)		0.47±0.02	0.46±0.02	1%

Data are reported as mean ± standard deviation. "OsteopS" refers to osteoporotic subject, "Diff" stands for difference between the osteoporotic subject and the control, "Ad" refers to a-dimensional. * indicates a p-value < 0.05.

The Student T-test analysis between the OL characteristics of the osteoporotic subject and the control showed a significative difference in the mean OL volume and surface ($p<0.01$ in both cases) and in the second and third principal axes of the inscribed ellipsoid in the OL ($p<0.05$ for both b and c axes). However, no statistical differences were registered for region of action, density, porosity, aspect ratios, sphericity index and fractal anisotropy.

To evaluate the dependency of the OL characteristics with the volume of bone, the correlation coefficient among each characteristic and the bone volume has been assessed in each VOI. The results showed an excellent correlation between the bone volume and the total number of individuated OL ($R^2 = 0.97$), and good correlation for the mean region of action ($R^2 = 0.59$), however modest to poor correlation were

assessed for OL volume (R^2 = 0.36), density (R^2 = 0.40), surface (R^2 = 0.27), sphericity (R^2 = 0.39) and fractal anisotropy (R^2 = 0.09) assessed in each analyzed region.

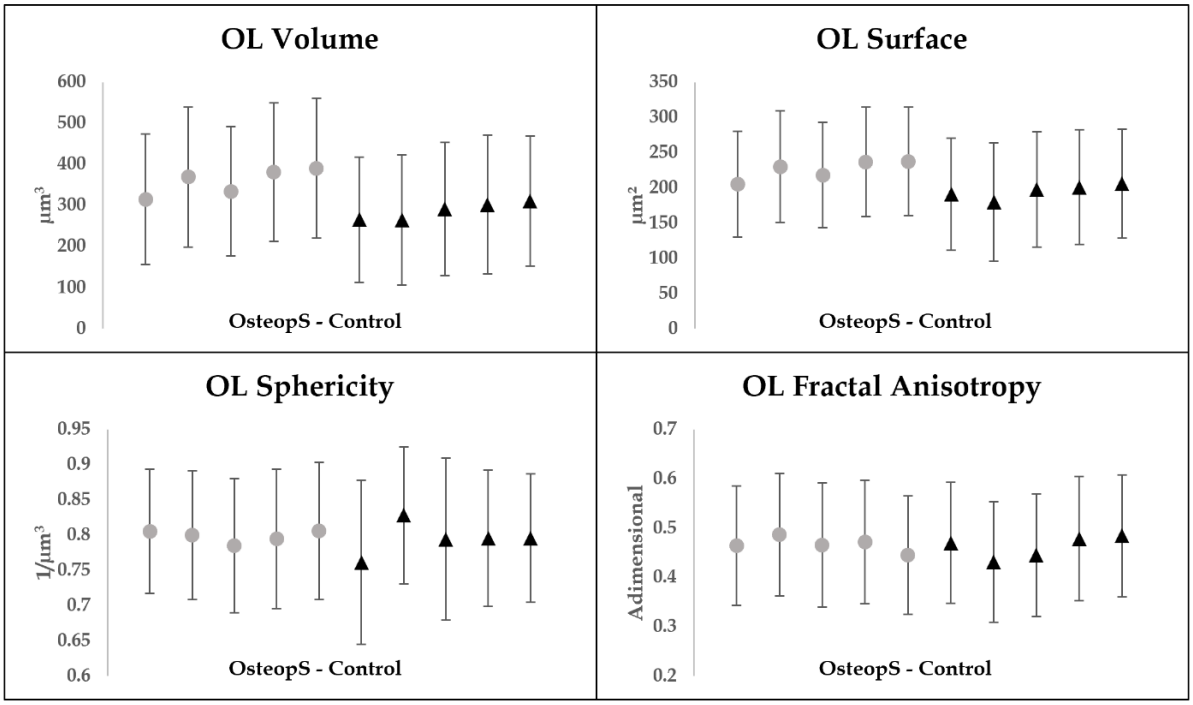

Figure 6. 7: osteocytes lacunae characteristics. The mean values and the SD are reported for each investigated region where "OsteopS" refers to osteoporotic sample and regions are marked with "●" while "Control" refers to the healthy subject and is marked as "▲". "OL" refers to Osteocytes lacunae.

Image Pre-Processing Effect on OL Characterization

We also investigated the possible effect of our image pre-processing. First, the pore regions distribution has been investigated to evaluate the classification efficacy between noise (pores volume <73 µm³), OL (pores between 73 and 1000 µm³) and vessels (pores >1000 µm³). The pore region distribution reported in Figure 6.8 showed that the range selected for the OL classification is coherent and allowed the separation between the three phases, and therefore could be used in further studies. Moreover, the OL image analysis described in the previous section has been performed on the same VOI choosing two different thresholds (+5 and -5% of the best manually identified threshold) and by comparing the effect of the median filter (kernel size 3×3) applied before performing the image analysis. The results of OL characteristics after the application of different thresholds showed errors in the same +5/-5% range. The committed maximum error in the number of individuated OL was -4% reducing the threshold of 5% and +4% when the threshold was increased. Similar results were assessed for the OL volume (-6% and +5% respectively for reduced and increased thresholds), surface (-4% and +4% respectively) and region of action (+6% and -5%). Regarding the OL shape the differences were even lower with a maximum error of

+2% in the principal axes and +1% in the aspect ratios, sphericity and fractal anisotropy for reduced thresholds of 5% and -3% in the principal axes and -1% in the aspect ratios, sphericity and fractal anisotropy for thresholds increased by 5%.

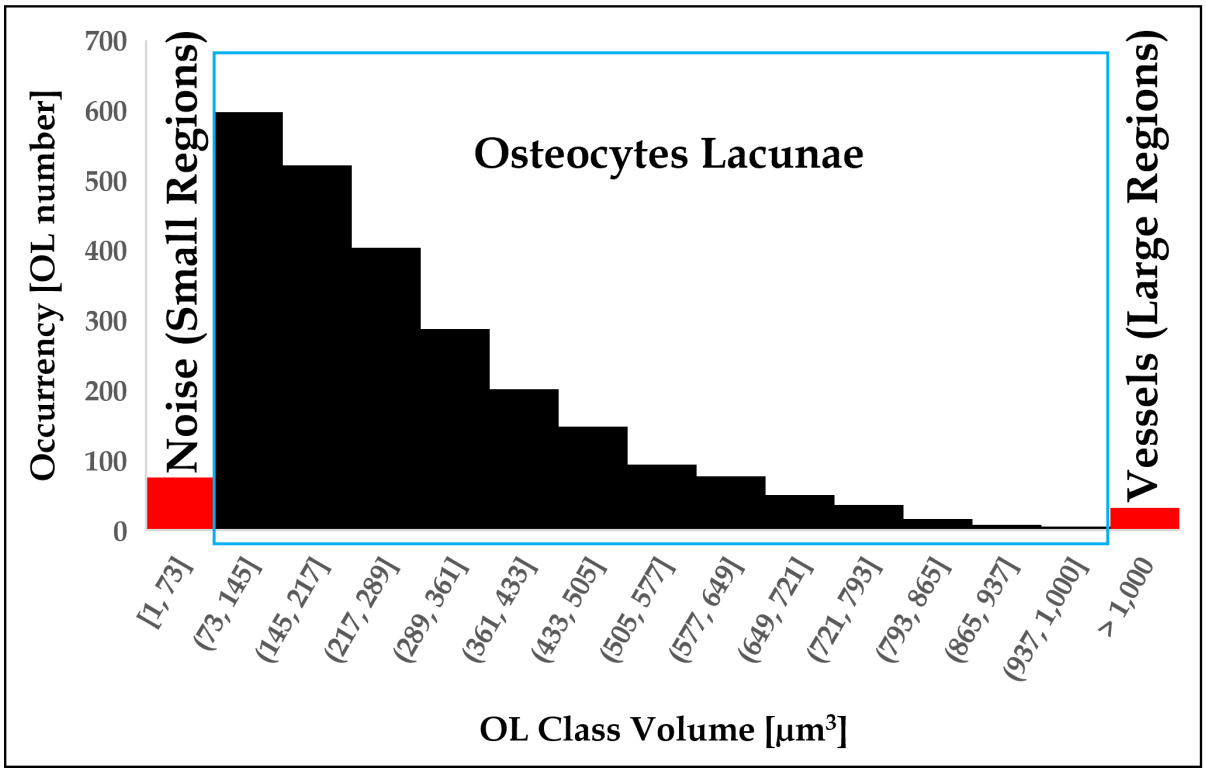

Figure 6. 8: Distribution of the individuated Osteocytes lacunae (OL) in the bone solid phase. Red bar shows the objects smaller than 73 µm³ classified as noise and re-added to the solid phase and the objects bigger than 1000 µm³ classified as blood vessels. The light blue square indicate the objects classified as osteocytes lacunae.

Furthermore, the binarization error concerns the voxels located at the level of the contours of the OL and around the optimal threshold, therefore the binarization error results in a positioning of the interface at ±1 voxel. To verify that healthy OL were statistically smaller than the osteoporotic OL, the effect of the variance of the threshold around the selected reference value has been investigated. Thus, the OL healthy was reduced by 5% resulting in an increase in the OL volumes, while this same threshold was increased by 5% for the osteoporotic images resulting in a decrease in the OL volumes. The average volumes of healthy OL remained lower than the average volumes of osteoporotic OL (-12%) which confirms the trend observed previously by using the same optimal threshold value for these 2 series of images (-25%).

Moreover, the investigation on the effect median filter on the image analysis showed that the filter application have left unchanged the total number of identified OL (maximum error on the OL number was 1%, where 4 more OL were individuated after the application of the median filter compared on a total of 475 found in the same

non-treated VOI). Higher impact was assessed on the OL volume, where the median filtered stack showed higher OL volumes (+6%) compared to the original stack, and surface (up to +9% for the median filtered stack). Although, similar incongruences were assessed in the principal axes of the inscribed ellipsoid, they resulted uniformly distributed therefore no difference between the median filtered and the original stack was assessed in the OL shape (0% difference in the aspect ratios, sphericity index and fractal anisotropy).

3.2. Trabeculae Mechanical Properties

The microindentation assays allowed the characterization of the mechanical properties of the lamellar bone at the micro scale. The first parameter analyzed, was the trabecular elastic modulus. The results presented in Fig. 6.9 showed that the FH of the control had the highest mean values, significantly different from the other two regions, 62 % higher compared to GT and 47% higher than FN (7.4±2.5 GPa vs. 2.8±1.3 GPa and 3.9±1.2 GPa, $p<0.0001$, respectively for the E_s of FH, GT and FN). Interestingly, the GT showed the lowest E_s mean value, moreover being significantly different ($p<0.001$) compared to the E_s in the FN area. However, in the OsteopS group, only the GT showed an E_s significantly different compared to the others with a mean value of 2.0±0.6 GPa vs. 3.9±1.3 GPa and 3.5±1.4 GPa for FH and FN respectively ($p<0.0001$). Those results showed that the GT region obtained the lowest E_s for both the osteoporotic subject and the sample, moreover being significantly different to the other ROIs. In addition, the intergroup differences has been assessed by comparing the E_s discrepancies in the same region of the two subjects. The FH and the GT of the control showed significantly higher elastic modulus compared to those derived from the osteoporotic subject (the mean E_s were 48% higher in the FH ($p<0.0001$) and 29% higher in the GT($p<0.01$)). Surprisingly, no statistical differences ($p>0.05$) have been assessed in the FN between the two groups.

The hardness was second parameter investigated. The results presented in Fig. 6.9 showed that the control FH hardness was statistically higher ($p<0.0001$) that the hardness of both the GT (+32%) and the FN (+36%) (hardness equal to 0.402±0.122 GPa in the FH, 0.274±0.175 GPa in the GT, and 0.258±0.070 GPa in the FN), while no statistical differences were assessed between GT and FN. For the Osteoporotic subject, the only difference assessed was between FH and GT with a mean value of 0.266±0.099 GPa vs. 0.215±0.059 GPa for FH and GT respectively, ($p<0.01$). Moreover, analyzing the intergroup differences, the pattern of distinctions was similar to the one observed for elastic modulus. Indeed, intergroup differences were assessed in the FH and GT while no differences were obtained in the FN. The hardness mean values obtained in the control FH were 34% higher compared to those from the Osteoporotic ($p<0.0001$),

while in the GT the control showed 22% greater hardness ($p<0.05$) compared to the osteoporotic subject.

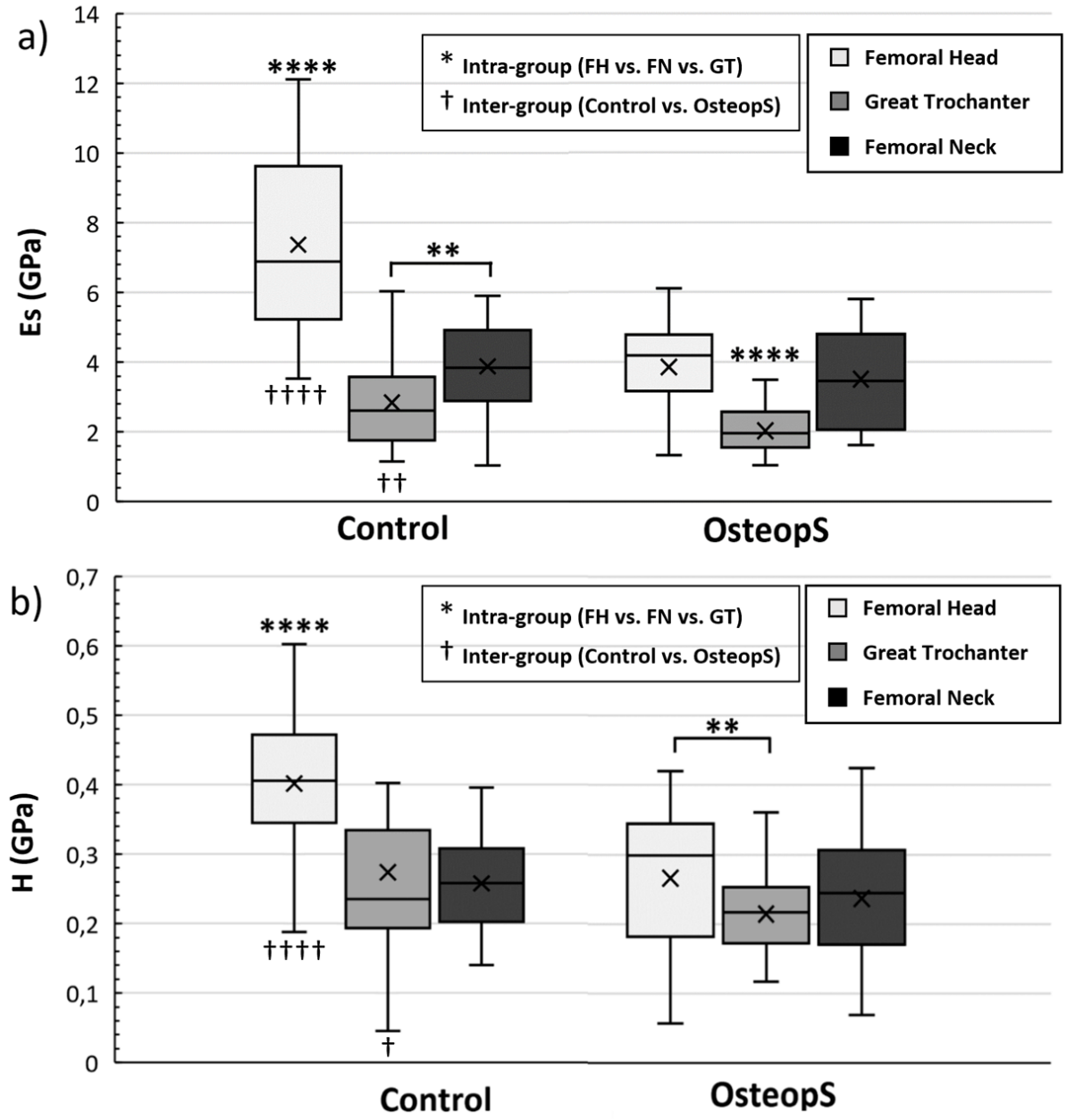

Figure 6. 9: Whisker plot of elastic modulus (Es) (a) and hardness (H) (b) obtained using microindentation on trabecular bone specimens. (a) Representation of intra-group variation of elastic modulus. On the left are presented the differences between the three ROIs in the control subject and on the right the differences for the osteoporotic subject. (b) Representation of intra-group variation of hardness. On the left are presented the differences between the three ROIs in the control subject and on the right the differences for the osteoporotic subject. * represent the variability between different region of the same group (intra-group) *$p < 0.05$, **$p < 0.01$ and **** $p < 0.0001$. † represent the variability between same regions of different group (inter-group) †$p < 0.05$, ††$p < 0.01$ and †††† $p < 0.0001$.

3.3. ATR-FTIR Results

The ATR-FT-IR spectra of the bones fragment are reported in Figure 6.10. Although a slight shift is observed in the main band of phosphates (1010 cm^{-1}), no significant variations were visible concerning the band position of the phosphate functional groups (962, 1010, 1090 cm^{-1}) among the spectra. Moreover, no changes were visible also about the bands of Amide I (1637 cm^{-1}) and Amide III (1239 cm^{-1}) organic-based compounds. Some considerations, however, could be made in the region of the of the carbonate group, namely 1300-1600 cm^{-1} (Fig. 6.11). In the spectra recorded in this study, the signal at 1540 cm^{-1} could indicate the presence of type A, but there was an evident difficulty to attribute it as it overlapped with the Amide II band at about 1550 cm^{-1}. Only in the FN of the osteoporotic subject a well-defined peaks at 1540,1570, and 1576 cm^{-1} were observed. Regarding the presence of type B, a shoulder was visible at 1465 cm^{-1}, which might indicate the presence of the compound in the spectra. However, the shoulder signal emerged best only in sample osteoporotic FN.

The band at 1408 and 1444 cm^{-1} are also attributed to the carbonate group. Still, they were not fully helpful in discriminating between type A and B. Concerning the control subject both in the FH and FN, a shoulder is visible at 1503 cm^{-1}, however not attributed.

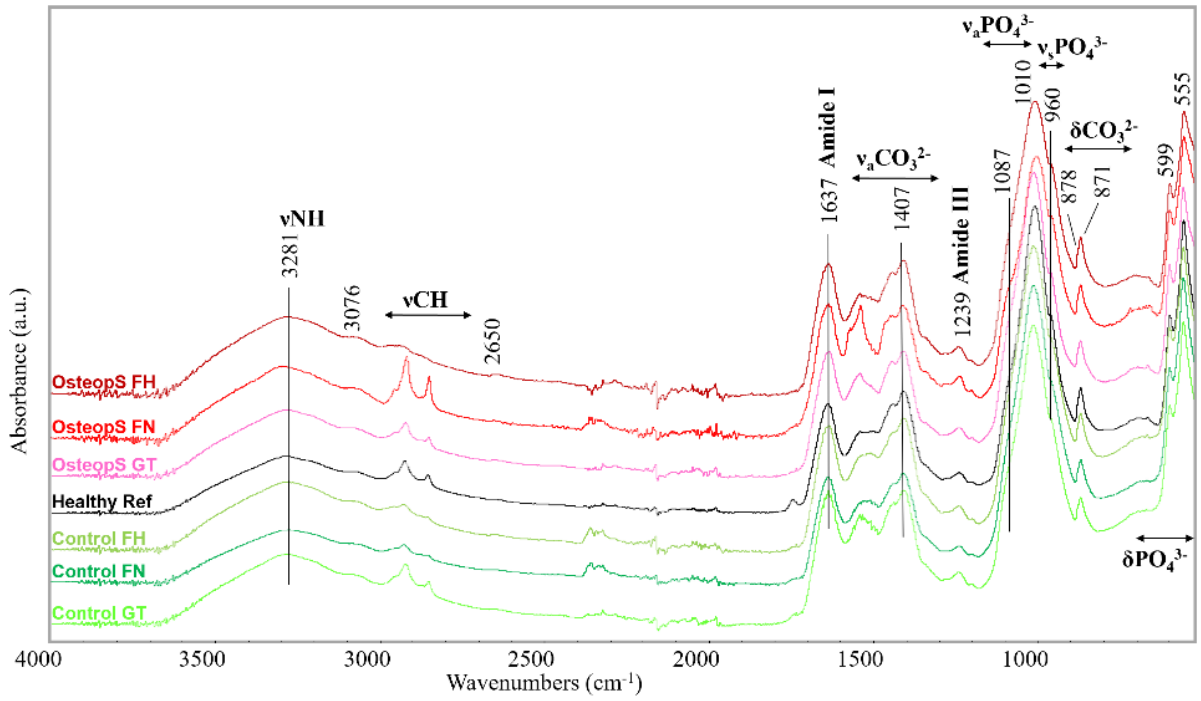

Figure 6. 10: ATR-FTIR spectra of the whole set of subjects and subregions. "OsteopS" refers to osteoporotic sample (S08); "Healthy Ref" refers to a refence sample of a healthy 61 years old male; "FH" refers to femoral head, "FN" refers to femoral neck; "GT" refers to great trochanter. (b) focus in the carbonated group region (1300-1600 cm^{-1}).

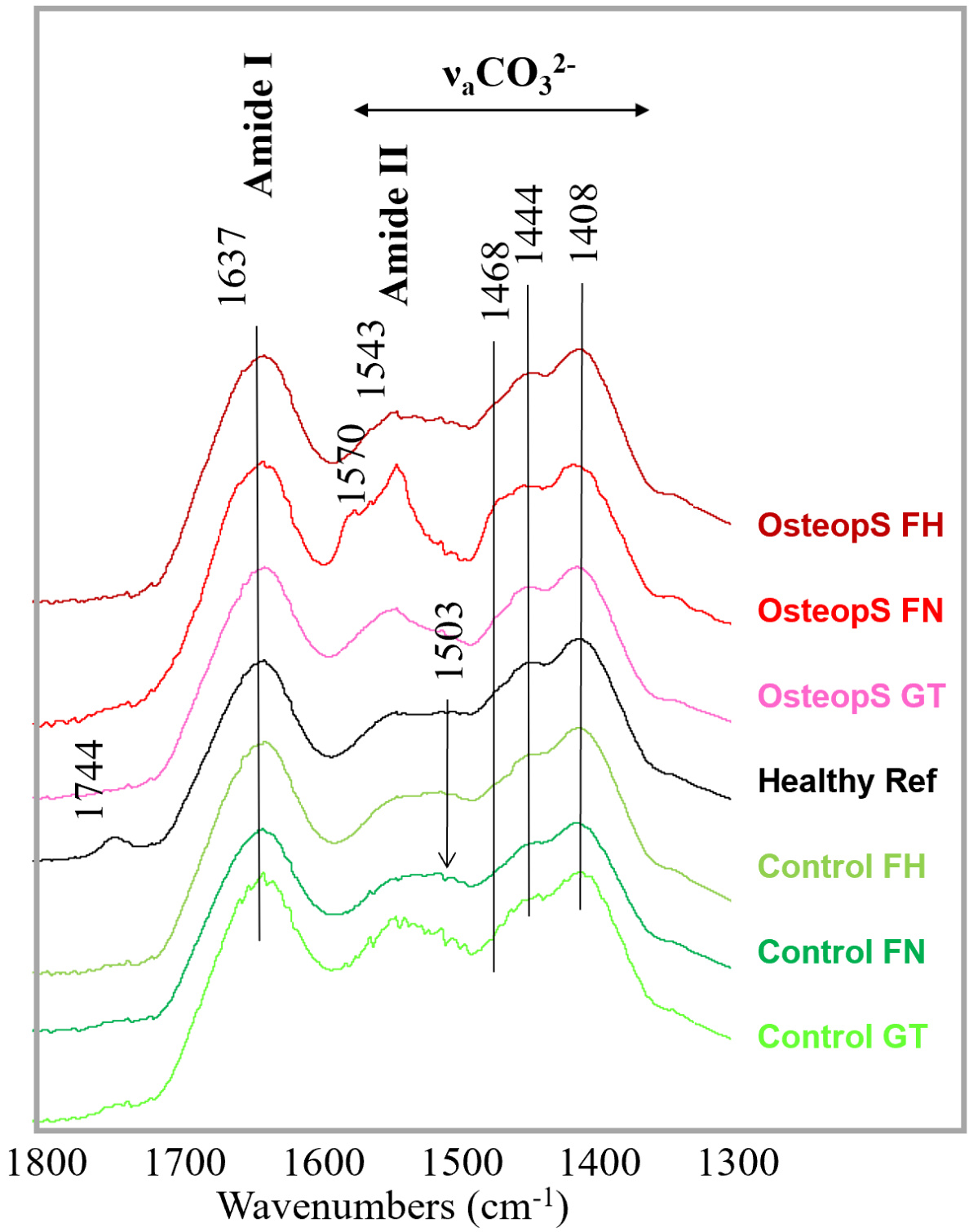

Figure 6. 11: ATR-FTIR spectra focus in the carbonated group region (1300-1600 cm^{-1}).

4. Discussion

The multiscale investigation of two femoral necks, one osteoporotic and one healthy subject, is of great interest for a reliable assessment of the bone quality from the macroscale to the microscale with the assessment of bone microarchitecture, trabecular mechanical properties and tissue composition, and osteocytes lacunae characterization. The Microindentation and the FTIR came to an additional support respectively assessing the differences in the trabeculae mechanical properties, and trabecular Hydroxyapatite composition between different proximal femur regions of the same sample and among different subjects by comparing one osteoporotic femur to one gender- and aged-matched control.

In the present study we addressed the issue related to bone composition and structure using a multiscale and multimodal approach. This approach allowed the acquisition and the analysis of femoral neck cortical and trabecular phase, the investigation of osteocytes lacunae morphology and organization, the assessment of the local quantitative mechanical properties of the trabeculae and the qualitative characterization of the bone composition and mineralization. Moreover, it provides the comparison of the corresponding results between one osteoporotic subject and one gender- and aged-matched control.

The analysis conducted using μCT images acquired at 51 μm^3 showed no difference in the cortical thickness and BMC between the osteoporotic and the control, however reporting differences in both the morphology and BMC in the trabecular phase. Similar bone morphology was assessed by Tjong et al. on a study conducted on 17 cadaveric radii scanned using μCT at 18 μm^3 (Tjong et al. 2012b). In their study, they reported a mean Ct.Th of 0.59±0.19 mm, Tb.Th of 0.17±0.01 mm and Tb.Sp of 0.75±0.15 mm, where the differences for both Ct.Th and Tb.Sp could be explained by the different anatomical site. Moreover, in a study conducted on 34 femoral neck (11 affected by rheumatoid arthritis, 15 affected by osteoarthritis and 8 controls), harvested during total hip replacement and scanned using μCT at 19 μm^3, Wang et al. reported that morphological parameters (Ct.Th = 0.64±0.2 mm, Tb.Th = 0.18±0.03 mm, BVF = 0.15±0.09 and Tb.Sp = 0.93±0.32 mm) in the same range of those reported in this study (B. Wang et al. 2016). However, Wang et al. reported that the patients showed greater Tb.Th and BVF and reduced Tb.Sp compared to controls (B. Wang et al. 2016). This opposite effect could be explained by the different bone disease (rheumatoid arthritis and osteoarthritis vs. osteoporosis in our case). This hypothesis was further supported by Li et al., where on a study conducted on 60 postmenopausal women (30 affected by osteoarthritis and 30 affected by osteoporosis) scanned in the femoral head using μCT

at 36 μm^3, reported that osteoporotic patients showed reduced BVF, trabecular thinning and increased Tb.Sp (Z.-C. Li et al. 2012).

Focusing in the central core of the femoral neck using SRμCT at 5 μm^3 the trabecular morphology provided lower Tb.Th and BVF and higher Tb.Sp than those previously reported at using μCT images at 51 μm^3. Although, those results were expected as the femoral neck is a highly in-homogeneous bone region with the solid phase progressively reducing its volume as approaching the central core, it was not expected to individuate greater discrepancies between the osteoporotic bone morphology and the control than those derived from the whole femoral necks. This result may suggest that the bone remodeling is not uniform and that works at different rate at different regions. Juan et al. on a study conducted on 5 different anatomic regions of both distal femurs of 10 postmenopausal women scanned using HRpQCT with an isotropic voxel size of 82 μm^3, reported significant regional variation in the trabecular architecture ($0.001<p<0.05$) with differences up to 106% between lowest (central) and highest (medial and posterior) regions (Juan Du et al. 2019). Local differences in the trabecular bone architecture were also been assessed in different anatomical sites, as for the calcaneus (Souzanchi et al. 2012), the glenoid (Jun et al. 2017) and the proximal femur (Issever et al. 2002) but not extensively investigated in the femoral neck, which is an osteoporotic fracture site and one of the most invalidating (van Oostwaard 2018). One could suggest that reducing the voxel size would allow a better characterization of the thinnest solid structures, however our results suggest that the bone morphology was already correctly characterized at 51 μm^3. In addition, using the μCT acquisition at 51 μm^3 it was possible to visualize the whole proximal femur in approximately 40 minutes therefore providing a more complete overview of the bone quality also allowing the characterization of both the cortical and the trabecular phase. SRμCT images at 5 μm^3 allowed the characterization of the smallest trabeculae present in the central femoral core reporting a minimum trabecular thickness of 50 μm and therefore suggesting that the bone morphology would be completely resolved using a voxel size in range 15-25 μm^3. These voxel dimensions would completely resolve both cortical and trabecular phase of the whole proximal femur in 2 to 3 acquisitions. In fact, using a voxel size of 25 μm^3 or 15 μm^3 the field of view would be respectively of 5.1 cm^3 and 3.1 cm^3 which would allow the acquisition of the great trochanter, the femoral neck and head in respectively 2 or 3 scans.

Reducing the voxel size from 5 to 0.9 μm^3 has the great advantage that the osteocytes lacunae became visible and characterizable since each OL had at least 152 voxels totally included in its volume (vs. 27 voxels using 5 μm^3 SRμCT images). In this study, OL differences have been assessed between the osteoporotic and the control in the volume, and the same result was also reflected in the OL surface and total solid phase porosity,

however no differences in the OL shape, sphericity and fractal anisotropy. Moreover, no statistical difference was assessed considering the OL as an interconnected network since OL region of action and density between the osteoporotic and the control were in the same range. Previous studies have investigated OL morphology in the cortical phase of femoral diaphysis (Carter et al. 2013; Dong et al. 2014; B. Yu et al. 2020), proximal tibiae (van Hove et al. 2009) and iliac crest (Qiu et al. 2006), however few studies have assessed the OL morphology in the trabecular bone phase. In a study conducted on the femoral diaphysis of 7 human cadavers (female, aging 75±15 years old) scanned SRnanoCT at 120 nm^3, Peyrin et al. reported a mean OL volume and surface of 315.6±51.7 μm^3 and 326.0±50.0 μm^2 respectively (B. Yu et al. 2020). Moreover, the principal axes of the inscribed ellipsoid were a = 16.7±1., b = 7.9±1.0 and c = 4.6±0.7 µm. They also reported a OL lacunae density of 3.2±1.2 $x10^4$ mm^{-3} (vs. 1.60±0.33 and 1.56±0.16 $x10^4$ mm^{-3} respectively for the osteoporotic and the control subject) and average volume of each Voronoi cell or region of action of 2.6±0.6 $x10^4$ μm^{-3} (vs. 5.7±2.7 and 6.0±4.0 $x10^4$ μm^{-3} in our case respectively for the osteoporotic and the control subject). The differences in the region of action, which were almost the double in our case, could be explained by the different bone region (cortical femoral diaphysis vs trabecular femoral neck). Similar results were reported by Dong et al. on a study conducted on 13 cortical specimens from the femoral mid-diaphysis of two female donors scanned using SRµCT at 1.4 μm^3, the mean volume and surface were in range 409.5±149.7 μm^3 and 336.2±94.5 μm^2 respectively (Dong et al. 2014). Moreover, they reported the average dimensions were of 18.9±4.9 µm in length, 9.2±2.1 µm in width and 4.8±1.1 µm in depth. In another study conducted on proximal tibial trabecular specimens extracted from 3 middle-aged women respectively affected by osteoarthritis, osteopenia due to rheumatoid arthritis and osteopetrosis and scanned using high-resolution nano-CT system at 580 nm^3, Van Hove et al. reported differences in OL shape between different pathologies with the osteopenic subject presenting relatively large and round OL (van Hove et al. 2009). Moreover, they suggested that the differences in 3D morphology of osteocytes and their lacunae in long bones of different pathologies with different BMD might reflect an adaptation to matrix strain due to different external loading conditions. In our case, although the osteoporotic and the control had different BMD, no difference in the OL shape was assessed, which might be due to the fact that both subject aged more than 90 years old and therefore one could suggest a reduced mobility of both cases. To further support this hypothesis, Van Oers et al. reported that osteocytes resulted aligned to collagen fibers which are affected by loading mode, moreover suggesting that variation in the lacunar and osteocytes shape undoubtedly effects the osteocytic mechanosensation and subsequent control of bone remodeling (van Oers, Wang, and Bacabac 2015).

The investigation of the pre-processing steps was necessary to evaluate the robustness of our analysis since the stack of images have been segmented using a threshold manually selected and the investigation was focusing on very small objects that could have been lost during the pre-processing. The analysis conducted applying two different thresholds (+5 and -5%) from the best manually individuated, demonstrated that the committed errors were small and the OL characteristics were comparable (maximum committed error in OL shape was in range +3 and -3%, therefore proving the robustness of our approach and the high image quality. Moreover, the application of the median filter showed that the OL volume uniformly increased by 6% compared to the original one, while no difference was assessed in the OL shape, sphericity nor fractal anisotropy. The median filter is usually applied to reduce the "salt and pepper" noise and it has been showed previously that median pre-filtering improves the thresholding performance while preserving the edges (Bovik, Huang, and Munson 1987).

Mechanical loading is an essential stimulus for skeletal tissues. Osteocytes are primarily responsible for sensing mechanical stimuli in bone and for orchestrating subsequent responses. This is critical for maintaining homeostasis, and responding to injury/disease (Hinton, Rackard, and Kennedy 2018). Therefore, microindentation assays were conducted to quantify the mechanical properties at the micro scale in the three different proximal femur regions allowing the overall characterization of the mechanical properties in the whole femur epiphysis in both the osteoporotic and the control subjects. The microindentation results showed statistical differences in the trabeculae elastic modulus and hardness depending from both their proximal femur anatomical location and bone health state. the FH showed greater E_s and H compared to the other two bone regions investigated, moreover, showing a statistical difference between the bone health state. Although reporting the lowest E_s and H, the GT showed similar results, this was not the case for the FN in which no differences was assessed between healthy and osteoporotic.

Surprisingly, to the best of our knowledge, trabecular data on osteoporotic bone at the femoral neck could not be found in the literature and only few studies have been found investigating the trabeculae mechanical properties in this regions (Philippe K Zysset et al. 1999; Hengsberger, Kulik, and Zysset 2002; Hoffler et al. 2000). Hengsberger et al., on a nanoindentation study using different maximum loadings (0.2, 0.4, 1 and 2 mN) conducted on the femoral neck of an 86 years old woman free of evident bone diseases reported greater E_s and H (respectively comprised between 7.4±0.45 GPa to 18.5±4.9 GPa and between 0.29±0.13 GPa to 0.95±0.44 GPa) (Hengsberger, Kulik, and Zysset 2002). However, the reported wide range was due to the several tested loading conditions which were found to be a significant factor for both parameters. In fact, as the elastic modulus and hardness decreased with the

increasing of the loading, the data with the highest loading condition, closer to our indentation protocol, was selected and the E_s range was reduced from 10 GPa to 14 GPa. Similar E_s values were also reported by Hoffler et al. on a study conducted on 10 FN trabeculae (male between 40 and 85 years old) in which a mean E_s of at 8.57±1.2 GPa and H of 0.37±0.05 GPa were assessed, however differences could be explained by the harvesting of the anatomical site which were closer to the cortical bone than in our case (Hoffler et al. 2000). Slightly greater values were also reported by Zysset et al. on a study conducted on the FN trabeculae of 4 males and 4 females (75±12 years old) with no previous history of fractures nor osteosarcoma using nanoindentation (E_s = 11.4±5.6 GPa and average H ranging from 0.234 to 0.760 GPa) (Philippe K Zysset et al. 1999). Finally KoKot et al. and Pawlikowski et al., on a study conducted respectively on 8 healthy FH (fame and female, 60+ years old) and 25 FH (male and female, 67±9 years old) affected by osteoarthritis, and both using comparable microindentation protocol (trapezoidal loading profile, maximum loading = 500 mN, loading rate = 500 mN/min, holding time = 20 sec) reported similar E_s and H (Kokot et al. 2018; Pawlikowski et al. 2017). In particular, the E_s and H reported were respectively 8.1±1.4 GPa and between 0.30 and 0.50 GPa (Kokot et al. 2018) vs. 7.4±2.5 GPa and 0.40±0.12 GPa in our case for the healthy subject and 4.8±1.1 GPa and 0.11±0.02 GPa (Pawlikowski et al. 2017) vs. 3.9±1.3 GPa and 0.27±0.05 GPa in our case for bones characterized by an altered remodeling process (osteoarthritis vs. osteoporosis). These results further support that elastic modulus and hardness are distinct parameters, as elastic modulus characterized rate-independent reversible material behavior and hardness explain resistance to plastic deformation as previously suggested (Rodriguez-Florez, Oyen, and Shefelbine 2013; Hoffler et al. 2000). The general slightly lower values obtained in our study could be explained by differences in the preparation protocol (embedded in exothermic resin (Philippe K Zysset et al. 1999; Hoffler et al. 2000) vs. stored in a optimized support in our case) and/or indentation protocol (different maximum loading (Hengsberger, Kulik, and Zysset 2002; Kokot et al. 2018; Pawlikowski et al. 2017), holding time of the maximum load (Kokot et al. 2018; Pawlikowski et al. 2017)). Supporting this hypothesis in the review article by Wu et al. has been reported a wide range of bone elastic modulus (1.3 GPa and 22.3 GPa) (D. Wu et al. 2018), moreover stating that this effect was due to different scale of analysis (micro, sub-micro and nano scale), different sample preparation (dry vs. wet) (Hengsberger, Kulik, and Zysset 2002), anatomical site and localization (Fratzl-Zelman et al. 2009), and orientation of the indentation (Dall'Ara et al. 2013). The patient age could also be a relevant factor which could have led to an already altered ECM in both the healthy and the osteoporotic sample by excessive bone remodeling process due to subjects reduced mobility and therefore to a reduced bone stress profile. Milovanovic et al. on a study conducted on 8 healthy FN specimens from female donors (5 young

aged 32±5 yrs, and 3 elderly aged 88±6 yrs) using nanoindentation, supported this hypothesis reporting that the bone trabeculae of elderly women expressed less elastic behavior (1.28±0.16 GPa in the young vs. 1.97±0.52 GPa in the elderly) at the material level, which makes them more vulnerable to unusual impact loads originating from a fall (Milovanovic et al. 2012). Therefore, we decided to repeat this microindentation assay on a sample harvested on a younger FN (61 years old) and the mean values obtained for elastic modulus were 7.6±0.6 GPa and the hardness was 0.36±0.05 GPa which was in the same range found in previous studies (Hengsberger, Kulik, and Zysset 2002; Hoffler et al. 2000; Kokot et al. 2018). For these reasons, knowing that mechanical parameters are correlated to ECM, composed by collagen, mineral and non-collagenous proteins and since no differences have been derived in the FN mechanical properties, one could suggest that the healthy and osteoporotic FN tissues were in the same bone remodeling state. Moreover, no differences in the OL characteristics have been assessed between the two types of tissue and the obtained mechanical properties were closer to those derived from osteoarthritis patients rather than from healthy subjects. However, differences in mechanical properties have been assessed in both FH and GT depending on the bone health state with healthy samples providing higher H and E_s. Therefore, one could suggest that healthy FN was already impacted by an intensive bone remodeling process and hence FN could be the first proximal femur region impacted by osteoporosis. Overall, the results showed that bone remodeling is a non-uniform process that evolves at different rate depending on the bone anatomical region. An extensive investigation of the OL characteristics in both FH and GT regions, could validate this hypothesis and reinforce the link between osteocyte network and bone quality.

The qualitative ATR-FTIR analysis aimed to assess trabecular mineral differences between the osteoporotic and the control. However, in this study, the spectra at 1540 cm^{-1} indicating the presence of A-type carbonated apatite was not possible due to band overlapping with the Amide II band. The band overlapping represents a well-known difficulty in peak attribution (F. Ren, Ding, and Leng 2014) which hamper the recognition of the presence of A-type apatite. Moreover, the well-defined peaks at 1540, 1570 and 1576 cm^{-1} found for the osteoporotic FN could not be attributed to A-type carbonated apatite as other compound absorb at these wavelength, i.e. degradation products derived from the interaction of calcium and fatty materials (calcium carboxylates). Furthermore, Madupalli et al. on a study conducted on synthesized apatites showed that the 1408 cm^{-1} band associated to type B carbonated apatite had la lower intensity than 1465 cm^{-1} (Madupalli, Pavan, and Tecklenburg 2017b), while in our case was higher. Finally, Figueiredo et al. on a study conducted on cadaveric femur of a 39 yrs male assigned the bands 1410/1445 cm^{-1} to the B-type apatite (Figueiredo et al. 2010) which were similar to those derived in this

study. The qualitative ATR-FTIR analysis showed that all spectra appeared similar with no possibilities to differentiate among the different proximal femur anatomical subregions (FH, FN and GT) nor depending on the health bone state (healthy vs. osteoporotic), suggesting a comparable chemical composition.

Some limitation have to be acknowledged, first the use of only two samples and second the synchrotron images focusing only in the FN of the two scanned proximal femurs. The synchrotron beamtime allowed us to fully explore and characterize only one bone region, therefore we decided to investigate the proximal femur region more exposed to fractures (Bouyer et al. 2020). Moreover, the two femurs have been accurately selected in order to have very different DXA-BMD while being extremely alike (gender-, age- and heigh-matched). Although, no differences in the OL shape have been assessed in the femoral neck, as a future perspective we may suggest that it would be interesting to evaluate the OL characteristics also in the great trochanter and the femoral head. In the femoral neck, the differences in the bone mineralized phase suggested by microindentation could be investigated at the molecular scale, as for the hydroxyapatite structure, organization and composition.

5. Conclusion

In this study, it has been characterized the bone quality in the femoral neck using a multiscale and multimodal approach of one osteoporotic and one gender- and age-matched control. This approach allowed the investigation of the bone quality from the macro scale assessing the whole proximal femur region, to the microscale with the assessment of the OL morphology and organization, and the trabeculae tissue properties, to the molecular scale with the investigation of the mineralization and carbonate accumulation. Our results suggested that small differences could be associated to osteoporosis in the cortical bone phase while the trabecular network resulted more impacted. Moreover, the analysis conducted at the microscale showed that while differences in the trabeculae mechanical properties were assessed between osteoporotic and healthy subject in both FN and GT, no differences in both the mechanical properties and OL shape and organization in the FN. This result suggested that healthy FN was already impacted by an intensive bone remodeling process and hence FN could be the first proximal femur region impacted by osteoporosis. Finally, no differences were assessed between spectra showing comparable chemical composition between subregions and regardless of bone health state.

Conclusion of the Chapter

In this chapter it has been show that osteoporosis could have a different impact in different proximal femur subregions. In particular from the microindetation essays it has been shown that FN subregion resulted the first region with an increase bone remodeling activity and therefore the subregion first affected by osteoporosis. Finally, the ATR-FTIR qualitative analysis of the spectra have suggested a comparable chemical composition between subregions and regardless of bone health state.

Interestingly would have been to compare the bone properties and the osteocytes lacunae characteristics of the osteoporotic and the control cortical phase together with the same properties derived from the trabeculae. However, while microindentation and FTIR in the cortical phase are planned for the following months, the granted shifts for the beamtime at ELETTRA synchrotron, where designed to assess only the trabecular phase leaving small extra time. Fortunately, in this extra time we managed to assess the cortical phase of the osteoporotic subject, which therefore has been acquired at both 5 and 0.9 μm^3. The SRμCT image analysis of images acquired at 5 μm^3 reported a cortical thickness of the upper part on the femoral neck of 0.65±0.22 mm which was in the same range of the Ct.Th derived from the whole femoral neck analysis at 51 μm^3. Moreover, the trabecular phase in proximity to the cortical shell confirmed the high inhomogeneities of the trabeculae depending from their position in the bone anatomy. In particular, as reported in Table 6.4 the trabecular phase close to the cortical shell compared to the trabecular phase of the central femoral core showed reduced Tb.Sp (-30%) and increased BVF (+133%) and Tb.Th (+27%).

The image analysis conducted on the cortical osteocytes lacunae acquired at 0.9 μm^3 showed some differences with those derived from the trabecular phase. The cortical phase (Fig. 6.12), compared to the trabecular one, showed lower total OL density (-20%), total lacunar porosity (-8%) and mean region of action (-6%). Moreover, while the cortical OL showed smaller mean volume and surface (-10% and -9% respectively), no statistical difference was assessed. Finally, while no difference has been assessed in the shape of OL embedded in the trabeculae between the osteoporotic and the healthy subject, small differences (up to 10%) were assessed in the OL principal axes and shape (up to -7% for b/c ratio) between cortical and trabecular phase. However, these differences were never statistically significant.

Table 6. 4: morphometric parameters of osteocytes lacunae (OL) of the trabecular and cortical phase of the osteoporotic subject.

Total Values		OsteopS (S08) Trabecular phase	OsteopS (S08) Cortical phase	Diff
Nb of Analyzed Regions		5	4	-
Bone Volume (mm^3)		0.28	1.45	-
OL Number		4030	25431	-
OL Volume (mm^3)		0.0016	0.0092	-
OL Density (10^4 mm^{-3})		1.44	1.80	-20%
Lacunar Porosity (%)		0.52%	0.64%	-8%
Mean values		**Trabecular phase (mean±SD)**	**Cortical phase (mean±SD)**	**Diff**
OL Volume (μm^3)		358.08±165.00	320.73±149.60	-10%
OL Surface (μm^2)		225.53±13.75	205.83±26.70	-9%
Lacunar Density (10^4 mm^{-3})		1.60±0.33	1.85±0.29	-13%
OL Region of Action (10^4 μm^{-3})		5.7±2.7	5.3±2.6	-6%
OL Principal Axes (µm)	a (length)	12.13±0.46	12.23±0.94	7%*
	b (width)	6.68±0.32	6.89±0.56	3%
	c (depth)	4.40±0.13	4.85±0.37	10%
OL Shape (Ad)	a/b	1.90±0.11	1.98±0.11	4%
	b/c	1.54±0.06	1.43±0.07	-7%
	a/c	2.85±0.07	2.76±0.23	-3%
	a/(b+c)	1.13±0.05	1.14±0.07	1%
OL Sphericity (Ad)		0.80±0.01	0.82±0.03	2%
OL Fractal Anisotropy (Ad)		0.47±0.02	0.46±0.03	-1%

Data are reported as mean ± standard deviation. "OsteopS" refers to osteoporotic subject, "Diff" stands for difference between the osteoporotic subject and the control, "Ad" refers to a-dimensional. * indicates a p-value < 0.05.

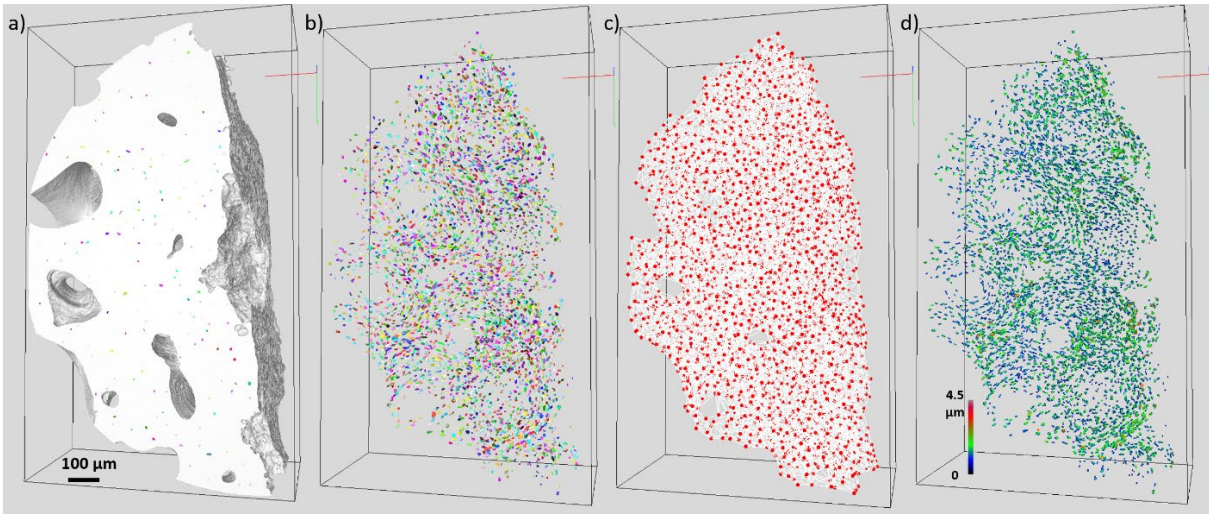

Figure 6. 12: SRµCT at 0.9 μm^3 of the cortical phase of the femoral neck. a) Cortical morphology with embedded colored osteocytes lacunae (OL), b) OL distribution, c) OL network and d) OL aperture map.

In the next chapter it is reported a multiscale and multimodal study conducted on small specimens (great trochanter, femoral neck and femoral head) extracted from five proximal femurs (from Sample01 to Sample05). The extracted samples were first scanned using μCT at 25 μm^3 to fully resolve the trabecular morphology and then the hydroxyapatite molecular composition have been investigated by performing X-ray absorption spectroscopy of the Calcium K-edge. This technique allowed the characterization of the Calcium to Phosphorous ratio and to retrieve qualitative information of the Hydroxyapatite crystal so that changes to the HA crystallinity have been investigated.

1

Chapter 7 : Fracture Risk Assessment in the Proximal Femur Based on Bone Microarchitecture and Hydroxyapatite Crystallinity Investigation: a Multimodal and Multiscale Approach (draft article)

Authors

Enrico Soldati [1,2,3], Jerome Vicente [1], Luis Alberto Macías-Pérez [4], Daphne Guenoun[2,5], Emilio Catelli [6], Giorgia Sciutto [6], Stefano Iotti [7], Emil Malucelli [7], Giulio Gorni [8], Carlo Marini [8], Martine Pithioux [2,9] and David Bendahan[3].

Affiliation

[1] Aix Marseille University, CNRS, IUSTI, Marseille, France

[2] Aix Marseille University, CNRS, ISM, Marseille, France

[3] Aix Marseille University, CNRS, CRMBM, Marseille, France

[4] Aix Marseille University, CNRS, IRD, INRAE, Collège de France, CEREGE, Technopôle de l'Arbois-Méditerranée, BP80, Aix-en-Provence, France

[5] Institute for Locomotion, Department of Radiology, Sainte-Marguerite Hospital, Aix Marseille University, APHM, CNRS, ISM, Marseille, France;

[6] University of Bologna, Department of Chemistry "G. Ciamician", Ravenna, Italy;

[7] Bologna University, Department of Pharmacy and Biotechnology, Bologna, Italy

[8] ALBA Synchrotron Light Facility, Carrer de la Llum 2-26, 08290 Cerdanyola del Vallès, Spain

[9] Department of Orthopaedics and Traumatology, Institute for Locomotion, Sainte-Marguerite Hospital, Aix Marseille University, APHM, CNRS, ISM, Marseille, France

1. Introduction

Osteoporosis is a bone disease characterized by an increased susceptibility to fractures mainly accounted by a reduced bone strength and quality associated to an altered bone mineralization (Gong et al. 2014). It is well accepted that bone remarkable mechanical properties are due to its complex hierarchical structure covering several length scales from the molecular level of collagen to the organ level (Fratzl and Gupta 2007). Bone extracellular matrix is made up of an organic matrix containing a collagen framework reinforced with mineral particles. Bone hydroxyapatite (HA) crystals precipitate and grow in intrafibrillar gap regions and at later stages also in extra-fibrillar spaces (Alexander et al. 2012). The crystals within the fibrils grow with the c-axis parallel to the collagen molecule and this phenomenon is named biomineralization (BM). BM is a process that takes place continuously in the whole life span, since bone has regenerative abilities that enable the self-repair and regeneration of fractures (Murshed 2018). However, there are pathological situations such as osteoporosis (proven to affects the whole bone with a dysfunctional remodeling function) in which BM is impaired and the bone loss extent is too important for a complete regeneration to occur, hence resulting in disrupted bone microarchitecture at both cortical and trabecular level (Soldati, Rossi, et al. 2021).

The fracture risk assessment up to now is based as a function of bone mineral density (BMD) calculated in the clinics using dual energy X-ray absorptiometry (DXA). However, this qualitative parameter derived from a 2D projection of the bone solid phase is sensed to misclassification (up to 30%) (Nayak et al. 2015a; Humadi, Alhadithi, and Alkudiari 2010a). The misdiagnose of osteoporosis could have a double impact, first false positives receive mistreatments responsible to fragilize bone increasing the resistance at the expense of the ductility, moreover false negatives are left without important treatments responsible to reduce the occurrence of fragility fractures (Odén et al. 2015). These double effect is responsible to increase both the patient hospitalization and the mortality risk (Odén et al. 2015; Burge et al. 2007). Therefore an increase on the osteoporosis diagnose is of utmost importance since would increase the quality of life of 158 million individuals worldwide at high fracture risk which could benefit from an early diagnosis and would prevent fragility fractures to occur (Sözen, Özışık, and Başaran, n.d.; Marcellusi et al. 2020; 'Epidemiology of Osteoporosis and Fragility Fractures | International Osteoporosis Foundation' n.d.). One possible strategy could be to increase the knowledge of osteoporosis responsibilities on bones degradation which could be obtained by comparing healthy

and osteoporotic bones with a multiscale and multimodal approach. This approach should take into consideration not only the bone density and morphology but also investigating the changes related to osteoporosis at nano and molecular scale. The overall collected information, could provide new insights of the osteoporosis effect on bones which could be eventually be added in the clinics, providing new investigative tools which would help clinicians in decision taking.

Calcium is a crucial element for bones and is an integral component of HA crystals of the extracellular mineralized matrix. Information related to both formation and evolution of the extracellular Ca-phosphates and polyphosphates compounds in the process of HA formation and deposition are still incomplete (Molino et al. 2019; Sindhupakorn and Kidkhunthod 2021). Moreover, bones are characterized by different types of HA crystals mainly due to the carbonate content whose range is about 2–8 wt.%1 (Landi et al. 2003b; F. Z. Ren and Leng 2011), in addition it has been previously showed the age dependency of HA types (Rey 1991). Within the HA structure, the carbonate group can substitute both the hydroxyl and the phosphate ions, giving rise to the A or B-type carbonation, respectively. A higher value of the A/B ratio has been observed in old tissues as compared to young ones (Landi et al. 2003b) thereby underlying the paramount importance of HA for our understanding of the BM process. One of the most promising approach in studying the BM process is the Synchrotron-based X-ray absorption near edge structure (XANES) spectroscopy at the HA central atom, the Calcium K-edge, which has been widely used to characterize apatite calcium phosphates or calcium carbonates (Politi et al. 2006; Monico et al. 2020; Hesse et al. 2016). The K-edge spectroscopy is a spectroscopic technique used to study the electronic structures of transition metal atoms and complexes. This method measures X-ray absorption caused by the excitation of a 1*s* electron to valence bound states localized on the metal, which creates a characteristic absorption peak called the K-edge. It has been suggested that this technique might be beneficial to gain further insights into tissue maturation processes and to assess the impact of bone diseases at mineral-level (Sindhupakorn and Kidkhunthod 2021; Zhai et al. 2019a). Clarifying the BM mechanism is necessary for a deeper understanding of the re-generation as well as the de-generation of bone, despite the fact that the obtainable information would be partial since whole bones are acquirable due to their volume.

The aim of this study is to qualitatively characterize the HA crystallinity in the trabecular network of the proximal femur taking advantage of the X-ray absorption spectroscopy of the Ca K-edges at micrometric scale and to evaluate the bone characteristics that better predict the fracture risk assessment due to osteoporosis. To evaluate the mechanism of osteoporotic fracture, numerous studies with different research methods have been carried out. Most of these studies were based on histomorphological and mechanical testing of bone specimens (D. Guenoun et al.

2020a; Nazarian et al. 2007; Katz and Yosibash 2020) whereas very few studies have assayed the molecular levels (Monico et al. 2020; Hesse et al. 2016; Taylor and Donnelly 2020). In this study, whole femurs have been initially scanned using industrial computed tomography (μCT) at resolution between 51 and 62 μm^3 to discriminate areas with high and low bone densities in three different proximal femur regions (femoral head, femoral neck and great trochanter) chosen to fully characterize the proximal femurs. Then, trabecular subregions (disks of 10 mm of diameter and 2 mm of thickness) have been extracted and rescanned using μCT at 25 μm^3 to fully characterize the subsamples morphology. Finally, the Calcium K-edge of these trabecular subregions have been investigated at CLÆSS beamline at ALBA synchrotron (Barcelona, Spain) to assess HA crystallinity properties. In this study, the corresponding results have been compared using an inter-gender approach (one healthy male vs. one healthy female) and an intra-gender approach (one healthy female vs. three osteoporotic females) focusing on the clinical state of the bone.

2. Materials and Methods

2.1. Sample Collection

All procedures were done in accordance with the ethical standards of the responsible committee on human experimentation of the thanatopraxy laboratory, University School of Medicine, Hôpital de la Timone, Marseille, France that provided the bodies coming from donation and in accordance with the Helsinki Declaration of 1975, as revised in 2000.

Table 7. 1: Description of the samples.

	Gender	**Age (y)**	**DXA-BMD (g/cm²)**	
			FN	**WPF**
Sample01	Male	80	0.796	0.884*
Sample02	Female	89	0.416	0.508
Sample03	Female	83	0.608	0.651
Sample04	Female	83	0.562	0.701
Sample05	Female	82	0.784	0.831*

FN: femoral neck; WPF: whole proximal femur; "*" refers to healthy bones accordingly to DXA-BMD analysis.

Five cadaveric human femurs from five different donors (from Sample01 to Sample05) have been collected thanks to the collaboration with the pathological department of LaTimone medical school, AixMarseille University. The whole femurs have been scanned using conventional DXA and the main sample characteristics have been reported in Table 7.1. They were then cut using a bandsaw along the axial direction right in the diaphysis (approximately 20-22 cm section proximal to the femur head) and then the specimens were stored at -25°C.

Sample Preparation for XAS

µCT images of whole proximal femurs have been acquired using Rx-Solution EasyTom XL ULTRA microtomograph ('RX Solutions SAS, 3D X-Ray Tomography Systems.', n.d.) with an isovolumetric voxel size between 51 and 62 µm, chosen depending on the femur anatomical sites, using a previously validated protocol (Soldati, Vicente, et al. 2021), able to fully resolve the proximal femur inner morphology. Based on µCT images, small specimens (10 mm of diameter and 2 mm of thickness) used in this translational study, were individuated and extracted using the following strategy.

The sections containing significative structural information and hence where the osteoporosis could be more impacting were individuated in three different regions of the proximal femur, the great trochanter (GT), the femoral neck (FN) and the femoral head (FH). The whole proximal femurs were first cored in correspondence to the individuated relevant subregions using drill press equipped with a hollow tip with an internal diameter of 10 mm and under constant water irrigation. Small disks of 2 mm width were then selected and extracted cutting the trabecular core using a saw equipped with a diamond disk (Fig. 7.1). The samples were conserved at low temperature (<-25°C) until use.

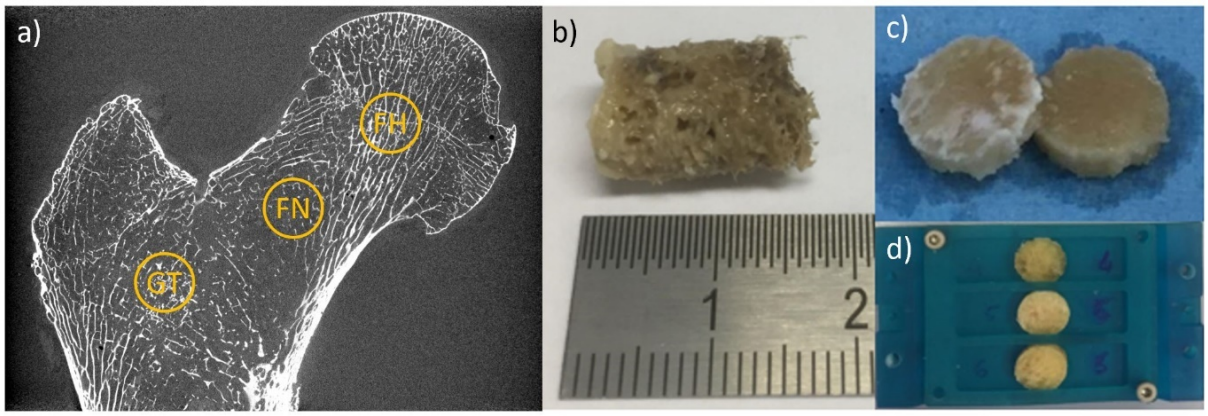

Figure 7. 1: Small sample extraction and conservation. a) core drilled from the proximal femur, b) extracted trabecular disks, c) and d) trabecular disks stored in sample holder for further experiments.

2.2. Biomechanical Fracture Tests

Before subregions extraction, each proximal femur was loaded to failure (i.e. fracture) in an universal testing machine (Instron 5566, Instron, Canton, MA, USA). Each femur was placed within the loading apparatus so as to simulate a sideways fall on the greater trochanter (Manske et al. 2009; Eckstein et al. 2003). Each specimens was first fixed in resin (Epoxy Axon F23) at 15° internal rotation and then the femoral head were oriented at 10° adduction within the testing machine. The load was applied to the greater trochanter (displacement rate 10 mm/min) through a pad, which simulated a soft tissue cover, and the femoral head was covered with resin to ensure force distribution over a larger surface area. Fractures were visually classified according to clinical criteria (femoral neck, intertrochanteric, subtrochanteric, or isolated greater trochanteric fractures) (D. Guenoun et al. 2020a). Moreover, the yielding strength (σSN) in MPa was individuated at the end of the linear stroke of the stress-strain curve, the failure load (in N) was defined as the first local maximum (F_{MAX}) after which the load declined by more than 10%, while the fracture load (in MPa) was defined as the first local maximum after which the load declined by more than 10% divided by the bone surface at the fracture site (σROTT) (Le Corroller et al. 2012). The area under the stress-strain curve (Work) have been calculated to assess the energy (in J) accommodated by the bone tissue until fracture.

2.3. µCT Imaging and Analysis

µCT images of all the proximal femurs subsamples were acquired using Rx-Solution EasyTom XL ULTRA microtomograph ('RX Solutions SAS, 3D X-Ray Tomography Systems.', n.d.), with a 150 kV X-Ray Hamamatsu Tube allowing a focus spot size of 5 µm. All the subsamples were acquired at once using an isovolumetric voxel size 25 μm^3 chosen to fully resolve the trabecular morphology of the extracted samples. The other parameters were, 219 mA current, 129 V voltage, 6 images/s and 1440 projections over 360 degrees of rotation. Each projection was obtained from the average of 10 images to increase the signal to noise ratio. The acquisition lasted approximatively 30 minutes.

The images of the proximal femur subsamples have been binarized and analyzed independently. The binarizations were straightforward as the contrast was high and the voxel size was smaller than the trabecular thickness. Based on binarized ROIs it has been computed the bone volume fraction (BVF), which refers to the ratio between the bone volume and the total volume, the trabecular thickness (Tb.Th) and spacing (Tb.Sp), which provide information about the trabecular diameters and distance between consecutive trabeculae respectively. Tb.Th and Tb.Sp have been extrapolated using the distance transform map from which it has been derived the aperture map

using the software iMorph (iMorph_v2.0.0, AixMarseille University, Marseille, France) (E. Brun, Ferrero, and Vicente 2017a; E. Brun et al., n.d.). The aperture map provides for every pixel of the bone the diameter of the maximal disk totally enclosed in the bone and containing this voxel. Tb.Th was then deduced from the mean values of the aperture map distribution. Tb.Sp was quantified from similar computations in the marrow phase of the trabecular ROI. The aperture map has been previously used for the 3D morphological evaluation of porous materials in different fields (E. Brun, Ferrero, and Vicente 2017a; Burghardt, Link, and Majumdar 2011b; Soldati, Escoffier, et al. 2020) and provides local information with a sub-voxel precision (E. Brun, Ferrero, and Vicente 2017a; Johansson et al. 2019). The bone morphology of all the different subsamples have been analyzed and each group of regions have been compared alone (e.g. healthy GT morphology vs. osteoporotic GT morphology). First, it has been investigated the differences due to the inter-gender variability by comparing the healthy male to the healthy female in the three different proximal femur regions, then the difference between osteoporotic and control has been investigated comparing the healthy female to osteoporotic female group.

2.4. X-ray Absorption Spectroscopy

The small samples extracted in the three regions of the proximal femur (great trochanter, femoral neck and femoral head) from Sample01 to Sample05 were simply kept stored at -25°C before and after acquisition. The acquisition has been performed keeping the samples in an under vacuum (10^{-2} bar) liquid nitrogen cryostat (LN_2-cryo) environment at -80°C, which allows fully automatized X-ray absorption measurements in both transmission and fluorescence modes.

Calcium K-edge XAS measurements were collected in the fluorescence mode at the CLÆSS (Core Level Absorption & Emission Spectroscopies) beamline of the ALBA Synchrotron (Barcelona, Spain) using a single channel silicon drift detector. The synchrotron radiation of a wiggler source was monochromatized by means of a Si(111) double crystal monochromator. The focus at the sample position was 200 x 200 µm. The calibration of the monochromator was performed by measuring the spectrum of the Calcium Phosphate $Ca_3(PO_4)_2$ pellet measured in transmission mode. The absolute energy reproducibility of the measured spectra was ±0.1 eV. The incoming energy resolution around the Calcium K-edge can be estimated below 0.4 eV. The incoming and outcoming flux have been measured by two customized ionization chambers to have respectively the ~10 and 75% of absorbance. The spectra, between 45 to 55 per sample depending on the sample size, have been selected and acquired following a grid with a step size of 1.25mm, were measured in fluorescence using a 6-channel

silicon drift detector (SDD) (Xspress'3 from Quantum Detectors). Energy scans were made from 3950 to 4460 eV using an integration time of 0.5 s per point.

Firstly, the raw spectra were imported in an opensource software, Athena a part of Demeter (v0.9.26)(Ravel and Newville 2005), which is a comprehensive opensource system for processing and analyzing X-ray Absorption Spectroscopy data. Athena's main function is to import and process XAS data which can be summed in three main steps: (i) import raw data and convert it to μ(E), (ii) normalize the data to make the measurements independent from sample details and detector setup, (iii) determine the background function and subtract it from the data in order to generate the EXAFS fine-structure function X(k). From each spectrum it has been possible to extrapolate four features: (i) the pre-peak area (I_G) providing a direct information on what is next to the Calcium element, (ii) the R distance representing the mean distance between the Calcium and its closest atoms, the Oxygens, (iii) the DebyeWaller (ss2) which represents the structure order of the Calcium providing information on the hydroxyapatite crystallinity, and (iv) the MapRatio which is the ratio between the Calcium and the Phosphorous present in the analyzed samples. The features have been calculated on the basis of kernel density estimation (KDE), which in statics is the non-parametric way to estimate the probability density function of a variable and it is a fundamental data smoothing problem where interferences about the population are made, based on a finite data sample. Therefore, we were able to provide a map for each of the described feature. The analysis of spectra variances (between 4000 and 4200 eV) (Figure 7.2) have been investigated to assess differences associated to gender, age or bone health state and is calculated as

$$\sigma^2 = \frac{\sum_N (X_i - \mu)^2}{N}$$

Where X_i is area of the spectrum between 4000 and 4200 eV, μ is the average spectra area and N is the total number of spectra acquired per each subregion.

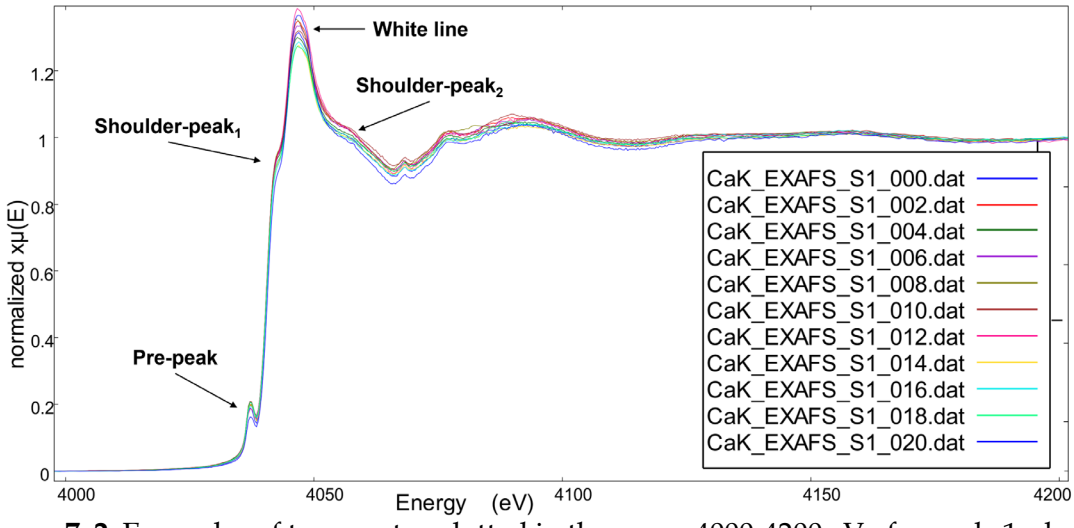

Figure 7. 2: Examples of ten spectra plotted in the range 4000-4200 eV of sample 1, showing the pre-peak, the shoulder before (1) and after (2) the principal peak or while line.

Moreover, the derived parameters have been compared based on gender (healthy female vs. healthy female) and clinical state (healthy vs. osteoporotic) using the female group alone (S02 to S05). Finally, the differences between samples spectra have been performed based on the Z-scores calculated based on the following formula:

$$Z = \frac{Y - \mu}{\sigma}$$

Where Y are the parameters occurrences, and μ and σ are the mean and the standard deviation of the parameter calculated in the reference, which in our case is represented by the Sample05 (healthy, female 82 yrs).

2.5. Statistical Analysis

To identify the variables that explain most of the variation in bone features, different Principal Component Analysis (PCA) were conducted by using the open-source software R (R Core Team, 2020) and the packages "FactoMineR" (Lê, Josse, and Husson 2008) and "factoextra" (Kassambara and Mundt 2020). PERMANOVA was then calculated with the package "vegan" (Oksanen et al. 2020) to examine whether the factors "bone health quality" and "bone region" influenced the characteristics of the bones. Moreover, to determine whether the samples could be grouped into healthy and osteoporotic, a k-means clustering allowing for two groups was calculated using the *kmeans* function.

The PCAs have been conducted using features from the same categories (biomechanical, morphological and spectroscopic) alone and by combining different categories. This multiple analysis would allow a complete overview of the usefulness of the extrapolated parameters for the fracture risk assessment considering that biomechanical parameters provide the real fracture information of the tested bones.

3. Results

3.1. Biomechanical Fracture Tests

Biomechanical fracture tests were performed to assess the real health state of each femur. The obtained results would provide the unquestionable insights of the bone resistance to fracture. We observed three femoral neck (Sample01, Sample03 and Sample04) and two intertrochanteric (Sample02 and Sample05) fractures. The mean failure load was equal to 1303.6 N (SD, 607.6 N) over a mean femoral neck cross-section of 966.8 mm² (SD, 246.9 mm²) computed between the femoral head and the

great trochanter and delimited by the cortical shell of high-resolution μCT images which were oriented perpendicularly to the neck axes. The resulting mean fracture strain was 1.38 MPa (SD, 0.61 MPa) with a mean work equal to 0.021 J (SD, 0.009 J).

The linear regression between DXA derived-BMD at the femoral neck region and the yielding strain reported in Figure 7.3, showed a moderate correlation (R^2 = 0.50). Lower correlation were assessed between DXA derived-BMD and both work (R^2 = 0.28) and fracture strain (R^2 = 0.40). Interestingly, the correlation coefficients increased using DXA derived-BMD and the biomechanical parameters derived only from the female donors respectively to R^2 = 0.90 for yielding strain, R^2 = 0.88 for fracture strain but not for Work R^2 = 0.01.

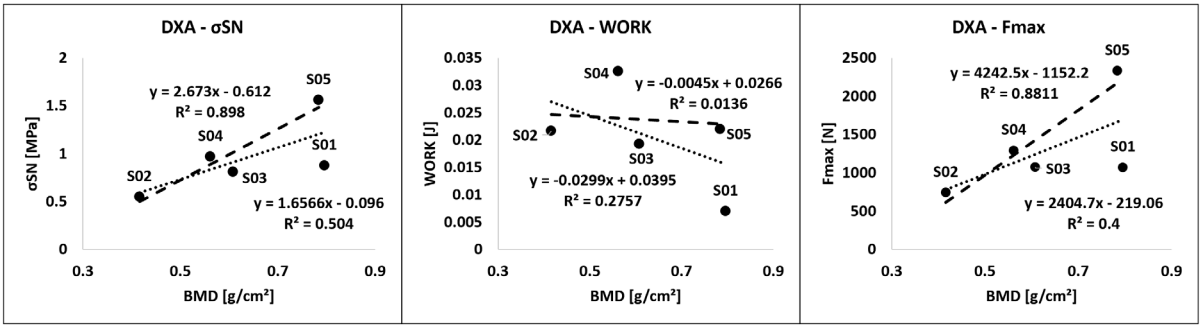

Figure 7. 3: Linear regression of DXA derive bone mineral density (BMD) and yielding strain (σSN), Work and fracture strain (Fmax) of all the samples (S) together (black dotted line) and of the female subgroup alone (S02-S05) (dashed line).

3.2. Bone Morphology

The bone morphology analysis between the two age-matched healthy specimens (male vs. female) has been conducted for comparative purposes. Differences in the morphological parameters have been compared region by region between the healthy female and the healthy male. The BVF and Tb.Th showed higher differences (+16% and +7% respectively) in the FH, the Tb.N and Tb.Sp showed higher differences (+12% and -10% respectively) in the FN. Interestingly, differences between bone morphology in the male and female specimens were more accentuated in both FH and FN but not in the GT where the derived differences were +3%, +1%, -2% and +2% respectively for BVF, Tb.Th, Tb.Sp and Tb.N.

The mean and SD of each morphological characteristic have been derived using the three subregions together. The healthy male specimens compared to the healthy female showed higher BVF and Tb.N (0.21±0.09 vs. 0.18±0.08 and 1.53±0.42 vs. 1.42±0.40 respectively for the BVF and Tb.N of the healthy male and female) similar Tb.Th (0.13±0.02 vs. 0.13±0.02 respectively for the male and female) and lower Tb.Sp (0.62±0.13 vs. 0.66±0.15 respectively for the healthy male and female).

Moreover, bone morphological differences between the healthy and the osteoporotic samples have been investigated using a gender specific approach,

focusing on the female samples alone (S02 to S05), and differences have been presented for each investigated proximal femur region. In the femoral head the healthy sample presented higher BVF (26%) and Tb.N (+36%), similar Tb.Th (-7%), lower Tb.Sp (-35%) compared to the osteoporotic (Figure 7.4). The GT showed similar results reporting higher BVF (+20%) and Tb.N (+23%), similar Tb.Th (-1%) and lower Tb.Sp (-22%). Finally, in the FN the healthy sample provided greater BVF (+19%) while similar parameters were assessed for both Tb.Th (+6%), Tb.Sp (-7%) and Tb.N (+7%).

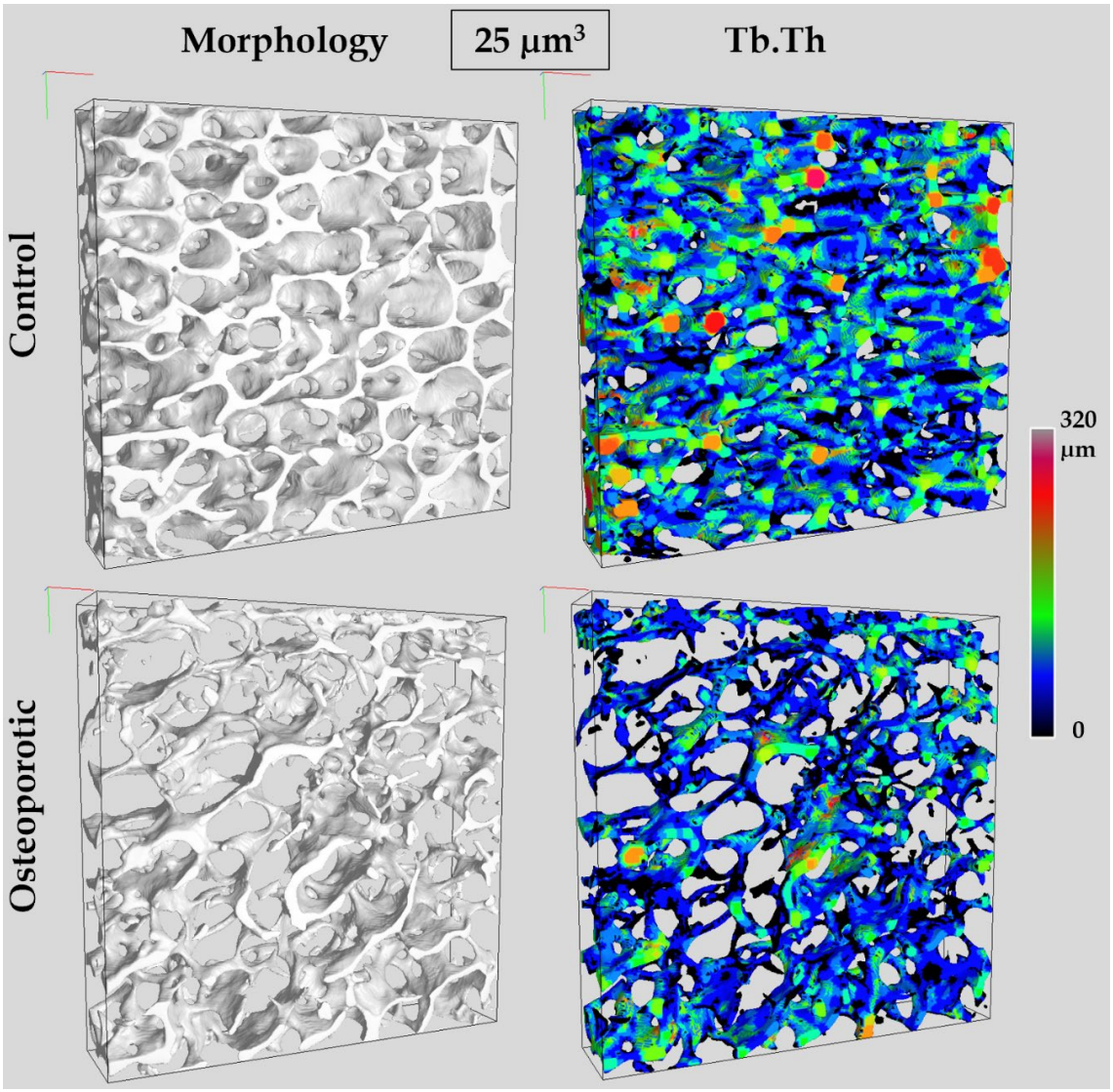

Figure 7. 4: Trabecular network morphology (left) and thickness (Tb.Th) (right) of respectively the female healthy (S05) (first row) and osteoporotic female (S04) (second row) proximal femur head.

The mean and SD of each morphological characteristic have been derived using the three subregions together and comparing the healthy female to the osteoporotic group. The healthy female compared to the osteoporotic female group showed higher BVF and Tb.N (0.18±0.08 vs. 0.14±0.06 and 1.46±0.46 vs. 1.09±0.22 respectively for the BVF and Tb.N of the healthy female and the osteoporotic group) similar Tb.Th (0.13±0.02

vs. 0.13±0.04 respectively for the healthy female and the osteoporotic group) and lower Tb.Sp (0.66±0.15 vs. 0.79±0.10 respectively for the healthy female and the osteoporotic group). However, performing the Student T-test between the healthy female and the osteoporotic group together and considering all the subregions together showed that differences were statistically significant for all the morphological parameters (BVF and Tb.Sp with a p-val<0.01 in both cases, and Tb.N with a p-val<0.05), but the Tb.Th (p-val>0.05).

The linear regression assessed between DXA derived-BMD in the FN and the corresponding morphological parameters derived in the same proximal femur region showed poor correlation for all the morphological characteristics (R^2 = 0.39, 0.18, 0.03 and 0.02 respectively for BVF Tb.Th, Tb.Sp and Tb.N) (Figure 7.5). Poor correlations were also assessed between BVF and Tb.Sp derived in the FN and the Work (R^2 respectively equal to 0.07 and 0.13) while the correlation between Tb.Th and Tb.N derived in the same region and Work showed moderate correlation (R^2 = 0.54 and 0.59 respectively for Tb.Th and Tb.N).

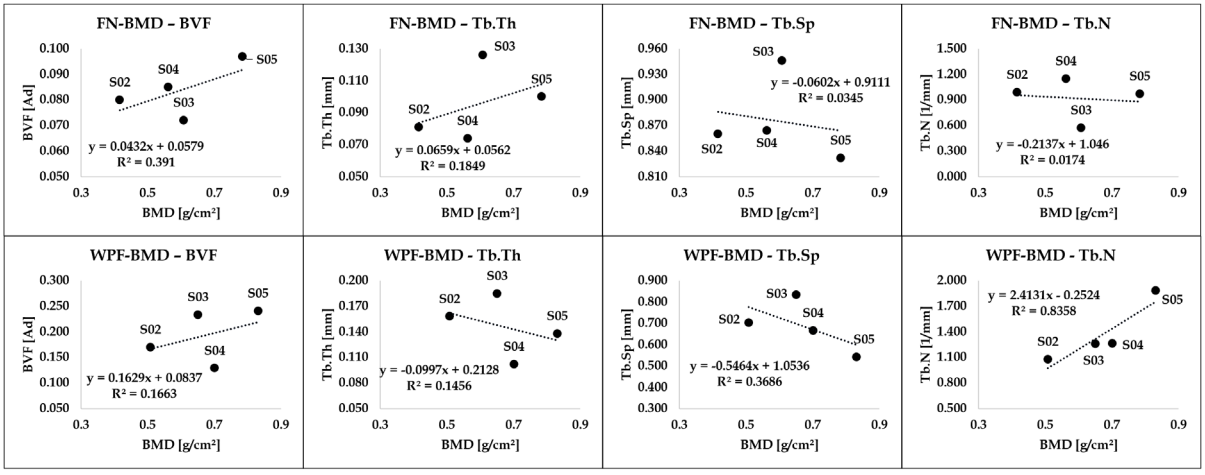

Figure 7. 5: Linear regression showing the coefficient of determination (R^2) between DXA derive-BMD in the femoral neck (FN) and morphological parameters derived in the FN (first row), and between DXA derive-BMD in the whole proximal femur (WPF) and morphological parameters derived in the femoral head (FH) (second row). S: Sample; BMD: bone mineral density; BVF: bone volume fraction; Tb.Th: trabecular thickness; Tb.Sp: trabecular Spacing; Tb.N: trabecular number; Ad: a dimensional.

Different results were assessed performing the linear regression between DXA derived-BMD in the whole proximal femur and the morphological parameters extracted from the FH. In particular, lower correlation was assessed for the BVF (R^2 = 0.17) and Tb.Th (R^2 = 0.15), while higher correlation was assessed between Tb.Sp and Tb.N (R^2 = 0.37 and 0.84 respectively). Regarding the linear regression between morphological parameters in the FH and the Work of female group, BVF and Tb.Th showed moderate to good correlation showing respectively a R^2 = 0.68 and 0.85.

However, slightly poor correlations were assessed for Tb.Sp and Tb.N R^2 = 0.08 and 0.01 respectively.

3.3. Calcium K-edge Spectroscopy

In Figure 7.6 and Table 7.2 are presented the Calcium concentration map and the four spectroscopic characteristics extracted from each sample. No differences (<1%) in the case of R parameter have been assessed between both clinical state (healthy vs. osteoporotic) and gender (healthy female vs. healthy male), while higher differences have been assessed for the other characteristics. In particular, small pre-peak intensity differences have been assessed between the healthy and the osteoporotic females in the FN (between -6% for S04 and +2% for S02) while higher differences were assessed in both FH (up to +19% for S04) and GT (up to -12% in the S03), moreover the healthy male had in general greater differences (11% for the FH, 16% for FN and -13% for the GT). MapRatio and ss2 reported greater differences comparing both healthy and osteoporotic females (between -36% and +52% for MapRatio respectively obtained in the S02 FH and FN, and between -48% and +84% for the ss2 respectively obtained in the S02 GT and S04 FH).

Table 7. 2: Spectroscopic results of each sample (S) and samples subregions.

ID	I_G	R	ss2	MapRatio
	mean±SD	**mean±SD**	**(*10^{-3}) mean±SD**	**mean±SD**
S01_FH	0.138±0.017	2.432±0.012	7.56±2.66	25.05±2.47
S01_FN	0.148±0.024	2.434±0.029	9.46±3.42	21.12±2.37
S01_GT	0.126±0.017	2.427±0.013	5.93±2.40	26.86±3.90
S02_FH	0.130±0.018	2.429±0.017	6.63±2.76	24.39±3.06
S02_FN	0.131±0.019	2.425±0.011	6.53±2.94	25.07±3.05
S02_GT	0.130±0.015	2.415±0.026	4.38±1.99	24.64±3.88
S03_FH	0.129±0.015	2.428±0.011	5.90±2.19	43.23±8.89
S03_FN	0.123±0.019	2.427±0.020	5.13±2.57	40.23±3.71
S03_GT	0.126±0.020	2.430±0.016	5.76±2.44	26.78±3.13
S04_FH	0.149±0.014	2.422±0.008	7.97±3.08	24.63±2.80
S04_FN	0.120±0.014	2.431±0.027	4.97±1.74	29.10±2.92
S04_GT	0.135±0.019	2.432±0.013	7.74±2.76	24.42±2.55
S05_FH	0.125±0.008	2.429±0.011	4.33±1.08	37.93±3.68
S05_FN	0.128±0.017	2.419±0.012	5.04±2.77	26.55±3.23
S05_GT	0.144±0.022	2.427±0.008	8.37±3.71	23.43±2.14

Data are presented as mean ± SD. FH: femoral head; FN: femoral neck; GT: great trochanter; I_G: pre-peak intensity; R: distance between Calcium and Oxygens; ss2: DebeyWaller; MapRatio: ratio between Calcium and Phosphorous.

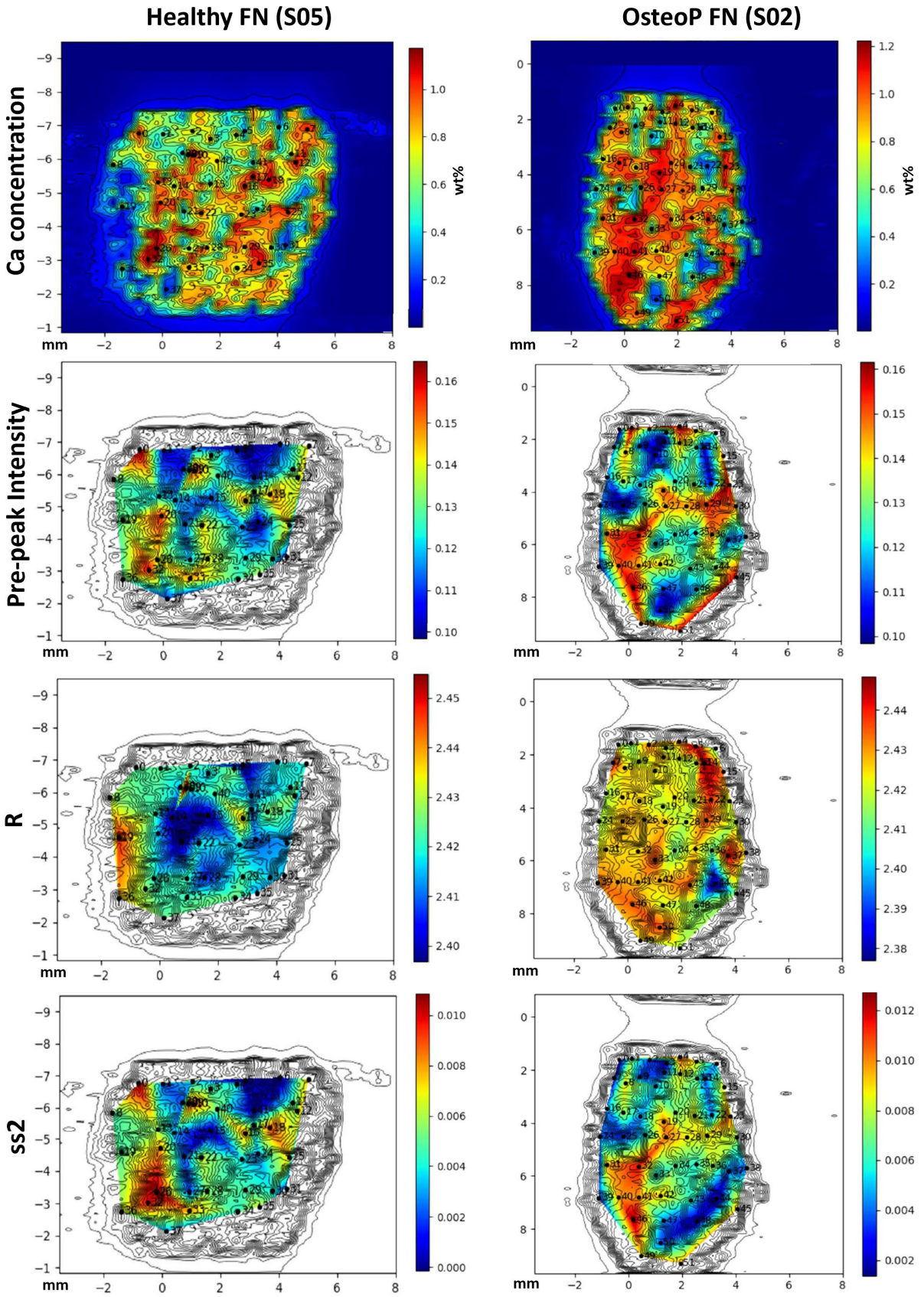
Healthy FN (S05)
OsteoP FN (S02)
Ca concentration
Pre-peak Intensity
R
ss2
wt%
mm

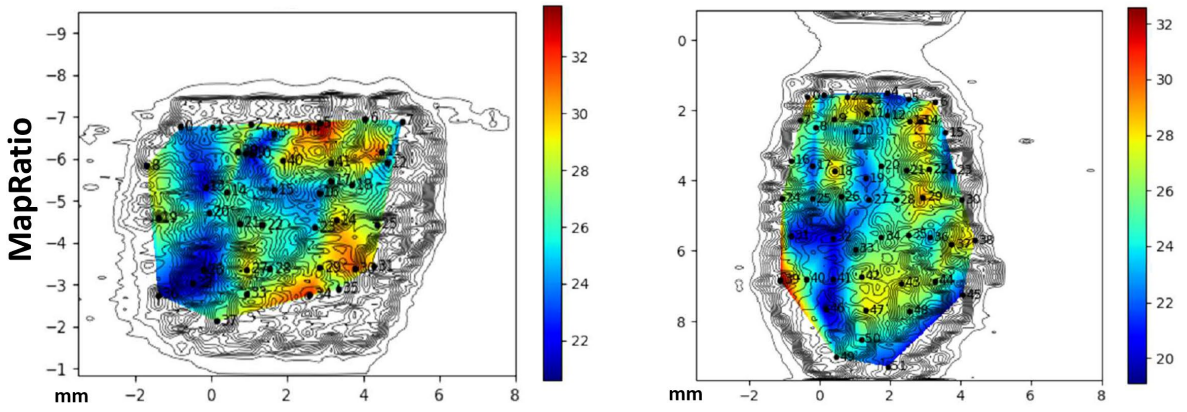

Figure 7. 6: X-ray absorption spectroscopy investigation of healthy (S5) and osteoporotic (OsteoP, S2) femoral neck (FN) comparing all the derived characteristics. Calcium concentration (first row); Pre-peak intensity (I_G) (second row); the distance, R, between Calcium and Oxygens (third line); the Calcium structure order descripted by the ss2 (forth row); and the MapRatio, which expresses the Ca/P ratio (fifth row). Calcium concentration is expressed ad weight per cent (wt%).

The variance of the spectra is calculated between 4000 and 4200 eV and has been assessed to investigate the variability of the spectra with respect to the average in the same subregion and between both different subregions and different samples (Figure 7.7). The results showed great variability between different spectra from the same subregion. Moreover, small differences were assessed comparing the spectra variance between healthy and osteoporotic samples, therefore the variability of spectra seemed more biological, i.e. depending by natural differences between different subjects, than linked to the bone health state.

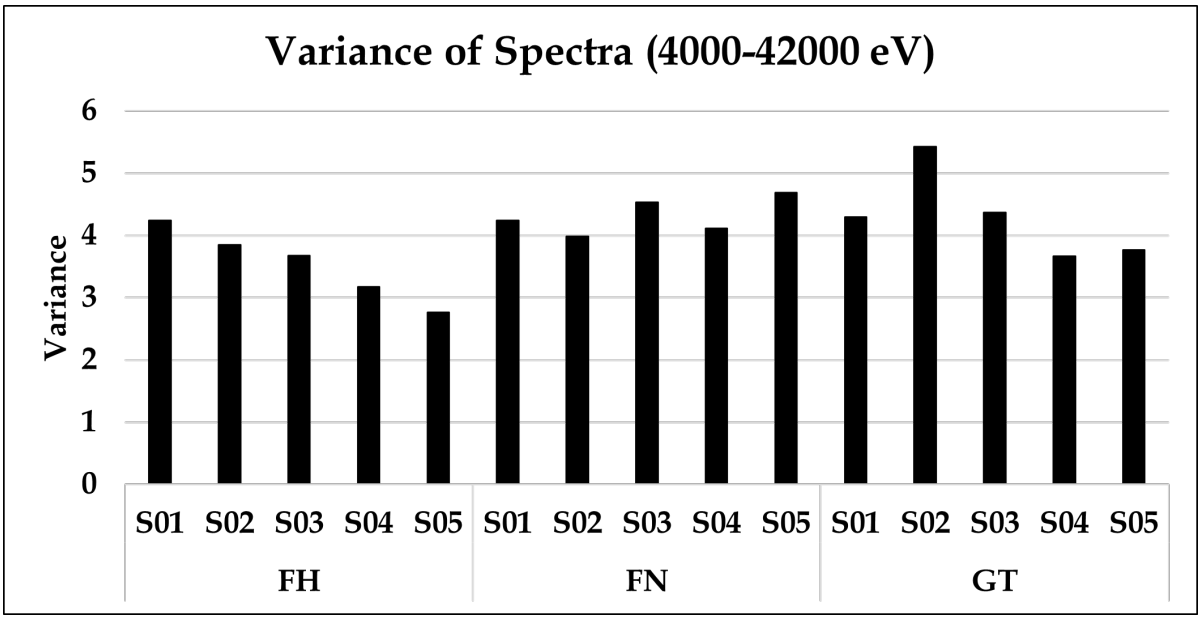

Figure 7. 7: (first row) Variance of the spectra calculated between 4000 and 4200 eV of each Sample (S) and subregion. FH: femoral head, FN: femoral neck, and GT: great trochanter.

The Z-scores, reported in Figure 7.8, has been calculated for each sample compared to the reference provided by the S05 with respect of the three investigated proximal femur regions and have been used to assess differences in the extrapolated features between osteoporotic samples and control, and between female and male. The results showed that in the FH all the samples compared to the S05 reference showed higher I_G and ss2 and similar R, however while S01, S02 and S04 showed lower Map ratio, this was not the case for S03. In the FN the Z-scores from S03 and S04, which had very similar DXA derived-BMD, showed the same trend (lower I_G, greater R and Map ratio and similar ss2), however the trend was almost opposite to both the S02 (older female with the lowest DXA derived BMD) and S01 (healthy male) which instead reported greater I_G, ss2 and R, and lower Map ratio. Finally, in the GT all the samples showed lower I_G, ss2 and greater Map ratio, while greater R was assessed for S01, S03 and 0S4 but not for S02 in which R was lower. In general, these results suggest that in the FH osteoporotic bones had higher phosphorous concentration responsible to increase the remodeling activity and were forming more ordered HA crystals (higher ss2). Opposite to FH, the GT showed a reduced bone remodeling and more disordered HA crystals. Finally, in the FN no clear trend was visible suggesting no differences neither in the HA crystals nor the bone remodeling activity.

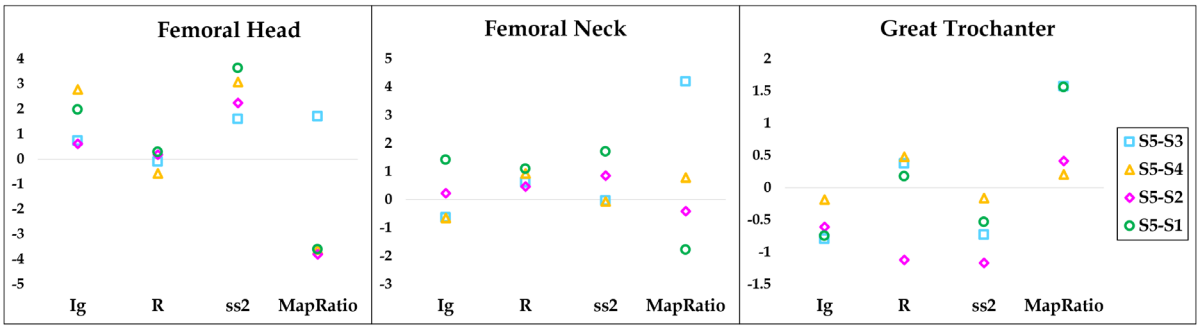

Figure 7. 8: Z-scores calculated for each XAS characteristic and subregion for all the investigated Samples (S) with respect to the healthy female (S05). I_G: pre-peak intensity; R: distance between Calcium and Oxygens; ss2: Calcium structure order; and MapRatio: ratio between Calcium and Phosphorous.

3.4. Bone Fracture Predictivity Risk Assessment

The PCA has been performed to assess the usefulness of each group of investigated parameters (biomechanical, morphological and spectroscopic) in the prediction of the proximal femur fracture risk assessment.

To interpret the PCA graphs, it is necessary to investigate and qualitative assess the separation between the healthy samples (light and dark green respectively corresponding to the healthy male S01 and female S05) and the osteoporotic group (S02, S03 and S04 respectively presented in bordeaux, red and orange). However, as will be presented further in the text, a clear separation between healthy and osteoporotic subjects never occurred since the healthy FN subregions seemed to systematically migrate towards the points representing the osteoporotic subregions.

Multimodal analysis

Biomechanics/Morphology/XAS

First the PCA derived using all the groups of investigated parameters combined has been performed as an exploratory investigation of bone quality changes (Fig. 7.9). PC1, PC2 and PC3 respectively explained 31.7%, 24.0 and 18.3% of the data variability, with PC1 primarily composed by morphological and biomechanical parameters, PC2 composed by biomechanical parameters and PC3 composed by XAS parameters. Moreover, samples were separated according to their bone health quality (healthy vs. osteoporotic), which was further confirmed by PERMANOVA analysis ($p<0.05$). The k-means cluster came to an additional support where the only subregions not correctly classified were the healthy FN of both S01 and S05 classified as osteoporotic.

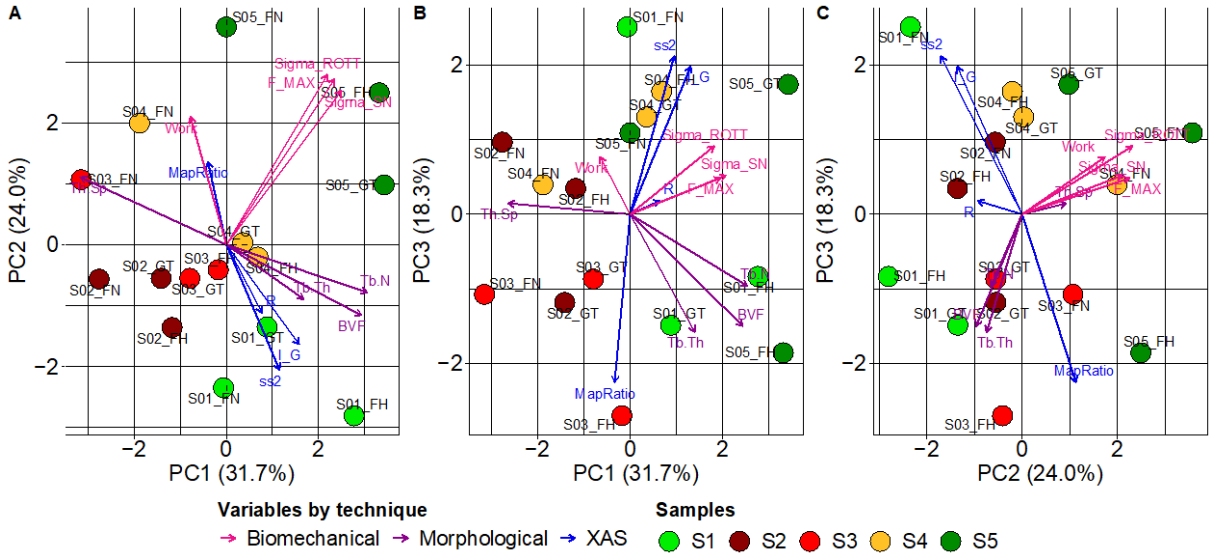

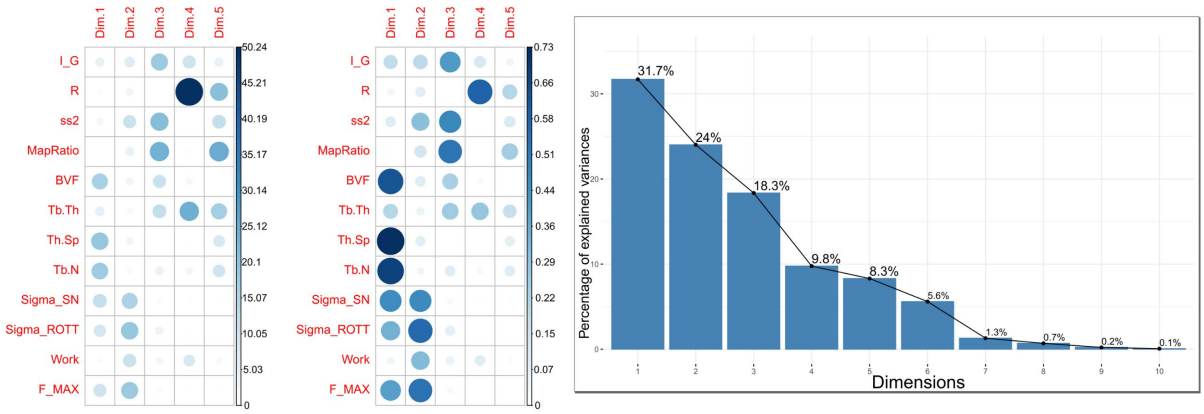

Figure 7. 9: Principal component analysis (PCA) of biomechanical, morphological and XAS parameters of control (S01 and S05) and osteoporotic (S02, S03 and S04) bone samples. Individuals are represented by dots and colored by sample. Variables are represented by arrows and colored by technique. The length of the arrows indicates the strength of the correlation of respective parameter with the samples. The graphs below show the contribution and the cos2 of each variable in each dimension as well as the percentage of variability contained in each dimension.

Biomechanics/Morphology/XAS*

The effect of XAS parameters on separating samples based on clinical condition has been further investigated. Additional PCAs have been performed using all the derived parameters (biomechanical, morphological and spectroscopic) and removing one XAS parameter at a time to explore whether the low data variability explanation was due to a specific XAS parameter. Interestingly, it has been observed that removing R the PCA seemed to provide a better separation rather than when removing the MapRatio, I_G or the ss2 (PC1-PC2-PC3 combined explained respectively 79.9% vs. 76.3% vs. 75.1% vs. 74% of the data variability).

Bi-Modal analysis

Biomechanics/Morphology

Then, each group of variables have been removed from the PCA one at a time to assess the usefulness of each investigative test in differentiating between osteoporotic and controls. The PCA using morphological and biomechanical parameters combined have been performed (Fig. 7.10). PC1, PC2 and PC3 respectively explained 45.8%, 33.1% and 11.3% of the data variability. No clear separation based on bone health quality was observed in PC1-PC2, while a better separation has been observed in the PC1-PC3 graph. PERMANOVA analysis corroborated the differences between osteoporotic and healthy subjects ($p<0.05$), but this hypothesis was not further supported by the k-means clustering. According to PCAs plots, the FN subregions remained the subregion of the proximal femur which migrates differently as compared to the other healthy subregions and positioning among the osteoporotic ones.

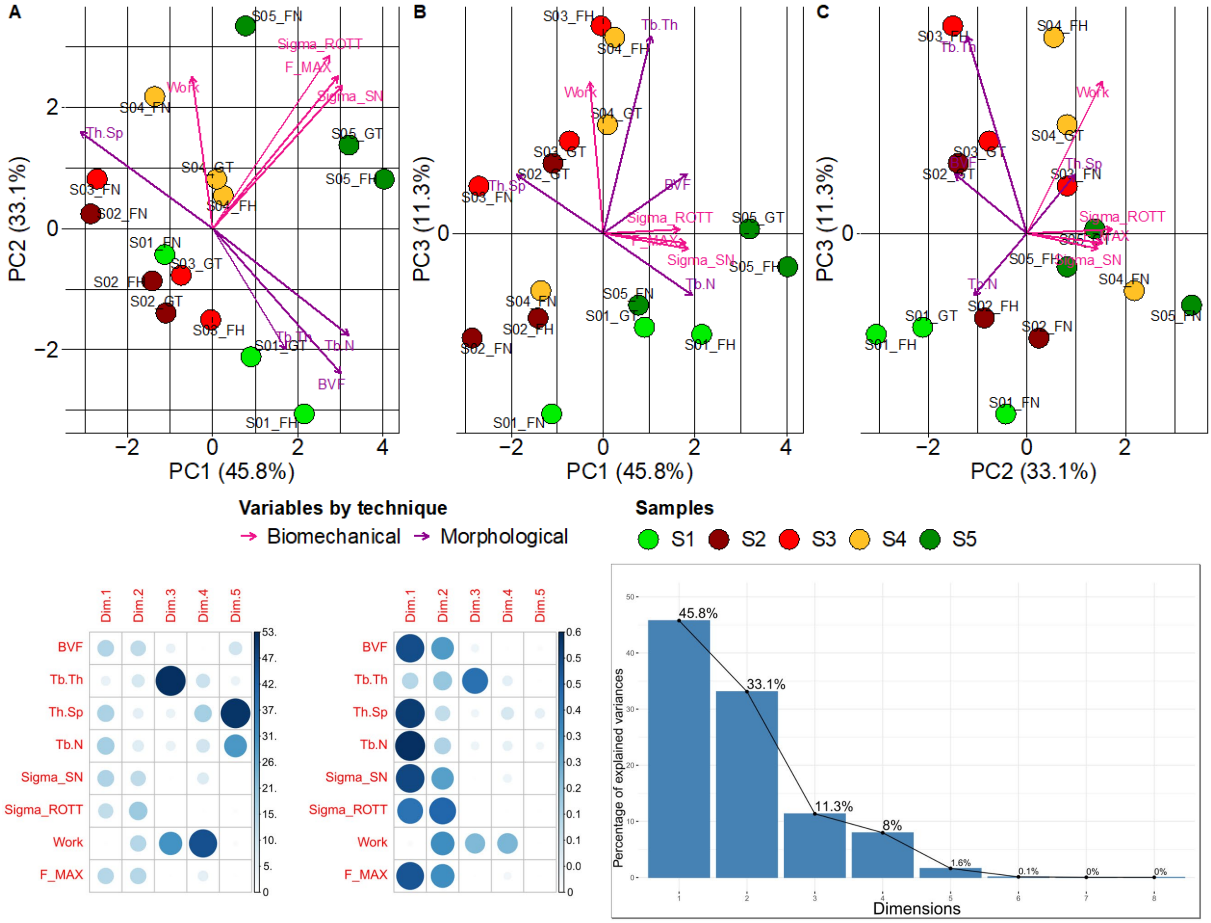

Figure 7. 10: Principal component analysis (PCA) of biomechanical and morphological parameters of control (S01 and S05) and osteoporotic (S02, S03 and S04) bone samples. Individuals are represented by dots and colored by sample. Variables are represented by arrows and colored by technique. The length of the arrows indicates the strength of the correlation of respective parameter with the samples. The graphs below show the contribution and the cos2 of each variable in each dimension as well as the percentage of variability contained in each dimension.

Biomechanics/XAS

Moreover, the PCA derived using biomechanical and XAS parameters showed that PC1, PC2 and PC3 combined explained 83.7% of the data variability, with PC1 primarily composed by biomechanical parameters, PC2 composed by I_G, ss2 and MapRatio and PC3 by R (Fig. 7.11). Although, the samples were significantly separated on bone health quality (PERMANOVA $p<0.05$) no clear separation was observed between proximal femur subregions in the principal component graphs.

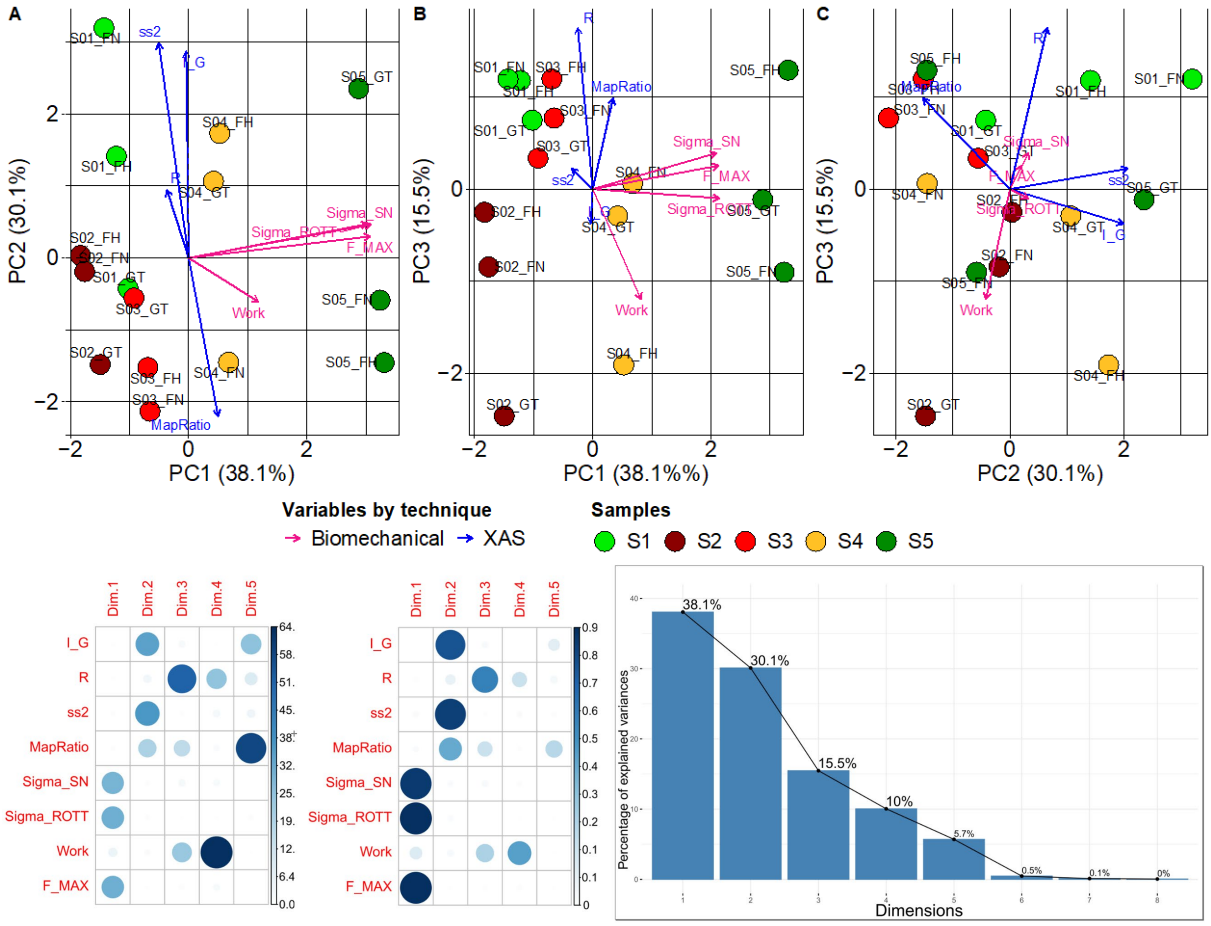

Figure 7. 11: Principal component analysis (PCA) of biomechanical and XAS parameters of control (S01 and S05) and osteoporotic (S02, S03 and S04) bone samples. Individuals are represented by dots and colored by sample. Variables are represented by arrows and colored by technique. The length of the arrows indicates the strength of the correlation of respective parameter with the samples. The graphs below show the contribution and the cos2 of each variable in each dimension as well as the percentage of variability contained in each dimension.

Morphology/XAS

The PCA has also been performed combining the morphological and the XAS parameters and the results are shown in Figure 7.12. PC1, PC2 and PC3 respectively explained 41.4, 28.1 and 14.0% of the variability of the samples with PC1 primarily composed by BVF, Tb.Sp and Tb.N, PC2 composed by MapRatio, ss2 and I_G, and PC3 by R. The PERMANOVA analysis was not significative, and the k-means clustering was not able to separate healthy subjects from those affected by osteoporosis. While no clear separation between healthy and osteoporotic groups was visible in the PC1-PC2-PC3 graphs, as previously observed also in this case all the FN subregions seemed migrating together with the osteoporotic subregions.

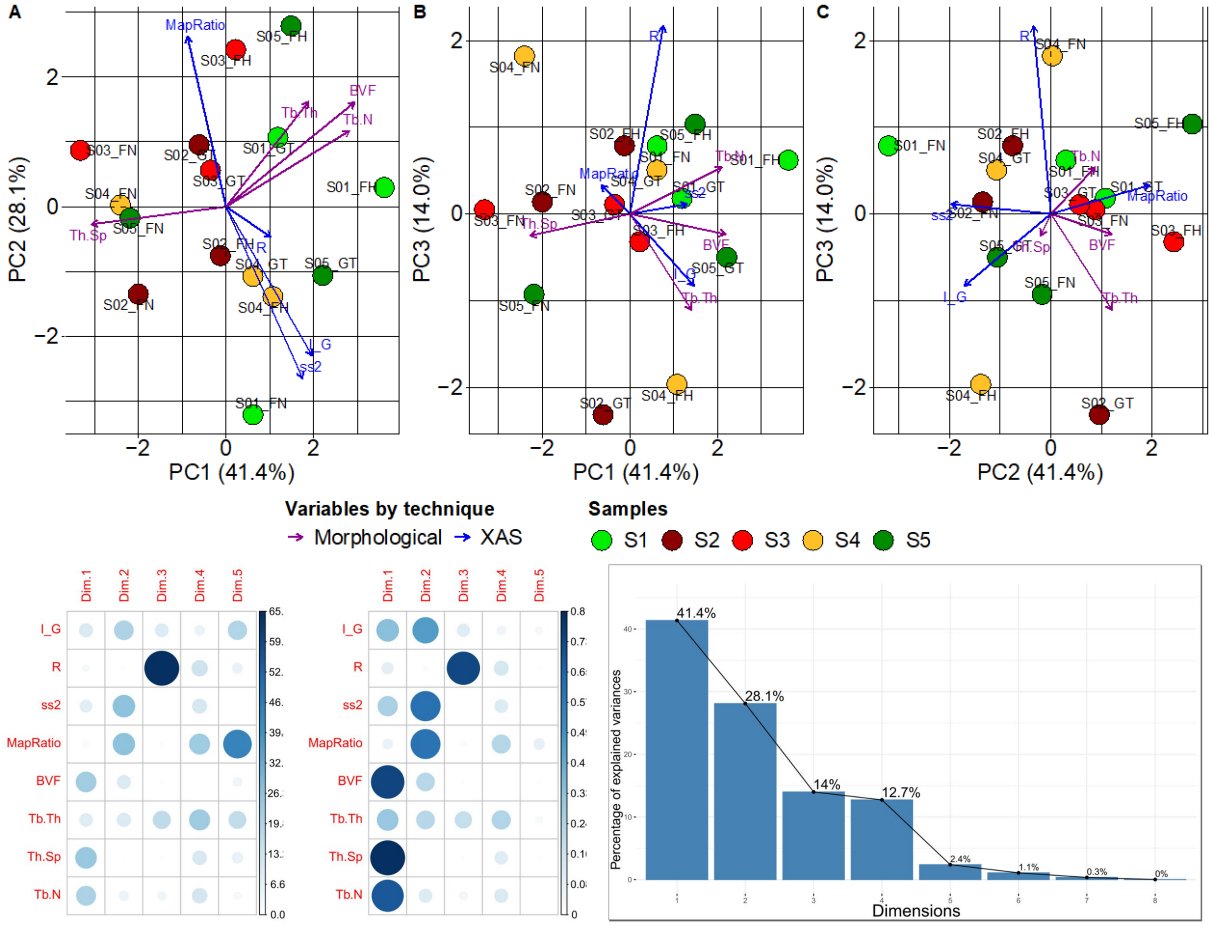

Figure 7. 12: Principal component analysis (PCA) of morphological and XAS parameters of control (S01 and S05) and osteoporotic (S02, S03 and S04) bone samples. Individuals are represented by dots and colored by sample. Variables are represented by arrows and colored by technique. The length of the arrows indicates the strength of the correlation of respective parameter with the samples. The graphs below show the contribution and the cos2 of each variable in each dimension as well as the percentage of variability contained in each dimension.

Mono-Modal analysis

Biomechanics

In addition, different PCAs using each group of variables alone have been performed to assess the ability of each group of techniques in separating bones based on the health condition. First, the PCA performed using only the biomechanical parameters showed the greatest explanation of variability, with PC1, PC2 and PC3 together explaining 99.9% of the variability of the data (Fig. 7.13). PC1 was mainly composed by σSN, σROTT and F_{MAX} and PC2 composed by Work. PERMANOVA showed a significant difference ($p<0.05$) between samples based on bone health condition, and a clear separation between healthy and osteoporotic subjects was also visible in both PC1-PC2 and PC2-PC3 graphs.

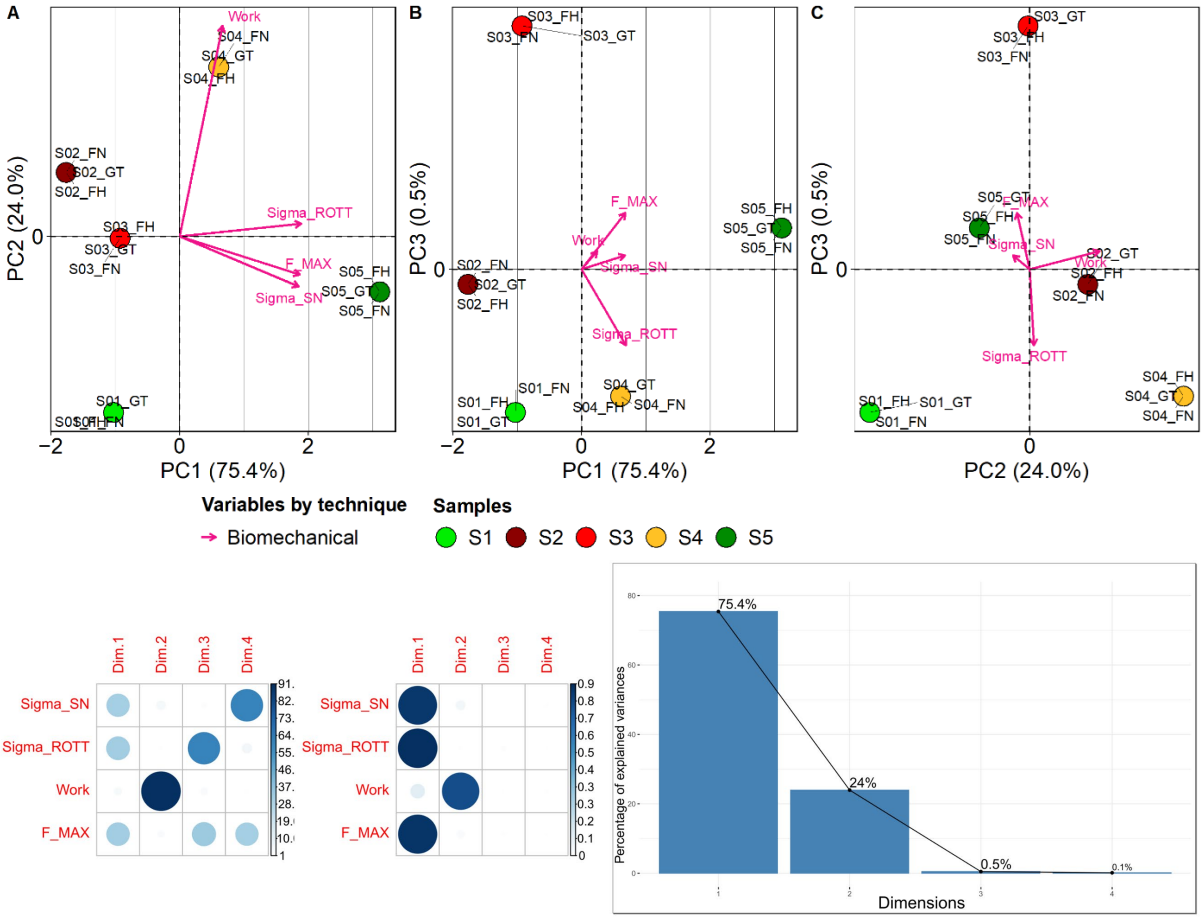

Figure 7. 13: Principal component analysis (PCA) of only biomechanical parameters of control (S01 and S05) and osteoporotic (S02, S03 and S04) bone samples. Individuals are represented by dots and colored by sample. Variables are represented by arrows and colored by technique. The length of the arrows indicates the strength of the correlation of respective parameter with the samples. The graphs below show the contribution and the cos2 of each variable in each dimension as well as the percentage of variability contained in each dimension.

Morphology

The same analysis has been performed using the morphological parameters derived from image analysis alone (Figure 7.14). In this case 96.5% of the data variability could be explained using PC1 and PC2 (75.4% for PC1 and 21.2% for PC2), with the whole set of morphological parameters having an influence on PC1, and PC2 being strongly influenced by Tb.Th. Healthy and osteoporotic samples were significantly separated according to PERMANOVA analysis ($p<0.05$), although no clear separation between healthy and osteoporotic subjects was possible using k-means clustering. Healthy subregions seemed to regroup (4/6 cases) along the positive PC1 axes, while in the PC1-PC2 plot all the FN subregions seemed to migrate on the negative part of the PC1 axes, and regrouping with the osteoporotic subregions.

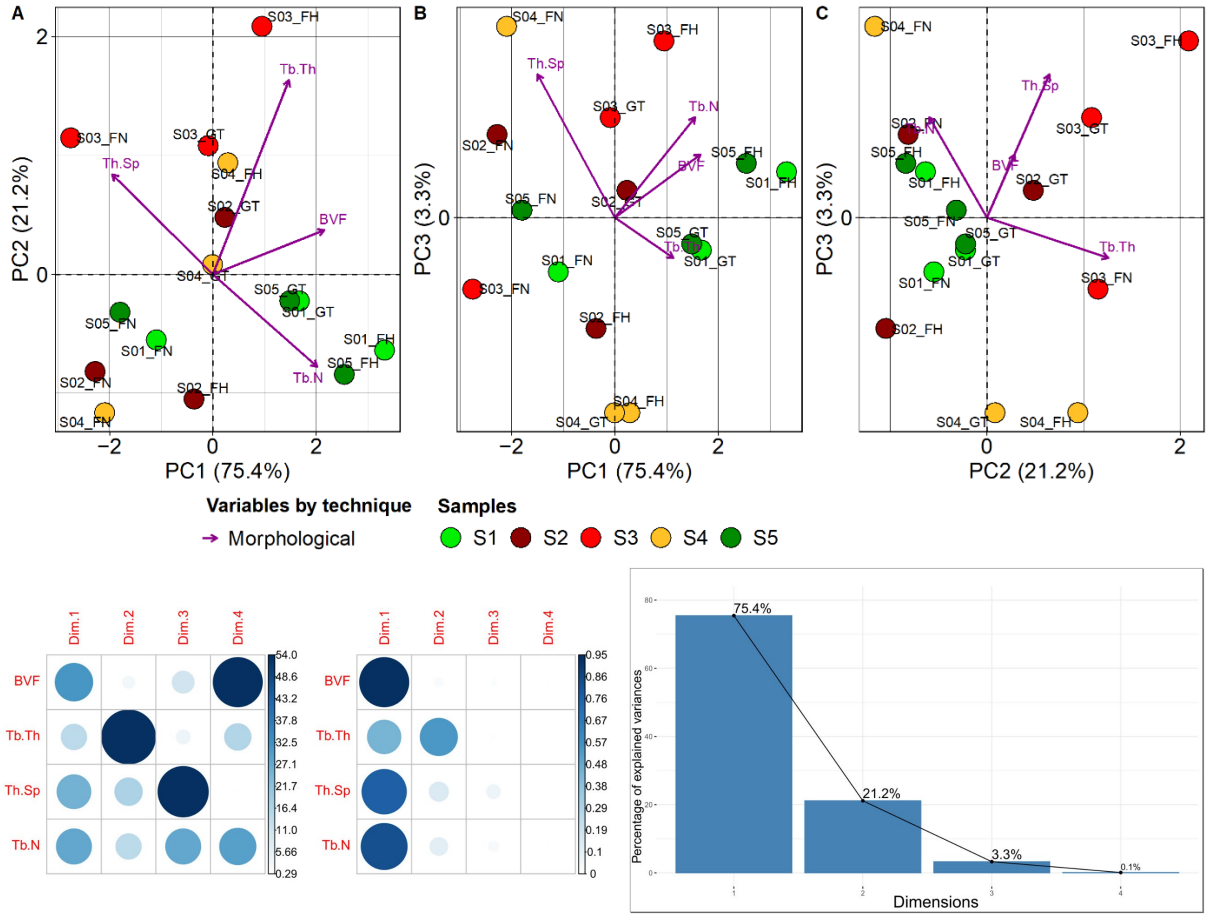

Figure 7. 14: Principal component analysis (PCA) of only morphological parameters of control (S01 and S05) and osteoporotic (S02, S03 and S04) bone samples. Individuals are represented by dots and colored by sample. Variables are represented by arrows and colored by technique. The length of the arrows indicates the strength of the correlation of respective parameter with the samples. The graphs below show the contribution and the cos2 of each variable in each dimension as well as the percentage of variability contained in each dimension.

XAS

Moreover, the PCA analysis has been performed using the parameters derived from XAS and the first three principal component axes (PC1, PC2 and PC3) explained 99% of the data variability between samples. Although, PC1 explained 59.5% and included I_G, ss2 and MapRatio, PC2 explained 27.8% of data variability and included R and MapRatio (Fig. 7.15), no clear separation between healthy and osteoporotic subjects was observed. PC3 explained 11.7% of the variance and was primarily composed by I_G and MapRatio. The PERMANOVA analysis was not significative and the k-means cluster analysis confirmed the tendencies observed in the PCA, not succeeding in separating the samples based on their health state.

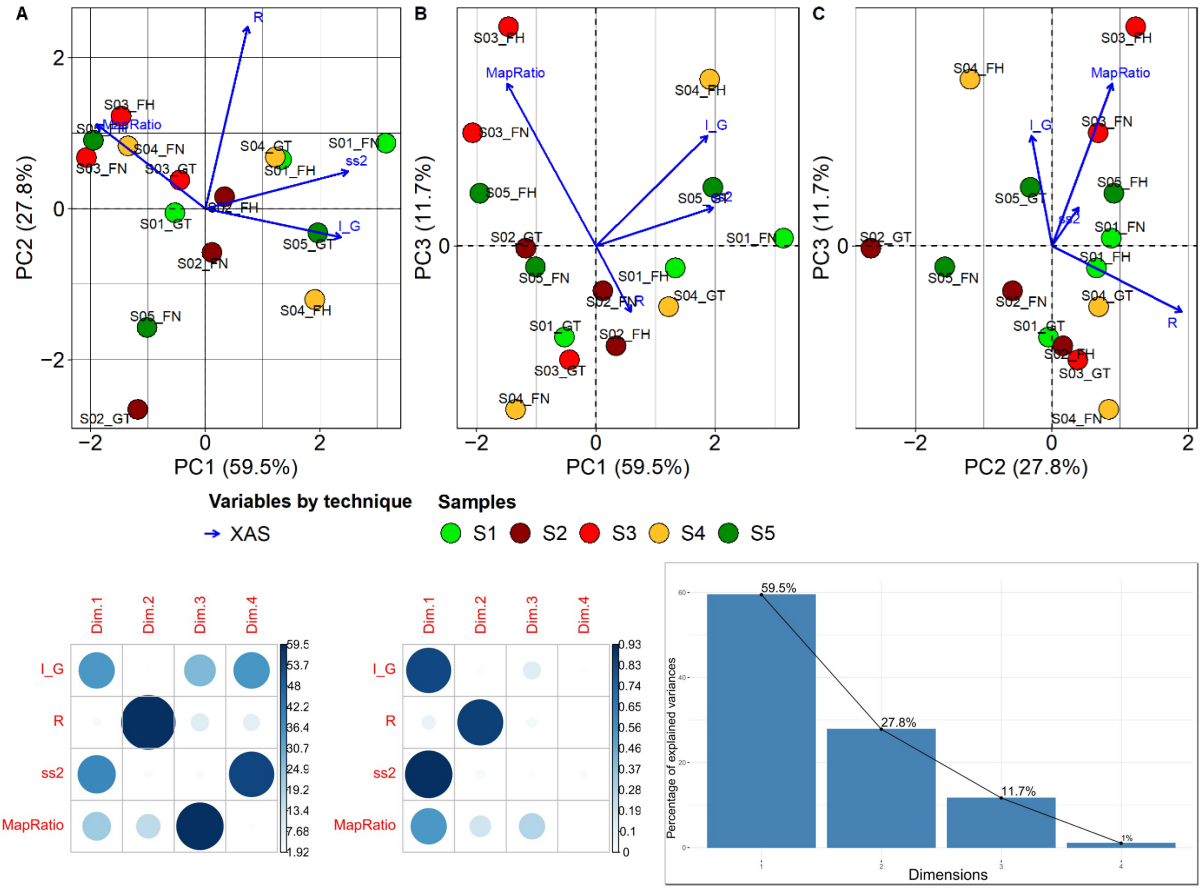

Figure 7. 15: Principal component analysis (PCA) of only XAS parameters of control (S01 and S05) and osteoporotic (S02, S03 and S04) bone samples. Individuals are represented by dots and colored by sample. Variables are represented by arrows and colored by technique. The length of the arrows indicates the strength of the correlation of respective parameter with the samples. The graphs below show the contribution and the cos2 of each variable in each dimension as well as the percentage of variability contained in each dimension.

Bi-Modal analysis (Clinical standard BMD/Morphology)

Finally, the PCA using the morphological parameters and the clinical standard BMD has been derived and the results are shown in Figure 7.16. PC1-PC2-PC3 explained 97.3% of data variability, with PC1 primarily composed by BVF, Tb.Sp and Tb.N, PC2 composed by Tb.Th, and BMD uniformly distributed between PC1, PC2 and PC3. The PERMANOVA showed that both the factor condition ($p<0.01$) and bone subregion ($p<0.05$) significantly explained the differences between the samples. Moreover, the k-means clustering provided statistical confirmation of the tendencies observed in the PCA with the healthy FN subregions being the only regions misclassified as osteoporotic for both S01 and S05 and providing the clearer separation between healthy and osteoporotic subjects above all the previously performed PCA.

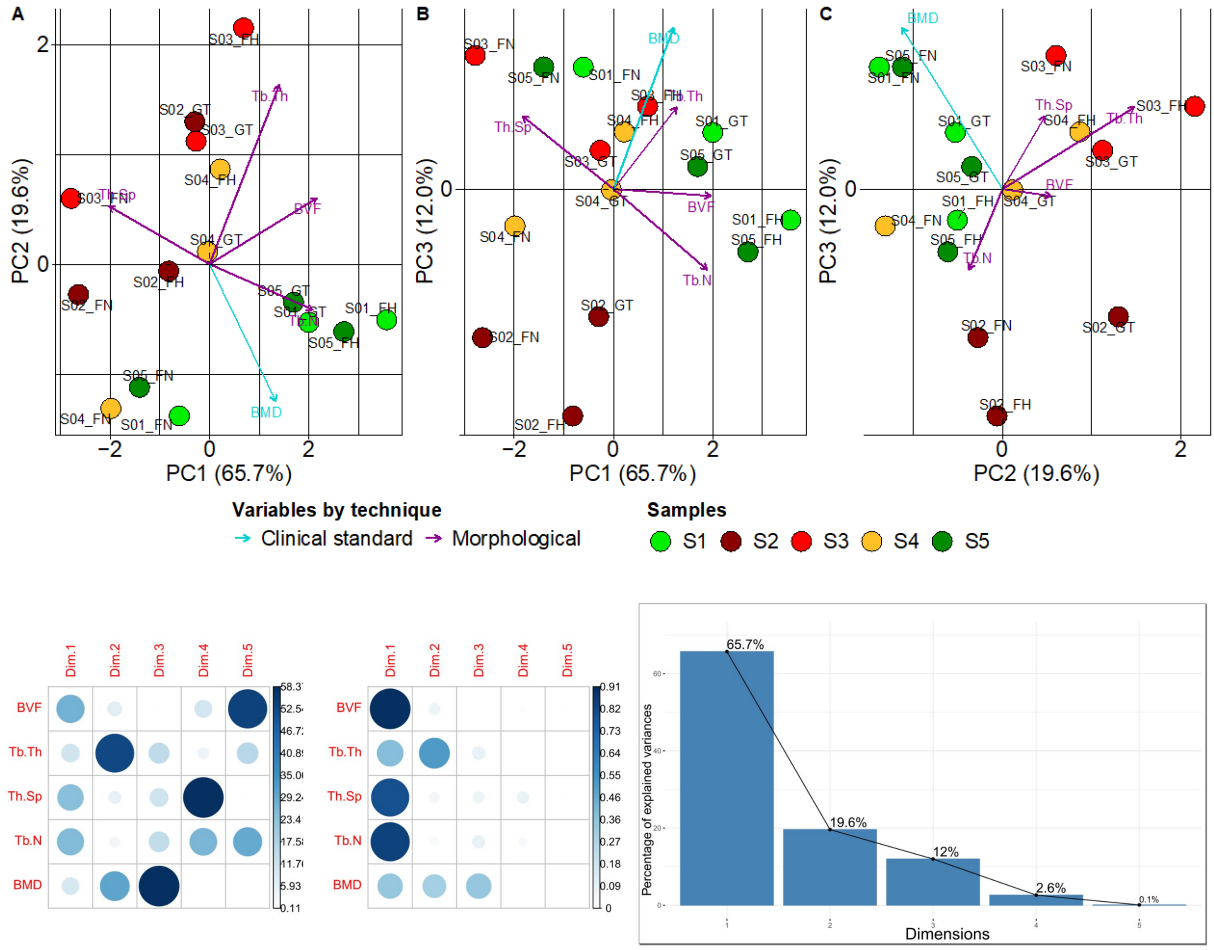

Figure 7. 16: Principal component analysis (PCA) of DXA derived-BMD providing the clinical standard and morphological parameters of control (S01 and S05) and osteoporotic (S02, S03 and S04) bone samples. Individuals are represented by dots and colored by sample. Variables are represented by arrows and colored by technique. The length of the arrows indicates the strength of the correlation of respective parameter with the samples. The graphs below show the contribution and the cos2 of each variable in each dimension as well as the percentage of variability contained in each dimension.

4. Discussion

The investigation of the HA crystallinity and trabeculae microarchitecture in the proximal femur trabecular network between osteoporotic and control subjects is of great interest since changes could modify the BM process and therefore impact the bone heath quality. The biomechanical fracture test came as an additional support since provided the real health condition of the proximal femur and therefore the provided information could be used as a reference.

In this study we addressed the issue related to trabecular microarchitecture and HA crystallinity using a multimodal approach, which combined image and spectra analysis, and biomechanical fracture tests. This approach allowed to completely resolve the trabecular microarchitecture and to investigate the Calcium K-edge of the HA structure in three different proximal femur regions specifically chosen to provide an overall picture of the whole proximal femur health quality. Moreover, it provides the comparison of the corresponding results of both an inter-gender approach (one healthy male vs. one healthy female) and intra-gender (one healthy female vs. three osteoporotic females).

The biomechanical fracture tests designed to imitate the sideway fall on the great trochanter provided reference values of the real proximal femur health quality and the obtained parameters were in accordance with those obtained from a previous studies (Le Corroller et al. 2012; D. Guenoun et al. 2020a; Manske et al. 2009; Soldati, Vicente, et al. 2021).

The analysis conducted using μCT images acquired at 25 μm^3 showed differences in the bone morphology based on the anatomical position (FH vs. FN vs. GT), on the patient gender (male vs. female), and on the bone health state (healthy vs. osteoporotic). In particular, higher BVF and Tb.N, similar Tb.Th and lower Tb.Sp have been assessed in the FH than in both the other two bone regions confirming regional structural variations of trabecular bone in the proximal femur previously assessed (Issever et al. 2002; Nazarian et al. 2007). Moreover, the differences based on the patients gender assessed in this study confirmed those previously reported, i.e. Mueller et al. on a study conducted on 163 cadaveric forearms of elderly subjects (>60 yrs) using high-resolution pQCT scanner (voxel size = 89x89x93 μm) reported that male had higher BVF and Tb.N (respectively +35% and +24%) and lower Tb.Sp (-49%) compared to females (Mueller et al. 2009). Differences in the bone morphology due to changes in the bone remodeling process caused by pathologies affecting the skeleton have also been assessed previously (among others, osteoporosis (Soldati, Vicente, et al. 2021; D. Guenoun et al. 2020a; Chamith S. Rajapakse et al. 2018a), psoriatic arthritis (Soldati, Escoffier, et al. 2020; Ogdie et al. 2017b; Chandran et al. 2016b), rheumatoid

arthritis (B. Wang et al. 2016) and, osteoarthritis (Z.-C. Li et al. 2012)). Furthermore, the obtained morphological parameters were in the same range of those previously reported in the literature from both inter-gender patients (Mueller et al. 2009; Khosla et al. 2005; Kazakia et al. 2013), different proximal femur subregions (Issever et al. 2002; Djuric et al. 2010) and different health state (Soldati, Vicente, et al. 2021; B. Wang et al. 2016; Z.-C. Li et al. 2012; Soldati, Escoffier, et al. 2021).

These results showed that bones are highly in-homogeneous structures whose inner microarchitecture is engineered to provide the maximum resistance performances which therefore is different based on gender, bones body position and anatomical location of the same bone. However, bone pathologies may affect bone microarchitecture reducing the trabeculae interconnection (lower BVF, Tb.N and higher Tb.Sp).

The XAS spectra showed identical spectral features for both male and female subjects and osteoporotic and healthy. The pre-peak, the shoulder peak before and after the higher peak (white line) and the white line were at same energy positions as previously reported for Ca K-edge XANES spectra of HA references (Monico et al. 2020; Sepulcre et al. 2004; Carpentier et al. 2010; Nguyen et al. 2011). The whole dominant peaks are in the same energy region suggesting the Ca local structure in all samples are mainly formed as HA. The great variability in the spectra intensities seemed due to the samples biological variability (normal variability between different subjects) and not related to the bone health state (Hesse et al. 2016). Differences were assessed between healthy and osteoporotic based on the spectra analysis of the four different parameters investigated. The healthy FH showed in general higher pre-peak intensity and DebyeWaller and lower Ca/P ratio, one could speculate that osteoporotic bones start collect P and increase the regenerative activity at the expenses of bone quality since more ordered crystals are sensed to increased rigidity. Supporting this hypothesis, Murshed et al. reported that ionic calcium (Ca^{2+}) and inorganic phosphate (P_i) are two critical determinants for bone mineralization (Murshed 2018). In addition, it has been previously reported that from patients and animal models of human diseases clearly demonstrates that the reduction of systemic P_i levels with or Ca^{2+} without any alteration of the levels lead to osteomalacia with the characteristic increase of unmineralized osteoid volume (Murshed 2018; Terkeltaub 2001; Dardenne et al. 2001; Masuyama et al. 2001). The GT on the contrary showed HA crystal more disordered and higher Ca/P ratio suggesting an overall higher flexibility and reduced regenerative activity. This effect could be explained by the anatomical position of the GT which is the proximal femur subregion less involved in the biomechanics of the bone. Usually, smaller differences between healthy and osteoporotic subjects have been assessed in the FN subregions suggesting that healthy

FN was already impacted by an intensive bone remodeling process and hence FN could be the first proximal femur region impacted by osteoporosis.

The principal component analysis has been performed to individuate the parameters contribution in the proximal femur fracture risk prediction. The first explorative PCA using all the investigated parameters showed no clear separation between healthy and osteoporotic subjects and the lowest data variability explanation with the first three principal component. This same effect has also been observed in all the PCAs using the spectroscopic features derived from XAS, while better separation could be appreciated removing XAS parameters from the equation. These results further support the hypothesis of Hesse at al. that no stoichiometric changes in the HA chemical composition can be associated to mineral maturation, anatomical site or disease (osteoporosis) (Hesse et al. 2016). The additional PCAs performed removing one XAS parameter at a time came as an additional support. In particular, the lower separation between healthy and osteoporotic obtained removing MapRatio rather than when removing ss2 suggested that no atomic changes can be associated to osteoporosis while changes could be associated to the HA crystal local order and microarchitecture. Finally, the best separation based on bone health condition has been obtained combining clinical standard BMD and the morphological parameters derived from image analysis. This result clearly support the hypothesis that the trabecular morphology provide additional information to the BMD and once added the diagnosis of osteoporosis and the fracture risk assessment resulted improved (Soldati, Vicente, et al. 2021).

Some limitation has to be acknowledged, first this work would have benefit of a larger sample population which could be chosen to be well distributed according to both bone health quality and patients gender. Second, the bone changes in both the morphology and HA crystallinity due to osteoporosis could be improved by adding the analysis of the cortical phase. Unfortunately, in our case it was not possible due to sample availability and beamtime shifts. Finally, quantitative or semi-quantitative information about trabeculae tissue properties and HA molecular composition and structure could be investigated performing both synchrotron experiments (i.e. X-ray Diffraction (XRD)) or laboratory analysis (i.e. Microindentation, Fourier transform infrared (FTIR) or Raman Spectroscopy) and further published. However, since these techniques require a specific sample preparation protocol, they have to be performed following a specific order (XRD, Microindentation, FTIR/Raman).

5. Conclusion

In this study, it has been qualitatively characterized the HA crystallinity in the trabecular network of three different proximal femur subregions taking advantage of the X-ray absorption spectroscopy of the Ca K-edges at micrometric scale. The obtained information has been compared to bone biomechanics and morphology to evaluate if the provided information would increase the proximal femur fracture risk assessment predictivity. Our results suggested that no stoichiometric changes in the HA chemical composition can be associated to mineral maturation, anatomical site or disease (osteoporosis). However, from the analysis of each feature extracted from XAS has been shown that while no HA atomic changes can be associated to osteoporosis, changes could be associated to the HA crystal local order and microarchitecture. Finally, the PCA conducted using clinical reference BMD and trabecular morphology provided a clear separation of the samples based on their bone health quality suggesting that the combination of these two bone properties could improve the osteoporosis diagnostic reliability and fracture risk assessment.

General Conclusion

Osteoporosis is a systemic bone pathology which is responsible to put at high risk of fragility fracture more than 300 million people by 2040. Hence, an early diagnose of osteoporosis is of utmost importance since would increase the quality of life of many patients. In this study, it has been presented an optimized approach for the diagnose of osteoporosis which aims to add the trabeculae inner morphology to the clinical standard reference, i.e. the bone mineral density, using MR imaging technology, which compared to DXA and qCT represent a non-invasive and radiation-free alternative.

This study, first assessed the possibility to acquire the trabeculae morphology using MR imaging technology showing that both the bone quality and the therapy delivery effect on a patient affected by psoriatic arthritis were assessable. However, the same first study also reported the limits of this imaging technique where due to the difference between image resolution and trabeculae dimension the bone inner morphology was not completely resolved.

To reliably assess the bone quality in both healthy and pathological situations with the aim of improving the in vivo diagnosis, ex vivo studies of large cadaveric bones are of utmost importance. The first issue on the investigation of large cadaveric bones using MR imaging are the air bubbles artefacts caused by bone decomposition. In our study, a vacuum procedure able to substitute the air bubbles inclusion with 1 mM Gd-DTPA saline solution which imitates the magnetic response of bone marrow has been designed and validated through image analysis. Then, the image resolution limit which would allow to resolve the bone trabeculae has been investigated showing that a minimum pixel size of 0.150 mm in plane is needed to assess bone trabeculae. Interestingly, the new introduced parameter based on the trabecular interconnectivity showed to highly correlate with fracture load proving that structural organization and morphological parameters could provide additional, rather than analogous, information to clinical standard BMD for a more comprehensive view of the bone health status and quality. Once determined the minimum pixel size to acquire the trabecular morphology, the second investigative problem was to identify the MRI field strength and pulse sequence that better differentiate bone and marrow phases. Hence the field strength and pulse sequence characterized by a reduced susceptibility to partial volume effects and susceptibility-induced broadening of the trabeculae has been investigated using different field strengths MRI (3T vs. 7T) and pulse sequences (GRE vs. TSE). The results showed that using TSE sequence at 7T MRI the morphological parameters acquired were comparable to those derived using the gold

standard μCT. Therefore, an optimized approach for the bone morphological assessment has been proposed.

Attested that the bone morphology could be assessed and provide additional information to clinical BMD, and hence could increase the diagnosis and the fracture risk prediction, the bone changes related to osteoporosis at lower scales (micro-, nano- and molecular) have been addressed. Interestingly, both the analysis conducted on the trabeculae osteocytes lacunae and mechanical properties in the femoral neck showed no changes based on clinical bone state. However, our results pointed that the femoral neck resulted the proximal femur subregion highly affected by osteoporosis with an increased bone remodeling process compared to both femoral head and great trochanter, confirming the higher occurrence of fragility fractures in the FN compared to both FH and GT. Moreover, the molecular investigation showed that no stoichiometric changes in the HA chemical composition could be associated to mineral maturation, anatomical site or osteoporosis, while changes in the HA could be associated to HA crystal order and microarchitecture. In addition, the principal component analysis conducted on the three different proximal femur subregions of 5 subjects showed that the healthy FN subregions were always migrating according to the osteoporotic. Finally, the PCA performed using BMD and morphological parameters showed a clear sample separation based on the bone health quality, confirming that the combination of these two bone properties could improve the osteoporosis diagnostic reliability and fracture risk assessment.

To better understand the implications of the HA nano- and molecular changes due to osteoporosis, future studies could address the structural properties of bone mineral platelets and collagen fibrils at the nanoscale and HA chemical composition. The structural properties of both bone mineral platelets and collagen fibrils could be assessed using synchrotron small-angle X-ray scattering (SAXS) and wide-angle X-ray diffraction (WAXD) techniques. Moreover, the HA chemical composition and the possible influence of different substitutes in the bone remodeling process could be assessed using atomic absorption spectroscopy (AAS) which is an analytical technique used for both quantitative and qualitative determination of metal ions in solution. Future works could also increase the sample population distributing samples based on bone quality and patients gender, and take into account both the bone cortical and trabecular phase. Finally, as presented in Chapter 1.4 promising MRI techniques could be used to assess non-invasively and in vivo the bone marrow fat quantification, the bone mineral composition, the bound, and pore water, and the magnetic susceptibility quantification, providing information of the bone health, quality and metabolic activity.

To conclude, in this PhD thesis the diagnostic power of osteoporosis in deep bone segments, as the proximal femur, has been increased by adding to the clinical reference

DXA derived-BMD, the bone inner morphology assessed using an optimized MR imaging approach, an in vivo and non-invasive clinical technology. Moreover, the proximal femur analysis at lower investigative scales have pointed that the femoral neck is the first proximal femur region affected by osteoporosis and with an increased bone remodeling activity, and therefore the more likely exposed to fragility fractures. Finally, the altered bone remodeling activity should be related to changes in the HA crystal order and microarchitecture rather than chemical composition.

Long Résumé de Thèse

Introduction

Les os ont de multiples fonctions fondamentales chez l'homme, il est possible de séparer 3 types de fonctions : (i) mécaniques, les os assurent la protection des organes internes, locomoteur permettant le mouvement mais aussi sensoriel transmettant le son et soutenant tous les tissus mous ; (ii) hématopoïétique, synthétisant les globules blancs ; et (iii) métaboliques, ils consistent en un stock de minéraux, lipides et facteurs de croissance, ils sont capables de détoxifier l'organisme de nombreux métaux lourds et leur sécrétion endocrinienne, entre autres, est chargée de réguler la sécrétion de phosphore et à travers l'ostéocalcine, de abaisser la glycémie. L'os est un tissu qui s'absorbe et se remplace continuellement en maintenant l'homéostasie, ce qui permet au tissu de résister également à toutes les forces extérieures auxquelles il est soumis dans la vie quotidienne de tous les humains. Des modifications de la résistance osseuse peuvent entraîner une augmentation de la susceptibilité aux fractures, principalement due à une diminution de la résistance et de la qualité des os. Alors que les deux déterminants sont étroitement liés à plusieurs paramètres liés à la géométrie osseuse, la macroarchitecture, la microarchitecture, les microlésions, la minéralisation osseuse et le remodelage osseux, de nombreuses maladies osseuses, à savoir l'ostéoporose, sont actuellement diagnostiquées sur la base de la mesure unique de la densité minérale osseuse (DMO) . La DMO est considérée comme un indice de perte de masse osseuse et sur cette base comme un prédicteur de fracture ostéoporotique. Cependant, les limites des mesures de la DMO ont été clairement reconnues étant donné qu'un pourcentage important de fractures ostéoporotiques surviennent chez des patients avec une DMO normale. L'os est en effet un matériau poreux et il est largement reconnu que la DMO ne peut pas prendre en compte d'autres paramètres morphométriques critiques pour le comportement mécanique de l'os. La BMD ne prend en compte ni la porosité osseuse, ni la distribution, la forme et l'organisation des pores osseux. En conséquence, la communauté scientifique manque encore d'une méthode de diagnostic fiable et sensible de la qualité osseuse qui devrait idéalement être basée sur des mesures de résistance osseuse in vivo.

L'imagerie par résonance magnétique (IRM) a été utilisée au cours des dernières décennies comme un outil de choix non invasif pour le diagnostic d'un grand nombre de troubles et elle est capable de fournir des images très contrastées et très résolues qui offrent des informations qualitatives et fonctionnelles. Les développements

technologiques récents ont permis d'améliorer encore la résolution de l'image grâce à l'utilisation d'un champ magnétique ultra-élevé (7T). Des images d'une résolution de 150 µm sont désormais disponibles dans un délai raisonnable (10 minutes). Une telle résolution a ouvert de nouvelles opportunités pour étudier la microarchitecture osseuse et pour évaluer in vivo la densité osseuse trabéculaire. Bien qu'intéressants, cet indice (DMO) et les indices correspondants liés à l'épaisseur trabéculaire et à la densité trabéculaire n'ont jamais fait l'objet d'une analyse comparative robuste avec des mesures in vivo de la résistance osseuse. Une telle analyse comparative devrait fournir une base incontestable soutenant le potentiel de l'IRM à ultra-haut champ dans le domaine de la qualité osseuse. S'il s'avère que ces indices de microarchitecture évalués par une technique non invasive sont liés à la résistance osseuse, ils pourraient être utilisés en complément de la DMO, comme indices diagnostiques sensibles et pour doser l'efficacité de stratégies thérapeutiques.

De plus, la qualité osseuse dépend non seulement de la densité et de la morphologie de sa phase solide mais aussi d'autres facteurs comme la minéralisation osseuse. Par conséquent, une enquête multi échelle et multimodale de l'effet de l'ostéoporose sur les os est d'un grand intérêt sachant qu'une meilleure compréhension du mécanisme de cette maladie, qui provoque des fractures de fragilité chez 1 femme sur 3 et 1 homme sur 5 âgés de 50 ans ou plus et est très invalidante, pourrait ouvrir la possibilité d'effectuer un diagnostic précoce et de commencer de nouveaux essais thérapeutiques.

Globalement, il existe un besoin de concevoir de nouvelles approches d'imagerie de la résistance osseuse qui pourraient être complémentaires à la DMO. Ces approches devraient fournir des informations clés concernant le comportement mécanique et le remodelage des os améliorant ainsi la fiabilité et la sensibilité des procédures de diagnostic, la stratification des risques et le suivi de la stratégie thérapeutique.

Objectif Général

L'objectif général de notre étude était d'améliorer le diagnostic in vivo de l'ostéoporose par IRM. L'ostéoporose est une maladie osseuse systémique caractérisée par une résistance osseuse réduite et une fréquence accrue de fractures de fragilité. L'ostéoporose est actuellement diagnostiquée à l'aide d'une absorptiométrie à double énergie X qui fournit des informations sur la densité osseuse tandis que pour augmenter la précision de l'outil de diagnostic, la microarchitecture osseuse pourrait être ajoutée car la structure interne de l'os joue un rôle important dans la résistance structurelle. La microarchitecture osseuse pourrait être évaluée in vivo en utilisant à la fois la tomodensitométrie à rayons X et l'IRM qui est reconnue comme totalement non invasive. Dans cette étude, une analyse multimodale et multi-échelle a été réalisée en se concentrant uniquement sur la qualité osseuse du fémur proximal, qui représente un site ostéoporotique important, l'un des plus invalidants, et un site anatomique

profond difficilement évaluable en utilisant ni la TDM ni l'IRM en raison à sa position, loin de la surface de la peau. Cependant, l'IRM UHF pourrait fournir une résolution d'image dans la même gamme de travées osseuses également dans ces sites anatomiques profonds, qui restent à la place non évaluables à l'aide de techniques de tomodensitométrie à haute résolution, c'est-à-dire de tomodensitométrie quantitative périphérique à haute résolution (HRpQCT).

Cette approche multimodale et multi-échelle comprenait i) une numérisation µCT de fémurs proximaux cadavériques qui vise à fournir la vérité terrain de l'architecture trabéculaire interne, ii) une numérisation IRM des mêmes spécimens à 3T et 7T à des fins comparatives et iii) des tests destructifs biomécaniques. Des méthodes de balayage supplémentaires telles que la tomographie par rayons X synchrotron, la spectroscopie d'absorptiométrie aux rayons X, l'infrarouge à transformée de Fourier et la microindentation ont été utilisées dans des spécimens plus petits et ainsi afin d'évaluer les propriétés mécaniques des trabécules, le réseau de lacunes des ostéocytes et la composition et la structure des cristaux d'hydroxyapatite. La figure I.1 présente la vue d'ensemble et le calendrier de ce projet de thèse. En particulier, il est rapporté la collecte d'échantillons, le calendrier de soumission et l'acceptation/le rejet des propositions de synchrotron pour effectuer un examen plus approfondi à l'échelle micro-moléculaire osseuse. Enfin, la figure I.1 rapporte toutes les techniques d'expérimentation, leur échelle d'investigation et le chapitre de la thèse où leurs résultats correspondants seront présentés et discutés.

Le premier objectif de la thèse était d'étudier la possibilité d'évaluer la microarchitecture du fémur proximal à l'aide de la technologie IRM et d'augmenter la précision du diagnostic de l'ostéoporose en utilisant des informations dérivées de la morphologie interne de l'os.

Le deuxième objectif était d'étudier les différences dans la qualité osseuse à l'échelle nanométrique et moléculaire pour évaluer à quel niveau l'ostéoporose commence son activité de détérioration, fournissant ainsi des implications directes dans la recherche préclinique, la stratégie thérapeutique et éventuellement la pratique clinique.

Afin d'étudier l'os à différentes échelles, plusieurs techniques d'investigation ont été appliquées. La macroéchelle a été étudiée en appliquant des modalités d'imagerie et des techniques biomécaniques à l'aide d'instruments à disposition dans nos laboratoires. Les plus petites échelles ont été étudiées en utilisant à la fois des instruments internes ou des appareils d'autres laboratoires après l'établissement d'un régime de collaboration basé sur des intérêts mutuels, et des techniques disponibles dans les installations synchrotron (spectroscopie d'absorption des rayons X et micro tomodensitométrie synchrotron). Cependant, si la collaboration avec différents laboratoires a été créée sur la base d'intérêts mutuels et donc immédiate, pour accéder aux installations synchrotron, il est nécessaire que la proposition soumise soit acceptée

et qu'un temps de faisceau soit attribué. Par conséquent, de la soumission de la proposition à l'acceptation, il faut généralement entre 3 et 4 mois et entre 5 et 7 mois avant l'heure du faisceau. Ces retards nécessitent une planification méticuleuse des expériences et la chronologie de la figure I.1 est nécessaire pour comprendre le motif appliqué pour effectuer les essais.

Structure de Manuscript

Ce manuscrit de thèse vise à caractériser la qualité osseuse à l'aide d'une approche multiéchelle et multimodale, en montrant de plus des différences à la fois in vivo, entre les patients atteints de troubles osseux et les témoins, et ex vivo à l'aide d'échantillons cadavériques sains et ostéoporotiques. Cependant, la collecte d'échantillons cadavériques est extrêmement compliquée en raison à la fois de la réglementation éthique et du manque effectif de corps humains donnés à la recherche. Par conséquent, au cours de ce projet de thèse, il a été tenté d'optimiser les échantillons en notre possession par une caractérisation systématique multimodale et multiéchelle.

Le manuscrit est organisé comme suit :

Le chapitre 1 présente une revue de la littérature, montrant les troubles osseux les plus importants et les outils d'investigation. De plus, il décrit l'approche clinique conventionnelle et l'applicabilité d'une approche basée sur l'IRM. Enfin, il décrit les applications IRM à venir, qui pourraient fournir des biomarqueurs supplémentaires pour l'évaluation de la qualité osseuse.

Le chapitre 2 présente une étude in vivo de l'évaluation de la microarchitecture du genou d'un patient atteint de rhumatisme psoriasique. Cette étude montre une application directe de l'IRM à ultra-haut champ pour quantifier les anomalies de la microarchitecture osseuse chez le patient par rapport aux témoins, présentant de plus une évaluation fiable de la qualité osseuse, la stratification du risque de maladie et pour le suivi des stratégies thérapeutiques.

Le chapitre 3, dédié aux matériels et méthodes, présente la base de données d'échantillons collectés au cours de la thèse et leur protocole de préparation en fonction des techniques expérimentales de caractérisation utilisées. De plus, toutes les techniques expérimentales de caractérisation osseuse multiéchelle et multimodale ont été présentées.

Le chapitre 4 présente une étude ex vivo sur la pertinence clinique de l'IRM UHF en évaluant la microarchitecture osseuse dans les fémurs proximaux cadavériques. Tout d'abord, il décrit le protocole de préparation des échantillons pour les grands fémurs cadavériques afin de réduire les artefacts dus aux effets de susceptibilité magnétique, puis il montre les techniques de quantification de la morphologie osseuse et l'effet de la résolution sur l'analyse morphologique. Enfin, les corrélations entre les mesures

cliniques de densité minérale osseuse standard et la morphologie osseuse sont présentées.

Le chapitre 5 présente une étude ex vivo visant à optimiser l'analyse de la microarchitecture des fémurs proximaux à partir d'acquisitions IRM. Les paramètres de microarchitecture des mêmes fémurs proximaux acquis à l'aide de différentes techniques d'imagerie µCT et IRM 3T et 7T et des séquences gradient re-appelées écho et turbo spin écho ont été comparés. De plus, il présente la corrélation entre la DMO clinique standard et la morphologie osseuse et la DMO dérivée de l'analyse d'images et la corrélation entre la morphologie osseuse et la charge de rupture osseuse dérivée du test de fracture biomécanique.

Le chapitre 6 présente une analyse multiéchelle et multimodale de deux cols fémurs, un ostéoporotique et un contrôle. Il décrit la qualité osseuse de la macro-échelle (µCT à 51 μm^3 et 5 μm^3) à la micro-échelle (X-ray synchrotron µCT à 0.9 μm^3 et microindentation) et à l'échelle moléculaire (Fourier Transform Infra-Red). La morphologie à l'échelle macroscopique, les changements dans la morphologie et la distribution des lacunes des ostéocytes ont été étudiés et les variations dans les propriétés mécaniques trabéculaires et dans les types d'hydroxyapatite, les fibrilles de collagène et les protéines ont été évaluées.

Le chapitre 7 présente l'étude des modifications moléculaires de l'hydroxyapatite dues à l'ostéoporose. En utilisant la spectroscopie d'absorption des rayons X, le Calcium K-edge a été étudié dans 15 échantillons provenant de 5 patients différents (3 femmes ostéoporotiques et 2 témoins, 1 femme et 1 homme). Les différences dans le rapport calcium et phosphore et l'ordre de cristallinité de l'hydroxyapatite ont été évaluées quant à leur pertinence dans la classification ostéoporotique/contrôle.

Enfin, une conclusion générale est présentée comme pour une ouverture à de nouvelles perspectives. Par ailleurs, une conclusion générale chapitre par chapitre est également présentée en français.

Chapitre 1 : état de l'art

Dans ce premier chapitre, il a été présenté la fonction et la structure osseuse en se concentrant sur sa hiérarchie multi-échelle. Les principales pathologies osseuses et les approches cliniques les plus courantes pour évaluer la qualité osseuse et l'état de santé ont été discutées, confirmant les doutes quant à l'utilisation de la DMO dérivée de la DXA comme seul outil d'investigation et soutenant la nécessité de fournir des informations supplémentaires concernant la microarchitecture osseuse. Ensuite, les techniques d'imagerie disponibles ont été présentés pour évaluer la morphologie interne de l'os. Les avantages et les inconvénients de chaque technique ont été présentées, nous suggérons que l'IRM UHC pourrait être une approche non invasive pour résoudre ce problème, bien que rapportant la nécessité d'une résolution du même

ordre de dimension des trabécules (100-150 µm). Enfin, de nouvelles techniques d'IRM d'investigation ont été rapportées dans des perspectives d'avenir montrant qu'avec l'IRM, il serait possible d'évaluer à la fois la microarchitecture osseuse du patient et la DMO dans une approche totalement non invasive et sans rayonnement.

Comme indiqué, la pathologie la plus courante liée aux altérations de la microstructure osseuse est l'ostéoporose et c'est donc la pathologie osseuse qu'il a été décidé d'étudier au cours de cette thèse. Dans l'ostéoporose, la densité osseuse et le volume de segments ou de régions osseuses spécifiques peuvent être progressivement réduits. Les patients atteints d'ostéoporose courent un risque élevé d'avoir une ou plusieurs fractures de fragilité, ce qui conduit éventuellement à un affaiblissement physique et potentiellement à une spirale descendante de la santé physique et mentale. Le mécanisme caché de l'ostéoporose est un déséquilibre entre la production et la résorption osseuse conduisant à une diminution de la masse osseuse. Habituellement, l'os est en constant remodelage et jusqu'à 10 % de la masse osseuse totale peut subir un remodelage à tout moment. Une interaction de différents mécanismes sous-tend le développement de tissus osseux fragiles, parmi lesquels une masse et une résistance insuffisantes pendant la croissance, une résorption osseuse excessive et une formation inadéquate d'os nouveau pendant le remodelage sont les plus importantes (Paccou et al., n.d.). Les facteurs hormonaux jouent un rôle important dans le taux de résorption osseuse comme pour la ménopause qui en raison d'un manque d'œstrogènes augmente la résorption osseuse et inhibe la formation d'os nouveau. D'autres facteurs, comme le métabolisme du calcium, ont joué un rôle important dans le remodelage osseux (Bendtzen 2015). L'os trabéculaire ostéoporotique perd non seulement de la densité, mais la microarchitecture est également perturbée, les plus petites trabécules se rompant créant des microfissures qui sont remplacées par des os plus faibles (Osterhoff et al. 2017). L'os cortical, lorsqu'il est atteint d'ostéoporose, diminue sa densité, perd une partie de sa résistance et de sa rigidité. Les sites les plus souvent touchés par les fractures ostéoporotiques sont le poignet, la colonne vertébrale et la hanche et se caractérisent par un rapport os trabéculaire/os cortical relativement élevé. Les sites de fracture reposent sur l'os trabéculaire pour la résistance et l'absorption de la charge, car ils correspondent aux articulations (Oftadeh et al. 2015). Le remodelage intense de ces régions osseuses provoque une dégénérescence progressive de ces zones lorsque le remodelage est déséquilibré. La dégradation osseuse est censée commencer entre 30 et 35 ans et les femmes peuvent en perdre jusqu'à 50 % tandis que les hommes environ 30 % (Koda-Kimble et al. 2008). L'ostéoporose peut être liée au vieillissement, en particulier chez les femmes ménopausées, ou peut survenir à la suite d'affections spécifiques, à savoir le diabète, l'anorexie mentale et l'obésité ou des traitements, comme la corticothérapie (Fig. 1.9). En effet, l'ostéoporose induite par les corticoïdes est la forme la plus fréquente d'ostéoporose secondaire et la première cause chez les

jeunes. La perte osseuse survient tôt après le début de la corticothérapie et est corrélée à la dose et à la durée du traitement (Bartl and Bartl 2017). Les fractures de fragilité ont été associées à une mortalité précoce et à une morbidité accrue ayant un effet significatif sur la qualité de vie des patients atteints de diabète (Keenan and Maddaloni 2016; S. C. Chen et al. 2019; Abdalrahaman et al. 2017), d'anorexie mentale (Singhal et al. 2018; Fazeli and Klibanski 2019) et d'obésité (Fintini et al. 2020; Cordes et al. 2016; 2015). De la même manière que l'ostéoporose, qui est l'objectif principal de cette thèse et qui est analysée plus en détail dans les chapitres suivants, le rhumatisme psoriasique est une maladie osseuse responsable de la dégradation des travées osseuses. Le rhumatisme psoriasique est ici introduit car avant le début de cette thèse, un patient atteint de rhumatisme psoriasique et huit témoins appariés selon le sexe et l'âge ont été acquis par IRM UHC au niveau du genou. Cette étude a été achevée au début de cette thèse, lorsque le patient a été évalué en utilisant l'IRM UHC une deuxième fois après un an de traitement. Les images IRM de cette étude clinique ont été utilisées pour étudier la microarchitecture du genou et les paramètres récupérés ont été comparés entre le patient et les témoins pour évaluer l'applicabilité de l'IRM à la fois à l'évaluation de la microarchitecture osseuse in vivo et au suivi des stratégies thérapeutiques. Cette étude a montré à la fois les limites et les potentialités de l'évaluation de la microarchitecture osseuse in vivo en utilisant la technologie d'imagerie par résonance magnétique au début de cette thèse.

Chapitre 2 : évaluation des modifications in vivo de la microarchitecture osseuse chez un patient atteint de psoriasis arthritique traité par anti-TNFα

Dans ce chapitre, les limites et les potentialités de l'applicabilité in vivo de l'IRM pour l'évaluation de la microarchitecture osseuse ont été montrés. Tout d'abord, les limitations techniques de l'IRM ont été exploitées, les séquences GRE ont été utilisées afin d'évaluer tout le volume du genou en un seul balayage, mais la résolution de l'image n'était pas suffisante pour résoudre la morphologie interne de l'os. Cependant, cet article a montré que l'IRM UHC était capable d'évaluer les caractéristiques osseuses les plus courantes et, à partir de leur analyse, de discriminer le patient PsA des témoins. De plus, il a été démontré l'amélioration de la qualité osseuse après un an de traitement montrant ainsi l'utilisation potentielle de l'IRM pour la stratification du risque de maladie et pour le suivi de la stratégie thérapeutique (Fig. 2.4). Ce chapitre a montré la valeur supplémentaire que l'imagerie IRM UHC de la microarchitecture osseuse pourrait apporter à la pratique clinique dans l'évaluation de la qualité osseuse, signalant toutefois le besoin d'amélioration et d'optimisation des techniques à la fois dans la séquence d'acquisition et les configurations, mais aussi dans l'analyse

d'images. . L'investigation de différentes séquences IRM, mais aussi l'optimisation entre résolution d'image, temps d'acquisition, taux d'absorption spécifique, SNR, … est d'un grand intérêt pour augmenter l'applicabilité in vivo de l'évaluation de la microarchitecture osseuse dans la pratique clinique.

Dans le chapitre suivant, toutes les techniques expérimentales et les configurations qui ont été appliquées dans ce projet de thèse ont été présentés . Le premier objectif était d'évaluer la qualité osseuse et de fournir une approche optimisée pour l'utilisation de l'IRM UHC pour l'évaluation de la microarchitecture osseuse des fémurs proximaux dans la pratique clinique. De plus, le deuxième objectif était d'étudier l'effet de l'ostéoporose sur la structure osseuse hiérarchique à plusieurs échelles.

Chapitre 3 : matériaux et méthodes

Dans le présent chapitre ont été rapportés tous les échantillons collectés, les techniques expérimentales utilisées, et les protocoles de préparation spécifiques à chaque technique. Les techniques expérimentales rapportées ont été divisées en trois groupes principaux, c'est-à-dire à l'échelle macro, micro et nano/moléculaire, en fonction de l'intérêt de la recherche. A l'échelle macroscopique ont été proposées deux techniques d'imagerie différentes (imagerie par résonance magnétique et de microtomographie à rayons X) et un test biomécanique pour l'ensemble du fémur proximal qui simule la chute latérale sur le grand trochanter. L'investigation microscopique du fémur proximal a été réalisée sur de multiples sous-échantillons extraits de trois régions différentes du fémur proximal (grand trochanter, col fémoral et tête fémorale) sur la base de tomographie à rayons X et de tests de microindentation sur les travées. Le SRμCT est capable de réduire la taille des pixels de l'image afin de résoudre complètement la microarchitecture osseuse et de caractériser les lacunes des ostéocytes tandis que la microindentation est capable de caractériser les propriétés matérielles des trabécules. Les échelles nanométrique et moléculaire ont été étudiées sur la base de deux techniques spectroscopiques appliquées à de petits échantillons extraits des trois régions fémorales proximales décrites précédemment. La spectroscopie d'absorption des rayons X a été réalisée pour étudier les changements autour du calcium du cristal d'hydroxyapatite osseux dus à l'ostéoporose, tandis que la transformée de Fourier infrarouge visait à évaluer les différences dans les propriétés minérales osseuses généralement signalées comme le rapport minéral sur matrice, la maturité minérale/ cristallinité et la maturité du collagène. Enfin, le dernier paragraphe rapportait l'analyse d'images réalisée pour caractériser la microarchitecture osseuse à partir d'images IRM et μCT, et les lacunes des ostéocytes évaluées à l'aide de SRμCT. En particulier, il a été rapporté que le processus d'enregistrement identifie deux images (une IRM et une μCT) représentant la même

région d'intérêt de sorte que l'analyse de la microarchitecture soit effectuée dans les mêmes régions fémorales proximales et que l'analyse morphologique soit comparable. De plus, les paramètres microarchitecturaux généralement récupérés dans la littérature ont été analysés, mesurés à l'aide d'une approche optimisée utilisant le logiciel iMorph qui fournit une précision sub-voxel. Un nouveau paramètre d'interconnectivité trabéculaire capable de fournir des informations sur l'adaptabilité osseuse à contraintes provenant de différentes directions est proposé. Enfin, il a été présenté deux techniques rapportées dans la littérature capables de réduire la résolution de l'image dans le post-traitement en divisant chaque pixel d'origine en quatre nouveaux sous-pixels tout en appliquant strictement la conservation de la masse osseuse.

Dans la figure 3.1, il a été présenté un aperçu de cette étude de thèse de doctorat, montrant comment les échantillons collectés ont été répartis entre les différentes études et examens dans le soucis de l'utilisation optimale de la banque d'échantillons pour ce projet de recherche. Dans le chapitre suivant, il est présenté une étude sur le protocole de préparation optimisé pour l'acquisition IRM de grands échantillons cadavériques et en particulier des fémurs proximaux. De plus, on évalue l'effet de la résolution de l'image sur l'évaluation des paramètres microarchitecturaux. L'étude présentée au chapitre 4 visait à valider le protocole de préparation d'échantillons développé pour de grands échantillons d'os cadavériques, et à identifier la limite de résolution d'image nécessaire pour caractériser la microarchitecture interne de l'os.

Chapitre 4 : évaluation de la microarchitecture osseuse dans les fémurs humains cadavériques frais : quelle pourrait être la pertinence clinique de l'IRM à ultra-haut champ ?

Dans ce chapitre, nous avons signalé la nécessité d'effectuer de grandes acquisitions d'images cadavériques pour étudier les difficultés et les potentialités de l'application de la technologie RM sur les os in vivo. Cependant, l'acquisition de gros os cadavériques présente plusieurs problèmes, le plus important est le processus de décomposition responsable de la génération de bulles d'air entre les travées. Les bulles d'air piégées entre les trabécules lors de l'examen par IRM créent des artefacts dus à l'effet de susceptibilité à l'air. Par conséquent, la nécessité de développer un protocole de préparation des échantillons pour réduire les artefacts dus aux bulles d'air est de la plus haute importance. Dans le présent chapitre, il a été présenté un protocole de préparation conçu pour de grands échantillons anatomiques cadavériques et le protocole a été validé à l'aide d'une analyse d'image µCT.

Le deuxième objectif de ce chapitre était d'étudier l'effet de la résolution dans l'analyse d'images de trabécules. Pour ce faire, les images µCT ont été dégradées de

deux à trois fois et les paramètres morphologiques dérivés ont été comparés entre différentes images de résolution et entre techniques (µCT vs. IRM). Cette étude avait un double objectif, le premier était d'individuer la limite de résolution nécessaire pour caractériser la microarchitecture osseuse et le second objectif était d'évaluer si le µCT et l'IRM fournissaient les mêmes informations morphologiques osseuses. L'approche conçue a révélé que l'IRM et le µCT pouvaient être utilisés pour évaluer la microarchitecture osseuse, mais il est important de concevoir les deux techniques d'acquisition d'images pour avoir une taille de pixel dans le plan comprise entre 100 et 150 µm indépendamment de l'épaisseur du pixel.

Enfin, ce chapitre a présenté un nouveau paramètre trabéculaire, à savoir l'interconnectivité trabéculaire, qui décrit la variabilité angulaire autour de la direction trabéculaire principale. Il a été démontré que la Tb.Int est corrélée avec la DMO dérivée de la DXA clinique standard, tandis que tous les autres paramètres morphologiques étudiés ont montré une faible corrélation. Par conséquent, notre hypothèse selon laquelle la microarchitecture osseuse pourrait fournir des informations supplémentaires sur la DMO dans la pratique clinique a été davantage étayée.

L'IRM est un outil puissant pour la quantification de la morphologie des tissus de manière non invasive. Cependant, lorsque la taille du voxel est plus grande que la structure analysée, un flou de volume partiel se produit, ce qui complique la précision des mesures. Des acquisitions à plus haute résolution sont possibles mais aux frais du SNR et ne présentent donc pas une alternative intéressante. Les contraintes de résolution restent l'obstacle majeur au développement de l'IRM comme outil de quantification in-vivo de la microarchitecture osseuse trabéculaire, dans le but final d'augmenter la prédiction du risque de fracture. Comme l'épaisseur trabéculaire (80 - 150 micro ? µm) est généralement inférieure à la taille de voxel réalisable in-vivo (environ 150 m), il est difficile d'obtenir des informations structurelles précises.

Dans le présent travail, parmi les techniques d'amélioration de la résolution d'image applicables au post-traitement présentes dans la littérature, nous avons identifié et testé le traitement sous-voxel (SubVoxel) et l'interpolation remplie de zéro (ZFI) ou interpolation Sinc. Les deux techniques d'amélioration de la résolution ont été appliquées à la fois aux images µCT et IRM de trois fémurs proximaux différents. Les images ont été analysées à l'aide d'iMorph récupérant le BVF, l'épaisseur et l'espacement trabéculaires. Les caractéristiques ont été comparées à celles dérivées des images originales de µCT et d'IRM.

Les images améliorées en résolution µCT ont montré des paramètres morphologiques dans la même gamme que ceux dérivés à l'aide de l'original. En particulier, les erreurs commises sur les paramètres morphologiques étaient toujours inférieures à 8%, les images rehaussées par interpolation Sinc montraient une BVF et une Tb.Th réduites (-4% que la référence µCT) et une Tb.Sp augmentée (+7%). Les

images µCT améliorées à l'aide de la résolution SubVoxel ont montré une augmentation de la BVF (+2 %) et une réduction de la Tb.Th et de la Tb.Sp (-7% et -6% respectivement) par rapport à la référence µCT. Des résultats similaires ont été évalués en comparant les images IRM rehaussées à la référence IRM. Les erreurs commises étaient toujours inférieures à 8%. En particulier, les images IRM améliorées à l'aide de l'interpolation Sinc ont montré une réduction de BVF (-1%) et de Tb.Sp (-3%) et une augmentation de Tb.Th (+5%), tandis que les images améliorées à l'aide de la technique SubVoxel ont montré une augmentation de BVF et Tb.Th (+6% et +4% respectivement) et Tb.Sp réduit (-8%). L'analyse statistique réalisée à l'aide du test T de Student n'a montré aucune différence significative entre les images originales et améliorées en utilisant à la fois les techniques d'interpolation Sinc et de SubVoxel pour toutes les caractéristiques morphologiques analysées.

L'analyse d'image a montré que l'interpolation Sinc et la résolution SubVoxel fournissaient des images deux fois plus grandes que l'original, fournissant ainsi des images avec une demi-dimension de pixel. De plus, les résultats ont montré des erreurs sur le BVF inférieures à 4% et jamais statistiquement différentes des images originales, ce qui signifie que la masse osseuse a été conservée en utilisant les deux techniques à résolution améliorée. Des différences légèrement plus élevées ont été signalées pour les caractéristiques morphologiques telles que Tb.Th et Tb.Sp. En particulier, les erreurs commises absolues à l'aide d'images µCT atteignaient jusqu'à 7 % pour le Tb.Sp récupéré à l'aide d'images µCT interpolées Sinc, tandis qu'en utilisant des images IRM, les erreurs commises absolues atteignaient jusqu'à 8 % pour le Tb.Sp récupéré à l'aide de l'IRM améliorée SubVoxel. Les deux techniques se sont révélées appropriées pour réduire la dimension des pixels tout en conservant la masse osseuse, mais les images améliorées n'ont pas fourni d'informations supplémentaires ni d'informations plus fiables sur la morphologie osseuse, tandis que le temps nécessaire pour obtenir les résultats morphologiques a été quadruplé. Des articles précédents ont montré la possibilité d'améliorer la résolution de l'image en utilisant à la fois les techniques d'interpolation Sinc (Yaroslavsky 2002; Khaire and Shelkikar 2013) et de résolution SubVoxel (Hwang and Wehrli 2002) en rapportant des contours mieux définis. Hwang et al. sur une étude menée à l'aide d'images IRM (137x137x350 µm) de deux rayons a rapporté que l'application de la résolution SubVoxel atténue avec succès le flou de volume partiel dans les images tomographiques de systèmes binaires (Hwang and Wehrli 2002), cependant les paramètres morphologiques ont été obtenus à l'aide d'images qui ont été binarisées à l'aide d'un seuil sélectionné manuellement alors que dans notre cas un seuil local adapté a été utilisé pour la binarisation des images IRM. De plus, l'application de la carte d'ouverture à l'aide d'iMorph est capable de fournir une analyse morphologique utilisant une précision subvoxel qui pourrait également expliquer pourquoi, dans notre cas, les paramètres morphologiques évalués à l'aide de

µCT et d'IRM n'ont pas changé après l'application de techniques d'amélioration de l'image. L'interpolation sinc s'est avérée fournir le même effet de flou que celui rapporté à l'aide de la résolution SubVoxel sur la caractérisation des contours de la structure en utilisant à la fois l'IRM (Puri, n.d.) et la tomodensitométrie (Zoroofi et al. 2003) mais elle a été principalement appliquée pour augmenter la taille des voxels dans les axes z plutôt que dans le plan. Dans notre cas, l'augmentation de la taille des pixels dans le plan à l'aide de l'interpolation Sinc et l'analyse des images à l'aide de la précision subvoxel fournie par la carte d'ouverture n'ont pas montré d'amélioration de l'analyse morphologique des structures osseuses.

L'IRM UHF s'est avérée fournir des images de résolution capables d'acquérir des travées osseuses, cependant une approche optimisée pour l'évaluation de la microarchitecture osseuse est d'un grand intérêt. Par conséquent, le chapitre suivant se concentre sur l'analyse morphologique osseuse de trois fémurs proximaux cadavériques acquis en utilisant différents champs magnétiques principaux (3T vs. 7T) et séquences d'impulsions (TSE vs. GRE) IRM. La comparaison entre les différentes intensités de champ principal de l'IRM et la séquence µCT de référence fournirait la configuration IRM optimale qui pourrait également être appliquée dans la pratique clinique.

Chapitre 5 : validation et optimisation de l'analyse de la microstructure des fémurs proximaux à l'aide d'IRM à haut champ et à ultra-haut champ

Dans ce chapitre, il a été présenté une approche optimisée pour l'évaluation de la microarchitecture osseuse des fémurs proximaux. Il a été montré qu'en utilisant l'IRM UHF les paramètres morphologiques obtenus étaient comparables à ceux dérivés de la référence µCT, cependant ce n'était pas le cas pour l'IRM à 3T. L'effet de séquence a également été exploité, montrant que les séquences TSE sont moins sujettes aux effets de volume partiel et doivent être préférées à celles GRE. Les différentes acquisitions IRM ont été réalisées en réduisant la taille des pixels à la limite de la machine et de la séquence dans un temps d'acquisition applicable in vivo. Le résultat obtenu soutient en outre l'hypothèse selon laquelle pour évaluer les travées osseuses, la résolution de l'image doit être du même ordre que l'épaisseur trabéculaire.

La technologie RM est un domaine en développement dont l'objectif principal est de fournir de meilleurs outils de diagnostic tout en augmentant le confort du patient. Au cours des dernières décennies, les avantages techniques se sont concentrés sur l'augmentation de l'intensité du champ principal de l'IRM jusqu'au nouveau 7T qui a également été lancé pour une utilisation clinique. L'augmentation de l'intensité du

champ principal fournit un SNR plus élevé tout en gardant le temps d'acquisition presque constant et n'affectant donc pas le confort du patient.

Les images précédemment rapportées dans ce manuscrit ont été acquises à l'aide du 7T MAGNETOM (Siemens Healthineers, Allemagne) qui était une machine UHF MR à usage de recherche uniquement. Comme indiqué précédemment, le 7T MAGNETOM a été en mesure d'évaluer la microarchitecture du fémur proximal, présentant toutefois certaines limites, à savoir le nombre d'images acquittables par session de balayage était limité par le dépôt SAR et le temps d'acquisition était à l'extrême limite de l'applicabilité in vivo. Tout récemment, un nouveau scanner UHF MR, le 7T MAGNETOM Terra (Siemens Healthineers, Allemagne) est sorti pour une utilisation clinique. L'application du protocole de numérisation présenté précédemment a montré de grands avantages par rapport au scanner décrit précédemment. Le dépôt SAR sur les patients a été considérablement réduit, permettant l'acquisition d'un nombre accru d'images par un seul balayage (de 10 à 20) ce qui a permis l'acquisition de la quasi-totalité du fémur proximal en une seule séance et le temps d'acquisition a été réduit à 11:59 min conduisant à un temps d'acquisition plus acceptable pour l'applicabilité des patients. Cependant, la qualité de l'image est restée inchangée.

Les avantages techniques qui viennent d'être décrits ont fourni des images IRM d'une qualité comparable à celles d'avant, mais ils ont permis l'acquisition de l'ensemble du fémur proximal en un seul balayage et en utilisant un temps d'acquisition plus acceptable pour les patients. Par conséquent, le confort du patient et l'applicabilité du protocole dans la pratique clinique ont augmenté.

Dans le chapitre suivant, il est présenté une analyse multiéchelle et multimodale de deux cols proximaux du fémur (un ostéoporotique et un sain). Le col fémoral a été choisi car il représente l'une des régions anatomiques les plus touchées par l'ostéoporose et une à haut risque de mortalité. L'analyse multi-échelle décrit la morphologie osseuse de la macro-échelle à la micro-échelle avec l'évaluation de la morphologie et de la distribution des lacunes des ostéocytes. De plus, la qualité osseuse a également été évaluée par une approche multimodale et les propriétés mécaniques trabéculaires ont été évaluées par microindentation tandis que la minéralisation et l'accumulation de carbonate ont été exploitées par FTIR.

Chapitre 6 : imagerie multi-échelle du col fémoral et caractérisation de la qualité des trabécules multimodales d'un sujet sain ostéoporotique et apparié selon l'âge

Dans ce chapitre, il a été montré que l'ostéoporose pouvait avoir un impact différent dans différentes sous-régions proximales du fémur. En particulier, à partir des essais

de micro-indentation, il a été montré que la sous-région FN était la première région avec une augmentation de l'activité de remodelage osseux et donc la sous-région la plus touchée par l'ostéoporose. Enfin, l'analyse qualitative ATR-FTIR des spectres a suggéré une composition chimique comparable entre les sous-régions et quel que soit l'état de santé des os.

Il aurait été intéressant de comparer les propriétés osseuses et les caractéristiques des lacunes des ostéocytes de la phase corticale ostéoporotique et témoin avec les mêmes propriétés dérivées des travées. Cependant, alors que la microindentation et le FTIR dans la phase corticale sont prévus pour les mois suivants, les décalages accordés pour le temps de faisceau au synchrotron ELETTRA, étaient conçus pour évaluer uniquement la phase trabéculaire, laissant un petit temps supplémentaire. Heureusement, dans ce temps supplémentaire, nous avons réussi à évaluer la phase corticale du sujet ostéoporotique, qui a donc été acquise à la fois à 5 et à 0.9 μm^3. L'analyse d'images SRμCT des images acquises à 5 μm^3 a rapporté une épaisseur corticale de la partie supérieure sur le col fémoral de 0.65±0.22 mm qui était dans la même gamme que le Ct.Th dérivé de l'analyse du col fémoral entier à 51 μm^3. De plus, la phase trabéculaire à proximité de la coquille corticale a confirmé les fortes inhomogénéités des trabécules en fonction de leur position dans l'anatomie osseuse. En particulier, comme indiqué dans le tableau 6.4, la phase trabéculaire proche de la coque corticale par rapport à la phase trabéculaire du noyau fémoral central a montré une Tb.Sp réduite (-30%) et une augmentation de la FV (+133%) et de la Tb.Th (+ 27%).

L'analyse d'images réalisée sur les lacunes des ostéocytes corticaux acquis à 0,9 μm^3 a montré quelques différences avec celles issues de la phase trabéculaire. La phase corticale (Fig. 6.12), par rapport à la phase trabéculaire, a montré une densité OL (-18%) et une région d'action (-6%). De plus, alors que l'OL cortical montrait un volume et une surface plus petits (-10% et -9% respectivement), aucune différence statistique n'a été évaluée. Enfin, alors qu'aucune différence n'a été évaluée dans la forme de l'OL intégré dans les trabécules entre le sujet ostéoporotique et le sujet sain, de petites différences (jusqu'à 10 %) ont été évaluées dans les axes principaux et la forme de l'OL (jusqu'à -7% pour b /c) entre la phase corticale et trabéculaire. Cependant, ces différences n'ont jamais été statistiquement significatives.

Dans le chapitre suivant, il est rapporté une étude multiéchelle et multimodale menée sur de petits spécimens (grand trochanter, col fémoral et tête fémorale) extraits de cinq fémurs proximaux (de Sample01 à Sample05). Les échantillons extraits ont d'abord été scannés à l'aide de μCT à 25 μm^3 pour résoudre complètement la morphologie trabéculaire, puis la composition moléculaire de l'hydroxyapatite a été étudiée en effectuant une spectroscopie d'absorption des rayons X du Calcium K-edge. Cette technique a permis de caractériser le rapport calcium/phosphore et de récupérer

des informations qualitatives sur le cristal d'hydroxyapatite afin d'étudier les modifications de la cristallinité de l'HA.

Chapitre 7 : évaluation du risque de fracture dans le fémur proximal basée sur la microarchitecture osseuse et l'investigation de la cristallinité de l'hydroxyapatite : une approche multimodale et multi-échelle

Dans cette étude, il a été caractérisé qualitativement la cristallinité HA dans le réseau trabéculaire de trois sous-régions fémorales proximales différentes en profitant de la spectroscopie d'absorption des rayons X des Ca K-edge à l'échelle micrométrique. Les informations obtenues ont été comparées à la biomécanique et à la morphologie osseuses pour évaluer si les informations fournies augmenteraient la prédictivité de l'évaluation du risque de fracture du fémur proximal. Nos résultats suggèrent qu'aucun changement stoechiométrique dans la composition chimique de l'AH ne peut être associé à la maturation minérale, au site anatomique ou à une maladie (ostéoporose). Cependant, à partir de l'analyse de chaque caractéristique extraite de XAS, il a été montré que bien qu'aucun changement atomique de l'HA ne puisse être associé à l'ostéoporose, des changements pourraient être associés à l'ordre local et à la microarchitecture du cristal HA. Enfin, l'ACP réalisée à l'aide de la DMO de référence clinique et de la morphologie trabéculaire a fourni une séparation claire des échantillons en fonction de leur qualité de santé osseuse, suggérant que la combinaison de ces deux propriétés osseuses pourrait améliorer la fiabilité du diagnostic de l'ostéoporose et l'évaluation du risque de fracture.

Conclusion General

L'ostéoporose est une pathologie osseuse systémique qui est responsable d'exposer à un risque élevé de fracture plus de 300 millions de personnes d'ici 2040. Par conséquent, un diagnostic précoce de l'ostéoporose est de la plus haute importance car cela augmenterait la qualité de vie de nombreux patients. Dans cette étude, il a été présenté une approche optimisée pour le diagnostic de l'ostéoporose qui vise à ajouter la morphologie interne des trabécules à la référence clinique standard, c'est-à-dire la densité minérale osseuse, en utilisant la technologie d'imagerie par résonance magnétique, qui par rapport à la DXA et la qCT représentent une non -alternative invasive et sans rayonnement.

Cette étude a d'abord évalué la possibilité d'acquérir la morphologie des trabécules à l'aide de la technologie d'imagerie par résonance magnétique, montrant que la qualité osseuse et l'effet de l'administration du traitement sur un patient atteint de rhumatisme psoriasique étaient évaluables. Cependant, la même première étude a

également signalé les limites de cette technique d'imagerie où, en raison de la différence entre la résolution de l'image et la dimension des travées, la morphologie interne de l'os n'était pas complètement résolue.

Pour évaluer de manière fiable la qualité osseuse dans des situations saines et pathologiques dans le but d'améliorer le diagnostic in vivo, les études ex vivo de gros os cadavériques sont de la plus haute importance. Le premier problème sur l'étude des gros os cadavériques à l'aide de l'imagerie par résonance magnétique concerne les artefacts de bulles d'air causés par la décomposition osseuse. Dans notre étude, une procédure sous vide capable de remplacer l'inclusion de bulles d'air par une solution saline de Gd-DTPA 1 mM qui imite la réponse magnétique de la moelle osseuse a été conçue et validée par analyse d'images. Ensuite, la limite de résolution d'image qui permettrait de résoudre les travées osseuses a été étudiée, montrant qu'une taille de pixel minimale de 0,150 mm dans le plan est nécessaire pour évaluer les travées osseuses. Fait intéressant, le nouveau paramètre introduit basé sur l'interconnectivité trabéculaire a montré une forte corrélation avec la charge de fracture, prouvant que l'organisation structurelle et les paramètres morphologiques pouvaient fournir des informations supplémentaires, plutôt qu'analogues, à la DMO clinique standard pour une vue plus complète de l'état de santé et de la qualité des os. Une fois déterminée la taille de pixel minimale pour acquérir la morphologie trabéculaire, le deuxième problème d'investigation était d'identifier l'intensité du champ IRM et la séquence d'impulsions qui différencient mieux les phases osseuses et médullaires. Par conséquent, l'intensité de champ et la séquence d'impulsions caractérisées par une sensibilité réduite aux effets de volume partiel et à l'élargissement induit par la susceptibilité des travées ont été étudiées en utilisant différentes intensités de champ IRM (3T vs 7T) et des séquences d'impulsions (GRE vs TSE). Les résultats ont montré qu'en utilisant la séquence TSE à l'IRM 7T, les paramètres morphologiques acquis étaient comparables à ceux dérivés de l'étalon-or μCT. Par conséquent, une approche optimisée pour l'évaluation morphologique osseuse a été proposée.

Attesté que la morphologie osseuse pourrait être évaluée et fournir des informations supplémentaires à la DMO clinique, et donc pourrait améliorer le diagnostic et la prédiction du risque de fracture. Les modifications osseuses liées à l'ostéoporose à des échelles inférieures (micro-, nano- et moléculaire) ont été abordées. Il est intéressant de noter que l'analyse menée sur les lacunes des ostéocytes de la trabécule et les propriétés mécaniques du col fémoral n'ont montré aucun changement en fonction de l'état clinique de l'os. Cependant, nos résultats ont montré que le col fémoral entraînait une sous-région proximale du fémur fortement affectée par l'ostéoporose avec un processus de remodelage osseux accru par rapport à la tête fémorale et au grand trochanter, confirmant la fréquence plus élevée de fractures de fragilité dans la FN par rapport à la FH et la GT. De plus, l'étude moléculaire a montré

qu'aucun changement stoechiométrique dans la composition chimique de l'HA ne pouvait être associé à la maturation minérale, au site anatomique ou à l'ostéoporose, tandis que les changements dans l'HA pouvaient être associés à l'ordre cristallin et à la microarchitecture de l'HA. De plus, l'analyse en composantes principales menée sur les trois sous-régions fémorales proximales différentes de 5 sujets a montré que les sous-régions FN saines migraient toujours en fonction de l'ostéoporose. Enfin, l'ACP réalisée à l'aide de paramètres BMD et morphologiques a montré une séparation claire des échantillons basée sur la qualité de la santé osseuse, confirmant que la combinaison de ces deux propriétés osseuses pourrait améliorer la fiabilité du diagnostic de l'ostéoporose et l'évaluation du risque de fracture.

Pour mieux comprendre les implications des changements nanométriques et moléculaires de l'HA dus à l'ostéoporose, des études futures pourraient aborder les propriétés structurelles des plaquettes minérales osseuses et des fibrilles de collagène à l'échelle nanométrique et la composition chimique de l'HA. Les propriétés structurelles des plaquettes minérales osseuses et des fibrilles de collagène ont pu être évaluées à l'aide des techniques de diffusion synchrotron aux petits angles des rayons X (SAXS) et de diffraction des rayons X aux grands angles (WAXD). De plus, la composition chimique de l'HA et l'influence possible de différents substituts dans le processus de remodelage osseux pourraient être évaluées à l'aide de la spectroscopie d'absorption atomique (AAS) qui est une technique analytique utilisée pour la détermination quantitative et qualitative des ions métalliques en solution. Les travaux futurs pourraient également augmenter la population de l'échantillon en répartissant les échantillons en fonction de la qualité osseuse et du sexe des patients, et prendre en compte à la fois la phase corticale osseuse et trabéculaire. Enfin, comme présenté au chapitre 1.4, des techniques d'IRM prometteuses pourraient être utilisées pour évaluer de manière non invasive et in vivo la quantification de la graisse de la moelle osseuse, la composition minérale osseuse, l'eau liée et interstitielle, et la quantification de la susceptibilité magnétique, fournissant des informations sur l'os, la santé, la qualité et l'activité métabolique.

Pour conclure, dans cette thèse, le pouvoir diagnostic de l'ostéoporose dans les segments osseux profonds, comme le fémur proximal, a été augmenté en ajoutant à la référence clinique dérivée de la DXA-DMO, la morphologie interne de l'os évaluée à l'aide d'une approche d'imagerie IRM optimisée, une technologie clinique in vivo et non invasive. De plus, l'analyse du fémur proximal à des échelles d'investigation inférieures a montré que le col fémoral est la première région fémorale proximale touchée par l'ostéoporose et avec une activité de remodelage osseux accrue, et donc la plus probablement exposée aux fractures de fragilité. Enfin, l'activité de remodelage osseux altérée devrait être liée à des changements dans l'ordre et la microarchitecture des cristaux de HA plutôt qu'à la composition chimique.

List of Figures

Figure I. 1: overview and timeline of the sample collection and acquisition performed. "MRI" refers to magnetic resonance imaging, "μCT" refers to industrial X-ray computed tomography, "SRμCT" refers to synchrotron radiation X-ray computed tomography, "XAS" refers to X-ray absorption spectroscopy, "FTIR" refers to Fourier transform infrared, "GT" refers to great trochanter, "FN" refers to femoral neck and "FH" refers to femoral head. 16

Figure 1. 1: Bone Structure. 22
Figure 1. 2: Bone hierarchical structure. 23
Figure 1. 3: Trabecular and cortical bone. 24
Figure 1. 4: (left) Osteocytes network and canaliculi scheme, (right) 3D rendering of the osteocyte network organized around a Haversian canal (reproduced from Med. Phys. 39 (4), April 2012). 26
Figure 1. 5: Collagen fiber structure. 28
Figure 1. 6: (left) Hydroxyapatite (HA) molecular structure, (right) HA type A and B substitutes. 29
Figure 1. 7: Comparison between MRI and CT. (first row) MR images of in vivo distal tibia acquired using gradient echo sequence at 7T MRI (a) (0.156×0.156×0.5 mm) and 3T MRI (b) (0.156×0.156×0.5 mm), and compared with high-resolution peripheral computed tomography (HR-pQCT) (c) (0.082 mm^3) (reproduced from J. of Mag. Res. Im. 27:854–859 (2008)). (second row) MR images of cadaveric proximal femur acquired using turbo spin echo sequence at 7T MRI (d) (0.13×0.13×1.5 mm) and 3T MRI (e) (0.21×0.21×1.1 mm), and compared with μCT (f) (0.051 mm^3). Note that using MRI, the trabecular bone appears black and bone marrow delivers the bright signal whereas for HR-pQCT and μCT the trabecular bone is shown bright. Additionally, note that the trabecular network is clearly more enhanced at 7T compared to 3T. 48
Figure 1. 8: Solid state MRI and quantitative susceptibility mapping. (first row) Maps of bone mineral ^{31}P density, and bound water density (second row) in central slices of 4 human tibial cortical bone specimens. Age and gender of bone specimen donors are indicated. Bone mineral ^{31}P and bound water ^{1}H densities are markedly lower in bones from elderly female donors than from younger females or males. ^{31}P maps also suffer from increased point spread function blurring because of the lower

gyromagnetic ratio and shorter T2* of ^{31}P. (reproduced from NMR Biomed. 27: 739–748 (2014)) (third row) (a) QSM map obtained through Cones 3D UTE-MRI scans (0.5×0.5×2 mm voxel size) of a tibial midshaft cortical bone (45-year-old female), (b) one μCT slice at 9 μm isotropic voxel size, (c) μCT-based porosity, and (d) BMD map of the same specimen. Local maxima in the QSM map correspond to high BMD regions and low porosity values in μCT-based maps (reproduced from Magn. Res. Im. 62: 104–110 (2019)). 58
Figure 1. 9: Factors leading to bone fractures. 62

Figure 2. 1: merged PET-UHF MRI. Sagittal, coronal, and axial plane of merged PET-UHF MRI of the knee articulation of the patient before (A) and after (B) treatment by TNF-antibodies. "[Ad]" refers to a dimensional. Values higher or equal to 2.5 are considered indicative of "hypermetabolic" activity. 70
Figure 2. 2: ROIs identification. PsA patient after treatment BVF maps showing the multiple ROIs identified in red. 71
Figure 2. 3: ROI1a extrapolated features box plot. Box plot for each extrapolated feature for the control reference (Healthy), patient before (P_before) and after (P_after) one year of anti-TNFα treatment in the trabecular region where the quadricep tendon attaches the patella (ROI1a). 75
Figure 2. 4: Bone Morphology characterization. Trabecular thickness and spacing of the PsA patient's patella before and after one year of anti-TNF treatment. 81

Figure 3. 1: Schematic representation of the different femurs and sample used in all the experimental setups and examination performed. 85
Figure 3. 2: Sample preparation. a) unfrozen femur head. b) cylindric plastic jar filled by 1mM Gd-DTPA saline solution. c) 3D-printed tool used for 3D volumes registration. d) vacuum pump. e) vibrating surfaces. 88
Figure 3. 3: Small sample extraction and conservation. a) core drilled from the proximal femur, b) extracted trabecular disks, c) and d) trabecular disks stored in sample holder for further experiments. 89
Figure 3. 4: Proximal femur coronal plane acquired using (a) 7T turbo spin echo MRI, and (b) 7T gradient re-called echo MRI. 91
Figure 3. 5: X-ray microtomography setup. 93
Figure 3. 6: Large femur biomechanical fracture test setup. 94
Figure 3. 7: X-ray synchrotron microtomography setup at the SYRMEP (SYnchrotron Radiation for MEdical Physics) beamline (Basovizza [Trieste], Italy). 96
Figure 3. 8: Microindentation test setup. 98

Figure 3. 9: X-ray absorption spectroscopy setup at CLÆSS (Core Level Absorption & Emission Spectroscopies) beamline of the ALBA Synchrotron (Barcelona, Spain). 100
Figure 3. 10: X-ray absorption spectroscopy of Calcium K-edge showing both the X-ray absorption near-edge spectroscopy (XANES) and extended X-ray absorption fine-structure spectroscopy (EXAFS) regions. 101
Figure 3. 11: X-ray absorption spectroscopy spectrum. a) Spectrum after positioning of the pre- and post-edge lines, b) spectrum after normalization and before deglitching, c) final XAS normalized spectrum, ready to be analyzed. 105
Figure 3. 12: Kernel density estimation of the derived features at CLÆSS beamline of the ALBA Synchrotron. 106
Figure 3. 13: Infrared Spectroscopy. a) Fourier Transform Infra-Red (FTIR) spectroscopy setup and b) FTIR spectra of bone sample showing principal tissue components and corresponding wavelength positions. 107
Figure 3. 14: Registration workflow. 110
Figure 3. 15: Preprocessing and elaboration steps for the microarchitecture characteristics assessment. 113
Figure 3. 16: Workflow for numerical bone mineral density estimation. 114
Figure 3. 17: Sinc Interpolation workflow. 116
Figure 3. 18: Synchrotron radiation X-ray micro computed tomography at 0.9 μm^3. (first column) Bone solid phase in the field of view, (second column) osteocytes lacunae distribution embedded in the bone solid phase and (third column) osteocytes lacunae network, where the red dots are the barycenter of the ellipsoid inscribed in the osteocytes lacunae and the white lines shows their connectivity (Delaunay graph that is the Voronoi graph dual) between osteocytes lacunae. 118

Figure 4. 1: Sample one same coronal plane before and after bubble removing. Sample05 (S05) same coronal plane for 3T MRI images (0.21x0.21x1.1 mm) before (left) and after (right) the application of air bubble reduction protocol. 124
Figure 4. 2: Sample preparation setup. First Fresh sample (S05) preparation. a.(left) unfrozen femur head. b.(middle) cylindric plastic jar filled by 1mM Gd-DTPA saline solution with 3D-printed tool (bottom left) used for 3D volumes registration. c. (Right) vacuum pump and vibrating surfaces. 126
Figure 4. 3: Same coronal µCT plane before and after sample preparation. Same S05 µCT coronal plane before (left) and after (right) the application of our sample preparation technique and acquired at 0.051 mm isovolumetric resolution. 127
Figure 4. 4: 7TMRI - µCT image registration. (left) 7T MR image, (center) µCT - 7T MRI best registration with highlighted ROI, (right) correlation score of one 7T MR image with a stack of 60 consecutive µCT images of the first analyzed sample (S05). 130

Figure 4. 5: Trabecular orientation quantification. (left) S05 µCT orientation map of the segmented bone phase. (center) µCT local orientation at pixel level. (right) Trabeculae orientation distribution expressed between 0 and 180 degrees obtained from all bone pixels - purple (µCT) - light blue (7T MRI), and gaussian curve fitting - black (µCT) - blue line (7T MRI). 131
Figure 4. 6: Resolution effect on the Sample05 morphology quantification. Box plot for S05 bone volume fraction, trabecular thickness, spacing, number, principal and secondary orientation, and trabecular interconnectivity for the reference value of the µCT, the degraded µCT at 2 (degµCT2) and 3 (degµCT3) times the original µCT spatial resolution, and the 7T turbo spin echo (TSE) MRI. 135
Figure 4. 7: Reproducibility analysis: µCT – 7T MRI linear regression. Linear regression between 7T MRI and reference µCT for bone volume fraction, trabecular thickness, spacing, number principal and secondary orientation, and trabecular interconnectivity for each of the 3 images of S05 '●', S06 '▲' and S07 '■'. – Each graph shows the slope, the coefficient of determination (R^2), the p-values (p-value<0.01 stands for representative feature and the degree of confidence (±2SD). 137
Figure 4. 8: Linear regression between DXA derived BMD and trabecular interconnectivity. Linear regression between DXA derived bone mineral density (BMD) and trabecular interconnectivity for µCT (left) and 7T MRI (right). – Each graph shows the slope, the coefficient of determination (R^2) and the degree of confidence (±2SD). 140

Figure 5. 1: Available characteristics from each imaging modality with their corresponding strength (+) and weaknesses (-). 150
Figure 5. 2: Registration workflow. 154
Figure 5. 3: Preprocessing and elaboration steps for the microarchitecture characteristics assessment. 156
Figure 5. 4: Workflow for bone mineral density estimation. 158
Figure 5. 5: (a–d) S05 best registration for the four different MRI acquisitions with µCT; (e–h) corresponding NCC efficiency profile. 159
Figure 5. 6: (a–e) S05 same coronal planes of the (a) µCT and four different MRI acquisitions ((b) 7T TSE, (c) 7T GRE, (d) 3T TSE and (e) 3T GRE). The red square identify the ROI extrapolated from all the registered images. (f–j) Corresponding ROI binarized (automatic local thresholding with a window size of 10×10 pixels). 160
Figure 5. 7: Data shows mean and SD of, respectively, BVF: bone volume fraction, Tb.Th: trabecular thickness, Tb.Sp: trabecular spacing, Tb.N: trabecular number, Tb.OrP: principal trabecular orientation, Tb.OrS: secondary trabecular orientation

and Tb.Int: trabecular interconnectivity of the three analyzed samples S05 '●', S06 '■' and S07 '▲' scanned with different scanners (μCT and MRI), field strengths (3T and 7T), sequences (TSE and GRE) and resolution. 162
Figure 5. 8: Linear regression between BMD calculated using standard DXA and all morphological parameters ((a-c) BVF, (d-f) Tb.Th, (g-i) Tb.Sp, (j-l) Tb.N, (m-o) Tb.OrP, (p-r) Tb.OrP, (s-u) Tb.Int) derived from μCT (left), 7T TSE MR (middle) and 7T GRE MR (right) images. "BVF" refers to bone volume fraction, "Tb.Th" refers to trabecular thickness, "Tb.Sp" refers to trabecular spacing, "Tb.N" refers to trabecular number, "Tb.OrP" refers to principal trabecula orientation, "Tb.OrS" refers to secondary trabecular orientation, "Tb.Int" refers to trabecular interconnectivity. 165
Figure 5. 9: Linear regression between BMD calculated using standard DXA analysis and BMD derived using (a) μCT 3D approach, (b) μCT 2D approach, (c) TSE 2D approach and (d) GRE 2D approach. 166
Figure 5. 10: Linear regression between fracture load and trabecular spacing (a-c) and trabecular interconnectivity (d-f) derived from μCT images (left), 7T TSE (middle) and 7T GRE (right) 167

Figure 6. 1: Sample extraction and preparation. a) localization of the three different bone regions extracted from each proximal femur, "GT" refers to great trochanter, "FN" refers to femoral neck and "FH" refers to femoral head; b) trabecular sample stored in the designed sample holder after sample preparation protocol; c) microscopic investigation of the preparation protocol efficacy before microindentation essays. 181
Figure 6. 2: multiscale characterization of femoral neck morphology acquired using μCT (51 μm^3) and SRμCT (5 and 0.9 μm^3). a) Proximal femur coronal plane acquired using μCT at 51 μm^3 showing the femoral neck ROI (orange rectangle) used to assess clinical standard bone mineral density using dual-energy X-ray absorptiometry; b) whole femoral neck acquired using μCT at 51 μm^3; c) central core of the femoral neck trabecular phase scanned using SRμCT at 5 μm^3; d) single trabecula acquired using SRμCT at 0.9 μm^3; e) osteocytes lacunae distribution and f) osteocytes lacune network. 184
Figure 6. 3: Trabeculae micro indentation. a) manually placed indents locations for each selected trabecula, b) indentation trapezoidal loading profile, c) stress-strain plot showing a single load–unload cycle, d) indented area and e) view of a single indent at original magnification x100. 186
Figure 6. 4: 3D morphology of the whole femoral neck acquired using μCT at 51 μm^3. 188

Figure 6. 5: 3D morphology of the osteoporotic and control femoral necks acquired using µCT at 51 µm^3 showing the cortical and trabecular phase alone (first row) and bone thickness (second row). 189
Figure 6. 6 : 3D morphology and trabecular thickness of the femoral neck central core acquired using SRµCT at 5 µm^3 of both the control and the osteoporotic subject. 189
Figure 6. 7: osteocytes lacunae characteristics. The mean values and the SD are reported for each investigated region where "OsteopS" refers to osteoporotic sample and regions are marked with "●" while "Control" refers to the healthy subject and is marked as "▲". "OL" refers to Osteocytes lacunae. 192
Figure 6. 8: Distribution of the individuated pores in the bone solid phase. Red bar shows the pores smaller than 73 µm^3 classified as noise and re-added to the solid phase and the pores bigger than 100µm^3 classified as blood vessels. The light blue square indicate the pore volumes classified as osteocytes lacunae (OL). 193
Figure 6. 9: Whisker plot of elastic modulus (Es) (a) and hardness (H) (b) obtained using microindentation on trabecular bone specimens. (a) Representation of intra-group variation of elastic modulus. On the left are presented the differences between the three ROIs in the control subject and on the right the differences for the osteoporotic subject. (b) Representation of intra-group variation of hardness. On the left are presented the differences between the three ROIs in the control subject and on the right the differences for the osteoporotic subject. * represent the variability between different region of the same group (intra-group) *$p < 0.05$, **$p < 0.01$ and **** $p < 0.0001$. † represent the variability between same regions of different group (inter-group) †$p < 0.05$, ††$p < 0.01$ and †††† $p < 0.0001$. 195
Figure 6. 10: ATR-FTIR spectra of the whole set of subjects and subregions. "OsteopS" refers to osteoporotic sample (S08); "Healthy Ref" refers to a refence sample of a healthy 61 years old male; "FH" refers to femoral head, "FN" refers to femoral neck; "GT" refers to great trochanter. (b) focus in the carbonated group region (1300-1600 cm^{-1}). 196
Figure 6. 11: ATR-FTIR spectra focus in the carbonated group region (1300-1600 cm^{-1}). 197
Figure 6. 12: SRµCT at 0.9 µm^3 of the cortical phase of the femoral neck. a) Cortical morphology with embedded colored osteocytes lacunae (OL), b) OL distribution, c) OL network and d) OL aperture map. 206

Figure 7. 1: Small sample extraction and conservation. a) core drilled from the proximal femur, b) extracted trabecular disks, c) and d) trabecular disks stored in sample holder for further experiments. 214

Figure 7. 2: Linear regression of DXA derive bone mineral density (BMD) and yielding strain (σSN) of all the samples (S) together (black dotted line) and of the female subgroup alone (dashed line). 219
Figure 7. 3: Trabecular network morphology (left) and thickness (Tb.Th) (right) of respectively the female healthy (S5) (first row) and osteoporotic (S4) (second row) proximal femur head..... 220
Figure 7. 4: Linear regression showing the coefficient of determination (R^2) between DXA derive-BMD in the femoral neck (FN) and morphological parameters derived in the FN (first row), and between DXA derive-BMD in the whole proximal femur (WPF) and morphological parameters derived in the femoral head (FN) (second row). S: Sample; BMD: bone mineral density; BVF: bone volume fraction; Tb.Th: trabecular thickness; Tb.Sp: trabecular Spacing; Tb.N: trabecular number; Ad: a dimensional. 221
Figure 7. 5: X-ray absorption spectroscopy investigation of healthy (S5) and osteoporotic (OsteoP, S2) femoral neck (FN) comparing all the derived characteristics. Calcium concentration (first row); Pre-peak intensity (second row); the distance, R, between Calcium and Oxygens (third line); the Calcium structure order descripted by the ss2 (forth row); and the MapRatio, which expresses the Ca/P ratio (fifth row). 224
Figure 7. 6: variance of the spectra calculated between 4000 and 4200 eV of each Sample and subregion. FH: femoral head, FN: femoral neck, and GT: great trochanter... 224
Figure 7. 7: Z-scores calculated for each XAS characteristic and subregion for all the investigated Samples (S) with respect to the healthy female (S5). Ig: pre-peak intensity; R: distance between Calcium and Oxygens; ss2: Calcium structure order; and MapRatio: ratio between Calcium and Phosphorous..... 225
Figure 7. 8: Principal component analysis (PCA) of biomechanical, morphological and XAS parameters of control (S1 and S5) and osteoporotic (S2, S3 and S4) bone samples. Individuals are represented by dots and colored by sample. Variables are represented by arrows and colored by technique. The length of the arrows indicates the strength of the correlation of respective parameter with the samples. The graphs below show the contribution and the cos2 of each variable in each dimension as well as the percentage of variability contained in each dimension. 227
Figure 7. 9: Principal component analysis (PCA) of biomechanical and morphological parameters of control (S1 and S5) and osteoporotic (S2, S3 and S4) bone samples. Individuals are represented by dots and colored by sample. Variables are represented by arrows and colored by technique. The length of the arrows indicates the strength of the correlation of respective parameter with the samples. The graphs below show the contribution and the cos2 of each variable in each dimension as well as the percentage of variability contained in each dimension. 228

Figure 7. 10: Principal component analysis (PCA) of biomechanical and XAS parameters of control (S1 and S5) and osteoporotic (S2, S3 and S4) bone samples. Individuals are represented by dots and colored by sample. Variables are represented by arrows and colored by technique. The length of the arrows indicates the strength of the correlation of respective parameter with the samples. The graphs below show the contribution and the cos2 of each variable in each dimension as well as the percentage of variability contained in each dimension. 229
Figure 7. 11: Principal component analysis (PCA) of morphological and XAS parameters of control (S1 and S5) and osteoporotic (S2, S3 and S4) bone samples. Individuals are represented by dots and colored by sample. Variables are represented by arrows and colored by technique. The length of the arrows indicates the strength of the correlation of respective parameter with the samples. The graphs below show the contribution and the cos2 of each variable in each dimension as well as the percentage of variability contained in each dimension. 230
Figure 7. 12: Principal component analysis (PCA) of only biomechanical parameters of control (S1 and S5) and osteoporotic (S2, S3 and S4) bone samples. Individuals are represented by dots and colored by sample. Variables are represented by arrows and colored by technique. The length of the arrows indicates the strength of the correlation of respective parameter with the samples. The graphs below show the contribution and the cos2 of each variable in each dimension as well as the percentage of variability contained in each dimension. 231
Figure 7. 13: Principal component analysis (PCA) of only morphological parameters of control (S1 and S5) and osteoporotic (S2, S3 and S4) bone samples. Individuals are represented by dots and colored by sample. Variables are represented by arrows and colored by technique. The length of the arrows indicates the strength of the correlation of respective parameter with the samples. The graphs below show the contribution and the cos2 of each variable in each dimension as well as the percentage of variability contained in each dimension. 232
Figure 7. 14: Principal component analysis (PCA) of only XAS parameters of control (S1 and S5) and osteoporotic (S2, S3 and S4) bone samples. Individuals are represented by dots and colored by sample. Variables are represented by arrows and colored by technique. The length of the arrows indicates the strength of the correlation of respective parameter with the samples. The graphs below show the contribution and the cos2 of each variable in each dimension as well as the percentage of variability contained in each dimension. 233
Figure 7. 15: Principal component analysis (PCA) of DXA derived-BMD providing the clinical standard and morphological parameters of control (S1 and S5) and osteoporotic (S2, S3 and S4) bone samples. Individuals are represented by dots and colored by sample. Variables are represented by arrows and colored by technique.

The length of the arrows indicates the strength of the correlation of respective parameter with the samples. The graphs below show the contribution and the cos2 of each variable in each dimension as well as the percentage of variability contained in each dimension. 234

List of Tables

Table 1. 1 : List of the main magnetic resonance imaging (MRI) parameters and sequences. 41

Table 2. 1: SUV results before and after treatment for all identified ROIs..... 73
Table 2. 2: Microarchitecture characteristics per ROI. 74

Table 3. 1: Description of the collected samples. 86
Table 3. 2: List of main parameters used for MRI acquisitions..... 90

Table 4. 1: Air bubbles reduction. 128
Table 4. 2: Morphological characteristics between registered µCT – 7T MR images. 133

Table 5. 1: List of main parameters used for MRI acquisitions..... 152
Table 5. 2: S05 normalized cross-correlation (NCC) scores and ΔIm, the number between two consecutive best registered µCT images used to evaluate the registration efficiency for the four stacks of MRI images. 159
Table 5. 3: Morphological characteristics between registered µCT—7T MR images. 161

Table 6. 1: Sample description. 180
Table 6. 2: Femoral neck morphological characteristics. 190
Table 6. 3: morphometric parameters of osteocytes lacunae (OL). 191
Table 6. 4: morphometric parameters of osteocytes lacunae (OL) of the trabecular and cortical phase of the osteoporotic subject..... 206

Table 7. 1: Description of the samples. 213
Table 7. 2: Spectroscopic results of each sample (S) and samples subregions..... 222

Bibliography

Aarle, Wim van, Willem Jan Palenstijn, Jan De Beenhouwer, Thomas Altantzis, Sara Bals, K. Joost Batenburg, and Jan Sijbers. 2015. 'The ASTRA Toolbox: A Platform for Advanced Algorithm Development in Electron Tomography'. *Ultramicroscopy* 157 (October): 35–47. https://doi.org/10.1016/j.ultramic.2015.05.002.

Abdalrahaman, N., C. McComb, J.E. Foster, R.S. Lindsay, R. Drummond, G.A. McKay, C.G. Perry, and S.F. Ahmed. 2017. 'The Relationship between Adiposity, Bone Density and Microarchitecture Is Maintained in Young Women Irrespective of Diabetes Status'. *Clinical Endocrinology* 87 (4): 327–35. https://doi.org/10.1111/cen.13410.

Abdulaal, O M. n.d. 'Evaluation of Optimised 3D Turbo Spin Echo and Gradient Echo MR Pulse Sequences of the Knee at 3T and 1.5T', 9.

Adams, Judith E. 2009. 'Quantitative Computed Tomography'. *European Journal of Radiology* 71 (3): 415–24. https://doi.org/10.1016/j.ejrad.2009.04.074.

Agten, Christoph A, Stephen Honig, Punam K Saha, Ravinder Regatte, and Gregory Chang. 2018. 'Subchondral Bone Microarchitecture Analysis in the Proximal Tibia at 7-T MRI'. *Acta Radiologica* 59 (6): 716–22. https://doi.org/10.1177/0284185117732098.

Albano, Domenico, Raffaele Giubbini, and Francesco Bertagna. 2018. '18F-FDG PET/CT in Splenic Marginal Zone Lymphoma'. *Abdominal Radiology* 43 (10): 2721–27. https://doi.org/10.1007/s00261-018-1542-z.

Alexander, Benjamin, Tyrone L. Daulton, Guy M. Genin, Justin Lipner, Jill D. Pasteris, Brigitte Wopenka, and Stavros Thomopoulos. 2012. 'The Nanometre-Scale Physiology of Bone: Steric Modelling and Scanning Transmission Electron Microscopy of Collagen–Mineral Structure'. *Journal of The Royal Society Interface* 9 (73): 1774–86. https://doi.org/10.1098/rsif.2011.0880.

Alford, Andrea I., Kenneth M. Kozloff, and Kurt D. Hankenson. 2015. 'Extracellular Matrix Networks in Bone Remodeling'. *The International Journal of Biochemistry & Cell Biology* 65 (August): 20–31. https://doi.org/10.1016/j.biocel.2015.05.008.

Andronache, Adrian, Philippe Cattin, and Gábor Székely. 2006. 'Local Intensity Mapping for Hierarchical Non-Rigid Registration of Multi-Modal Images Using the Cross-Correlation Coefficient'. In *Biomedical Image Registration*, edited by Josien P. W. Pluim, Boštjan Likar, and Frans A. Gerritsen, 4057:26–33. Lecture Notes in Computer Science. Berlin, Heidelberg: Springer Berlin Heidelberg. https://doi.org/10.1007/11784012_4.

Appelman-Dijkstra, Natasha M., and Socrates E. Papapoulos. 2018. 'Paget's Disease of Bone'. *Best Practice & Research Clinical Endocrinology & Metabolism* 32 (5): 657–68. https://doi.org/10.1016/j.beem.2018.05.005.

Aprovitola, Andrea, and Luigi Gallo. 2016. 'Knee Bone Segmentation from MRI: A Classification and Literature Review'. *Biocybernetics and Biomedical Engineering* 36 (2): 437–49. https://doi.org/10.1016/j.bbe.2015.12.007.

Arcocha, M. de, H. Portilla-Quattrociocchi, P. Medina-Quiroz, and J.M. Carril. 2012. 'Estado Actual Del Uso Del (18F)Fluoruro Sódico En La Patología Ósea'. *Revista Española de Medicina Nuclear e Imagen Molecular* 31 (1): 51–57. https://doi.org/10.1016/j.remn.2011.05.008.

Arokoski, Merja H., Jari P.A. Arokoski, Pauli Vainio, Lea H. Niemitukia, Heikki Kröger, and Jukka S. Jurvelin. 2002a. 'Comparison of DXA and MRI Methods for Interpreting Femoral Neck Bone Mineral Density'. *Journal of Clinical Densitometry* 5 (3): 289–96. https://doi.org/10.1385/JCD:5:3:289.

———. 2002b. 'Comparison of DXA and MRI Methods for Interpreting Femoral Neck Bone Mineral Density'. *Journal of Clinical Densitometry* 5 (3): 289–96. https://doi.org/10.1385/JCD:5:3:289.

Arsigny, Vincent, Olivier Commowick, Nicholas Ayache, and Xavier Pennec. 2009. 'A Fast and Log-Euclidean Polyaffine Framework for Locally Linear Registration'. *Journal of Mathematical Imaging and Vision* 33 (2): 222–38. https://doi.org/10.1007/s10851-008-0135-9.

Ascenzi, A., E. Bonucci, P. Generali, A. Ripamonti, and N. Roveri. 1979. 'Orientation of Apatite in Single Osteon Samples as Studied by Pole Figures'. *Calcified Tissue International* 29 (1): 101–5. https://doi.org/10.1007/BF02408064.

Ashinsky, Beth G., Kenneth W. Fishbein, Erin M. Carter, Ping-Chang Lin, Nancy Pleshko, Cathleen L. Raggio, and Richard G. Spencer. 2016. 'Multiparametric Classification of Skin from Osteogenesis Imperfecta Patients and Controls by Quantitative Magnetic Resonance Microimaging'. Edited by Kewei Chen. *PLOS ONE* 11 (7): e0157891. https://doi.org/10.1371/journal.pone.0157891.

Ashique, A.M., L.S. Hart, C.D.L. Thomas, J.G. Clement, P. Pivonka, Y. Carter, D.D. Mousseau, and D.M.L. Cooper. 2017. 'Lacunar-Canalicular Network in Femoral Cortical Bone Is Reduced in Aged Women and Is Predominantly Due to a Loss of Canalicular Porosity'. *Bone Reports* 7 (December): 9–16. https://doi.org/10.1016/j.bonr.2017.06.002.

Attia, Enas A. S., Ayman Khafagy, Sameh Abdel-Raheem, Sahar Fathi, and Abeer A. Saad. 2011. 'Assessment of Osteoporosis in Psoriasis with and without Arthritis: Correlation with Disease Severity: Assessment of Osteoporosis in Psoriasis'. *International Journal of Dermatology* 50 (1): 30–35. https://doi.org/10.1111/j.1365-4632.2010.04600.x.

Baker, D.R., L. Mancini, M. Polacci, M.D. Higgins, G.A.R. Gualda, R.J. Hill, and M.L. Rivers. 2012. 'An Introduction to the Application of X-Ray Microtomography to the Three-Dimensional Study of Igneous Rocks'. *Lithos* 148 (September): 262–76. https://doi.org/10.1016/j.lithos.2012.06.008.

Bandirali, Michele, Giovanni Di Leo, Giacomo Davide Edoardo Papini, Carmelo Messina, Luca Maria Sconfienza, Fabio Massimo Ulivieri, and Francesco Sardanelli. n.d. 'A New Diagnostic Score to Detect Osteoporosis in Patients Undergoing Lumbar Spine MRI'. *Eur Radiol*, 9.

Bartl, Reiner, and Christoph Bartl. 2017. 'Corticosteroid-Induced Osteoporosis'. In *Bone Disorders*, by Reiner Bartl and Christoph Bartl, 431–34. Cham: Springer International Publishing. https://doi.org/10.1007/978-3-319-29182-6_78.

Baum, Thomas, Samuel P. Yap, Michael Dieckmeyer, Stefan Ruschke, Holger Eggers, Hendrik Kooijman, Ernst J. Rummeny, Jan S. Bauer, and Dimitrios C. Karampinos. 2015. 'Assessment of Whole Spine Vertebral Bone Marrow Fat Using Chemical Shift-

Encoding Based Water-Fat MRI: Whole Spine Water-Fat Imaging'. *Journal of Magnetic Resonance Imaging* 42 (4): 1018–23. https://doi.org/10.1002/jmri.24854.

Bazin, Dominique, Arnaud Dessombz, Christelle Nguyen, Hang Korng Ea, Frédéric Lioté, John Rehr, Christine Chappard, et al. 2014. 'The Status of Strontium in Biological Apatites: An XANES/EXAFS Investigation'. *Journal of Synchrotron Radiation* 21 (1): 136–42. https://doi.org/10.1107/S1600577513023771.

Bembey, A. K., M. L. Oyen, A. J. Bushby, and A. Boyde. 2006. 'Viscoelastic Properties of Bone as a Function of Hydration State Determined by Nanoindentation'. *Philosophical Magazine* 86 (33–35): 5691–5703. https://doi.org/10.1080/14786430600660864.

Bendtzen, Klaus. 2015. 'Immunogenicity of Anti-TNF-α Biotherapies: I. Individualized Medicine Based on Immunopharmacological Evidence'. *Frontiers in Immunology* 6 (April). https://doi.org/10.3389/fimmu.2015.00152.

Benouali, A.-H., L. Froyen, T. Dillard, S. Forest, and F. N'guyen. 2005. 'Investigation on the Influence of Cell Shape Anisotropy on the Mechanical Performance of Closed Cell Aluminium Foams Using Micro-Computed Tomography'. *Journal of Materials Science* 40 (22): 5801–11. https://doi.org/10.1007/s10853-005-4994-9.

Blake, Glen M., So-Jin Park-Holohan, and Ignac Fogelman. 2002. 'Quantitative Studies of Bone in Postmenopausal Women Using 18F-Fluoride and 99mTc-Methylene Diphosphonate'. *Journal of Nuclear Medicine* 43 (3): 338–45.

Bolbos, R.I., Jin Zuo, Suchandrima Banerjee, Thomas M. Link, C. Benjamin Ma, Xiaojuan Li, and Sharmila Majumdar. 2008. 'Relationship between Trabecular Bone Structure and Articular Cartilage Morphology and Relaxation Times in Early OA of the Knee Joint Using Parallel MRI at 3T'. *Osteoarthritis and Cartilage* 16 (10): 1150–59. https://doi.org/10.1016/j.joca.2008.02.018.

Boskey, A, and N Pleshkocamacho. 2007. 'FT-IR Imaging of Native and Tissue-Engineered Bone and Cartilage'. *Biomaterials* 28 (15): 2465–78. https://doi.org/10.1016/j.biomaterials.2006.11.043.

Boskey, Adele L. 1996. 'Matrix Proteins and Mineralization: An Overview'. *Connective Tissue Research* 35 (1–4): 357–63. https://doi.org/10.3109/03008209609029212.

Boskey, A.L., and R. Coleman. 2010. 'Aging and Bone'. *Journal of Dental Research* 89 (12): 1333–48. https://doi.org/10.1177/0022034510377791.

Boutroy, Stephanie, Mary L. Bouxsein, Francoise Munoz, and Pierre D. Delmas. 2005a. '*In Vivo* Assessment of Trabecular Bone Microarchitecture by High-Resolution Peripheral Quantitative Computed Tomography'. *The Journal of Clinical Endocrinology & Metabolism* 90 (12): 6508–15. https://doi.org/10.1210/jc.2005-1258.

———. 2005b. 'In Vivo Assessment of Trabecular Bone Microarchitecture by High-Resolution Peripheral Quantitative Computed Tomography'. *The Journal of Clinical Endocrinology & Metabolism* 90 (12): 6508–15. https://doi.org/10.1210/jc.2005-1258.

Bouyer, Benjamin, Fanny Leroy, Jérémie Rudant, Alain Weill, and Joël Coste. 2020. 'Burden of Fractures in France: Incidence and Severity by Age, Gender, and Site in 2016'. *International Orthopaedics* 44 (5): 947–55. https://doi.org/10.1007/s00264-020-04492-2.

Bovik, Alan Conrad, Thomas S. Huang, and David C. Munson. 1987. 'The Effect of Median Filtering on Edge Estimation and Detection'. *IEEE Transactions on Pattern Analysis*

and Machine Intelligence PAMI-9 (2): 181–94. https://doi.org/10.1109/TPAMI.1987.4767894.

Brage, Sören, Jan F. Nygard, and Gunnar Tellnes. 1998. 'The Gender Gap in Musculoskeletal-Related Long Term Sickness Absence in Norway'. *Scandinavian Journal of Social Medicine* 26 (1): 34–43. https://doi.org/10.1177/14034948980260010901.

Brian C. Smith. 2011. *Fundamentals of Fourier Transform Infrared Spectroscopy*. CRC Press.

Briot, Karine, Christian Roux, Thierry Thomas, Hubert Blain, Daniel Buchon, Roland Chapurlat, Françoise Debiais, et al. 2018. '2018 Update of French Recommendations on the Management of Postmenopausal Osteoporosis'. *Joint Bone Spine* 85 (5): 519–30. https://doi.org/10.1016/j.jbspin.2018.02.009.

Brismar, T. B. 2000. 'MR Relaxometry of Lumbar Spine, Hip, and Calcaneus in Healthy Premenopausal Women: Relationship with Dual Energy X-Ray Absorptiometry and Quantitative Ultrasound'. *European Radiology* 10 (8): 1215–21. https://doi.org/10.1007/s003300000438.

Brown, RW, YCN Cheng, MR Thompson, E. Mark Haacke, and Ramesh Venkatesan. 2014. *Magnetic Resonance Imaging: Physical Principles and Sequence Design*. John Wiley & Sons.

Brun, Emmanuel, Claudio Ferrero, and Jerome Vicente. 2017a. 'Fast Granulometry Operator for the 3D Identification of Cell Structures'. Edited by Paolo Dulio, Andrea Frosini, and Grzegorz Rozenberg. *Fundamenta Informaticae* 155 (4): 363–72. https://doi.org/10.3233/FI-2017-1590.

———. 2017b. 'Fast Granulometry Operator for the 3D Identification of Cell Structures'. Edited by Paolo Dulio, Andrea Frosini, and Grzegorz Rozenberg. *Fundamenta Informaticae* 155 (4): 363–72. https://doi.org/10.3233/FI-2017-1590.

Brun, Emmanuel, Jérôme Vicente, Frédéric Topin, and René Occelli. n.d. 'IMorph : A 3D Morphological Tool to Fully Analyze All Kind of Cellular Materials', 6.

Brun, Francesco, Serena Pacilè, Agostino Accardo, George Kourousias, Diego Dreossi, Lucia Mancini, Giuliana Tromba, and Roberto Pugliese. 2015. 'Enhanced and Flexible Software Tools for X-Ray Computed Tomography at the Italian Synchrotron Radiation Facility Elettra'. Edited by Paolo Dulio, Andrea Frosini, and Grzegorz Rozenberg. *Fundamenta Informaticae* 141 (2–3): 233–43. https://doi.org/10.3233/FI-2015-1273.

Burge, Russel, Bess Dawson-Hughes, Daniel H Solomon, John B Wong, Alison King, and Anna Tosteson. 2007. 'Incidence and Economic Burden of Osteoporosis-Related Fractures in the United States, 2005-2025'. *Journal of Bone and Mineral Research* 22 (3): 465–75. https://doi.org/10.1359/jbmr.061113.

Burghardt, Andrew J., Thomas M. Link, and Sharmila Majumdar. 2011a. 'High-Resolution Computed Tomography for Clinical Imaging of Bone Microarchitecture'. *Clinical Orthopaedics and Related Research*® 469 (8): 2179–93. https://doi.org/10.1007/s11999-010-1766-x.

———. 2011b. 'High-Resolution Computed Tomography for Clinical Imaging of Bone Microarchitecture'. *Clinical Orthopaedics and Related Research*® 469 (8): 2179–93. https://doi.org/10.1007/s11999-010-1766-x.

Cammilleri, Serge, Sophie Gabriel, Arnaud Le Troter, Christophe Chagnaud, Jean Pierre Mattei, David Bendahan, and Sandrine Guis. 2019. 'Knee Psoriatic Enthesitis Assessed Using Positron Emission Tomography (PET) - FNa Merged to Ultrahigh Field

Magnetic Resonance Imaging (UHF-MRI)'. *Joint Bone Spine* 86 (3): 387–88. https://doi.org/10.1016/j.jbspin.2019.01.002.

Carpentier, Xavier, Dominique Bazin, Paul Jungers, Solenn Reguer, Dominique Thiaudière, and Michel Daudon. 2010. 'The Pathogenesis of Randall's Plaque: A Papilla Cartography of Ca Compounds through an *Ex Vivo* Investigation Based on XANES Spectroscopy'. *Journal of Synchrotron Radiation* 17 (3): 374–79. https://doi.org/10.1107/S0909049510003791.

Carter, Yasmin, C. David L. Thomas, John G. Clement, Andrew G. Peele, Kevin Hannah, and David M.L. Cooper. 2013. 'Variation in Osteocyte Lacunar Morphology and Density in the Human Femur — a Synchrotron Radiation Micro-CT Study'. *Bone* 52 (1): 126–32. https://doi.org/10.1016/j.bone.2012.09.010.

Casali, P.G., S. Bielack, N. Abecassis, H.T. Aro, S. Bauer, R. Biagini, S. Bonvalot, et al. 2018. 'Bone Sarcomas: ESMO–PaedCan–EURACAN Clinical Practice Guidelines for Diagnosis, Treatment and Follow-Up'. *Annals of Oncology* 29 (October): iv79–95. https://doi.org/10.1093/annonc/mdy310.

Chandran, Shelly, Ali Aldei, Sindhu R. Johnson, Angela M. Cheung, David Salonen, and Dafna D. Gladman. 2016a. 'Prevalence and Risk Factors of Low Bone Mineral Density in Psoriatic Arthritis: A Systematic Review'. *Seminars in Arthritis and Rheumatism* 46 (2): 174–82. https://doi.org/10.1016/j.semarthrit.2016.05.005.

———. 2016b. 'Prevalence and Risk Factors of Low Bone Mineral Density in Psoriatic Arthritis: A Systematic Review'. *Seminars in Arthritis and Rheumatism* 46 (2): 174–82. https://doi.org/10.1016/j.semarthrit.2016.05.005.

Chang, Gregory, Sean Boone, Dimitri Martel, Chamith S. Rajapakse, Robert S. Hallyburton, Mitch Valko, Stephen Honig, and Ravinder R. Regatte. 2017a. 'MRI Assessment of Bone Structure and Microarchitecture'. *Journal of Magnetic Resonance Imaging : JMRI* 46 (2): 323–37. https://doi.org/10.1002/jmri.25647.

———. 2017b. 'MRI Assessment of Bone Structure and Microarchitecture: Bone Structure and Microarchitecture'. *Journal of Magnetic Resonance Imaging* 46 (2): 323–37. https://doi.org/10.1002/jmri.25647.

Chang, Gregory, Cem M. Deniz, Stephen Honig, Chamith S. Rajapakse, Kenneth Egol, Ravinder R. Regatte, and Ryan Brown. 2014a. 'Feasibility of Three-Dimensional MRI of Proximal Femur Microarchitecture at 3 Tesla Using 26 Receive Elements without and with Parallel Imaging: 3D MRI of Proximal Femur Microarchitecture'. *Journal of Magnetic Resonance Imaging* 40 (1): 229–38. https://doi.org/10.1002/jmri.24345.

———. 2014b. 'Feasibility of Three-Dimensional MRI of Proximal Femur Microarchitecture at 3 Tesla Using 26 Receive Elements without and with Parallel Imaging: 3D MRI of Proximal Femur Microarchitecture'. *Journal of Magnetic Resonance Imaging* 40 (1): 229–38. https://doi.org/10.1002/jmri.24345.

Chang, Gregory, Stephen Honig, Ryan Brown, Cem M. Deniz, Kenneth A. Egol, James S. Babb, Ravinder R. Regatte, and Chamith S. Rajapakse. 2014a. 'Finite Element Analysis Applied to 3-T MR Imaging of Proximal Femur Microarchitecture: Lower Bone Strength in Patients with Fragility Fractures Compared with Control Subjects'. *Radiology* 272 (2): 464–74. https://doi.org/10.1148/radiol.14131926.

———. 2014b. 'Finite Element Analysis Applied to 3-T MR Imaging of Proximal Femur Microarchitecture: Lower Bone Strength in Patients with Fragility Fractures

Compared with Control Subjects'. *Radiology* 272 (2): 464–74. https://doi.org/10.1148/radiol.14131926.

Chang, Gregory, Stephen Honig, Yinxiao Liu, Cheng Chen, Kevin K. Chu, Chamith S. Rajapakse, Kenneth Egol, Ding Xia, Punam K. Saha, and Ravinder R. Regatte. 2015a. '7 Tesla MRI of Bone Microarchitecture Discriminates between Women without and with Fragility Fractures Who Do Not Differ by Bone Mineral Density'. *Journal of Bone and Mineral Metabolism* 33 (3): 285–93. https://doi.org/10.1007/s00774-014-0588-4.

———. 2015b. '7 Tesla MRI of Bone Microarchitecture Discriminates between Women without and with Fragility Fractures Who Do Not Differ by Bone Mineral Density'. *Journal of Bone and Mineral Metabolism* 33 (3): 285–93. https://doi.org/10.1007/s00774-014-0588-4.

Chang, Gregory, Chamith S. Rajapakse, Cheng Chen, Arakua Welbeck, Kenneth Egol, Ravinder R. Regatte, Punam K. Saha, and Stephen Honig. 2018a. '3-T MR Imaging of Proximal Femur Microarchitecture in Subjects with and without Fragility Fracture and Nonosteoporotic Proximal Femur Bone Mineral Density'. *Radiology* 287 (2): 608–19. https://doi.org/10.1148/radiol.2017170138.

———. 2018b. '3-T MR Imaging of Proximal Femur Microarchitecture in Subjects with and without Fragility Fracture and Nonosteoporotic Proximal Femur Bone Mineral Density'. *Radiology* 287 (2): 608–19. https://doi.org/10.1148/radiol.2017170138.

Chang, Gregory, Chamith S. Rajapakse, Ravinder R. Regatte, James Babb, Amit Saxena, H. Michael Belmont, and Stephen Honig. 2015a. '3 Tesla MRI Detects Deterioration in Proximal Femur Microarchitecture and Strength in Long-Term Glucocorticoid Users Compared with Controls: Changes in Proximal Femur Microarchitecture in GIO'. *Journal of Magnetic Resonance Imaging* 42 (6): 1489–96. https://doi.org/10.1002/jmri.24927.

———. 2015b. '3 Tesla MRI Detects Deterioration in Proximal Femur Microarchitecture and Strength in Long-Term Glucocorticoid Users Compared with Controls: Changes in Proximal Femur Microarchitecture in GIO'. *Journal of Magnetic Resonance Imaging* 42 (6): 1489–96. https://doi.org/10.1002/jmri.24927.

Chang, Rong, Xiaowen Ma, Yonghong Jiang, Dageng Huang, Xiujin Chen, Ming Zhang, and Dingjun Hao. 2020. 'Percentage Fat Fraction in Magnetic Resonance Imaging: Upgrading the Osteoporosis-Detecting Parameter'. *BMC Medical Imaging* 20 (1): 30. https://doi.org/10.1186/s12880-020-00423-0.

Chappard, Christine, Gilles André, Michel Daudon, and Dominique Bazin. 2016. 'Analysis of Hydroxyapatite Crystallites in Subchondral Bone by Fourier Transform Infrared Spectroscopy and Powder Neutron Diffraction Methods'. *Comptes Rendus Chimie* 19 (11–12): 1625–30. https://doi.org/10.1016/j.crci.2015.03.015.

Chaudhari, Abhijit J, Andrea Ferrero, Felipe Godinez, Kai Yang, David K Shelton, John C Hunter, Stanley M Naguwa, John M Boone, Siba P Raychaudhuri, and Ramsey D Badawi. 2016. 'High-Resolution ^{18} F-FDG PET/CT for Assessing Disease Activity in Rheumatoid and Psoriatic Arthritis: Findings of a Prospective Pilot Study'. *The British Journal of Radiology* 89 (1063): 20160138. https://doi.org/10.1259/bjr.20160138.

Chen, Jun, Michael Carl, Yajun Ma, Hongda Shao, Xing Lu, Bimin Chen, Eric Y. Chang, Zhihong Wu, and Jiang Du. 2016. 'Fast Volumetric Imaging of Bound and Pore Water in Cortical Bone Using Three-Dimensional Ultrashort-TE (UTE) and Inversion Recovery UTE

Sequences: Bound and Pore Water Imaging in Cortical Bone Using 3D UTE Sequences'. *NMR in Biomedicine* 29 (10): 1373–80. https://doi.org/10.1002/nbm.3579.

Chen, Suet Ching, Sheila Shepherd, Martin McMillan, Jane McNeilly, John Foster, Sze Choong Wong, Kenneth J Robertson, and S Faisal Ahmed. 2019. 'Skeletal Fragility and Its Clinical Determinants in Children With Type 1 Diabetes'. *The Journal of Clinical Endocrinology & Metabolism* 104 (8): 3585–94. https://doi.org/10.1210/jc.2019-00084.

Chen, Weiwei, Wenzhen Zhu, IIhami Kovanlikaya, Arzu Kovanlikaya, Tian Liu, Shuai Wang, Carlo Salustri, and Yi Wang. 2014. 'Intracranial Calcifications and Hemorrhages: Characterization with Quantitative Susceptibility Mapping'. *Radiology* 270 (2): 496–505. https://doi.org/10.1148/radiol.13122640.

Chen, Yanjun, Yihao Guo, Xintao Zhang, Yingjie Mei, Yanqiu Feng, and Xiaodong Zhang. 2018. 'Bone Susceptibility Mapping with MRI Is an Alternative and Reliable Biomarker of Osteoporosis in Postmenopausal Women'. *European Radiology* 28 (12): 5027–34. https://doi.org/10.1007/s00330-018-5419-x.

Cheng, Xiaoguang, Huishu Yuan, Jingliang Cheng, Xisheng Weng, Hao Xu, Jianbo Gao, Mingqian Huang, et al. 2020. 'Chinese Expert Consensus on the Diagnosis of Osteoporosis by Imaging and Bone Mineral Density'. *Quantitative Imaging in Medicine and Surgery* 10 (10): 12.

Chiba, K., M. Uetani, Y. Kido, M. Ito, N. Okazaki, K. Taguchi, and H. Shindo. 2012. 'Osteoporotic Changes of Subchondral Trabecular Bone in Osteoarthritis of the Knee: A 3-T MRI Study'. *Osteoporosis International* 23 (2): 589–97. https://doi.org/10.1007/s00198-011-1585-2.

Chung, H., F. W. Wehrli, J. L. Williams, and S. D. Kugelmass. 1993. 'Relationship between NMR Transverse Relaxation, Trabecular Bone Architecture, and Strength.' *Proceedings of the National Academy of Sciences* 90 (21): 10250–54. https://doi.org/10.1073/pnas.90.21.10250.

Chung, Hsiao-Wen, Felix W. Wehrli, John L. Williams, and Suzanne L. Wehrli. 2009. 'Three-Dimensional Nuclear Magnetic Resonance Microimaging of Trabecular Bone'. *Journal of Bone and Mineral Research* 10 (10): 1452–61. https://doi.org/10.1002/jbmr.5650101005.

Coates, Laura C, and Philip S Helliwell. 2017. 'Psoriatic Arthritis: State of the Art Review'. *Clinical Medicine* 17 (1): 65–70. https://doi.org/10.7861/clinmedicine.17-1-65.

Corbett, Mary C., Matthew J. Latimer, Thomas L. Poulos, Irina F. Sevrioukova, Keith O. Hodgson, and Britt Hedman. 2007. 'Photoreduction of the Active Site of the Metalloprotein Putidaredoxin by Synchrotron Radiation'. *Acta Crystallographica Section D Biological Crystallography* 63 (9): 951–60. https://doi.org/10.1107/S0907444907035160.

Cordes, Christian, Thomas Baum, Michael Dieckmeyer, Stefan Ruschke, Maximilian N. Diefenbach, Hans Hauner, Jan S. Kirschke, and Dimitrios C. Karampinos. 2016. 'MR-Based Assessment of Bone Marrow Fat in Osteoporosis, Diabetes, and Obesity'. *Frontiers in Endocrinology* 7 (June). https://doi.org/10.3389/fendo.2016.00074.

Cordes, Christian, Michael Dieckmeyer, Beate Ott, Jun Shen, Stefan Ruschke, Marcus Settles, Claudia Eichhorn, et al. 2015. 'MR-Detected Changes in Liver Fat, Abdominal Fat, and Vertebral Bone Marrow Fat after a Four-Week Calorie Restriction in Obese Women:

MR-Detected Fat Changes After a Diet'. *Journal of Magnetic Resonance Imaging* 42 (5): 1272–80. https://doi.org/10.1002/jmri.24908.

Cowin, S. 2001. *Bone Mechanics Handbook*. Boca Raton.

Cowin, Stephen C. 1999. 'Bone Poroelasticity'. *Journal of Biomechanics* 32: 217–38. https://doi.org/10.1016/s0021-9290(98)00161-4.

Cowin, Stephen C., and Stephen B. Doty. 2007. *Tissue Mechanics*. Springer-Verlag New York.

Cundy, Tim. 2018. 'Paget's Disease of Bone'. *Metabolism* 80 (March): 5–14. https://doi.org/10.1016/j.metabol.2017.06.010.

D. C. Koningsberger and R. Prins. 1988. *X-Ray Absorption: Principles, Applications, Techniques of EXAFS, SEXAFS and XANES*. Wiley.

Dachena, Chiara, Sergio Casu, Alessandro Fanti, Matteo Bruno Lodi, and Giuseppe Mazzarella. 2019. 'Combined Use of MRI, FMRIand Cognitive Data for Alzheimer's Disease: Preliminary Results'. *Applied Sciences* 9 (15): 3156. https://doi.org/10.3390/app9153156.

Dall'Ara, E., C. Karl, G. Mazza, G. Franzoso, P. Vena, M. Pretterklieber, D. Pahr, and P. Zysset. 2013. 'Tissue Properties of the Human Vertebral Body Sub-Structures Evaluated by Means of Microindentation'. *Journal of the Mechanical Behavior of Biomedical Materials* 25 (September): 23–32. https://doi.org/10.1016/j.jmbbm.2013.04.020.

Damilakis, John, Judith E. Adams, Giuseppe Guglielmi, and Thomas M. Link. 2010a. 'Radiation Exposure in X-Ray-Based Imaging Techniques Used in Osteoporosis'. *European Radiology* 20 (11): 2707–14. https://doi.org/10.1007/s00330-010-1845-0.

———. 2010b. 'Radiation Exposure in X-Ray-Based Imaging Techniques Used in Osteoporosis'. *European Radiology* 20 (11): 2707–14. https://doi.org/10.1007/s00330-010-1845-0.

Dardenne, O., J. Prud'homme, A. Arabian, F. H. Glorieux, and R. St-Arnaud. 2001. 'Targeted Inactivation of the 25-Hydroxyvitamin D(3)-1(Alpha)-Hydroxylase Gene (CYP27B1) Creates an Animal Model of Pseudovitamin D-Deficiency Rickets'. *Endocrinology* 142 (7): 3135–41. https://doi.org/10.1210/endo.142.7.8281.

Deistung, Andreas, Ferdinand Schweser, and Jürgen R. Reichenbach. 2017. 'Overview of Quantitative Susceptibility Mapping: Overview of Quantitative Susceptibility Mapping'. *NMR in Biomedicine* 30 (4): e3569. https://doi.org/10.1002/nbm.3569.

Del Puente, A., A. Esposito, L. Costa, C. Benigno, A. Del Puente, F. Foglia, A. Oriente, P. Bottiglieri, F. Caso, and R. Scarpa. 2015. 'Fragility Fractures in Patients with Psoriatic Arthritis'. *The Journal of Rheumatology Supplement* 93 (0): 36–39. https://doi.org/10.3899/jrheum.150633.

Di Munno, Ombretta, and Francesco Ferro. 2019. 'The Effect of Biologic Agents on Bone Homeostasis in Chronic Inflammatory Rheumatic Diseases'. *Clinical and Experimental Rheumatology* 37 (3): 502–7.

Dieckmeyer, Michael, Daniela Junker, Stefan Ruschke, Muthu Rama Krishnan Mookiah, Karupppasamy Subburaj, Egon Burian, Nico Sollmann, Jan S. Kirschke, Dimitrios C. Karampinos, and Thomas Baum. 2020. 'Vertebral Bone Marrow Heterogeneity Using Texture Analysis of Chemical Shift Encoding-Based MRI: Variations in Age, Sex, and Anatomical Location'. *Frontiers in Endocrinology* 11 (October): 555931. https://doi.org/10.3389/fendo.2020.555931.

Diefenbach, Maximilian N., Jakob Meineke, Stefan Ruschke, Thomas Baum, Alexandra Gersing, and Dimitrios C. Karampinos. 2019. 'On the Sensitivity of Quantitative

Susceptibility Mapping for Measuring Trabecular Bone Density'. *Magnetic Resonance in Medicine* 81 (3): 1739–54. https://doi.org/10.1002/mrm.27531.

Diez-Perez, Adolfo, Roberto Güerri, Xavier Nogues, Enric Cáceres, Maria Jesus Peña, Leonardo Mellibovsky, Connor Randall, et al. 2010. 'Microindentation for in Vivo Measurement of Bone Tissue Mechanical Properties in Humans'. *Journal of Bone and Mineral Research* 25 (8): 1877–85. https://doi.org/10.1002/jbmr.73.

Dimov, Alexey V., Zhe Liu, Pascal Spincemaille, Martin R. Prince, Jiang Du, and Yi Wang. 2018. 'Bone Quantitative Susceptibility Mapping Using a Chemical Species-Specific R2* Signal Model with Ultrashort and Conventional Echo Data: Bone QSM Using a R_2* Signal Model With UTE Conventional Echo Data'. *Magnetic Resonance in Medicine* 79 (1): 121–28. https://doi.org/10.1002/mrm.26648.

Djuric, Marija, Danijela Djonic, Petar Milovanovic, Slobodan Nikolic, Robert Marshall, Jelena Marinkovic, and Michael Hahn. 2010. 'Region-Specific Sex-Dependent Pattern of Age-Related Changes of Proximal Femoral Cancellous Bone and Its Implications on Differential Bone Fragility'. *Calcified Tissue International* 86 (3): 192–201. https://doi.org/10.1007/s00223-009-9325-8.

Dong, Pei, Sylvain Haupert, Bernhard Hesse, Max Langer, Pierre-Jean Gouttenoire, Valérie Bousson, and Françoise Peyrin. 2014. '3D Osteocyte Lacunar Morphometric Properties and Distributions in Human Femoral Cortical Bone Using Synchrotron Radiation Micro-CT Images'. *Bone* 60 (March): 172–85. https://doi.org/10.1016/j.bone.2013.12.008.

Dougherty, R, and K-H Kunzelmann. 2007a. 'Computing Local Thickness of 3D Structures with ImageJ'. *Microscopy and Microanalysis* 13 (S02). https://doi.org/10.1017/S1431927607074430.

———. 2007b. 'Computing Local Thickness of 3D Structures with ImageJ'. *Microscopy and Microanalysis* 13 (S02). https://doi.org/10.1017/S1431927607074430.

Du, Jiang, Juan C Hermida, Eric Diaz, Jacqueline Corbeil, Richard Znamirowski, Darryl D D'Lima, and Graeme M Bydder. n.d. 'Assessment of Cortical Bone with Clinical and Ultrashort Echo Time Sequences', 8.

Du, Juan, Katherine Brooke-Wavell, Margaret A. Paggiosi, Chris Hartley, Jennifer S. Walsh, Vadim V. Silberschmidt, and Simin Li. 2019. 'Characterising Variability and Regional Correlations of Microstructure and Mechanical Competence of Human Tibial Trabecular Bone: An in-Vivo HR-PQCT Study'. *Bone* 121 (April): 139–48. https://doi.org/10.1016/j.bone.2019.01.013.

Dwan, Kerry, Carrie A Phillipi, Robert D Steiner, and Donald Basel. 2016. 'Bisphosphonate Therapy for Osteogenesis Imperfecta'. Edited by Cochrane Cystic Fibrosis and Genetic Disorders Group. *Cochrane Database of Systematic Reviews*, October. https://doi.org/10.1002/14651858.CD005088.pub4.

E Soldati, M Pithioux, D Bendahan, and J Vicente. 2020. 'MRI Assessment of Bone Microarchitecture in Human Femurs: The Issue of Air Bubbles Artefacts'. https://doi.org/10.13140/RG.2.2.15937.79203.

Eckstein, Felix, Caecilia Wunderer, Holger Boehm, Volker Kuhn, Mathias Priemel, Thomas M Link, and Eva-Maria Lochmüller. 2003. 'Reproducibility and Side Differences of Mechanical Tests for Determining the Structural Strength of the Proximal Femur'. *Journal of Bone and Mineral Research* 19 (3): 379–85. https://doi.org/10.1359/JBMR.0301247.

Eisenberger, P., and B. M. Kincaid. 1978. 'EXAFS: New Horizons in Structure Determinations'. *Science* 200 (4349): 1441–47.

'Epidemiology of Osteoporosis and Fragility Fractures | International Osteoporosis Foundation'. n.d. Accessed 18 November 2021. https://www.osteoporosis.foundation/facts-statistics/epidemiology-of-osteoporosis-and-fragility-fractures.

Faibish, Dan, Susan M Ott, and Adele L Boskey. 2006. 'Mineral Changes in Osteoporosis A Review', 19.

Fantner, Georg E., Jonathan Adams, Patricia Turner, Philipp J. Thurner, Larry W. Fisher, and Paul K. Hansma. 2007. 'Nanoscale Ion Mediated Networks in Bone: Osteopontin Can Repeatedly Dissipate Large Amounts of Energy'. *Nano Letters* 7 (8): 2491–98. https://doi.org/10.1021/nl0712769.

Fazeli, Pouneh K, Mark C Horowitz, Ormond A MacDougald, Erica L Scheller, Matthew S Rodeheffer, Clifford J Rosen, and Anne Klibanski. 2013. 'Marrow Fat and Bone—New Perspectives'. *J Clin Endocrinol Metab*, 11.

Fazeli, Pouneh K., and Anne Klibanski. 2019. 'The Paradox of Marrow Adipose Tissue in Anorexia Nervosa'. *Bone* 118 (January): 47–52. https://doi.org/10.1016/j.bone.2018.02.013.

Figueiredo, M., A. Fernando, G. Martins, J. Freitas, F. Judas, and H. Figueiredo. 2010. 'Effect of the Calcination Temperature on the Composition and Microstructure of Hydroxyapatite Derived from Human and Animal Bone'. *Ceramics International* 36 (8): 2383–93. https://doi.org/10.1016/j.ceramint.2010.07.016.

Fintini, Danilo, Stefano Cianfarani, Marta Cofini, Angela Andreoletti, Grazia Maria Ubertini, Marco Cappa, and Melania Manco. 2020. 'The Bones of Children With Obesity'. *Frontiers in Endocrinology* 11 (April): 200. https://doi.org/10.3389/fendo.2020.00200.

Florenzano, Pablo, Iris R. Hartley, Macarena Jimenez, Kelly Roszko, Rachel I. Gafni, and Michael T. Collins. 2021. 'Tumor-Induced Osteomalacia'. *Calcified Tissue International* 108 (1): 128–42. https://doi.org/10.1007/s00223-020-00691-6.

Folkesson, Jenny, Janet Goldenstein, Julio Carballido-Gamio, Galateia Kazakia, Andrew J. Burghardt, Ana Rodriguez, Roland Krug, Anne E. de Papp, Thomas M. Link, and Sharmila Majumdar. 2011. 'Longitudinal Evaluation of the Effects of Alendronate on MRI Bone Microarchitecture in Postmenopausal Osteopenic Women'. *Bone* 48 (3): 611–21. https://doi.org/10.1016/j.bone.2010.10.179.

for the International Osteoporosis Foundation, Fredrik Borgström, Linda Karlsson, Gustav Ortsäter, Nicolas Norton, Philippe Halbout, Cyrus Cooper, et al. 2020. 'Fragility Fractures in Europe: Burden, Management and Opportunities'. *Archives of Osteoporosis* 15 (1): 59. https://doi.org/10.1007/s11657-020-0706-y.

Fratzl, Peter. 2005. 'Hierarchical Structure and Mechanical Adaptation of Biological Materials'. In *Learning from Nature How to Design New Implantable Biomaterialsis: From Biomineralization Fundamentals to Biomimetic Materials and Processing Routes*, edited by R. L. Reis and S. Weiner, 171:15–34. NATO Science Series II: Mathematics, Physics and Chemistry. Dordrecht: Kluwer Academic Publishers. https://doi.org/10.1007/1-4020-2648-X_2.

Fratzl, Peter, and Himadri S. Gupta. 2007. 'Nanoscale Mechanisms of Bone Deformation and Fracture'. In *Handbook of Biomineralization*, edited by Edmund Buerlein, 397–414.

Weinheim, Germany: Wiley-VCH Verlag GmbH. https://doi.org/10.1002/9783527619443.ch23.

Fratzl-Zelman, N., P. Roschger, A. Gourrier, M. Weber, B. M. Misof, N. Loveridge, J. Reeve, K. Klaushofer, and P. Fratzl. 2009. 'Combination of Nanoindentation and Quantitative Backscattered Electron Imaging Revealed Altered Bone Material Properties Associated with Femoral Neck Fragility'. *Calcified Tissue International* 85 (4): 335–43. https://doi.org/10.1007/s00223-009-9289-8.

Frediani, Bruno, Alessandra Allegri, Paolo Falsetti, Lara Storri, Stefania Bisogno, Fabio Baldi, Paolo Filipponi, and Roberto Marcolongo. n.d. 'Bone Mineral Density in Patients with Psoriatic Arthritis'. *The Journal of Rheumatology*, 6.

Frost, Michelle L., Gary J. R. Cook, Glen M. Blake, Paul K. Marsden, Nigel A. Benatar, and Ignac Fogelman. 2003. 'A Prospective Study of Risedronate on Regional Bone Metabolism and Blood Flow at the Lumbar Spine Measured by 18F-Fluoride Positron Emission Tomography'. *Journal of Bone and Mineral Research: The Official Journal of the American Society for Bone and Mineral Research* 18 (12): 2215–22. https://doi.org/10.1359/jbmr.2003.18.12.2215.

Ganie, Mohd Ashraf, Nishant Raizada, Himika Chawla, Arun Kumar Singh, Sandeep Aggarwala, and Chandra Sekhar Bal. 2016. 'Primary Hyperparathyroidism May Masquerade as Rickets-Osteomalacia in Vitamin D Replete Children'. *Journal of Pediatric Endocrinology and Metabolism* 29 (10). https://doi.org/10.1515/jpem-2016-0018.

Gennari, Luigi, Domenico Rendina, Alberto Falchetti, and Daniela Merlotti. 2019. 'Paget's Disease of Bone'. *Calcified Tissue International* 104 (5): 483–500. https://doi.org/10.1007/s00223-019-00522-3.

Genthial, Rachel, Emmanuel Beaurepaire, Marie-Claire Schanne-Klein, Françoise Peyrin, Delphine Farlay, Cécile Olivier, Yohann Bala, et al. 2017. 'Label-Free Imaging of Bone Multiscale Porosity and Interfaces Using Third-Harmonic Generation Microscopy'. *Scientific Reports* 7 (1): 3419. https://doi.org/10.1038/s41598-017-03548-5.

Gervais, Christel, Christian Bonhomme, and Danielle Laurencin. 2020. 'Recent Directions in the Solid-State NMR Study of Synthetic and Natural Calcium Phosphates'. *Solid State Nuclear Magnetic Resonance* 107 (June): 101663. https://doi.org/10.1016/j.ssnmr.2020.101663.

Gherase, Mihai R., and David E. B. Fleming. 2019. 'Probing Trace Elements in Human Tissues with Synchrotron Radiation'. *Crystals* 10 (1): 12. https://doi.org/10.3390/cryst10010012.

Glover, Gary H., John M. Pauly, and Kenneth M. Bradshaw. 1992. 'Boron-11 Imaging with a Three-Dimensional Reconstruction Method'. *Journal of Magnetic Resonance Imaging* 2 (1): 47–52. https://doi.org/10.1002/jmri.1880020109.

Gómez, Maria Pilar Aparisi, Carmen Ayuso Benavent, Paolo Simoni, Francisco Aparisi, Giuseppe Guglielmi, and Alberto Bazzocchi. 2020. 'Fat and Bone: The Multiperspective Analysis of a Close Relationship'. *Quantitative Imaging in Medicine and Surgery* 10 (8): 22.

Gong, Bo, Gurjit S. Mandair, Felix W. Wehrli, and Michael D. Morris. 2014. 'Novel Assessment Tools for Osteoporosis Diagnosis and Treatment'. *Current Osteoporosis Reports* 12 (3): 357–65. https://doi.org/10.1007/s11914-014-0215-2.

Gonzalezballester, M. 2002. 'Estimation of the Partial Volume Effect in MRI'. *Medical Image Analysis* 6 (4): 389–405. https://doi.org/10.1016/S1361-8415(02)00061-0.

Gossec, Laure, Xenofon Baraliakos, Andreas Kerschbaumer, Maarten de Wit, Iain McInnes, Maxime Dougados, Jette Primdahl, et al. 2020. 'EULAR Recommendations for the Management of Psoriatic Arthritis with Pharmacological Therapies: 2019 Update'. *Annals of the Rheumatic Diseases* 79 (6): 700–712. https://doi.org/10.1136/annrheumdis-2020-217159.

Griffin, Lindsay M., Stephen Honig, Cheng Chen, Punam K. Saha, Ravinder Regatte, and Gregory Chang. 2017. '7T MRI of Distal Radius Trabecular Bone Microarchitecture: How Trabecular Bone Quality Varies Depending on Distance from End-of-Bone: 7T MRI of Distal Radius'. *Journal of Magnetic Resonance Imaging* 45 (3): 872–78. https://doi.org/10.1002/jmri.25398.

Griffith, James F., David K. W. Yeung, Gregory E. Antonio, Francis K. H. Lee, Athena W. L. Hong, Samuel Y. S. Wong, Edith M. C. Lau, and Ping Chung Leung. 2005. 'Vertebral Bone Mineral Density, Marrow Perfusion, and Fat Content in Healthy Men and Men with Osteoporosis: Dynamic Contrast-Enhanced MR Imaging and MR Spectroscopy'. *Radiology* 236 (3): 945–51. https://doi.org/10.1148/radiol.2363041425.

Griffiths, Christopher Em, and Jonathan Nwn Barker. 2007. 'Pathogenesis and Clinical Features of Psoriasis'. *Lancet (London, England)* 370 (9583): 263–71. https://doi.org/10.1016/S0140-6736(07)61128-3.

Grodzki, David M., Peter M. Jakob, and Bjoern Heismann. 2012. 'Ultrashort Echo Time Imaging Using Pointwise Encoding Time Reduction with Radial Acquisition (PETRA)'. *Magnetic Resonance in Medicine* 67 (2): 510–18. https://doi.org/10.1002/mrm.23017.

Groot, Frank de. 2001. 'High-Resolution X-Ray Emission and X-Ray Absorption Spectroscopy'. *Chemical Reviews* 101 (6): 1779–1808. https://doi.org/10.1021/cr9900681.

Groot, Frank de, and Akio Kotani. 2008. *Core Level Spectroscopy of Solids*. 0 ed. CRC Press. https://doi.org/10.1201/9781420008425.

Guenoun, D., M. Pithioux, J.-C. Souplet, S. Guis, T. Le Corroller, A. Fouré, V. Pauly, et al. 2020a. 'Assessment of Proximal Femur Microarchitecture Using Ultra-High Field MRI at 7 Tesla'. *Diagnostic and Interventional Imaging* 101 (1): 45–53. https://doi.org/10.1016/j.diii.2019.06.013.

———. 2020b. 'Assessment of Proximal Femur Microarchitecture Using Ultra-High Field MRI at 7 Tesla'. *Diagnostic and Interventional Imaging* 101 (1): 45–53. https://doi.org/10.1016/j.diii.2019.06.013.

———. 2020c. 'Assessment of Proximal Femur Microarchitecture Using Ultra-High Field MRI at 7 Tesla'. *Diagnostic and Interventional Imaging* 101 (1): 45–53. https://doi.org/10.1016/j.diii.2019.06.013.

Guenoun, Daphne, Alexandre Fouré, Martine Pithioux, Sandrine Guis, Thomas Le Corroller, Jean-Pierre Mattei, Vanessa Pauly, et al. 2017a. 'Correlative Analysis of Vertebral Trabecular Bone Microarchitecture and Mechanical Properties: A Combined Ultra-High Field (7 Tesla) MRI and Biomechanical Investigation'. *SPINE* 42 (20): E1165–72. https://doi.org/10.1097/BRS.0000000000002163.

———. 2017b. 'Correlative Analysis of Vertebral Trabecular Bone Microarchitecture and Mechanical Properties: A Combined Ultra-High Field (7 Tesla) MRI and

Biomechanical Investigation'. *Spine* 42 (20): E1165–72. https://doi.org/10.1097/BRS.0000000000002163.

Guglielmi, Giuseppe, Kathy Selby, Barbara A. Blunt, Michael Jergas, David C. Newitt, Harry K. Genant, and Sharmila Majumdar. 1996. 'Magnetic Resonance Imaging of the Calcaneus: Preliminary Assessment of Trabecular Bone-Dependent Regional Variations in Marrow Relaxation Time Compared with Dual X-Ray Absorptiometry'. *Academic Radiology* 3 (4): 336–43. https://doi.org/10.1016/S1076-6332(96)80254-6.

Güler-Yüksel, M., J. Bijsterbosch, Y. P. M. Goekoop-Ruiterman, J. K. de Vries-Bouwstra, H. M. J. Hulsmans, W. M. de Beus, K. H. Han, et al. 2008. 'Changes in Bone Mineral Density in Patients with Recent Onset, Active Rheumatoid Arthritis'. *Annals of the Rheumatic Diseases* 67 (6): 823–28. https://doi.org/10.1136/ard.2007.073817.

Gupta, Himadri S., Wolfgang Wagermaier, Gerald A. Zickler, D. Raz-Ben Aroush, Sérgio S. Funari, Paul Roschger, H. Daniel Wagner, and Peter Fratzl. 2005. 'Nanoscale Deformation Mechanisms in Bone'. *Nano Letters* 5 (10): 2108–11. https://doi.org/10.1021/nl051584b.

Gustafson, M.B., R.B. Martin, V. Gibson, D.H. Storms, S.M. Stover, J. Gibeling, and L. Griffin. 1996. 'Calcium Buffering Is Required to Maintain Bone Stiffness in Saline Solution'. *Journal of Biomechanics* 29 (9): 1191–94. https://doi.org/10.1016/0021-9290(96)00020-6.

Haacke, E. Mark, Saifeng Liu, Sagar Buch, Weili Zheng, Dongmei Wu, and Yongquan Ye. 2015. 'Quantitative Susceptibility Mapping: Current Status and Future Directions'. *Magnetic Resonance Imaging* 33 (1): 1–25. https://doi.org/10.1016/j.mri.2014.09.004.

Haacke, E Mark, Yingbiao Xu, and Yu-Chung N Cheng. n.d. 'Susceptibility Weighted Imaging (SWI)', 7.

Hao, Yuewen, Rui An, Yingsen Xue, Fan Li, Hong Wang, Jianmin Zheng, Linni Fan, Jixin Liu, Hongbin Fan, and Hong Yin. 2020. 'Prognostic Value of Tumoral and Peritumoral Magnetic Resonance Parameters in Osteosarcoma Patients for Monitoring Chemotherapy Response'. *European Radiology*, November. https://doi.org/10.1007/s00330-020-07338-y.

Harrison, Douglas J., David S. Geller, Jonathan D. Gill, Valerae O. Lewis, and Richard Gorlick. 2018. 'Current and Future Therapeutic Approaches for Osteosarcoma'. *Expert Review of Anticancer Therapy* 18 (1): 39–50. https://doi.org/10.1080/14737140.2018.1413939.

Hasegawa, Tomoka, Tomomaya Yamamoto, Hiromi Hongo, Zixuan Qiu, Miki Abe, Takuma Kanesaki, Kawori Tanaka, et al. 2018. 'Three-Dimensional Ultrastructure of Osteocytes Assessed by Focused Ion Beam-Scanning Electron Microscopy (FIB-SEM)'. *Histochemistry and Cell Biology* 149 (4): 423–32. https://doi.org/10.1007/s00418-018-1645-1.

He, Jie, Hao Fang, and Xiaona Li. 2019. 'Vertebral Bone Marrow Fat Content in Normal Adults with Varying Bone Densities at 3T Magnetic Resonance Imaging'. *Acta Radiologica* 60 (4): 509–15. https://doi.org/10.1177/0284185118786073.

Henderson, G. S., F. M. F. de Groot, and B. J. A. Moulton. 2014. 'X-Ray Absorption Near-Edge Structure (XANES) Spectroscopy'. *Reviews in Mineralogy and Geochemistry* 78 (1): 75–138. https://doi.org/10.2138/rmg.2014.78.3.

Hengsberger, S, A Kulik, and Ph Zysset. 2002. 'Nanoindentation Discriminates the Elastic Properties of Individual Human Bone Lamellae under Dry and Physiological Conditions'. *Bone* 30 (1): 178–84. https://doi.org/10.1016/S8756-3282(01)00624-X.

Hermie, Isabeau, Monique Horvath, and Sofie Van Cauter. 2017. 'Temporal Bone Imaging Features in Osteogenesis Imperfecta'. *Journal of the Belgian Society of Radiology* 101 (1): 27. https://doi.org/10.5334/jbr-btr.1321.

Hernlund, E., A. Svedbom, M. Ivergård, J. Compston, C. Cooper, J. Stenmark, E. V. McCloskey, B. Jönsson, and J. A. Kanis. 2013. 'Osteoporosis in the European Union: Medical Management, Epidemiology and Economic Burden: A Report Prepared in Collaboration with the International Osteoporosis Foundation (IOF) and the European Federation of Pharmaceutical Industry Associations (EFPIA)'. *Archives of Osteoporosis* 8 (1–2): 136. https://doi.org/10.1007/s11657-013-0136-1.

Hesse, Bernhard, Murielle Salome, Hiram Castillo-Michel, Marine Cotte, Barbara Fayard, Christoph J. Sahle, Wout De Nolf, et al. 2016. 'Full-Field Calcium K-Edge X-Ray Absorption Near-Edge Structure Spectroscopy on Cortical Bone at the Micron-Scale: Polarization Effects Reveal Mineral Orientation'. *Analytical Chemistry* 88 (7): 3826–35. https://doi.org/10.1021/acs.analchem.5b04898.

Hinton, Paige V., Susan M. Rackard, and Oran D. Kennedy. 2018. 'In Vivo Osteocyte Mechanotransduction: Recent Developments and Future Directions'. *Current Osteoporosis Reports* 16 (6): 746–53. https://doi.org/10.1007/s11914-018-0485-1.

Hipp, John A., Alan Jansujwicz, Craig A. Simmons, and Brian D. Snyder. 2009. 'Trabecular Bone Morphology from Micro-Magnetic Resonance Imaging'. *Journal of Bone and Mineral Research* 11 (2): 286–92. https://doi.org/10.1002/jbmr.5650110218.

Hisham, M. B., Shahrul Nizam Yaakob, R. A. A Raof, A.B A. Nazren, and N.M. Wafi Embedded. 2015a. 'Template Matching Using Sum of Squared Difference and Normalized Cross Correlation'. In *2015 IEEE Student Conference on Research and Development (SCOReD)*, 100–104. Kuala Lumpur, Malaysia: IEEE. https://doi.org/10.1109/SCORED.2015.7449303.

———. 2015b. 'Template Matching Using Sum of Squared Difference and Normalized Cross Correlation'. In *2015 IEEE Student Conference on Research and Development (SCOReD)*, 100–104. Kuala Lumpur, Malaysia: IEEE. https://doi.org/10.1109/SCORED.2015.7449303.

Hoff, Mari, Arthur Kavanaugh, and Glenn Haugeberg. 2013. 'Hand Bone Loss in Patients with Psoriatic Arthritis: Posthoc Analysis of IMPACT II Data Comparing Infliximab and Placebo'. *The Journal of Rheumatology* 40 (8): 1344–48. https://doi.org/10.3899/jrheum.121376.

Hoffler, C.E., K.E. Moore, K. Kozloff, P.K. Zysset, M.B. Brown, and S.A. Goldstein. 2000. 'Heterogeneity of Bone Lamellar-Level Elastic Moduli'. *Bone* 26 (6): 603–9. https://doi.org/10.1016/S8756-3282(00)00268-4.

Hove, Ruud P. van, Peter A. Nolte, Aviral Vatsa, Cornelis M. Semeins, Philip L. Salmon, Theo H. Smit, and Jenneke Klein-Nulend. 2009. 'Osteocyte Morphology in Human Tibiae of Different Bone Pathologies with Different Bone Mineral Density — Is There a Role for Mechanosensing?' *Bone* 45 (2): 321–29. https://doi.org/10.1016/j.bone.2009.04.238.

Hoyer-Kuhn, Heike, Christian Netzer, and Oliver Semler. 2015. 'Osteogenesis Imperfecta: Pathophysiology and Treatment'. *Wiener Medizinische Wochenschrift* 165 (13–14): 278–84. https://doi.org/10.1007/s10354-015-0361-x.

Huang, Raymond Y, Lisa M Miller, Cathy S Carlson, and Mark R Chance. 2003. 'In Situ Chemistry of Osteoporosis Revealed by Synchrotron Infrared Microspectroscopy'. *Bone* 33 (4): 514–21. https://doi.org/10.1016/S8756-3282(03)00233-3.

Humadi, Ali, RajitH Alhadithi, and SabhanI Alkudiari. 2010a. 'Validity of the DEXA Diagnosis of Involutional Osteoporosis in Patients with Femoral Neck Fractures'. *Indian Journal of Orthopaedics* 44 (1): 73. https://doi.org/10.4103/0019-5413.58609.

———. 2010b. 'Validity of the DEXA Diagnosis of Involutional Osteoporosis in Patients with Femoral Neck Fractures'. *Indian Journal of Orthopaedics* 44 (1): 73. https://doi.org/10.4103/0019-5413.58609.

Hwang, Scott N., and Felix W. Wehrli. 2002. 'Subvoxel Processing: A Method for Reducing Partial Volume Blurring with Application to in Vivo MR Images of Trabecular Bone'. *Magnetic Resonance in Medicine* 47 (5): 948–57. https://doi.org/10.1002/mrm.10138.

Ian Goodfellow, Yoshua Bengio, and Aaron Courville. 2016. *Deep Learning (Adaptive Computation and Machine Learning Series)*. The MIT Press.

Idiyatullin, Djaudat, Curt Corum, Jang-Yeon Park, and Michael Garwood. 2006. 'Fast and Quiet MRI Using a Swept Radiofrequency'. *Journal of Magnetic Resonance*, 8.

Idiyatullin, Djaudat, Curtis A. Corum, Donald R. Nixdorf, and Michael Garwood. 2014. 'Intraoral Approach for Imaging Teeth Using the Transverse B_1 Field Components of an Occlusally Oriented Loop Coil: Intraoral Approach for Imaging Teeth'. *Magnetic Resonance in Medicine* 72 (1): 160–65. https://doi.org/10.1002/mrm.24893.

Idiyatullin, Djaudat, Steven Suddarth, Curtis A. Corum, Gregor Adriany, and Michael Garwood. 2012. 'Continuous SWIFT'. *Journal of Magnetic Resonance* 220 (July): 26–31. https://doi.org/10.1016/j.jmr.2012.04.016.

Ismail, Umi Nabilah, Che Ahmad Azlan, Shasha Khairullah, Raja Rizal Azman, Nur Farhayu Omar, Mohammad Nazri Md Shah, Chai Hong Yeong, Nicholas Jackson, and Kwan Hoong Ng. 2021. 'Marrow Fat Content and Composition in B-Thalassemia: A Study Using ^{1}H-MRS '. *Journal of Magnetic Resonance Imaging* 53 (1): 190–98. https://doi.org/10.1002/jmri.27294.

Issever, Ahi Sema, Volker Vieth, Albrecht Lotter, Norbert Meier, Andres Laib, David Newitt, Sharmila Majumdar, and Thomas M Link. 2002. 'Local Differences in the Trabecular Bone Structure of the Proximal Femur Depicted with High-Spatial-Resolution MR Imaging and Multisection CT'. *Academic Radiology* 9 (12): 1395–1406. https://doi.org/10.1016/S1076-6332(03)80667-0.

Jarraya, Mohamed, Rafael Heiss, Jeffrey Duryea, Armin M. Nagel, John A. Lynch, Ali Guermazi, Marc-André Weber, et al. 2021. 'Bone Structure Analysis of the Radius Using Ultrahigh Field (7T) MRI: Relevance of Technical Parameters and Comparison with 3T MRI and Radiography'. *Diagnostics* 11 (1): 110. https://doi.org/10.3390/diagnostics11010110.

Jenkinson, Mark, Peter Bannister, Michael Brady, and Stephen Smith. 2002. 'Improved Optimization for the Robust and Accurate Linear Registration and Motion Correction of Brain Images'. *NeuroImage* 17 (2): 825–41. https://doi.org/10.1006/nimg.2002.1132.

Jerban, Saeed, Douglas G. Chang, Yajun Ma, Hyungseok Jang, Eric Y. Chang, and Jiang Du. 2020. 'An Update in Qualitative Imaging of Bone Using Ultrashort Echo Time Magnetic Resonance'. *Frontiers in Endocrinology* 11 (September): 555756. https://doi.org/10.3389/fendo.2020.555756.

Jerban, Saeed, Xing Lu, Hyungseok Jang, Yajun Ma, Behnam Namiranian, Nicole Le, Ying Li, Eric Y. Chang, and Jiang Du. 2019. 'Significant Correlations between Human Cortical Bone Mineral Density and Quantitative Susceptibility Mapping (QSM) Obtained with 3D Cones Ultrashort Echo Time Magnetic Resonance Imaging (UTE-MRI)'. *Magnetic Resonance Imaging* 62 (October): 104–10. https://doi.org/10.1016/j.mri.2019.06.016.

Jerban, Saeed, Yajun Ma, Liang Li, Hyungseok Jang, Lidi Wan, Tan Guo, Adam Searleman, Eric Y. Chang, and Jiang Du. 2019. 'Volumetric Mapping of Bound and Pore Water as Well as Collagen Protons in Cortical Bone Using 3D Ultrashort Echo Time Cones MR Imaging Techniques'. *Bone* 127 (October): 120–28. https://doi.org/10.1016/j.bone.2019.05.038.

Jiang, Jian-Guo, Yanrong Guo, Shu Zhan, and Hong Li. 2008. 'Segmentation of Knee Joints Based on Improved Multiphase Chan-Vese Model'. In *2008 2nd International Conference on Bioinformatics and Biomedical Engineering*, 2418–22. Shanghai, China: IEEE. https://doi.org/10.1109/ICBBE.2008.937.

Johansson, M.V., F. Testa, P. Perrier, J. Vicente, J.P. Bonnet, P. Moulin, and I. Graur. 2019. 'Determination of an Effective Pore Dimension for Microporous Media'. *International Journal of Heat and Mass Transfer* 142 (October): 118412. https://doi.org/10.1016/j.ijheatmasstransfer.2019.07.062.

Johnell, O, and J A Kanis. 2006. 'An Estimate of the Worldwide Prevalence and Disability Associated with Osteoporotic Fractures'. *Osteoporos Int*, 8.

Jun, Bong-Jae, Amit Vasanji, Eric T. Ricchetti, Eric Rodriguez, Naveen Subhas, Zong-Ming Li, and Joseph P. Iannotti. 2017. 'Quantification of Regional Variations in Glenoid Trabecular Bone Architecture and Mineralization Using Clinical Computed Tomography Images: GLENOID TRABECULAR BONE ARCHITECTURAL VARIATIONS'. *Journal of Orthopaedic Research*, June. https://doi.org/10.1002/jor.23620.

Kaflak, Agnieszka, Dariusz Chmielewski, and Waclaw Kolodziejski. 2016. 'Solid-State NMR Study of Discrete Environments of Bone Mineral Nanoparticles Using Phosphorus-31 Relaxation'. *Journal of Applied Biomedicine* 14 (4): 321–30. https://doi.org/10.1016/j.jab.2016.07.001.

Kamel-ElSayed, Suzan A., LeAnn M. Tiede-Lewis, Yongbo Lu, Patricia A. Veno, and Sarah L. Dallas. 2015. 'Novel Approaches for Two and Three Dimensional Multiplexed Imaging of Osteocytes'. *Bone* 76 (July): 129–40. https://doi.org/10.1016/j.bone.2015.02.011.

Kang, C., M. Paley, R. Ordidge, and R. Speller. 1999. 'In Vivo MRI Measurements of Bone Quality in the Calcaneus: A Comparison with DXA and Ultrasound'. *Osteoporosis International* 9 (1): 65–74. https://doi.org/10.1007/s001980050117.

Karamat, Muhammad Irfan, Sahar Darvish-Molla, and Alejandro Santos-Diaz. 2016a. 'Opportunities and Challenges of 7 Tesla Magnetic Resonance Imaging: A Review'. *Critical Reviews in Biomedical Engineering* 44 (1–02): 73–89. https://doi.org/10.1615/CritRevBiomedEng.2016016365.

———. 2016b. ‘Opportunities and Challenges of 7 Tesla Magnetic Resonance Imaging: A Review’. *Critical Reviews in Biomedical Engineering* 44 (1–02): 73–89. https://doi.org/10.1615/CritRevBiomedEng.2016016365.

Karampinos, Dimitrios C., Stefan Ruschke, Michael Dieckmeyer, Maximilian Diefenbach, Daniela Franz, Alexandra S. Gersing, Roland Krug, and Thomas Baum. 2018. ‘Quantitative MRI and Spectroscopy of Bone Marrow: Quantitative MR of Bone Marrow’. *Journal of Magnetic Resonance Imaging* 47 (2): 332–53. https://doi.org/10.1002/jmri.25769.

Karampinos, Dimitrios C, Stefan Ruschke, Olga Gordijenko, Eduardo Grande Garcia, Hendrik Kooijman, Rainer Burgkart, Ernst J Rummeny, Jan S Bauer, and Thomas Baum. n.d. ‘Association of MRS-Based Vertebral Bone Marrow Fat Fraction with Bone Strength in a Human In Vitro Model’. *Journal of Osteoporosis*, 8.

Kassambara, A., and Fabian Mundt. 2020. ‘Extract and Visualize the Results of Multivariate Data Analyses [R Package Factoextra Version 1.0.7]’. *Undefined*. https://www.semanticscholar.org/paper/Extract-and-Visualize-the-Results-of-Multivariate-Kassambara-Mundt/5cb503e3db8609405d9f286fadc2a8bb867e5b6e.

Katsamenis, Orestis L., Harold M.H. Chong, Orestis G. Andriotis, and Philipp J. Thurner. 2013. ‘Load-Bearing in Cortical Bone Microstructure: Selective Stiffening and Heterogeneous Strain Distribution at the Lamellar Level’. *Journal of the Mechanical Behavior of Biomedical Materials* 17 (January): 152–65. https://doi.org/10.1016/j.jmbbm.2012.08.016.

Katz, Yekutiel, and Zohar Yosibash. 2020. ‘New Insights on the Proximal Femur Biomechanics Using Digital Image Correlation’. *Journal of Biomechanics* 101 (March): 109599. https://doi.org/10.1016/j.jbiomech.2020.109599.

Kazakia, Galateia J., Julio Carballido-Gamio, Andrew Lai, Lorenzo Nardo, Luca Facchetti, Courtney Pasco, Chiyuan A. Zhang, et al. 2018. ‘Trabecular Bone Microstructure Is Impaired in the Proximal Femur of Human Immunodeficiency Virus-Infected Men with Normal Bone Mineral Density’. *Quantitative Imaging in Medicine and Surgery* 8 (1): 5–13. https://doi.org/10.21037/qims.2017.10.10.

Kazakia, Galateia J, Benedict Hyun, Andrew J Burghardt, Roland Krug, David C Newitt, Anne E de Papp, Thomas M Link, and Sharmila Majumdar. 2007. ‘In Vivo Determination of Bone Structure in Postmenopausal Women: A Comparison of HR-PQCT and High-Field MR Imaging’. *Journal of Bone and Mineral Research* 23 (4): 463–74. https://doi.org/10.1359/jbmr.071116.

Kazakia, Galateia J., Jasmine A. Nirody, Gregory Bernstein, Miki Sode, Andrew J. Burghardt, and Sharmila Majumdar. 2013. ‘Age- and Gender-Related Differences in Cortical Geometry and Microstructure: Improved Sensitivity by Regional Analysis’. *Bone* 52 (2): 623–31. https://doi.org/10.1016/j.bone.2012.10.031.

Keenan, Hillary A., and Ernesto Maddaloni. 2016. ‘Bone Microarchitecture in Type 1 Diabetes: It Is Complicated’. *Current Osteoporosis Reports* 14 (6): 351–58. https://doi.org/10.1007/s11914-016-0338-8.

kemmak, Asma Rashki, Aziz Rezapour, Reza Jahangiri, Shima Nikjoo, Hiro Farabi, and Samira Soleimanpour. 2020. ‘Economic Burden of Osteoporosis in the World: A Systematic Review’. Preprint. In Review. https://doi.org/10.21203/rs.2.22372/v1.

Khaire, Mr G M, and R P Shelkikar. 2013. ‘Resolution Enhancement of Images with Interpolation and DWT-SWT Wavelet Domain Components’ 2 (9): 7.

Khosla, Sundeep, B Lawrence Riggs, Elizabeth J Atkinson, Ann L Oberg, Lisa J McDaniel, Margaret Holets, James M Peterson, and L Joseph Melton. 2005. 'Effects of Sex and Age on Bone Microstructure at the Ultradistal Radius: A Population-Based Noninvasive In Vivo Assessment'. *Journal of Bone and Mineral Research* 21 (1): 124–31. https://doi.org/10.1359/JBMR.050916.

Khurama, Jasvir S. 2009. *Bone Phatology*. 2nd edition. Humana Press.

Kijowski, Richard, Michael Tuite, Diane Kruger, Alejandro Munoz Del Rio, Michael Kleerekoper, and Neil Binkley. 2012. 'Evaluation of Trabecular Microarchitecture in Nonosteoporotic Postmenopausal Women with and without Fracture'. *Journal of Bone and Mineral Research* 27 (7): 1494–1500. https://doi.org/10.1002/jbmr.1595.

Kindler, Joseph M., Norman K. Pollock, Hannah L. Ross, Christopher M. Modlesky, Harshvardhan Singh, Emma M. Laing, and Richard D. Lewis. 2017. 'Obese Versus Normal-Weight Late-Adolescent Females Have Inferior Trabecular Bone Microarchitecture: A Pilot Case-Control Study'. *Calcified Tissue International* 101 (5): 479–88. https://doi.org/10.1007/s00223-017-0303-2.

Knothe Tate, Melissa L, Josée R Adamson, Andrea E Tami, and Thomas W Bauer. 2004. 'The Osteocyte'. *The International Journal of Biochemistry & Cell Biology* 36 (1): 1–8. https://doi.org/10.1016/S1357-2725(03)00241-3.

Kocijan, Roland, Matthias Englbrecht, Judith Haschka, David Simon, Arnd Kleyer, Stephanie Finzel, Sebastian Kraus, et al. 2015. 'Quantitative and Qualitative Changes of Bone in Psoriasis and Psoriatic Arthritis Patients'. *Journal of Bone and Mineral Research: The Official Journal of the American Society for Bone and Mineral Research* 30 (10): 1775–83. https://doi.org/10.1002/jbmr.2521.

Koda-Kimble, Mary A., Brian Alldredge, Joseph Guglielmo, Wayne Kradjan, and Lloyd Y. Young. 2008. *Applied Therapeutics : The Clinical Use of Drugs*. 9th Edition. Lippincott Williams & Wilkins.

Kokot, Grzegorz, Anna Makuch, Konstanty Skalski, and Jakub Bańczerowski. 2018. 'Mechanical Properties of Cancellous Tissue in Compression Test and Nanoindentation'. *Bio-Medical Materials and Engineering* 29 (4): 415–26. https://doi.org/10.3233/BME-180999.

Koo, Terry K., and Mae Y. Li. 2016a. 'A Guideline of Selecting and Reporting Intraclass Correlation Coefficients for Reliability Research'. *Journal of Chiropractic Medicine* 15 (2): 155–63. https://doi.org/10.1016/j.jcm.2016.02.012.

———. 2016b. 'A Guideline of Selecting and Reporting Intraclass Correlation Coefficients for Reliability Research'. *Journal of Chiropractic Medicine* 15 (2): 155–63. https://doi.org/10.1016/j.jcm.2016.02.012.

Koshi, Rachel. 2017. *Cunningham's Manual of Practical Anatomy VOL 1 Upper and Lower limbs*. 16th ed. Vol. 1. OUP Oxford.

———. n.d. *Cunningham's Manual of Practical Anatomy VOL 1 Upper and Lower Limbs*.

Kravets, Igor. 2018. 'Paget's Disease of Bone: Diagnosis and Treatment'. *The American Journal of Medicine* 131 (11): 1298–1303. https://doi.org/10.1016/j.amjmed.2018.04.028.

Kröger, H., P. Vainio, J. Nieminen, and A. Kotaniemi. 1995. 'Comparison of Different Models for Interpreting Bone Mineral Density Measurements Using DXA and MRI Technology'. *Bone* 17 (2): 157–59. https://doi.org/10.1016/S8756-3282(95)00162-X.

Krug, R., J. Carballido-Gamio, A. J. Burghardt, G. Kazakia, B. H. Hyun, B. Jobke, S. Banerjee, M. Huber, T. M. Link, and S. Majumdar. 2008a. 'Assessment of Trabecular Bone Structure Comparing Magnetic Resonance Imaging at 3 Tesla with High-Resolution Peripheral Quantitative Computed Tomography Ex Vivo and in Vivo'. *Osteoporosis International* 19 (5): 653–61. https://doi.org/10.1007/s00198-007-0495-9.

———. 2008b. 'Assessment of Trabecular Bone Structure Comparing Magnetic Resonance Imaging at 3 Tesla with High-Resolution Peripheral Quantitative Computed Tomography Ex Vivo and in Vivo'. *Osteoporosis International* 19 (5): 653–61. https://doi.org/10.1007/s00198-007-0495-9.

Krug, Roland, S. Banerjee, E. T. Han, D. C. Newitt, T. M. Link, and S. Majumdar. 2005a. 'Feasibility of in Vivo Structural Analysis of High-Resolution Magnetic Resonance Images of the Proximal Femur'. *Osteoporosis International* 16 (11): 1307–14. https://doi.org/10.1007/s00198-005-1907-3.

———. 2005b. 'Feasibility of in Vivo Structural Analysis of High-Resolution Magnetic Resonance Images of the Proximal Femur'. *Osteoporosis International* 16 (11): 1307–14. https://doi.org/10.1007/s00198-005-1907-3.

Krug, Roland, Julio Carballido-Gamio, Suchandrima Banerjee, Andrew J. Burghardt, Thomas M. Link, and Sharmila Majumdar. 2008a. 'In Vivo Ultra-High-Field Magnetic Resonance Imaging of Trabecular Bone Microarchitecture at 7 T'. *Journal of Magnetic Resonance Imaging* 27 (4): 854–59. https://doi.org/10.1002/jmri.21325.

———. 2008b. 'In Vivo Ultra-High-Field Magnetic Resonance Imaging of Trabecular Bone Microarchitecture at 7 T'. *Journal of Magnetic Resonance Imaging* 27 (4): 854–59. https://doi.org/10.1002/jmri.21325.

Kuethe, Dean O., Arvind Caprihan, Irving J. Lowe, David P. Madio, and H.Michael Gach. 1999. 'Transforming NMR Data Despite Missing Points'. *Journal of Magnetic Resonance* 139 (1): 18–25. https://doi.org/10.1006/jmre.1999.1767.

Ladinsky, Glenn A, Branimir Vasilic, Andra M Popescu, Michael Wald, Babette S Zemel, Peter J Snyder, Louise Loh, et al. 2007. 'Trabecular Structure Quantified With the MRI-Based Virtual Bone Biopsy in Postmenopausal Women Contributes to Vertebral Deformity Burden Independent of Areal Vertebral BMD'. *Journal of Bone and Mineral Research* 23 (1): 64–74. https://doi.org/10.1359/jbmr.070815.

Lam, Diana, Sandra L. Wootton-Gorges, John P. McGahan, Robin Stern, and John M. Boone. 2011a. 'Abdominal Pediatric Cancer Surveillance Using Serial Computed Tomography: Evaluation of Organ Absorbed Dose and Effective Dose'. *Seminars in Oncology* 38 (1): 128–35. https://doi.org/10.1053/j.seminoncol.2010.11.009.

———. 2011b. 'Abdominal Pediatric Cancer Surveillance Using Serial Computed Tomography: Evaluation of Organ Absorbed Dose and Effective Dose'. *Seminars in Oncology* 38 (1): 128–35. https://doi.org/10.1053/j.seminoncol.2010.11.009.

Landi, E., G. Celotti, G. Logroscino, and A. Tampieri. 2003a. 'Carbonated Hydroxyapatite as Bone Substitute'. *Journal of the European Ceramic Society* 23 (15): 2931–37. https://doi.org/10.1016/S0955-2219(03)00304-2.

———. 2003b. 'Carbonated Hydroxyapatite as Bone Substitute'. *Journal of the European Ceramic Society* 23 (15): 2931–37. https://doi.org/10.1016/S0955-2219(03)00304-2.

Landis, William J, Karen J Hodgens, James Arena, and Min J A Song. n.d. 'Structural Relations between Collagen and Mineral in Bone as Determined by High Voltage Electron Microscopic Tomography', 11.

Lange, U., J. Teichmann, U. Müller-Ladner, and J. Strunk. 2005. 'Increase in Bone Mineral Density of Patients with Rheumatoid Arthritis Treated with Anti-TNF-Alpha Antibody: A Prospective Open-Label Pilot Study'. *Rheumatology (Oxford, England)* 44 (12): 1546–48. https://doi.org/10.1093/rheumatology/kei082.

Laval-Jeantet, Anne-Marie, Catherine Bergot, Roberta Carroll, and Françoise Garcia-Schaefer. 1983a. 'Cortical Bone Senescence and Mineral Bone Density of the Humerus'. *Calcified Tissue International* 35 (1): 268–72. https://doi.org/10.1007/BF02405044.

———. 1983b. 'Cortical Bone Senescence and Mineral Bone Density of the Humerus'. *Calcified Tissue International* 35 (1): 268–72. https://doi.org/10.1007/BF02405044.

Le Corroller, T., J. Halgrin, M. Pithioux, D. Guenoun, P. Chabrand, and P. Champsaur. 2012. 'Combination of Texture Analysis and Bone Mineral Density Improves the Prediction of Fracture Load in Human Femurs'. *Osteoporosis International* 23 (1): 163–69. https://doi.org/10.1007/s00198-011-1703-1.

Lê, Sébastien, Julie Josse, and François Husson. 2008. '**FactoMineR**: An *R* Package for Multivariate Analysis'. *Journal of Statistical Software* 25 (1). https://doi.org/10.18637/jss.v025.i01.

Leijten, Emmerik F. A., Tessa S. van Kempen, Marianne Boes, Jocea M. R. Michels-van Amelsfort, Dirkjan Hijnen, Sarita A. Y. Hartgring, Joel A. G. van Roon, Mark H. Wenink, and Timothy R. D. J. Radstake. 2015. 'Brief Report: Enrichment of Activated Group 3 Innate Lymphoid Cells in Psoriatic Arthritis Synovial Fluid'. *Arthritis & Rheumatology (Hoboken, N.J.)* 67 (10): 2673–78. https://doi.org/10.1002/art.39261.

Leonard, Mary B., Felix W. Wehrli, Susan L. Ziolkowski, Erica Billig, Jin Long, Thomas L. Nickolas, Jeremy F. Magland, et al. 2019. 'A Multi-Imaging Modality Study of Bone Density, Bone Structure and the Muscle - Bone Unit in End-Stage Renal Disease'. *Bone* 127 (October): 271–79. https://doi.org/10.1016/j.bone.2019.05.022.

Li, Cheng, Alan C. Seifert, Hamidreza Saligheh Rad, Yusuf A. Bhagat, Chamith S. Rajapakse, Wenli Sun, Shing Chun Benny Lam, and Felix W. Wehrli. 2014. 'Cortical Bone Water Concentration: Dependence of MR Imaging Measures on Age and Pore Volume Fraction'. *Radiology* 272 (3): 796–806. https://doi.org/10.1148/radiol.14132585.

Li, Guanwu, Zheng Xu, Hao Gu, Xuefeng Li, Wei Yuan, Shixin Chang, Jingzheng Fan, Horea Calimente, and Jiani Hu. 2017. 'Comparison of Chemical Shift-Encoded Water-Fat MRI and MR Spectroscopy in Quantification of Marrow Fat in Postmenopausal Females: Water-Fat Imaging Quantifies Marrow Fat'. *Journal of Magnetic Resonance Imaging* 45 (1): 66–73. https://doi.org/10.1002/jmri.25351.

Li, Wei, Bing Wu, and Chunlei Liu. 2011. 'Quantitative Susceptibility Mapping of Human Brain Reflects Spatial Variation in Tissue Composition'. *NeuroImage* 55 (4): 1645–56. https://doi.org/10.1016/j.neuroimage.2010.11.088.

Li, Zhan-Chun, Li-Yang Dai, Lei-Sheng Jiang, and Shijing Qiu. 2012. 'Difference in Subchondral Cancellous Bone between Postmenopausal Women with Hip Osteoarthritis and Osteoporotic Fracture: Implication for Fatigue Microdamage, Bone Microarchitecture, and Biomechanical Properties'. *Arthritis & Rheumatism* 64 (12): 3955–62. https://doi.org/10.1002/art.34670.

Lim, Stephen S, Theo Vos, Abraham D Flaxman, Goodarz Danaei, Kenji Shibuya, Heather Adair-Rohani, Mohammad A AlMazroa, et al. 2012. 'A Comparative Risk Assessment of Burden of Disease and Injury Attributable to 67 Risk Factors and Risk Factor Clusters in 21 Regions, 1990–2010: A Systematic Analysis for the Global Burden of Disease Study 2010'. *The Lancet* 380 (9859): 2224–60. https://doi.org/10.1016/S0140-6736(12)61766-8.

Link, Thomas M., Sharmila Majumdar, Peter Augat, John C. Lin, David Newitt, Ying Lu, Nancy E. Lane, and Harry K. Genant. 1998. 'In Vivo High Resolution MRI of the Calcaneus: Differences in Trabecular Structure in Osteoporosis Patients'. *Journal of Bone and Mineral Research* 13 (7): 1175–82. https://doi.org/10.1359/jbmr.1998.13.7.1175.

Link, Thomas M., Volker Vieth, Christoph Stehling, Albrecht Lotter, Ambros Beer, David Newitt, and Sharmila Majumdar. 2003a. 'High-Resolution MRI vs Multislice Spiral CT: Which Technique Depicts the Trabecular Bone Structure Best?' *European Radiology* 13 (4): 663–71. https://doi.org/10.1007/s00330-002-1695-5.

———. 2003b. 'High-Resolution MRI vs Multislice Spiral CT: Which Technique Depicts the Trabecular Bone Structure Best?' *European Radiology* 13 (4): 663–71. https://doi.org/10.1007/s00330-002-1695-5.

Link, T.M., V. Vieth, R. Langenberg, N. Meier, A. Lotter, D. Newitt, and S. Majumdar. 2003. 'Structure Analysis of High Resolution Magnetic Resonance Imaging of the Proximal Femur: In Vitro Correlation with Biomechanical Strength and BMD'. *Calcified Tissue International* 72 (2): 156–65. https://doi.org/10.1007/s00223-001-2132-5.

Liu, Chenglei, Chang Liu, Xvhua Ren, Liping Si, Hao Shen, Qian Wang, and Weiwu Yao. 2017. 'Quantitative Evaluation of Subchondral Bone Microarchitecture in Knee Osteoarthritis Using 3T MRI'. *BMC Musculoskeletal Disorders* 18 (1): 496. https://doi.org/10.1186/s12891-017-1865-x.

Liu, Chenglei, Chang Liu, Liping Si, Hao Shen, Qian Wang, and Weiwu Yao. 2018. 'Relationship between Subchondral Bone Microstructure and Articular Cartilage in the Osteoarthritic Knee Using 3T MRI: Interrelationships in the OA Knee'. *Journal of Magnetic Resonance Imaging* 48 (3): 669–79. https://doi.org/10.1002/jmri.25982.

Liu, X Sherry, Adi Cohen, Elizabeth Shane, Perry T Yin, Emily M Stein, Halley Rogers, Shannon L Kokolus, et al. 2010. 'Bone Density, Geometry, Microstructure, and Stiffness: Relationships between Peripheral and Central Skeletal Sites Assessed by DXA, HR-PQCT, and CQCT in Premenopausal Women'. *Journal of Bone and Mineral Research* 25 (10): 2229–38. https://doi.org/10.1002/jbmr.111.

Liu, X Sherry, X Henry Zhang, Chamith S Rajapakse, Michael J Wald, Jeremy Magland, Kiranjit K Sekhon, Mark F Adam, Paul Sajda, Felix W Wehrli, and X Edward Guo. 2010. 'Accuracy of High-Resolution in Vivo Micro Magnetic Resonance Imaging for Measurements of Microstructural and Mechanical Properties of Human Distal Tibial Bone'. *Journal of Bone and Mineral Research* 25 (9): 2039–50. https://doi.org/10.1002/jbmr.92.

Lu, Xing, Hyungseok Jang, Yajun Ma, Saeed Jerban, Eric Chang, and Jiang Du. 2019. 'Ultrashort Echo Time Quantitative Susceptibility Mapping (UTE-QSM) of Highly Concentrated Magnetic Nanoparticles: A Comparison Study about Different Sampling Strategies'. *Molecules* 24 (6): 1143. https://doi.org/10.3390/molecules24061143.

MacKay, J.W., P.J. Murray, B. Kasmai, G. Johnson, S.T. Donell, and A.P. Toms. 2017. 'Subchondral Bone in Osteoarthritis: Association between MRI Texture Analysis and

Histomorphometry'. *Osteoarthritis and Cartilage* 25 (5): 700–707. https://doi.org/10.1016/j.joca.2016.12.011.

Madupalli, Honey, Barbara Pavan, and Mary M.J. Tecklenburg. 2017a. 'Carbonate Substitution in the Mineral Component of Bone: Discriminating the Structural Changes, Simultaneously Imposed by Carbonate in A and B Sites of Apatite'. *Journal of Solid State Chemistry* 255 (November): 27–35. https://doi.org/10.1016/j.jssc.2017.07.025.

———. 2017b. 'Carbonate Substitution in the Mineral Component of Bone: Discriminating the Structural Changes, Simultaneously Imposed by Carbonate in A and B Sites of Apatite'. *Journal of Solid State Chemistry* 255 (November): 27–35. https://doi.org/10.1016/j.jssc.2017.07.025.

Magland, J.F., M.J. Wald, and F.W. Wehrli. 2009. 'Spin-Echo Micro-MRI of Trabecular Bone Using Improved 3D Fast Large-Angle Spin-Echo (FLASE)'. *Magnetic Resonance in Medicine* 61 (5): 1114–21. https://doi.org/10.1002/mrm.21905.

Majumdar, S., H. K. Genant, S. Grampp, D. C. Newitt, V.-H. Truong, J. C. Lin, and A. Mathur. 1997a. 'Correlation of Trabecular Bone Structure with Age, Bone Mineral Density, and Osteoporotic Status: In Vivo Studies in the Distal Radius Using High Resolution Magnetic Resonance Imaging'. *Journal of Bone and Mineral Research* 12 (1): 111–18. https://doi.org/10.1359/jbmr.1997.12.1.111.

———. 1997b. 'Correlation of Trabecular Bone Structure with Age, Bone Mineral Density, and Osteoporotic Status: In Vivo Studies in the Distal Radius Using High Resolution Magnetic Resonance Imaging'. *Journal of Bone and Mineral Research* 12 (1): 111–18. https://doi.org/10.1359/jbmr.1997.12.1.111.

Majumdar, S., T. M. Link, Peter Augat, J. C. Lin, D. Newitt, N. E. Lane, and H. K. Genant. 1999a. 'Trabecular Bone Architecture in the Distal Radius Using Magnetic Resonance Imaging in Subjects with Fractures of the Proximal Femur'. *Osteoporosis International* 10 (3): 231–39. https://doi.org/10.1007/s001980050221.

———. 1999b. 'Trabecular Bone Architecture in the Distal Radius Using Magnetic Resonance Imaging in Subjects with Fractures of the Proximal Femur'. *Osteoporosis International* 10 (3): 231–39. https://doi.org/10.1007/s001980050221.

Majumdar, S., D. Newitt, A. Mathur, D. Osman, A. Gies, E. Chiu, J. Lotz, J. Kinney, and H. Genant. 1996a. 'Magnetic Resonance Imaging of Trabecular Bone Structure in the Distal Radius: Relationship with X-Ray Tomographic Microscopy and Biomechanics'. *Osteoporosis International* 6 (5): 376–85. https://doi.org/10.1007/BF01623011.

———. 1996b. 'Magnetic Resonance Imaging of Trabecular Bone Structure in the Distal Radius: Relationship with X-Ray Tomographic Microscopy and Biomechanics'. *Osteoporosis International* 6 (5): 376–85. https://doi.org/10.1007/BF01623011.

Makki, Karim, Bhushan Borotikar, Marc Garetier, Sylvain Brochard, Douraied Ben Salem, and François Rousseau. 2019. 'In Vivo Ankle Joint Kinematics from Dynamic Magnetic Resonance Imaging Using a Registration-Based Framework'. *Journal of Biomechanics* 86 (March): 193–203. https://doi.org/10.1016/j.jbiomech.2019.02.007.

Manenti, Guglielmo, Silvia Capuani, Ezio Fanucci, Elie Parfait Assako, Salvatore Masala, Roberto Sorge, Riccardo Iundusi, Umberto Tarantino, and Giovanni Simonetti. 2013. 'Diffusion Tensor Imaging and Magnetic Resonance Spectroscopy Assessment of Cancellous Bone Quality in Femoral Neck of Healthy, Osteopenic and Osteoporotic

Subjects at 3T: Preliminary Experience'. *Bone* 55 (1): 7–15. https://doi.org/10.1016/j.bone.2013.03.004.

Manhard, Mary Kate, R. Adam Horch, Daniel F. Gochberg, Jeffry S. Nyman, and Mark D. Does. 2015. 'In Vivo Quantitative MR Imaging of Bound and Pore Water in Cortical Bone'. *Radiology* 277 (1): 221–29. https://doi.org/10.1148/radiol.2015140336.

Manske, S. L., T. Liu-Ambrose, D. M. L. Cooper, S. Kontulainen, P. Guy, B. B. Forster, and H. A. McKay. 2009. 'Cortical and Trabecular Bone in the Femoral Neck Both Contribute to Proximal Femur Failure Load Prediction'. *Osteoporosis International* 20 (3): 445–53. https://doi.org/10.1007/s00198-008-0675-2.

Marcellusi, Andrea, Maria Assunta Rotundo, Claudia Nardone, Paolo Sciattella, Simone Gazzillo, Maurizio Rossini, Mario Barbagallo, Amalia Antenori, Domenico Valle, and Francesco Saverio Mennini. 2020. 'Osteoporosis: Economic Burden of Disease in Italy'. *Clinical Drug Investigation* 40 (5): 449–58. https://doi.org/10.1007/s40261-020-00904-8.

Marini, Joan C., Antonella Forlino, Hans Peter Bächinger, Nick J. Bishop, Peter H. Byers, Anne De Paepe, Francois Fassier, et al. 2017. 'Osteogenesis Imperfecta'. *Nature Reviews Disease Primers* 3 (1): 17052. https://doi.org/10.1038/nrdp.2017.52.

Marotte, Hubert, Beatrice Pallot-Prades, Laurent Grange, Philippe Gaudin, Christian Alexandre, and Pierre Miossec. 2007. 'A 1-Year Case-Control Study in Patients with Rheumatoid Arthritis Indicates Prevention of Loss of Bone Mineral Density in Both Responders and Nonresponders to Infliximab'. *Arthritis Research & Therapy* 9 (3): R61. https://doi.org/10.1186/ar2219.

Martel, Dimitri, Benjamin Leporq, Mary Bruno, Ravinder R. Regatte, Stephen Honig, and Gregory Chang. 2018. 'Chemical Shift-Encoded MRI for Assessment of Bone Marrow Adipose Tissue Fat Composition: Pilot Study in Premenopausal versus Postmenopausal Women'. *Magnetic Resonance Imaging* 53 (November): 148–55. https://doi.org/10.1016/j.mri.2018.07.001.

Martel, Dimitri, Benjamin Leporq, Amit Saxena, H. Michael Belmont, Gabrielle Turyan, Stephen Honig, Ravinder R. Regatte, and Gregory Chang. 2018. '3T Chemical Shift-encoded MRI: Detection of Altered Proximal Femur Marrow Adipose Tissue Composition in Glucocorticoid Users and Validation with Magnetic Resonance Spectroscopy'. *Journal of Magnetic Resonance Imaging*, December, jmri.26586. https://doi.org/10.1002/jmri.26586.

Martin, R. Bruce, David B. Burr, Neil A. Sharkey, and David P. Fyhrie. 2015. *Skeletal Tissue Mechanics*. New York, NY: Springer New York. https://doi.org/10.1007/978-1-4939-3002-9.

Maruotti, N., A. Corrado, and F. P. Cantatore. 2014. 'Osteoporosis and Rheumatic Diseases'. *Reumatismo* 66 (2): 125–35. https://doi.org/10.4081/reumatismo.2014.785.

Mastrogiacomo, Simone, Weiqiang Dou, John A. Jansen, and X. Frank Walboomers. 2019. 'Magnetic Resonance Imaging of Hard Tissues and Hard Tissue Engineered Bio-Substitutes'. *Molecular Imaging and Biology* 21 (6): 1003–19. https://doi.org/10.1007/s11307-019-01345-2.

Masuyama, R., Y. Nakaya, S. Tanaka, H. Tsurukami, T. Nakamura, S. Watanabe, T. Yoshizawa, S. Kato, and K. Suzuki. 2001. 'Dietary Phosphorus Restriction Reverses the Impaired Bone Mineralization in Vitamin D Receptor Knockout Mice'. *Endocrinology* 142 (1): 494–97. https://doi.org/10.1210/endo.142.1.8050.

Menon, Bina, Nicola J. Gullick, Gina J. Walter, Megha Rajasekhar, Toby Garrood, Hayley G. Evans, Leonie S. Taams, and Bruce W. Kirkham. 2014. 'Interleukin-17+CD8+ T Cells Are Enriched in the Joints of Patients with Psoriatic Arthritis and Correlate with Disease Activity and Joint Damage Progression'. *Arthritis & Rheumatology (Hoboken, N.J.)* 66 (5): 1272–81. https://doi.org/10.1002/art.38376.

Milovanovic, Petar, Jelena Potocnik, Danijela Djonic, Slobodan Nikolic, Vladimir Zivkovic, Marija Djuric, and Zlatko Rakocevic. 2012. 'Age-Related Deterioration in Trabecular Bone Mechanical Properties at Material Level: Nanoindentation Study of the Femoral Neck in Women by Using AFM'. *Experimental Gerontology* 47 (2): 154–59. https://doi.org/10.1016/j.exger.2011.11.011.

Minisola, Salvatore, Munro Peacock, Seijii Fukumoto, Cristiana Cipriani, Jessica Pepe, Sri Harsha Tella, and Michael T. Collins. 2017. 'Tumour-Induced Osteomalacia'. *Nature Reviews Disease Primers* 3 (1): 17044. https://doi.org/10.1038/nrdp.2017.44.

Modlesky, C. M., P. Subramanian, and F. Miller. 2008. 'Underdeveloped Trabecular Bone Microarchitecture Is Detected in Children with Cerebral Palsy Using High-Resolution Magnetic Resonance Imaging'. *Osteoporosis International* 19 (2): 169–76. https://doi.org/10.1007/s00198-007-0433-x.

Molino, Giulia, Alessio Dalpozzi, Gabriela Ciapetti, Massimo Lorusso, Chiara Novara, Marco Cavallo, Nicola Baldini, Fabrizio Giorgis, Sonia Fiorilli, and Chiara Vitale-Brovarone. 2019. 'Osteoporosis-Related Variations of Trabecular Bone Properties of Proximal Human Humeral Heads at Different Scale Lengths'. *Journal of the Mechanical Behavior of Biomedical Materials* 100 (December): 103373. https://doi.org/10.1016/j.jmbbm.2019.103373.

Moll, J. M., and V. Wright. 1973. 'Psoriatic Arthritis'. *Seminars in Arthritis and Rheumatism* 3 (1): 55–78. https://doi.org/10.1016/0049-0172(73)90035-8.

Monico, Letizia, Laura Cartechini, Francesca Rosi, Wout De Nolf, Marine Cotte, Riccardo Vivani, Celeste Maurich, and Costanza Miliani. 2020. 'Synchrotron Radiation Ca K-Edge 2D-XANES Spectroscopy for Studying the Stratigraphic Distribution of Calcium-Based Consolidants Applied in Limestones'. *Scientific Reports* 10 (1): 14337. https://doi.org/10.1038/s41598-020-71105-8.

Mow, Van C., and Rik Huiskes. 2004. *Basic Orthopaedic Biomechanics and Mechano-Biology, 3rd Ed.* 3rd ed. LWW.

Mueller, Thomas L., G. Harry van Lenthe, Martin Stauber, Christian Gratzke, Felix Eckstein, and Ralph Müller. 2009. 'Regional, Age and Gender Differences in Architectural Measures of Bone Quality and Their Correlation to Bone Mechanical Competence in the Human Radius of an Elderly Population'. *Bone* 45 (5): 882–91. https://doi.org/10.1016/j.bone.2009.06.031.

Mulder, Martijn J., Max C. Keuken, Pierre-Louis Bazin, Anneke Alkemade, and Birte U. Forstmann. 2019a. 'Size and Shape Matter: The Impact of Voxel Geometry on the Identification of Small Nuclei'. Edited by Niels Bergsland. *PLOS ONE* 14 (4): e0215382. https://doi.org/10.1371/journal.pone.0215382.

———. 2019b. 'Size and Shape Matter: The Impact of Voxel Geometry on the Identification of Small Nuclei'. Edited by Niels Bergsland. *PLOS ONE* 14 (4): e0215382. https://doi.org/10.1371/journal.pone.0215382.

Murray, Christopher J L. 2012. 'Disability-Adjusted Life Years (DALYs) for 291 Diseases and Injuries in 21 Regions, 1990–2010: A Systematic Analysis for the Global Burden of Disease Study 2010' 380: 27.

Murshed, Monzur. 2018. 'Mechanism of Bone Mineralization'. *Cold Spring Harbor Perspectives in Medicine* 8 (12): a031229. https://doi.org/10.1101/cshperspect.a031229.

Murugan, R, and S Ramakrishna. 2005. 'Development of Nanocomposites for Bone Grafting'. *Composites Science and Technology* 65 (15–16): 2385–2406. https://doi.org/10.1016/j.compscitech.2005.07.022.

Nayak, S., D. L. Edwards, A. A. Saleh, and S. L. Greenspan. 2015a. 'Systematic Review and Meta-Analysis of the Performance of Clinical Risk Assessment Instruments for Screening for Osteoporosis or Low Bone Density'. *Osteoporosis International* 26 (5): 1543–54. https://doi.org/10.1007/s00198-015-3025-1.

———. 2015b. 'Systematic Review and Meta-Analysis of the Performance of Clinical Risk Assessment Instruments for Screening for Osteoporosis or Low Bone Density'. *Osteoporosis International* 26 (5): 1543–54. https://doi.org/10.1007/s00198-015-3025-1.

Nazarian, Ara, John Muller, David Zurakowski, Ralph Müller, and Brian D. Snyder. 2007. 'Densitometric, Morphometric and Mechanical Distributions in the Human Proximal Femur'. *Journal of Biomechanics* 40 (11): 2573–79. https://doi.org/10.1016/j.jbiomech.2006.11.022.

Nguyen, Christelle, Hang Korng Ea, Dominique Thiaudiere, Solenn Reguer, Didier Hannouche, Michel Daudon, Frédéric Lioté, and Dominique Bazin. 2011. 'Calcifications in Human Osteoarthritic Articular Cartilage: *Ex Vivo* Assessment of Calcium Compounds Using XANES Spectroscopy'. *Journal of Synchrotron Radiation* 18 (3): 475–80. https://doi.org/10.1107/S0909049511006984.

Nikolov, Svetoslav, and Dierk Raabe. 2008. 'Hierarchical Modeling of the Elastic Properties of Bone at Submicron Scales: The Role of Extrafibrillar Mineralization'. *Biophysical Journal* 94 (11): 4220–32. https://doi.org/10.1529/biophysj.107.125567.

Nyman, Jeffry S., Anuradha Roy, Xinmei Shen, Rae L. Acuna, Jerrod H. Tyler, and Xiaodu Wang. 2006a. 'The Influence of Water Removal on the Strength and Toughness of Cortical Bone'. *Journal of Biomechanics* 39 (5): 931–38. https://doi.org/10.1016/j.jbiomech.2005.01.012.

———. 2006b. 'The Influence of Water Removal on the Strength and Toughness of Cortical Bone'. *Journal of Biomechanics* 39 (5): 931–38. https://doi.org/10.1016/j.jbiomech.2005.01.012.

Odén, A., E. V. McCloskey, J. A. Kanis, N. C. Harvey, and H. Johansson. 2015. 'Burden of High Fracture Probability Worldwide: Secular Increases 2010–2040'. *Osteoporosis International* 26 (9): 2243–48. https://doi.org/10.1007/s00198-015-3154-6.

Oers, René F. M. van, Hong Wang, and Rommel G. Bacabac. 2015. 'Osteocyte Shape and Mechanical Loading'. *Current Osteoporosis Reports* 13 (2): 61–66. https://doi.org/10.1007/s11914-015-0256-1.

Oftadeh, Ramin, Miguel Perez-Viloria, Juan C. Villa-Camacho, Ashkan Vaziri, and Ara Nazarian. 2015. 'Biomechanics and Mechanobiology of Trabecular Bone: A Review'. *Journal of Biomechanical Engineering* 137 (1): 010802. https://doi.org/10.1115/1.4029176.

Ogdie, Alexis, Lauren Harter, Daniel Shin, Joshua Baker, Junko Takeshita, Hyon K. Choi, Thorvardur Jon Love, and Joel M. Gelfand. 2017a. 'The Risk of Fracture among Patients with Psoriatic Arthritis and Psoriasis: A Population-Based Study'. *Annals of the Rheumatic Diseases* 76 (5): 882–85. https://doi.org/10.1136/annrheumdis-2016-210441.

Ogdie, Alexis, Lauren Harter, Daniel Shin, Joshua Baker, Junko Takeshita, Hyon K Choi, Thorvardur Jon Love, and Joel M Gelfand. 2017b. 'The Risk of Fracture among Patients with Psoriatic Arthritis and Psoriasis: A Population-Based Study'. *Annals of the Rheumatic Diseases* 76 (5): 882–85. https://doi.org/10.1136/annrheumdis-2016-210441.

Ogdie, Alexis, and Pamela Weiss. 2015. 'The Epidemiology Psoriatic Arthritis'. *Rheumatic Diseases Clinics of North America* 41 (4): 545–68. https://doi.org/10.1016/j.rdc.2015.07.001.

Ohs, Nicholas, Caitlyn J. Collins, and Penny R. Atkins. 2020. 'Validation of HR-PQCT against Micro-CT for Morphometric and Biomechanical Analyses: A Review'. *Bone Reports* 13 (December): 100711. https://doi.org/10.1016/j.bonr.2020.100711.

Oksanen, Jari, F. Guillaume Blanchet, Michael Friendly, Roeland Kindt, Pierre Legendre, Dan McGlinn, Peter R. Minchin, et al. 2020. *Vegan: Community Ecology Package* (version 2.5-7). https://CRAN.R-project.org/package=vegan.

Oliver, W.C., and G.M. Pharr. 1992. 'An Improved Technique for Determining Hardness and Elastic Modulus Using Load and Displacement Sensing Indentation Experiments'. *Journal of Materials Research* 7 (6): 1564–83. https://doi.org/10.1557/JMR.1992.1564.

Oostwaard, Marsha van. 2018. 'Osteoporosis and the Nature of Fragility Fracture: An Overview'. In *Fragility Fracture Nursing*, edited by Karen Hertz and Julie Santy-Tomlinson, 1–13. Perspectives in Nursing Management and Care for Older Adults. Cham: Springer International Publishing. https://doi.org/10.1007/978-3-319-76681-2_1.

Osterhoff, Georg, Elise F Morgan, Sandra J Shefelbine, Lamya Karim, Laoise M McNamara, and Peter Augat. 2017. 'Bone Mechanical Properties and Changes with Osteoporosis', 26.

Ottani, V, D Martini, M Franchi, A Ruggeri, and M Raspanti. 2002. 'Hierarchical Structures in FIbrillar Collagens', 10.

Ovejero Crespo, Diana. 2020. 'Microindentation: A New Technique for Bone Quality Assessment'. *Advances in Therapy* 37 (S2): 47–54. https://doi.org/10.1007/s12325-019-01175-2.

Özarslan, Evren, Baba C. Vemuri, and Thomas H. Mareci. 2005. 'Generalized Scalar Measures for Diffusion MRI Using Trace, Variance, and Entropy: Generalized Scalar Measures for Diffusion MRI'. *Magnetic Resonance in Medicine* 53 (4): 866–76. https://doi.org/10.1002/mrm.20411.

Paccou, Julien, Pierre Hardouin, Anne Cotten, Guillaume Penel, and Bernard Cortet. n.d. 'The Role of Bone Marrow Fat in Skeletal Health: Usefulness and Perspectives for Clinicians'. *J Clin Endocrinol Metab*, 10.

Pacureanu, Alexandra, Max Langer, Elodie Boller, Paul Tafforeau, and Françoise Peyrin. 2012. 'Nanoscale Imaging of the Bone Cell Network with Synchrotron X-Ray Tomography: Optimization of Acquisition Setup: Synchrotron x-Ray Tomography

Reveals the Bone Cell Network'. *Medical Physics* 39 (4): 2229–38. https://doi.org/10.1118/1.3697525.

Paganin, D., S. C. Mayo, T. E. Gureyev, P. R. Miller, and S. W. Wilkins. 2002. 'Simultaneous Phase and Amplitude Extraction from a Single Defocused Image of a Homogeneous Object'. *Journal of Microscopy* 206 (1): 33–40. https://doi.org/10.1046/j.1365-2818.2002.01010.x.

Palomo, Telma, Tatiane Vilaça, and Marise Lazaretti-Castro. 2017. 'Osteogenesis Imperfecta: Diagnosis and Treatment'. *Current Opinion in Endocrinology & Diabetes and Obesity* 24 (6): 381–88. https://doi.org/10.1097/MED.0000000000000367.

Paschalis, Eleftherios P. 2019a. 'Fourier Transform Infrared Imaging of Bone'. In *Bone Research Protocols*, edited by Aymen I. Idris, 1914:641–49. Methods in Molecular Biology. New York, NY: Springer New York. https://doi.org/10.1007/978-1-4939-8997-3_34.

———. 2019b. 'Fourier Transform Infrared Imaging of Bone'. In *Bone Research Protocols*, edited by Aymen I. Idris, 1914:641–49. Methods in Molecular Biology. New York, NY: Springer New York. https://doi.org/10.1007/978-1-4939-8997-3_34.

Pawlikowski, Marek, Konstanty Skalski, Jakub Bańczerowski, Anna Makuch, and Krzysztof Jankowski. 2017. 'Stress–Strain Characteristic of Human Trabecular Bone Based on Depth Sensing Indentation Measurements'. *Biocybernetics and Biomedical Engineering* 37 (2): 272–80. https://doi.org/10.1016/j.bbe.2017.01.002.

Penner-Hahn, J E. n.d. '1.59 CCC01063.0005 X-Ray Absorption Spectroscopy', 28.

Penney, Graeme P, Jurgen Weese, John A Little, Paul Desmedt, Derek L G Hill, and David J Hawkes. 1998. 'A Comparison of Similarity Measures for Use in 2-D–3-D Medical Image Registration'. *IEEE TRANSACTIONS ON MEDICAL IMAGING* 17 (4): 10.

Perez-Chada, Lourdes M., and Joseph F. Merola. 2020. 'Comorbidities Associated with Psoriatic Arthritis: Review and Update'. *Clinical Immunology (Orlando, Fla.)* 214 (May): 108397. https://doi.org/10.1016/j.clim.2020.108397.

Pérez-Sáez, María José, Sabina Herrera, Daniel Prieto-Alhambra, Xavier Nogués, María Vera, Dolores Redondo-Pachón, Marisa Mir, et al. 2017. 'Bone Density, Microarchitecture, and Tissue Quality Long-Term After Kidney Transplant'. *Transplantation* 101 (6): 1290–94. https://doi.org/10.1097/TP.0000000000001328.

Peter Larkin. 2011. *Infrared and Raman Spectroscopy: Principles and Spectral Interpretation*. Elsevier.

Peter R. Griffiths and James De Haseth. 2007. *Fourier Transform Infrared Spectrometry*. 2nd Edition. James D. Winefordner.

Pierre-Marie Robitaille and Lawrence Berliner. 2006. *Ultra High Field Magnetic Resonance Imaging*. Springer US.

Pietro, Giulia Di. 2015. 'Bone Marrow Lipid Profiles from Peripheral Skeleton as Potential Biomarkers for Osteoporosis: A 1H-MR Spectroscopy Study'. *Academic Radiology*, 11.

Politi, Y., Y. Levi-Kalisman, S. Raz, F. Wilt, L. Addadi, S. Weiner, and I. Sagi. 2006. 'Structural Characterization of the Transient Amorphous Calcium Carbonate Precursor Phase in Sea Urchin Embryos'. *Advanced Functional Materials* 16 (10): 1289–98. https://doi.org/10.1002/adfm.200600134.

Poundarik, A. A., T. Diab, G. E. Sroga, A. Ural, A. L. Boskey, C. M. Gundberg, and D. Vashishth. 2012. 'Dilatational Band Formation in Bone'. *Proceedings of the National Academy of Sciences* 109 (47): 19178–83. https://doi.org/10.1073/pnas.1201513109.

Puri, Basant K. n.d. 'High-Resolution Magnetic Resonance Imaging Sinc-Interpolation-Based Subvoxel Registration and Semi-Automated Quantitative Lateral Ventricular Morphology Employing Threshold Computation and Binary Image Creation in the Study of Fatty Acid Interventions in Schizophrenia, Depression, Chronic Fatigue Syndrome and Huntington's Disease', 6.

Qiu, Shijing, D. Sudhaker Rao, Saroj Palnitkar, and A. Michael Parfitt. 2006. 'Differences in Osteocyte and Lacunar Density between Black and White American Women'. *Bone* 38 (1): 130–35. https://doi.org/10.1016/j.bone.2005.07.004.

Rad, Hamidreza Saligheh, Shing Chun Benny Lam, Jeremy F. Magland, Henry Ong, Cheng Li, Hee Kwon Song, James Love, and Felix W. Wehrli. 2011. 'Quantifying Cortical Bone Water *in Vivo* by Three-Dimensional Ultra-Short Echo-Time MRI: QUANTIFYING CORTICAL BONE WATER *IN VIVO* BY 3D UTE MRI'. *NMR in Biomedicine* 24 (7): 855–64. https://doi.org/10.1002/nbm.1631.

Rajapakse, C. S., E. A. Phillips, W. Sun, M. J. Wald, J. F. Magland, P. J. Snyder, and F. W. Wehrli. 2014. 'Vertebral Deformities and Fractures Are Associated with MRI and PQCT Measures Obtained at the Distal Tibia and Radius of Postmenopausal Women'. *Osteoporosis International* 25 (3): 973–82. https://doi.org/10.1007/s00198-013-2569-1.

Rajapakse, Chamith S., Mahdieh Bashoor-Zadeh, Cheng Li, Wenli Sun, Alexander C. Wright, and Felix W. Wehrli. 2015. 'Volumetric Cortical Bone Porosity Assessment with MR Imaging: Validation and Clinical Feasibility'. *Radiology* 276 (2): 526–35. https://doi.org/10.1148/radiol.15141850.

Rajapakse, Chamith S., Elizabeth A. Kobe, Alexandra S. Batzdorf, Michael W. Hast, and Felix W. Wehrli. 2018a. 'Accuracy of MRI-Based Finite Element Assessment of Distal Tibia Compared to Mechanical Testing'. *Bone* 108 (March): 71–78. https://doi.org/10.1016/j.bone.2017.12.023.

———. 2018b. 'Accuracy of MRI-Based Finite Element Assessment of Distal Tibia Compared to Mechanical Testing'. *Bone* 108 (March): 71–78. https://doi.org/10.1016/j.bone.2017.12.023.

Rajapakse, Chamith S., Mary B. Leonard, Yusuf A. Bhagat, Wenli Sun, Jeremy F. Magland, and Felix W. Wehrli. 2012a. 'Micro–MR Imaging–Based Computational Biomechanics Demonstrates Reduction in Cortical and Trabecular Bone Strength after Renal Transplantation'. *Radiology* 262 (3): 912–20. https://doi.org/10.1148/radiol.11111044.

———. 2012b. 'Micro–MR Imaging–Based Computational Biomechanics Demonstrates Reduction in Cortical and Trabecular Bone Strength after Renal Transplantation'. *Radiology* 262 (3): 912–20. https://doi.org/10.1148/radiol.11111044.

Rajapakse, Chamith S., Jeremy F. Magland, Michael J. Wald, X. Sherry Liu, X. Henry Zhang, X. Edward Guo, and Felix W. Wehrli. 2010a. 'Computational Biomechanics of the Distal Tibia from High-Resolution MR and Micro-CT Images'. *Bone* 47 (3): 556–63. https://doi.org/10.1016/j.bone.2010.05.039.

———. 2010b. 'Computational Biomechanics of the Distal Tibia from High-Resolution MR and Micro-CT Images'. *Bone* 47 (3): 556–63. https://doi.org/10.1016/j.bone.2010.05.039.

Rajapakse, Chamith S., Jeremy Magland, X. Henry Zhang, X. Sherry Liu, Suzanne L. Wehrli, X. Edward Guo, and Felix W. Wehrli. 2009a. 'Implications of Noise and Resolution on

Mechanical Properties of Trabecular Bone Estimated by Image-Based Finite-Element Analysis'. *Journal of Orthopaedic Research* 27 (10): 1263–71. https://doi.org/10.1002/jor.20877.

———. 2009b. 'Implications of Noise and Resolution on Mechanical Properties of Trabecular Bone Estimated by Image-Based Finite-Element Analysis'. *Journal of Orthopaedic Research* 27 (10): 1263–71. https://doi.org/10.1002/jor.20877.

Ramponi, Denise R., Judith Kaufmann, and Gwendolen Drahnak. 2018. 'Hip Fractures': *Advanced Emergency Nursing Journal* 40 (1): 8–15. https://doi.org/10.1097/TME.0000000000000180.

Rauscher, Alexander, Jan Sedlacik, Andreas Deistung, Hans-Joachim Mentzel, and Jürgen R. Reichenbach. 2006. 'Susceptibility Weighted Imaging: Data Acquisition, Image Reconstruction and Clinical Applications'. *Zeitschrift Für Medizinische Physik* 16 (4): 240–50. https://doi.org/10.1078/0939-3889-00322.

Ravel, B., and M. Newville. 2005. '*ATHENA* , *ARTEMIS* , *HEPHAESTUS* : Data Analysis for X-Ray Absorption Spectroscopy Using *IFEFFIT*'. *Journal of Synchrotron Radiation* 12 (4): 537–41. https://doi.org/10.1107/S0909049505012719.

Raynor, William, Cyrus Ayubcha, Sara Pourhassan Shamchi, Mahdi Zirakchian Zadeh, Sahra Emamzadehfard, Thomas Werner, Poul Flemming Hoilund-Carlsen, and Abass Alavi. 2017. 'Assessing Global Uptake of 18F-Sodium Fluoride in the Femoral Neck: A Novel Quantitative Technique to Evaluate Changes in Bone Turnover with Age.' *Journal of Nuclear Medicine* 58 (supplement 1): 1223–1223.

Reeder, Scott B., Houchun H. Hu, and Claude B. Sirlin. 2012. 'Proton Density Fat-Fraction: A Standardized Mr-Based Biomarker of Tissue Fat Concentration'. *Journal of Magnetic Resonance Imaging* 36 (5): 1011–14. https://doi.org/10.1002/jmri.23741.

Rehr, J. J., and R. C. Albers. 2000. 'Theoretical Approaches to X-Ray Absorption Fine Structure'. *Reviews of Modern Physics* 72 (3): 621–54. https://doi.org/10.1103/RevModPhys.72.621.

Rehr, J.J., and A.L. Ankudinov. 2001. 'New Developments in the Theory of X-Ray Absorption and Core Photoemission'. *Journal of Electron Spectroscopy and Related Phenomena* 114–116 (March): 1115–21. https://doi.org/10.1016/S0368-2048(00)00341-8.

Ren, Fu Zeng, and Yang Leng. 2011. 'Carbonated Apatite, Type-A or Type-B?' *Key Engineering Materials* 493–494 (October): 293–97. https://doi.org/10.4028/www.scientific.net/KEM.493-494.293.

Ren, Fuzeng, Yonghui Ding, and Yang Leng. 2014. 'Infrared Spectroscopic Characterization of Carbonated Apatite: A Combined Experimental and Computational Study: Ir Spectroscopic Characterization of CAp'. *Journal of Biomedical Materials Research Part A* 102 (2): 496–505. https://doi.org/10.1002/jbm.a.34720.

Renault, Jean-Baptiste, Maximiliano Carmona, Chris Tzioupis, Matthieu Ollivier, Jean-Noël Argenson, Sébastien Parratte, and Patrick Chabrand. 2020. 'Tibial Subchondral Trabecular Bone Micromechanical and Microarchitectural Properties Are Affected by Alignment and Osteoarthritis Stage'. *Scientific Reports* 10 (1): 3975. https://doi.org/10.1038/s41598-020-60464-x.

Rey, C. 1991. 'A Resolution-Enhanced Fourier Transform Infrared Spectroscopic Study of the Environment of the CO32- Ion in the Mineral Phase of Enamel during Its Formation and Maturation'. *Calcified Tissue International*, 10.

Rey, C., C. Combes, C. Drouet, and D. Grossin. 2011. 'Bioactive Ceramics: Physical Chemistry'. In *Comprehensive Biomaterials*, 187–221. Elsevier. https://doi.org/10.1016/B978-0-08-055294-1.00178-1.

Rho, Jae-Young, Liisa Kuhn-Spearing, and Peter Zioupos. 1998. 'Mechanical Properties and the Hierarchical Structure of Bone'. *Medical Engineering & Physics* 20 (2): 92–102. https://doi.org/10.1016/S1350-4533(98)00007-1.

Ritchlin, Christopher T., Robert A. Colbert, and Dafna D. Gladman. 2017. 'Psoriatic Arthritis'. Edited by Dan L. Longo. *New England Journal of Medicine* 376 (10): 957–70. https://doi.org/10.1056/NEJMra1505557.

Ritchlin, Christopher T., Sally A. Haas-Smith, Ping Li, David G. Hicks, and Edward M. Schwarz. 2003. 'Mechanisms of TNF-Alpha- and RANKL-Mediated Osteoclastogenesis and Bone Resorption in Psoriatic Arthritis'. *The Journal of Clinical Investigation* 111 (6): 821–31. https://doi.org/10.1172/JCI16069.

Rodriguez-Florez, Naiara, Michelle L. Oyen, and Sandra J. Shefelbine. 2013. 'Insight into Differences in Nanoindentation Properties of Bone'. *Journal of the Mechanical Behavior of Biomedical Materials* 18 (February): 90–99. https://doi.org/10.1016/j.jmbbm.2012.11.005.

Rosen, Daniel, Bruce Herrington, Peeyush Bhargava, Rodolfo Laucirica, and Gordana Verstovsek. 2011. 'Correlation of Tissue Biopsy and Fine Needle Aspiration Cytology with Positron Emission Tomography Results'. *Pathology Research International* 2011 (April): 1–7. https://doi.org/10.4061/2011/323051.

Rossi, Vittoria, Brendan Lee, and Ronit Marom. 2019. 'Osteogenesis Imperfecta: Advancements in Genetics and Treatment'. *Current Opinion in Pediatrics* 31 (6): 708–15. https://doi.org/10.1097/MOP.0000000000000813.

Ruderman, Irene, Chamith S. Rajapakse, Angelica Opperman, Patricia L. Robertson, Rosemary Masterson, Mark K. Tiong, and Nigel D. Toussaint. 2020. 'Bone Microarchitecture in Patients Undergoing Parathyroidectomy for Management of Secondary Hyperparathyroidism'. *Bone Reports* 13 (December): 100297. https://doi.org/10.1016/j.bonr.2020.100297.

Ruschke, Stefan. n.d. 'Measurement of Vertebral Bone Marrow Proton Density Fat Fraction in Children Using Quantitative Water–Fat MRI'. *Magn Reson Mater Phy*, 12.

Ruschke, Stefan, Holger Eggers, Hendrik Kooijman, Maximilian N. Diefenbach, Thomas Baum, Axel Haase, Ernst J. Rummeny, Houchun H. Hu, and Dimitrios C. Karampinos. 2017. 'Correction of Phase Errors in Quantitative Water-Fat Imaging Using a Monopolar Time-Interleaved Multi-Echo Gradient Echo Sequence: Phase Error Correction in Time-Interleaved Water-Fat Imaging'. *Magnetic Resonance in Medicine* 78 (3): 984–96. https://doi.org/10.1002/mrm.26485.

'RX Solutions SAS, 3D X-Ray Tomography Systems.' n.d.

Saleh, Mahmoud Mohamed, Tamer Moustafa Abdelrahman, Youusef Madney, Ghada Mohamed, Ahmed Mohammed Shokry, and Amr Farouk Moustafa. 2020. 'Multiparametric MRI with Diffusion-Weighted Imaging in Predicting Response to Chemotherapy in Cases of Osteosarcoma and Ewing's Sarcoma'. *The British Journal of Radiology* 93 (1115): 20200257. https://doi.org/10.1259/bjr.20200257.

Sasaki, Muneteru, Shinichiro Kuroshima, Yuri Aoki, Nao Inaba, and Takashi Sawase. 2015. 'Ultrastructural Alterations of Osteocyte Morphology via Loaded Implants in Rabbit

Tibiae'. *Journal of Biomechanics* 48 (15): 4130–41. https://doi.org/10.1016/j.jbiomech.2015.10.025.

Sato, Y., C. Westin, A. Bhalerao, S. Nakajima, N. Shiraga, S. Tamura, and R. Kikinis. 2000. 'Tissue Classification Based on 3D Local Intensity Structures for Volume Rendering'. *IEEE Transactions on Visualization and Computer Graphics* 6 (2): 160–80. https://doi.org/10.1109/2945.856997.

Sayers, Dale E., Edward A. Stern, and Farrel W. Lytle. 1971. 'New Technique for Investigating Noncrystalline Structures: Fourier Analysis of the Extended X-Ray—Absorption Fine Structure'. *Physical Review Letters* 27 (18): 1204–7. https://doi.org/10.1103/PhysRevLett.27.1204.

Scheiner, S, A Théoval, P Pivonka, D W Smith, and L F Bonewald. 2010. 'Investigation of Nutrient Transport Mechanisms in the Lacunae-Canaliculi System'. *IOP Conference Series: Materials Science and Engineering* 10 (June): 012129. https://doi.org/10.1088/1757-899X/10/1/012129.

Schmeel, Frederic Carsten, Julian Alexander Luetkens, Simon Jonas Enkirch, Andreas Feißt, Christoph Hans-Jürgen Endler, Leonard Christopher Schmeel, Peter Johannes Wagenhäuser, Frank Träber, Hans Heinz Schild, and Guido Matthias Kukuk. 2018. 'Proton Density Fat Fraction (PDFF) MR Imaging for Differentiation of Acute Benign and Neoplastic Compression Fractures of the Spine'. *European Radiology* 28 (12): 5001–9. https://doi.org/10.1007/s00330-018-5513-0.

Schmeel, Frederic Carsten, Julian Alexander Luetkens, Andreas Feißt, Simon Jonas Enkirch, Christoph Hans-Jürgen Endler, Peter Johannes Wagenhäuser, Leonard Christopher Schmeel, Frank Träber, Hans Heinz Schild, and Guido Matthias Kukuk. 2018. 'Quantitative Evaluation of T2* Relaxation Times for the Differentiation of Acute Benign and Malignant Vertebral Body Fractures'. *European Journal of Radiology* 108 (November): 59–65. https://doi.org/10.1016/j.ejrad.2018.09.021.

Schmidt, F.N., E.A. Zimmermann, G.M. Campbell, G.E. Sroga, K. Püschel, M. Amling, S.Y. Tang, D. Vashishth, and B. Busse. 2017a. 'Assessment of Collagen Quality Associated with Non-Enzymatic Cross-Links in Human Bone Using Fourier-Transform Infrared Imaging'. *Bone* 97 (April): 243–51. https://doi.org/10.1016/j.bone.2017.01.015.

———. 2017b. 'Assessment of Collagen Quality Associated with Non-Enzymatic Cross-Links in Human Bone Using Fourier-Transform Infrared Imaging'. *Bone* 97 (April): 243–51. https://doi.org/10.1016/j.bone.2017.01.015.

Schuit, S.C.E, M van der Klift, A.E.A.M Weel, C.E.D.H de Laet, H Burger, E Seeman, A Hofman, A.G Uitterlinden, J.P.T.M van Leeuwen, and H.A.P Pols. 2004. 'Fracture Incidence and Association with Bone Mineral Density in Elderly Men and Women: The Rotterdam Study'. *Bone* 34 (1): 195–202. https://doi.org/10.1016/j.bone.2003.10.001.

Schweser, Ferdinand. 2015. 'Foundations of MRI Phase Imaging and Processing for Quantitative Susceptibility Mapping (QSM)', 29.

Sebbag, Eden, Renaud Felten, Flora Sagez, Jean Sibilia, Hervé Devilliers, and Laurent Arnaud. 2019. 'The World-Wide Burden of Musculoskeletal Diseases: A Systematic Analysis of the World Health Organization Burden of Diseases Database'. *Annals of the Rheumatic Diseases* 78 (6): 844–48. https://doi.org/10.1136/annrheumdis-2019-215142.

Seifert, Alan C., Cheng Li, Chamith S. Rajapakse, Mahdieh Bashoor-Zadeh, Yusuf A. Bhagat, Alexander C. Wright, Babette S. Zemel, Antonios Zavaliangos, and Felix W. Wehrli. 2014a. 'Bone Mineral ^{31} P and Matrix-Bound Water Densities Measured by Solid-State

^{31} P and ^{1} H MRI: BONE DENSITY QUANTIFICATION BY MRI'. *NMR in Biomedicine* 27 (7): 739–48. https://doi.org/10.1002/nbm.3107.

———. 2014b. 'Bone Mineral ^{31} P and Matrix-Bound Water Densities Measured by Solid-State ^{31} P and ^{1} H MRI: BONE DENSITY QUANTIFICATION BY MRI'. *NMR in Biomedicine* 27 (7): 739–48. https://doi.org/10.1002/nbm.3107.

Seifert, Alan C., and Felix W. Wehrli. 2016. 'Solid-State Quantitative 1H and 31P MRI of Cortical Bone in Humans'. *Current Osteoporosis Reports* 14 (3): 77–86. https://doi.org/10.1007/s11914-016-0307-2.

Sepulcre, Francesc, M. Grazia Proietti, Maurizio Benfatto, Stefano Della Longa, Joaquin García, and Esteve Padrós. 2004. 'A Quantitative XANES Analysis of the Calcium High-Affinity Binding Site of the Purple Membrane'. *Biophysical Journal* 87 (1): 513–20. https://doi.org/10.1529/biophysj.103.030080.

Sharir, Amnon, Meir Max Barak, and Ron Shahar. 2008. 'Whole Bone Mechanics and Mechanical Testing'. *The Veterinary Journal*, 10.

Sharma, Ashish K., Nigel D. Toussaint, Grahame J. Elder, Rosemary Masterson, Stephen G. Holt, Patricia L. Robertson, Peter R. Ebeling, Paul Baldock, Rhiannon C. Miller, and Chamith S. Rajapakse. 2018. 'Magnetic Resonance Imaging Based Assessment of Bone Microstructure as a Non-Invasive Alternative to Histomorphometry in Patients with Chronic Kidney Disease'. *Bone* 114: 14–21. https://doi.org/10.1016/j.bone.2018.05.029.

Sharma, Ashish K., Nigel D. Toussaint, Grahame J. Elder, Chamith S. Rajapakse, Stephen G. Holt, Paul Baldock, Patricia L. Robertson, Peter R. Ebeling, Olivia R. Sorci, and Rosemary Masterson. 2018. 'Changes in Bone Microarchitecture Following Kidney Transplantation-Beyond Bone Mineral Density'. *Clinical Transplantation* 32 (9): e13347. https://doi.org/10.1111/ctr.13347.

Shen, W., J. Chen, M. Punyanitya, S. Shapses, S. Heshka, and S. B. Heymsfield. 2007. 'MRI-Measured Bone Marrow Adipose Tissue Is Inversely Related to DXA-Measured Bone Mineral in Caucasian Women'. *Osteoporosis International* 18 (5): 641–47. https://doi.org/10.1007/s00198-006-0285-9.

Sheu, Yahtyng, Francesca Amati, Ann V Schwartz, Michelle E Danielson, Xiaojuan Li, Robert Boudreau, and Jane A Cauley. 2018. 'Vertebral Bone Marrow Fat, Bone Mineral Density and Diabetes: The Osteoporotic Fractures in Men (MrOS) Study', 18.

Sindhupakorn, Bura, and Pinit Kidkhunthod. 2021. 'Structural Investigation in Subchondral Bone of Osteoarthritic Knee: Phosphorous K-Edge XAS'. *Radiation Physics and Chemistry* 187 (October): 109584. https://doi.org/10.1016/j.radphyschem.2021.109584.

Singhal, Vibha, and Miriam A. Bredella. 2019. 'Marrow Adipose Tissue Imaging in Humans'. *Bone* 118 (January): 69–76. https://doi.org/10.1016/j.bone.2018.01.009.

Singhal, Vibha, Shreya Tulsiani, Karen Joanie Campoverde, Deborah M. Mitchell, Meghan Slattery, Melanie Schorr, Karen K. Miller, Miriam A. Bredella, Madhusmita Misra, and Anne Klibanski. 2018. 'Impaired Bone Strength Estimates at the Distal Tibia and Its Determinants in Adolescents with Anorexia Nervosa'. *Bone* 106 (January): 61–68. https://doi.org/10.1016/j.bone.2017.07.009.

Soldado-Folgado, Jade, Elisabeth Lerma-Chippirraz, Itziar Arrieta-Aldea, Daniel Bujosa, Natalia García-Giralt, Marta Pineda-Moncusi, Marta Trenchs-Rodríguez, et al. 2020. 'Bone Density, Microarchitecture and Tissue Quality after 1 Year of Treatment with

Dolutegravir/Abacavir/Lamivudine'. *Journal of Antimicrobial Chemotherapy* 75 (10): 2998–3003. https://doi.org/10.1093/jac/dkaa254.

Soldati, Enrico, David Bendahan, Martine Pithioux, and Jerome Vicente. 2020. 'MRI Assessment of Bone Microarchitecture in Human Bone Samples: The Issue of Air Bubbles Artefacts'. *Bone Reports* 13 (October): 100541. https://doi.org/10.1016/j.bonr.2020.100541.

Soldati, Enrico, Lucas Escoffier, Sophie Gabriel, Jean Pierre Mattei, Serge Cammilleri, David Bendahan, and Sandrine Guis. 2020. 'Assessment of in Vivo Bone Microarchitecture Changes in a Psoriatic Arthritic Patient Resulting from an Anti-TNFα Treatment'. Preprint. In Review. https://doi.org/10.21203/rs.3.rs-115381/v1.

Soldati, Enrico, Lucas Escoffier, Sophie Gabriel, Augustin C. Ogier, Christophe Chagnaud, Jean P. Mattei, Serge Cammilleri, David Bendahan, and Sandrine Guis. 2021. 'Assessment of in Vivo Bone Microarchitecture Changes in an Anti-TNFα Treated Psoriatic Arthritic Patient'. Edited by Ewa Tomaszewska. *PLOS ONE* 16 (5): e0251788. https://doi.org/10.1371/journal.pone.0251788.

Soldati, Enrico, Martine Pithioux, Jerome Vicente, and David Bendahan. 2020. 'Trabecular Bone Microarchitecture: A Comparative Analysis between High Field, Ultra High Field MRI and X-Ray Micro CT in Humans Anatomical Samples'. *Bone Reports* 13 (October): 100542. https://doi.org/10.1016/j.bonr.2020.100542.

Soldati, Enrico, Francesca Rossi, Jerome Vicente, Daphne Guenoun, Martine Pithioux, Stefano Iotti, Emil Malucelli, and David Bendahan. 2021. 'Survey of MRI Usefulness for the Clinical Assessment of Bone Microstructure'. *International Journal of Molecular Sciences* 22 (5): 2509. https://doi.org/10.3390/ijms22052509.

Soldati, Enrico, Jerome Vicente, Daphne Guenoun, David Bendahan, and Martine Pithioux. 2021. 'Validation and Optimization of Proximal Femurs Microstructure Analysis Using High Field and Ultra-High Field MRI'. *Diagnostics* 11 (9): 1603. https://doi.org/10.3390/diagnostics11091603.

Sollmann, Nico, Maximilian T. Löffler, Sophia Kronthaler, Christof Böhm, Michael Dieckmeyer, Stefan Ruschke, Jan S. Kirschke, et al. 2020. 'MRI -Based Quantitative Osteoporosis Imaging at the Spine and Femur'. *Journal of Magnetic Resonance Imaging*, June, jmri.27260. https://doi.org/10.1002/jmri.27260.

Souzanchi, Mohammad F, Paolo Palacio-Mancheno, Yury A Borisov, Luis Cardoso, and Stephen C Cowin. 2012. 'Microarchitecture and Bone Quality in the Human Calcaneus: Local Variations of Fabric Anisotropy'. *Journal of Bone and Mineral Research* 27 (12): 2562–72. https://doi.org/10.1002/jbmr.1710.

Sözen, Tümay, Lale Özışık, and Nursel Çalık Başaran. n.d. 'An Overview and Management of Osteoporosis', 11.

Stephan Grampp, Sharmila Majumdar, Michael Jergas, David Newitt, Philipp Lang, and Harry K. Genant. 1996. 'Distal Radius: In Vivo Assessment with Quantitative MR Imaging, Peripheral Quantitative CT, and Dual X-Ray Absorptiometry', January. https://doi.org/10.1148/radiology.198.1.8539382.

Stockhausen, Kilian E., Mahan Qwamizadeh, Eva M. Wölfel, Haniyeh Hemmatian, Imke A. K. Fiedler, Silja Flenner, Elena Longo, et al. 2021. 'Collagen Fiber Orientation Is Coupled with Specific Nano-Compositional Patterns in *Dark* and *Bright* Osteons Modulating

Their Biomechanical Properties'. *ACS Nano* 15 (1): 455–67. https://doi.org/10.1021/acsnano.0c04786.

Studholme, Colin, Derek L. G. Hill, and David J. Hawkes. 1997. 'Automated Three-Dimensional Registration of Magnetic Resonance and Positron Emission Tomography Brain Images by Multiresolution Optimization of Voxel Similarity Measures'. *Medical Physics* 24 (1): 25–35. https://doi.org/10.1118/1.598130.

Takizawa, Masahiro, Hikaru Hanada, Kuniharu Oka, Tetsuhiko Takahashi, Etsuji Yamamoto, and Masahiko Fujii. 2013. 'A Robust Ultrashort TE (UTE) Imaging Method With Corrected k-Space Trajectory by Using Parametric Multiple Function Model of Gradient Waveform'. *IEEE TRANSACTIONS ON MEDICAL IMAGING* 32 (2): 11.

Tamimi, Iskandar, Arthur Rodríguez González Cortes, Juan-Manuel Sánchez-Siles, Jerome L. Ackerman, David González-Quevedo, Ángel García, Farid Yaghoubi, et al. 2020. 'Composition and Characteristics of Trabecular Bone in Osteoporosis and Osteoarthritis'. *Bone* 140 (November): 115558. https://doi.org/10.1016/j.bone.2020.115558.

Tang, Yuanjiao, Shan Cheng, Yujia Yang, Xi Xiang, Liyun Wang, Lingyan Zhang, and Li Qiu. 2020. 'Ultrasound Assessment in Psoriatic Arthritis (PsA) and Psoriasis Vulgaris (Non-PsA): Which Sites Are Most Commonly Involved and What Features Are More Important in PsA?' *Quantitative Imaging in Medicine and Surgery* 10 (1): 86–95. https://doi.org/10.21037/qims.2019.08.09.

Tassani, Simone, Caroline Öhman, Fabio Baruffaldi, Massimiliano Baleani, and Marco Viceconti. 2011. 'Volume to Density Relation in Adult Human Bone Tissue'. *Journal of Biomechanics* 44 (1): 103–8. https://doi.org/10.1016/j.jbiomech.2010.08.032.

Taylor, Erik A., and Eve Donnelly. 2020. 'Raman and Fourier Transform Infrared Imaging for Characterization of Bone Material Properties'. *Bone* 139 (October): 115490. https://doi.org/10.1016/j.bone.2020.115490.

Techawiboonwong, Aranee, Hee Kwon Song, Mary B. Leonard, and Felix W. Wehrli. 2008. 'Cortical Bone Water: In Vivo Quantification with Ultrashort Echo-Time MR Imaging'. *Radiology* 248 (3): 824–33. https://doi.org/10.1148/radiol.2482071995.

Techawiboonwong, Aranee, Hee Kwon Song, Jeremy F. Magland, Punam K. Saha, and Felix W. Wehrli. 2005a. 'Implications of Pulse Sequence in Structural Imaging of Trabecular Bone'. *Journal of Magnetic Resonance Imaging* 22 (5): 647–55. https://doi.org/10.1002/jmri.20432.

———. 2005b. 'Implications of Pulse Sequence in Structural Imaging of Trabecular Bone'. *Journal of Magnetic Resonance Imaging* 22 (5): 647–55. https://doi.org/10.1002/jmri.20432.

Terkeltaub, R. A. 2001. 'Inorganic Pyrophosphate Generation and Disposition in Pathophysiology'. *American Journal of Physiology. Cell Physiology* 281 (1): C1–11. https://doi.org/10.1152/ajpcell.2001.281.1.C1.

Tjong, Willy, Galateia J. Kazakia, Andrew J. Burghardt, and Sharmila Majumdar. 2012a. 'The Effect of Voxel Size on High-Resolution Peripheral Computed Tomography Measurements of Trabecular and Cortical Bone Microstructure: HR-PQCT Voxel Size Effects on Bone Microstructural Measurements'. *Medical Physics* 39 (4): 1893–1903. https://doi.org/10.1118/1.3689813.

———. 2012b. 'The Effect of Voxel Size on High-Resolution Peripheral Computed Tomography Measurements of Trabecular and Cortical Bone Microstructure: HR-

PQCT Voxel Size Effects on Bone Microstructural Measurements'. *Medical Physics* 39 (4): 1893–1903. https://doi.org/10.1118/1.3689813.

Trejo, P., and F. Rauch. 2016. 'Osteogenesis Imperfecta in Children and Adolescents—New Developments in Diagnosis and Treatment'. *Osteoporosis International* 27 (12): 3427–37. https://doi.org/10.1007/s00198-016-3723-3.

Tresguerres, F.G.F., J. Torres, J. López-Quiles, G. Hernández, J.A. Vega, and I.F. Tresguerres. 2020. 'The Osteocyte: A Multifunctional Cell within the Bone'. *Annals of Anatomy - Anatomischer Anzeiger* 227 (January): 151422. https://doi.org/10.1016/j.aanat.2019.151422.

Uchida, Kenzo, Hideaki Nakajima, Tsuyoshi Miyazaki, Takafumi Yayama, Hideo Kawahara, Shigeru Kobayashi, Tatsuro Tsuchida, Hidehiko Okazawa, Yasuhisa Fujibayashi, and Hisatoshi Baba. 2009. 'Effects of Alendronate on Bone Metabolism in Glucocorticoid-Induced Osteoporosis Measured by 18F-Fluoride PET: A Prospective Study'. *Journal of Nuclear Medicine: Official Publication, Society of Nuclear Medicine* 50 (11): 1808–14. https://doi.org/10.2967/jnumed.109.062570.

Villani, Axel Patrice, Marie Rouzaud, Morgane Sevrain, Thomas Barnetche, Carle Paul, Marie-Aleth Richard, Marie Beylot-Barry, et al. 2015. 'Prevalence of Undiagnosed Psoriatic Arthritis among Psoriasis Patients: Systematic Review and Meta-Analysis'. *Journal of the American Academy of Dermatology* 73 (2): 242–48. https://doi.org/10.1016/j.jaad.2015.05.001.

Vis, M., E. A. Havaardsholm, G. Haugeberg, T. Uhlig, A. E. Voskuyl, R. J. van de Stadt, B. a. C. Dijkmans, A. D. Woolf, T. K. Kvien, and W. F. Lems. 2006. 'Evaluation of Bone Mineral Density, Bone Metabolism, Osteoprotegerin and Receptor Activator of the NFkappaB Ligand Serum Levels during Treatment with Infliximab in Patients with Rheumatoid Arthritis'. *Annals of the Rheumatic Diseases* 65 (11): 1495–99. https://doi.org/10.1136/ard.2005.044198.

Vis, M., Gj Wolbink, M. C. Lodder, P. J. Kostense, R. J. van de Stadt, M. H. M. T. de Koning, B. a. C. Dijkmans, and W. F. Lems. 2003. 'Early Changes in Bone Metabolism in Rheumatoid Arthritis Patients Treated with Infliximab'. *Arthritis & Rheumatism* 48 (10): 2996–97. https://doi.org/10.1002/art.11292.

Vos, Theo, Abraham D Flaxman, Mohsen Naghavi, Rafael Lozano, Catherine Michaud, Majid Ezzati, Kenji Shibuya, et al. 2012. 'Years Lived with Disability (YLDs) for 1160 Sequelae of 289 Diseases and Injuries 1990–2010: A Systematic Analysis for the Global Burden of Disease Study 2010'. *The Lancet* 380 (9859): 2163–96. https://doi.org/10.1016/S0140-6736(12)61729-2.

Wang, Bailiang, Søren Overgaard, John Chemnitz, and Ming Ding. 2016. 'Cancellous and Cortical Bone Microarchitectures of Femoral Neck in Rheumatoid Arthritis and Osteoarthritis Compared with Donor Controls'. *Calcified Tissue International* 98 (5): 456–64. https://doi.org/10.1007/s00223-015-0098-y.

Wang, X., J.S. Nyman, X. Dong, H. Leng, and M. Reyes. 2010. 'Fundamental Biomechanics in Bone Tissue Engineering'. *Synthesis Lectures on Tissue Engineering* 2 (1): 1–225. https://doi.org/10.2200/S00246ED1V01Y200912TIS004.

Wehrli, Felix W. 2007. 'Structural and Functional Assessment of Trabecular and Cortical Bone by Micro Magnetic Resonance Imaging'. *Journal of Magnetic Resonance Imaging* 25 (2): 390–409. https://doi.org/10.1002/jmri.20807.

Weiger, Markus, Klaas P. Pruessmann, and Franciszek Hennel. 2011. 'MRI with Zero Echo Time: Hard versus Sweep Pulse Excitation: MRI With Zero Echo Time'. *Magnetic Resonance in Medicine* 66 (2): 379–89. https://doi.org/10.1002/mrm.22799.

Weiger, Markus, Marco Stampanoni, and Klaas P. Pruessmann. 2013. 'Direct Depiction of Bone Microstructure Using MRI with Zero Echo Time'. *Bone* 54 (1): 44–47. https://doi.org/10.1016/j.bone.2013.01.027.

Weir, Connor, and Arif Jan. 2020. 'BMI Classification Percentile and Cut Off Points'. Treasure Island (FL): StatPearls Publishing. https://www.ncbi.nlm.nih.gov/books/NBK541070/.

Wijbrandts, C. A., R. Klaasen, M. G. W. Dijkgraaf, D. M. Gerlag, B. L. F. van Eck-Smit, and P. P. Tak. 2009. 'Bone Mineral Density in Rheumatoid Arthritis Patients 1 Year after Adalimumab Therapy: Arrest of Bone Loss'. *Annals of the Rheumatic Diseases* 68 (3): 373–76. https://doi.org/10.1136/ard.2008.091611.

Winn, Naomi, Radhesh Lalam, and Victor Cassar-Pullicino. 2017. 'Imaging of Paget's Disease of Bone'. *Wiener Medizinische Wochenschrift* 167 (1–2): 9–17. https://doi.org/10.1007/s10354-016-0517-3.

Wolff, Julius. 1986. 'Concept of the Law of Bone Remodelling'. In *The Law of Bone Remodelling*, by Julius Wolff, 1–1. Berlin, Heidelberg: Springer Berlin Heidelberg. https://doi.org/10.1007/978-3-642-71031-5_1.

Woods, Gina N, Susan K Ewing, Sigurdur Sigurdsson, Deborah M Kado, Gudny Eiriksdottir, Vilmundur Gudnason, Trisha F Hue, et al. 2020. 'Greater Bone Marrow Adiposity Predicts Bone Loss in Older Women'. *Journal of Bone and Mineral Research* 35 (2): 326–32. https://doi.org/10.1002/jbmr.3895.

Woolf, Anthony D. 2015. 'Global Burden of Osteoarthritis and Musculoskeletal Diseases'. *BMC Musculoskeletal Disorders* 16 (S1): S3, 1471-2474-16-S1–3. https://doi.org/10.1186/1471-2474-16-S1-S3.

Wopenka, Brigitte, and Jill D. Pasteris. 2005. 'A Mineralogical Perspective on the Apatite in Bone'. *Materials Science and Engineering: C* 25 (2): 131–43. https://doi.org/10.1016/j.msec.2005.01.008.

Wu, Dan, Per Isaksson, Stephen J. Ferguson, and Cecilia Persson. 2018. 'Young's Modulus of Trabecular Bone at the Tissue Level: A Review'. *Acta Biomaterialia* 78 (September): 1–12. https://doi.org/10.1016/j.actbio.2018.08.001.

Wu, Hui-Zhao, Xiao-Fei Zhang, Shu-Man Han, Lei Cao, Jin-Xu Wen, Wen-Juan Wu, and Bu-Lang Gao. 2020. 'Correlation of Bone Mineral Density with MRI T2* Values in Quantitative Analysis of Lumbar Osteoporosis'. *Archives of Osteoporosis* 15 (1): 18. https://doi.org/10.1007/s11657-020-0682-2.

Wu, Yaotang, Jerome L. Ackerman, David A. Chesler, Lila Graham, Yan Wang, and Melvin J. Glimcher. 2003. 'Density of Organic Matrix of Native Mineralized Bone Measured by Water- and Fat-Suppressed Proton Projection MRI'. *Magnetic Resonance in Medicine* 50 (1): 59–68. https://doi.org/10.1002/mrm.10512.

Yano, Junko, and Vittal K. Yachandra. 2009. 'X-Ray Absorption Spectroscopy'. *Photosynthesis Research* 102 (2–3): 241–54. https://doi.org/10.1007/s11120-009-9473-8.

Yaroslavsky, Leonid P. 2002. 'Fast Signal Sinc-Interpolation Methods for Signal and Image Resampling'. In , edited by Edward R. Dougherty, Jaakko T. Astola, and Karen O. Egiazarian, 120–29. San Jose, CA. https://doi.org/10.1117/12.467973.

Yavropoulou, M P, and J G Yovos. n.d. 'The Molecular Basis of Bone Mechanotransduction', 16.

Yon, Maxime, Vincent Sarou-Kanian, Ulrich Scheler, Jean-Michel Bouler, Bruno Bujoli, Dominique Massiot, and Franck Fayon. 2017. 'Solid-State 31P and 1H Chemical MR Micro-Imaging of Hard Tissues and Biomaterials with Magic Angle Spinning at Very High Magnetic Field'. *Scientific Reports* 7 (1): 8224. https://doi.org/10.1038/s41598-017-08458-0.

Yu, Boliang, Alexandra Pacureanu, Cécile Olivier, Peter Cloetens, and Françoise Peyrin. 2020. 'Assessment of the Human Bone Lacuno-Canalicular Network at the Nanoscale and Impact of Spatial Resolution'. *Scientific Reports* 10 (1): 4567. https://doi.org/10.1038/s41598-020-61269-8.

Yu, Elaine W., Logan Greenblatt, Alireza Eajazi, Martin Torriani, and Miriam A. Bredella. 2017. 'Marrow Adipose Tissue Composition in Adults with Morbid Obesity'. *Bone* 97 (April): 38–42. https://doi.org/10.1016/j.bone.2016.12.018.

Zaia, Annamaria, Roberto Rossi, Roberta Galeazzi, Manuela Sallei, Pierluigi Maponi, and Pietro Scendoni. 2021. 'Fractal Lacunarity of Trabecular Bone in Vertebral MRI to Predict Osteoporotic Fracture Risk in Over-Fifties Women. The LOTO Study'. *BMC Musculoskeletal Disorders* 22 (1): 108. https://doi.org/10.1186/s12891-021-03966-7.

Zhai, Mingyang, Yanfei Lu, Juanjuan Fu, Yongkang Zhu, Yuan Zhao, Linwei Shang, and Jianhua Yin. 2019a. 'Fourier Transform Infrared Spectroscopy Research on Subchondral Bone in Osteoarthritis'. *Spectrochimica Acta Part A: Molecular and Biomolecular Spectroscopy* 218 (July): 243–47. https://doi.org/10.1016/j.saa.2019.04.020.

———. 2019b. 'Fourier Transform Infrared Spectroscopy Research on Subchondral Bone in Osteoarthritis'. *Spectrochimica Acta Part A: Molecular and Biomolecular Spectroscopy* 218 (July): 243–47. https://doi.org/10.1016/j.saa.2019.04.020.

Zhang, Ning, Jeremy F. Magland, Chamith S. Rajapakse, Yusuf A. Bhagat, and Felix W. Wehrli. 2013. 'Potential of *in Vivo* MRI-Based Nonlinear Finite-Element Analysis for the Assessment of Trabecular Bone Post-Yield Properties: Potential of *in Vivo* MRI-Based Nonlinear Finite-Element Analysis'. *Medical Physics* 40 (5): 052303. https://doi.org/10.1118/1.4802085.

Zhang, X Henry, X Sherry Liu, Branimir Vasilic, Felix W Wehrli, Maria Benito, Chamith S Rajapakse, Peter J Snyder, and X Edward Guo. 2008. 'In Vivo MMRI-Based Finite Element and Morphological Analyses of Tibial Trabecular Bone in Eugonadal and Hypogonadal Men Before and After Testosterone Treatment'. *Journal of Bone and Mineral Research* 23 (9): 1426–34. https://doi.org/10.1359/jbmr.080405.

Zhao, Can, Aaron Carass, Amod Jog, and Jerry L. Prince. 2016. 'Effects of Spatial Resolution on Image Registration'. In , edited by Martin A. Styner and Elsa D. Angelini, 97840Y. San Diego, California, United States. https://doi.org/10.1117/12.2217322.

Zhao, Xia, Hee Kwon Song, Alan C. Seifert, Cheng Li, and Felix W. Wehrli. 2017. 'Feasibility of Assessing Bone Matrix and Mineral Properties in Vivo by Combined Solid-State 1H and 31P MRI'. Edited by Deepak Vashishth. *PLOS ONE* 12 (3): e0173995. https://doi.org/10.1371/journal.pone.0173995.

Zhao, Xia, Hee Kwon Song, and Felix W. Wehrli. 2018. 'In Vivo Bone ^{31} P Relaxation Times and Their Implications on Mineral Quantification: Zhao et Al.' *Magnetic Resonance in Medicine* 80 (6): 2514–24. https://doi.org/10.1002/mrm.27230.

Zhao, Yinxia, Mingqian Huang, Jie Ding, Xintao Zhang, Karl Spuhler, Shaoyong Hu, Mianwen Li, et al. 2019. 'Prediction of Abnormal Bone Density and Osteoporosis From Lumbar Spine MR Using Modified Dixon Quant in 257 Subjects With Quantitative Computed Tomography as Reference: Bone Density Prediction From MDixon MR'. *Journal of Magnetic Resonance Imaging* 49 (2): 390–99. https://doi.org/10.1002/jmri.26233.

Zoroofi, Reza A, Yoshinobu Sato, Toshihiko Sasama, Takashi Nishii, Nobuhiko Sugano, Kazuo Yonenobu, Hideki Yoshikawa, Takahiro Ochi, and Shinichi Tamura. 2003. 'Automated Segmentation of Acetabulum and Femoral Head From 3-D CT Images'. *IEEE TRANSACTIONS ON INFORMATION TECHNOLOGY IN BIOMEDICINE* 7 (4): 15.

Zysset, P. K. 2009. 'Indentation of Bone Tissue: A Short Review'. *Osteoporosis International* 20 (6): 1049–55. https://doi.org/10.1007/s00198-009-0854-9.

Zysset, Philippe K, X Edward Guo, C Edward Hoffler, Kristin E Moore, and Steven A Goldstein. 1999. 'Elastic Modulus and Hardness of Cortical and Trabecular Bone Lamellae Measured by Nanoindentation in the Human Femur'. *Journal of Biomechanics* 32 (10): 1005–12. https://doi.org/10.1016/S0021-9290(99)00111-6.